

*Advanced Materials Series*

# ADVANCED MAGNETIC AND OPTICAL MATERIALS



*Edited By*

**Ashutosh Tiwari, Parameswar K. Iyer,  
Vijay Kumar and Hendrik Swart**



# Advanced Magnetic and Optical Materials

**Scrivener Publishing**  
100 Cummings Center, Suite 541J  
Beverly, MA 01915-6106

**Advanced Materials Series**

The Advanced Materials Series provides recent advancements of the fascinating field of advanced materials science and technology, particularly in the area of structure, synthesis and processing, characterization, advanced-state properties, and applications. The volumes will cover theoretical and experimental approaches of molecular device materials, biomimetic materials, hybrid-type composite materials, functionalized polymers, supramolecular systems, information- and energy-transfer materials, biobased and biodegradable or environmental friendly materials. Each volume will be devoted to one broad subject and the multidisciplinary aspects will be drawn out in full.

**Series Editor: Ashutosh Tiwari**  
Biosensors and Bioelectronics Centre  
Linköping University  
SE-581 83 Linköping  
Sweden  
E-mail: ashutosh.tiwari@liu.se

Managing Editor: Sophie Thompson

Publishers at Scrivener  
Martin Scrivener ([martin@scrivenerpublishing.com](mailto:martin@scrivenerpublishing.com))  
Phillip Carmical ([pcarmical@scrivenerpublishing.com](mailto:pcarmical@scrivenerpublishing.com))

# **Advanced Magnetic and Optical Materials**

Edited by

**Ashutosh Tiwari, Parameswar K. Iyer,  
Vijay Kumar and Hendrik Swart**



**WILEY**

Copyright © 2017 by Scrivener Publishing LLC. All rights reserved.

Co-published by John Wiley & Sons, Inc. Hoboken, New Jersey, and Scrivener Publishing LLC, Beverly, Massachusetts.

Published simultaneously in Canada.

No part of this publication may be reproduced, stored in a retrieval system, or transmitted in any form or by any means, electronic, mechanical, photocopying, recording, scanning, or otherwise, except as permitted under Section 107 or 108 of the 1976 United States Copyright Act, without either the prior written permission of the Publisher, or authorization through payment of the appropriate per-copy fee to the Copyright Clearance Center, Inc., 222 Rosewood Drive, Danvers, MA 01923, (978) 750-8400, fax (978) 750-4470, or on the web at [www.copyright.com](http://www.copyright.com). Requests to the Publisher for permission should be addressed to the Permissions Department, John Wiley & Sons, Inc., 111 River Street, Hoboken, NJ 07030, (201) 748-6011, fax (201) 748-6008, or online at <http://www.wiley.com/go/permission>.

**Limit of Liability/Disclaimer of Warranty:** While the publisher and author have used their best efforts in preparing this book, they make no representations or warranties with respect to the accuracy or completeness of the contents of this book and specifically disclaim any implied warranties of merchantability or fitness for a particular purpose. No warranty may be created or extended by sales representatives or written sales materials. The advice and strategies contained herein may not be suitable for your situation. You should consult with a professional where appropriate. Neither the publisher nor author shall be liable for any loss of profit or any other commercial damages, including but not limited to special, incidental, consequential, or other damages.

For general information on our other products and services or for technical support, please contact our Customer Care Department within the United States at (800) 762-2974, outside the United States at (317) 572-3993 or fax (317) 572-4002.

Wiley also publishes its books in a variety of electronic formats. Some content that appears in print may not be available in electronic formats. For more information about Wiley products, visit our web site at [www.wiley.com](http://www.wiley.com).

For more information about Scrivener products please visit [www.scrivenerpublishing.com](http://www.scrivenerpublishing.com).

Cover design by Russell Richardson

***Library of Congress Cataloging-in-Publication Data:***

ISBN 978-1-119-24191-1

Printed in the United States of America

10 9 8 7 6 5 4 3 2 1

# Contents

---

Preface	xix
---------	-----

## Part 1 Magnetic Materials

1 Superconducting Order in Magnetic Heterostructures	3
<i>Sol H. Jacobsen, Jabir Ali Ouassou and Jacob Linder</i>	
1.1 Introduction	3
1.2 Fundamental Physics	6
1.2.1 The Superconducting Gap	6
1.2.2 The Proximity Effect	9
1.2.2.1 Singlet-triplet Conversion	10
1.2.2.2 Experimental Signatures	11
1.3 Theoretical Framework	15
1.3.1 Quasiclassical Theory	16
1.3.1.1 Diffusive Limit: Usadel Equation	19
1.3.2 Notation and Parameterizations	21
1.4 Experimental Status	23
1.4.1 Materials and Techniques	23
1.4.1.1 Material Choice	24
1.4.1.2 Experimental Techniques	24
1.4.2 Recent Experimental Advances	28
1.5 Novel Predictions	33
1.5.1 $\phi_0$ -junctions	34
1.5.2 Control of $T_c$	35
1.5.3 Giant Proximity Effect and Control of Spin Supercurrent	36
1.5.4 Inducing Magnetism via Superconductivity	36
1.6 Outlook	37
Acknowledgements	38
References	39

<b>2 Magnetic Antiresonance in Nanocomposite Materials</b>	<b>47</b>
<i>Anatoly B. Rinkevich, Dmitry V. Perov and Olga V. Nemytova</i>	
2.1 Introduction: Phenomenon of Magnetic Antiresonance	47
2.2 Magnetic Antiresonance Review	49
2.3 Phase Composition and Structure of Nanocomposites Based on Artificial Opals	54
2.4 Experimental Methods of the Antiresonance Investigation	56
2.4.1 Measurements of the Transmission and Reflection Coefficients in the Waveguide	58
2.4.2 Measurements in the Hollow Resonator	60
2.5 Nanocomposites where the Antiresonance is Observed in	60
2.5.1 Metallic Particles	60
2.5.2 Ferrite Garnet Particles	61
2.5.3 Lanthanum–Strontium Manganite Particles	62
2.6 Conditions of Magnetic Antiresonance Observation in Non-conducting Nanocomposite Plate	63
2.7 Magnetic Field Dependence of Transmission and Reflection Coefficients	70
2.8 Frequency Dependence of Resonance Amplitude	72
2.9 Magnetic Resonance and Antiresonance upon Parallel and Perpendicular Orientation of Microwave and Permanent Magnetic Fields	74
2.10 Conclusion	76
Acknowledgement	77
References	77
<b>3 Magnetic Bioactive Glass Ceramics for Bone Healing and Hyperthermic Treatment of Solid Tumors</b>	<b>81</b>
<i>Andrea Cochis, Marta Miola, Oana Bretcanu, Lia Rimondini and Enrica Vernè</i>	
3.1 Bone and Cancer: A Hazardous Attraction	82
3.1.1 The Pre-metastatic Niche of Bone Colonization	82
3.1.2 Bone Invasion via Matrix Proteins	83
3.1.3 Tumor Formation and Metastatic Growth	84
3.1.4 Bone Metastases Management	85
3.2 Hyperthermia Therapy for Cancer Treatment	86
3.2.1 Hyperthermia as Alternative to Traditional Therapies	86

3.2.2	Activating Hyperthermia	87
3.2.2.1	Hot Bath, Incubator, or Injection	88
3.2.2.2	Perfusion	88
3.2.2.3	Magnetic Induction	88
3.2.2.4	Ultrasounds	89
3.2.2.5	Microwaves and Radiofrequency	89
3.2.3	Hyperthermia Mechanisms	90
3.2.3.1	Heat Shock Proteins	91
3.2.3.2	Surface Molecules	92
3.2.3.3	Tumor Vasculature	93
3.2.3.4	Exosomes	93
3.3	Evidences of Hyperthermia Efficacy	94
3.3.1	Optimal Hyperthermia Temperature	94
3.4	Magnetic Composites for Hyperthermia Treatment	95
3.5	Magnetic Glass Ceramics	99
3.6	Conclusions	103
	References	103
<b>4</b>	<b>Magnetic Iron Oxide Nanoparticles: Advances on Controlled Synthesis, Multifunctionalization, and Biomedical Applications</b>	<b>113</b>
	<i>Dung The Nguyen and Kyo-Seon Kim</i>	
4.1	Introduction	114
4.2	Controlled Synthesis of $\text{Fe}_3\text{O}_4$ Nanoparticles	115
4.2.1	Size-controlled Synthesis of $\text{Fe}_3\text{O}_4$ Nanoparticles	117
4.2.2	Structure-controlled Synthesis of $\text{Fe}_3\text{O}_4$ Nanoparticles	118
4.2.3	Component-controlled Synthesis of $\text{Fe}_3\text{O}_4$ Nanoparticles	121
4.3	Surface Modification of $\text{Fe}_3\text{O}_4$ Nanoparticles for Biomedical Applications	122
4.3.1	Surface Modification of $\text{Fe}_3\text{O}_4$ Nanoparticles	122
4.3.2	Design of $\text{Fe}_3\text{O}_4$ Nanoparticles for Biomedical Applications	125
4.4	Magnetism and Magnetically Induced Heating of $\text{Fe}_3\text{O}_4$ Nanoparticles	126
4.4.1	Magnetism of $\text{Fe}_3\text{O}_4$ Nanoparticles	126
4.4.2	Magnetically Induced Heating of $\text{Fe}_3\text{O}_4$ Nanoparticles	128
4.5	Applications of $\text{Fe}_3\text{O}_4$ Nanoparticles to Magnetic Hyperthermia	130

4.6 Applications of $\text{Fe}_3\text{O}_4$ Nanoparticles to Hyperthermia-based Controlled Drug Delivery	132
4.7 Conclusions	134
Acknowledgment	135
References	135
<b>5 Magnetic Nanomaterial-based Anticancer Therapy</b>	<b>141</b>
<i>Catalano Enrico</i>	
5.1 Introduction	142
5.2 Magnetic Nanomaterials	144
5.2.1 Cobalt Ferrite	144
5.2.2 Manganese Ferrite	145
5.2.3 Zinc-doped Ferrites	145
5.3 Biomedical Applications of Magnetic Nanomaterials	145
5.4 Magnetic Nanomaterials for Cancer Therapies	146
5.5 Relevance of Nanotechnology to Cancer Therapy	147
5.6 Cancer Therapy with Magnetic Nanoparticle Drug Delivery	148
5.7 Drug Delivery in the Cancer Therapy	149
5.7.1 Drug Targeting	150
5.7.2 Passive and Active Drug Targeting	150
5.8 Magnetic Hyperthermia	151
5.8.1 Application of Hyperthermia for Cancer Therapy	152
5.8.2 Catabolism of Tumors by Hyperthermia	153
5.9 Role of Theranostic Nanomedicine in Cancer Treatment	154
5.10 Magnetic Nanomaterials for Chemotherapy	155
5.11 Magnetic Nanomaterials as Carrier for Cancer Gene Therapeutics	156
5.12 Conclusions	156
5.13 Future Prospects	158
References	159
<b>6 Theoretical Study of Strained Carbon-based Nanobelts: Structural, Energetic, Electronic, and Magnetic Properties of [n]Cyclacenes</b>	<b>165</b>
<i>E. San-Fabián, A. Pérez-Guardiola, M. Moral, A. J. Pérez-Jiménez and J. C. Sancho-García</i>	
6.1 Introduction	166
6.2 Computational Strategy and Associated Details	168
6.3 Results and Discussion	171
6.3.1 [6]CC as a Test Case	171

6.3.2 Geometries and Strain Energy Evolution with the Size of the Nanobelt	173
6.3.3 Electronic Structure Issues	177
6.4 Conclusions	181
Acknowledgments	182
References	182
<b>7 Room Temperature Molecular Magnets: Modeling and Applications</b>	<b>185</b>
<i>Mihai A. Girțu and Corneliu I. Oprea</i>	
7.1 Introduction	186
7.2 Experimental Background	187
7.3 Ideal Structure and Sources of Structural Disorder	193
7.4 Exchange Coupling Constants and Ferrimagnetic Ordering	200
7.4.1 Exchange Interactions	200
7.4.2 Broken-Symmetry DFT Band Calculations of Exchange Constants	202
7.4.3 Broken-Symmetry DFT Calculations of Exchange Constants of Finite Models	204
7.4.4 CASSCF Calculations of Exchange Constants	212
7.4.5 MRPT2 Calculations of Exchange Constants	216
7.4.6 Mechanism of Ferrimagnetic Coupling	217
7.4.7 Role of the Transition Metal Ion	221
7.5 Magnetic Anisotropy	224
7.5.1 Anisotropy in Pure and Disordered Magnets	224
7.5.2 Applicability of the Spin Glass Model	229
7.5.3 Uniform and Random Magnetic Anisotropy in V[TCNE] <sub>x</sub>	230
7.6 Applications of V[TCNE] <sub>x</sub>	233
7.7 Conclusions	241
Acknowledgments	243
References	243

## Part 2 Optical Materials

<b>8 Advances and Future of White LED Phosphors for Solid-State Lighting</b>	<b>253</b>
<i>Xianwen Zhang and Xin Zhang</i>	
8.1 Light Generation Mechanisms and History of LEDs Chips	253
8.1.1 Light Generation Mechanisms	253
8.1.2 History of LED Chips	254

8.2	Fabrication of WLEDs	256
8.3	Evaluation Criteria of WLEDs	259
8.3.1	Physical Requirements	259
8.3.2	Optical Requirements	259
8.3.2.1	Color Temperature	259
8.3.2.2	Color Rendering Index	261
8.3.2.3	Emission Spectrum	261
8.3.2.4	Excitation Spectrum	262
8.3.2.5	Quantum Efficiency	262
8.3.2.6	Luminous Efficiency ( $\eta$ )	263
8.3.3	Thermal Requirements	263
8.4	Phosphors for WLEDs	263
8.4.1	Dopants in WLEDs Phosphors	267
8.4.1.1	Broad-band Emitting Rare-earth Ions as Dopants	267
8.4.1.2	Line Emitting Rare-Earth Ions as Dopants	267
8.4.1.3	Other Dopants	268
8.4.2	Choice of Host Material in WLEDs Phosphors	268
8.4.2.1	Garnet	268
8.4.2.2	Orthosilicates	269
8.4.2.3	Sulfides and Oxysulfides	269
8.4.2.4	Nitrides and Oxynitrides	270
8.4.2.5	Other Host Materials	270
8.4.3	Synthetic Approaches for WLEDs Phosphors	271
8.5	Conclusions	273
	References	274
9	<b>Design of Luminescent Materials with “Turn-On/Off” Response for Anions and Cations</b>	279
	<i>Serkan Erdemir and Sait Malkondu</i>	
9.1	Introduction	280
9.2	Luminescent Materials for Sensing of Cations	283
9.2.1	Luminescent Materials for Alkaline and Alkaline Earth Metals	284
9.2.2	Luminescent Materials for Transition Metal Ions	287
9.3	Luminescent Materials for Sensing of Anions	302
9.4	Conclusion	307
	Acknowledgments	308
	References	308

<b>10 Recent Advancements in Luminescent Materials and Their Potential Applications</b>	<b>317</b>
<i>Devender Singh, Vijeta Tanwar, Shri Bhagwan and Ishwar Singh</i>	
10.1 Phosphor	317
10.2 An Overview on the Past Research on Phosphor	318
10.3 Luminescence	319
10.4 Mechanism of Emission of Light in Phosphor Particles	320
10.5 How Luminescence Occur in Luminescent Materials?	321
10.5.1 Excitation	324
10.5.2 Emission	325
10.5.3 Nonradiative Transitions	325
10.5.4 Energy Transfer	326
10.6 Luminescence Is Broadly Classified within the Following Categories	326
10.6.1 Photoluminescence	326
10.6.1.1 Fluorescence	327
10.6.1.2 Phosphorescence	328
10.6.2 Bioluminescence	330
10.6.3 Chemiluminescence	330
10.6.4 Crystalloluminescence	330
10.6.5 Electroluminescence	330
10.6.6 Cathodoluminescence	330
10.6.7 Mechanoluminescence	331
10.6.8 Radioluminescence	331
10.6.9 Sonoluminescence	331
10.6.10 Thermoluminescence	331
10.7 Inorganic Phosphors	332
10.8 Organic Phosphors	332
10.9 Optical Properties of Inorganic Phosphors	333
10.10 Role of Activator and Coactivator	333
10.11 Role of Rare Earth as Activator and Coactivator in Phosphors	334
10.11.1 Rare Earths as Activator	335
10.11.2 Luminescence of Rare Earths	337
10.11.2.1 Tetravalent Ions	337
10.11.2.2 Trivalent Ions	338
10.11.2.3 Bivalent Ions	340
10.11.3 Rare Earths as Coactivator	341

10.12	There are Different Classes of Phosphors, which May be Classified According to the Host Lattice	342
10.12.1	Oxide Lattice Phosphors	342
10.12.2	Sulphide Lattice Phosphors (ZnS)	342
10.12.3	Aluminate Lattice Phosphors	342
10.12.4	Silicate Lattice Phosphor	343
10.12.5	Phosphate Lattice Phosphors	343
10.12.6	Zirconates Lattice Phosphor	344
10.12.7	Vanadates Lattice Phosphors	344
10.12.8	Titanate Lattice Phosphors	344
10.12.9	Other Lattice Phosphors	345
10.13	Applications of Phosphors	345
10.13.1	Fluorescent Lamps	345
10.13.2	Cathode Ray Tubes	346
10.13.3	Luminescent Paints	346
10.13.4	Textiles	347
10.13.5	X-ray Intensifying/Scintillation	347
10.13.6	Vacuum Fluorescent Displays	347
10.13.7	Field Emission Displays	347
10.13.8	Plasma Display Panels	348
10.13.9	Safety Indicators	348
10.14	Future Prospects of Phosphors	348
10.15	Conclusions	349
	References	349
<b>11</b>	<b>Strongly Confined PbS Quantum Dots: Emission Limiting, Photonic Doping, and Magneto-optical Effects</b>	<b>353</b>
	<i>P. Barik, A. K. Singh, E. V. García-Ramírez, J. A. Reyes-Esqueda, J. S. Wang, H. Xi and B. Ullrich</i>	
11.1	Introduction	354
11.2	QDs Used and Sample Preparation	356
11.3	Basic Properties of PbS Quantum Dots	356
11.4	Measuring Techniques and Equipment Employed	358
11.4.1	Fourier Transform Infrared Spectroscopy of PbS Quantum Dots	358
11.4.2	Two-photon Excited Emission in PbS Quantum Dots	359
11.4.3	Magneto-optical Measurements	360
11.5	Photoluminescence Limiting of Colloidal PbS Quantum Dots	361
11.6	Photonic Doping of Soft Matter	364

11.7	Magneto-optical Properties	370
11.7.1	Quantum Dot Absorption	370
11.7.2	Basics of the Magneto-optical Effects in Semiconductors	370
11.7.3	Reflection of Quantum Dots Under Low Magnetic Fields	371
11.7.4	Transmittance of Quantum Dots Under Low Magnetic Fields	374
11.7.5	Magneto-photoluminescence of Colloidal PbS Quantum Dots at Room Temperature	377
11.8	Conclusions	380
	Acknowledgment	380
	References	380
<b>12</b>	<b>Microstructure Characterization of Some Quantum Dots Synthesized by Mechanical Alloying</b>	<b>385</b>
	<i>S. Sain and S. K. Pradhan</i>	
12.1	Introduction	386
12.2	Brief History of QDs	387
12.3	Theory of QDs	388
12.3.1	Band Gap and Quantization of Energy Levels	388
12.3.2	The Density of States	388
12.3.3	The Excitons	389
12.3.4	The Effective Mass Theory	390
12.4	Different Processes of Synthesis of QDs	391
12.4.1	Bottom-up Method	392
12.4.2	Top-down Method	392
12.5	Structure of QDs	392
12.6	Applications of QDs	393
12.6.1	Photovoltaic Devices	393
12.6.2	Electroluminescence Devices	394
12.6.3	Infrared Photodetectors	394
12.6.4	Downconversion of UV Light	394
12.6.5	QD Lasers	394
12.6.6	Cancer Diagnosis	395
12.7	Mechanical Alloying	395
12.7.1	Sample Preparation by MA	395
12.7.2	Optimization of Different Parameters of MA	396
12.8	The Rietveld Refinement Method	398
12.8.1	The Rietveld Method: Mathematical Approach	398
12.8.2	Quantitative-phase Analysis by the Rietveld Method	400

12.8.3	Coherently Diffracting Domain (Particle) Size and R.M.S. Strain	400
12.8.4	Lognormal Size Distribution	400
12.8.5	Planar Defects	401
12.8.6	Rietveld Refinement Software: MAUD	401
12.9	Some Previous Work on Metal Chalcogenide QDs Prepared by Mechanical Alloying from Other Groups	402
12.10	Results and Discussion	402
12.10.1	Some Interesting Features Noticed in ZnS QDs Synthesized by MA	402
12.10.1.1	Coexistence of Minor Wurtzite Phase with Major Zinc Blende Phase	402
12.10.1.2	Presence of Planar Defects in Ball-milled ZnS	403
12.10.1.3	Core–Shell ZnS	406
12.10.2	Some Key Features in Mechanically Alloyed ZnTe QDs	406
12.10.2.1	Formation of ZnTe in Quickest Time by MA	406
12.10.2.2	Variation of Particle Size and R.M.S Lattice Strain	407
12.10.2.3	Quantitative and Qualitative Analysis of Stacking Faults	408
12.10.3	Few Special Features of CdTe QDs Synthesized by MA	409
12.10.3.1	Formation of CdTe QDs in Quickest Time	409
12.10.3.2	Planar Defects Formed During the Synthesis of CdTe QDs	411
12.10.3.3	Variation in Coherently Diffracting Domain (Particle) Size and R.M.S Lattice Strain	412
12.10.4	Ternary CdZnS with Different Cd:Zn Ratio	412
12.10.4.1	X-ray Diffraction Study of $\text{Cd}_x \text{Zn}_{1-x} \text{S}$ Nanocrystalline Semiconductors	412
12.10.4.2	Simultaneous Presence of Zinc–Blende and Wurtzite Phases	414

12.10.4.3	Variation in Lattice Parameters in $\text{Cd}_x\text{Zn}_{1-x}\text{S}$	415
12.10.4.4	Variation of Formation Time in $\text{Cd}_x\text{Zn}_{1-x}\text{S}$	415
12.10.4.5	Variation of Mol Fraction of Cubic and Hexagonal Phases	416
12.10.4.6	Presence of Planar Defects in $\text{Cd}_x\text{Zn}_{1-x}\text{S}$	416
12.10.4.7	Variation of Optical Band Gap in $\text{Cd}_x\text{Zn}_{1-x}\text{S}$ with Different Cd:Zn Ratio	418
12.11	Conclusions	419
	References	419
<b>13</b>	<b>Advances in Functional Luminescent Materials and Phosphors</b>	<b>425</b>
	<i>Radhaballabh Debnath</i>	
13.1	Introduction	425
13.2	Some Theoretical Aspects of the Processes of Light Absorption/Emission by Matter	427
13.2.1	Electric Dipole Induced Electronic Transition Probability in a System	427
13.2.2	Optical Parameters of an Optical Center Doped in a Host	429
13.2.3	Experimentally Measurable Parameters and Their Correlation with Theoretical Expressions	431
13.3	Sensitization/Energy Transfer Phenomenon in Luminescence Process	433
13.3.1	Resonant Energy Transfer	433
13.3.2	Phonon-assisted Non-resonant Energy Transfer	434
13.4	Functional Phosphors	435
13.4.1	Preparation of Functional Phosphors	435
13.4.2	Functional Nanophosphors and Their Preparation	437
13.5	Classifications of Functional Phosphors	438
13.5.1	Phosphors for X-ray Fluorescence Imaging	439
13.5.2	Phosphors for Fluorescent Display	440
13.5.2.1	CRT-display Phosphors	440
13.5.2.2	Color Plasma Display Phosphors	443
13.5.2.3	Luminescent Diode Materials for Display	446

13.5.3	Phosphors for Fluorescent Lamps	447
13.5.3.1	Sb <sup>3+</sup> and Mn <sup>2+</sup> -based Lamp Phosphor	448
13.5.3.2	Rare Earth-based Lamp Phosphors	449
13.5.3.3	Phosphors for LED Lamps	452
13.5.4	Phosphors for Upconversion Luminescence	455
13.5.4.1	Sodium Yttrium Fluoride Co-doped with Yb <sup>3+</sup> and Tm <sup>3+</sup>	457
13.5.4.2	Er <sup>3+</sup> and Yb <sup>3+</sup> Co-doped Barium Fluorotellurite Glass	458
13.5.4.3	(Tm <sup>3+</sup> , Ho <sup>3+</sup> , and Yb <sup>3+</sup> )-tridoped Fluorolead Germanate Glass	459
13.6	Solid-state Luminescent Materials for Laser	460
13.6.1	Nd <sup>3+</sup> -YAG/Nd <sup>3+</sup> -glass Laser	463
13.6.2	Yb <sup>3+</sup> -YAG Laser	465
13.6.3	Ho <sup>3+</sup> /Yb <sup>3+</sup> Co-doped Tellurite-based Laser Glass	465
	Acknowledgments	467
	References	467
<b>14</b>	<b>Development in Organic Light-emitting Materials and Their Potential Applications</b>	<b>473</b>
	<i>Devender Singh, Shri Bhagwan, Raman Kumar Saini, Vandna Nishal and Ishwar Singh</i>	
14.1	Luminescence in Organic Molecules	473
14.2	Types of Luminescence	475
14.3	Mechanism of Luminescence	479
14.4	Organic Compounds as Luminescent Material	480
14.4.1	Small Organic Materials	481
14.4.2	Polymers	493
14.5	Possible Transitions in Organic Molecules	494
14.6	OLED's Structure and Composition	495
14.6.1	Mono-layered OLED Devices	495
14.6.2	Double-layered OLED Devices	496
14.6.3	Multi-layered OLED Devices	497
14.7	Basic Principle of OLEDs	502
14.8	Working of OLEDs	502
14.9	Light Emission in OLEDs	504

14.10	Types of OLED Displays	505
14.11	Techniques of Fabrication of OLEDs Devices	506
14.12	Advantages of OLEDs	507
14.13	Potential Applications of OLEDs	511
14.13.1	Conventional Applications	511
14.13.2	Applications Convertible to OLEDs (Which Can Boost Their Commercial Development)	512
14.14	Future Prospects of OLEDs	512
14.15	Conclusions	512
	References	513
	<b>Index</b>	<b>521</b>



## Preface

---

Throughout the decades, semiconductors, metals and ceramics have been used in highly complex systems, viz., optical and magnetic mass storage media, sensors, therapeutics, light-emitting diodes, and optoelectronic devices. In this regard, a large number of materials with modified and improved properties carry out various functions such as data collection, processing, transmission, storage and display information. Technological advancements in magnetic and optical materials are shaping the boundaries shared by the various fields of physics, chemistry, engineering, medicine and materials science. This book gives comprehensive information on the progress made in magnetic and optical materials. It also provides a few of the interesting features of these materials that have particular significance in their performance in various fields of science and technology. Furthermore, this book is the sole compilation of important discussions about magnetic and optical materials such as their synthesis, properties, characterizations and applications in a single platform.

The work included in this book has been organized into two parts. The first part consists of magnetic materials. Different aspects of magnetic materials are discussed in detail by various authors in a way that should allow the scientific community to select the best materials for a particular application. On the other hand, the second part consists of optical materials, providing past and most recent breakthrough discoveries in optics and photonics. This book is organized into fourteen chapters, the agendas of which are briefly described below.

Chapter 1 gives an introduction to the primary concepts of superconductivity, magnetism and their interaction in composite structures. It includes an overview of the structure and phase diagram as well as the properties of the superconducting and magnetic parts of these composites. The magnetic anisotropy in different ferromagnetic materials is also reviewed. A survey of current experimental results is summarized, along with the theoretical calculations regarding different magnetic heterostructures. In chapter 2, magnetic antiresonance in different metallic nanocomposites is reviewed in detail. The criterion needed for magnetic antiresonance to

occur at frequencies of millimeter waveband along with the ferromagnetic resonance is also presented in a detailed manner. Furthermore, the possible reasons for antiresonance existing in the reflection and absorption waves are discussed. Chapter 3 presents the recent development of glass ceramics with good bioactivity and magnetic property for bone healing and hyperthermia treatments of solid tumors. In this chapter, various magnetic materials and their oxides doped with bioactive matrix and magnetic bioactive glass ceramic in different systems are investigated in detail. Recent developments and various strategies in the preparation, microstructure, and magnetic properties of pure and surface functionalized iron oxide nanoparticles and their corresponding biological application are presented in chapter 4. Also discussed are new functionalized strategies, problems and major challenges, along with current directions for the synthesis, surface functionalization and biomedical applications of iron oxide nanoparticles. The direction and scope for further research in the area of functionalized iron oxide nanoparticles are also suggested.

Further on, nanocarriers based on magnetic nanomaterials for anticancer therapy are presented in chapter 5. This chapter reveals the great potential of magnetic nanomaterials for anticancer therapy by reporting and discussing promising examples of the published data. The principles of anticancer therapy, as well as recent studies on magnetic nanomaterials for biomedical applications, are offered as a basis for understanding the mechanism of magnetic nanoparticle-mediated anticancer therapy. A detailed theoretical study on the strain energy of carbon nanobelts, i.e., the belt-shaped molecules representing the sidewall structures of carbon nanotubes, is presented in chapter 6. Chapter 7 gives an extensive overview of room-temperature molecular magnets modeling and applications based on metals and metal oxides. The mechanism by which molecule-based magnets stabilize and display a net magnetic moment is also given in this chapter.

The scientific societies have recognized 2015 as the International Year of Light and Light-based Technologies owing to the importance of lighting and display systems in every part of human evolution. Driven by the superior optical and photoluminescence properties of luminescent materials in a wide range of areas, there have been shared research efforts in this sector aimed at achieving better material features. The development of white light-emitting diodes with enhanced color and efficiency for lighting and display industries is presented in chapter 8. This chapter also discusses the important requirements and scientific questions that come up in synthesizing cost-effective and environmentally friendly light-emitting diodes based on different rare-earth doped inorganic host materials. Also

suggested are opportunities for new research for future development in this area. Chapter 9 presents the design of luminescent materials with Turn-on/off response for anion and cations. Recent advances in various lanthanides and transition metals doped/co-doped nanomaterials for lighting, sensing and biomedical applications are reported in chapter 10. Also, the current status and future prospects of luminescent materials are presented along with appropriate documents taken from the scientific literature. The synthesis, characterization and applications of quantum dots based on different materials are presented in chapters 11 and 12, respectively. Chapter 13 gives the development of functional luminescent materials and phosphors for use in solid-state lighting. The discussion starts with some history of phosphors based on different materials and continues with the progress in this direction resulting from various research studies that have been carried out. Finally, the progress in organic light-emitting materials and their potential applications are presented in chapter 14. This chapter explains the breakthroughs and characteristics of organic materials-based phosphors. The main motive of this chapter is not to encompass all the accessible literature, but to include, to a certain extent, some of the most recent accomplishments and concise information in this area.

Thus, this book brings together fundamental synthesis techniques and approaches implemented in the research and development of advanced magnetic and optical materials. Included are contributions from well-known researchers from around the world on (1) synthesis, characterizations, modeling and properties, (2) state-of-the-art design and (3) innovative uses of magnetic and optical materials. Such advanced investigations are a milestone along the path of real-time applications of magnetic and optical materials. Because it is well known that research works on advanced magnetic and optical materials are based on various aspects of physics, chemistry, biology and engineering, this book is written for readers from diverse backgrounds across chemistry, physics, materials science and engineering, nanoscience and nanotechnology, biotechnology, and biomedical engineering. It offers a comprehensive overview of cutting-edge research on advanced magnetic and optical materials.

Editors

Ashutosh Tiwari, PhD, DSc

Parameswar K. Iyer, PhD

Vijay Kumar, PhD

Hendrik Swart, PhD

October 2016



# **Part 1**

## **MAGNETIC MATERIALS**



# Superconducting Order in Magnetic Heterostructures

Sol H. Jacobsen, Jabir Ali Ouassou and Jacob Linder\*

*Department of Physics, NTNU, Norwegian University of Science and Technology, Trondheim, Norway*

---

## **Abstract**

In the rapidly developing field of spintronics, information is encoded and processed in the form of quantum spins. Although phenomena such as the giant magnetoresistance effect and spin-transfer torque have already found use in commercialized devices, two main challenges remaining in spintronic circuits based on electron transport are Joule heating and short decay lengths due to spin-flip scattering. The incorporation of superconducting elements into spintronic architectures has recently emerged as a potential solution to this problem. Recent advances in understanding the underlying physics of the interface between superconductors and ferromagnets has revealed a wealth of new features that can be enhanced and controlled to create improved spintronic devices. In this chapter, we present an introduction to the superconducting proximity effect in magnetic materials that opens the tantalizing prospect of combining the dissipationless transport offered by superconductors with the spin-polarized order existing in magnetic thin-film heterostructures. This includes an outline of theoretical frameworks and conventions in the field, as well as a discussion of some key experimental and theoretical advances that may indicate where the field is heading.

**Keywords:** Superconducting spintronics, proximity effect, ferromagnetism

## **1.1 Introduction**

In the rapidly developing field of *spintronics*, information is encoded and processed in the form of quantum spins – either in place of, or in conjunction

---

\*Corresponding author: jacob.linder@ntnu.no

#### 4 ADVANCED MAGNETIC AND OPTICAL MATERIALS

with, the traditional charge-based processing schemes. This has high potential with respect to computational processing, both in terms of time and energy efficiency, as well as significantly increased stability and longer coherence times than conventional electronic components. Although several spintronic architectures have already been widely adopted, *e.g.* in hard drives and random access memory based on the giant magnetoresistive effect (GMR) [1, 2], two main challenges in spintronic circuits based on electron transport are Joule heating and short decay lengths due to spin-flip scattering. The incorporation of superconducting elements into existing spintronic architectures has recently emerged as a potential solution to this problem [3]. Recent advances in understanding the underlying physics of the interface between superconductors and ferromagnets has revealed a wealth of new features that can be enhanced and controlled to create improved spintronic devices. In this chapter, we present an introduction to the superconducting proximity effect that opens the tantalizing prospect of combining the dissipationless transport offered by superconductors with the spin-polarized order existing in magnetic thin-film heterostructures. This includes an outline of theoretical frameworks and conventions in the field, as well as a discussion of some key experimental and theoretical advances that may indicate where the field is heading.

Spin-polarized currents are typically generated by passing an electric current through a ferromagnet, such that the magnetization in the ferromagnet acts to align the electron spins. Spintronic nanostructures are designed as a series of thin-film layers of normal-metal and ferromagnetic elements, which can be incorporated into conventional semiconductor-based systems. Emergent features of such spintronic devices can then be used to harness and control aspects of the device, for which GMR provides an exemplary case. GMR manifests as a change in the electrical resistance according to the relative magnetization directions of adjacent ferromagnetic layers: the resistance is low for parallel alignment and high for anti-parallel alignment. This effect has been implemented in a wide variety of experimental structures, an important example being *spin valves* [4, 5], which switch an electric current on or off based on a magnetic input signal. Experimentally, spin valves consist of two ferromagnetic layers and an interstitial normal metal. The coercivity of one ferromagnetic layer can be enhanced due to proximity with an antiferromagnetic base layer, meaning that the application of an external magnetic field can be used to control the magnetization of the other ferromagnet. Albert Fert and Peter Grünberg shared the 2007 Nobel Prize in Physics for the discovery of the GMR effect.

In order to utilize the GMR effect, one needs a way to alter the magnetization direction of a ferromagnet. Spin-polarized electric currents

can induce magnetization dynamics via the so-called spin-transfer torque effect [6, 7], but this typically requires very large current densities of order  $10^6 \text{ A/cm}^2$ . This causes excessive Joule heating and ultimately destroys the properties of the thin-film structure. Recent investigations of the proximity effect, where the properties of adjacent materials leak across the interfacial barrier, have indicated that it will be possible to harness the dissipationless currents offered by superconductors to overcome the problem of excessive heating by making these supercurrents spin-polarized [3].

Superconductivity was discovered as early as 1911, when Heike Kamerlingh Onnes observed that the electrical resistivitiy of certain materials vanished abruptly at cryogenic temperatures [8]. Kamerlingh Onnes received the Nobel Prize in Physics in 1913 for this discovery. The temperature at which the transition to zero resistivity occurs is called the *critical temperature* ( $T_c$ ) of the material, and as a material transitions into this superconducting state it displays a second characteristic feature: all magnetic fields are expelled from the material. This was discovered in 1933 by Walther Meissner and Robert Ochsenfeld [9], and subsequently became known as the *Meissner effect*.

Historically, experiments on spin transport in superconductors [10–13] predated experiments with non-superconducting materials [14]. Now that the advantage of superconducting elements in spintronics is becoming increasingly evident, the field is re-emerging as a highly active avenue of research. Recent results have exposed the tremendous potential offered by superconducting spintronics, with experiments demonstrating not only infinite magnetoresistance [15], but also strongly enhanced quasiparticle spin lifetimes [16], spin relaxation lengths [17], spin Hall effects [18], and thermoelectric currents [19] compared with non-superconducting structures. The enhancement is truly monumental: the magnitude of the superconducting spin Hall effect, for example, exceeded its non-superconducting equivalent by a factor of more than two thousand, as we will discuss further in Section 1.4.2.

This chapter is intended to provide an introduction to superconductivity in magnetic thin-film heterostructures for readers who are primarily familiar with magnetic materials. We give only a peripheral mention to examples of *bulk coexistence* of magnetic and superconducting order, as seen in certain heavy-fermion compounds, focusing instead on induced superconductivity via the proximity effect. We will explain the underlying physics and introduce the most commonly used approaches, notation and conventions, before discussing key experimental and theoretical advances and speculating on where the field is heading. The chapter is *not* intended to be a comprehensive review of the field; instead, we refer readers to the bibliography to gain a more complete overview.

## 6 ADVANCED MAGNETIC AND OPTICAL MATERIALS

In Section 1.2, we provide an introduction to superconductivity and the proximity effect in magnetic materials, and discuss the process of singlet-triplet conversion and typical experimental signatures of the proximity effect. In Section 1.3, we provide a brief introduction to the so-called *quasiclassical theory*, which is a useful theoretical framework with which one can address a vast number of physical phenomena that occur in superconductor/ferromagnet hybrid structures, and we include explanations of the different parametrizations and conventions that populate the field. In Section 1.4 we consider the frontier of current experimental research, providing first an introduction to the techniques and materials most readily available in the laboratory setting before discussing recent experimental breakthroughs in superconducting spintronics. In Section 1.5 we discuss novel predictions and speculate about future developments and technological applications before concluding in Section 1.6.

### 1.2 Fundamental Physics

In this section we will present a brief introduction to superconductivity, with emphasis on how superconducting correlations can manifest in other materials near an interface via the proximity effect. We give particular weight to the differences between manifestation in ferromagnetic materials compared with normal metals. We discuss the process of converting between different superconductive species, *i.e.* singlet-triplet conversion, and sources thereof, and outline the broadly applicable experimental signatures to provide an intuitive introduction to the interaction before more details are provided in the subsequent sections.

#### 1.2.1 The Superconducting Gap

Superconductors are often categorized as conventional or unconventional, where *conventional superconductors* refer to materials that can be described fully by the Bardeen–Cooper–Schrieffer (BCS) theory [20], the Bogoliubov theory [21] and minor extensions thereof. These have an *s*-wave pairing symmetry, *i.e.* the order parameter is spherically symmetric in momentum space, and typically manifest only at very low temperatures at atmospheric pressure.<sup>1</sup> There are several common elemental superconductors of this kind. For instance, tin (Sn), aluminium (Al), and lead (Pb) all have critical

---

<sup>1</sup> At higher pressures, it is possible to increase the critical temperature of conventional superconductors significantly, *e.g.* the recent world record of 203 K at 150 GPa [22].

temperatures  $T_c$  in the range 0.4–7.2 K. The critical temperature is often higher in compounds and alloys compared to their constituent elements. For example, elemental titanium (Ti) and niobium (Nb) have critical temperatures of 0.4 K and 9.2 K, respectively, while the niobium-titanium alloys have critical temperatures of up to 11 K. At atmospheric pressures, the current record for highest critical temperature in a conventional bulk superconductor is 39 K for magnesium diboride ( $\text{MgB}_2$ ) [23].

In the late 1970s, an unconventional superconductor dominated by  $d$ -wave pairing instead of the conventional  $s$ -wave pairing was discovered (see Figure 1.1). This turned out to be a class of materials known as high-temperature superconductors, and Johannes G. Bednorz and Karl A. Müller shared the 1987 Nobel Prize in Physics for the discovery of the first of many high-temperature cuprate superconductors [24]. Although this is a highly active research branch, a major restriction in their implementation is the requirement for extreme sample purity imposed by the  $d$ -wave pairing. Due to the prevalence and natural abundance of conventional singlet  $s$ -wave superconductors which do not suffer this restriction, it is highly desirable to use these as superconductive sources in spintronics for immediate application, and for the remainder of the chapter we shall primarily consider such sources.

Conventional superconductivity is caused by electron-phonon interactions, *i.e.* a weak coupling between the conduction electrons and the lattice vibrations of the material. This coupling distorts the lattice and causes a long-range attraction between electrons. This can therefore lead to a pair of electrons having lower energy than the Fermi energy, meaning these

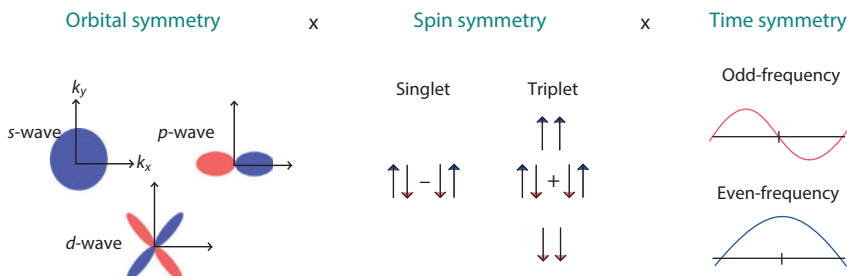


**Figure 1.1** The possible symmetry combinations of a superconducting order parameter  $\Delta$ . The total Cooper pair wave function must in general be antisymmetric at equal times in order to satisfy the Pauli principle, while the particular combination of underlying symmetries governs the properties and class of superconductor. The axis for the curves displaying the two types of time-symmetries (even and odd frequency) is *frequency*, essentially obtained by Fourier-transforming the relative time-coordinate  $t = t_1 - t_2$  for electrons 1 and 2 in the Cooper pair.

two electrons become paired as long as they maintain the lower energy state. Since the pairing energy is typically very small, the pairs are easily destroyed by thermal lattice vibrations, which is why the materials must be cooled far below room temperature to exhibit the effect. The quasiparticle pairing of two fermions is called a Cooper pair, after Leon N. Cooper [25], and, since the range of the pairing effect far exceeds the interelectron distance, the distortion typically leads to the creation of a high number of pairs within the same volume. Individual pairs easily become unpaired due to the low pairing energy, but a new pair is just as easily created; it is the *net number* of pairs which is of importance for superconductivity, not the persistence of individual pairs over time.

The cumulative effect of many Cooper pairs in a material is to open up a gap in the continuous energy spectrum of possible electron states. This gap in the density of states means that any excitations with energies that fall within that gap, *e.g.* typical electron scattering, are forbidden. Materials in their superconducting state exhibit dissipationless charge flow precisely because these energy states are forbidden, since electron scattering is the microscopic origin of electrical resistance, and because the Cooper pairs are quantum mechanically coherent. The gap is by itself not sufficient to create superconductivity: one also needs phase coherence, as known from studies of the pseudogap phase in the high- $T_c$  cuprates [26]. The energy threshold that delineates the gap is typically denoted by the norm  $|\Delta| = \Delta_0$ , which is known as the bulk *superconducting energy gap*, *i.e.* one that has not been modified due to for instance the restricted geometry of a sample or a proximity to non-superconducting materials. Note that it is nevertheless not possible to run an arbitrarily large dissipationless current through superconductors – beyond a so-called *critical current*, the current again becomes resistive.

The electron-phonon interaction and appearance of the superconducting gap are encapsulated in the mean-field Hamiltonian [20]

$$H = - \int d^3x \left[ \Delta(\mathbf{x}, t) \psi_\downarrow^\dagger(\mathbf{x}, t) \psi_\uparrow^\dagger(\mathbf{x}, t) + \Delta^*(\mathbf{x}, t) \psi_\uparrow(\mathbf{x}, t) \psi_\downarrow(\mathbf{x}, t) \right]. \quad (1.1)$$

Here the operators  $\psi_\sigma^\dagger(\mathbf{x}, t)$  and  $\psi_\sigma(\mathbf{x}, t)$  create and annihilate electrons with  $\sigma$  spin at position  $\mathbf{x}$  and time  $t$ , respectively, and the mean-field is defined as

$$\Delta(\mathbf{x}, t) \equiv |\Delta(\mathbf{x}, t)| e^{i\varphi(\mathbf{x}, t)} \equiv \lambda \langle \psi_\uparrow(\mathbf{x}, t) \psi_\downarrow(\mathbf{x}, t) \rangle, \quad (1.2)$$

where  $\lambda > 0$  is the effective coupling constant of the electron-phonon interaction. The superconducting phase  $\varphi$  may be removed by a U(1) gauge transformation to a gauge where  $\Delta$  is real. In that case, the superconducting

phase only becomes relevant insofar as a material is affected by relative phase differences, *e.g.* due to interference between multiple superconducting elements. For a more complete introduction to superconductivity, see *e.g.* the textbook by Tinkham [27] or Sudbø and Fossheim [28].

According to Eq. (1.2), we see that the superconducting order parameter  $\Delta$  originates from a finite expectation value of a two-fermion operator. As a result, the Pauli principle places restrictions on which symmetries  $\Delta$  can have, as illustrated in Figure 1.1. Conventional superconductors would in this scheme be characterized as *s*-wave (even parity under exchange of spatial coordinates), spin-singlet (odd under exchange of spin coordinates), even-frequency (even under exchange of time-coordinates). This satisfies the Pauli principle at equal times of electron 1 and 2 in the Cooper pair ( $t_1 = t_2$ ). However, as indicated in Figure 1.1 there exist other combinations. For instance, it is possible to have a spin-triplet (even under exchange of spin-coordinates) and *s*-wave order parameter if it is antisymmetric in time, meaning it vanishes when  $t_1 = t_2$  [29]. This corresponds to a strong retardation effect in the correlation function of the electrons. When the order parameter is restricted to having *s*-wave symmetry in order to survive the frequent impurity scattering, which effectively leads to an averaging over the Fermi surface, it is precisely this kind of odd-frequency triplet pairing that is realized in diffusive superconductor/ferromagnet (SF) structures.

### 1.2.2 The Proximity Effect

By *proximity effect*, we refer to the processes by which properties of adjacent materials diffuse into one another across their mutual interface, creating a region with properties derived from both materials. In SF hybrid structures, the superconductive proximity effect therefore concerns the leakage of superconducting correlations into the ferromagnet. As well as inducing superconducting correlations in the ferromagnet, the drainage of correlations from the superconductor diminishes its superconducting properties. Furthermore, the ferromagnet may also induce magnetic order in the superconductor close to its interface. The presence of magnetic impurities causes spin-flip scattering of the constituent electrons in individual Cooper pairs, thus further suppressing the superconducting properties. The combined effect of drainage and induced magnetic order in the superconductor is called the *inverse proximity effect*, with *proximity effect* typically denoting the effect of the superconductor on the ferromagnet only. Conversely, when both effects are considered, one may refer to this as the *full proximity effect*.

In this chapter we will primarily be examining the superconductive proximity effect, but note that the inverse proximity effect typically acts to lower the superconducting gap from its bulk value, especially near the interface. When considering proximity structures where the superconductive layer is very large compared to the superconducting correlation length, and the temperature is far below the critical temperature of the hybrid structure, the inverse proximity effect can usually be neglected. In this case, to calculate physical features of the ferromagnet affected by superconductivity, such as the modification to the density of states, it is sufficient to use the bulk superconducting gap at the interface. However, ignoring the inverse proximity effect is only legitimate when it is very weak, and that is not the case in *e.g.* spin valves with thin superconducting regions of size similar to the superconducting coherence length. For such systems, the inverse proximity effect decreases the superconducting gap throughout the entire proximity structure, and therefore needs to be included in a full, self-consistent manner.

### 1.2.2.1 Singlet-triplet Conversion

Singlet superconducting correlations in realistic diffusive ferromagnets typically decay over distances of the order of the ferromagnetic coherence length  $\xi_F = \sqrt{D/h}$ , where  $D$  is the diffusion coefficient and  $h$  is the exchange strength of the ferromagnet [30]. This is because the exchange field causes the misaligned spins of the singlet Cooper pair to be energetically unequal and therefore destroys the correlation: the coherence is lost due to a difference in the phase accumulated by electrons with spin-up ( $\uparrow$ ) and spin-down ( $\downarrow$ ) as they propagate into the ferromagnet. The Cooper pairs thus acquire a nonzero centre-of-mass momentum, resulting in the so-called FFLO-state (after Fulde, Ferell, Larkin and Ovchinnikov [31, 32]), which is a mixture of the singlet state and the triplet state with zero spin projection along the magnetization. However, for certain configurations the superconducting correlations may instead be carried by triplet spin-pairings with a finite spin projection along the exchange field, rendering them immune to this pair-breaking effect. In this case physical quantities such as the supercurrent will decay over length scales comparable with the much longer correlation length in a normal metal  $\xi_N = \sqrt{D/T}$ . That is, the decay length is independent of the exchange field and instead limited by the temperature,  $T$ . At low temperatures this allows the condensate to penetrate deep into the ferromagnet, and the isolation and enhancement of this feature has been the primary focus for research into superconducting spintronics [3, 33].

Heavy-fermion compounds that display intrinsic coexistence of superconductivity and ferromagnetism garnered significant attention upon their discovery [34, 35], and by now well-established intrinsically triplet-paired superconductors such as the noncentrosymmetric cerium platinum silicon CePt<sub>3</sub>Si [36] and the chiral strontium ruthenate Sr<sub>2</sub>RuO<sub>4</sub> [37] feature regularly in the scientific literature. These materials have proven difficult to use in thin-film heterostructures for a variety of reasons to be discussed further in Section 1.4.1. They typically suffer from restrictions such as a requirement of very high pressures, exceedingly low critical temperatures ( $\sim 1$  K), or that they only superconduct at extreme sample purity because their pairing symmetry is *p*-wave rather than *s*-wave, but they are nevertheless interesting candidates for harnessing the long-range triplet pairs [38, 39]. However, it is now well known that in the presence of magnetic inhomogeneities, *i.e.* a spatially varying exchange field, singlet superconducting correlations may be converted into the long-range triplet correlations [40–42]. These magnetic inhomogeneities may arise from *e.g.* spin-polarized interfaces, multiple magnetic layers and conical-field magnets such as holmium (Ho), and enables the generation of triplet superconductivity from the wide variety of available singlet superconductors.

The conversion from singlet pairing to spin-polarized triplet pairing can be understood as a two-step process. In the first step, spin-mixing [42] occurs from for instance spin-dependent scattering at interfaces [43]. This generates the zero spin triplet projection which then coexists with the singlet component. By changing basis, the triplet component with zero spin projection can then be transformed into the triplet components with equal spin and this happens precisely in the presence of magnetic inhomogeneities. Ref. [33] provides a nice introduction to the topic.

Until recently, magnetic inhomogeneities were believed to be the primary source of the singlet-to-long-range-triplet conversion, and correspondingly the majority of research on isolating and enhancing the long-range component focused on such setups [44–55]. However, in very recent developments, it has been shown that intrinsic spin-orbit coupling can also convert the singlet pairs to long-range triplets in a ferromagnet [56, 57]. This has given rise to several novel phenomena including significant effects on the superconducting critical temperature and modification of the electronic density of states [58, 59], and this will be discussed further in Section 1.5.

### 1.2.2.2 Experimental Signatures

Before presenting the underlying theory in more detail below, we will first reinforce the intuitive picture of the superconductive proximity effect by

outlining some typical experimental signatures of the effect and the most general physical principles behind this behaviour.

*Andreev Reflection.* A central feature of the proximity effect is the process of Andreev reflection [60], which describes the conversion of normal current into supercurrent at a superconducting interface. Incoming electrons with energy  $\epsilon < \Delta_0$  cannot be transmitted from the normal metal into the superconductor, as there are no quasiparticle states with this energy in the superconductor. There are then two possibilities: the electron can either be reflected as an electron, or it can be retroreflected as a hole with opposite spin, thereby transmitting a Cooper pair of two electrons into the superconductor in the process. Since the retroreflected hole is phase coherent with the transmitted electrons, the hole will also be phase coherent with the superconducting condensate at large, and can therefore carry information about the superconducting correlations into the normal metal, *i.e.* what we call the proximity effect.

*Josephson effect.* With two or more superconducting layers, such as in a Josephson junction [61, 62] where two superconducting layers sandwich one or more magnetic or non-magnetic layers, the phase difference  $\phi$  between the superconductors becomes an important factor. Analogously to electron tunneling, the Cooper pairs can tunnel through the interstitial barrier, resulting in a flow of *supercurrent* between the two superconductors. The mechanism of multiple Andreev reflections is an intuitive candidate for explaining this tunneling effect. Consider an electron from the middle layer of a superconductor/normal-metal/superconductor structure that has an energy  $\epsilon < \Delta_0$ . If this electron hits the interface shared with the right superconductor, a Cooper pair may be transmitted into the superconductor, while the electron is Andreev retroreflected as a hole. The hole may then move through the normal metal to the left interface where it can annihilate a Cooper pair in this superconductor as it becomes Andreev reflected as an electron again. Through the mechanism of multiple Andreev reflections, we see that a Cooper pair can be effectively phase-coherently transmitted through a non-superconducting region from the left to right superconductor. Since the Andreev processes at both interfaces are phase-coherent processes, this tunneling phenomenon is highly sensitive to the relative phases of the two superconducting condensates. The phase difference between the superconductors therefore governs the magnitude of supercurrent that can flow in the junction via the expression  $I = I_c \sin \phi$ , where  $I_c$  is the critical supercurrent above which a feedback resistance enters into the system, reducing the supercurrent to conventional resistive current. Note that while  $I_c > 0$  for typical superconductor/normal-metal/superconductor (SNS) structures, and  $I_c < 0$  often occurs for superconductor/ferromagnet/

superconductor (SFS) structures, the current-phase relations for Josephson junctions with more involved interstitial regions can take entirely different forms. A review of the current-phase relations for a range of different Josephson junctions was given by Golubov *et al.* [63].

*Oscillating superconducting order.* In the presence of a large magnetic field, the FFLO state should in certain cases manifest as spatially oscillating superconducting order, but the originally proposed state has never been unambiguously observed experimentally in a superconductor due to its extreme sensitivity to impurity scattering. However, oscillation of both the order parameter and the critical temperature with the thickness of a proximized ferromagnet has been predicted and observed [64] in diffusive SF systems. From this one can infer the existence of a spatially modulated superconducting FFLO state which is also naturally manifested in other physical observables of SF systems, such as the supercurrent, as will be discussed further in Section 1.4.2.

*Density of states.* The density of states is a measure of the number of available microstates that a system might occupy in a particular energy range and, as discussed above, superconductors display a gap in this continuous spectrum below their critical temperature (see Figure 1.2). The normal state density of states at the Fermi level can be taken to be of the order  $N_0 \sim 10^{22}/\text{eV cm}^3$  (see e.g. [65]). Compared to a normal metal, the presence of singlet superconductivity will lower the density of states at the Fermi level, while triplet superconductivity will increase the density of states, an effect which can be traced back to the symmetry of the superconducting order parameter [66]. The experimentally measured

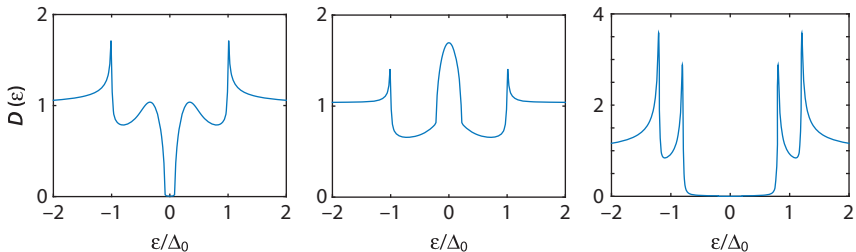


**Figure 1.2** *Left panel:* Typical density of states  $D(\varepsilon)$  vs. quasiparticle energy  $\varepsilon$  measured on the non-superconducting side of an SF bilayer setup when the singlet proximity effect dominates. *Middle panel:* Typical density of states measured on the non-superconducting side of an SF bilayer setup when the triplet proximity effect dominates. *Right panel:* Spin-split density of states in a thin-film superconductor exposed to an in-plane magnetic field. Here shown for an externally induced Zeeman field of  $h = 0.3\Delta_0$ . In all cases the background density of states of a normal metal is here normalized as  $D(\varepsilon) = 1$ .

enhancement of the density of states in an SF bilayer without spin-orbit coupling in the first experiments probing this effect was about 1% from the normal-state [64, 67]. On the other hand, a large effect on the density of states can be seen for a thin-film superconductor in the presence of a weak in-plane magnetic field. Meservey, Tedrow and Fulde observed a spin splitting in the electronic density of states of a superconductor with two maxima near  $\Delta \pm \mu_B H$ , where  $\mu_B$  is the Bohr magneton and  $H$  the magnetic field [10] and showed this can be used to determine the polarization of the electron spin in a ferromagnet [13]. Such systems were recently shown to feature strong odd-frequency correlations despite the absence of a zero-energy peak [68].

In the case of a Josephson junction with an interstitial normal metal (N) or even a simpler superconductor/normal metal bilayer, the proximity effect in N manifests as a *minigap*, *i.e.* the N displays a gap  $\Delta_N < \Delta_0$  [69]. This minigap extends throughout the N, even featuring on the superconducting side of the contact with the same value, and along with its dependence on phase difference this was recently measured in experiment with great accuracy [70]. When the superconductor phase difference  $\phi$  is increased from 0 to  $\pi$ , the magnitude of the gap decreases. In agreement with theoretical prediction, it closes entirely at  $\phi = \pi$  [71].

When the material is magnetic, the oscillating order parameter leads to a corresponding oscillation in the density of states as a function of the penetration distance into the ferromagnet due to the alternating dominance of singlet and triplet pairing [64, 72]. The density of states in the ferromagnet is *inverted* compared with SN structures when the superconducting order parameter is negative (called the  $\pi$ -phase) and triplet pairings dominate. Whenever the Thouless energy is much greater than the exchange field strength one expects to see a spectroscopic minigap, which closes when the resonant condition  $h \sim E_g$  is fulfilled, where  $E_g$  is the zero-field minigap [73, 74]. Beyond this a zero-energy peak emerges until the field strength overcomes all correlations and the density of states becomes essentially featureless [75]. In contrast to SNS junctions where the phase-difference  $\phi \rightarrow \pi$  closes the gap, triplet-dominated SFS junctions can now exhibit a giant proximity effect at  $\phi = \pi$ , manifesting as a uniform zero-energy peak throughout the magnetic material [59].

*Critical temperature.* The critical temperature  $T_c$  of a superconductor is the temperature at which the superconducting correlations vanish. Mathematically, this means that the superconducting gap  $\Delta$  drops to zero above the critical temperature. One of the main aspects of the inverse proximity effect is that it reduces the gap in a superconductor at all temperatures, and this in turn causes the gap to drop to zero at lower temperatures

than for a bulk superconductor. Because of this, the critical temperature of a superconductor can be directly manipulated if the inverse proximity effect can be controlled. One prime example of this is the so-called *absolute spin-valve*, which consists of a singlet superconductor sandwiched between two individually controlled ferromagnetic layers. If the ferromagnetic layers are parallel, their magnetic exchange fields add up constructively inside the superconductor. This causes strong pair-breaking and drastically lowers the critical temperature to some value  $T_{c,1}$ . On the other hand, if the ferromagnetic layers are antiparallel, then their magnetic fields instead partially cancel each other inside the superconductor. The superconducting condensate is thus less disturbed by the presence of magnetic order, resulting in a higher critical temperature  $T_{c,2}$ . Thus, by keeping the structure at a temperature  $T_{c,1} < T < T_{c,2}$ , whether the structure is above or below its critical temperature will depend on the relative magnetizations of the two ferromagnets. In other words, by rotating the magnetization of one (soft) ferromagnet while keeping the magnetization of the other (hard) ferromagnet fixed, superconductivity can be toggled on and off in the structure, which corresponds to an infinite GMR effect. This has been experimentally demonstrated in Ref. [15].

### 1.3 Theoretical Framework

One theoretical approach to examining heterostructures that combine superconducting and ferromagnetic materials is the Bogoliubov–de Gennes formalism [76]. The Bogoliubov–de Gennes equations take the form

$$\begin{pmatrix} H_0 & \Delta(x) \\ \Delta^*(x) & -H_0^* \end{pmatrix} \begin{pmatrix} \phi_e(x) \\ \phi_h(x) \end{pmatrix} = E \begin{pmatrix} \phi_e(x) \\ \phi_h(x) \end{pmatrix}, \quad (1.3)$$

where  $H_0$  is the Hamiltonian of a single electron, including both kinetic energy and all non-superconducting interactions;  $\phi_e$  and  $\phi_h$  are complex wave functions that describe electron-like and hole-like excitations respectively;  $E$  is the energy of the excitations;  $*$  denotes complex conjugation; and  $\Delta(x)$  is a complex field that describes superconductivity. We note that this bears a lot of resemblance to the Schrödinger equation  $H_0\phi_e(x) = E\phi_e(x)$  for an electron. The obvious difference is that the corresponding Bogoliubov–de Gennes equation  $H_0\phi_e(x) + \Delta(x)\phi_h(x) = E\phi_e(x)$  couples electron-like and hole-like excitations. However, in the non-superconducting limit  $\Delta \rightarrow 0$ , we see that the Bogoliubov–de Gennes equations reduce to the Schrödinger equations.

In the ballistic limit, there is negligible resistivity due to the lack of scattering. Although seemingly a severe restriction, this can be a suitable limit when the mean free path of the conduction particles, *i.e.* the electrons and holes, is longer than the transporting medium, as can be the case for very pure metal nanowires, for example. The fewer defects there are in the medium, and the lower the temperature at which it is held, the longer the mean free path. However, the introduction of interfaces introduces an inevitable source of scattering due to the mismatch between the crystal structures of the two materials on either side of the interface. Therefore, we will focus primarily on the more widely applicable diffusive regime for the remainder of the chapter.

The Bogoliubov-de Gennes framework can be substantially simplified by making a quasiclassical approximation which in the ballistic limit provides the Eilenberger equation [77], while the diffusive limit is described by the Usadel equation [78]. Refs. [69, 79] review the use of quasiclassical Green's functions in normal-metal/superconductor heterostructures, and in this section we will provide a very brief introduction to quasiclassical theory with an overview of the primary conventions and parameterization regimes that populate the literature. The motivation for including this section is to give the reader an idea of the theoretical “toolbox” that can be used to describe the emergent quantum physics in SF systems.

### 1.3.1 Quasiclassical Theory

In quantum mechanics, a *Green's function*  $G_{\sigma\sigma'}(\mathbf{x}, t; \mathbf{x}', t')$  can usually be thought of as a probability amplitude.<sup>2</sup> More precisely, it is a measure of the probability that a particle that was at position  $\mathbf{x}'$  with spin  $\sigma'$  at time  $t'$ , will appear at some other position  $\mathbf{x}$  with spin  $\sigma$  at some later time  $t$ . In quasiclassical theory, the two main Green's function formalisms in use are the *Keldysh real-time formalism* [81] and the *Matsubara imaginary-time formalism* [82]. Here, we will consider the Keldysh technique for ordering Green's functions, and briefly discuss the Matsubara technique in the section on conventions and notations 1.3.2.

The Keldysh technique identifies a *retarded* and *advanced* component describing particle propagation in the positive and negative temporal directions respectively, as well as a *Keldysh* component which describes any non-equilibrium component. As usual, a particle travelling backwards

---

<sup>2</sup> Depending on the personal preferences of the authors, the same mathematical object may be referred to as either a Green's function, Green function, or propagator [80].

in time may also be interpreted as an antiparticle travelling forwards in time, so a more natural interpretation might be that the retarded component describes the propagation of electrons while the advanced component describes the propagation of holes. The full  $8 \times 8$  Green's function  $\check{G} = \check{G}(\mathbf{x}, t; \mathbf{x}', t')$  is written as a combination of these,

$$\check{G} = \begin{pmatrix} \hat{G}^R & \hat{G}^K \\ 0 & \hat{G}^A \end{pmatrix}, \quad (1.4)$$

where  $\hat{G}^R$ ,  $\hat{G}^A$  and  $\hat{G}^K$  refer to the retarded, advanced and Keldysh components respectively. The two  $2 \times 2$  diagonal blocks of these component matrices are termed *normal* Green's functions  $G_{\sigma\sigma'}$ , while the off-diagonal blocks are called *anomalous* Green's functions  $F_{\sigma\sigma'}$ . The normal Green's functions are given by the following expectation values:

$$\begin{aligned} G_{\sigma\sigma'}^R(\mathbf{x}, t; \mathbf{x}', t') &= -i \langle \{ \psi_\sigma(\mathbf{x}, t), \psi_{\sigma'}^\dagger(\mathbf{x}', t') \} \rangle \Theta(t - t'), \\ G_{\sigma\sigma'}^A(\mathbf{x}, t; \mathbf{x}', t') &= +i \langle \{ \psi_\sigma(\mathbf{x}, t), \psi_{\sigma'}^\dagger(\mathbf{x}', t') \} \rangle \Theta(t' - t), \\ G_{\sigma\sigma'}^K(\mathbf{x}, t; \mathbf{x}', t') &= -i \langle [\psi_\sigma(\mathbf{x}, t), \psi_{\sigma'}^\dagger(\mathbf{x}', t')] \rangle, \end{aligned} \quad (1.5)$$

where  $\Theta(\cdot)$  is the Heaviside step function. The anomalous counterparts  $F_{\sigma\sigma'}$  are defined in the same way except for the  $\dagger$ , *i.e.* they are proportional to  $\langle \{\psi, \psi'\} \rangle$  and  $\langle [\psi, \psi'] \rangle$  instead.

The Green's function displays a wavepacket-like oscillatory profile, where the relative coordinate describes the internal, rapid oscillations of the order of the Fermi wavelength  $\lambda_p$ , that occur due to self-interference effects. Conversely, the center-of-mass coordinate describes the spatial evolution of the wavepacket envelope. Only the average of the fast oscillations is relevant for the superconductivity of the material since the superconducting coherence length of the Cooper pairs  $\xi_s \gg \lambda_p$  and thus one averages out the relative coordinate (also known as the *gradient approximation*). This is equivalent to assuming that all relevant length scales in the system must be much greater than  $\lambda_p$  and is the starting point for the *quasiclassical approximation*, which goes on to consider only momenta of the order of the Fermi momentum. All physical quantities are therefore confined to the Fermi surface, and since all quasiparticles have the same magnitude of momentum in this approximation, the relevant information is the transport direction.

Explicitly, the approximation enters as an integration over the kinetic energy, such that the quasiclassical Green's function  $\check{g}(\mathbf{x}, \mathbf{p}_F, \epsilon, t)$  is given by

$$\check{g}(\mathbf{x}, \mathbf{p}_F, \epsilon, t) \equiv \frac{i}{\pi} \int_{-\infty}^{\infty} d\xi_p \check{G}(\mathbf{x}, \mathbf{p}, \epsilon, t), \quad (1.6)$$

where  $\epsilon$  is the quasiparticle energy,  $\mathbf{p}$  is the momentum,  $\mathbf{p}_F$  is the Fermi momentum, and  $\xi_p = \mathbf{p}^2/2m - \mu$  is the kinetic energy measured from the Fermi level  $\mu$ . It is straight forward to verify that this definition is equivalent to the approximation  $\check{G}(\mathbf{x}, \mathbf{p}, \epsilon, t) \approx -i\pi\delta(\xi_p)\check{g}(\mathbf{x}, \mathbf{p}_F, \epsilon, t)$  where the delta function  $\delta(\xi_p)$  constrains the quasiparticle momentum to the Fermi surface. In other words, this integral definition is equivalent to our previous qualitative discussion of the approximation as confining physical quantities to the Fermi surface. This integral is not well-defined for large kinetic energies  $\xi_p$ , so in practice the integral is solved by contour integration. For the details of this procedure, we refer the reader to Refs. [83–85].

The  $4 \times 4$  retarded block of  $\check{g}$  has the structure:

$$\hat{g} = \begin{pmatrix} g & f \\ -\tilde{f} & -\tilde{g} \end{pmatrix}, \quad (1.7)$$

and is normalized such that  $\hat{g}^2 = \hat{1}$ , where  $\hat{1}$  is the  $4 \times 4$  unit matrix. It is worth noting that the choice of normalization convention for  $\hat{g}$  is governed by the ordering of particle creation and annihilation operators when these are combined in a convenient 4-vector form [86]. The normalization of the Green's function matrix can also be set to  $\hat{g}^2 = -\hat{1}$  or  $\hat{g}^2 = -\pi^2\hat{1}$  depending on the prefactor in Eq. (1.6). The advanced and Keldysh blocks have a similar structure to the retarded block, and the notation  $\dots$  denotes a  $2 \times 2$  matrix. The tilde-operation  $\dots$  denotes a combination of complex conjugation  $i \rightarrow -i$  and energy  $\epsilon \rightarrow -\epsilon$ . Note that the Green's functions of the system can be used to directly calculate physical observables for a superconducting system. For instance, the normalized density of states  $D(\epsilon) = \frac{1}{2} \operatorname{Re} \operatorname{Tr} g$  corresponds to the real part of the normal Green's function, and the critical temperature  $T_c$  can be defined as the temperature where the anomalous Green's function  $f$  drops to zero for all energies. Moreover, a small imaginary component is often added to the energy to model inelastic scattering, such that  $\epsilon \rightarrow \epsilon + i\delta$ . This has the effect of smoothing out divergences in the density of states.

### 1.3.1.1 Diffusive Limit: Usadel Equation

In the diffusive limit, we are able to take account of particle scattering by impurities and rough interfaces. In this case the system is described by a set of second-order partial differential equations for the Green's function of a material collectively termed the Usadel equation. The Usadel equation reads:

$$D \nabla \cdot (\check{g} \nabla \check{g}) + i \left[ \epsilon \hat{\rho}_3 + \hat{\Delta} + \hat{M} - \check{\sigma}_{sf} - \check{\sigma}_{so}, \check{g} \right] = 0. \quad (1.8)$$

Here we have written the equation in a quite general form, where  $D$  denotes the diffusion coefficient of the material,  $\epsilon$  is the quasiparticle energy and  $\hat{\rho}_3 = \text{diag}(+1, +1, -1, -1)$ . Moreover, it should be noted that  $\check{g}$  in the above equation refers to the isotropic part of the quasiclassical Green's function defined in Eq. (1.6), which is independent of the direction of motion (the position on the Fermi surface). The magnetization matrix  $\hat{M} = \mathbf{h} \cdot \text{diag}(\boldsymbol{\sigma}, \boldsymbol{\sigma}^*)$ , where  $\mathbf{h}$  is the magnetization exchange field and  $\boldsymbol{\sigma}$  is the Pauli vector. Products of matrices with incompatible dimensions should be interpreted by taking Kronecker products with the appropriate identity matrices, so that e.g.  $\hat{\rho}_3 \check{g} = [\hat{\rho}_3 \otimes \text{diag}(1, 1)] \check{g} = \text{diag}(\hat{\rho}_3, \hat{\rho}_3) \check{g}$ . The effects of spin-orbit coupling and randomly aligned magnetic spin-flip processes caused by impurities have been included via the terms

$$\begin{aligned} \check{\sigma}_{so} &= -\frac{1}{8\tau_{so}} \hat{\sigma} \hat{\rho}_3 \check{g} \hat{\rho}_3 \hat{\sigma}, \\ \check{\sigma}_{sf} &= -\frac{1}{8\tau_{sf}} \hat{\sigma} \check{g} \hat{\sigma}, \end{aligned} \quad (1.9)$$

where  $\tau_{so}$  and  $\tau_{sf}$  are the mean spin-flip and spin-orbit scattering times, and we have defined the matrix  $\hat{\sigma} = \text{diag}(\boldsymbol{\sigma}, \boldsymbol{\sigma}^*)$ . Impurity scattering in the Usadel equation is typically treated in the Born approximation, which means that the strength of the impurity potential (the phase-shift imposed on the electron wave function when it scatters on the impurity) is sufficiently weak, although the impurity concentration may still be high. This is in contrast to the opposite regime of the unitary limit where the scattering potential is strong, imposing a large phase-shift.

### A note on the derivation and applicability of the Usadel equation

The Usadel formalism assumes that the impurity scattering rate is the largest energy scale in the system besides the Fermi level (typically several eV in metals), and may therefore be inaccurate for strong ferromagnets where

the exchange field is a significant fraction of the Fermi energy. In this case the Eilenberger equations [77] should be used instead. These are the kinetic equations for the superconductor before the standard battery of assumptions and approximations are applied in order to make more complicated scenarios tractable. A detailed derivation of the Usadel equation in the dirty limit, starting from the equation of motions for the field operators, can be found in Ref. [85]. One first finds the equation of motion for the Green's functions, and the Eilenberger equation is found by setting their difference equal to zero. This is done within the BCS mean field approximation, which reduces two-particle operators to single-particle operators by assuming short range interactions and taking the average. This is the first of many necessary approximations, and we provide a brief overview and discussion of the most common cases and the associated nomenclature typically met in the literature:

- *Mean-field Approximation*: One here assumes that electron-electron interactions can be described effectively by each electron moving in a net background field set up by the other electrons. Mathematically, this amounts to taking the average of two-particle operators to yield single-particle operators. In the case of a superconducting order parameter, this results in  $\Delta(\mathbf{x}, t) = \lambda\langle\psi_{\downarrow}(\mathbf{x}, t)\psi_{\uparrow}(\mathbf{x}, t)\rangle$ , where  $\lambda$  is the coupling constant of the effective electron-electron interaction that causes superconductivity.
- *Gradient Approximation*: This assumes all quantities vary slowly compared with the Fermi wavelength, so that one may neglect short-ranged oscillations and keep only spatial derivatives up to first order.
- *Clean Limit*: The clean limit applies to very pure materials, where the mean free path  $\ell$  is greater than the coherence length  $\xi$  and length  $L$  of the medium,  $\ell \gg \xi, L$ . At low temperatures, the proximity effect is therefore long ranged. Ferromagnets with increasingly high Curie temperatures, *i.e.* the temperature beyond which it loses its permanent magnetization and becomes a paramagnet, tend towards the clean limit. Typical examples are iron (Fe) and cobalt (Co).
- *Born Approximation*: This assumes that the strength of the impurity potential is so weak that it imposes a phase-shift  $\delta$  on the electron wave function upon scattering, satisfying  $\delta \ll 1$ . In effect one introduces a self-energy term (*i.e.* quantifying the contribution to the particle or quasiparticle's

energy given by interactions with the system) by averaging over the positions of the impurities (and averaging over spin states in the case of magnetic impurities).

- *Dirty Limit:* In contrast to the clean limit, the dirty limit is defined by  $\xi \gg \ell$  or  $L \gg \ell$ , and the proximity effect decays exponentially because the Usadel formalism takes the ensemble average over impurities. By taking the dirty limit one assumes that the elastic scattering self-energy term from the Born approximation dominates all terms in the equation of motion for the Green's function,  $1/\tau_{\text{imp}} \gg \Delta, T$ , and in this way models quasiparticle diffusion.
- *Equilibrium:* In equilibrium, there are no applied voltages or temperature gradients, allowing the Keldysh component of the quasiclassical Green's function to be written purely in terms of the retarded Green's function since  $\hat{g}^K = (\hat{g}^R - \hat{g}^A) \tanh(\epsilon/2k_B T)$  and  $\hat{g}^A = -(\hat{\rho}_3 \hat{g}^R \hat{\rho}_3)^\dagger$ , where  $k_B$  is the Boltzmann constant.
- *Weak Proximity Limit:* The limit of weak proximity effect is a reasonable approximation when the non-superconducting layers are very long, or the interface transparency is very low. Mathematically, this limit implies that the anomalous Green's function can be treated as a perturbation  $\|f\| \ll 1$ , since the presence of an anomalous Green's function is invariably linked to the presence of superconducting phenomena. The resultant simplification allows for analytic results which facilitates the understanding of the underlying physical mechanisms. In contrast, the strong proximity limit can typically only be solved numerically but allows for more accurate predictions of physically relevant signatures.

### 1.3.2 Notation and Parameterizations

The  $4 \times 4$  components of the retarded Green's function  $\hat{g}(\mathbf{x}, \epsilon)$  (dropping the superscript 'R' for brevity) are not all independent. Firstly, the particle-hole symmetries  $\tilde{g}(\mathbf{x}, \epsilon) = g^*(\mathbf{x}, -\epsilon)$  and  $\tilde{f}(\mathbf{x}, \epsilon) = f^*(\mathbf{x}, -\epsilon)$  relates the top two  $2 \times 2$  blocks of the matrix to the bottom ones. Secondly, writing out the normalization condition  $\hat{g}^2 = \hat{1}$  reveals two further constraints:  $\underline{g}\underline{g} - \underline{f}\underline{f} = 1$  and  $\underline{g}\underline{f} - \underline{f}\underline{g} = 0$ . By picking a parametrization of the Green's function such that these normalization and symmetry constraints are automatically satisfied, the relevant physical equations can be significantly simplified. We will discuss two such parametrizations in this section.

In analytical treatments of superconductivity, the most popular parametrization is the so-called  *$\theta$ -parametrization*, which is usually written

$$\hat{g} = \begin{pmatrix} c_\uparrow & 0 & 0 & s_\uparrow \\ 0 & c_\downarrow & -s_\downarrow & 0 \\ 0 & s_\downarrow & -c_\downarrow & 0 \\ -s_\uparrow & 0 & 0 & -c_\uparrow \end{pmatrix}, \quad (1.10)$$

where  $\sinh \theta_\sigma \equiv s_\sigma$  and  $\cosh \theta_\sigma \equiv c_\sigma$ . Thus, with this parametrization, the equations of motion can be recast in terms of only two scalar parameters  $\theta_\uparrow$  and  $\theta_\downarrow$ . While this choice can be very useful for analytical considerations, it has several limitations. Firstly, in the form presented here, it can only be used to describe singlet pairing and short-range triplet pairing, although there exists a generalization which captures all pairing components [87]. We recall that short-range triplet pairs are those which have zero spin-projection along the local magnetization direction, whereas the long-ranged pairs have spins aligned with the magnetization direction. When it comes to long-range triplet pairs, these would specifically be described by the elements that are set to zero in this parametrization. Secondly, the hyperbolic functions and their inverses are multi-valued. This is usually not a problem in analytical treatments, but can lead to convergence problems and instability when treating the problem numerically.

These problems bring us to the other popular parametrization, namely the Riccati parametrization [88, 89]. This parametrization is defined as

$$\hat{g} = \begin{pmatrix} \underline{N} & 0 \\ 0 & -\tilde{\underline{N}} \end{pmatrix} \begin{pmatrix} 1 + \underline{\gamma}\tilde{\underline{\gamma}} & 2\underline{\gamma} \\ 2\tilde{\underline{\gamma}} & 1 + \underline{\gamma}\underline{\gamma} \end{pmatrix}, \quad (1.11)$$

where the normalization matrices<sup>3</sup>  $\underline{N} \equiv (1 - \underline{\gamma}\tilde{\underline{\gamma}})^{-1}$  and  $\tilde{\underline{N}} \equiv (1 - \tilde{\underline{\gamma}}\underline{\gamma})^{-1}$ . In contrast to the multi-valued and unbounded  $\theta$ -parametrization, the Riccati parametrization is both single-valued and bounded  $\|\underline{\gamma}\| < 1$ , and is therefore the most popular parametrization for numerical work. Finally, the parametrization is completely general as it can be used to analyze all combinations of singlet, short-range triplet, and long-range triplet pairing that may occur in hybrid structures.

---

<sup>3</sup> In some literature, one uses the convention that  $\underline{\gamma}(e) = [-\underline{\gamma}(-e)]^*$  instead of changing the sign structure of Eq. (1.11).

We conclude this section by noting that a common alternative to the Keldysh real-time framework discussed herein is the Matsubara imaginary-time formalism. In that case, the physical equations are expressed in terms of only a single Matsubara Green's function  $\hat{g}^M(\mathbf{x}, t)$ , which can be related to the retarded and advanced Green's functions of the real-time formalism by analytical continuation to complex energies. We have for instance  $\hat{g}^R(\epsilon) = \hat{g}^M(i\omega \rightarrow \epsilon + i\eta)$  where  $\eta$  is a positive infinitesimal.<sup>4</sup> The imaginary energy  $\omega$  is restricted to one of the discrete *Matsubara frequencies*  $\omega_n = (2n+1)\pi T$ , where  $T$  is the temperature of the system and  $n$  is an arbitrary integer. In superconductors, the relevant Matsubara frequencies are those below the Debye frequency  $\omega_c$ , so we only need to consider  $n \in (-n_c, +n_c)$  in practice, where  $n_c \approx \omega_c / 2\pi T$ . Thus, at high temperatures, the number of Matsubara frequencies below the Debye frequency decreases, which means the Matsubara formalism becomes more computationally efficient in this regime. This explains why the formalism has become quite popular for critical temperature calculations, for example. Nevertheless, the Matsubara formalism is less general than the Keldysh formalism; the former can only be used to treat systems in thermal equilibrium, while the latter is valid also for non-equilibrium systems.

## 1.4 Experimental Status

In this section we will provide a brief introduction to the techniques and materials most readily available in the laboratory setting, and use the theory developed in the preceding chapter to explain the latest experimental breakthroughs in superconducting spintronics. Three comprehensive reviews of proximity effects in superconductor-ferromagnet heterostructures appeared in 2005 [29, 30, 90], as well as an overview of experimental devices in 2014 [91] and thorough review of spin-polarized supercurrents in 2015 [92]. We thus limit the scope of this section to provide a broad but brief overview of the most important experimental features affecting superconducting order in magnetic materials, primarily from the last decade.

### 1.4.1 Materials and Techniques

To help newcomers to superconducting spintronics or heterostructures in general, and to set the stage for the state-of-the-art experimental frontier,

---

<sup>4</sup> Although  $\eta$  enters in a similar way to  $\delta$ , which models the inelastic scattering in the Keldysh formalism, the mathematical equivalence here requires  $\eta = 0^+$ .

we provide a brief overview of the primary materials and experimental techniques typically used in the construction of such thin-film architectures. For an in-depth explanation of experimental techniques we refer readers to Ref. [93], sections of which we briefly paraphrase in 1.4.1.2. The overarching process requires an appropriate construction environment, methods of generating clean surfaces and well-formed interfaces, and methods for measuring the efficacy of all aspects of the process.

#### 1.4.1.1 *Material Choice*

The range of available ferromagnetic and superconducting elements is too extensive to discuss all implemented combinations here with any degree of justice, so we provide just a few common examples in order to give the unfamiliar reader a feeling for the appropriate parameter range of operation. Although we assume the reader to be familiar with ferromagnetism, we highlight a few examples that work particularly well in combination with superconductivity. The common elemental ferromagnets are of course the transition metals iron (Fe), nickel (Ni) and cobalt (Co). We mentioned above that Fe and Co are in the clean limit due to their high Curie temperature, featuring an exchange field which is a substantial fraction of the Fermi energy (high polarization), and these are routinely used in their pure state in superconducting heterostructures. Ferromagnetic compounds are preferred when specifically tailored characteristics of the heterostructure, such as a desired magnitude of the exchange field, is required. Examples include PdNi and CuNi, which can feature a canted magnetization orientation relative to the film-plane due to the competition between shape- and magnetocrystalline anisotropy [49]. The diffusion constant of CuNi is of the order  $D \sim 5 \text{ cm}^2/\text{s}$  [94]. Of the elemental superconductors, niobium has one of the biggest gaps at around  $\Delta \approx 3 \text{ meV}$ . In the diffusive limit one typically expects superconducting coherence lengths in the range  $\xi_s = 10\text{--}30 \text{ nm}$ , although it should be noted that its magnitude decreases when the thickness of the superconductor becomes comparable or smaller than this regime.

#### 1.4.1.2 *Experimental Techniques*

The preparation of reasonably impurity-free nanoscale heterostructures requires extremely low ambient pressures, typically under  $10^{-8} \text{ Pa}$ , as the ambient pressure governs the rate at which external particles impinge on a surface. For this reason all operations are performed inside an ultra-high vacuum chamber, and such vacuum technology has undergone a series of steady improvements in recent years [93]. If the crystal is brittle, a

well-defined crystal surface can be prepared by cleavage, where mechanical pressure is applied to the crystal via externally controlled magnetic or electric devices. The cleavage then occurs along a particular crystallographic direction, meaning noncentrosymmetric materials are quite unsuited for cleaving due to their lack of inversion symmetry.

Since cleavage only works well for brittle crystals, and as a cleaved surface may contain rough edges or defects, an alternative preparation method is ion bombardment and annealing. In this case noble gas ions are fired at the surface of the crystal, removing the top layer along with any defects, and high-temperature annealing ( $\sim 500\text{--}1200\text{ }^{\circ}\text{C}$ ) removes any noble gas remnants on the surface. The purity and crystallographic order of the remaining surface are checked by spectroscopic and diffraction methods (see more below), and the bombardment/annealing process may be repeated a number of times until a satisfactory surface is achieved.

Thin-film layers are typically deposited by simple evaporation and condensation in general, creating a transversal “pancake-stack”. When a specific crystallographic orientation is required, the evaporation-condensation conditions are chosen more carefully and deposited with a technique called Molecular Beam Epitaxy (MBE). Here a beam of the sublimated/evaporated elements or compounds from which one wishes to make a layer is directed onto the substrate, and the layer deposition can be controlled to within a single monolayer by the rapid switching of this beam. Epitaxy refers to the deposition of a thin crystalline layer on top of a crystalline substrate, where the epitaxial layer has a fixed crystallographic orientation with respect to this substrate. The substrate provides a base structure from which the epitaxial layer is “grown” – that is it acts as a so-called *seed crystal*, which lowers the interaction potential of molecules to form a crystal lattice near the surface. The quality of the interface is therefore quite dependent on the crystallographic matching/lattice constants of the two layers. The III-V semiconductor gallium arsenide (GaAs) is a commonly used substrate, which has a zincblende crystal structure, *i.e.* the atoms form two interlocked face-centered cubic lattices where the four nearest neighbours at the tetrahedral vertices are of opposite type. The epitaxy may also occur through chemical reactions, in which case the technique is called Metal-Organic MBE, or Chemical Beam Epitaxy.

For materials that have very high melting points, making the evaporation step difficult, the *sputter deposition* technique provides an alternative. This term actually denotes a range of related vapour deposition methods, many of which can still be operated at ultra-high vacuum for increased purity and epitaxial growth for structural control. In this case accelerated gaseous ions are fired onto the material from which one wishes to create a

thin-film layer (the “target”). The impact causes a number of particles to be ejected (sputtered) from the surface and are subsequently deposited as a thin-film on a substrate. By choosing reactive gases, one may also sputter compounds. The deposition with sputtering, and to a large extent also with MBE, is primarily homogeneous; patterning is significantly more of a challenge because of the lack of control over deposition direction. Thus, if particular structural features are required, these must be created by removing surface layers via etching with a focused beam of particles or by using electron-beam lithography. In the latter case, the pattern is drawn by firing an electron beam at an electron-sensitive coating, after which selective removal is possible in a solvent bath.

High-quality thin-film interfaces are crucial for efficient spin-transport between the layers, and the atomic structures of such interfaces are studied in detail using microscopy, spectroscopy and diffraction methods. Using Auger electron microscopy or X-ray photoemission spectroscopy, the intensity of the characteristic transitions or emission lines corresponding to electrons from individual atoms in the sample decays exponentially with the thin-film thickness. This is due to the often short mean free path (~tens of nm) of electrons in matter, the length of which changes according to material structure and impurity level. If the deposition occurs as an island on the substrate rather than a full monolayer, the intensity profile, which is measured as a function of the layer coverage, will instead tend to be linear [93].

Using electron diffraction techniques, bright Bragg spots show the crystallographic order of the reciprocal lattice, accurate to within the electron beam’s coherence length. If one requires a more accurate real-space image, a range of tools are available, with various advantages and drawbacks. They may yield significantly increased resolution for example, but may not be compatible with ultra-high vacuum conditions, meaning contamination of the sample might occur during transfer to the microscope. This is the case for scanning electron microscopy (SEM), which is among the most common high-resolution tools, along with transmission electron microscopy (TEM) and scanning tunneling microscopy (STM). Optical methods may also be used, such as using inelastic scattering to study vibrational properties of the lattice. For buried interfaces, ion scattering is another indispensable tool, where the subsequent analysis can yield information about the chemical composition, crystallographic quality and lattice matching between the layers. For further reading, we refer again to the book by Lüth [93] and references therein.

So far we have been concerned with the construction of thin-film architectures. Now we turn to techniques for controlling and measuring the

physical features of interest in spintronics. The practicalities of control in experimental setups can be quite unintuitive – for example, it is often easier in experiment to rotate the sample itself rather than the magnetic field source in order to probe the influence of different magnetic field orientations on the system. The pace at which interesting new features are being uncovered makes the physics of control and measurement a rapidly expanding field in itself, and this discussion will lead us naturally into the next section, where we consider the frontier of experimental research.

The differential conductance  $dI/dV$  is directly proportional to the density of states in the tunneling limit (where Andreev reflection is suppressed) and so is a common measure in which to present such analysis experimentally. It is typically normalized to the normal-state conductance at high bias (5 mV in a Nb superconductor, for a concrete example [95]). An STM can be used to generate the current-voltage sweep since the tunneling current depends on the voltage between the STM tip and the electronic structure to be probed. For this reason differential conductance and tunneling spectroscopy are sometimes used interchangeably in the literature. Numerical differentiation is very sensitive to noise, so typically an averaging over several sweeps must be taken to get an accurate mapping.

The Josephson junction (Section 1.2.2.2) is a mainstay of spintronic architectures in the context of superconducting hybrids, but the approach to its construction depends on the intended purpose. The phase difference between the superconductors can be adjusted by applying a current bias. As long as the current is smaller than the critical current  $I_c$ , the superconducting phase difference then adjusts in order to support the applied current via the relation  $I = I_c \sin(\phi)$ . The phase may also be modified continuously by applying an external magnetic flux in a loop geometry [70]. In an SNS junction, the superconductors have zero phase difference between them in the ground state. However, due to the oscillating behavior of the order parameter in SFS junctions described previously, the ground state in this case can occur at a phase difference equal to  $\pi$ . Whether 0 or  $\pi$  is the ground state depends on the system parameters, such as the length of the interstitial ferromagnetic layer and temperature. It has also been predicted that, in special circumstances, the ground state may be manufactured to give an arbitrary  $\phi_0$ -junction (see Section 1.5 for more details).

A highly influential application of Josephson junctions is their use in superconducting quantum interference devices (SQUIDs). These are typically made by joining two junctions in a loop [96], but single-junction designs which are less sensitive but more easily manufactured also exist [97, 98]. When a magnetic flux passes through the loop, it induces a circulating current. If an external current is applied to the SQUID, the induced

current will enhance the current in one arm of the loop and suppress it in the other. It will then be energetically favourable for the induced current to change direction as a function of the magnetic flux in units of  $h/2e$ , where  $h$  is Planck's constant and  $e$  is the electronic charge, *i.e.* in practice the induced current increases or decreases the flux through the loop. A SQUID may then in turn be used to measure properties of other thin-film heterostructures, as their high sensitivity to external flux means they function as high-precision magnometers (equivalently magnetometers). The recently developed nanoSQUIDs can even resolve the magnetization of individual spins [99–101], and we expand on this in the following section.

#### 1.4.2 Recent Experimental Advances

The full theoretical basis of spin transport between materials in thin-film heterostructures involving superconductors is still incomplete, but as the potential benefits have emerged the field has undergone rapid development. The race is now on to harness the full potential of superconducting correlations for spin transport in experimental devices, and a number of important steps have already been achieved in this regard. Key features include spin injection, spin accumulation, control of spin diffusion as well as dynamical detection and manipulation of the spin state of the system. Here we briefly discuss some of the superconducting counterparts to these conventional procedures from spintronics.

*Spin injection and spin Hall effects.* A compelling reminder of the enhanced capabilities promised by superconducting spintronics was provided recently with the report of a quasiparticle-mediated spin Hall effect – *i.e.* spin accumulation on the lateral surfaces due to spin-orbit coupling – in an *s*-wave superconductor. The magnitude of this effect exceeded its non-superconducting equivalent by a factor of more than 2000 [18]. In that experiment, a lateral superconductor-ferromagnet structure was created by using a non-magnetic Cu wire to join a ferromagnetic  $\text{Ni}_{81}\text{Fe}_{19}$  wire to a wire of compound superconductor NbN, which has  $T_c = 10$  K. A spin current was injected into the NbN via diffusion of spin accumulation in the Cu wire resulting from driving a current from the ferromagnet to the Cu. The inverse spin Hall effect causes scattering of the injected spin current and converts it to charge current, which below  $T_c$  is carried by quasiparticles. The electrical signatures of the inverse spin Hall effect thus manifest as a charge imbalance at the edges of the sample [102].

Spin injection in conventional spintronics typically occurs as above, through diffusion of spins across a ferromagnet/non-ferromagnet interface. At a superconducting interface, a range of novel phenomena have been shown when spin-polarized currents are injected into superconductors,

such as quasiparticle spin lifetimes close to one million times longer than the normal-state lifetime [16], which is a result of the unique properties of quasiparticles in superconductors. While they carry spin-1/2, their effective charge depends on their energy. In fact, near the gap edge  $\epsilon \approx \Delta_0$ , their effective charge  $Q \rightarrow 0$  at the same time as their group velocity  $v_g$  slows down. This means that close to the gap edge, one has chargeless spin-1/2 fermion excitations which should then be insensitive to processes that cause decoherence due to coupling to the charge degree of freedom. Importantly, a recent experiment has indeed given an exposition of near-chargeless spin imbalance [17], which could have interesting consequences with regard to overcoming the problem of Joule heating associated with the large charge current densities (order  $10^6$  A/cm<sup>2</sup>) currently required for domain wall motion and magnetization dynamics. The fact that the group velocity of quasiparticles in superconductors slows down at  $\epsilon \approx \Delta_0$  also means that it takes a much longer time for them to experience e.g. spin-orbit scattering on impurities. Spin diffusion via quasiparticles in superconductors has been shown to be strongly enhanced in Zeeman-split superconductors [103].

*Spin-polarized Cooper pairs.* Whereas the above examples show how spin transport in superconductors can be dramatically improved compared to its non-superconducting counterpart even at the level of quasiparticles, much attention has also been devoted to the role of spin-polarized Cooper pairs that can emerge in SF structures. This triplet component of the superconducting correlations has been enhanced in experiments both via the introduction of a ferromagnet with an inhomogeneous magnetization texture to produce long-ranged supercurrents [48, 104], and in multilayered SFS junctions [49] (see the left panel of Figure 1.3). The pioneering experiment with regard to long-ranged triplet supercurrents was done by Keizer *et al.* [105], demonstrating transfer of a supercurrent through an extreme magnetic environment: a half-metal. Half-metals are ferromagnets with so strong magnetic fields that one spin band becomes electrically insulating, while the other band is a metallic conductor. Since conventional singlet Cooper pairs consist of electrons from both spin bands, such pairs cannot exist in a half-metal. In the presence of magnetic disorder near the interfaces connecting the half-metal to a superconductor, effectively producing a local misalignment of the magnetization there compared to its direction in the bulk, a net Josephson coupling via triplet Cooper pairs can be established [106]. The history and properties of spin-polarized supercurrents has been covered in great detail in a recent review [92]. Martinez *et al.* reported recently an important step forward with regard to exerting well-defined control of such triplet supercurrents [107]. The key idea in this experiment was to use an external magnetic field to switch on and off a triplet supercurrent by controlling the relative magnetization orientation in a Ni/Co/NiFe ferromagnetic

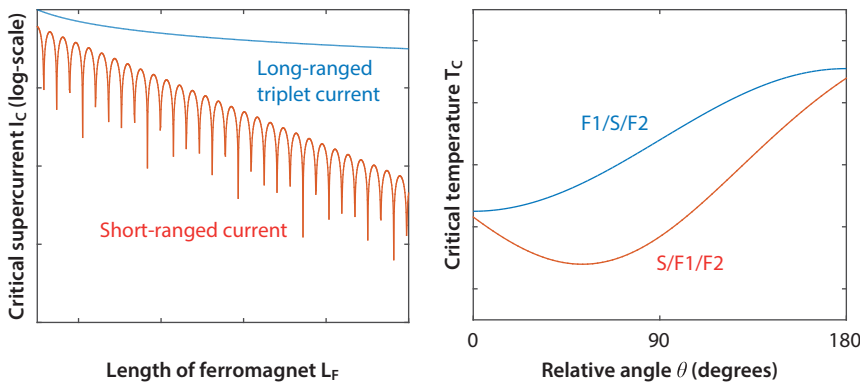


**Figure 1.3** Left panel: The critical supercurrent can display two types of behavior in ferromagnetic Josephson junctions. If no long-ranged triplet pairs are generated (due to e.g. magnetic inhomogeneities), the supercurrent is suppressed very quickly with increasing junction length  $L_F$  (note the logarithmic scale). In contrast, if triplet pairs with spin-polarization aligned with the magnetization direction are created, these can carry a long-ranged current through the system which is only weakly suppressed with increasing  $L_F$ . Right panel: Magnetic control over the superconducting critical temperature  $T_c$  and its characteristic behaviour in two types of spin-valve junctions: FSF and SFF.

stack sandwiched between two conventional superconductors. Whereas Ni is a hard ferromagnet (high coercivity field), NiFe switches much more easily and could be rotated with a small field less than 20 mT. When the NiFe was rotated into a non-collinear orientation, a triplet supercurrent could flow through the junction, whereas it was otherwise strongly suppressed. In this way, the authors obtained “on-off ratios” up to 20 for the supercurrent.

The existence of triplet Cooper pairs is inferred indirectly via long-ranged supercurrents through ferromagnets. More direct proof can be obtained by considering how triplet Cooper pairs should influence the spectroscopic properties of superconducting structures, such as the energy-dependent density of states. The first *direct* experimental signatures of an odd-frequency triplet pairing state in a conventional superconductor was in fact reported as recently as 2015 [96], using scanning tunneling spectroscopy of a niobium/holmium bilayer. Using a sapphire substrate topped with a thin layer of non-superconducting Nb as a seed crystal,<sup>5</sup> a 9.5 nm layer of Ho was grown epitaxially followed by a 20 nm layer of superconducting Nb. The sample was protected from oxidization by applying a final thin layer of

<sup>5</sup> Typically, a superconducting layer needs to be longer than the order of half a coherence length of the material in order to display superconductivity, since there are otherwise insufficient Cooper pairs to form a condensate.

gold. Having noted that spin-active interfaces can enhance odd-frequency pairing on the superconducting side of an SF interface [106], the authors used the *controllable* magnetic order in Ho to gain such an amplification of the triplets. By measuring the density of states on the superconducting side, the authors also avoid the normal-state background, thus in principle getting a clearer conductance signal. By applying an external field the Ho was then driven through a metamagnetic transition from helical antiferromagnet to homogeneous ferromagnet and the authors recorded a change in the subgap density of states from a double peak indicating spin splitting to an enhanced peak at zero energy, characteristic of the behavior of odd-frequency triplets in the presence of a spin-active interface (see Figure 1.2). A similar effect was reported shortly thereafter in a superconductor/half-metal bilayer [108].

*Control of  $T_c$ .* In the last few years, there has been increasing activity in the quest for controlling the superconducting critical temperature  $T_c$  in spin-valve geometries, *i.e.* by changing the relative magnetization orientation of two or more ferromagnetic layers. It is also possible to alter  $T_c$  by altering the width  $L_F$  of the ferromagnetic layer. This can obviously not be done *in situ*, which is a practical hinderance, but in return the change in  $T_c$  becomes potentially much larger and in some cases fully suppresses superconductivity,  $T_c \rightarrow 0$ . Controlling  $T_c$  via the relative magnetization direction in an FSF spin-valve can be done with a single sample, as shown recently in Refs. [109–112]. As discussed previously, the configuration of antiparallel magnetizations should be more compatible with the superconducting state (higher  $T_c$ ) compared with the parallel alignment where the fields add [113, 114]. However, there is an additional effect that must be taken into account when the fields are non-collinear. In this case, an additional proximity channel through which Cooper pairs may “leak” into the ferromagnet is opened since long-ranged Cooper pairs can now be generated. As a result, one could expect that  $T_c$  is in fact not at its lowest in the parallel alignment, but instead at misalignment angles close to  $\pi/2$ . This has been experimentally confirmed in [109–111]. It is worth noting that this effect becomes much more pronounced in an SFF structure than in an FSF structure, since the additive, destructive effect of the ferromagnetic layers become less severe in the former case (see the right panel of Figure 1.3).

Recently, an unusually large change in  $T_c$  of order 1 K was reported by using half-metallic ferromagnets in a spin-valve setup [115]. In their device, the authors exploited precisely the extra leakage channel via long-ranged triplet Cooper pairs which becomes of crucial importance in half-metallic ferromagnets. In this case, a proximity effect is indeed only possible when such Cooper pairs are allowed to exist. Whereas previous experiments

(mentioned above) had achieved a maximum suppression of  $T_c$  of around 100 mK, a change of 1 K was obtained in Ref. [115] by utilizing a CrO<sub>2</sub>/Cu/Ni/MoGe structure (half-metal/normal metal/ferromagnet/superconductor). The normal Cu spacer serves to reduce exchange coupling between the CrO<sub>2</sub> and Ni which otherwise would have their magnetizations locked to each other. Using an external magnetic field to thus accomplish rotation of the Ni layer magnetization to a 90 degree orientation relative to the CrO<sub>2</sub> magnetization, the large shift in  $T_c$  was observed due to the long-ranged triplet proximity effect. This finding has relevance to applications utilizing superconducting switches that are controlled magnetically, as discussed in Ref. [116]. One reason for this is that when the range of  $T_c$  varies widely, the resistance state (“off”-state) of the device is more stable with respect to thermal fluctuations. For a small change in  $T_c$ , thermal fluctuations could accidentally turn the device “on” by lowering the temperature below the  $T_c$  dictated by the magnetic configuration. A superconducting GMR device like this should be able to perform the same type of logic operations as its non-superconducting equivalent, but with much lower dissipation of energy.

*Thermoelectric effects.* Part of what makes the transport properties of superconductors so exciting is the strong coupling between not only the spin and charge degree of freedom, but also *heat*. In fact, quasiparticle spin accumulation in superconductors can be intimately related to thermoelectric effects. Although overall electron-hole symmetry may be preserved, spin-dependent order in superconductors induced either via a proximate magnetic host or an in-plane magnetic field in thin-film structures, breaks the spin-resolved electron-hole degeneracy. In turn, this allows for very large thermoelectric effects as predicted in [117, 118]. Interestingly, this has very recently been experimentally confirmed in [19]. In this work, the authors measured thermoelectric currents in tunnel junctions comprised of superconductor/ferromagnet layers in the presence of a high magnetic field. The resulting Seebeck coefficients were found to exceed 100  $\mu\text{V/K}$ , far beyond what is typically obtained in conventional metallic structures. It is encouraging to note that these results were obtained without very strongly polarized magnetic materials, alluding to the fact that even larger Seebeck coefficients might be possible when using *e.g.* strongly polarized ferromagnetic insulators such as EuO or GdN.

*Imaging.* SQUID technology is advancing rapidly, with nanoSQUIDS reducing noise and allowing increased magnetic field sensitivity over their traditional micrometre counterparts [99, 100]. Until very recently however, it was not possible to measure the magnetic field generated by single electron spins using a SQUID. Such precision could be gained via magnetic resonance force microscopy [119] or nitrogen-vacancy magnetometers [120],

the latter enabling imaging at atmospheric conditions, which is a considerable advantage for biological and chemical applications. However, the ubiquitous use of SQUIDs for imaging in condensed matter where low temperatures are not a practical hinderance has made this pursuit a long-standing goal. In 2013 Vasyukov *et al.* manufactured a nanoSQUID on the apex of a hollow quartz tube, with a diameter down to 56 nm [101]. This construction gives single-spin sensitivity and, being mounted on a thin tip, is straightforwardly applied as a scanning probe. They report improved flux noise due to the small effective area and increased spin sensitivity that are orders of magnitude better than previous nanoSQUIDs. By utilizing Nb and Pb, which have relatively short coherence lengths, their nanoSQUID can operate at reasonably high magnetic fields and temperatures, making this a very promising new imaging tool whose increased sensitivity will allow for much more careful experimental examination of individual spintronic architectures.

On the experimental side, Blamire and Robinson point out [92] that the missing ingredient in order to gain the required level of control of the spin transport is the ability to manipulate the spins or the magnetic state. However, there is also evidence that the underlying physics of long-range proximity effects is still not entirely understood. These are cases in which magnetic inhomogeneities and spin orbit effects both appear to be negligible, so that no known mechanism for generating the triplet component is available. In 2010, Wang *et al.* reported zero resistance for single-crystal Co nanowires up to 600 nm in length [121]. Ref. [56] argues that this could mean there exists Rashba-type coupling in the system, but this is perhaps a contentious issue. Rashba coupling is typically a surface effect (unless the lattice itself is noncentrosymmetric), and currently there exist no precise experimental estimates of how deep such effects can penetrate into the bulk of a material, although an order of  $\sim 1$  nm is typically assumed. A recent alternative suggestion argues that giant mesoscopic fluctuations control the emergent behaviour [122].

## 1.5 Novel Predictions

Although triplet superconductivity may not be at the heart of all long-range effects, its generation and control has received increasing focus over the last decade due to its pivotal role in overcoming the problem of Joule heating in spintronics. The importance of combining spin-orbit coupling and magnetic materials has in this regard become increasingly apparent, and below we take a look at some of the most recent novel predictions and benefits in superconducting spintronics.

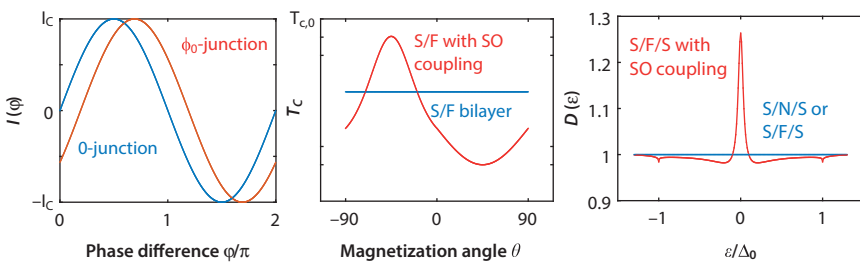


**Figure 1.4** *Left panel:* In a  $\phi_0$ -junction, the entire current-phase relation is shifted so that a net supercurrent flows even at zero phase difference. *Middle panel:* Magnetic control of superconducting  $T_c$  in the presence of Rashba and Dresselhaus spin-orbit coupling requires only one single homogeneous ferromagnet, in contrast to all previous proposals which have required two or more magnetic materials. Here,  $T_{c0}$  is the bulk superconducting critical temperature and the angle  $\theta$  is given in degrees. *Right panel:* Giant triplet proximity effect in spin-orbit coupled Josephson junction at  $\pi$  phase difference. Note the absence of a proximity effect without spin-orbit coupling at  $\pi$  phase difference for conventional SNS or SFS junctions.

### 1.5.1 $\phi_0$ -junctions

The phase difference  $\phi$  between the superconductors of a Josephson junction determines the supercurrent flowing in the junction according to  $I = I_c \sin(\phi)$ , with higher order harmonics appearing only at very low temperatures, and systems are routinely manufactured to have ground state  $\phi = 0$  and  $\phi = \pi$  by altering the sample length as discussed above. In principle, however, junctions may have any arbitrary single ground state between 0 and  $\pi$  e.g. if the superconducting state breaks time-reversal symmetry.<sup>6</sup> Such junctions have been dubbed the  $\phi_0$ -junctions since they follow the general current-phase relation  $I = I_c \sin(\phi + \phi_0)$  (see left panel of Figure 1.4). They were allowed for in Josephson's original work [61] and have been predicted to occur with unconventional superconductors [123–125]. Moreover, it was predicted by Buzdin in 2008 [126] that junctions with an interstitial noncentrosymmetric magnetic material<sup>7</sup> should provide direct coupling between the supercurrent and the magnetic moment in the interstitial material. This would create a  $\phi_0$ -junction with  $\phi_0$  proportional to the strength of the spin-orbit coupling and the exchange field in

<sup>6</sup> The current-phase relation must be antisymmetric if time reversal symmetry is preserved [63].

<sup>7</sup> Alternatively, a centrosymmetric ferromagnet could be used if only surface properties are probed.

the metal, consequently shifting the current-phase relation as shown in the left panel of Figure 1.4 so that a net supercurrent flows even for zero phase difference between the superconductors. The model was originally formulated for pure Rashba-type spin-orbit coupling before being developed for arbitrary Rashba-Dresselhaus coupling in diffusive systems [127], and could be incorporated into spintronic circuits as a phase-shifter, to generate spin precession or utilizing precession to generate supercurrent [126]. The superconducting  $\phi_0$ -junction has very recently been experimentally observed [128].

### 1.5.2 Control of $T_c$

Most previous endeavours to control the critical temperature of superconducting hybrid structures have focused on the use of multiple magnetic elements. For instance, the critical temperature  $T_c$  of FSF' and SFF' junctions can be toggled between a low state  $T_{c,1}$  and high state  $T_{c,2}$  by rotating the magnetization of the soft F' layer relative to the hard F layer, as discussed in previous sections. However, it becomes increasingly challenging to exert control over individual layers in the presence of multiple magnetic elements, especially if these are in immediate proximity. Recently, it was discovered that inclusion of spin-orbit coupling in superconducting spintronics opens up a rich new avenue of physical phenomena. As the authors show in Ref. [58], the presence of both Rashba and Dresselhaus spin-orbit coupling in an SF bilayer causes its superconducting properties to become strongly dependent upon the magnetization direction, in contrast to the case without spin-orbit coupling. The magnetization will always suppress the triplet pairs with spin projections perpendicular to the field, *i.e.* the singlet pairs and short-range triplet pairs. The spin-orbit coupling, on the other hand, suppresses triplet pairs depending on their spin projections relative to the crystal structure, and not the magnetization direction. Depending on the direction of magnetization relative to the spin-orbit coupling then, the latter may either suppress the short-range triplet pairs, long-range triplet pairs, or both. Finally, whether the short-range triplet pairs can be converted into long-range triplet pairs or not in a homogeneous ferromagnet depends on the magnetization direction relative to the spin-orbit coupling. The net result is that the magnetization and spin-orbit coupling can either conspire to suppress or enhance the proximity effect in the ferromagnet, and these two situations result in vastly different inverse proximity effects in the superconductor. It has been shown theoretically that this can lead to a difference  $T_{c,2} - T_{c,1}$  of up to  $0.2T_{c,0}$ , which for a niobium-titanium alloy would correspond to a 2 K change, in comparison with the current

world record for structures with multiple magnetic elements of 1 K [115] as discussed above. This result is illustrated in the middle panel of Figure 1.4, and at the time of writing it has not yet been experimentally verified.

### 1.5.3 Giant Proximity Effect and Control of Spin Supercurrent

In Ref. [58], the authors derive the Riccati-parameterized Usadel equation with spin-orbit coupling and go on to provide a detailed account of the effect of spin-orbit coupling on the density of states and  $T_c$  in transversal thin-films. It is shown that the density of states depends strongly on the direction of magnetization, so that in fact the direction of the exchange field can be used to tune the minigap from open to closed. Moreover, when the spin-orbit coupling direction corresponds to the transverse layering direction, the presence of spin-orbit coupling leads to an enhanced proximity effect at a phase difference  $\phi = \pi$ , in contrast to the well-known suppression of such effects when no spin-orbit coupling is present [59]. In fact, it is possible to fully isolate the triplet component without any contamination from singlets, and this triplet-only state persists throughout the entire interstitial layer, all the way up to the superconducting contacts. This effect is illustrated in the right panel of Figure 1.4. The density of states has a nonmonotonic dependence on the spin-orbit coupling, and, when the exchange field lies along the junction, large coupling can again lead to a magnetically tunable gap, with a gap at  $\phi = 0$  and zero-energy peak at  $\phi = \pi$ . The significant impact of spin-orbit coupling on the density of states translates into an equally dramatic effect on the supercurrent that can flow between the superconductors of a Josephson junction. The authors have shown that for an SNFNS junction, with very thin normal-metal layers (N) and a *homogeneous* ferromagnet, it is possible generate and control a spin supercurrent that displays spin-flip immunity [129]. Normal spin currents remain polarized only up to the spin relaxation length, so the lack of spatial decay of the current is remarkable.

### 1.5.4 Inducing Magnetism via Superconductivity

Whereas so far we have discussed mainly how the presence of magnetic order influences superconductivity, the reciprocal phenomenon is also possible. As an example, one can consider Ref. [130] where it was proposed that it is possible to control magnetism via supercurrents. The concrete system under consideration was an SFNFS junction which supports a supercurrent when phase-biased. Due to the appearance of triplet Cooper pairs in such a junction, there exists a proximity induced magnetization

$M$  in the normal metal, which depends sensitively on the superconducting phase difference  $\phi$  and the length  $d$  of the junction. Interestingly, the total induced magnetization  $M = M_1 + M_2$  could be decomposed into a phase-independent part  $M_1 = M_1(d)$  and a phase-dependent part  $M_2 = M_2(\phi, d)$ . The authors found that whereas  $M_2$  decays rapidly with the length  $d$ , the phase-independent part only weakly decreased upon increasing  $d$ . This proposal is interesting because it goes beyond discussing the long-ranged effect of triplet supercurrents and instead links Cooper pairs directly to their spin-properties, which could possibly be integrated with other magnetic components in a cryogenic spintronic device. The spin supercurrent flowing through a similar system was found to behave similarly as the magnetization [55]. The fact that a triplet proximity effect can induce a magnetization could also be a possible explanation for the remotely induced magnetism via a superconductor reported in Ref. [131], a topic which deserves further exploration.

## 1.6 Outlook

The field of superconducting spintronics is developing rapidly and a number of challenges can be identified from the above discussions. Theoretical models of spin-orbit coupling show great potential for enhancing features such as long-range superconducting proximity effects and realizing  $\phi_0$ -junctions, but a number of experimental challenges must be overcome before the effect can be adequately included in real thin-films. Consensus has not yet been reached regarding the precise penetration depth of surface Rashba-coupling into the bulk of materials. Although the relative strengths of Rashba and Dresselhaus couplings in e.g. semiconducting quantum wells can be measured separately [132], tuning them separately in a controllable manner has proven more challenging. We see the benefits of noncentrosymmetric materials come up again and again in the context of SF structures, and one of the most promising experimental directions to study their significance could be to make use of very thin heavy normal metals to induce Rashba coupling.

The upswing in experimental activity in the field of superconductor/ferromagnet structures has been notable over the last few years. We believe that one of the most interesting experimental directions to explore in the coming years will be the direct measurement of the triplet Cooper pair spin (as opposed to indirect via long-ranged supercurrents through ferromagnets or spectroscopic measurements of the frequency-symmetry). There are different ways in which this can be achieved. Experiments measuring effects such as domain wall motion, spin-transfer torques, and

magnetization switching due to spin-polarized supercurrents are likely to have a transformative effect on the field as it would open up a whole new avenue of possible cryogenic applications via superconducting spintronics. Moreover, the theory of equilibrium physics in SF structures is mostly well-developed at present, but there remains much work to be done on the non-equilibrium side. Spin and charge dynamics in systems combining superconducting and magnetic elements remain far less explored. Developing these aspects of the theory will be a necessary step in order to further advance the field and identify novel dynamic effects involving triplet Cooper pairs, both with regard to thermoelectric effects and magnetization dynamics.

Another interesting avenue to explore is the electromagnetic response of magnetic structures including superconducting elements. Ref. [131] demonstrated remotely induced magnetism mediated by a superconductor, leaving the question of how this phenomenon occurred open and thus also indicating that novel electromagnetic phenomena in superconductors may still lie undiscovered. Superconductivity is usually defined by its two hallmark properties of zero electrical resistance and the tendency to expel magnetic flux. Previous works have nanoengineered superconducting films with a lattice of magnetic dots in order to control the existence of superconductivity by the interplay of an applied field and the stray field of the dipole array of dots [133]. However, the role of odd-frequency superconductivity with regard to the electromagnetic response appears to be of crucial importance, as recently indicated by Di Bernardo *et al.* who reported an *inverse Meissner effect*, *i.e.* the enhancement of magnetic flux via a superconductor [134]. This finding is in agreement with theoretical predictions regarding how odd-frequency pairing in SF layers should influence the Meissner effect [135, 136]. Remarkably, this finding may cause us to rethink what the fundamental properties of superconductivity really are.

We have no doubt that the coming years will see a number of exciting experimental and theoretical advances with regard to the role of spin-orbit coupling and magnetization dynamics in SF structures, and thereby open up a rich new testing-ground for the further development of superconducting spintronics.

## Acknowledgements

We have benefitted from discussions and collaborations with a number of researchers, but we would like to mention in particular M. Eschrig, J. W. A. Robinson, A. Di Bernardo, A. Pal, N. Banerjee, M. Blamire,

M. Cuoco, K. Halterman, M. Amundsen, V. Risinggård, and I. Kulagina. We acknowledge funding and support via the “Outstanding Academic Fellows” programme at NTNU, the COST Action MP-1201 and the Research Council of Norway Grant numbers 205591, 216700, and 240806.

## References

1. Baibich, M.N. *et al.* Giant Magnetoresistance of (001)Fe/(001)Cr Magnetic Superlattices. *Phys. Rev. Lett.* 61, 2472, 1988.
2. Binasch, G. *et al.* Enhanced magnetoresistance in layered magnetic structures with antiferro magnetic interlayer exchange *Phys. Rev. B* 39, 4828(R), 1989.
3. Linder, J. and Robinson, J.W.A. Superconducting spintronics. *Nat. Phys.* 11, 307, 2015.
4. Huertas-Hernando, D., Nazarov, Y.V., and Belzig, W. Absolute spin-valve effect with super-conducting proximity structures. *Phys. Rev. Lett.* 88, 047003, 2002.
5. Fominov, Y.V. *et al.* Superconducting triplet spin valve. *JETP Lett.* 91, 308–313, 2010.
6. Slonczewski, J.C. Mechanism of interlayer exchange in magnetic multilayers. *J. Magn. Magn. Mater.* 126, 374, 1993.
7. Slonczewski, J.C. Current-driven excitation of magnetic multilayers. *J. Magn. Magn. Mater.* 159, L1–L7, 1996.
8. Kamerlingh Onnes, H. The resistance of pure mercury at helium temperatures. *Commun. Phys. Lab. Univ. Leiden* 12, 120, 1911.
9. Meissner, W. and Ochsenfeld, R. Ein neuer Effekt bei Eintritt der Supraleitfähigkeit. *Natur-wissenschaften* 21(44): 787–788, 1933.
10. Meservey, R., Tedrow, P.M. and Fulde, P. Magnetic Field Splitting of the Quasiparticle States in Superconducting Aluminium Films. *Phys. Rev. Lett.* 25, 1270, 1970.
11. Tedrow, P. M. & Meservey, R. Spin-dependent tunneling into ferromagnetic nickel. *Phys. Rev. Lett.* 26, 192–195, 1971.
12. Tedrow, P. M. & Meservey, R. Spin polarization of electrons tunneling from films of Fe, Co, Ni, and Gd. *Phys. Rev. B* 7, 318–326, 1973.
13. Tedrow, P. M. & Meservey, R. Spin-polarized electron tunneling. *Phys. Rep.* 238, 173–243, 1994.
14. Johnson, M. & Silsbee, R. H. Interfacial charge-spin coupling: Injection and detection of spin magnetization in metals. *Phys. Rev. Lett.* 55, 1790–1793, 1985.
15. Li, B. *et al.* Superconducting spin switch with infinite magnetoresistance induced by an internal exchange field. *Phys. Rev. Lett.* 110, 097001, 2013.
16. Yang, H., Yang, S-H., Takahashi, S., Maekawa, S. & Parkin, S. S. P. Extremely long quasiparticle spin lifetimes in superconducting aluminium using MgO tunnel spin injectors. *Nature Mater.* 9, 586–593, 2010.

17. Quay, C. H. L., Chevallier, D., Bena, C. & Aprili, M. Spin imbalance and spin-charge separation in a mesoscopic superconductor. *Nature Phys.* 9, 84–88, 2013.
18. Wakamura, T., Omori, Y., Niimi, Y., Takahashi, S., Fujimaki, A., Maekawa, S. & Otani, Y. Quasiparticle-mediated spin Hall effect in a superconductor. *Nature Materials* 14, 675–678, 2015.
19. Kolenda, S., Wolf, M. J., and Beckmann, D. Observation of thermoelectric currents in high-field superconductor-ferromagnet tunnel junctions. *Phys. Rev. Lett.* 116, 097001, 2016.
20. Bardeen, J., Cooper, L.N. and Schrieffer, J.R. Microscopic Theory of Superconductivity. *Phys. Rev.* 106, 162, 1957.
21. Bogoliubov, N.N. A new method in the theory of superconductivity I. *Soviet Phys. JETP* 34, 41, 1958.
22. Drozdov, A.P. *et al.* Conventional superconductivity at 203 kelvin at high pressures in the sulfur hydride system. *Nature* 525, 73, 2015.
23. Nagamatsu, J. *et al.* Superconductivity at 39 K in magnesium diboride. *Nature* 410, 63, 2001.
24. Bednorz, J.G. and Müller, K.A. Possible high  $T_c$  superconductivity in the Ba-La-Cu-O system. *Z. Physik*, B. 64(1), 189, 1986.
25. Cooper, L.N. Bound electron pairs in a degenerate Fermi gas. *Phys. Rev.* 104(1), 1189, 1956.
26. Loram, J. W., Mirza, K. A., Cooper, J. R., and Liang, W. Y. Electronic specific heat of  $\text{YBa}_2\text{Cu}_3\text{O}_{6+x}$  from 1.8 to 300 K. *Phys. Rev. Lett.* 71, 1740, 1993.
27. Tinkham, M. *Introduction to Superconductivity*, (McGraw-Hill, 1996), 2nd Edition.
28. Sudbø, A. and Fossheim, K. *Superconductivity: Physics and Applications*. Wiley, 2004.
29. Bergeret, F.S., Volkov, A.F. and Efetov, K.B. Odd triplet superconductivity and related phenomena in superconductor-ferromagnet structures. *Rev. Mod. Phys.* 77(4), 1321, 2005.
30. Buzdin, A.I. Proximity effects in superconductor-ferromagnet heterostructures. *Rev. Mod. Phys.* 77(3), 935, 2005.
31. Fulde, P. and Ferrell, R.A. Superconductivity in a strong spin-exchange field. *Phys. Rev.* 135, A550, 1964.
32. Larkin, A.I. and Ovchinnikov, Y.N. Nonuniform state of superconductors. *Sov. Phys. JETP* 20, 762, 1965.
33. Eschrig, M. Spin-polarized supercurrents for spintronics. *Phys. Today*. 64, 43, 2011.
34. Saxena, S.S. *et al.* Superconductivity on the border of itinerant-electron ferromagnetism in  $\text{UGe}_2$ . *Nature (London)* 406, 587, 2000.
35. Aoki, D. *et al.* Coexistence of superconductivity and ferromagnetism in URhGe. *Nature (London)* 413, 613, 2001.
36. Bauer, E. *et al.* Heavy Fermion Superconductivity and Magnetic Order in Noncentrosymmetric  $\text{CePt}_3\text{Si}$ . *Phys. Rev. Lett.* 92, 027003, 2004.

37. Maeno, Y. *et al.* Superconductivity in a layered perovskite without copper. *Nature* 372, 532, 1994.
38. Mackenzie, A.P. and Maeno, Y. The superconductivity of  $\text{Sr}_2\text{RuO}_4$  and the physics of spin-triplet pairing. *Rev. Mod. Phys.* 75, 657, 2003.
39. Annunziata, G. *et al.* Spin-sensitive long-range proximity effect in ferromagnet/spin-triplet-superconductor bilayers. *Phys. Rev. B* 83, 060508(R), 2011.
40. Bergeret, F. S., Volkov, A. F. & Efetov, K. B. Long-Range Proximity Effects in Superconductor-Ferromagnet Structures. *Phys. Rev. Lett.* 86, 4096, 2001.
41. Kadigrobov, A., Shekhter, R. and Jonson, M. Quantum spin fluctuations as a source of long-range proximity effects in diffusive ferromagnet-superconductor structures. *Europhys. Lett.* 54, 394, 2001.
42. Eschrig, M., Kopu, J., Cuevas, J.C. and Schön, G. Theory of half-metal/superconductor heterostructures. *Phys. Rev. Lett.* 90, 137003, 2003.
43. Yokoyasu, T., Sauls, J.A. and Rainer, D. Proximity effect of a ferromagnetic insulator in contact with a superconductor. *Phys. Rev. B* 38, 8823, 1988.
44. Halterman, K., Barsic, P.H. and Valls, O.T. Odd triplet pairing in clean superconductor/ferromagnet heterostructures. *Phys. Rev. Lett.* 99, 127002, 2007.
45. Cottet, A. Inducing odd-frequency triplet superconducting correlations in a normal metal. *Phys. Rev. Lett.* 107, 177001, 2011.
46. Asano, Y., Sawa, Y., Tanaka, Y. and Golubov, A.A. Odd-frequency pairs and Josephson current through a strong ferromagnet. *Phys. Rev. B* 76, 224525, 2007.
47. Kalcheim, Y. *et al.* Magnetic field dependence of the proximity-induced triplet superconductivity at ferromagnet/superconductor interfaces. *Phys. Rev. B* 89, 180506(R), 2014.
48. Robinson, J.W.A., Witt, J.D., and Blamire, M. Controlled injection of spin-triplet supercurrents into a strong ferromagnet. *Science* 329, 59, 2010.
49. Khaire, T.S. *et al.* Observation of spin-triplet superconductivity in Co-based Josephson Junctions. *Phys. Rev. Lett.* 104, 137002, 2010.
50. Alidoust, M. and Linder, J. Spin-triplet supercurrent through inhomogeneous ferromagnetic trilayers. *Phys. Rev. B* 82, 224504, 2010.
51. Sperstad, I.B., Linder, J. and Sudbø, A. Josephson current in diffusive multilayer superconductor/ferromagnet/superconductor junctions *Phys. Rev. B* 78, 104509, 2008.
52. Trifunovic, L. and Radović, Z. Long-range spin-triplet proximity effect in Josphson junctions with multilayered ferromagnets. *Phys. Rev. B* 82, 020505(R), 2010.
53. Sosnin, I., Cho, H., Petrushov, V.T. and Volkov, A.F. Superconducting phase coherent electron transport in proximity conical ferromagnets. *Phys. Rev. Lett.* 96, 157002, 2006.
54. Shomali, Z., Zareyan, M. and Belzig, W. Spin supercurrent in Josephson contacts with noncollinear ferromagnets. *New J. Phys.* 13, 083033, 2011.
55. Gomperud, I. and Linder, J. Spin supercurrent and phase-tunable triplet Cooper pairs via magnetic insulators. *Phys. Rev. B* 92, 035416, 2015.

56. Bergeret, F.S. and Tokatly, I.V. Singlet-triplet conversion and the long-range proximity effect in superconductor-ferromagnet structures with generic spin dependent fields. *Phys. Rev. Lett.* 110, 117003, 2013.
57. Bergeret, F.S. and Tokatly, I.V. Spin-orbit coupling as a source of long-range triplet proximity effect in superconductor-ferromagnet hybrid structures. *Phys. Rev. B* 89, 134517, 2014.
58. Jacobsen, S.H., Ouassou, J.A. and Linder, J. Critical temperature and tunneling spectroscopy of superconductor-ferromagnet hybrids with intrinsic Rashba-Dresselhaus spin-orbit coupling. *Phys. Rev. B* 92, 024510, 2015.
59. Jacobsen, S.H. and Linder, J. Giant triplet proximity effect in  $\pi$ -biased Josephson Junctions with spin-orbit coupling. *Phys. Rev. B* 92, 024501, 2015.
60. Andreev, A.F. Thermal conductivity of the intermediate state of superconductors. *Sov. Phys. JETP* 19, 1228, 1964.
61. Josephson, B.D. Possible new effects in superconductive tunnelling. *Phys. Lett.* 1, 251, 1962.
62. Josephson, B.D. The discovery of tunnelling supercurrents. *Rev. Mod. Phys.* 46(2), 251, 1974.
63. Golubov, A.A., Kupriyanov, M.Yu. and Il'ichev, E. The current-phase relation in Josephson junctions. *Rev. Mod. Phys.* 76(2), 411, 2004.
64. Kontos, T. *et al.* Inhomogeneous superconductivity induced in a ferromagnet by proximity effect. *Phys. Rev. Lett.* 86, 304, 2001.
65. Hummel, R.E. *Electronic Properties of Materials*, Springer, New York, 2011, 4th Edition.
66. Tanaka, Y. and Golubov, A.A. Theory of the Proximity Effect in Junctions with Unconventional Superconductors. *Phys. Rev. Lett.* 98, 037003, 2007.
67. SanGiorgio, P. *et al.* Anomalous Double Peak Structure in Superconductor/Ferromagnet Tunneling Density of States. *Phys. Rev. Lett.* 100, 237002, 2008.
68. Linder, J. and Robinson, J.W.A. Strong odd-frequency correlations in fully gapped Zeeman-split superconductors. *Sci. Rep.* 5, 15483, 2015.
69. Belzig, W. *et al.* Quasiclassical Green's function approach to mesoscopic superconductivity. *Superlattices and Microstructures* 25, 1251, 1999.
70. Le Sueur, H. *et al.* Controlled Superconducting Proximity Effect Probed by Tunneling Spectroscopy. *Phys. Rev. Lett.* 100, 197002, 2008.
71. Zhou, F. *et al.* Density of States in Superconductor-Normal-Metal-Superconductor Junctions. *J. Low Temp. Phys.* 110, 841, 1998.
72. Ryazanov, V.V. *et al.* Coupling of Two Superconductors through a Ferromagnet: Evidence for a Junction. *Phys. Rev. Lett.* 86, 2427, 2001.
73. Yokoyama, T., Tanaka, Y. and Golubov, A.A. Resonant peak in the density of states in normal-metal/diffusive-ferromagnet/superconductor junctions. *Phys. Rev. B* 72, 052512, 2005.
74. Yokoyama, T., Tanaka, Y. and Golubov, A.A. Resonant proximity effect in normal metal/diffusive ferromagnet/superconductor junctions. *Phys. Rev. B* 73, 094501, 2006.

75. Kawabata, S. *et al.* Robustness of Spin-Triplet Pairing and Singlet-Triplet Pairing Crossover in Superconductor/Ferromagnet Hybrids. *J. Phys. Soc. Jpn.* 82, 124702, 2013.
76. de Gennes, P.G. *Superconductivity of Metals and Alloys*. Benjamin, New York, 1966.
77. Eilenberger, G. Transformation of Gorkov's Equation for Type II Superconductors into Transport-Like Equations. *Z. Phys.* 214, 195, 1968.
78. Usadel, K. Generalized Diffusion Equation for Superconducting Alloys. *Phys. Rev. Lett.* 25, 507, 1970.
79. Chandrasekhar, V. *An introduction to the quasiclassical theory of superconductivity for diffusive proximity-coupled systems*, book chapter in *The Physics of Superconductors: Vol. II*, Ed. K. H. Bennemann and J. B. Ketterson, Springer, Berlin, 2004.
80. Wright, M.C.M. Green function or Green's function? *Nature Physics* 2, 464, 2006.
81. Keldysh, L.V. Diagram technique for nonequilibrium processes. *Soviet Physics JETP* 20, 1018, 1965.
82. Matsubara, T. A new approach to quantum statistical mechanics. *Prog. Theor. Phys.* 14, 351, 1955.
83. Schmid, A. *Nonequilibrium Superconductivity*. Ed. K.E. Gray (Plenum, New York, 1981).
84. Rammer, J. and Smith, H. Quantum field-theoretical methods in transport theory of metals. *Rev. Mod. Phys.* 58, 323, 1986.
85. Morten, J.P. Spin and Charge Transport in Dirty Superconductors. *Norwegian University of Science and Technology*, Master thesis, 2005.
86. Maki, K. Gapless Superconductivity, in *Superconductivity*, edited by R.D. Parks, vol. 2, pages 1035–1106, Marcel Dekker, New York, 1969.
87. Ivanov, D.A. and Fominov, Ya.V. Minigap in superconductor-ferromagnet junctions with inhomogeneous magnetization. *Phys. Rev. B* 73, 214524, 2006.
88. Schopohl, N. and Maki, K. Quasiparticle spectrum around a vortex line in a d-wave superconductor. *Phys. Rev. B* 52, 490, 1995.
89. Schopohl, N. Transformation of the Eilenberger Equations of Superconductivity to a Scalar Riccati Equation. *arXiv: cond-mat/9804064*, 1998.
90. Lyuksyutov, I.F. and Pokrovsky, V.L. Ferromagnet-superconductor hybrids. *Adv. Phys.* 54, 67, 2005.
91. Blamire, M.G. and Robinson, J.W.A. The interface between superconductivity and magnetism: understanding and device prospects. *J. Phys.: Condens. Matter* 26, 453201, 2014.
92. Eschrig, M. Spin-polarized supercurrents for spintronics: a review of current progress. *Rep. Prog. Phys.* 78, 10, 2015.
93. Lüth, H. *Solid Surfaces, Interfaces and Thin Films*, (Springer, Berlin Heidelberg 2010), 5th Edition.
94. Oboznov, V. A., Bol'ginov, V. V., Feofanov, A. K., Ryazanov, V. V. & Buzdin, A. I. Thickness Dependence of the Josephson Ground States of

- Superconductor-Ferromagnet-Superconductor Junctions. *Phys. Rev. Lett.* 96, 197003, 2006.
95. Di Bernardo, A. *et al.* Signature of magnetic-dependent gapless odd frequency states at superconductor/ferromagnet interfaces. *Nat. Commun.* 6, 8053, 2015.
  96. Jaklevic, R.C. *et al.* Quantum Interference Effects in Josephson Tunneling. *Phys. Rev. Lett.* 12, 159, 1964.
  97. Silver, A.H. and Zimmerman, J.E. Quantum States and Transitions in Weakly Connected Superconducting Rings. *Phys. Rev.* 157, 317, 1967.
  98. Sternickel, K. and Braginski, A.I. Biomagnetism using SQUIDs: Status and perspectives. *Supercond. Sci. Technol.* 19, S160, 2006.
  99. Cleuziou, J.-P. *et al.* Carbon nanotube superconducting quantum interference device. *Nat. Nanotech.* 1, 53, 2006.
  100. Foley, C.P. and Hilgenkamp, H. Why NanoSQUIDs are important: an introduction to the focus issue. *Supercond. Sci. Technol.* 22, 064001, 2009.
  101. Vasyukov, D. *et al.* A scanning superconducting quantum interference device with single electron spin sensitivity. *Nature Nanotech.* 8, 639, 2013.
  102. Kimura, T *et al.* Room-Temperature Reversible Spin Hall Effect. *Phys. Rev. Lett.* 98, 156601, 2007.
  103. Hübler, F., Wolf, M.J., Beckmann, D. and v. Löhneysen, H. Long-Range Spin-Polarized Quasiparticle Transport in Mesoscopic Al Superconductors with a Zeeman Splitting. *Phys. Rev. Lett.* 109, 207001, 2012.
  104. Sprungmann, D., Westerholt, K., Zabel, H., Weides, M. and Kohlstedt, H. Evidence for triplet superconductivity in Josephson junctions with barriers of the ferromagnetic Heusler alloy Cu<sub>2</sub>MnAl. *Phys. Rev. B* 82, 060505(R), 2010.
  105. Keizer, R.S., Goennenwein, S.T.B., Klapwijk, T.M., Miao, G., Xiao, G. and Gupta, A. A spin triplet supercurrent through the half-metallic ferromagnet CrO<sub>2</sub>. *Nature* 439, 825, 2006.
  106. Eschrig, M. & Löfwander, T. Triplet supercurrents in clean and disordered half-metallic ferromagnets. *Nature Physics* 4, 138, 2008.
  107. Martinez, W., Pratt, Jr., W.P., Birge, N.O. Amplitude control of spin-triplet supercurrent in S/F/S Josephson junctions. *Phys. Rev. Lett.* 116, 077001, 2016.
  108. Kalcheim, Y., Millo, O., Di Bernardo, A., Pal, A. and Robinson, J.W.A. Inverse proximity effect at superconductor-ferromagnet interfaces: Evidence for induced triplet pairing in the superconductor. *Phys. Rev. B* 92, 060501(R), 2015.
  109. Leksin, P. V., Garif'yanov, N. N., Garifullin, I. A., Fominov, Ya. V., Schumann, J., Krupskaya, Y., Kataev, V., Schmidt, O. G., and Buchner. Evidence for Triplet Superconductivity in a Superconductor-Ferromagnet Spin Valve. *Phys. Rev. Lett.* 109, 057005, 2012.
  110. Jara, A. A., Safranski, C., Krivorotov, I., Wu, C.-T., Malmi-Kakkada, A. N., Valls, O. T., and Halterman. K. Angular dependence of superconductivity in superconductor/spin-valve heterostructures. *Phys. Rev. B* 89, 184502, 2014.

111. Wang, X. L., Di Bernardo, A., Banerjee, N., Wells, A., Bergeret, F. S., Blamire, M. G. & Robinson, J. W. A. Giant triplet proximity effect in superconducting pseudo spin valves with engineered anisotropy. *Phys. Rev. B* 89, 140508(R), 2014.
112. Banerjee, N., Smiet, C. B., Ozaeta, A., Bergeret, F. S., Blamire, M. G., and Robinson, J. W. A. Evidence for spin-selectivity of triplet pairs in superconducting spin-valves. *Nature Communications* 5, 3048, 2014.
113. Gu, J. Y., You, C.-Y., Jiang, J. S., Pearson, J., Bazaliy, Ya. B., and Bader, S. D. Magnetization-Orientation Dependence of the Superconducting Transition Temperature in the Ferromagnet-Superconductor-Ferromagnet System: CuNi/Nb/CuNi. *Phys. Rev. Lett.* 89, 267001, 2002.
114. Moraru, I. C., Pratt Jr., W. P., and Birge, N. O. Magnetization-Dependent  $T_c$  Shift in Ferromagnet/Superconductor/Ferromagnet Trilayers with a Strong Ferromagnet. *Phys. Rev. Lett.* 96, 037004, 2006.
115. Singh, A., Voltan, S., Lahabi, K. and Aarts, J. Colossal Proximity Effect in a Superconducting Triplet Spin Valve Based on the Half-Metallic Ferromagnet CrO<sub>2</sub>. *Phys. Rev. X* 5, 021019, 2015.
116. Robinson, J.W.A. Viewpoint: A Boost for Superconducting Logic. *Physics* 8, 49, 2015.
117. Machon, P., Eschrig, M. and Belzig, W. Nonlocal Thermoelectric Effects and Nonlocal Onsager relations in a Three-Terminal Proximity-Coupled Superconductor-Ferromagnet Device. *Phys. Rev. Lett.* 110, 047002, 2013.
118. Ozaeta, A., Virtanen, P., Bergeret, F.S. and Heikkilä, T.T. Predicted Very Large Thermoelectric Effect in Ferromagnet-Superconductor Junctions in the Presence of a Spin-Splitting Magnetic Field. *Phys. Rev. Lett.* 112, 057001, 2014.
119. Rugar, D. *et al.* Single spin detection by magnetic resonance force microscopy. *Nature* 430, 329, 2004.
120. Grinolds, M.S. *et al.* Nanoscale magnetic imaging of a single electron spin under ambient conditions. *Nature Phys.* 9, 215, 2013.
121. Wang, J. *et al.* Interplay between superconductivity and ferromagnetism in crystalline nanowires. *Nature Phys.* 6, 389, 2010.
122. Melnikov, A.S. and Buzdin, A.I., Giant Mesoscopic Fluctuations and Long-Range Superconducting Correlations in Superconductor-Ferromagnet Structures, *Phys. Rev. Lett.* 117, 077001, 2016.
123. Geschkenbein, V.B. and Larkin, A.I. The Josephson effect in superconductors with heavy fermions. *JETP Lett.* 43, 395, 1986 [*Pis'ma Zh. Eksp. Teor. Fiz.* 43, 306, 1986].
124. Yip, S. Josephson current-phase relationships with unconventional superconductors. *Phys. Rev. B* 52, 3087, 1995.
125. Sigrist, M. Time-reversal symmetry breaking states in high-temperature superconductors. *Prog. Theor. Phys.* 99, 899, 1998.
126. Buzdin, A. Direct coupling between magnetism and superconducting current in the Josephson  $\phi_0$  junction. *Phys. Rev. Lett.* 101, 107005, 2008.

127. Bergeret, F.S. and Tokatly, I.V. Theory of diffusive  $\phi_0$  Josephson junctions in the presence of spin-orbit coupling. *Euro. Phys. Lett.* 110, 57005, 2015.
128. Szombati, D.B., Nadj-Perge, S., Car, D., Plissard, S.R., Bakkers, E.P.A.M. and Kouwenhoven, L.P. Josephson  $\phi_0$ -junction in nanowire quantum dots. *Nature Physics* 12, 568–572, 2016.
129. Jacobsen, S.H., Kulagina, I. and Linder, J. Controlling superconducting spin flow with spin-flip immunity using a single homogeneous ferromagnet. *Sci. Rep.* 6, 23926, 2016.
130. Hikino, S. and Yunoki, S. Magnetization induced by odd-frequency spin-triplet Cooper pairs in a Josephson junction with metallic trilayers. *Phys. Rev. B* 92, 024512, 2015.
131. Flokstra, M.G. *et al.* Remotely induced magnetism in a normal metal using a superconducting spin-valve. *Nat. Phys.* 12, 57–61, 2016.
132. Ganichev, S.D. *et al.* Experimental Separation of Rashba and Dresselhaus Spin Splittings in Semiconductor Quantum Wells. *Phys. Rev. Lett.* 92, 256601, 2004.
133. Lange, M., van Bael, M.J., Bruynseraede, Y. and Moshchalkov, V.V. Nanoengineered Magnetic-Field-Induced Superconductivity. *Phys. Rev. Lett.* 90, 197006, 2003.
134. Di Bernardo, A. *et al.* Intrinsic paramagnetic Meissner effect due to *s*-wave odd frequency superconductivity. *Phys. Rev. X* 5, 041021, 2015.
135. Yokoyama, T., Tanaka, Y. and Nagaosa, N. Anomalous Meissner Effect in a Normal-Metal-Superconductor Junction with a Spin-Active Interface. *Phys. Rev. Lett.* 106, 246601, 2011.
136. Mironov, S., Mel'nikov, A. and Buzdin, A. Vanishing Meissner effect as a Hallmark of in-Plane Fulde-Ferrell-Larkin-Ovchinnikov Instability in Superconductor-Ferromagnet Layered Systems. *Phys. Rev. Lett.* 109, 237002, 2012.

# Magnetic Antiresonance in Nanocomposite Materials

Anatoly B. Rinkevich\*, Dmitry V. Perov and Olga V. Nemytova

*M.N. Miheev Institute of Metal Physics of Ural Branch of Russian Academy of Sciences, Ekaterinburg, Russia*

---

## Abstract

The magnetic antiresonance phenomenon occurs when the real part of effective permeability becomes equal to zero. At that in the antiresonance point, the imaginary part of effective permeability has little value. As a rule, the magnetic antiresonance has been studied in thin ferromagnetic metal films. Provided antiresonance, a pronounced maximum of passing of microwave field through the film is typically observed. In this chapter, the magnetic antiresonance in nanocomposite media is studied. Besides the metal films, massive inhomogeneous media, such as the lanthanum manganite, the antiresonance can occur in the nanocomposite materials with the particles of ferromagnetic and ferrimagnetic substances. It is experimentally shown in the chapter that the antiresonance is observed in the nanocomposite media on the basis of opal matrixes. The phenomenon occurs in the nanocomposites not only with the particles of transition metals but also with the particles of dielectrics such as ferrite spinels and ferrite garnets.

**Keywords:** Magnetic antiresonance, magnetic resonance, nanocomposite, microwave magnetic fields, opal matrix, permeability

## 2.1 Introduction: Phenomenon of Magnetic Antiresonance

There are frequencies in multi-degree-of-freedom systems at which a dynamic force applied at a point does not cause any motion of the system at that point. In general, these frequencies are known as antiresonances.

---

\*Corresponding author: rin@imp.uran.ru

Provided antiresonance, the input impedance of given system is very high. A generally known example of antiresonance is an electric circuit consisting of a capacitor and a coil in parallel. Antiresonance occurs when a voltage of alternating-current line and a resultant current are in phase. Upon these conditions, the line current is very small because of high impedance of the parallel circuit at antiresonance. The branch currents are almost equal in magnitude and opposite in phase. The *magnetic* antiresonance phenomenon occurs when the real part of effective permeability becomes equal to zero. At that in the antiresonance point, the imaginary part of effective permeability has small value. For the first time, the antiresonance minimum was observed by Yager [1] when investigating a surface impedance of thin film of supermalloy. When changing a magnetic field provided the antiresonance a surface impedance of metal has a minimum. The theory of magnetic antiresonance is developed in [2]. The surface impedance of ferromagnetic metal film is calculated taking into account boundary conditions for a magnetization, as well as the shape of line of the magnetic antiresonance is calculated.

As a rule, the magnetic antiresonance has been studied in thin ferromagnetic metal films. The antiresonance condition does not depend on the direction of magnetization and has the form [3]:

$$\omega_{FMAR} = \omega_M + \omega_H \quad (2.1)$$

where  $\omega_{FMAR}$  is the ferromagnetic antiresonance frequency (FMAR),  $\omega_M = \gamma 4\pi M_0$ ,  $\gamma$  is the magnetomechanical ratio,  $M_0$  is the saturation magnetization of the film, and  $H_0$  is the external magnetic field. It is seen from (2.1) that the antiresonance can be observed only at frequencies  $\omega > \omega_M$ .

This chapter is schemed in the following way. Next section is a brief overview of publications devoted to the magnetic antiresonance. The works are devoted not only to thin films. Other media – heterogeneous and nanocomposite – will be also considered. Furthermore, in Section 2.3, brief information about a method of samples preparation, their structure, and phase composition is described. Then, the results of microwave measurements are presented. In Section 2.4, a specificity of observation of magnetic antiresonance when placing a sample in waveguide or resonator is illuminated. Next, in Section 2.5, examples of observation of magnetic antiresonance in nanocomposite media based on the opal matrix with particles of different materials are outlined. In Section 2.6, the conditions of magnetic antiresonance observation in nanocomposite plate which is non-conducting on DC are analyzed. Magnetic field dependence of transmission and reflection coefficients and frequency dependence of resonance

amplitude are considered in Sections 7 and 8, respectively. Finally, in Section 2.9, the examples of magnetic antiresonance observation upon the different orientations of constant and microwave magnetic fields are adduced. The basic features of magnetic antiresonance in nanocomposite media are summarized in the Conclusion section.

## 2.2 Magnetic Antiresonance Review

The works of B. Heinrich and his co-authors [4–6] play the important part in an experimental investigation of antiresonance in metal films. A method of experimental investigation was proposed in [4] where a metal film covers a coupling hole between two hollow cavities which are tuned to the same frequency. Provided antiresonance, a pronounced maximum of passing the microwave field through the film is observed. The maximum occurs due to the sharp increasing of skin depth when the real part of effective permeability becomes equal to zero. After this work, the maximum of transmitted electromagnetic power has been considered as a main feature of antiresonance.

Measurements of the antiresonance field and the shape of line in permalloy are reported in [5] for various values of frequency, temperature, and thickness of sample. The magnetic field dependence of microwave signal transmitted through a ferromagnetic plate is calculated in the antiresonance region. Optimum values of the sample thickness for the determination of the spin–spin relaxation time are found for ferromagnetic metals. The angular dependence of antiresonance transmission of microwave radiation through metallic ferromagnetic specimens has been studied in [6, 7]. It was found experimentally that rotation of the field gives a transmission signal having a double peak. That observation is inconsistent with the simple theory of antiresonance transmission which neglects the exchange interaction between spins. Several material constants could be extracted from investigation of magnetic antiresonance. The magnetic field dependence of the transmission of GHz radiation through ferromagnetic plates of supermalloy has been investigated in paper [8]. The results of the measurements on supermalloy discs resulted in the average values g-factor and a damping parameter. Transmission studies carried out on specimens thick of which is compared to the skin depth are very useful for obtaining the magnetic damping parameter and magnetostatic parameters. These parameters for nickel and permalloy single crystals were obtained in paper [9]. The microwave transmission experiments through the pure iron plate at high frequency of 73 GHz are carried out in [10]. Magnetic attenuation

parameter is investigated over the temperature range 140–300 K. At room temperature, the results are consistent with the accepted value of the attenuation parameter for iron of  $G = 0.7 \cdot 10^8$  Hz. The damping increases when reducing the temperature and reaches a value of approximately  $1.4 \cdot 10^8$  Hz at 140 K.

The calculations of resonance phenomena were carried out based on the theory developed in [11]. Analytical expressions for the surface impedance are obtained in [12]. In the same work, numerical calculations in the cases of spins fixed and unfixed on the boundary are realized. In the case of fixed spins, the surface impedance is expressed as a sum of two components: A contribution from edge of ferromagnetic resonance line, which depends on the conductivity, and a superposition of spin-wave resonances. FMAR is studied in detail, and it is shown that this phenomenon depends mainly on phenomenological magnetic damping parameter.

Penetration of millimeter-waveband electromagnetic waves through the permalloy films under magnetic resonance and antiresonance conditions has been studied experimentally and theoretically [13]. The measurements are undertaken on the film samples from 40 to 200 nm in thickness in frequency range from 26 to 38 GHz. The magnetic resonance, antiresonance, and spin-wave resonance are observed. The resonance spectrum is reconstructed. The Gilbert damping constant is determined for series of the films. It is shown that the damping constant decreases when increasing the film thickness. The resonance line shape is calculated, and the dependences of the resonance line amplitude and width upon the experimental conditions and material parameters of the film are determined. The method developed in [14, 15] makes it possible to calculate theoretically the transmission and reflection coefficients of the electromagnetic waves passed through and reflected from the thin ferromagnetic metallic film. The calculation takes into account the exchange interaction, conductivity of the film and conditions of the spin pinning at boundaries. For close agreement with the experimental conditions in the calculation, it is assumed that the metallic film is deposited on a dielectric substrate. A set of equations is written taking into consideration all the existing waves. The transmission and reflection coefficients can be obtained from the solution of the set of equations. Computations are carried out using the material constants corresponding to permalloy films and the experimental conditions of measurements in millimeter waveband. The intervals of values of parameters have been determined where resonances of definite type are realized. If the exchange constant is relatively small and pinning of spins at the boundaries is weak, only ferromagnetic resonance is realized in the film. If the exchange constant is about  $10^{-7}$  erg cm<sup>-1</sup>, then the peaks of

spin-wave resonance are present in addition to ferromagnetic resonance, and the amplitude of spin-wave resonance peaks increases if pinning of spins at the boundaries increases. In this interval of the exchange constant values, spin-wave resonance expressed as the oscillation-type variations of the transmission coefficient is possible.

Several methods of experimental investigation of spin-wave resonance and magnetic antiresonance are known. Besides method using the conventional spectrometer of magnetic resonance, two other methods are known and successfully used. In first method, the sample of metallic film covers the coupling hole between two cavities tuned to one and the same frequency [4, 5]. This method is especially effective for investigation of electromagnetic wave transmission upon the magnetic antiresonance condition. In the second method, the sample covers the cross section of a rectangular waveguide, and the transmission coefficient modulus through the film is measured [16]. The advantage of this method is in the possibility to vary continuously the frequency of the wave. It can be applied for investigation of microwave magnetoresistive effect in metallic nanostructures besides investigation of resonance phenomena. Area of application of this method, however, is limited by the films with thickness not more than few hundred of nanometers because of sensitivity of the receiver.

Microwave absorption in bulk polycrystalline and thin-film  $\text{La}_{1-x}\text{Ba}_x\text{MnO}_3$  manganites was studied in [17]. The availability of two features at the microwave-absorption curves as a function of magnetic field was established. These features were identified as stipulated by the ferromagnetic resonance and ferromagnetic antiresonance. The surface impedance at frequencies 10 and 60 GHz in the range of metal-insulator transition was studied for thin-film  $\text{Nd}_{0.7}\text{Sr}_{0.3}\text{MnO}_3$  and bulk  $\text{La}_{1-x}\text{Sr}_x\text{MnO}_3$ ,  $\text{La}_{1-x}\text{Ba}_x\text{MnO}_3$  in [18]. The ferromagnetic antiresonance and its relation to microwave magneto-impedance in  $\text{La}_{0.7}\text{Sr}_{0.3}\text{MnO}_3$  single crystals were discussed in [19]. The antiresonance disappearance with the decrease of frequency was found in [20]. Absorption of electromagnetic waves by  $\text{La}_{0.68}\text{Y}_{0.07}\text{Ba}_{0.25}\text{MnO}_3$  and  $\text{La}_{0.67}\text{Sr}_{0.33}\text{MnO}_3$  manganites at the frequencies from 5 to 9 GHz was investigated experimentally [21]. The ferromagnetic resonance FMR and ferromagnetic antiresonance FMAR were observed as microwave absorption vs. the applied magnetic field dependences. The relative contribution of FMR and FMAR depends on the sample size, microwave frequency, and position of the sample in the resonator. The shape of the microwave absorption curves depends critically on the type of the resonator's mode and mutual orientation of the high-frequency and static magnetic fields. The applicability of the thin-film model for theoretical description of ferromagnetic resonance in bulk samples was verified.

It is shown that the FMR linewidth for bulk polycrystalline manganites is determined by two major factors: porosity and nonuniform broadening. The FMR linewidth is larger for the highest modes having the smaller lateral scale. The FMAR curve is more symmetric than the FMR one.

Magnetic antiresonance has specific features for the nanocomposite media. In principle, it could be observable even in nonconducting media. Observation of magnetic antiresonance phenomenon is reported in 3D nanocomposite based on opal packages with embedded ferrite particles [22]. Antiresonance is seen at microwave frequencies of millimeter waveband, and it results above all in a sharp maximum of the reflection coefficient of electromagnetic wave. Measurements are carried out in frequency range of 26–38 GHz with two compositions of embedded particles, namely,  $\text{Co}_{0.5}\text{Zn}_{0.5}\text{Fe}_2\text{O}_4$  and  $\text{Ni}_{0.5}\text{Zn}_{0.5}\text{Fe}_2\text{O}_4$  ferrite spinels. The reasons of physical nature of antiresonance are discussed. In paper [23], the microwave properties of nanocomposite materials obtained by embedding opal matrices (regular packing of  $\text{SiO}_2$  spheres about 250 nm in diameter) of ferrite spinel nanoparticles in the interspherical space are analyzed. It is found that the main reason for microwave changes is the magnetic resonance in a nanocomposite. In addition to the resonance, antiresonance also takes place. Antiresonance manifested itself as a minimum of absorbed power at frequencies higher than a certain frequency characteristic of the given type of ferrite particles. Antiresonance appears in the fields smaller than the resonance field. The amplitude of the reflected signal in antiresonance increases up to fourfold. The measurements are taken in frequency range from 26 to 38 GHz. The change in the moduli of transmission and reflection coefficients in the external magnetic field in a rectangular waveguide containing a nanocomposite is analyzed. The modulus of the wave transmittance through a rectangular resonator with a nanocomposite specimen is measured.

Investigations of microwave properties of Ni-based inverse ferromagnetic opal-like film with the [111] axis of the fcc structure along the normal direction to the film have been carried out in the 2–18 GHz frequency band [24]. The multiple spin-wave resonances for the magnetic field applied perpendicular to the film, i.e. along the [111] axis of this artificial crystal were observed.

Magnetic properties of magnetophotonic crystals based on opal matrices have been studied as well as their electromagnetic properties in millimeter waveband. The particles of cobalt oxide are embedded into the inter-sphere voids of the matrix [25]. After annealing in hydrogen the cobalt oxide particles transform to metallic cobalt. Magnetic field influences essentially on the microwave transmission and reflection coefficients only after annealing in hydrogen that is if the ferromagnetic phase presents in the sample. The

spectra of magnetic resonance and antiresonance are studied. Microwave properties of the 3D-nanocomposite media based on opal matrix with the metallic cobalt nanoparticles embedded have been investigated [26]. It is shown that the magnetic antiresonance is observable at frequencies of millimeter waveband along with the ferromagnetic resonance. The experimental magnetic field dependence of transmission coefficient is compared to the theoretically calculated one. The magnetic field dependence of the refraction coefficient is restored, and it is shown that on submicron scale the refraction coefficient is close to zero in weak magnetic fields.

Problem of homogenization of nanostructured media in magnetic field has been considered in paper [27]. Possibility of introduction of effective material parameters dielectric permittivity and magnetic permeability for three classes of media such as magnetic metallic nanostructures, film metal–dielectric composite media and 3D nanocomposites on the base of opal matrices has been investigated. It has been stated that the introduction of effective parameters far from magnetic resonance conditions is possible at millimeter waveband frequencies. Strict introduction of effective magnetic permeability of nanostructured media near magnetic resonance is not possible.

The complex diagonal and off-diagonal components of the effective permeability tensor were calculated for the case of a realistic 3D opal, infiltrated with  $\text{Ni}_{0.7}\text{Zn}_{0.3}\text{Fe}_2\text{O}_4$  nanoparticles [28]. First, an accurate electrodynamic effective medium permeability tensor approach is formulated. Next, Maxwell's equations were solved rigorously for the case of an interacting system of ferrite particles in the opal matrix, having a normal distribution of the ferromagnetic resonance fields.

Metamaterials based on opal matrix and containing magnetic particles are studied both experimentally and theoretically and their complex refractive coefficients at frequencies of millimeter waveband are obtained by comparing the results of calculations with the experimental data on transmission and reflection coefficients and their variations with an applied magnetic field [29]. The metamaterials under study contain metallic cobalt, nickel and iron particles, nickel–zinc ferrite and silver particles, or ferrite–garnet  $\text{Nd}_3\text{Fe}_5\text{O}_{12}$  particles. A parameter characterizing the non-uniformity of electromagnetic fields at different distances from a magnetic particle has been introduced and calculated. It is found that the nonuniformity drastically varies depending on the distance from magnetic particle and on external magnetic field.

The ferromagnetic resonance and ferromagnetic antiresonance of FeCoNi magnetic tubes created by electroplating on CuBe wire have been investigated in [30]. Important parameters such as the g-factor,

magnetization, anisotropy field, and damping parameter were obtained from the measurements. One sample, prepared by a method which entails rf-sputtering deposition of an additional FeNi layer, shows a clear ferromagnetic antiresonance.  $(\text{NiZn})\text{Fe}_2\text{O}_4$  carbon nanofiber (CNF) nanocomposites with concentrations up to 5% in volume of CNFs were prepared in [31] by traditional ceramic processing and a subsequent spark plasma sintering at 860 °C with a holding time of 1 min. Low-frequency conductivity and magnetic properties were studied. Revealing the appearance of a ferromagnetic antiresonance when a certain value of conductivity is reached due to the introduction of a conductive second-phase CNF in the ferromagnetic matrix (ferrite), thereby opening a route to induce magnetically tunable transparency in these composites.

## 2.3 Phase Composition and Structure of Nanocomposites Based on Artificial Opals

Nanocomposite materials based on artificial opals were obtained from the opal matrix with  $\text{SiO}_2$  spheres of 260–270 nm in diameter by the following procedure (see, e.g. [32]). The amorphous  $\text{SiO}_2$  is obtained by hydrolysis of ether of orthosilicic acid  $\text{Si}(\text{OC}_2\text{H}_5)_4$  with ethanol solution in the form of small branched nanoparticles. During polycondensation process, these particles turn into the amorphous silica particles of spherical shape. When settling a suspension a hydrogel containing liquid up to 50–60% precipitates. For the strengthening of opal matrices and almost total removal of water, the samples are heat-treated after drying.

The nanocomposites based on the opal matrix which contains magnetic particles are obtained by the impregnation of matrix by a precursor with the following heat treatment. During heat treatment in the interspherical areas of opal matrix, the particles with required chemical composition are created. The impregnation procedure is repeated iteratively (up to 10 times). At that, the interspherical areas of opal matrix are gradually infilled. Before the impregnation of nanoparticles, the opal matrix has a periodical structure which consists of closely packed submicron spheres. The results of X-ray diffraction (XRD) and electron microscopy point to it. The particles embedded in the interspherical voids by the impregnation with following drying consist of metal oxides. Under the subsequent heat treatment at temperatures from 500 to 700 °C the spinel structure ferrites are formed and the unstructured water is completely removed. To obtain the nanocomposite with the metal particles, the samples are annealed in the hydrogen atmosphere at temperature 600–700 °C for 7 h.

The particles of entered phases have irregular shape with sizes from 10 to 60 nm. In Figure 2.1, the structure of nanocomposite with the nanoparticles of nickel–zinc ferrite spinel  $\text{Ni}_{0.5}\text{Zn}_{0.5}\text{Fe}_2\text{O}_4$  is seen, which is obtained by the scanning electron microscope Quanta-200. The concentration of incorporated substance is about 5–15% (vol.). The structure of nanocomposite with the nanoparticles of two metals – palladium and cobalt – is shown in Figure 2.1b. When comparing Figure 2.1a and b, it should be taken into account that these figures are presented in the different scales. By the example of sample No.155/7-700 with the particles of cobalt and palladium one can explain the scheme of samples marking. First the serial number is indicated, e.g. 155. Then, after the slash the impregnations numbers are denoted (7), and finally the heat treatment temperature is shown (700 °C).

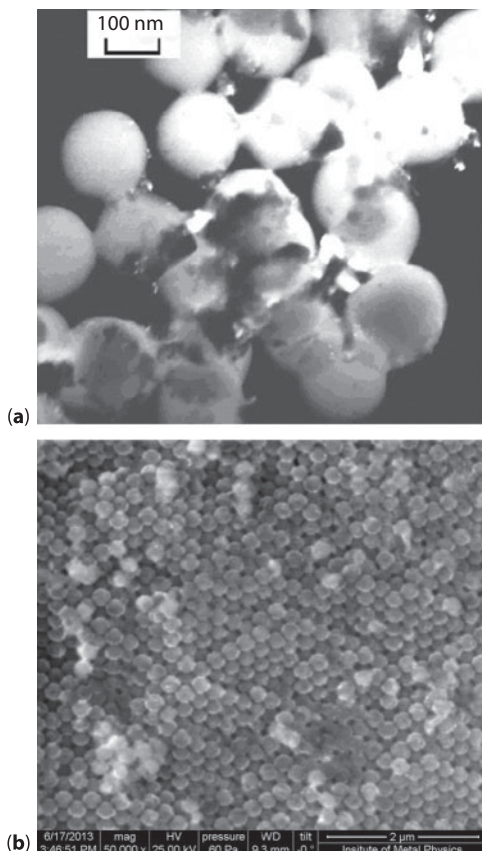


**Figure 2.1** Electron microscopic image of structure of nanocomposite based on the artificial opal with the particles of nickel–zinc ferrite spinel (a) and particles of cobalt and palladium (b).

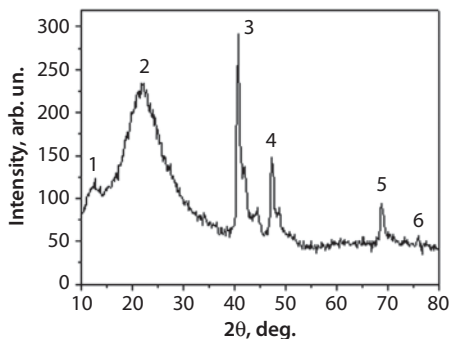


**Figure 2.2** XRD pattern of nanocomposite sample No. 155/7-700 with the particles of cobalt and palladium.

X-ray phase analysis or XRD of incorporated substance was implemented by using diffractometer DRON 3M with  $\text{CuK}_\alpha$  – radiation, flat graphite monochromator, upon rotating of sample either with the step of  $0.02^\circ$  or continuously with the rate of  $1^\circ$  per minute. XRD analysis of opal matrix sample No.155/7-700 (see Figure 2.2) with the compounds synthesized in nanovoides, based on cobalt and palladium, allows us to establish the availability of following phases (see Table 2.1): Pd – cubic syngony, Fm-3m (87-0645); Co – hexagonal syngony,  $P6_3/mmc$  (89-7373). XRD analysis of other investigated samples revealed that the magnetically ordered materials which are indicated in the sample title is basic or sole contributed substance into the opal matrix with nanoparticles.

## 2.4 Experimental Methods of the Antiresonance Investigation

For the experimental investigation of magnetic antiresonance, two techniques are used here. The first one is to placing the sample in a cross section of rectangular waveguide. The sample completely covers all waveguide's cross-section. Transmission and reflection coefficients of waves are measured [16, 33]. Using this technique, the antiresonance in the nanocomposite material was revealed [22]. The possibility of continuous changes of frequency is an advantage of this technique.

The second technique is to placing the sample inside the hollow resonator which is inserted in microwave tract through the coupling hole in transmission scheme. In this case, the transmission and reflection coefficients of waves from the resonator are measured. More precisely, in the microwave

Table 2.1 XRD data of sample No. 155/7-700.

No.	Experimental data				Pd, Co Data ICDD PDF-2			
	Intensity, arb. un.	Intensity, %	Bragg's angle 2θ, deg.	Peak half-width, deg.	Interplanar spacing d, Å	Pd - cubic syngony, Fm-3n (87-0645)	Co - hexagonal syngony, P6 <sub>3</sub> /mmc (89-7373)	
1.	164	100.00	40.407	0.423	2.2303	2.2326	111	100
2.	45	27.44	41.627	0.423	2.1677			2.1702
3.	20	12.20	43.921	0.423	2.0597		2.0355	100
4.	78	47.56	46.955	0.478	1.9334	1.9335	200	44.1
5.	18	10.98	48.381	0.478	1.8797		2.0355	002
6.	36	21.95	68.446	0.452	1.3695	1.3671	220	20.8

experiments the relative change of transmission coefficient module in the external magnetic field was measured  $d_m = [|D(H)| - |D(0)|]/|D(0)|$ , where  $|D(H)|$  is the transmission coefficient module in the magnetic field  $H$  and the reflection coefficients module  $r_m = [|R(H)| - |R(0)|]/|R(0)|$ , where  $|R(H)|$  is the reflection coefficients module.

All experiments were carried out at the room temperature. At first, let's consider the results obtained by the first technique.

#### 2.4.1 Measurements of the Transmission and Reflection Coefficients in the Waveguide

Microwave measurements were implemented in frequency range from 26 to 38 GHz by using the standard waveguide and rectangular resonators with  $TE_{10}$  mode. To perform the microwave measurements the sample was placed into the waveguide (see Figure 2.3a). At that, the long side of sample was placed across the axis of microwave path. External DC magnetic field  $\mathbf{H}$  produced by an electromagnet lies in the plane of sample either in

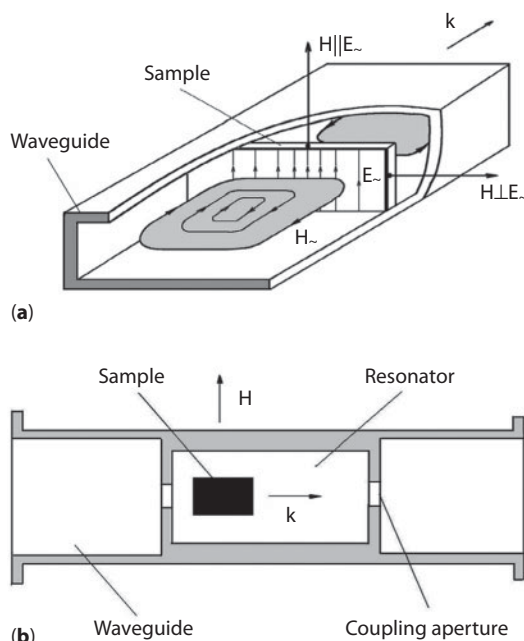


**Figure 2.3** The scheme of magnetic antiresonance observation in the transmission and reflection of waves from the sample in the waveguide (a) and upon the placement in the resonator (b).

parallel or in perpendicular with the vector of microwave electric field  $\mathbf{E}_\perp$ . In the first case, vector  $\mathbf{H}$  is in perpendicular with the plane where vector of microwave magnetic field  $\mathbf{H}_\perp$  lies,  $\mathbf{H} \perp \mathbf{H}_\perp$ . And in the second case,  $\mathbf{H}$  lies in this plane and  $\mathbf{H} \parallel \mathbf{H}_\perp$ . The results of the measurements of field dependence of reflection coefficients from the sample No.169/6-700 with the particles of iron, nickel, and palladium are shown in Figure 2.4. Reflection coefficient minimum corresponds to a homogeneous mode of magnetic resonance and is designated in Figure 2.4 as FMR. Besides the minimum, the maxima which were identified as the magnetic antiresonance in [22] still present in the dependences. The position of maxima in the figure is indicated by the arrow labeled as FMAR. Some characteristic features of antiresonance can be traced in Figure 2.4. At first, in contrast to the resonance, the magnetic antiresonance leads to maximum on the magnetic field dependence of the reflection coefficient, and sometimes on the transmission coefficient.

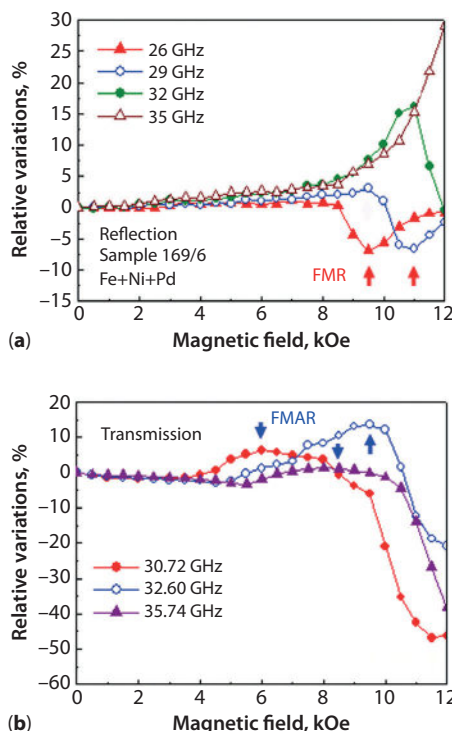


**Figure 2.4** The magnetic antiresonance upon the reflection of waves for nanocomposite No. 169/6-700 with the metal particles (a); the dependence of coefficient of wave's transmission through the resonator with the nanocomposite containing dielectric particles of nickel–zinc ferrite  $\text{Ni}_{0.5}\text{Zn}_{0.5}\text{Fe}_2\text{O}_4$  (b).

Second, the field FMAR is less than the field FMR. In the third place, there is a frequency limit of observation of FMAR. For example, it can be seen in Figure 2.4 that the antiresonance occurs at frequencies of 29 GHz and higher ones. But there is no antiresonance at lower frequency of 26 GHz. Fourthly, in Figure 2.4, the amplitude of the antiresonance increases when increasing the frequency. It is typically for antiresonance, but this rule is not universal as we shall see later. It is easily seen that all these characteristic features were previously marked for the magnetic antiresonance upon the transmission of the electromagnetic wave through a thin ferromagnetic metallic film [3, 4].

#### **2.4.2 Measurements in the Hollow Resonator**

To perform the microwave measurements in the resonator, the sample was placed into rectangular waveguide, as it is shown in Figure 2.3b. At that, the sample was placed along the axis of microwave path. The external constant magnetic field  $\mathbf{H}$  is applied in perpendicular to wave vector of wave  $\mathbf{q}$ . The results of measurements of field dependence of coefficient of waves transmission through the resonator with the nanocomposite sample which contains the particles of Ni–Zn ferrite are shown in Figure 2.4b. It should be noted that the magnetic resonance and magnetic antiresonance are observed in Figure 2.4b. Next, when placing the sample in the waveguide, the experimental results will be presented.

### **2.5 Nanocomposites where the Antiresonance is Observed in**

In this section, we present the experimental results obtained with the nanocomposites of different compositions which contains nonconductive and conductive nanoparticles. The nanocomposites with metal particles, with the particles of lanthanum–strontium manganite and particles of ferrite garnet are considered. The results for nanocomposite with the particles of ferrite spinel are shown above.

#### **2.5.1 Metallic Particles**

Let us consider the results of measurements of field dependences of transmission and reflection coefficients for the nanocomposite sample No. 155/7-700 with the metallic particles of cobalt and palladium. The field

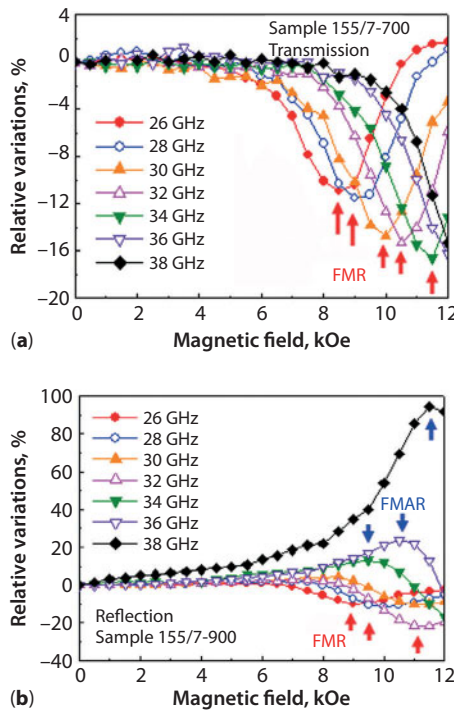


**Figure 2.5** The field dependence of changes of modules of transmission (a) and reflection coefficients (b) for the nanocomposite with the metallic particles of cobalt and palladium.

dependences of transmission coefficient, measured at the several frequencies, are shown in Figure 2.5. It can be noted (Figure 2.5) that there is resonance minimum caused by the ferromagnetic resonance for all frequencies. At that, the maximum concerned with the antiresonance is not visible. On the magnetic field dependences of reflection coefficient, which are shown in Figure 2.5b, both maxima and minima are present. So, for the nanocomposite with the particles of cobalt and palladium, the antiresonance is observed upon the reflection of wave.

### 2.5.2 Ferrite Garnet Particles

Let's consider the results of measurements of transmission and reflection coefficients for the nanocomposite with the dielectric particles of neodymium ferrite garnet (see Figure 2.6). In contrast to the previous case in this nanocomposite, both the opal matrix and entered ferrite garnet particles are dielectrics. Therefore, from the point of view of antiresonance

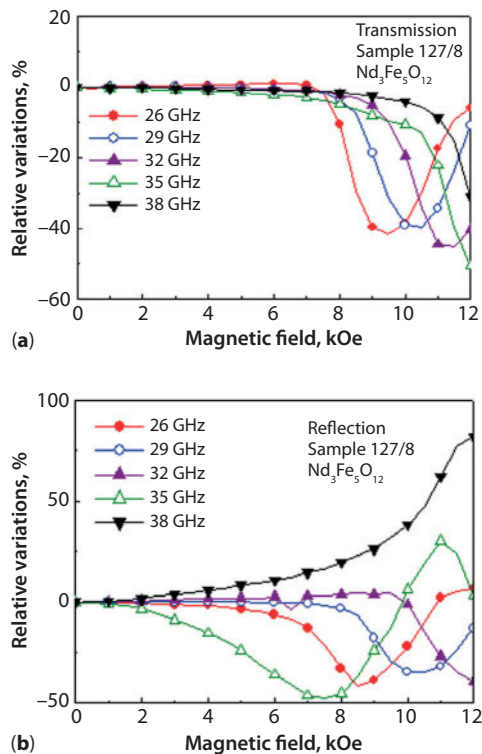


**Figure 2.6** The magnetic field dependence of changes of modules of transmission (a) and reflection coefficients (b) for the nanocomposite with the dielectric particles of neodymium ferrite garnet.

theory which is developed earlier [2, 3], there is no reason to expect the appearance of antiresonance. However, actually there is the antiresonance in reflected wave. In particular, we can see the maximum at frequency of 38 GHz. On the field dependence of transmission coefficient, there is the magnetic resonance, but the antiresonance is not visible.

### 2.5.3 Lanthanum–Strontium Manganite Particles

The magnetic field dependences of transmission (a) and reflection coefficients (b) for the nanocomposite with the particles of lanthanum–strontium manganite  $\text{La}_{0.75}\text{Sr}_{0.25}\text{MnO}_3$  are shown in Figure 2.7. Earlier, the antiresonance was observed in the bulk and powder samples of manganite [18–21]. As is well known, the conductivity of the bulk samples of lanthanum–strontium manganite is significantly less than for a typical metal. Both in the transmission and reflection of the waves, we can observe

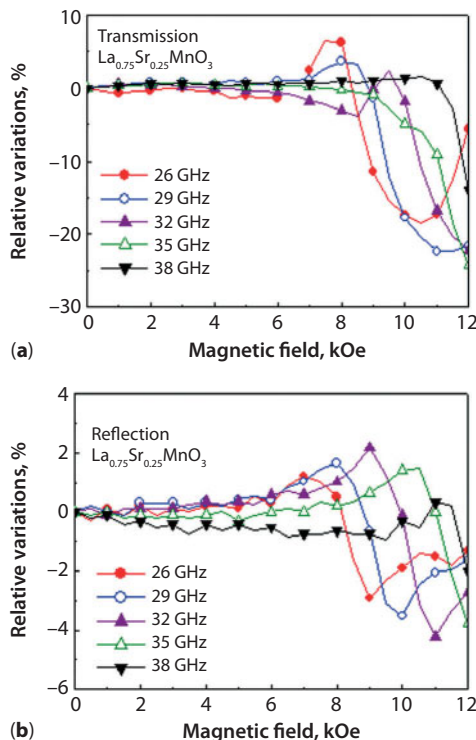


**Figure 2.7** The field dependence of changes of modules of transmission (a) and reflection coefficients (b) for the nanocomposite with the particles of lanthanum–strontium ( $\text{La}–\text{Sr}$ ) manganite.

the minimum which is caused by FMR. Also, we can see the maximum produced by the antiresonance. This maximum is observed when the values of magnetic fields are smaller than FMR field at a given frequency. Moreover, it can be seen from Figure 2.7 that, as usual, the amplitude of FMR increases when increasing the frequency. However, we can see that in this case the amplitude of FMAR decreases when increasing the frequency. The reasons of this anomaly will be discussed in next section.

## 2.6 Conditions of Magnetic Antiresonance Observation in Non-conducting Nanocomposite Plate

Let us list the characteristic feature of magnetic antiresonance which is observed experimentally in the plate made of the nanocomposite.

1. The antiresonance is observed for the nanocomposites which contain conductive (metallic particles), poorly conducting (lanthanum–strontium manganite), and nonconductive (ferrites garnet, ferrites spinel) particles.
2. The field of magnetic antiresonance is less than FMR field.
3. The magnetic antiresonance is observed only at the frequencies which exceed some fixed frequency for given material.
4. The maximum of transmission or reflection coefficient is the characteristic feature of magnetic antiresonance.
5. As a rule, the amplitude of FMAR increases when increasing the frequency. However, there is the exclusion from this rule.
6. Frequently, the antiresonance is observed in the field dependence of the reflection coefficient.

Some of these characteristic features were earlier noted for nanocomposites [22, 23]. Next, in this section, we will consider the reasons of existence of antiresonance features. According to [26], a condition of smallness of period of opal matrix structure, as well as the randomness of orientation of magnetic particles in the matrix, enables one to use a model of continuous medium which possesses of dielectric  $\epsilon_{eff}$  permittivity and magnetic  $\mu_{eff}$  permeability.

Assume that in the waveguide, only the mode  $TE_{10}$  can propagate within the considered frequency range. The length of sample along the waveguide axis is  $d$ , and the lateral dimensions of waveguide are  $a$  and  $b$ ,  $a > b$ . As it is shown in Figure 2.3a, the sample completely occupies the cross-section of waveguide. Let us consider at first the faces magnetized tangentially. Assume also that  $H_0$  is the DC magnetic field inside the sample, and  $M_0$  is the magnetization. For the calculation of reflection and transmission coefficients, it is essential that the waveguide sections have a different wave resistance: filled by the sample –  $Z_2$ , and unfilled by the sample –  $Z_1$ . The wave resistance can be expressed through the characteristic impedance  $W_1$  and  $W_2$ . Let's follow [34] to write an expression for  $TE_{10}$  mode:

$$Z_1 = \frac{\pi}{2} \frac{b}{a} W_1; Z_2 = \frac{\pi}{2} \frac{b}{a} W_2;$$

at that

$$W_1 = \frac{120\pi}{\sqrt{1 - \left(\frac{c}{2af}\right)^2}}; W_2 = \frac{120\pi \mu_{eff}}{\sqrt{\epsilon_{eff} \mu_{eff} - \left(\frac{c}{2af}\right)^2}}.$$

The wavenumber  $k$  of electromagnetic wave which propagates in the ferromagnetic medium is determined by the formula

$$\dot{k} = k' - ik'' = \frac{\omega}{c} \sqrt{\dot{\epsilon}_{eff} \dot{\mu}_{eff}}, \quad (2.2)$$

where где  $\dot{\epsilon}_{eff} = \epsilon' - i\epsilon''$  and  $\dot{\mu}_{eff} = \mu' - i\mu'$ ,  $c = \frac{1}{\sqrt{\epsilon_0 \mu_0}}$  – the speed of light in vacuum. The components of wavenumber are defined by the following equations:

$$k' = \sqrt{\frac{1}{2} \left( \sqrt{\Re^4 + \Im^4} + \Re^2 \right)}, \quad (2.3a)$$

$$k'' = \sqrt{\frac{1}{2} \left( \sqrt{\Re^4 + \Im^4} - \Re^2 \right)}, \quad (2.3b)$$

where

$$\Re = \frac{\omega}{c} \sqrt{(\epsilon'_{eff} \mu'_{eff} - \epsilon''_{eff} \mu''_{eff})} \quad (2.4)$$

and

$$\Im = \frac{\omega}{c} \sqrt{(\epsilon''_{eff} \mu'_{eff} + \epsilon'_{eff} \mu''_{eff})}. \quad (2.5)$$

In the case of magnetic conductive media we suppose that  $\dot{\epsilon}_{eff} = -i \frac{\sigma}{\omega \epsilon_0}$  and  $\dot{\mu}_{eff} = \mu$ . Then, it follows from the formulas (2.4) and (2.5) that  $\Re = 0$  and  $\Im = \frac{\omega}{c} \sqrt{\frac{\mu \sigma}{\omega \epsilon_0}} = \sqrt{\mu \mu_0 \sigma \omega}$ . Next, inserting these ratios in formula (2.3), we obtain that  $k' = k'' = \sqrt{\frac{\mu \mu_0 \sigma \omega}{2}}$ . Consequently,

$$\dot{k} = (1 - i) \cdot \sqrt{\frac{\mu \mu_0 \sigma \omega}{2}} = \frac{1 - i}{\Delta}, \quad (2.6)$$

where  $\Delta = \sqrt{\frac{2}{\mu\mu_0\sigma\omega}}$  – the skin depth.

The function of square root from a complex value is multivalued. Therefore, when finding the complex wavenumber in (2.3), it is necessary to choose the solution which corresponds to the principle of saturable absorption. According to [3], the following result is obtained:

$$k = k' - ik'' = \frac{\sqrt{|\mu_{ef}| - \mu''_{ef}} - i\sqrt{|\mu_{ef}| + \mu''_{ef}}}{\delta}. \quad (2.7)$$

Then, using notation  $\mu_{eL} = |\mu_{ef}| - \mu''_{ef}$  и  $\mu_{eR} = |\mu_{ef}| + \mu''_{ef}$ , we obtain the formula (2.8):

$$k = k' - ik'' = \frac{\sqrt{\mu_{eL}} - i\sqrt{\mu_{eR}}}{\delta}. \quad (2.8)$$

The effective permittivity and permeability are expressed through the tensor components of effective material constants of permittivity  $\hat{\epsilon}$  and permeability  $\hat{\mu}$ . Below the type of permittivity and permeability for the selected orientation of fields upon the propagation of wave of  $TE_{10}$  type is shown. The wavenumber, impedances  $Z_1$  and  $Z_2$ , and ratio of these impedances  $\xi = Z_2/Z_1$  depend on the strength of the external magnetic field. When  $\mathbf{H} \perp \mathbf{H}_0$ , where  $\mathbf{H}$  is the vector of intensity of constant field, and  $\mathbf{H}_0$  is the vector of intensity of high-frequency magnetic field, the wavenumber in the section of the waveguide with the sample is calculated by the following formula:

$$k_2 = \sqrt{\left(\frac{\omega}{c}\right)^2 \epsilon_{||} \mu_{\perp} - \left(\frac{\pi}{a}\right)^2}. \quad (2.9)$$

In formula (2.9),  $\epsilon_{||}$  is a component  $\epsilon_{33}$  of permittivity tensor and  $\mu_{\perp}$  is expressed through the diagonal component  $\mu$  and off-diagonal component  $\mu_a$  of tensor  $\hat{\mu}$  in the following way

$$\mu_{\perp} = \mu - \frac{\mu_a^2}{\mu}. \quad (2.10)$$

Let's express the permeability tensor components through susceptibilities:  $\mu = 1 + 4\pi\chi$ ,  $\mu_a = 4\pi\chi_a$ , and  $\mu_{||} = 1 + 4\pi\chi_{||}$ . In the simplest case of Lorentz-type expressions for the susceptibilities, we have

$$\begin{aligned}\chi &= \chi' - i\chi'' \\ &= \gamma M m_F \frac{\omega_H [\omega_H^2 - (1 - \alpha^2)\omega^2] - i\alpha\omega[\omega_H^2 + (1 + \alpha^2)\omega^2]}{D},\end{aligned}\quad (2.11a)$$

$$\chi_a = \chi'_a - i\chi''_a = \gamma M_0 m_F \omega \frac{[\omega_H^2 - (1 + \alpha^2)\omega^2] - i2\alpha\omega\omega_H}{D},\quad (2.11b)$$

$$\chi_{||} = -\frac{i\alpha\gamma m_F M_0}{\omega - i\alpha\omega_H},\quad (2.11c)$$

Where  $D = [\omega_H^2 - (1 + \alpha^2)\omega^2]^2 + 4\alpha^2\omega^2\omega_H^2$ ,  $\omega_H = \gamma H_0$ ,  $m_F$  is the mass share of ferromagnetic phase in the nanocomposite.

The frequency dependences of real and imaginary parts of effective permeability calculated by formulas (2.10) and (2.11) for the nanocomposite with the particles of nickel-zinc ferrite spinel  $\text{Ni}_{0.5}\text{Zn}_{0.5}\text{Fe}_2\text{O}_4$  are shown in Figure 2.8.

In the following experimental part of this chapter, FMR and antiresonance in the samples of plate form which are magnetized in the plane of plate are discussed. The following conditions for FMR and FMAR are valid for the part of samples magnetized tangentially [3]:

$$\omega_R = \gamma [H_0(H_0 + 4\pi M_0)]^{1/2}, \quad (\text{FMR}),\quad (2.12a)$$

$$\omega_{AR} = \gamma B_0, \quad (\text{FMAR}),\quad (2.12b)$$

where  $\omega_R$  and  $\omega_{AR}$  are the frequencies of magnetic resonance and antiresonance, respectively;  $B_0$  and  $H_0$  are the permanent induction and magnetic field inside the sample, respectively.

Upon small dissipation at the antiresonance point  $(\mu_{ef}''')_{\text{FMAR}} = \alpha\omega/\omega_M$   $\alpha$  is the dimensionless Gilbert damping constant. A width of antiresonance lines is a distance between points where  $\mu_{ef}''' = 2(\mu_{ef}''')_{\text{FMAR}}$ . The width of antiresonance lines  $\Delta H_{\text{FMAR}}$  is equal to the width of FMR line, namely,  $2\alpha\omega/\gamma$ . According to [23], the complex transmission  $D$  and reflection  $R$  coefficients are expressed by following formulas:

$$D = \frac{1}{\operatorname{ch}\beta_2 d + \frac{1}{2}(\xi + \xi^{-1})\operatorname{sh}\beta_2 d},\quad (2.13)$$

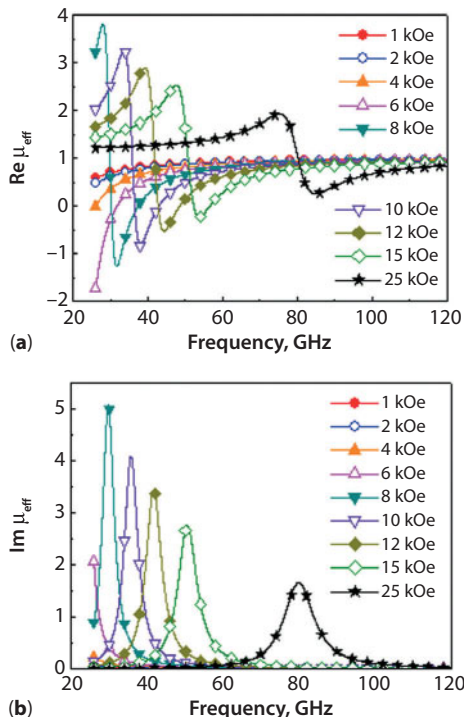


**Figure 2.8** The frequency dependences of real (a) and imaginary (b) parts of effective permeability, calculated by formulas (2.10) and (2.11) for the nanocomposite with the particles of nickel–zinc ferrite spinel  $\text{Ni}_{0.5}\text{Zn}_{0.5}\text{Fe}_2\text{O}_4$ .

$$R = \frac{\frac{1}{2}(\xi - \xi^{-1}) \operatorname{sh} \beta_2 d}{\operatorname{ch} \beta_2 d + \frac{1}{2}(\xi + \xi^{-1}) \operatorname{sh} \beta_2 d}, \quad (2.14)$$

where  $\xi = Z_2/Z_1$  is the ratio of impedances of filled and unfilled sections of waveguide.

The view of frequency dependences of transmission and reflection coefficients is determined by several factors. Far from the conditions of magnetic resonance and antiresonance under the conditions where the real part of material constants is significantly more than imaginary part, the points of maxima and minima on the frequency dependences of coefficients which are close to the conditions for a quarter- and half-wave plate. However, near the magnetic resonance and upon the frequencies

which are inside the interval between FMR and FMAR, the real part of effective permeability is negative. This fact very strongly effects on the view of frequency dependence of coefficients. The frequency dependences of transmission and reflection coefficients, which are calculated in the fields of different intensity for the nanocomposite with the particles of nickel–zinc ferrite spinel  $\text{Ni}_{0.5}\text{Zn}_{0.5}\text{Fe}_2\text{O}_4$  are shown in Figure 2.9. The calculation is carried out by formulas (2.13) and (2.14), and the effective permeability is calculated by formulas (2.10), (2.11), and shown in Figure 2.8. It can be seen from Figure 2.9 that the ratio between the maxima and minima in the frequency dependences of coefficients is absolutely different upon the different values of magnetic field. Thus, in the field of 8 kOe the transmission coefficient varies from 0.02 to 0.56, and in the field of 25 kOe the transmission coefficient is from 0.59 to 0.7. As even upon the positive real part of permeability the frequency dependence of coefficients has an oscillatory view, the peculiarities which are

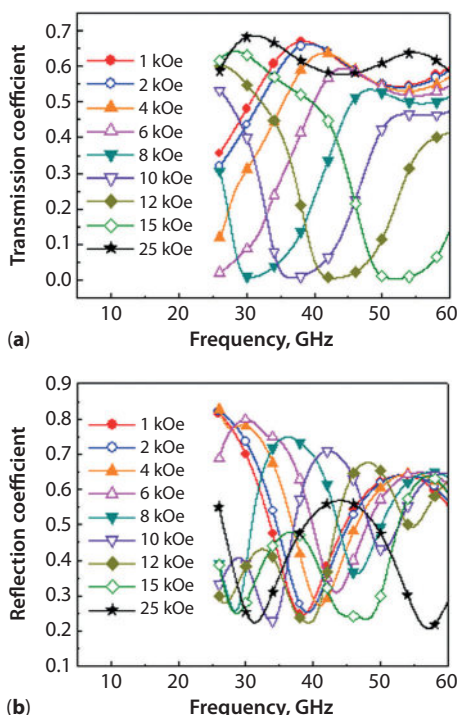


**Figure 2.9** The frequency dependences of transmission (a) and reflection coefficients (b), which are calculated by formulas (2.13) and (2.14) for the nanocomposite with the particles of nickel–zinc ferrite spinel  $\text{Ni}_{0.5}\text{Zn}_{0.5}\text{Fe}_2\text{O}_4$ .

directly associated with FMR and FMAR can be conveniently studied by using the field dependences of coefficients. It will be discussed at next section.

## 2.7 Magnetic Field Dependence of Transmission and Reflection Coefficients

In this section, the experimentally measured and calculated field dependences of reflection and transmission coefficients are compared each other taking into account the dielectric and magnetic parameters of sample of opal matrix with the particles of ferrite spinel  $\text{Ni}_{0.5}\text{Zn}_{0.5}\text{Fe}_2\text{O}_4$ . Let's suppose that the sample is placed in the metallic waveguide of rectangular cross-section with sizes  $7.2 \times 3.4$  mm, as shown in Figure 2.3a. For calculation, the expression for impedance of waveguide is used. In this expression, the real part of permittivity of nanocomposite  $\epsilon' = 5.5$  is determined by the frequency dependences of transmission and reflection coefficients into the zero magnetic field with the use of technique described in [33].

The effective permeability of nanocomposite is calculated by formulas (2.10) and (2.11) at that  $M_0 = 5000/4p \Gamma_c$ ,  $a = 0.06$ . Its frequency dependence is shown in Figure 2.8. Complex transmission  $D$  and reflection  $R$  coefficients are calculated by formulas (2.13) and (2.14) as the functions of magnetic field. The calculation results for three frequencies  $f = 26, 32$  and  $38$  GHz are shown in Figure 2.10. The sample thickness is  $1.9$  mm. It is convenient to count off the position of FMR and FMAR by the dependence of dissipation. It is seen that the position of FMR shifts toward higher fields when increasing the frequency. The position of antiresonance can be defined for the dependence at frequency  $f = 38$  GHz. The counting out of FMR and FMAR fields is complicated by the fact that the position of extrema also depends on the implementation of conditions of quarter- or half-wave plates. Nevertheless, it is seen from the carried out calculations that the condition of FMR affects both the transmission and reflection coefficients – the minima appear in the field dependence. In FMAR field, the reflection coefficient has pronounced maximum.

Let's note also that the extremes of reflection and transmission coefficients upon FMR and FMAR occur in the fields which differ from the fields where dissipation extremes. Apparently, for the recovery of FMR and FMAR spectra, it is more accurately to use the field values of dissipation extremes.

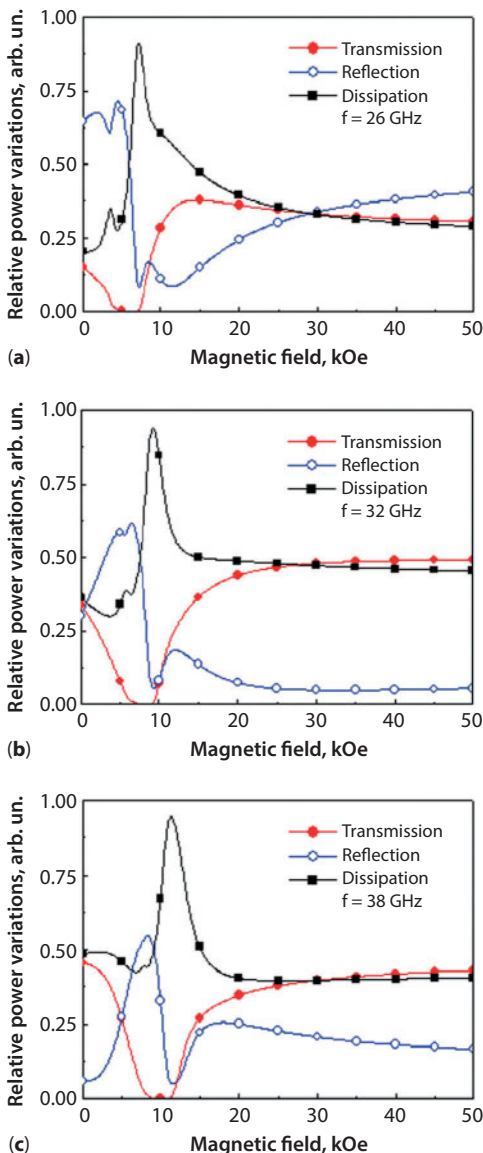


**Figure 2.10** The dependences of transmission, reflection coefficients and dissipation, calculated by formulas (2.13) and (2.14) for the nanocomposite with the particles of nickel-zinc ferrite spinel  $\text{Ni}_{0.5}\text{Zn}_{0.5}\text{Fe}_2\text{O}_4$  for three frequencies  $f = 26 \text{ GHz}$  (a),  $f = 32 \text{ GHz}$  (b), and  $f = 38 \text{ GHz}$  (c).

## 2.8 Frequency Dependence of Resonance Amplitude

Let us more closely consider the dependence of reflection coefficient of wave from the nanocomposite plate with the particles of nickel–zinc ferrite  $\text{Ni}_{0.5}\text{Zn}_{0.5}\text{Fe}_2\text{O}_4$ , which is experimentally measured at a few frequencies of millimeter range. The sample thickness is about 1.9 mm. The measurement result is shown in Figure 2.11. The maximum of reflection coefficient is clearly visible at the dependences measured at frequencies of 26, 28, 30, and 32 GHz. The maximum value for this nanocomposite is 300%. Therefore, the reflection maximum is called as giant in [23]. It can be seen that prior to frequency of 30 GHz when increasing the frequency there is a tendency to amplitude increasing of reflection coefficient in the resonance. However, when subsequent increasing the frequency, the amplitude of changes of the reflection coefficient upon FMAR reduces. This decreasing is concerned with the approach to the condition of quarter-wave plate. An influence of condition of quarter- and half-wave plates on the frequency dependences of coefficients is theoretically considered above when discussing Figure 2.9. The calculations of field dependence of reflection coefficient, shown in Figure 2.9, do not contrary to the experimental observations. For example, it can be noted in Figure 2.9 that the absolute value of reflection coefficient module at the maximum about 7–8 kOe at frequency of 32 GHz is greater than at frequency of 38 GHz. One more feature of the nonmonotony of frequency dependence of wave characteristics near the antiresonance can be seen in Figure 2.9b and c. If we compare the relative depth of dissipation minimum upon FMAR at frequencies of 32, 38 GHz, and about 4–6 kOe, it can be seen that at higher frequency of

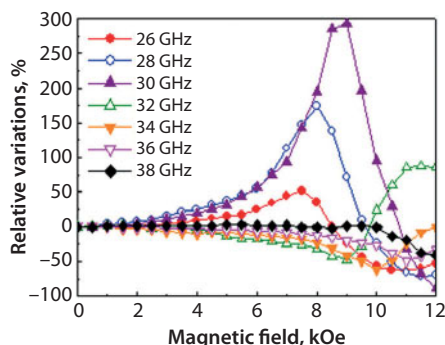


**Figure 2.11** The giant antiresonance in the nanocomposite with Ni–Zn ferrite particles. The dependences of reflection coefficient from the plate of 1.9 mm in thickness, measured at several frequencies of millimeter waveband.

38 GHz the dissipation minimum is less pronounced. The nonmonotonic frequency dependence of changes of reflection coefficient upon FMAR near the minimum of reflection coefficient from the plate is illustrated in Figure 2.12. Two frequency dependences of reflection coefficient from the plate are schematically shown in this figure. One of these dependences is drawn in zero external magnetic field,  $H = 0$ . The second dependence is drawn for  $H \neq 0$ . Let this dependence corresponds to FMAR field. The minimum at first dependence is achieved at frequency  $f_1$ , and for second dependence – at frequency  $f_3$ . Since when increasing the magnetic field from  $H = 0$  the dynamic permeability decreases, then  $f_3 > f_1$ . These two dependences intersect at frequency  $f_2$ , at that  $f_1 < f_2 < f_3$ . When turning on the magnetic field the value of reflection coefficient passes from first frequency dependence to second one with the same frequency. It is easy to see from Figure 2.12, that upon  $f < f_2$  the changes sign is positive. That is when increasing the field value up to FMAR condition the reflection coefficient increases. It turns out that the reflection coefficient upon FMAR has a maximum. When  $f > f_2$ , the changes sign should be negative. Let us note that upon  $f < f_1$  when increasing the frequency  $f$  the value of changes of reflection coefficient should increase, and upon  $f_1 < f < f_2$  – should decrease.

This simple scheme illustrates the nonmonotony of amplitude of maximum upon FMAR observed at the experimental dependences of Figure 2.11.

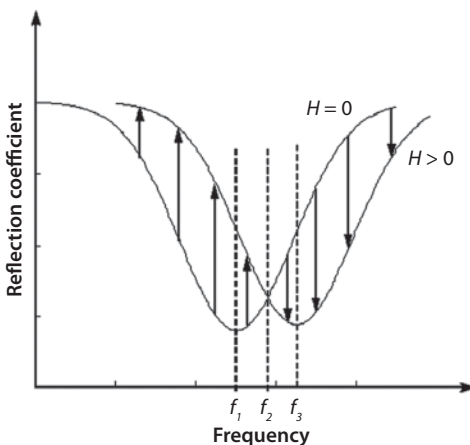


**Figure 2.12** A schematic representation of frequency dependences of reflection coefficient upon  $H = 0$  and  $H \neq 0$ . The minimum positions are designated as  $f_1$  and  $f_3$ . Upon  $f < f_2$  when increasing the magnetic field the reflection coefficient increases. Upon  $f < f_1$  when increasing the frequency  $f$  the value of changes of reflection coefficient should increase, and upon  $f_1 < f < f_2$  – should decrease.

## 2.9 Magnetic Resonance and Antiresonance upon Parallel and Perpendicular Orientation of Microwave and Permanent Magnetic Fields

In this section, the results of experiments performed in two orientation of external DC magnetic field relative to the surface where the microwave magnetic field of  $H_{10}$  mode lies are considered. Both these orientation are shown in Figure 2.3a. The condition  $\mathbf{H} \perp \mathbf{H}_\sim$  fulfills at one of them. In particular, the microwave experiments are performed upon this orientation. These results are shown above. Upon another orientation, the condition  $\mathbf{H} / \mathbf{H}_\sim$  fulfills. In both cases, the DC magnetic field lies in the plane of plate of nanocomposite, and the condition  $\mathbf{H} \perp \mathbf{k}$  is valid. The results of measurements of field dependences of transmission and reflection coefficients for these two orientations for the nanocomposite plate with the particles of nickel-zinc ferrite spinel  $\text{Ni}_{0.5}\text{Zn}_{0.5}\text{Fe}_2\text{O}_4$  are shown in Figures 2.13 and 2.14. The field dependences of transmission coefficients for the sample with the thickness of about 1 mm are

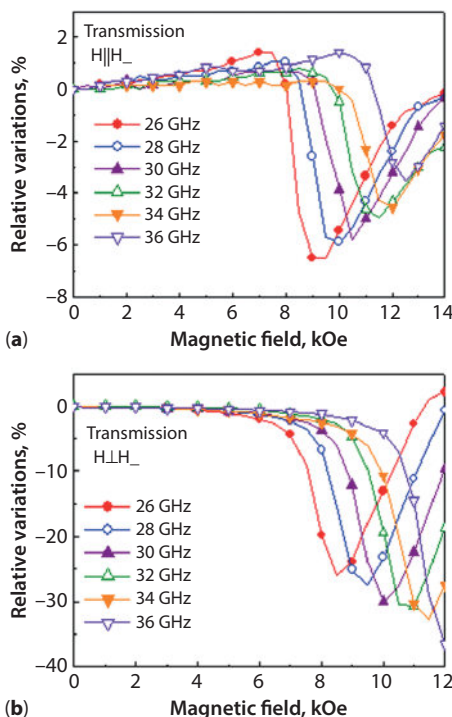


**Figure 2.13** The field dependence of transmission coefficients through the plate of Ni-Zn ferrite: parallel orientation of  $\mathbf{H} \parallel \mathbf{H}_\sim$  (a) and perpendicular orientation  $\mathbf{H} \perp \mathbf{H}_\sim$  (b).

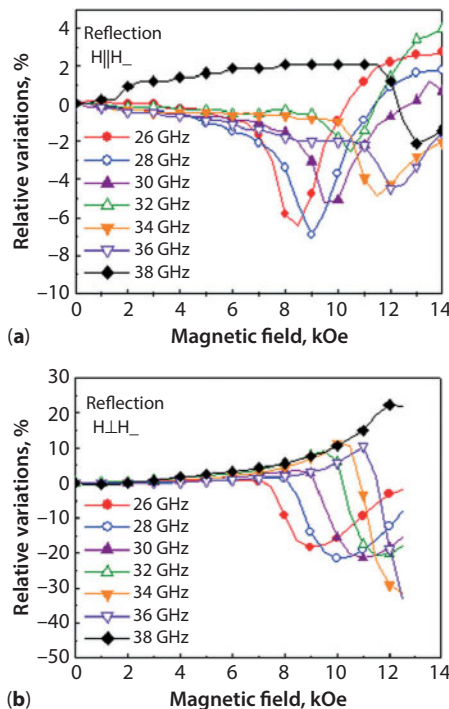


**Figure 2.14** The field dependence of reflection coefficients from the plate of Ni-Zn ferrite: parallel orientation of  $\mathbf{H} \parallel \mathbf{H}_{\perp}$  (a) and perpendicular orientation  $\mathbf{H}_{\perp} \parallel \mathbf{H}_{\perp}$  (b).

compared. It is easy to see that there are minima at the dependences, which are caused by FMR. When increasing the frequency, the resonance field increases. At the dependences measured upon  $\mathbf{H} \perp \mathbf{H}_{\perp}$  orientation, the maximum caused FMAR for the transmission coefficient is not visible. However, upon another orientation  $\mathbf{H} \parallel \mathbf{H}_{\perp}$  at frequencies below 34 GHz the maximum is present. In this parallel orientation, there is the minimum of transmission and reflection coefficients, caused by FMR. These results – in particular, the presence of FMR in the parallel orientation – testify significant and very important magnetic inhomogeneity of the nanocomposite specimen. As it is well known for homogeneous and film samples, the acoustic branch of spectrum of ferromagnetic resonance upon the parallel orientation is unobservable [3, 16]. The heterogeneity is present both in the microwave fields and in DC magnetic field. The heterogeneity of microwave fields inherent to the different spatial scales is studied in [29]. It is shown that the parameter of

heterogeneity  $\frac{1}{E_{n,in}^0 H_{n,in}^0} \int_S E_{n,in} H_{n,in}^* dS$ , where  $E_{n,in}$  and  $H_{n,in}$  are normal components of the electric and magnetic microwave fields on the inner surface of

sphere which is about 1–10 mm in radius with the surface S,  $E_{n,in}^0$  and  $H_{n,in}^0$  are the respective amplitude values of components which are introduced in order the parameter to be made dimensionless (introduced to make the dimensionless parameter). The evaluations carried out for the nanocomposite with the particles of ferrite  $\text{Ni}_{0.5}\text{Zn}_{0.5}\text{Fe}_2\text{O}_4$  and metallic silver shows that depending on the spatial scale of selected sphere the heterogeneity parameter changes no less than for four times both in lower and in bigger sides as compared with its macroscopic value.

However, here it is more signify for us the heterogeneity of DC magnetic field. There is no doubt that near the ferromagnetic or ferrimagnetic particles DC magnetic field is highly heterogeneous both by the magnitude and direction. In other words, the direction of magnetic field near the magnetic particles can be very different from the direction of field outside the sample, i.e. the condition  $\mathbf{H} \perp \mathbf{H}$  is violated. The result is the fact that the effective permeability is not precisely defined by formula (2.12) (see [26]). For the existence of minimum in FMR, it is important that the heterogeneity leads to the appearance of DC component of magnetic field near the magnetic particles. This component is perpendicular to the microwave field  $\mathbf{H}_\perp$  and leads to the presence of FMR. The experimental fact observed in Figures 2.13a and 2.14a testifies for benefit of this interpretation. It consists in that with increasing the frequency the amplitude of FMR decreases. This tendency differs from the perpendicular orientation FMR – there FMR amplitude increases with the frequency increasing. An assumption that when increasing the frequency the FMR field increases and the resonance moves to the region of technical magnetic saturation can serve as a possible explanation of anomaly in the parallel orientation. The heterogeneity of DC magnetic field is reduced in this region. The decreasing of amplitude of resonance testifies about it. The results presented in Figure 2.14a show that the antiresonance upon the parallel orientation in the reflection coefficient is not observed.

## 2.10 Conclusion

The magnetic antiresonance phenomenon occurs when the real part of effective permeability becomes equal to zero. At that, in the antiresonance point, the imaginary part of the effective permeability has small value. For nanocomposites, FMAR has some features which are similar to FMAR in thin metallic ferromagnetic films. In particular, FMAR leads to the minimum of electromagnetic absorption, in contrast to its maximum upon FMR. Antiresonance occurs at the frequencies exceeding a certain

characteristic frequency of a given material. This characteristic frequency is determined by the magnetization of a material. However, the antiresonance in metals differs significantly from it in nanocomposites. In metals, the wave equation has the skin-type solution due to their high conductivity. Hence, the electromagnetic field distribution corresponding to the skin effect is realized in a metal plate. The nanocomposites considered in this paper do not have conductivity at DC, so the solution of wave equation is in the form of traveling electromagnetic waves. As a result, there are some differences between FMAR in nanocomposites and in metals. Firstly, whereas for a metallic film the antiresonance to a greater extent causes a sharp increasing of the amplitude of transmitted wave, for the nanocomposite the reflection coefficient substantially changes. Provided FMAR, the maximum of reflection coefficient is observed. Secondly, the frequency dependence of this maximum is determined by the interference of direct and reflected waves into the plate nanocomposite, besides the frequency dependence of the magnetic permeability. As a result, the frequency dependence of reflection coefficient upon the antiresonance can be nonmonotonic.

It can be shown from the experiments carried out that FMAR can be observed both upon the parallel orientation of the constant and microwave magnetic fields. It comes out of the strong inhomogeneity of the field near the magnetic nanoparticles.

## Acknowledgement

The work is carried out within the RAS plan (theme “Spin” No. 01.2.006 01201463330), with partial support of grant from Russian Ministry of Education and Science No. 14.Z50.31.0025 and NSh-7539.2016.2 grant.

## References

1. Yager, W.A., Additional ferromagnetic resonance absorption measurements on supermalloy. *Phys. Rev.*, 75, 316, 1949.
2. Kaganov, M.I., The excitation of standing spin waves in a film. *Sov. Phys. JETP*, 1, 7, 114, 1960.
3. Gurevich, A.G. and Melkov, G.A., *Magnetic Oscillations and Waves*, pp. 1–445, CRC Press, 1996.
4. Heinrich, B. and Meshcheryakov, V., Antiresonance transmission in ferromagnetic metals. *Sov. Phys. JETP*, 9, 11, 378, 1969.

5. Heinrich, B. and Meshcheryakov, V., Temperature, thickness, frequency dependences of antiresonance transmissions in PY. *Sov. Phys. JETP*, 32, 2, 232, 1971.
6. Heinrich, B. and Cochran, J. F., Anomalous behavior of the antiresonance transmission through supermalloy at 23.7 GHz. *Phys. Rev.*, 29, 1175, 1972.
7. Cochran, J. F., Heinrich, B. and G. Dewar, G., Apparatus for study of the transmission of 24 GHz radiation through metal plates and for the study of FMR absorption lineshapes. *Can. J. Phys.*, 55, 834, 1977.
8. Cochran, J. F., Heinrich, B. and G. Dewar, G., Ferromagnetic antiresonance transmission through supermalloy at 24 GHz. *Can. J. Phys.*, 55, 787, 1977.
9. Heinrich, B., Cochran, J. F., Liaw, J.H., Barker, R.C., Transmission resonance experiments with nickel and permalloy platelets. *Magnetism and Magnetic Materials, Proceedings of the First Joint MMM-Intermag Conference. AIP Conference Proceedings*, 34, 250, 1976.
10. Rudd, J. M., Cochran, J. F., Urquhart, K. B., Myrtle, K., Heinrich, B., Ferromagnetic antiresonance transmission through pure Fe at 73 GHz. *J. Appl. Phys.* 63, 3811, 1988.
11. Ament, W. S., Rado, G. T., Electromagnetic effect of spin wave resonance in ferromagnetic metals. *Phys. Rev.*, 97, 1558, 1955.
12. De Wames, R.E., Wolfram, T., Spin wave resonance in conducting films: parallel resonance. *J. Appl. Phys.*, 13, 68, 1974.
13. Rinkevich, A. B., Perov, D. V., Vas'kovskii, V. O., Lepalovskii, V. N., Regularities in penetration of electromagnetic waves through metallic magnetic films. *Tech. Phys.*, 54, 1339, 2009.
14. Rinkevich, A. B., Perov, D. V., Shape of magnetic resonance line in electromagnetic wave transmission through permalloy films, in *Recent Research Development in Material Sciences*, Pandalai, S. G. (Ed.), Research Signpost, India, 9, 157, 2012.
15. Rinkevich, A. B., Perov, D. V., Vaskovsky, V. O., Types of magnetic resonances in electromagnetic wave penetration through thin magnetic films. *Phys. Scr.*, 83, 13, 2011.
16. Rinkevich, A. B., Romashev, L. N., Ustinov, V. V., Kuznetsov, E. A., High frequency properties of magnetic multilayers. *JMMM*, 254–255, 603, 2003.
17. Tyagi, S., Lofland, S., Dominguez, M., Bhagat, S., Kwon, C., Robson, M., Ramesh, R., Venkatesan, T., Low-field microwave magnetoabsorption in manganites. *J. Appl. Phys.*, 68, 2893, 1996.
18. Lofland, S., Dominguez, M., Tyagi, S., Bhagat, S., Robson, M., Kwon, C., Trajanovic, Z., Takeuchi, I., Ramesh, R., Venkatesan, T., Surface resistance of thin Perovskite films – high-temperature superconductors and giant magnetoresistance manganites. *Thin Solid Films*, 288, 256, 1996.
19. Lofland, S., Kim, P., Dahiroc, P., Bhagat, S., Tyagi, S., Kwon, C., Shreekala, R., Ramesh, R., Venkatesan, T., Microwave surface resistance of colossal magnetoresistance manganites. *J. Phys. Condens. Matter*, 9, 6697, 1997.
20. Lofland, S., Bhagat, S., Tyagi, S., Mukovski, Y., Karabashev, S., Balbashov, A., Giant microwave magneto-impedance in a single crystal of  $\text{La}_{0.7}\text{Sr}_{0.3}\text{MnO}_3$ : the effect of ferromagnetic antiresonance. *J. Appl. Phys.* 80, 3592, 1996.

21. Nossov, A., Rinkevich, A., Zainullina, R., Vassiliev, V., Slobodin, B., Bebenin, N., Ustinov, V., Frequency dependence of microwave absorption in barium manganites. *Phys. Met. Metallogr.*, 85, 428, 1998.
22. Ustinov, V. V., Rinkevich, A. B., Perov, D. V., Samoilovich, M. I., Klescheva, S. M., Anomalous magnetic antiresonance and resonance of ferrite-spinel nanoparticles embedded in opal matrix package. *JMMM*, 324, 78, 2012.
23. Ustinov, V. V., Rinkevich, A. B., Perov, D. V., Burkhanov, A. M., Klescheva, S. M., Kuznetsov, E. A., Giant antiresonance in electromagnetic wave reflection from a 3D structure with ferrite spinel nanoparticles. *Tech. Phys.*, 58, 568, 2013.
24. Kostylev, M., Stashkevich, A. A., Roussigné, Y., Grigoryeva, N. A., Mistonov, A. A., Menzel, D., Sapoletova, N. A., Napol'skii, K. S., Eliseev, A. A., Lukashin, A. V., Grigoriev, S. V., Samarin, S. N., Microwave properties of Ni-based ferromagnetic inverse opals *Phys. Rev.*, 86, 184431(1–10), 2012.
25. Rinkevich, A. B., Burkhanov, A. M., Perov, D. V., Samoilovich, M. I., Kleshcheva, S. M., Kuznetsov, E. A., Electromagnetic and magnetic properties of magnetophotonic crystal based on opal matrix with Co and CoO nanoparticles. *Phot. Nano. Fund. Appl.*, 12, 144, 2014.
26. Rinkevich, A. B., Perov, D. V., Samoilovich, M. I., Klescheva, S. M., Magnetic antiresonance in metamaterial based on opal matrix with metallic cobalt nanoparticles embedded. *Metamaterials*, 6, 27, 2012.
27. Rinkevich, A. B., Perov, D. V., Homogenization of nanostructured media in magnetic field. *Phot. Nano. Fund. Appl.*, 12, 447, 2014.
28. Makeeva, G. S., Golovanov, O. A., Pardavi-Horvath, M. and Rinkevich, A. B., A probabilistic model for the interaction of microwaves with 3-dimensional magnetic opal nanocomposites. *J. Appl. Phys.*, 113, 173901(1–6), 2013.
29. Rinkevich, A. B., Perov, D. V., Demokritov, S. O., Samoylovich, M. I., Nemytova, O. V., Interaction of microwave electromagnetic waves with 3D magnetic metamaterials. *Phot. Nano. Fund. Appl.*, 15, 59, 2015.
30. García-Miquel, H., Bhagat, S. M., Lofland, S. E., Kurlyandskaya, G. V., Svalov, A. V., Ferromagnetic resonance in FeCoNi electroplated wires. *J. Appl. Phys.*, 94, 1868, 2003.
31. Fernández-García, L., Suárez, M., Menéndez, J. L., Pecharromán, C., Torrecillas, R., Peretyagin, P. Y., Petzelt, J., Savinov, M., Frait, Z., Antiresonance in (Ni, Zn) ferrite-carbon nanofibres nanocomposites. *Mater. Res. Express*, 2, 055003, 1–6, 2015.
32. Rinkevich, A. B., Burkhanov, A. M., Samoilovich, M. I., Belyanin, A. F., Kleshcheva, S. M., Kuznetsov, E. A., Three-dimensional nanocomposite metal dielectric materials on the basis of opal matrices. *Russ. J. Gen. Chem.*, 83, 2148, 2013.
33. Rinkevich, A. B., Samoilovich, M. I., Klescheva, S. M., Perov, D. V., Burkhanov, A. M., Kuznetsov, E. A., Millimeter-wave properties and structure of gradient Co-Ir films deposited on opal matrix. *IEEE Trans. Nanotech.*, 13, 3, 2014.
34. Collin, R. E., *Field Theory of Guided Waves*, pp. 1–852, Wiley-Interscience, 1991.



# Magnetic Bioactive Glass Ceramics for Bone Healing and Hyperthermic Treatment of Solid Tumors

Andrea Cochis<sup>1,2,3#</sup>, Marta Miola<sup>1,4#</sup>, Oana Bretcanu<sup>5#</sup>,  
Lia Rimondini<sup>1,3\*</sup> and Enrica Verne<sup>4</sup>

<sup>1</sup>Biomedical Materials Lab, Department of Health Sciences,  
Università del Piemonte Orientale, Novara, Italy

<sup>2</sup>Department of Biomedical, Surgical and Dental Sciences,  
Università di Milano, Milano, Italy

<sup>3</sup>Consorzio Interuniversitario Nazionale per la Scienza  
e Tecnologia dei Materiali (INSTM), Firenze, Italy

<sup>4</sup>Institute of Materials Physics and Engineering, Applied Science and  
Technology Department, Politecnico di Torino, Torino, Italy

<sup>5</sup>School of Mechanical and System Engineering,  
Newcastle upon Tyne, United Kingdom

---

## Abstract

Bone tumor cases have risen on average 0.4% each year over the past decade. Surgery, chemotherapy, and radiotherapy represent the mainstay of malignant bone tumors. However, these procedures are invasive and often related with strong side effects. Hyperthermia was recognized as an effective treatment of solid tumors: it consists of cancer wound temperature increase above the physiological values by means of microwave or radiofrequency devices. So, healthy cells survive, whereas cancer cells die due to coagulative necrosis or apoptosis. Moreover, generated heat is able to enhance chemotherapeutic agents' effect favoring penetration via vasodilatation. Hyperthermic heating of tissues can be performed by implantable magnetic materials heated by alternating magnetic field. Magnetic bioceramics have been developed in order to replace damaged bone tissue and at the same time provide a local treatment of tumor. They can be synthesized by

---

\*Corresponding author: lia.rimondini@med.uniupo.it

#Authors equally contributed.

melt and quenching or sol-gel process and combined with hydroxyapatite by dip-coating or ferrofluids containing iron oxide nanoparticles. Magnetic bioceramics and nanoparticles can also be exploited as filler in acrylic or calcium phosphate bone cements. All these approaches are meant to improve the current bone tumor treatments by surgeon-friendly devices capable to combine replacement of damaged bone tissue with local cancer treatment.

**Keywords:** Hyperthermia, magnetic glass ceramics, bone, tumor

### 3.1 Bone and Cancer: A Hazardous Attraction

#### 3.1.1 The Pre-metastatic Niche of Bone Colonization

The bone microenvironment is comprised of a mineralized extracellular matrix (ECM) and specific cell types that are under the control of local and systemic factors. This special milieu provides a fertile soil for many cancers to thrive. Certain types of solid tumors metastasize to bone and induce destructive osteolytic and/or bone-forming osteoblastic lesions, with most solid tumors commonly producing both. Tumor cells secrete a vast array of proteins, many of which interact with resident cells in the bone marrow to induce the differentiation, recruitment, and activation of osteoclasts and osteoblasts. During the process of bone resorption, stored growth factors and ionized calcium are released from the mineralized bone matrix, and these factors feed back to promote tumor cell growth and further production of osteolytic and osteoblastic factors. This vicious cycle can support tumor growth in bone [1, 2].

The concept of a pre-metastatic niche has emerged as a means through which a primary tumor is able to prepare sites of metastasis. In the bone microenvironment, most evidence in support of a pre-metastatic niche is in the context of endocrine-like actions. Primary tumors may condition the bone marrow through the production of circulating factors that target cells in the bone microenvironment and thus render it conducive to tumor localization and colonization. Examples include heparanase that is produced by breast cancer cells increasing bone resorption [3]; osteopontin (OPN) that is secreted by tumor cells and/or senescent fibroblasts promoting bone marrow cell recruitment or tumor formation [4–6]; and matrix metalloproteinase (MMP) production from osteoclasts supporting prostate cancer skeletal metastasis [7]. Parathyroid hormone-related protein (PTHRP; also known as PTHLH) is produced by various tumors and can promote bone resorption [5, 14] and can enhance the production of local factors in the bone marrow, such as the chemokine CCL2 [8]. Tumor cells

preferentially adhere to the bone marrow endothelium, a potentially initial and key event in their introduction to the bone microenvironment [9]. Tumor cells that metastasize to bone can use the same physiological mechanisms as those used by hematopoietic stem cells (HSCs) homing to bone [10–12]. Osteoblasts and bone marrow stromal cells attract and regulate HSCs and provide a niche through protein interactions that include integrins, such as  $\alpha 4\beta 1$ -vascular cell adhesion molecule 1 (VCAM1); chemokines, such as CXCL12 (also known as SDF1)–CXCR4; BMPs, Notch, nestin, and OPN [13–19].

CXCL12 is expressed at high levels by osteoblasts and bone marrow stromal cells, and expression of its receptor, CXCR4, on cancer cells has an important role in tumor cell homing to bone [20–23]. IL-11 and MMP1 stimulate bone resorption by increasing osteoblast production of RANKL, and CTGF can stimulate osteoblast proliferation, as well as neoangiogenesis. When expressed together, these proteins can act cooperatively to cause osteolytic metastasis, but overexpression of individual proteins was insufficient to accelerate bone metastases [24].

Finally, tumor cell surface integrins interact with ECM proteins that are expressed in the bone microenvironment. The  $\alpha v\beta 3$  integrin interacts with bone-derived OPN, fibronectin, and vitronectin, and expression of  $\alpha v\beta 3$  by breast and prostate cancer cells is associated with higher rates of bone metastasis, tumor-associated osteolysis and colonization in bone [25, 26].

### 3.1.2 Bone Invasion via Matrix Proteins

Bone matrixellular proteins that could affect tumor localization include OPN, which is also released by stromal and tumor cells, secreted protein acidic and rich in cysteine (SPARC), periostin, bone sialoprotein, dentin matrix acidic phosphoprotein 1 (DMP1), syndecan 1, and decorin. SPARC, which is produced by osteoblasts, leukocytes, and cancer cells, induces cancer cell migration by interacting with  $\alpha v\beta 5$  [27]. OPN, which is derived from bone matrix, stromal and tumor cells, has an important role in tumor metastasis. Experiments in mice deficient for OPN or overexpressing OPN revealed that levels of OPN correlate with skeletal metastatic potential [28].

CXCL12 is expressed at high levels by osteoblasts and bone marrow stromal cells, and expression of its receptor, CXCR4, on cancer cells has an important role in tumor cell homing to bone [26–28]. CXCL12 expression from bone marrow endothelial monolayers has been demonstrated to promote prostate cancer cell migration and upregulation of both MMP9 and  $\alpha v\beta 3$  on prostate cancer cells [27, 28]. Tumor cell surface integrins interact with ECM proteins that are expressed in the bone microenvironment.

Tumor cell expression of the  $\beta 1$  integrin family members  $\alpha 5\beta 1$ ,  $\alpha 2\beta 1$ , and  $\alpha 4\beta 1$ —which are receptors for fibronectin, collagen I and VCAM1, respectively—has been implicated in the interactions of leukemia, myeloma, prostate, and breast cancer cells with bone marrow stroma, and can result in enhanced colonization and survival in bone [29–32].

### 3.1.3 Tumor Formation and Metastatic Growth

Tumor metastasis to bone can alter normal bone physiology, resulting in uncoupled bone remodeling (Figure 3.1). Enhanced osteoclast activity exacerbates the growth and progression of bone metastases. By contrast, the administration of osteoclast inhibitors, such as bisphosphonates, OPG, RANKL antagonists, and  $\beta 3$  integrin antagonists, before tumor inoculation diminishes the growth of solid tumor bone metastases and myeloma tumor burden in bone [33, 34].

Thus, osteoclastic changes are essential for both tumor cell colonization and growth in bone. Together, these data indicate that the state of the bone

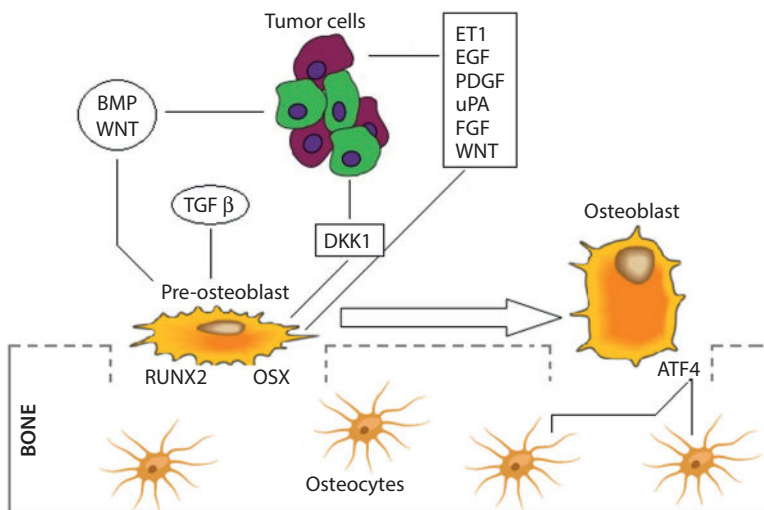


**Figure 3.1** Tumors induce the release of various factors regulating bone formation at different steps of osteoblast development. Bone morphogenetic proteins (BMPs), Wingless-type MMTV integration site family member (WNTs), and TGF- $\beta$  provide signals to mesenchymal stem cells to differentiate towards osteoblast lineage. Osteoblast progenitors and pre-osteoblastic cells are sensitive to positive osteoblastic factors produced by tumor cells: BMPs, endothelin 1 (ET1), insulin-like growth factors (IGFs), platelet-derived growth factor (PDGF), urinary plasminogen activator (uPA), and fibroblast growth factors (FGFs), as well as the negative regulator dickkopf 1 (DKK1). Osteoblast-associated transcription factors include RUNX2, osterix (OSX), and activating transcription factor 4 (ATF4).

microenvironment before bone metastasis can modulate tumor growth and the subsequent behavior of tumors in bone, and thus it represents an important target for metastasis prevention.

Interestingly, reports suggest that cancer cells can fuse with macrophages or can induce the fusion of osteoclast precursors to promote multinucleated giant cells [35], leading to mature osteoclasts with tumor cell nuclei and increased function [36–38]. This identification of tumor cells with osteoclast properties shows that tumor cells are able to behave like bone cells in some circumstances, and this is known as osteomimicry. Another form of osteomimicry involving osteoblasts has been identified in breast and prostate cancer cells. The osteoblastic nature of prostate cancer skeletal metastases results in bone that is of a poor quality, immature, and woven type [118]. Various mechanisms for a tumor-associated increase in bone tissue have been proposed. Tumor cells in the metastatic prostate lesion may transdifferentiate to become mesenchymal cells that are capable of osteoblastic activity, cancer cells may induce resident cells in the marrow microenvironment to enter the osteoblast lineage, and prostate cancer cells may induce the proliferation and/or differentiation of osteoblast lineage cells. RUNX2 has been implicated in the osteomimicry that is attributed to breast and prostate skeletal metastasis [39–40]. Osteoblasts are a vital component in certain aspects of tumor localization in bone. Tumors that display the phenotypic ‘osteoblastic’ response are thought to be dependent on osteoblasts in the bone microenvironment for their continued growth and survival, resulting in a co-dependent cycle.

### 3.1.4 Bone Metastases Management

Carcinoma-derived metastases are the most recognized malignant tumors disturbing bone [41].

According to Canada and US statistics [42], about 50% of confirmed invasive carcinoma is able to metastasize to bone. Moreover, different tissues carcinomas such as prostate (65–75%), thyroid (60%), lung (30–40%), and renal (20–25%) [43] showed tendency to metastasize to bone.

Vertebrae are not the unique bones affected by metastasis; long bones and the pelvis are also commonly affected by metastatic bone disease (MBD) [44]. Thus, even if clinical presentation of patients with MBD to the long bones and pelvis is varied, patients with bone metastases sometimes require surgical intervention to prevent deterioration of quality of life due to pathological fractures, which commonly occur as a result of lytic lesions in weight-bearing bones. The annihilation of both trabecular and cortical bone represents a very severe damage from a structurally point of view. In

fact, fractures are highly unlikely to occur (2.3%) when less than 50% of the cortex is destroyed, while are most expected to occur (80%) when over 75% of the cortex is compromised [45–47].

Thus, new strategies to improve MBD management still represents a major focus in clinical oncology. In fact, current treatment options for MBD are limited and often only palliative: they include chemotherapy, pharmacological treatment (by bisphosphonates administration), radiation therapy, and surgery [43, 46].

Radiotherapy is the most common, safe, and effective treatment, and it is well established for patients presenting MDB. However, if radiotherapy treatment is not reinforced by surgery, it is not possible to prevent pathological fractures in patients presenting impending fractures of long tubular bones. The addition of internal fixation before localized radiotherapy can reduce the risk of further bone destruction, which leads to increased pain, loss of fixation, and the need for additional orthopedic procedures [48, 49]. Radiotherapy also lead sometimes to soft tissue injuries, including muscle induration and joint contracture [49–52].

Surgical reconstruction strategies include different techniques: open reduction internal fixation (ORIF), intramedullary nailing (IMN), the use of methylmethacrylate bone cement, arthroplasty, intercalary or tumor prostheses, and resection alone [47]. However, the decision to advance with surgery represents a crucial step involving clinicians and patients. The risks of surgery may outweigh the proposed benefits of improved pain and function [43, 46]. Patients affected by MBD are often also immunocompromised: therefore, they present an increased risk of developing surgical site infections, as well as other surgical complications [43, 46]. Finally, recovery time after surgery can be extensive and can further reduce patients' quality of life.

## 3.2 Hyperthermia Therapy for Cancer Treatment

### 3.2.1 Hyperthermia as Alternative to Traditional Therapies

Hyperthermia therapy is a treatment approach in which the temperature of a particular area of the body or the whole body is heated above normal temperatures to achieve therapeutic effects. There are three basic hyperthermia categories: local, regional, and whole body. When local hyperthermia is used for cancer treatment, heat is applied to a solid tumor. The heating temperature can be as high as 80 °C when the purpose is to completely ablate the tumor [53], or can be in the range of 41–45 °C when aiming for

certain physiological effects including cell death without causing serious injury to adjoining normal tissues [54]. Alternatively, the temperature of 39–41 °C can be used to mimic fever-range effects that do not damage any tissues. Regional hyperthermia is applied to a relatively large area, such as the peritoneal cavity or a limb. Whole-body hyperthermia is used in conjunction with other therapies to treat metastatic cancer that has spread throughout the body by systemic heating, and usually the fever-range temperature of 39–41 °C is used [55]. Currently, most cancer patients die not from the primary tumor, but from metastatic disease, and the only approach to treating unrecognized metastases is chemotherapy. Immune-based cancer therapies are on the cusp of becoming part of the standard of care for many cancers because the immune system can actively seek and eliminate occult metastatic disease that may often survive chemotherapy. Recent studies indicate that many cytotoxic chemotherapeutic drugs mediate their effects in part by stimulating antitumor immunity [56–58]. With the increasing appreciation of the important role of the immune system in cancer treatment, there is growing interest in the potential of local tumor hyperthermia to activate antitumor immune responses.

### 3.2.2 Activating Hyperthermia

Usually, hyperthermia treatments can be subdivided into three types based on the heated surface area or volume: (i) local hyperthermia, (ii) regional hyperthermia, and (iii) whole-body hyperthermia. Local hyperthermia allows the heating of the tumoral mass and a restricted contiguous area of both superficial (external) and deep-seated (interstitial and intraluminal) subcutaneous tumors. Tumors can be heated externally, by means of high-frequency waves, or internally, by using heated wire probes inside the body. Regional (or part-body) hyperthermia is often used to treat large areas of the body affected by a tumor, usually in organs or limbs. This type of hyperthermic treatment can be applied by using external devices or thermal perfusion. Finally, whole-body hyperthermia is used to hinder metastatic cancer spread through the body, such as melanoma or soft tissue sarcoma. For this approach, all the body is heated at about 41–42 °C for about 1 h or at lower temperature for more time, in order to limit the adverse effects (thermal stress to the heart, lungs, liver, or brain). Whole-body hyperthermia has been applied using different systems: thermal chambers, warm-water blankets, hot wax, infrared radiators, inductive coils, or extracorporeal heating of blood through a heat exchanger. However, most of these methods were abandoned since they showed intolerable toxic effect and today only radiant systems are in clinical use.

Other classifications of hyperthermia treatments are based on (i) the system of energy production, (ii) the frequency or electromagnetic waves, (iii) the clinical application, (iv) kind of energy delivery, and (v) the level of invasivity.

The different physical effects and energy production systems used to induce hyperthermia are described below.

### *3.2.2.1 Hot Bath, Incubator, or Injection*

One of the simplest hyperthermia methods is to increase the patient temperature by means of hot-water bath, hot-wax bath (Pettigrew technique), or a moist hot-air incubator. The temperature of the fluid is controlled to raise the patient temperature to approximately 41–42 °C. One of the adverse effects that can occur is the possibility of superficial lesions.

A slightly different method consists of injecting a hot fluid (generally water—normal saline heated at about 96 °C) directly to the tumor. This technique was used increasingly in recent years to treat hepatocellular carcinoma.

### *3.2.2.2 Perfusion*

Regional perfusion is a method used to treat malignancies located in arms, legs, or some organs (mainly liver and lung). It consists of bypassing a large artery of an organ or limb to externally heat the blood before reintroducing the heated blood to the affected organ. This technique has now been used for over 40 years, often in conjunction with chemotherapy.

Systemic perfusion hyperthermia was also adopted by extracting all of the patient's blood over a sustained period and heating it up to 42 °C using systemic perfusion systems.

Isolated hepatic perfusion (IHP) is a regional treatment technique used for liver tumors, which implies the separation of the liver from the rest of the circulatory system and its perfusion using heated (40–44 °C) fluids which contain cytotoxic agents. Continuous hyperthermic peritoneal perfusion (CHPP) is a thermal therapy used to treat dispersed tumors within the abdominal cavity. After tumor removal by surgery, CHPP is administered post-operatively using warmed (40–42 °C) washing fluid (usually saline solution), sometimes loaded with antineoplastic agents.

### *3.2.2.3 Magnetic Induction*

Magnetically induced hyperthermia is probably the most recent developed technique. It consists of heat generation by means of magnetizable devices

subjected to an external magnetic field. This process can be applied for superficial as well as deep-seated tumors since the heat source can easily cross tissues. Moreover, the therapy is targeted at the tumor site, safeguarding the surrounding healthy tissues [59–61]. Hyperthermia can be induced by a wide range of magnetic materials, such as metallic particles, magnetic glass ceramics, magnetic bone cements, and magnetic fluids (suspensions of superparamagnetic nanoparticles). These materials can be implanted or injected in the tumor site and generate heat through hysteresis loss and eddy current loss. The heat produced depends on different factors, such as material properties, frequency and intensity of applied magnetic field, and tissue characteristics.

### 3.2.2.4 *Ultrasounds*

Ultrasound waves with a frequency range between 2 and 20 MHz are used in certain hyperthermia treatment where the tissue absorbs high-energy waves [62–65]. Depending on the application and equipment used, the beam can be focused or unfocused, stationary, or translocating. One or multiple applicators with phasing and power guiding can be adopted. This technique allows for the generation of uniform heating and permits controlled depth of penetration with precise definition of the boundaries of the heated tissue volume. However, ultrasound waves can decay rapidly in air and are reflected at tissue surfaces, so they cannot be used for air-containing tissue and they rarely reach deep-seated tumors.

### 3.2.2.5 *Microwaves and Radiofrequency*

The use of microwaves is one of the most promising methods for hyperthermia. This technique was clinically applied to breast and prostate cancers and can be used alone or in conjunction with other treatments, such as radiotherapy. Microwaves hyperthermia is based on the conversion of the energy carried by the waves into thermal energy by dielectric and resistive loss. In the past, this technique used a single-waveguide antenna at frequencies between 300 and 2500 MHz and a temperature sensor to check and adjust the microwave power in order to maintain a uniform temperature in the tissue. However, since this system showed some limitations, recently multiple applicators are used, especially to treat large tumors.

Microwaves hyperthermia can treat large regional tissue volume, and it is usually applied for superficial tumors, by using an external microwave radiator. It can also be used for tumors situated in natural cavities (i.e. esophagus, uterine neck, rectum), using an internal intracavitary radiator.

Radiofrequency waves are one of the most used methods of externally applied hyperthermia, to treat large tumors, especially liver cancer, in a frequency range of 10–120 MHz. Generally, the system consists of a generator and two opposite electrodes (dispersive and needle) situated over the patient, who acts as a resistor. The generated electric field within the patient tissue causes the vibration and movement of the free charges and ions present in the tumor and rotation of polar molecules, leading to heating (frictional heating, mainly produced by the formation of conduction currents and dielectric losses). This technique can be used to treat tumors seated in deep tissue, and it has been recently applied for whole-body hyperthermia treatment, maintaining the body temperature between 39.5 and 41.5 °C for more than 2 h. The side effects related to the use of radiofrequency waves are associated to superficial skin burns and focal fat necrosis, while the most important limitation of this technique is the absence of tumor targeting.

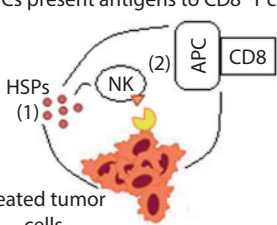
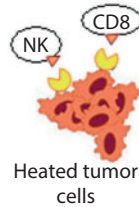
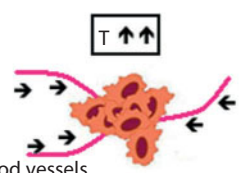
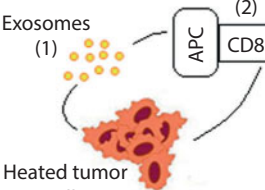
### 3.2.3 Hyperthermia Mechanisms

Temperatures in the range of 39–45 °C can arrest cell proliferation and kill cells. The effects are dependent on a combination of temperature and time of exposure to that temperature that together are referred to as thermal dose [66]. When cells are exposed to elevated temperature, several changes occur (Figure 3.2).

Heat alters membrane characteristics, leading to modification in cell morphology, intracellular sodium and calcium levels, and membrane potential [67–70]. Other than membranes, secondary structures of proteins are thought to be the most sensitive biomolecules to heat and protein denaturation likely mediates many of the effects of mild hyperthermia [66]. Although DNA itself is not damaged at temperatures of 39–45 °C, *de novo* synthesis and polymerization of DNA are more temperature sensitive due to denaturation and aggregation of synthetases and polymerases [71–74], and this is thought to greatly contribute to cell cycle arrest and cell death. Impaired functions of proteins responsible for other essential cell activities, such as DNA repair, are likely also involved.

In general, following a sufficient thermal dose, cells die through either necrosis, in which the cell rapidly loses membrane integrity, or apoptosis, in which programmed cell death is triggered, and each of these deaths has different immune modulatory activities [75].

Different mechanisms of immune activation occur at different temperatures within the mentioned range. The most important of them are described in 3.2.3.1–3.2.3.4 subchapters.

Heat shock proteins	Surface molecules
(1) Tumor cells release HSPs (2) HSPs activate NK (3) APCs present antigens to CD8 <sup>+</sup> T cells  	T = 39–43 °C ↑ MICA ↑ MHCI  
Tumor vasculature	Exosomes
• Improve tumor perfusion • Facilitate immune trafficking  	(1) Tumor cells release exosomes (2) APCs present antigens to CD8 <sup>+</sup> T cells  

**Figure 3.2** Different mechanisms of immune activation induced by locally heating tumors.  
 (a) Heated tumor cells are induced to release HSPs, which activate NK cells and APCs which take up the HSP-antigen complex and cross-present the antigen to CD8<sup>+</sup> T cells.  
 (b) Heated tumor cells increase the surface expression of MICA, a NKG2D ligand, and MHC class I, making the tumor cells more sensitive to lysis by NK cells and CD8<sup>+</sup> T cells, respectively.  
 (c) The tumor vasculature becomes more permeable and may have increased adhesion molecule expression after heating, which may facilitate better trafficking of immune cells between the tumor and dLN.  
 (d) Finally, heated tumor cells release exosomes containing potential tumor antigens that APCs recognize and presents to the CD8<sup>+</sup> T cells.

### 3.2.3.1 Heat Shock Proteins

Heat shock proteins (HSPs) are a heterogeneous group of molecular chaperones with various functions that are upregulated when cells are stressed in a variety of manners, including heat exposure [76]. HSPs are usually divided into subgroups based on the molecular size; small HSP (540 kDa), Hsp40, Hsp60, Hsp70, Hsp90, and Hsp100–110, among which Hsp70 is most recognized to be immunostimulatory. Hsp70 has an epitope that is recognized by natural killer (NK) cells and stimulates NK cell proliferation and cytolytic activities [77–79]. Hsp70 is also released by heat-stressed cells and directly binds to TLR2 and TLR4 on antigen-presenting cells (APCs)

such as dendritic cells (DCs) to activate cytokine production and antigen uptake by the APCs [80–82]. Because HSPs are chaperones, HSPs released into the extracellular environment are often bound to proteins from within tumor cells, and therefore by being engulfed by APCs HSPs can transfer potential tumor antigens to APCs [82, 83]. APCs are able to cross-present tumor antigens from HSP complexes to CD8+ T cells via MHC class I and thus elicit tumor-specific CD8+ T cell responses [84–86].

While many HSPs are considered generally immunostimulatory and hence would help suppress tumor growth, negative roles of some HSPs in suppressing tumor growth are also reported [87–90]. Hsp90, for example, blocks apoptosis by directly interacting with and repressing the tumor suppressor protein p53 [87]. Although Hsp110–tumor antigen complex can stimulate DCs to produce inflammatory cytokines and prime antigen-specific naïve T cells, binding of Hsp110 to scavenger receptor A expressed on DCs reduces those activities by DCs [90]. Since HSPs are not only danger signals but also are lifeguards of the cell that protect cells against environmental stress, it is not surprising that some HSPs activate the immune system to attack the heated tumor cells, while other HSPs prevent the heated cells from dying from the heat itself or from overly activated immune attack. Therefore, when applying *in situ* local hyperthermia, it should be noted that the overall outcome is influenced by the sum of all the effects by different HSPs.

Besides heat, many kinds of physiological and chemical stresses induce HSP expression. One of the most striking findings in recent cancer therapy research is that the efficacy of many chemotherapy drugs that have been used historically to kill cancer cells was actually relying on immune activation by chemotherapy-induced immunogenic cell stress and death. In fact, tumor cells treated with those chemotherapy drugs release HSPs, and those treated tumor cells activate DCs and T cells. Therefore, it is not surprising if local tumor hyperthermia also works as an immunotherapy by inducing HSPs that stimulates antitumor immune responses. Furthermore, while HSP induction by local tumor hyperthermia is largely tumor-specific but only in the heated tumor, HSP induction by systemically administered therapeutics is nonspecific but also occurring in tumors of any location including unidentified tumors. This suggests that combination of local hyperthermia with certain chemotherapeutics may be synergistic in stimulating systemic antitumor immune responses.

### 3.2.3.2 Surface Molecules

Hyperthermia can increase the visibility of tumor cells to the immune system. Repasky's group showed that heating tumor cells *in vitro* at 39.5 °C

for 6 h increased surface expression of MICA, an NKG2D ligand, but not MHC class I [91], making the cells more sensitive to lysis by NK cells [91]. Kobayashi's group showed that tumor cells heated *in vitro* at 43 °C for 30 min had increased surface MHC class I levels [92], which allows better recognition by CD8+ T cells. Increased lysis of tumor cells by NK cells and CD8+ T cells within the heated tumor can further improve antitumor immune responses, for instance by creating a more inflammatory cytokine milieu.

### 3.2.3.3 *Tumor Vasculature*

Changes in the vasculature within the tumor may help immune cell mobilization. *In situ* local hyperthermia increases the permeability of tumor vasculature. Dewhirst's group showed that heating rat tumors at 42 °C for 1 h using a water bath increases the diameter of arterioles entering tumors by 35%, resulting in better tumor perfusion [93]. Others show better perfusion in an indirect manner, through increase in pO<sub>2</sub> [94] or better delivery of therapeutic materials [95], but overall there is agreement that blood flow in the tumor is improved upon local hyperthermia in the range of 40–43 °C and that the effect is abrogated at temperatures higher than 43 °C due to hemorrhage. Since better perfusion has the potential to facilitate increased trafficking of immune cells including DCs and T cells between tumors and draining lymph node (dLN), heating to temperatures of 40–43 °C may add further immune-mediated benefit. Immune cell trafficking may be further improved through changes in the vasculature adhesion molecules. Evans' group showed that whole body hyperthermia of 39.5 °C for 5 h in mice increased intratumoral IL-6 trans-signaling [96]. This increases ICAM-1 expression on the tumor vasculature and tumor-specific CD8+ effector/memory T cell trafficking into the tumor, both of which are recapitulated by intravenously administering IL-6 instead of giving whole body hyperthermia. Locally heating tumors at 43 °C for 30 min increases the intratumoral concentration of IL-6. Therefore, it is possible that this local tumor hyperthermia treatment also increases ICAM-1 on the tumor vasculature and enhances trafficking of T cells or other immune cells into the tumor.

### 3.2.3.4 *Exosomes*

Tumor cell-derived exosomes contain enriched amounts of tumor antigens [97–99] and therefore are now recognized as potential immunostimulatory factors. Studies show that pulsing DCs with tumor-derived exosomes results in transfer of tumor antigens to DCs, and those DCs stimulate

tumor antigen-specific CD8+ T cell responses in mice [97] and human *ex vivo* systems [98, 99].

Tumor cells experiencing stress, such as hypoxia and heat, also release increased amounts of exosomes [100–103]. The stress conditions are generally reflected in the content of exosomes [101] and hence also likely in the effects of the exosomes. Exosomes from heated tumor cells do seem to have increased ability to stimulate antitumor immune responses.

Immunosuppressive properties of tumor-derived exosomes are also known. For example, some exosomes of tumor origin express death ligands such as FasL and TRAIL, triggering apoptosis of activated T cells [104, 105]. Exosomes can contain NKG2D ligands and inhibit NKG2D-dependent cytotoxicity of NK cells and CD8+ T cells by blocking the NKG2D receptor [106]. There are also exosomes that induce the differentiation of and support functions of myeloid-derived suppressor cells and regulatory T cells through a transforming growth factor- $\beta$  (TGF- $\beta$ )-dependent mechanism [106, 107]. Although these negative roles of tumor-derived exosomes in immune stimulation are not reported in the context of heat stress, the question of whether exosomes induced by locally heating tumors stimulate or suppress the antitumor immune response in total needs to be assessed carefully. Likely this balance will again depend on details of the specific tumor, the thermal dose and the existing immune response prior to treatment.

### 3.3 Evidences of Hyperthermia Efficacy

A variety of animal studies demonstrate the ability of hyperthermia of one tumor to affect the growth of other tumors not exposed to heat. Most researchers utilize subcutaneous or dermal tumor models for experimental feasibility. While many successful studies heat tumors at 42–45 °C, some studies show hyperthermia at ablation temperatures is also effective in eliciting antitumor immunity. The most immunostimulatory thermal dose parameters are not fully determined yet, and this is further exacerbated by limited information regarding temperature gradients across tumors during treatment. Once again, it would not be surprising if the optimal thermal dose differed for different tumor types.

#### 3.3.1 Optimal Hyperthermia Temperature

Hyperthermia is usually performed with temperatures ranging between 42 and 45 °C. With these parameters, very promising results were obtained by several research groups in the treatment of different kind of tumors *in vivo*.

Yanase *et al.* obtained awesome results by applying an alternating magnetic field to induce heat production by nanosized liposomes containing iron oxide that are directly injected into the tumor [108]. Upon heating of T-9 rat glioma on one flank for 30 min (approximately 42–45 °C throughout the heating process), not only the heated tumor, but also the unheated T-9 tumor implanted on the contralateral flank of the same rat completely disappeared. This coincided with increased infiltration of NK cells, CD4+ T cells and CD8+ T cells in both the heated and unheated tumors, indicating possible roles of these lymphocytes. They also showed that mice whose primary subcutaneous B16 melanoma was heated at 43 °C for 30 min have splenocytes with increased cytotoxicity specifically against B16 cells and show better resistance against secondary B16 rechallenge on the other flank compared to naive mice [109]. Although the comparison was done with naive mice, this at least implies that a single hyperthermia treatment is possibly capable of inducing antitumor efficacy, considering that B16 cells are in general poorly immunogenic. Furthermore, they found that DCs in the heated tumor migrate to the dLN better than DCs in the unheated tumor [110]. Interestingly, the rechallenge resistance was more efficiently induced when the heating was at 43 °C than at 41 °C or 46 °C, which means that the antitumor efficacy is sensitive to small temperature differences and an optimal temperature exists at least within this narrow range of heating temperatures.

Some studies using non-nanomaterial heating methods also produced valuable results. Kubes *et al.* heated subcutaneous B16 tumors at 42 °C for 7 min 3 times by applying microwaves [111]. This treatment increased CD8+ T cells and NK cells in the spleen, and splenocytes from treated mice showed higher cytotoxicity against B16 and NK-sensitive YAC-1 target cells than the untreated controls. Chen *et al.* heated subcutaneous Lewis lung tumors at 42–43 °C for 1 h 3 times using microwaves [112]. They showed that Hsp70 produced by heated tumor cells activated tumor cells to produce chemokines that increased recruitment of DCs and CD4+ and CD8+ T cells into the tumor and that the recruitment was dependent on TLR4 expressed by tumor cells and DCs. Although these two studies did not show whether the immunological changes were sufficient to affect tumor growth of unheated tumors, the results at least tell us that heating tumors at 42–43 °C using microwave methods is also able to elicit antitumor immune responses.

### 3.4 Magnetic Composites for Hyperthermia Treatment

A new approach to enable hyperthermic treatment of bone tumors concerns the realization of an *in situ* forming implant, generally composed of

a polymeric matrix and a magnetic filler. Once exposed to an alternating magnetic field this implant is able to increase the temperature of surrounding tissues.

These intraosseous implants allow localized heating, safeguarding the tissues not colonized by the tumor. They avoid the adverse effects associated with common therapies (such as chemotherapy and radiotherapy), and they are minimally invasive since the thermal therapy can be carried out without further invasive procedures.

The *in situ* implants are a composite material generally based on a polymeric matrix, like polymethyl methacrylate (PMMA), filled with a magnetic ceramic or glass ceramic phase (as represented in Figure 3.3). Several authors proposed the use of micro- and nanoparticles of magnetite as magnetic fillers for the treatment of bone tumors.

For example, Kawashita *et al.* [113] reported a study concerning the synthesis of a PMMA-based cement containing  $\text{Fe}_3\text{O}_4$  particles (5  $\mu\text{m}$ , 40–50–60 wt.%). The authors evaluated the curing parameters of the composites and noted an increase in setting time by increasing the amount of magnetite; the compression strength increased as did the ability to generate heat useful for clinical applications. Other authors synthesized composite bone cements containing two different fillers: magnetite powders and bioactive glass ceramics or silica microparticles [114, 115]. *In vitro* studies on a rabbit animal model evidenced that composite cements are able to generate regulated heat when an external magnetic field is applied, generating a regression of the tumor without any systemic adverse effect.

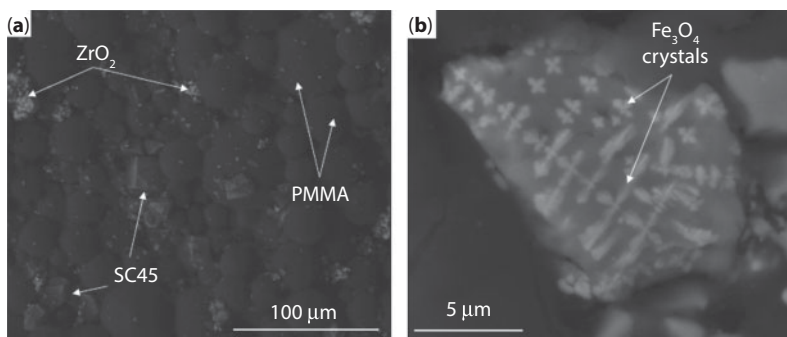


**Figure 3.3** SEM images of composite bone cements. The SC 45 powders appear uniformly distributed into the polymeric matrix, without signs of agglomeration. (a) The compositional analyses evidence the presence of the peaks characteristic of the glass ceramic and of the  $\text{ZrO}_2$ , together with the PMMA peaks. In (b) is also possible to appreciate the presence of the ferromagnetic counterpart. Bar scale = 100  $\mu\text{m}$  (magnification 200 $\times$ ) for (a) and 5  $\mu\text{m}$  (magnification 10,000 $\times$ ) for (b).

These studies demonstrated that a controlled hyperthermic treatment for bone tumors can be achieved.

Clinical studies using magnetic composite cements were reported only for calcium phosphate cements containing magnetite microparticles [114, 115]. These first clinical studies evidenced the possibility to treat metastatic bone tumor by means of *in situ* formed magnetic implant.

Finally, a recent branch of research concerns the development of composite bone cements containing magnetite nanoparticles in order to obtain a material useful both to fill the cavities created following bone cancer removal and to apply a local hyperthermia treatment [116]. In these composites, the heat generation strongly depends on the dimension of the magnetic nanoparticles and on the intensity and frequency of the applied magnetic field. The inclusion of nanoparticles in the polymeric matrix did not affect the compression strength.

However, the proposed composite cements do not promote the integration of the implant with bone tissue. Recently, Bruno *et al.* investigated a new and innovative bone cement formulation composed of a PMMA matrix and a ferrimagnetic (containing magnetite) and bioactive glass ceramic (named SC45), which was studied and characterized by Bretcanu *et al.* [117, 118].

In a first work, the authors investigated the possibility to incorporate the SC45 powders, milled and sieved below 20  $\mu\text{m}$ , in the polymeric matrix (PMMA—Palamed<sup>®</sup>, produced by Heraeus Kulzer S.r.l.). They added different amount of SC45 powders (10, 15, and 20 wt.%), which were mixed with pre-polymerized PMMA and subsequently both phases were blended with monomer (methacrilate—MMA) using a solid/liquid phase ratio of 2 g/ml.

Composite bone cements were characterized in terms of morphology and composition by means of scanning electron microscopy (SEM), microcomputed tomography (micro-CT), and energy dispersion spectrometry (EDS). Morphological and compositional characterizations demonstrated a good dispersion of glass ceramic powders in the polymeric phase. Moreover, the SC45 glass ceramic appears well exposed to the cement surface and this is an essential feature to impart bioactive behavior to the composite cement.

Since the addition of fillers could reduce the mechanical strength of the cement, the influence of the addition of SC45 powders on mechanical properties was investigated by means of compression and bending tests in accordance with ISO 5833-2002. The authors demonstrated that tailoring the size and the amount of the inorganic phase the composite cement maintained good compression and bending strength. In fact, even if the

mechanical strength of composites is slightly lower than that of commercial cements, both compression and bending strength are higher than values required from ISO 5833 standard.

The ability of the composite cements to develop heat was estimated using a magnetic induction furnace Egma 6 (Felmi S.r.l) generating a magnetic field intensity in the range 0–50 mT at fixed working frequency of 220 kHz. These test demonstrated that all cement compositions are able to generate heat useful for hyperthermia treatment when exposed to and alternate magnetic field. Moreover, the authors showed that the power loss increased with the amount of SC45 powders inserted in the cement and with the applied magnetic field.

In a second paper by Vernè *et al.*, the *in vitro* properties of SC45-containing composite cements were evaluated [119]. Leaching test of iron ions was performed by means of graphite furnace atomic absorption spectrometer to assess the iron release, which can cause an iron overloading in the fluids and so a potential toxic risk. The bioactivity of the composite cements was evaluated by *in vitro* test in simulated body fluid (SBF) for up to 1 month. SEM–EDS analyses performed after the bioactivity test demonstrated the composite cements ability to induce the precipitation of hydroxyapatite (HAp) after 1 month of immersion in SBF.

Cytocompatibility test was carried out using human osteosarcoma cells MG63; composites bone cements (containing 10, 15, and 20 wt.% of SC45 powders) and commercial control were subjected to both indirect and direct test (as represented in Figure 3.4). The obtained cell viability was very good, cells adhered and spread on composite cements creating bridge-like

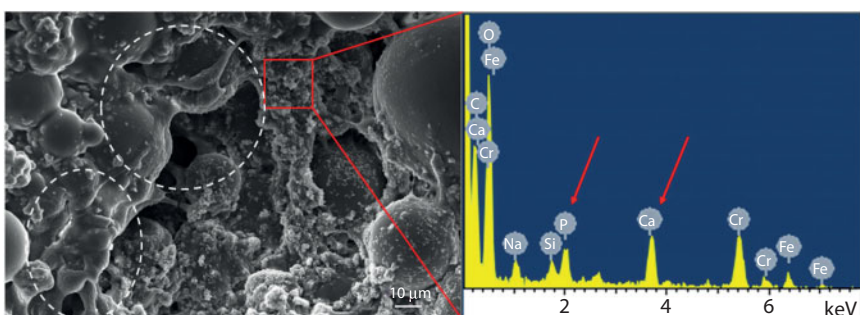


**Figure 3.4** Field emission scanning electron microscopy (FESEM) micrograph of human osteoblasts-like Mg63 cells (white circles) cultured on ferrimagnetic and bioactive composite cement (left panel) and EDS analysis of calcium phosphate crystal grown onto specimen surface (right panel). Cells successfully adhered to the cements surface where the HAp typical Ca and P peaks were detected. Bar scale = 10  $\mu$ m (magnification 5000 $\times$ ).

structures and tridimensional multilayers. In particular, a synergistic effect between cells metabolism and bioactivity of ferrimagnetic glass ceramic was observed; HAp crystals were evidenced at very early stage (72 h) of culture on composite samples suggesting a stimulation of cell mineralization process by the SC45 glass. The obtained results are very promising, and the studied ferrimagnetic and bioactive composite cement represents innovative multifunctional biomaterials for bone tumor therapies.

### 3.5 Magnetic Glass Ceramics

Magnetic glass ceramics can be useful for magnetic hyperthermia treatment of cancer, especially for deep-seated cancers such as bone tumors. When they are implanted into tumors after surgical curettage, they develop heat under oscillating magnetic fields (mainly due to magnetic hysteresis and eddy current losses), destroying the recurrent cancer cells. The hyperthermic process on tumoral cells is extremely complex, and the mechanism of cells destruction is not fully understood. Hyperthermia studies have shown that thermal energy leads to metabolic modifications at the cellular level as well as important changes in the tumor microenvironment. The heat generation depends on the magnetic properties of the glass ceramics, magnetic field parameters (intensity and frequency), and tissue characteristics (thermal conductivity, heat capacity, local blood perfusion, etc.).

During the past decade, the development of bioactive ferrimagnetic glass ceramics has attracted considerable interest. Bioactive materials form a biologically active bone-like apatite, augmenting the formation of new bone tissue and reinforcing the bone structure. The dual effect of magnetic properties and bioactivity makes these glass ceramics extremely attractive for the treatment of bone tumors.

The first magnetic glass ceramics were reported in the 1980s. Luderer *et al.* showed that ferrimagnetic glass ceramics containing lithium ferrite  $\text{LiFe}_5\text{O}_8$  could cause significant tumor regrowth delay and a permanent control of murine breast adenocarcinoma [120, 121]. However, those glass ceramics were not bioactive [122]. Ferrimagnetic glass ceramics containing magnetite in a  $\text{CaO}-\text{SiO}_2$  glassy matrix were obtained by crystallization of  $\text{CaO}-\text{SiO}_2-\text{Fe}_2\text{O}_3$  glasses. Lee and Choi fabricated ferrimagnetic glass ceramics in the system  $\text{Fe}_2\text{O}_3-\text{CaO}-\text{SiO}_2$  by a controlled two-step crystallization method [123, 124].  $\text{B}_2\text{O}_3$  and  $\text{P}_2\text{O}_5$  were added to reduce the glass viscosity and the crystallization temperature. To prevent magnetite decomposition, glasses were covered by carbon powders and then heat-treated at temperatures between 650 and 1000 °C. During the crystallization process,

magnetite, hematite, and  $\beta$ -wollastonite were formed. A preclinical evaluation of cytotoxicity by an agar phantom containing L929 cells showed that those glass ceramics were biocompatible.

Ebisawa *et al.* also reported the synthesis of  $\text{Fe}_2\text{O}_3$ – $\text{CaO}$ – $\text{SiO}_2$  glass ceramics by crystallization [125]. They showed that after heat treatment of a glass with the composition of 40 ( $\text{FeO}$ ,  $\text{Fe}_2\text{O}_3$ )–60  $\text{CaO}$ – $\text{SiO}_2$  (wt.%) at 950 °C, a glass ceramic containing 36 wt.% of magnetite in a  $\beta$ -wollastonite matrix was formed. However, those glass ceramics were not bioactive. The absence of bioactivity was attributed to small amounts of iron ions remaining in the glassy matrix.

In order to overcome the bioactivity problem, small amounts of  $\text{Na}_2\text{O}$ ,  $\text{B}_2\text{O}_3$ , and/or  $\text{P}_2\text{O}_5$  were added in the glass matrix [122, 126, 127]. *In vivo* experiments confirmed that these new glass-ceramics form an apatite layer on their surface and bond tightly with living bone. Glass ceramic granules with the diameter of 2–3 mm and composition of 27.3  $\text{CaO}$ –29.4  $\text{SiO}_2$ –37.7  $\text{Fe}_2\text{O}_3$ –2.8  $\text{P}_2\text{O}_5$ –2.8  $\text{B}_2\text{O}_3$  (wt.%) were used to fill a defect created by drilling a hole in the bone marrow of a tibial metaphysis of a rabbit. The glass ceramic-filled defect was heated in an oscillating magnetic field of 300 Oe at a frequency of 100 kHz. The temperature fields of the glass ceramic and the surrounding bone were measured by two fluoroptic thermometers inserted in the glass ceramic and at the interface between the bone and muscle (Figure 3.3). Due to their magnetic properties, the glass ceramic granules were heated up to 45 °C in 10 min, and the heat was transmitted by conduction to the surrounding bone. The temperature outside the bone was 43 °C. This glass ceramic is bioactive and bonds directly with bone within 8 weeks of implantation.

During the 1990s, Kokubo *et al.* developed glass ceramics containing  $\alpha$ -Fe magnetic phase in a wollastonite-based glassy matrix. As Kokubo's research team had considerable experience using apatite–wollastonite glass ceramics for bone tissue applications, they precipitated  $\alpha$ -Fe magnetic phase in the  $\text{Fe}_2\text{O}_3$ – $\text{CaO}$ – $\text{SiO}_2$  system using a heat treatment of the glass under a  $\text{H}_2$  atmosphere (to avoid the formation of hematite) [128]. The resultant glass ceramic had improved magnetic properties.

Arcos *et al.* studied magnetic composite materials based on a sol-gel-derived glass S58 (58 $\text{SiO}_2$ –36 $\text{CaO}$ –6 $\text{P}_2\text{O}_5$  mol%) and a melt-derived glass FeG (45  $\text{SiO}_2$ –45  $\text{CaO}$ –10  $\text{Fe}_2\text{O}_3$  mol%) [129, 130]. Bioactive sol-gel glasses showed increased *in vitro* bioactivity compared to the melt-derived bioglasses. S58 and FeG components are both bioactive, but they have different bioactivity kinetics. S58 has a fast bioactivity kinetics (forming an apatite-like layer in one day), while FeG has a slow bioactivity kinetics (forming an apatite-like layer in 1 month).  $\text{Na}_2\text{O}$  (3 wt.%) was added to decrease the glass viscosity.

Bretcanu *et al.* developed bioactive and ferrimagnetic glass ceramics in the system  $\text{SiO}_2\text{-Na}_2\text{O}\text{-CaO-P}_2\text{O}_5\text{-FeO-Fe}_2\text{O}_3$  by melting coprecipitation-derived raw materials [131]. These glass ceramics contained only one crystalline phase, magnetite, which was embedded in an amorphous matrix (Figure 3.4). They did not require any further thermal treatment to promote nucleation and growth, as the magnetic phase (magnetite) precipitated during glass quenching (during cooling from melting temperature) [132]. The hysteresis loops of the glass ceramic compared to pure magnetite are shown in Figure 3.5. The glass ceramic presented a very narrow magnetic hysteresis, characteristic of ferrimagnetic materials. The same authors studied the magnetic properties of similar glass ceramics prepared by traditional melting and quenching method [133]. The heat generation of these glass ceramic samples was estimated from calorimetric measurements. Glass ceramics produced by the two methods (coprecipitation-derived and melt-derived) had similar magnetic and calorimetric behavior. This thermal energy is influenced by the melting temperature of the glasses and by the glass ceramic microstructure [133, 134]. The highest power loss was obtained for a melt-derived sample (SC45), melted at 1500 °C.

Saqlain *et al.* analyzed the magnetic properties and bioactivity of  $\text{ZnO-Fe}_2\text{O}_3\text{-SiO}_2\text{-CaO-P}_2\text{O}_5\text{-Na}_2\text{O}$  glass ceramics containing ferrimagnetic  $\text{ZnFe}_2\text{O}_4$ . Heat generation increased with the increase of  $\text{ZnO}$  content in the glass [135]. Similarly, Singh *et al.* studies on  $\text{MgO-CaO-SiO}_2\text{-P}_2\text{O}_5\text{-CaF}_2\text{-Fe}_2\text{O}_3$  glass ceramics showed that the bioactivity kinetics and magnetic hysteresis increased when the iron content was increased [136]. Abdel-Hameed *et al.* studied the influence of  $\text{CuO}$  on magnetic properties

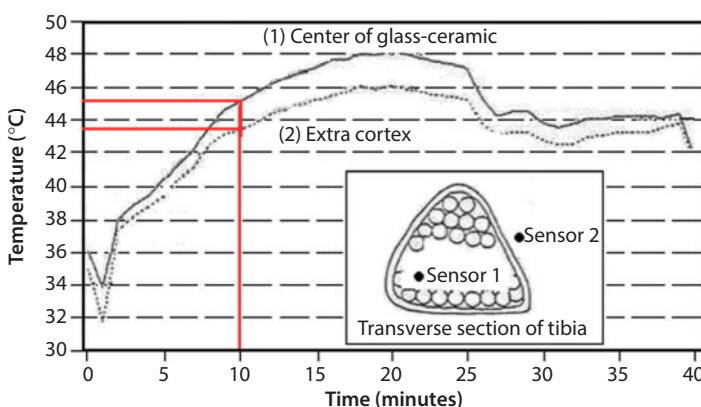
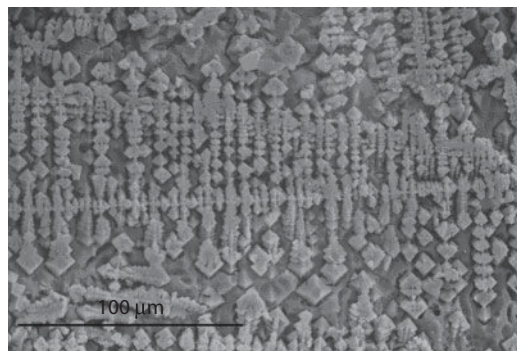
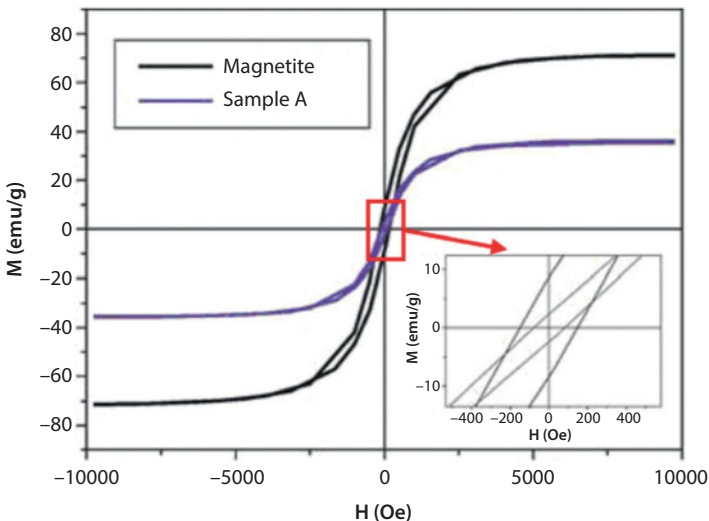


Figure 3.5 Bone heating ability of glass ceramics (adapted from ref. [120]).



**Figure 3.6** SEM image of magnetite crystals after glass ceramic etching. Bar scale = 100  $\mu\text{m}$  (magnification 2000 $\times$ ).



**Figure 3.7** Room temperature hysteresis cycle up to 10 kOe for a coprecipitation-derived magnetic glass ceramic (sample A) and magnetite (adapted from ref. [132]).

of  $\text{Fe}_2\text{O}_3$ – $\text{CaO}$ – $\text{ZnO}$ – $\text{SiO}_2$ – $\text{B}_2\text{O}_3$ – $\text{P}_2\text{O}_5$  glass ceramics [137]. Increasing the amount of  $\text{CuO}$ , decreased the saturation magnetization.

Recently, Sharma *et al.* investigated magnetic glass ceramics with antibacterial properties, belonging to the system  $\text{SiO}_2$ – $\text{CaO}$ – $\text{P}_2\text{O}_5$ – $\text{Fe}_2\text{O}_3$ – $\text{ZnO}$ – $\text{AgO}$  [138]. These materials released Ag ions which attach to the negatively charged bacterial cell wall and break it, leading to the cell death. The antibacterial activity of  $\text{AgO}$ –glass ceramics was evaluated using *E. coli* MG1655, a Gram-negative coliform bacteria. The bacterial growth

inhibition increased with the increase in Ag ions concentration in the glass matrix.

The development of magnetic materials for hyperthermia treatment of cancer is a continuously progressing research field which provides new alternatives for the treatment of cancer. Tailoring the materials' properties and the magnetic field parameters has a significant effect on heat generation in biological tissues. *In vivo* studies of the temperature distribution over time under oscillating magnetic fields will bring new knowledge on the successful elimination of tumoral tissue by magnetic hyperthermia.

### 3.6 Conclusions

About two decades ago, the median survival of patients with bone metastasis from advanced lung cancer was typically measured in months, while the median survival of the patients with bone metastases from prostate cancer or breast cancer was measurable in years [39, 40]. However, recent development of new chemotherapies, including targeted therapies, has dramatically improved these patients' prognoses. Paradoxically, the improvement of prognosis of these cancer patients will lead to an increase in the number of patients with pathological fracture or impending fractures due to bone metastases, even if systemic therapy for bone metastases makes great progress. The results of first series of clinical hyperthermia using magnetic materials achieved good local control of metastatic bone lesions. However, further investigations are needed before this technique can be employed as a standard therapy for bone metastases.

## References

1. Mundy, G.R. Metastasis to bone: causes, consequences and therapeutic opportunities. *Nat. Rev. Cancer.*, 2, 584, 2002.
2. Guise, T.A., et al. Evidence for a causal role of parathyroid hormone-related protein in the pathogenesis of human breast cancer-mediated osteolysis. *J. Clin. Invest.*, 98, 1544, 1996.
3. Kelly, T., et al. Expression of heparanase by primary breast tumors promotes bone resorption in the absence of detectable bone metastases. *Cancer Res.*, 65, 5778, 2005.
4. Pazolli, E., et al. Senescent stromal-derived osteopontin promotes preneoplastic cell growth. *Cancer Res.*, 69, 1230, 2009.
5. McAllister, S.S., et al. Systemic endocrine instigation of indolent tumor growth requires osteopontin. *Cell*, 133, 994, 2008.

6. Anborgh, P.H., Mutrie, J.C., Tuck, A.B., Chambers, A.F. Role of the metastasis-promoting protein osteopontin in the tumor microenvironment. *J. Cell. Mol. Med.*, 14, 2037, 2006.
7. Lynch, C.C., et al. MMP-7 promotes prostate cancer-induced osteolysis via the solubilization of RANKL. *Cancer Cell*, 7, 485, 2005.
8. Li, X., et al. A destructive cascade mediated by CCL2 facilitates prostate cancer growth in bone. *Cancer Res.*, 69, 1685, 2009.
9. Lehr, J.E., Pienta, K.J. Preferential adhesion of prostate cancer cells to a human bone marrow endothelial cell line. *J. Natl. Cancer Inst.*, 90, 118, 1998.
10. Brenner, S., et al. CXCR4-transgene expression significantly improves marrow engraftment of cultured hematopoietic stem cells. *Stem Cells*, 22, 1128, 2004.
11. Kahn, J., et al. Overexpression of CXCR4 on human CD34+ progenitors increases their proliferation, migration, and NOD/SCID repopulation. *Blood*, 103, 2942, 2004.
12. Yoneda, T. Cellular and molecular basis of preferential metastasis of breast cancer to bone. *J. Orthop. Sci.*, 5, 75, 2000.
13. Stier, S., et al. Osteopontin is a hematopoietic stem cell niche component that negatively regulates stem cell pool size. *J. Exp. Med.*, 201, 1781, 2005.
14. Christopher, M.J., Liu, F., Hilton, M.J., Long, F., Link, D.C. Suppression of CXCL12 production by bone marrow osteoblasts is a common and critical pathway for cytokine-induced mobilization. *Blood*, 114, 1331, 2009.
15. Calvi, L.M., et al. Osteoblastic cells regulate the haematopoietic stem cell niche. *Nature*, 425, 841, 2003.
16. Zhang, J., et al. Identification of the haematopoietic stem cell niche and control of the niche size. *Nature*, 425, 836, 2003.
17. Papayannopoulou, T. Mechanisms of stem-/progenitor-cell mobilization: the anti-VLA-4 paradigm. *Semin. Hematol.*, 37, 11, 2000.
18. Hidalgo, A., Peired, A.J., Weiss, L.A., Katayama, Y., Frenette, P.S. The integrin  $\alpha$ M $\beta$ 2 anchors hematopoietic progenitors in the bone marrow during enforced mobilization. *Blood*, 104, 993, 2004.
19. Mendez-Ferrer, S., et al. Mesenchymal and haematopoietic stem cells form a unique bone marrow niche. *Nature*, 466, 829, 2010.
20. Muller, A., et al. Involvement of chemokine receptors in breast cancer metastasis. *Nature*, 410, 50, 2001.
21. Sun, Y.X., et al. Expression and activation of  $\alpha$ v $\beta$ 3 integrins by SDF-1/CXC12 increases the aggressiveness of prostate cancer cells. *Prostate*, 67, 61, 2007.
22. Sun, Y.X., et al. Skeletal localization and neutralization of the SDF-1(CXCL12)/CXCR4 axis blocks prostate cancer metastasis and growth in osseous sites *in vivo*. *J. Bone Miner. Res.*, 20, 318, 2005.
23. Smith, M.C., et al. CXCR4 regulates growth of both primary and metastatic breast cancer. *Cancer Res.*, 64, 8604, 2004.
24. Kang, Y., et al. A multigenic program mediating breast cancer metastasis to bone. *Cancer Cell*, 3, 537, 2003.

25. Clezardin, P. Integrins in bone metastasis formation and potential therapeutic implications. *Curr. Cancer Drug Targets*, 9, 801, 2009.
26. Schneider, J.G., Amend, S.R., Weilbaecher, K.N. Integrins and bone metastasis: integrating tumor cell and stromal cell interactions. *Bone*, 48, 54, 2010.
27. Sangaletti, S., et al. Macrophage-derived SPARC bridges tumor cell-extracellular matrix interactions toward metastasis. *Cancer Res.*, 68, 9050, 2008.
28. Shevde, L.A., Das, S., Clark, D.W., Samant, R.S. Osteopontin: an effector and an effect of tumor metastasis. *Curr. Mol. Med.*, 10, 71, 2010.
29. Korah, R., Boots, M., Wieder, R. Integrin  $\alpha 5\beta 1$  promotes survival of growth-arrested breast cancer cells: an *in vitro* paradigm for breast cancer dormancy in bone marrow. *Cancer Res.*, 64, 4514, 2004.
30. Liesveld, J.L., Dipersio, J.F., Abboud, C.N. Integrins and adhesive receptors in normal and leukemic CD34+ progenitor cells: potential regulatory checkpoints for cellular traffic. *Leuk. Lymphoma*, 14, 19, 1994.
31. Lang, S.H., Clarke, N.W., George, N.J., Testa, N.G. Primary prostatic epithelial cell binding to human bone marrow stroma and the role of  $\alpha 2\beta 1$  integrin. *Clin. Exp. Metastasis*, 15, 218, 1997.
32. Hall, C.L., et al. Type I collagen receptor ( $\alpha 2\beta 1$ ) signaling promotes prostate cancer invasion through RhoC GTPase. *Neoplasia*, 10, 797, 2008.
33. Boissier, S., et al. Bisphosphonates inhibit breast and prostate carcinoma cell invasion, an early event in the formation of bone metastases. *Cancer Res.*, 60, 2949, 2000.
34. Croucher, P.I., et al. Osteoprotegerin inhibits the development of osteolytic bone disease in multiple myeloma. *Blood*, 98, 3534, 2001.
35. Pawelek, J.M., Chakraborty, A.K. Fusion of tumor cells with bone marrow-derived cells: a unifying explanation for metastasis. *Nat. Rev. Cancer*, 8, 377, 2008.
36. Andersen, T.L., et al. Osteoclast nuclei of myeloma patients show chromosome translocations specific for the myeloma cell clone: a new type of cancer-host partnership? *J. Pathol.*, 211, 10, 2007.
37. Vignery, A. Macrophage fusion: are somatic and cancer cells possible partners? *Trends Cell. Biol.*, 15, 188, 2005.
38. Lu, X., Kang, Y. Efficient acquisition of dual metastasis organotropism to bone and lung through stable spontaneous fusion between MDA-MB-231 variants. *Proc. Natl. Acad. Sci. USA*, 106, 9385, 2009.
39. Brubaker, K.D., Vessella, R.L., Brown, L.G., Corey, E. Prostate cancer expression of runt-domain transcription factor Runx2, a key regulator of osteoblast differentiation and function. *Prostate*, 56, 13, 2003.
40. Leong, D.T., et al. Cancer-related ectopic expression of the bone-related transcription factor RUNX2 in non-osseous metastatic tumor cells is linked to cell proliferation and motility. *Breast Cancer Res.*, 12, R89, 2010.
41. Virk, M.S., Lieberman, J.R. Tumor metastasis to bone. *Arthritis. Res. Ther.*, 9, S5, 2007.

42. Harrington, K.D. Metastatic disease of the spine. *J. Bone Joint Surg. Am.*, 68, 1110, 1986.
43. Coleman, R.E. Metastatic bone disease: clinical features, pathophysiology and treatment strategies. *Cancer Treat. Rev.*, 27, 165, 2001.
44. Bauer, H.C. Controversies in the surgical management of skeletal metastases. *J. Bone Joint Surg. Br.*, 87, 608, 2005.
45. Fidler, M. Incidence of fracture through metastases in long bones. *Acta Orthop. Scand.*, 52, 623, 1981.
46. Nathan, S.S., Chan, L., Tan, W.L., Tan, I., Go, M., Chuah, B., *et al.* The need for a system of prognostication in skeletal metastasis to decide best end-of-life care: a call to arms. *Ann. Acad. Med. Singapore*, 39, 476, 2010.
47. Wedin, R. Surgical treatment for pathologic fracture. *Acta Orthop. Scand.*, 72, 21, 2001.
48. Frassica, D.A., Frassica, F.J. Nonoperative management. Simon M.A., Springfield D. (eds) *Surgery for Bone and Soft-tissue Tumors*. Lippincott-Raven, Philadelphia, pp. 633–637, 1998.
49. Yazawa, Y., Frassica, F.J., Chao, E.Y. *et al.* Metastatic bone disease. A study of the surgical treatment of 166 pathologic humeral and femoral fractures. *Clin. Orthop. Relat. Res.*, 251, 213, 1990.
50. Mirels, H. Metastatic disease in long bones: a- proposed scoring system for diagnosing impending pathologic fractures. *Clin. Orthop. Relat. Res.*, 249, 256, 1989.
51. Harrington, K.D. Impending pathologic fractures from metastatic malignancy: evaluation and management. *Instr. Course Lect.*, 35, 357, 1986.
52. Damron, T.A., Morgan, H., Prakash, D., Grant, W., Aronowitz, J., Heiner, J. Critical evaluation of Mirels' rating system for impending pathologic fractures. *Clin. Orthop. Relat. Res.*, 415, S201, 2003.
53. den Brok, M.H., Sutmuller, R.P., van der Voort, R., Bennink, E.J., Figdor, C.G., Ruers, T.J., *et al.* *In situ* tumor ablation creates an antigen source for the generation of antitumor immunity. *Cancer Res.*, 64, 4024, 2004.
54. van der Zee, J. Heating the patient: A promising approach? *Ann. Oncol.*, 13, 1173, 2002.
55. Wust, P., Hildebrandt, B., Sreenivasa, G., Rau, B., Gellermann, J., Riess, H., *et al.* Hyperthermia in combined treatment of cancer. *Lancet Oncol.*, 3, 487, 2002.
56. Obeid, M., Tesniere, A., Panaretakis, T., Tufi, R., Joza, N., van Endert, P., *et al.* Ecto-calreticulin in immunogenic chemotherapy. *Immunol. Rev.*, 220, 22, 2007.
57. Cao, C., Han, Y., Ren, Y., Wang, Y. Mitoxantrone-mediated apoptotic B16-F1 cells induce specific anti-tumor immune response. *Cell. Mol. Immunol.*, 6, 469, 2009.
58. Schiavoni, G., Sistigu, A., Valentini, M., Mattei, F., Sestili, P., Spadaio, F., *et al.* Cyclophosphamide synergizes with type I interferons through systemic dendritic cell reactivation and induction of immunogenic tumor apoptosis. *Cancer Res.*, 71, 768, 2011.

59. Curley, S.A. Radiofrequency ablation of malignant liver tumors. *Oncologist*, 6, 14, 2001.
60. Takada, T., Yamashita, T., Sato, M., Sato, A., Ono, I., Tamura, Y., *et al.* Growth inhibition of re-challenge B16 melanoma transplant by conjugates of melanogenesis substrate and magnetite nanoparticles as the basis for developing melanoma-targeted chemo-thermo-immunotherapy. *J. Biomed. Biotechnol.*, 2009, 457936, 2009.
61. Toraya-Brown, S., Sheen, M.R., Zhang, P., Chen, L., Baird, J.R., Demidenko, E., *et al.* Local hyperthermia treatment of tumors induces CD8(+) T cell-mediated resistance against distal and secondary tumors. *Nanomed. Nanotechnol. Biol. Med.*, 10, 1273, 2014.
62. Xiaoping, L., Leizhen, Z. Advances of high intensity focused ultrasound (HIFU) for pancreatic cancer. *Int. J. Hyperthermia*, 29, 678, 2013.
63. Partanen, A., Tillander, M., Yarmolenko, P.S., Wood, B.J., Dreher, M.R., Kohler, M.O. Reduction of peak acoustic pressure and shaping of heated region by use of multifoci sonifications in MR-guided high-intensity focused ultrasound mediated mild hyperthermia. *Med. Phys.*, 40, 013301, 2013.
64. Krishnan, S., Diagaradjane, P., Cho, S.H. Nanoparticle-mediated thermal therapy: Evolving strategies for prostate cancer therapy. *Int. J. Hyperthermia*, 26, 775, 201.
65. Wust, P., Gneveckow, U., Johannsen, M., Bohmer, D., Henkel, T., Kahmann, F., *et al.* Magnetic nanoparticles for interstitial thermo-therapy – Feasibility, tolerance and achieved temperatures. *Int. J. Hyperthermia*, 22, 673, 2006.
66. Hildebrandt, B., Wust, P., Ahlers, O., Dieing, A., Sreenivasa, G., Kerner, T., *et al.* The cellular and molecular basis of hyperthermia. *Crit. Rev. Oncol. Hematol.*, 43, 33, 2002.
67. Vidair, C.A., Dewey, W.C. Evaluation of a role for intracellular Na<sup>+</sup>, K<sup>+</sup>, Ca<sup>2+</sup>, and Mg<sup>2+</sup> in hyperthermic cell killing. *Radiat. Res.*, 105, 187, 1986.
68. Stevenson, M.A., Calderwood, S.K., Hahn, G.M. Effect of hyperthermia (45 °C) on calcium flux in Chinese hamster ovary HA-1 fibroblasts and its potential role in cytotoxicity and heat resistance. *Cancer Res.*, 47, 3712, 1987.
69. Malhotra, A., Heynen, M.L., Lepock, J.R. Role of extracellular calcium in the hyperthermic killing of CHLV79 cells. *Radiat. Res.*, 112, 478, 1987.
70. Nishida, T., Akagi, K., Tanaka, Y. Correlation between cell killing effect and cell membrane potential after heat treatment: Analysis using fluorescent dye and flow cytometry. *Int. J. Hyperthermia*, 13, 227, 1997.
71. Henle, K.J., Leeper, D.B. Effects of hyperthermia (45 °C) on macromolecular synthesis in Chinese hamster ovary cells. *Cancer Res.*, 39, 2665, 1979.
72. Spiro, I.J., Denman, D.L., Dewey, W.C. Effect of hyperthermia on CHO DNA polymerases alpha and beta. *Radiat. Res.*, 89, 134, 1982.
73. Kampinga, H.H., Jorritsma, J.B., Konings, A.W. Heat-induced alterations in DNA polymerase activity of HeLa cells and of isolated nuclei. Relation to cell survival. *Int. J. Radiat. Biol. Relat. Stud. Phys. Chem. Med.*, 47, 29, 1985.

74. Jorritsma, J.B., Kampinga, H.H., Scaf, A.H., Konings, A.W. Strand break repair, DNA polymerase activity and heat radiosensitization in thermotolerant cells. *Int. J. Hyperthermia*, 1, 131, 1985.
75. Green, D.R., Ferguson, T., Zitvogel, L., Kroemer, G. Immunogenic and tolerogenic cell death. *Nat. Rev. Immunol.*, 9, 353, 2009.
76. Jaattela, M. Heat shock proteins as cellular lifeguards. *Ann. Med.*, 31, 261, 1999.
77. Multhoff, G., Botzler, C., Jennen, L., Schmidt, J., Ellwart, J., Issels, R. Heat shock protein 72 on tumor cells: A recognition structure for natural killer cells. *J. Immunol.*, 158, 4341, 1997.
78. Botzler, C., Li, G., Issels, R.D., Multhoff, G. Definition of extracellular localized epitopes of Hsp70 involved in an NK immune response. *Cell. Stress Chaperon*, 3, 6, 1998.
79. Roigas, J., Wallen, E.S., Loening, S.A., Moseley, P.L. Heat shock protein (Hsp72) surface expression enhances the lysis of a human renal cell carcinoma by IL-2 stimulated NK cells. *Adv. Exp. Med. Biol.*, 451, 225, 1998.
80. Vabulas, R.M., Ahmad-Nejad, P., Ghose, S., Kirschning, C.J., Issels, R.D., Wagner, H. Hsp70 as endogenous stimulus of the Toll/interleukin-1 receptor signal pathway. *J. Biol. Chem.*, 277, 15107, 2002.
81. Asea, A., Rehli, M., Kabingu, E., Boch, J.A., Bare, O., Auron, P.E., et al. Novel signal transduction pathway utilized by extracellular Hsp70: Role of Toll-like receptor (TLR) 2 and TLR4. *J. Biol. Chem.*, 277, 15028, 2002.
82. Todryk, S., Melcher, A.A., Hardwick, N., Linardakis, E., Bateman, A., Colombo, M.P., et al. Heat shock protein 70 induced during tumor cell killing induces Th1 cytokines and targets immature dendritic cell precursors to enhance antigen uptake. *J. Immunol.*, 163, 1398, 1999.
83. Noessner, E., Gastpar, R., Milani, V., Brandl, A., Hutzler, P.J., Kuppner, M.C., et al. Tumor-derived heat shock protein 70 peptide complexes are cross-presented by human dendritic cells. *J. Immunol.*, 169, 5424, 2002.
84. Suzue, K., Zhou, X., Eisen, H.N., Young, R.A. Heat shock fusion proteins as vehicles for antigen delivery into the major histocompatibility complex class I presentation pathway. *Proc. Natl. Acad. Sci. USA*, 94, 13146, 1997.
85. Suto, R., Srivastava, P.K. A mechanism for the specific immunogenicity of heat shock protein-chaperoned peptides. *Science*, 269, 1585, 1995.
86. Binder, R.J., Srivastava, P.K. Peptides chaperoned by heat-shock proteins are a necessary and sufficient source of antigen in the cross-priming of CD8+ T cells. *Nat. Immunol.*, 6, 593, 2005.
87. Neckers, L. Hsp90 inhibitors as novel cancer chemotherapeutic agents. *Trends. Mol. Med.*, 8, S55, 2002.
88. Lin, K., Rockliffe, N., Johnson, G.G., Sherrington, P.D., Pettitt, A.R. Hsp90 inhibition has opposing effects on wild-type and mutant p53 and induces p21 expression and cytotoxicity irrespective of p53/ATM status in chronic lymphocytic leukaemia cells. *Oncogene*, 27, 2445, 2008.
89. Huntoon, C.J., Nye, M.D., Geng, L., Peterson, K.L., Flatten, K.S., Haluska, P., et al. Heat shock protein 90 inhibition depletes LATS1 and LATS2, two

- regulators of the mammalian hippo tumor suppressor pathway. *Cancer. Res.*, 70, 8642, 2010.
90. Qian, J., Yi, H., Guo, C., Yu, X., Zuo, D., Chen, X., *et al.* CD204 suppresses large heat shock protein-facilitated priming of tumor antigen gp100-specific T cells and chaperone vaccine activity against mouse melanoma. *J. Immunol.*, 187, 2905, 2011.
91. Ostberg, J.R., Dayanc, B.E., Yuan, M., Oflazoglu, E., Repasky, E.A. Enhancement of natural killer (NK) cell cytotoxicity by fever-range thermal stress is dependent on NKG2D function and is associated with plasma membrane NKG2D clustering and increased expression of MICA on target cells. *J. Leukoc. Biol.*, 82, 1322, 2007.
92. Ito, A., Tanaka, K., Kondo, K., Shinkai, M., Honda, H., Matsumoto, K., *et al.* Tumor regression by combined immunotherapy and hyperthermia using magnetic nanoparticles in an experimental subcutaneous murine melanoma. *Cancer. Sci.*, 94, 308, 2003.
93. Meyer, R.E., Braun, R.D., Rosner, G.L., Dewhirst, M.W. Local 42 °C hyperthermia improves vascular conductance of the R3230Ac rat mammary adenocarcinoma during sodium nitroprusside infusion. *Radiat. Res.*, 154, 196, 2000.
94. Song, C.W., Shakil, A., Griffin, R.J., Okajima, K. Improvement of tumor oxygenation status by mild temperature hyperthermia alone or in combination with carbogen. *Semin. Oncol.*, 24, 626, 1997.
95. Kong, G., Braun, R.D., Dewhirst, M.W. Characterization of the effect of hyperthermia on nanoparticle extravasation from tumor vasculature. *Cancer Res.*, 61, 3027, 2001.
96. Fisher, D.T., Chen, Q., Skitzki, J.J., Muhitch, J.B., Zhou, L., Appenheimer, M.M., *et al.* IL-6 trans-signaling licenses mouse and human tumor microvascular gateways for trafficking of cytotoxic T cells. *J. Clin. Invest.*, 121, 3846, 2011.
97. Wolfers, J., Lozier, A., Raposo, G., Regnault, A., Thery, C., Masurier, C., *et al.* Tumor-derived exosomes are a source of shared tumor rejection antigens for CTL cross-priming. *Nat. Med.*, 7, 297, 2001.
98. Andre, F., Schartz, N.E., Movassagh, M., Flament, C., Pautier, P., Morice, P., *et al.* Malignant effusions and immunogenic tumor-derived exosomes. *Lancet*, 360, 295, 2002.
99. Bu, N., Wu, H., Sun, B., Zhang, G., Zhan, S., Zhang, R., *et al.* Exosome-loaded dendritic cells elicit tumor-specific CD8+ cytotoxic T cells in patients with glioma. *J. Neurooncol.*, 104, 659, 2011.
100. King, H.W., Michael, M.Z., Gleadle, J.M. Hypoxic enhancement of exosome release by breast cancer cells. *BMC Cancer*, 12, 421, 2012.
101. de Jong, O.G., Verhaar, M.C., Chen, Y., Vader, P., Gremmels, H., Posthuma, G., *et al.* Cellular stress conditions are reflected in the protein and RNA content of endothelial cell-derived exosomes. *J. Extracell. Vesicles*, 1, 18396, 2012.

102. Dai, S., Wan, T., Wang, B., Zhou, X., Xiu, F., Chen, T., *et al.* More efficient induction of HLA-A\*0201-restricted and carcinoembryonic antigen (CEA)-specific CTL response by immunization with exosomes prepared from heat-stressed CEA-positive tumor cells. *Clin. Cancer. Res.*, 11, 7554, 2005.
103. Chen, T., Guo, J., Yang, M., Zhu, X., Cao, X. Chemokine-containing exosomes are released from heat-stressed tumor cells via lipid raft-dependent pathway and act as efficient tumor vaccine. *J. Immunol.*, 186, 2219, 2011.
104. Andreola, G., Rivoltini, L., Castelli, C., Huber, V., Perego, P., Deho, P., *et al.* Induction of lymphocyte apoptosis by tumor cell secretion of FasL-bearing microvesicles. *J. Exp. Med.*, 195, 1303, 2002.
105. Huber, V., Fais, S., Iero, M., Lugini, L., Canese, P., Squarcina, P., *et al.* Human colorectal cancer cells induce T-cell death through release of proapoptotic microvesicles: Role in immune escape. *Gastroenterology*, 128, 1796, 2005.
106. Clayton, A., Tabi, Z. Exosomes and the MICA-NKG2D system in cancer. *Blood Cells Mol. Dis.*, 34, 206, 2005.
107. Valenti, R., Huber, V., Filipazzi, P., Pilla, L., Sovena, G., Villa, A., *et al.* Human tumor-released microvesicles promote the differentiation of myeloid cells with transforming growth factor-beta-mediated suppressive activity on T lymphocytes. *Cancer Res.*, 66, 9290, 2006.
108. Yanase, M., Shinkai, M., Honda, H., Wakabayashi, T., Yoshida, J., Kobayashi, T. Antitumor immunity induction by intracellular hyperthermia using magnetite cationic liposomes. *Jpn. J. Cancer Res.*, 89, 775, 1998.
109. Suzuki, M., Shinkai, M., Honda, H., Kobayashi, T. Anticancer effect and immune induction by hyperthermia of malignant melanoma using magnetite cationic liposomes. *Melanoma Res.*, 13, 129, 2003.
110. Tanaka, K., Ito, A., Kobayashi, T., Kawamura, T., Shimada, S., Matsumoto, K., *et al.* Intratumoral injection of immature dendritic cells enhances antitumor effect of hyperthermia using magnetic nanoparticles. *Int. J. Cancer*, 116, 624, 2005.
111. Kubes, J., Svoboda, J., Rosina, J., Starec, M., Fiserova, A. Immunological response in the mouse melanoma model after local hyperthermia. *Physiol. Res.*, 57, 459, 2008.
112. Chen, T., Guo, J., Han, C., Yang, M., Cao, X. Heat shock protein 70, released from heat-stressed tumor cells, initiates antitumor immunity by inducing tumor cell chemokine production and activating dendritic cells via TLR4 pathway. *J. Immunol.*, 182, 1449, 2009.
113. Kawashita, M., Kawamura, K., Li, Z. PMMA-based bone cements containing magnetite particles for the hyperthermia of cancer. *Acta Biomater.*, 6, 3187, 2010.
114. Matsumine, A., Kenji Takegami, K., Asanuma, K., Matsubara, T., Nakamura, T., Uchida, A., *et al.* A novel hyperthermia treatment for bone metastases using magnetic materials. *Int. J. Clin. Oncol.*, 16, 101, 2011.
115. Kusaka, M., Takegami, K., Sudo, A., Yamazaki, T., Kawamura, J., *et al.* Effect of hyperthermia by magnetite cement on tumor-induced bone destruction. *J. Orthop. Sci.*, 7, 354, 2002.

116. Li, Z., Kawamura, K., Kawashita, M., Kudo, T., Kanetaka, H., Hiraoka, M. *In vitro* assessment of poly(methylmethacrylate)-based bone cement containing magnetite nanoparticles for hyperthermia treatment of bone tumor. *J. Biomed. Mater. Res. A.*, 100, 2537, 2012.
117. Bruno, M., Miola, M., Bretcanu, O., Vitale-Brovarone, C., Gerbaldo, R., Laviano, F., et al. Composite bone cements loaded with a bioactive and ferrimagnetic glass-ceramic. Part I: Morphological, mechanical and calorimetric characterization. *J. Biomat. Applicat.*, 29, 254, 2014.
118. Bretcanu, O., Verne', E., Coisson, M., et al. Magnetic properties of the ferrimagnetic glass-ceramics for hyperthermia. *J. Magn. Magn. Mater.*, 305, 529, 2006.
119. Verné, E., Bruno, M., Miola, M., Maina, G., Bianco, C., Andrea Cochis, A., et al. Composite bone cements loaded with a bioactive and ferrimagnetic glass-ceramic: Leaching, bioactivity and cytocompatibility. *Mat. Sci. Eng. C.*, 53, 95, 2015.
120. Ohura, K., Nakamura, T., Yamamuro, T., Ebisawa, Y., Kokubo, T., Kotoura, Y., et al. A bioactive ferromagnetic glass-ceramic for hyperthermia. *Ceramic in Substitutive and Reconstructive Surgery*, pp. 131–136, Vincenzini, 1991.
121. Borrelli, P. et al., Radio frequency induced hyperthermia for tumor therapy, US Patent 4323056, year 1982
122. Ebisawa, Y., Miyaji, F., Kokubo, T., Ohura, K., Nakamura, T., Bioactivity of ferrimagnetic glass-ceramics in the system  $\text{FeO}-\text{Fe}_2\text{O}_3-\text{CaO}-\text{SiO}_2$ . *Biomaterials*, 18, 1277, 1997.
123. Lee, Y.K., Choi, S.Y. Crystallisation and properties of  $\text{Fe}_2\text{O}_3-\text{CaO}-\text{SiO}_2$  glasses. *J. Am. Ceram. Soc.*, 79, 992, 1996.
124. Oh, SH., Choi, S., Lee, Y.K., Kim, K.N. Research on annihilation of cancer cells by glass-ceramics for cancer treatment with external magnetic field. I. Preparation and citotoxicity. *J. Biomed. Mater. Res.*, 54, 360, 2001.
125. Ebisawa, Y., Sugimoto, Y., Hayashi, T., Kokubo, T., Ohura, K., Yamamuro, T. *Crystallisation of ( $\text{FeO}, \text{Fe}_2\text{O}_3$ )-CaO-SiO<sub>2</sub> glasses and magnetic properties of their crystallized products*. Sermikkusu Ronbunshi, pp. 7–13, 1, 1991.
126. Ebisawa, Y., Kokubo, T., Ohura, K., Yamamuro, T. Bioactivity of  $\text{Fe}_2\text{O}_3$ -containing CaO-SiO<sub>2</sub> glasses: *in vitro* evaluation. *J. Mater Sci: Mater in Med.*, 4, 225, 1992.
127. Ohura, K., Nakamura, T., Yamamuro, T., Ebisawa, T., Kokubo, T., Kotoura, Y., et al. Bioactivity of CaO-SiO<sub>2</sub> glasses added with various ions. *J. Mater Sci: Mater in Med.*, 3, 95, 1992.
128. Konaka, H., Miyaji, F., Kokubo, T. Preparation and magnetic properties of glass-ceramics containing  $\alpha$ -Fe for hyperthermia. *J. Ceram. Soc. Jpn.*, 105, 833, 1997.
129. Arcos, D., del Real, R.P., Vallet-Regi, M. A novel bioactive and magnetic biphasic material. *Biomaterials*, 23, 2151, 2002.
130. Arcos, D., del Real, R.P., Vallet-Regi, M. Biphasic materials for bone grafting and hyperthermia treatment of cancer. *J. Biomed. Mater. Res.*, 65A, 71, 2003.
131. Bretcanu, O., Spriano, S., Verne' E., Coisson M., Tiberto P., Allia P. The influence of crystallised  $\text{Fe}_3\text{O}_4$  on the magnetic properties of

- coprecipitation-derived ferrimagnetic glass–ceramics. *Acta Biomater.*, 1, 421, 2005.
132. Bretcanu, O., Spriano, S., Brovarone Vitale, C., Verne', E. Synthesis and characterization of coprecipitation-derived ferrimagnetic glass-ceramic. *J. Mater. Sci.*, 41, 1029, 2006.
133. Bretcanu, O., Verne', E., Coisson, M., Tiberto, P., Allia, P. Magnetic properties of the ferrimagnetic glass-ceramics for hyperthermia. *J. Magnetism Magnetic Mater.*, 305, 529, 2006.
134. Bretcanu, O., Verné, E., Coisson, M., Tiberto, P., Allia, P. Temperature effect on the magnetic properties of the coprecipitation derived ferrimagnetic glass-ceramics. *J. Magnetism Magnetic Mater.*, 300, 412, 2006.
135. Saqlain, A.S., Hashmi, M.U., Alam, S., Shamim, A. Magnetic and bioactivity evaluation of ferrimagnetic  $ZnFe_2O_4$  containing glass ceramics for the hyperthermia treatment of cancer. *J. Magnetism Magnetic Mater.*, 322, 375, 2010.
136. Singh, R.K., Srinivasan, A. Bioactivity of ferrimagnetic  $MgO-CaO-SiO_2-P_2O_5-Fe_2O_3$  glass-ceramics. *Ceram. Internat.*, 36, 283, 2010.
137. Abdel-Hameed, S.A.M., Marzouk, M.A., Abdel-Ghany, A.E. Magnetic properties of nanoparticles glass–ceramic rich with copper ions. *J. Non-Crystall. Solids.*, 357, 3888, 2011.
138. Sharma, K., Meena, S.S., Saxena, S., Yusuf, S.M., Srinivasan, A., Kothiyal, G.P. Structural and magnetic properties of glass-ceramics containing silver and iron oxide. *Mater. Chem. Phys.*, 133, 144, 2012.

# Magnetic Iron Oxide Nanoparticles: Advances on Controlled Synthesis, Multifunctionalization, and Biomedical Applications

Dung The Nguyen and Kyo-Seon Kim\*

*Department of Chemical Engineering, Kangwon National University, Chuncheon, Kangwon-do, Korea*

---

## **Abstract**

This chapter focuses on the controlled synthesis, multifunctionalization, and biomedical applications of magnetic iron oxide nanoparticles. Substantial progresses in the size, shape, and component control of iron oxide nanoparticles have been made by developing various methods such as co-precipitation, thermal decomposition, micelle synthesis, and hydrothermal synthesis. Precise control over the synthesis as well as surface functionalization of iron oxide nanoparticles is crucial because it governs their magnetic characteristics, physicochemical properties, colloidal stability, and biological behavior. For biomedical purposes, the magnetic iron oxide nanoparticles should possess a very high homogeneity of particle morphology and composition with narrow size distribution along with high magnetization values. Their proper surface coating is required to ensure their dispersion, stability, and biocompatibility in order to prevent endocytosis by macrophages as well as to extend their residence time in circulating blood. In this chapter, key technical principles of magnetic iron oxide nanoparticle synthesis with subsequent multifunctionalization of nanoparticles are discussed thoroughly. Also, the ongoing advancement of biomedical treatments using magnetic iron oxide nanoparticles are highlighted. Finally, some challenges, future trends, and perspectives in these research areas are outlined.

**Keywords:** Magnetic nanoparticles, iron oxide nanoparticles, controlled synthesis, multifunctionalization, biomedical applications

---

\*Corresponding author: kkyoseon@kangwon.ac.kr

## 4.1 Introduction

In recent years, the magnetic  $\text{Fe}_3\text{O}_4$  nanoparticles have been of great interest to worldwide researchers for biomedical applications because of their magnetic behaviors under magnetic fields and field gradients. They have their own advantages that provide many exciting opportunities in many applications, specifically, in biomedical treatments such as controlled drug delivery and hyperthermia [1–4]. The particle size, shape, and surface structure of  $\text{Fe}_3\text{O}_4$  nanomaterials can be prepared controllably to match with the requirements in specific applications. Due to their response to an external magnetic field, the  $\text{Fe}_3\text{O}_4$  nanoparticles play an important role as the contrast enhancement agents of magnetic resonance imaging. In addition, the  $\text{Fe}_3\text{O}_4$  nanoparticles can also be manipulated by an external magnetic force, and this action at a distance provides tremendous advantages for many applications such as magnetic hyperthermia and targeted drug delivery as well as controlled drug release.

It is still a great challenge to controllably synthesize  $\text{Fe}_3\text{O}_4$  nanoparticles of customized size and shape with appropriate surface engineering. For biomedical treatments, the  $\text{Fe}_3\text{O}_4$  nanoparticles should possess very uniform morphology with high magnetization values to ensure the external controllability. They also must have good dispersion, stability and biocompatibility to prevent endocytosis by macrophages as well as to extend their residence time in circulating blood. Precise control over the synthetic conditions as well as surface functionalization of magnetic nanoparticles is crucial because it governs their magnetic characteristics, colloidal stability, physicochemical properties, and biological responses.

In this chapter, we highlight the recent progresses on the synthesis of  $\text{Fe}_3\text{O}_4$  nanostructures with corresponding formation mechanisms. We also provide a basic background on the physical properties of magnetic nanoparticles and then introduce design strategies for magnetic nanoparticles as a platform for hyperthermia-based treatments. Furthermore, we introduce and discuss some typical developments of mechanical actuation and manipulation of drug release which are important to accomplish highly effective therapeutics in a noninvasive and remote fashion. Finally, we conclude this review with our outlook and perspectives on the future research in this field. We believe that what is presented in this chapter can be considered as a collection of protocols for controlled synthesis and multifunctionalization of magnetic  $\text{Fe}_3\text{O}_4$  nanoparticles as well as their applications in biomedical research.

## 4.2 Controlled Synthesis of $\text{Fe}_3\text{O}_4$ Nanoparticles

Magnetite nanoparticles of various sizes, surfaces, and spatial confinements have been successfully synthesized by a number of different methods such as chemical co-precipitation, thermal decomposition and oxidation-reduction, microemulsion, and hydrothermal/solvothermal synthesis. Table 4.1 shows the features of iron oxide nanoparticles fabricated through different methods. The gas-phase methods for preparing iron oxide nano-materials depend on thermal decomposition reduction, oxidation, or other reactions to solidify particles from gas-phase precursors. Although gas-phase methods are able to produce a large amount of particles, it is difficult to control precisely various process variables such as oxygen concentration and impurities to obtain homogeneous products.

The co-precipitation and sol-gel methods are convenient ways to synthesize iron oxides at either room temperature or elevated temperature. The main advantage of these methods is that a large amount of nanoparticles can be synthesized. However, iron oxide nanoparticles synthesized under these conditions usually exhibit a low degree of crystallinity and large polydispersity which result in nonideal magnetic behavior for many applications.

To obtain monodisperse magnetite nanoparticles of different sizes, significant advances have been developed by providing a constrained environment for particle nucleation and growth such as microemulsion synthesis. The microemulsions are currently being used to synthesize iron oxide nanoparticles with a narrow size range and uniform physical properties. However, in comparison with other methods, the yield of product through microemulsion synthesis is low, while a large amount of solvent is required and thus this method is not a very efficient process and also difficult to scale up.

High-temperature synthesis techniques such as hydrothermal/solvothermal processes are alternative methods for the preparation of highly crystalline iron oxide nanoparticles. The magnetic nanoparticles prepared from thermal decomposition and hydrothermal/solvothermal approaches exhibit high uniformity in both size and shape with excellent magnetic properties and the preparation processes show high potential on a large-scale production. Herein, we highlight several typical synthesis processes to control magnetic properties of nanoparticles with the corresponding particle formation mechanisms, focusing on the preparation of  $\text{Fe}_3\text{O}_4$ -based materials through high-temperature synthesis techniques which allow the fabrication of high-quality nanoparticles on a relatively large-scale production.

**Table 4.1** Features of iron oxide nanoparticles fabricated through different methods.

Features	Methods	Gas phase	Co-precipitation	Sol-gel	Microemulsion	Solvothermal
Size and size distribution	~5–60 nm, broad distribution	~10–50 nm, broad distribution	~20–200 nm, broad distribution	~4–15 nm, narrow distribution	~5–500 nm, narrow distribution	
Dispersity	Large aggregates	Large aggregates	Large aggregates	Mono-dispersity	Mono-dispersity	
Shape control	Not good	Not good	Not good	Good	Good	
Magnetization	10–50 emu/g	20–50 emu/g	10–40 emu/g	30–50 emu/g	70–90 emu/g	
Yield	High/scalable	High/scalable	High/scalable	Low	Medium/scalable	

#### 4.2.1 Size-controlled Synthesis of $\text{Fe}_3\text{O}_4$ Nanoparticles

Monodisperse iron oxide nanoparticles were widely synthesized by high-temperature methods. The high-temperature processes resulted in rapid nucleation and growth of the newly formed particles, leading to the formation of small-sized nanoparticles. The precursors included metal acetylacetones,  $[\text{M}(\text{acac})_n]$ , ( $\text{M} = \text{Fe}, \text{Mn}, \text{Co}, \text{Ni}, \text{Cr}; n = 2 \text{ or } 3$ , acac = acetylacetone), metal cupferronates  $[\text{MxCupx}]$  ( $\text{M} = \text{metal ion}$ ; Cup =  $N$ -nitrosophenylhydroxylamine,  $\text{C}_6\text{H}_5\text{N}(\text{NO})\text{O}^-$ ), or carbonyls. Fatty acids, oleic acid, and hexadecylamine were often used as surfactants. The reaction conditions such as solvent, temperature, precursors, and processing time strongly affected the product properties. For instance, the particle size could be controlled by using different solvents of different boiling points. Sun *et al.* [5, 6] reported a synthesis of 4 nm monodisperse magnetite nanoparticles by refluxing a reaction mixture containing the iron (III) acetylacetone ( $\text{Fe}(\text{acac})_3$ ) 1,2-hexadecanediol, oleic acid, and oleylamine in diphenyl ether solvent (boiling point of 265 °C), while 6-nm monodisperse  $\text{Fe}_3\text{O}_4$  nanoparticles were obtained in benzyl ether solvent (boiling point of 300 °C). To make larger  $\text{Fe}_3\text{O}_4$  nanoparticles, a seeded growth process was demonstrated for generating nanoparticles up to 16 nm by controlling the ratio of seed to additional precursor. Hyeon *et al.* prepared 5-, 9-, 12-, 16-, and 22-nm-sized iron oxide nanoparticles from Fe–oleate complex by using different solvents including 1-hexadecene, octyl ether, 1-octadecene, 1-eicosene, and trioctylamine which have the boiling point of 274 °C, 287 °C, 317 °C, 330 °C, and 365 °C, respectively [7]. They also developed an ultra-large-scale synthesis of 40-g monodisperse  $\text{Fe}_3\text{O}_4$  nanoparticles using Fe–oleate complex [8]. In this process, Fe–oleate complex prepared from hydrated iron chloride and sodium oleate was transferred to an appropriate high-boiling-point solvent, and slowly heated to around 300 °C to produce monodisperse  $\text{Fe}_3\text{O}_4$  nanoparticles. The synthesis process was composed of two sequential steps: the thermal decomposition of iron–oleate complex to generate intermediate species, and the nucleation and growth of iron oxide nanoparticles from these intermediate species. Uniform-sized nanocrystals of other metal oxides such as  $\text{MnO}$ ,  $\text{CoO}$ , and  $\text{ZnO}$  and  $\text{MFe}_2\text{O}_4$  ( $\text{M} = \text{Mn}, \text{Zn}, \text{Co}$ ) were also produced by using a similar synthetic procedure involving the pyrolysis of corresponding metal–oleate complexes.

The molar ratios of starting reagents including organometallic compounds, surfactant, and solvent were decisive parameters for the control of particle size and morphology. Jana *et al.* [9] reported the synthesis of monodisperse  $\text{Fe}_3\text{O}_4$  colloidal nanoparticles of larger size via the pyrolysis of iron oleate salt with presences of octadecane and oleic acid. By changing

the ratio of iron oleate salt to oleic acid from 0.1 to 10, the diameter of the  $\text{Fe}_3\text{O}_4$  nanoparticles could be controlled between 6 and 50 nm. Another study reported that triethylene glycol directly reacted with  $\text{Fe}(\text{acac})_3$  at an elevated temperature to prepare nonagglomerated  $\text{Fe}_3\text{O}_4$  nanoparticles with uniform shape and narrow size distribution.

Hyeon's group prepared monodisperse iron oxide nanoparticles by thermal decomposition of an iron–oleate complex which was synthesized from pentacarbonyliron,  $[\text{Fe}(\text{CO})_5]$ , and oleic acid, followed by controlled chemical oxidation with trimethylamine N-oxide as a mild oxidant [10]. Particle sizes of 4, 8, and 11 nm were obtained by using reaction mixtures of  $[\text{Fe}(\text{CO})_5]$  and oleic acid at molar ratios of 1:1, 1:2, and 1:3, respectively. In this synthesis, monodisperse iron nanoparticles were initially generated, and these were further oxidized controllably to produce iron oxide nanoparticles.

Hyeon's group achieved the synthesis of monodisperse magnetic iron oxide nanocrystals controlled in a 1 nm level by seed-mediated growth of monodisperse nanoparticle seeds previously synthesized [11]. Monodisperse iron nanoparticles with sizes of 6, 7, 9, 10, 12, 13, and 15 nm could be synthesized by heating solutions of various combinations of 4-, 8-, or 11-nm iron seed nanoparticles with solutions of 1.5, 3.0, or 4.5 mmol iron–oleate complex. These synthesized iron nanoparticles were readily oxidized to highly crystalline iron oxide when exposed to air. These monodisperse nanoparticles were obtained directly without a size-selection process. The synthetic procedure was highly reproducible and could be applicable to synthesize monodisperse nanoparticles of other materials.

#### 4.2.2 Structure-controlled Synthesis of $\text{Fe}_3\text{O}_4$ Nanoparticles

Formation of structured  $\text{Fe}_3\text{O}_4$  porous/hollow nanoparticles is expected to integrate the valuable characteristics of porous/hollow structure and unique magnetic property of  $\text{Fe}_3\text{O}_4$  material in a single platform which can provide opportunities to tune their properties for specific applications. Porous and/or hollow magnetic nanoparticles are expected to have similar magnetic, chemical, and biological properties as the solid nanoparticles, while their structures offer the additional opportunity to store and release drugs at a target.

Ge *et al.* [12] reported the synthesis of highly water dispersible and porous  $\text{Fe}_3\text{O}_4$  nanoparticles with uniform size from about 31 to about 174 nm. Each nanoparticle was composed of many primary smaller nanoparticles of approximately 10 nm in diameter. In their process, iron (III) chloride and diethylene glycol (DEG) were used as precursor and solvent,

respectively. Polyacrylic acid (PAA) was selected as surfactant. Introduction of NaOH into the hot mixture of DEG,  $\text{FeCl}_3$ , and PAA resulted in the hydrolysis of  $\text{FeCl}_3$ . Under the reductive atmosphere provided by DEG at high temperature,  $\text{Fe(OH)}_3$  was partially transformed into  $\text{Fe(OH)}_2$ , and finally  $\text{Fe}_3\text{O}_4$  nanoparticles were formed through dehydration. These  $\text{Fe}_3\text{O}_4$  primary nanoparticles spontaneously aggregated to form larger-sized  $\text{Fe}_3\text{O}_4$  nanoparticles. The size of the  $\text{Fe}_3\text{O}_4$  nanoparticles could be precisely controlled by simply increasing the amount of NaOH, while keeping all other parameters fixed.

Zhao *et al.* [13] reported the formation of nanoporous  $\text{Fe}_3\text{O}_4$  particles with excellent magnetic properties and various specific morphologies by simply changing the solvent system and amount of KOH. In a typical process, the  $\text{FeSO}_4$  was dissolved in ethylene glycol or glycerol to form a homogeneous solution, followed by a quick addition of KOH at room temperature. The mixture was then transferred into a Teflon-lined stainless steel autoclave, sealed, and maintained at 200 °C for 24 h for the complete formation of product particles. The KOH concentration and solvent properties determined the growth of particles, leading to the evolution of different particle morphologies including cube, truncated octahedron, octahedron, sphere, truncated cube, and equilateral octahedron.

It has been reported that the  $\text{Fe}_3\text{O}_4$  hollow nanoparticles were successfully prepared through the controlled oxidation of the Fe nanoparticles as templates [14, 15]. The Fe nanoparticles were not chemically stable and would be oxidized to form  $\text{Fe}/\text{Fe}_3\text{O}_4$  core/shell structures. Controlled oxidation of these core/shell nanoparticles eventually led to the formation of hollow  $\text{Fe}_3\text{O}_4$  nanoparticles. In this process, the Fe metal diffused outward faster than oxygen did inward and  $\text{Fe}_3\text{O}_4$  was formed at the metal–oxide interface rather than in the interior. The Fe template directly determined the shape and cavity size of the final hollow structure. Although this process was efficient, it still required a complicated chemical and physical control for the formation of robust shells [16]. For example, the specific geometry, diffusivity, and concentration profile of materials should satisfy the conditions by which the diffusivity of core material exceeds that of shell material. For the Fe templates larger than the critical size of 8 nm, voids were not observed and only metal/metal oxide core/shell solid spheres were obtained [17].

Recently, one template-free method to prepare  $\text{Fe}_3\text{O}_4$  hollow nanoparticles has been developed based on the inside-out Ostwald ripening of primary particles inside a crystallite aggregate. The plausible mechanism was supported by several experimental observations. The dissolution-relocation of grains which built the aggregates could be rationalized by considering the different chelation modes between the outer and inner grains

or by the existence of bubbles inside the aggregates [18–22]. The chemical conversion has been also demonstrated as an important factor for the hollowing process [23]. The chemical conversions of solid material caused a shrinkage of the grain size. The reduced grains around the exterior surface of the aggregates quickly became compact and were transformed to be a solid and stable surface shell while the reduced grains within the aggregates led to the formation of a loosely packed structure. The inner grains which were possibly less stable than solid shell became objects of the inside-out Ostwald ripening and would migrate and deposit onto the stable exterior shell, resulting in continuous expansion of cavity space inside the aggregates. The hollow structure was well developed with the complete chemical conversions of core grains. By simply adjusting the initial concentrations of Fe precursor and additive or varying other process variables such as processing time and temperature, the  $\text{Fe}_3\text{O}_4$  porous/hollow nanoparticles were synthesized controllably with tunable particle size and porosity [24, 25]. Schematic of the particle formation and hollow structure development of  $\text{Fe}_3\text{O}_4$  porous/hollow nanoparticles is given in Figure 4.1.

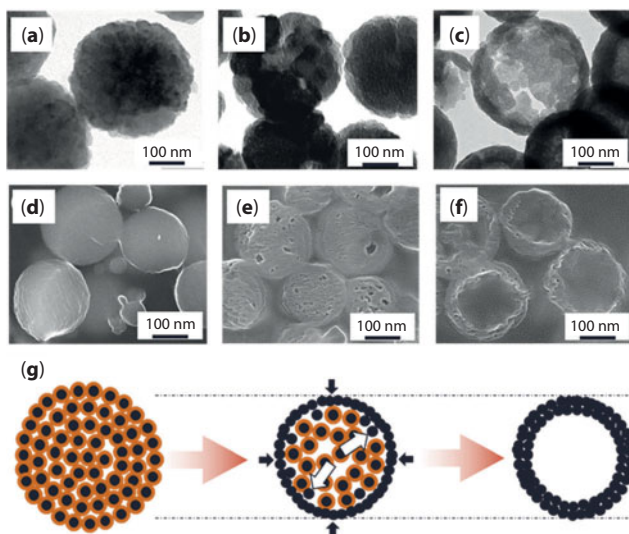


**Figure 4.1** (a–c) TEM images and (d–f) corresponding SEM images of cross-section of  $\text{Fe}_3\text{O}_4$  nanoparticles prepared by solvothermal process for 6, 8, and 12 h of processing times, respectively, showing the evolution of porous/hollow structures, and (g) schematic of the hollow structure development in solvothermal process. The chemical conversion caused the nonuniformities of tiny grains and the empty spaces within the spheres and thus enhanced the outward migration and relocation of the core grains toward the outer layer, resulting in generation and development of hollow structure.

#### 4.2.3 Component-controlled Synthesis of $\text{Fe}_3\text{O}_4$ Nanoparticles

Considering that the effects of magnetic nanoparticles for biomedical applications are strongly depend on their magnetic characteristics, it is important to synthesize monodisperse nanoparticles with high magnetization saturation values. The partial substitution of iron with other transition metal (e.g. Cu, Ni, Co, Mn) in the crystal lattice of magnetite ( $\text{Fe}_3\text{O}_4$ ) may display enhanced properties, such as higher magnetic permeability and electrical resistivity than those of magnetite. Jang *et al.* [26] synthesized  $\text{Zn}^{2+}$ -doped ferrite nanoparticles by thermal decomposition of a metal chloride ( $\text{MCl}_2$ , M =  $\text{Zn}^{2+}$ ,  $\text{Mn}^{2+}$ , and  $\text{Fe}^{2+}$ ) and  $\text{Fe}(\text{acac})_3$ . A large-scale (ca. 10 g) synthesis was achieved. The  $\text{Zn}^{2+}$  doping level was carefully controlled by varying the initial molar ratio of the metal chloride precursors. The magnetization saturation gradually increased as the  $\text{Zn}^{2+}$  doping level of nanoparticles increased from  $x = 0$  to 0.1, 0.2, 0.3, and 0.4. The magnetization saturation reached maximum for  $x = 0.4$ . Structure investigation revealed that  $\text{Zn}^{2+}$  dopant mainly occupied tetrahedral sites of the spinel matrix. When  $x < 0.4$ , Zn dopant induced the partial removal of antiferromagnetic coupling interactions between  $\text{Fe}^{3+}$  ions in the tetrahedral and octahedral sites. For higher  $\text{Zn}^{2+}$  doping levels ( $x > 0.4$ ), anti-ferromagnetic interaction of  $\text{Fe}^{3+}$  at nearby octahedral sites was dominant and the net magnetization moment decreased. According to the results, the Zn-doped nanoparticles exhibited an 8- to 14-fold increase in MRI contrast and a fourfold enhancement in hyperthermic effects compared to the commercial Feridex nanoparticles.

Elemental iron (Fe) has a higher magnetization than that of metal oxide form, and this concept has led to creation of Fe–core and  $\text{Fe}_3\text{O}_4$ –shell magnetic nanoparticles with unique characteristics. Yoon *et al.* [27] presented the formation of nanoparticles consisted of an elemental iron (Fe) core and an artificial ferrite shell ( $\text{Fe}@\text{MFe}_2\text{O}_4$ , M=Fe, Mn, Co) by thermally decomposing iron complex  $[\text{Fe}(\text{CO})_5]$  in the presence of oleylamine under air-free conditions. By adding Fe–oleate complexes and co-injecting Mn–oleate or Co–oleate complexes with Fe–oleate to Fe nanoparticles suspension and annealing the mixture at elevated temperatures, the Fe nanoparticles with protective shells of the ferrite structure ( $\text{Fe}@\text{Fe}_3\text{O}_4$ ,  $\text{Fe}@\text{MnFe}_2\text{O}_4$  or  $\text{Fe}@\text{CoFe}_2\text{O}_4$ ) were obtained. The core-shell nanoparticles displayed a hysteresis loop with high saturation magnetization but negligible coercivity and remanence. Consequently, their magnetic dipole interaction was negligible, resulting in good colloidal stability in aqueous media after suitable surface treatments. Increasing the crystallinity of ferrite shells could further improve the magnetization of such core–shell

nanoparticles [28]. Generally, the overall synthesis procedure was similar to seed-mediated growth method. The shell material is controlled by the heterogeneous nucleation of the shell precursor on the surface of core material. The homogeneous nucleation of shell precursor which results in the formation of new particles must be prohibited. Obviously, this method allows an independent control of the core and the shell during the synthesis, resulting in a controllable size ratio between the core diameter and shell thickness. This method had been also developed in the synthesis of various core–shell nanoparticles such as  $\text{CoFe}_2\text{O}_4/\text{ZnFe}_2\text{O}_4$ ,  $\text{CoFe}_2\text{O}_4/\text{MnFe}_2\text{O}_4$ ,  $\text{Mn}_{x}\text{Fe}_{3-x}\text{O}_4/\text{Fe}_x\text{Mn}_{3-x}\text{O}_4$ ,  $\text{Fe}_3\text{O}_4/\text{Mn}_3\text{O}_4$ , and  $\text{Mn}_3\text{O}_4/\text{Fe}_3\text{O}_4$  [29–34].

## 4.3 Surface Modification of $\text{Fe}_3\text{O}_4$ Nanoparticles for Biomedical Applications

### 4.3.1 Surface Modification of $\text{Fe}_3\text{O}_4$ Nanoparticles

The biomedical applications of magnetic nanoparticles depend on a number of factors related to the size, shape, and magnetism of the biocompatible nanoparticles as well as the physicochemical properties of the drug-loaded nanoparticles, field strength and geometry, depth of target tissue, rate of blood flow, and so on. Surface coating of  $\text{Fe}_3\text{O}_4$  nanoparticles is required to protect particle agglomeration and to provide functional groups for the conjugation of other materials such as drugs, targeting ligands, proteins and DNA sequences. Additionally, surface coating of  $\text{Fe}_3\text{O}_4$  nanoparticles enhances nanoparticle pharmacokinetics, endosomal release, and tailored drug loading and release behaviors. To serve these coating functions, a diverse group of materials have been investigated including inorganic materials such as gold, silica, and organic materials such as dextran, chitosan, polyethylene glycol, and so on as shown in Figure 4.2.

When polymeric materials are employed as stabilizers, the adsorption of polymers onto the magnetic nanoparticles provides protective steric repulsion and acts as a barrier against the interaction between the particles and thus keeping the particles from aggregation. The key characteristics of polymeric materials should be considered including length and molecular weight, biodegradability and hydrophobic/hydrophilic nature, conformation, degree of surface coverage, and attachment mechanism to the particle surface. The polymeric coatings could introduce new chemical functionality and surface charge to the nanoparticles for further attachment of other materials. For example, the functionalized  $\text{Fe}_3\text{O}_4$  nanoparticles with extended amine groups could carry other active targeting moieties, drugs,

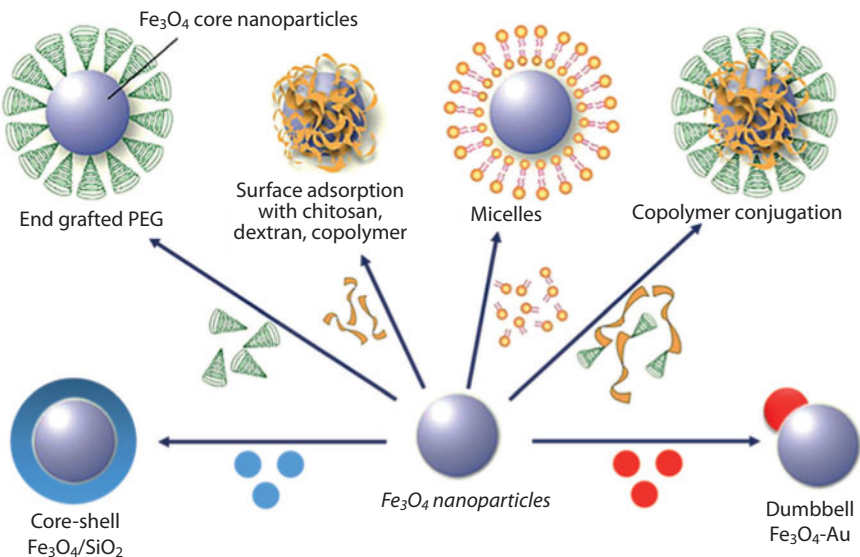


**Figure 4.2** Illustration depicting the modification of various materials onto the surface of magnetic nanoparticle cores.

and imaging agents by both physical interactions and covalent linkages such as disulfide bound formation, carbon-thiol formation, amide formation, ether, and ester formation [35–38].

The adsorption of block-copolymers such as poloxamers and poloxamines has been widely studied [39–41]. Such copolymers adsorbed onto the surface of hydrophobic  $\text{Fe}_3\text{O}_4$  nanoparticles via their hydrophobic poly(propylene oxide) (PPO) component, extending the hydrophilic poly(ethylene oxide) (PEO) side arms outward from the particle surface. The strength of polymer adsorption and the resultant polymer conformation strongly depended on the proportion and the size of both PPO and PEO blocks as well as the physicochemical properties and the curvature of the  $\text{Fe}_3\text{O}_4$  nanoparticles.

A heterobifunctional PEG such as carboxyl-terminated PEG could covalently attach to the  $\text{Fe}_3\text{O}_4$  nanoparticle surface through carboxyl groups by one end and be conjugated with other specific molecules by other end [42–44]. Dextran-coated iron oxide nanoparticles and cross-linked iron oxide nanoparticles have been developed for magnetic resonance imaging applications [45, 46]. The cross-linked iron oxide nanoparticles were also treated with ammonia to provide primary amino groups for the attachment of other biomolecules [47, 48]. Chitosan-coated  $\text{Fe}_3\text{O}_4$  nanoparticles have been produced by physical adsorption of chitosan onto oleic acid-coated

nanoparticles [49, 50]. Because of having both amino and hydroxyl functional groups, chitosan and its derivatives could form polymeric nanoparticles with nucleic acids and various pharmaceutical formulations through electrostatic interactions.

Inorganic coatings such as  $\text{SiO}_2$  and gold are other useful coating materials. The advantage of using  $\text{SiO}_2$  as coating material relies on its ease of synthesis and stability of modified particles in aqueous medium. A reverse microemulsion method has been developed for silica coating using non-ionic surfactants such as Triton X100, Brij-97, and Igepal CO-520, giving a uniform silica coating of 1 nm encapsulating the bare nanoparticles [51]. The resulting silica-coated magnetic nanoparticles could be further either functionalized or modified with polymers, yielding multifunctional hybrid nanomaterials.

Gold has been another inorganic coating candidate to implement functionality to magnetic nanoparticles. The  $\text{Au}-\text{Fe}_3\text{O}_4$  nanoparticles could be synthesized by controlling growth of Au on the surface of  $\text{Fe}_3\text{O}_4$  [52–53], and the Au could provide new surface to be functionalized with various ligands such as protein, oligonucleotide, DNA sequences through Au-S covalent bonding as reviewed [54]. Robinson *et al.* [55] reported that surface coating of  $\text{Fe}_3\text{O}_4$  by Au nanoparticles and subsequent functionalization with thiolated DNA slightly reduced the magnetization saturation due to addition of nonmagnetic materials but helped particles to remain stable in aqueous solution. It was also discussed that gold coating could modify the magnetic properties by isolating the magnetic cores and thus could provide possibility of producing very efficient nanostructures [56]. For example, a gold coating of approximately 0.4–0.5 nm thickness around superparamagnetic iron oxide nanoparticles resulted in a four-to five-fold increase in the amount of heat release in comparison with uncoated nanoparticles on application of low-frequency oscillating magnetic fields [57].

A critical question in this process is how to organize the functional groups on particle surface since it is related to the final particle size, density, and magnetic behavior of functional particles. A disadvantage arising from the surface modification of  $\text{Fe}_3\text{O}_4$  nanoparticles was a significant increase in the hydrodynamic diameter of the final particles. For example, the hydrodynamic diameters of magnetic nanoparticles with core sizes of 5 and 8 nm increased to 45 and 90 nm by coating with dextran and poly(acrylic acid), respectively [58–59]. It has been reported that the larger particle size led to rapid systemic clearance resulting in a shorter systemic half-life. The size distribution of the nanoparticles should be carefully considered depending on the desired pharmacokinetic and distribution [60–63]. For instance, the

nanoparticles of size larger than 4  $\mu\text{m}$  could be mainly captured and withheld in lungs, while the nanoparticles of size larger than 200 nm could be filtrated in the spleen, resulting in spleen uptake [64, 65]. It should be also noticed that surface modification of iron oxide nanoparticles with a non-magnetic shell usually led to the decrease in magnetization which could be attributed to different mechanisms such as the weight contribution of nonmagnetic material, the existence of a magnetically dead layer on the particle's surface and/or the existence of canted spins [66–68]. In fact, no correlation between the magnetic property of functionalized nanoparticles and the surface functionalization has been clearly established since the magnetic response of a system to the surface modification is complex and system specific.

#### 4.3.2 Design of $\text{Fe}_3\text{O}_4$ Nanoparticles for Biomedical Applications

Design of  $\text{Fe}_3\text{O}_4$  nanoparticles for biomedical applications requires careful considerations to the physicochemical stability, targeting ability, drug loading, and release. Figure 4.3 describes the general design of magnetic nanoparticles for biomedical treatments. The functionalized  $\text{Fe}_3\text{O}_4$  nanoparticles could carry other active targeting moieties, drug molecules, cell penetrating agent, DNA sequences, and imaging agents by both physical interactions and covalent linkages. At the targeted location, different release mechanisms could be activated depending on the choice

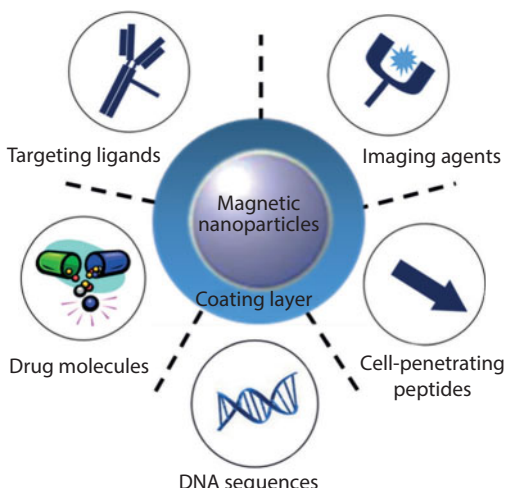


**Figure 4.3** Illustration of multifunctional magnetic nanoparticles.

of therapeutic technique integrated onto the magnetic nanoparticles. For example, doxorubicin was loaded on dextran cross-linked iron oxide nanoparticles based on the electrostatic interaction between the positively charged doxorubicin and the negatively charged polymer layer on the surface of nanoparticles [69], while methotrexate (MTX) drug was chemically conjugated to the surface of iron oxide nanoparticles via amide bond [70]. As a result, the doxorubicin could be released in the acidic condition of tumor due to the pH change of the surrounding medium, while the MTX drug could be released through an enzymatic reaction by the presence of lysozymes in the lysosomal compartments.

## 4.4 Magnetism and Magnetically Induced Heating of $\text{Fe}_3\text{O}_4$ Nanoparticles

### 4.4.1 Magnetism of $\text{Fe}_3\text{O}_4$ Nanoparticles

The properties of magnetic materials are characterized by the alignment of atomic magnetic moments generated by the spinning of electrons. The atomic magnetic moments can be aligned in either parallel or antiparallel fashion with respect to the neighboring ones in the crystal lattice. The alignment of the magnetic moments gives rise to the macroscopic magnetic behaviors which are usually measured by magnetization, coercivity, and magnetocrystalline anisotropy constant. Figure 4.4 shows the magnetism of  $\text{Fe}_3\text{O}_4$  nanoparticles as a function of particle size and the theoretical magnetization versus applied magnetic field curves for superparamagnetic and ferromagnetic nanoparticles.

At a certain level of particle size ( $D_{sd}$ ), the magnetic nanoparticles consist of all spins aligned in the same direction and thus exhibit single-domain structure. As the particle size continues to decrease and reaches a critical size where thermal energy exceeds the magnetic anisotropy energy barrier, the magnetization measured in a finite time interval or that in a removal of an external magnetic field is zero. This particle size represents critical size for superparamagnetism behavior,  $D_{sp}$ , and such particles are superparamagnetic. The critical sizes for single-domain structure and for superparamagnetic behavior of various magnetic materials could be predicted by using the physical theories for domain stability in crystalline particles as well as the bulk properties of these materials. The characteristic temperature which defines a transition from ferromagnetic to a thermally unstable or superparamagnetic behavior is called the blocking temperature,  $T_B$ . Under an applied field, the magnetic moments tend to align themselves in

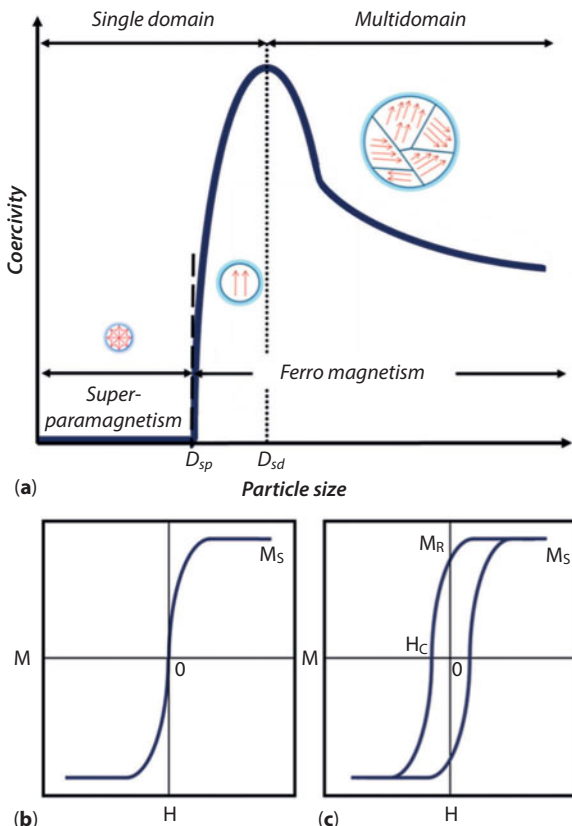


**Figure 4.4** (a) Schematic illustration of domain structure and magnetism of magnetic nanoparticles as a function of size. (b and c) Schematic illustrations of the theoretical magnetization versus applied magnetic field curves for superparamagnetic and ferromagnetic nanoparticles, respectively.

the same direction of applied field and thus the magnetization increases with the increase of magnetic field until a saturation value ( $M_s$ ) is reached. However, as long as the magnetic field is removed, the thermal energy of the superparamagnetic nanoparticles randomizes their magnetization and the overall magnetic moment of these nanoparticles drops back to zero. The corresponding magnetization curve of the superparamagnetic material exhibits a saturation of the magnetization ( $M_s$ ) and no hysteresis around the origin (Figure 4.4b). The negligible remnant magnetization of superparamagnetic nanoparticles is advantageous because the nanoparticles can avoid their aggregation during preparation and storage and after administration.

Above the critical size for single-domain structure, the magnetic material usually consists of a number of domains in order to minimize its internal

energy and exhibits ferromagnetic characteristics. As shown in Figure 4.4c, when an external magnetic field of strength is applied to a multidomain magnetic particle, the magnetization increases with the increase of magnetic field until a saturation value ( $M_s$ ) is reached. When magnetic field reduces and drops to zero, the magnetic domains do not return to their original orientations and cause a remnant magnetization ( $M_R$ ). The remnant magnetization can only be removed by applying a coercive field ( $H_c$ ) in the opposite direction to the initially applied field. The coercivity strictly depend on the magnetocrystalline anisotropy constant (K) which reflects the energy required to change the direction of magnetic moments.

#### 4.4.2 Magnetically Induced Heating of $\text{Fe}_3\text{O}_4$ Nanoparticles

When the magnetic nanoparticles are exposed to an alternating magnetic field, the magnetization of the particles is continuously reversed, which converts magnetic into thermal energy. This heat immediately releases to the surrounding tumor cells. By raising the temperature of tissues to between 42 °C and 46 °C, the viability of the disease tissues is reduced and their sensitivity to chemotherapy and radiation is increased [71–74]. In addition to selectively killing tumor cells, a potential of developing antitumor immunity after hyperthermia treatment has also been suggested [75, 76].

General mechanisms for heat generation of different magnetic nanoparticles are given in Figure 4.5. For superparamagnetic nanoparticles, the

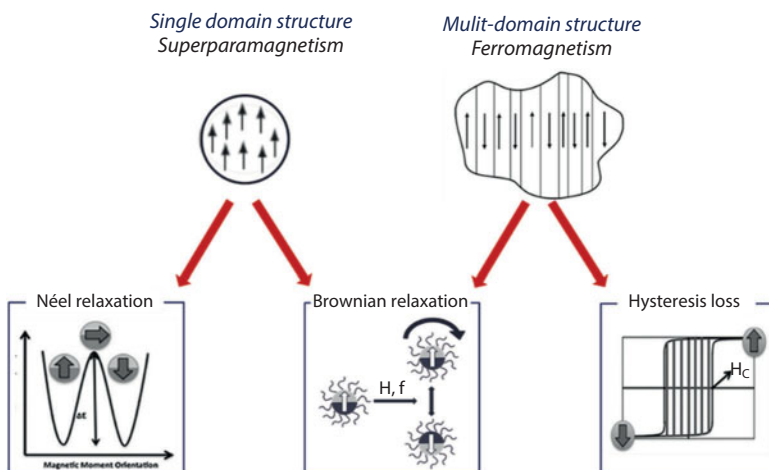


**Figure 4.5** Magnetism and general mechanisms for heat generation of magnetic nanoparticles.

external magnetic field supplies energy and assists the magnetic moment rotation inside particles. This energy is dissipated with the relaxation of the magnetic moment to its equilibrium orientation. For ferromagnetic materials whose sizes exceed the domain wall width, the so-called hysteresis loss mechanism dominates heat generation. Under application of an alternative field, the magnetic moments oscillate and cause domain wall displacement, which generates heat. It has been found that, when the applied field is small, the hysteresis loops are different from full hysteresis loops in that they are minor loops having relatively smaller areas. The amount of generated heat is considered to be proportional to the frequency multiplied by the area of the minor loop [77]. In both mechanisms, the relaxation of magnetic moments as well as the domain wall displacement depends on the magnetic anisotropy of magnetic material which depends on two main parameters: the intrinsic anisotropy of particle (material, surface, and shape) and the volume of particle.

Heat generation is also caused by the rotational Brownian motion of magnetic nanoparticles within a dispersed media. This movement is caused by the torque exerted on the magnetic moment under an external alternating magnetic field. The rotation ability of magnetic nanoparticles is characterized by the viscosity of medium and the global hydrodynamic diameter of particle. The Brownian relaxation and other primary heating mechanisms take place in parallel but with different contributions to overall heat generation. In practice, it has been reported that the Brownian relaxation mechanisms can be significantly hindered due to the high viscosity of intracellular medium, and thus the heat generation of magnetic nanoparticles mainly depends on their primary heating mechanisms [78–80].

Magnetic particles which have been studied for use in hyperthermia treatment have been focused on the magnetite  $\text{Fe}_3\text{O}_4$  and the nanoparticles related with cobalt, nickel, or other substitutions in size from several nanometers to a few tenths of a micron. The main parameter to determine the heating of tissue is the specific loss power (SLP) or specific absorption rate (SAR), which can be calculated based on the following equation:

$$\text{SLP(SAR)} = \frac{C}{m} \frac{\Delta T}{\Delta t}$$

where  $C$  represents the sample specific heat capacity,  $m$  is the amount of magnetic material per mass or volume of sample used in the experiment and  $(\Delta T/\Delta t)$  is the initial slope of heating curve.

The SLP achievable for a given condition of magnetic field, frequency, and nature of magnetic particles must be determined experimentally. The

SLP depends on various factors, including the effect of coating layer on surface spin dynamics as well as on the Brownian relaxation, the particle size, shape, and crystallinity which govern the magnetization of nanoparticles. Practically, optimization of nanoparticle properties is utmost important to achieve the highest heating efficiency.

## 4.5 Applications of $\text{Fe}_3\text{O}_4$ Nanoparticles to Magnetic Hyperthermia

The higher the SLP is, the lower the injected dose to the patient can be. The hyperthermia efficiency which could be reflected by heating rate or SLP values depended on various factors, including the intrinsic factors of material such as particle structure, magnetic properties, and the external factors such as amplitude and frequency of the applied magnetic field. Rosensweig [81] formulated and computed the heating rates for various magnetic samples and reported that the heating rate of a given particle size depended on the applied field intensity but the optimum particle size of a given material at which the heating rate is maximal was nearly independent of the applied field intensity. A very sharp maximum of the heating rate was observed for monodisperse  $\text{Fe}_3\text{O}_4$  nanoparticles of about 14 nm diameter and an increase of the particle size distribution caused a very fast decrease of the heating rate.

Practically, the effect of each significant parameter such as particle size and shape, functionalization, and magnetic properties on the hyperthermia efficiency has been independently investigated from study to study with different particle synthesis methods and different magnetic-induced heating systems. Ma *et al.* [82] reported that the SLP values depended on the particle size and the coercivity of  $\text{Fe}_3\text{O}_4$  nanoparticles. Under an applied field of 80 kHz frequency and  $32.5 \text{ kA m}^{-1}$  amplitude, a maximum SLP was recorded for sample containing 46 nm diameter of  $\text{Fe}_3\text{O}_4$  nanoparticles which also has the highest coercivity. Gonzales-Weimuller *et al.* [83] demonstrated that SLP values of superparamagnetic  $\text{Fe}_3\text{O}_4$  nanoparticles varied with particle size and the highest SLP was measured for 11.2 nm particles under an applied field of 400 kHz frequency and  $24.5 \text{ kA m}^{-1}$  amplitude. Gonzalez-Fernandez *et al.* [84] used an alternative magnetic field of 260 kHz frequency and 100 Oe (about  $8 \text{ kA m}^{-1}$ ) amplitude to induce heat generation and showed that a maximum SLP was recorded for particles of around 30 nm diameter.

The choices of ligand and coating thickness are important because it can modify the magnetic properties of the magnetic nanoparticles. Larumbe *et al.* [85] showed that silica coating on magnetite nanoparticles resulted

in the decreases of the magnetic properties and the SLP values due to an enhancement of spin disorder caused by the silica coating. The  $\text{SiO}_2$  shell also hindered the heat outflow, thus decreasing the heating efficiency [84]. However, with a proper coating, a ferromagnetic nanoparticle could give a fast heating rate for disease treatment. For instance, chitosan oligosaccharide-stabilized iron oxide nanocubes (Chito-FIONs) were developed for cancer hyperthermia [86]. The magnetic heating test revealed that Chito-FIONs encapsulated with multiple 30 nm sized iron oxide nanocubes showed the higher hyperthermal efficiency than single nanocube and more than 30 times higher than that of the Feridex particles as reference. In this study, it should be noticed that an evolution of aggregation of the nanoparticles caused a modification of the SLP values due to the effect of dipolar interparticle coupling with the Néel relaxation.

There are potential opportunities to enhance hyperthermia through manipulation of magnetic properties utilizing core-shell architecture such as  $\text{MnFe}_2\text{O}_4/\text{CoFe}_2\text{O}_4$  or  $\text{CoFe}_2\text{O}_4/\text{MnFe}_2\text{O}_4$  or  $\text{CoFe}_2\text{O}_4/\text{NiFe}_2\text{O}_4$  nanoparticles [29]. A remarkable enhancement of SLP values has been obtained in cubic  $\text{Zn}_{0.4}\text{Fe}_{2.6}\text{O}_4/\text{CoFe}_2\text{O}_4$  core/shell nanoparticles for achieving SLP values of 14 times higher than the single  $\text{Fe}_3\text{O}_4$  nanoparticles [87].

The temperature control during heating is essential but still remains challenges because heat conduction and energy adsorption *in vivo* are widely unknown. Furthermore, a local overheating may damage the healthy tissue. As a result, the magnetic materials with a maximum self-heating temperature are very attractive for hyperthermia applications. Achieving self-controlled and self-regulated heating has been considered as an effective method to prevent such local overheating problem. The candidate materials for self-controlled and self-regulated heating should exhibit Curie temperature ( $T_C$ ) slightly above the therapeutic temperature. The Curie temperature is the maximal temperature reachable by magnetic particles to maintain their magnetic properties. Above this temperature, the magnetic particles lose their magnetic properties, and thus they are unable to convert electromagnetic energy into heat. For instance, syntheses of several materials including  $\text{M}_{1-x}\text{Zn}_x\text{Fe}_2\text{O}_4$  (with M = Ni, Cu, Co, Mn) and alloy such as  $\text{Ni}_{1-x}\text{Cr}_x$  with adjustable  $T_C$  were reported. The  $T_C$  of  $\text{Ni}_{1-x}\text{Cr}_x$  increased with decreasing Cr content and was found equal to 44 °C at  $x = 5.63$  [88]. Yao *et al.* [89] reported that the  $T_C$  of Gd-substituted Zn-ferrite ( $\text{ZnGd}_x\text{Fe}_{2-x}\text{O}_4$ ) increased with an increasing Gd content and was found to be around 45 °C at  $x = 0.02$ . Other studies reported that the  $T_C$  of 46 °C could be achieved for  $\text{Mn}_{1+x}\text{Ti}_x\text{Fe}_2\text{O}_4$  with  $x = 0.55$  [90] and for  $\text{Mg}_{1+x}\text{Fe}_{2-2x}\text{Ti}_x\text{O}_4$  with  $x = 0.37$  [91]. Certainly, an ideal material with optimal physical features for self-controlled and self-regulated magnetic

heating has not been well developed yet but, indeed, this concept offers a smart way to control hyperthermia treatment.

## 4.6 Applications of $\text{Fe}_3\text{O}_4$ Nanoparticles to Hyperthermia-based Controlled Drug Delivery

Controlled drug delivery by nanostructured functional materials is attracting great attention because of the high opportunities in cancer therapy. The magnetic nanoparticles have been widely used for targeted delivery and controlled drug release due to their response to a magnetic field. A controlled drug delivery system should be able to deliver drugs to a targeted location in the body and to maintain drug levels within the required concentration range for therapy. A high gradient of external magnetic fields could be used to guide and concentrate the magnetic nanocarriers at targeted site in order to reduce the systemic distribution of cytotoxic compounds and to enhance drug uptake, resulting in more effective treatment at lower doses.

Once the magnetic carrier was concentrated at the target, the therapeutic agent was then released from the magnetic carrier by changes in the local physicochemical environment. For example, drug molecule was loaded into the  $\text{Fe}_3\text{O}_4$  porous/hollow nanoparticles and its release was studied as a function of pH, showing a higher release rate in acidic conditions [92]. It was supposed that the acidic environment could weaken the binding between drug molecule and polymer layer on the surface of  $\text{Fe}_3\text{O}_4$  porous/hollow nanoparticles [93]. One unit decrease in the pH of media caused a pronounced increase in polymer degradation as well as drug release [94]. A higher release in acidic conditions was also attributed to the enlargement of the pores of porous/hollow nanoparticles due to the acid etching of  $\text{Fe}_3\text{O}_4$  shell [95]. Since the pH of release medium played a critical role in the drug release from the polymeric coating layer, a small change in biological pH occurred by disease would result in polymer degradation enough for drug release from the nanocarriers.

Magnetic nanoparticles embedded in a polymer matrix which could be mechanically deformed upon application of a static magnetic field or generate heat under an alternating current field was used to deliver drug and control drug release. For example, upon applying a static magnetic field, the magnetic particles in the polymer matrix aggregated instantly and produced a bulk magnetic moment leading to a “close” configuration and resulted in a slower drug release than that when the static magnetic field was off [96, 97]. This magnetic-induced mechanical deformation of the polymer could be utilized to sustain drug levels within the desired therapeutic range for a long time.

On the contrary with the static magnetic field, drug release could be enhanced under an alternating magnetic field. Several systems have been developed to demonstrate the remotely controlled pulsatile drug release for a number of “on-off” durations of an alternating magnetic fields. Hoare *et al.* [98] developed nanocomposite membranes based on poly(*N*-isopropylacrylamide)-based nanogels and magnetite nanoparticles entrapped in ethyl cellulose to achieve “on-demand” drug delivery upon the application of an oscillating magnetic field. A small-scale device made by gluing two 1 cm diameter membrane disks to the ends of a 1 cm length of silicone tubing filled with a sodium fluorescein solution was mounted inside a flow cell placed in a solenoid coil. Under an oscillating applied field, heat generated by magnetite nanoparticles caused the shrinkage of nanogels and permitted drug diffusion out of the device. When the magnetic field was turned off, the nanogels reswelled and refilled the membrane pores, resulting in return to a near-zero value of drug flux. In another study, poly(D,L-lactic-co-glycolic acid) (PLGA) microcapsules (1–3 mm in diameter) with a 250-nm-thick membrane containing a high density of iron oxide nanoparticles loaded with doxorubicin were prepared and then used in cancer treatment [99]. It was demonstrated that, for magnetic nanoparticles loading of at least 25 wt.%, an application of alternative magnetic field of 100 kHz and 2.5 kA m<sup>-1</sup> could induce heating above the glass temperature of PLGA and thus could allow controlled pulsatile release of the drug.

The thermal energy from magnetic heating was utilized to open the gates of inorganic carriers which contain drugs for therapy. Thomas *et al.* [100] synthesized 15 nm ( $Zn_{0.4}Fe_{0.6}$ ) $Fe_2O_4$  nanoparticles and then incorporated these nanoparticles inside porous drug carrier nanoparticles. Nanovalves which consisted of *N*-(6-*N*-aminohexyl) aminomethyltrioxysilane and cucurbit[6]uril were capped onto the pores to keep the drug inside. When an external alternating magnetic field was applied, heat generation and a subsequent pressure buildup inside the porous nanoparticles caused the rapid removal of molecular valves and the rapid release of drug molecules. These magnetic nanoparticles were considered as effective actuators for controlled drug release from a carrier. When breast cancer cells (MDA-MB-231) were treated with doxorubicin-loaded particles and exposed to an alternating magnetic field, cell death occurred. This material promises to be a noninvasive, externally controlled drug delivery system with cancer-killing properties.

Furthermore, the heat generation from magnetic nanoparticles can be used to activate temperature-sensitive cation channels within cells in order to enhance drug uptake without observable toxic effects. Huang *et al.* [101] targeted superparamagnetic  $MnFe_2O_4$  nanoparticles onto the plasma

membrane of cells exposing the transient receptor potential cation channel subfamily V member 1 (TRPV1), and then heated the particles by a radio frequency magnetic field. On the application of oscillating magnetic field, the local temperature increased resulting in heat-induced opening of TRPV1 and caused an influx of calcium ions into the cells. This approach could be applied to activate cells uniformly across a large volume, making it feasible for *in vivo* whole-body applications.

The combination of hyperthermia and traditional chemotherapeutic functions in the same system could utilize the great potentials of individual hyperthermia and controlled drug delivery as well as could raise synergistic effects in the treatment of cancer. Kulshrestha *et al.* [102] developed paclitaxel-loaded magnetoliposomes and achieved a better cell-killing efficacy than individual magnetoliposomes or paclitaxel-loaded liposomes. The drug release behaviors were studied under an AC magnetic field at 37 °C and 43 °C, exhibiting released amounts of 1.2% and 55.6%, respectively. The hyperthermia was performed on HeLa cells at  $42.5 \pm 1$  °C for a duration of 30 min with magnetoliposomes containing 6 mg mL<sup>-1</sup> of magnetic nanoparticles only or in combination with 100 nM paclitaxel. The cell viability was decreased by 37% after the heat treatment with magnetic particle alone and by about 50% and 89% for paclitaxel-loaded magnetoliposomes without and with application of an alternative magnetic field, respectively. This study demonstrated that the magnetoliposomes exhibit promising potential for combined thermo-chemotherapy due to its good biocompatibility, slow drug release at 37 °C, burst drug release at 43 °C and synergistic cancer cell-killing effect.

## 4.7 Conclusions

Controlled drug delivery and hyperthermia treatment by magnetic nanoparticles exhibited high opportunities in biomedical treatments. High-gradient, external magnetic fields could be utilized to guide and concentrate the magnetic nanocarriers at target locations where the therapy has to act specifically. Once the magnetic carrier was concentrated at the target, the therapeutic agent was released from the magnetic carrier by changes in the local physicochemical environment or by application of an external magnetic field, leading to the increased uptake of drug by the tumor cells. By applying an alternative magnetic field with sufficient amplitude and frequency, the magnetization of the particles was continuously reversed, which converted magnetic to thermal energy. A combination of hyperthermia-based therapy and controlled drug release has strong potential to develop an

intelligent therapy for cancer treatment. The hyperthermia and traditional chemotherapeutic functions combined in the same system could utilize the great potential of individual hyperthermia and controlled drug delivery as well as could raise the synergistic effects in the treatment of cancer.

It is still a great challenge to develop a system that minimizes nanoparticle dose for actual treatment. This could be overcome by synthesis and surface modification of nanoparticles able to circulate in the blood compartment for a long period and preservation of ligands able to facilitate their specific internalization in tumor cells. It is crucial to develop systematic strategies of controlled synthesis and surface modification of magnetic nanoparticles to obtain the nanoparticles of customized size and shape with high homogeneity as well as sufficient magnetization. Even though different kinds of monodisperse magnetic nanoparticles with controllable particle sizes and compositions could be synthesized by various synthetic procedures, the magnetic nanoparticles obtained under different synthetic conditions may exhibit big differences due to formation of structural disorder and antiphase boundaries, or the existence of a magnetically dead layer at the particle surface. We believe that the synthesis and functionalization of high-quality magnetic nanoparticles in a controlled manner are still the critical challenges to be faced in the coming years. It will also be desirable to develop the large-scale synthesis of highly functional magnetic nanoparticles with the requirement of reproducible and industrial processes without any laborious purification step to ensure cost-effective synthetic procedures. Finally, it should be pointed out that the biomedical uses of magnetic nanoparticles are not restricted to controlled drug delivery and hyperthermia and, indeed, they are also applicable to magnetic resonance imaging, sensing, enzyme immobilization, immunoassays, bioseparation, and so on.

## Acknowledgment

This research was supported by the Converging Research Center Program through the Ministry of Science, ICT and Future Planning, Republic of Korea (Grant number 2014048827).

## References

1. C.S.S.R. Kumar, F. Mohammad, *Adv. Drug Deliv. Rev.*, 63, 789, 2011.
2. A. Hervault, N.T.K. Thanh, *Nanoscale*, 6, 11553, 2014.

3. D.T. Nguyen, K.-S. Kim, *Korean J. Chem. Eng.*, 31, 1289, 2014.
4. D.T. Nguyen, K.-S. Kim, *KONA Powder Part. J.*, 33, 2016.
5. S. Sun, H. Zeng, *J. Am. Chem. Soc.*, 124, 8204, 2002.
6. S. Sun, H. Zeng, D.B. Robinson, S. Raoux, P.M. Rice, S.X. Wang, G. Li, *J. Am. Chem. Soc.*, 126, 273, 2004.
7. J. Park, J. Joo, S.G. Kwon, Y. Jang, T. Hyeon, *Angew. Chem. Int. Ed.*, 46, 4630, 2007.
8. J. Park, K. An, Y. Hwang, J.G. Park, H.J. Noh, J.Y. Kim, J.H. Park, N.M. Hwang, T. Hyeon, *Nat. Mater.*, 3, 891, 2004.
9. N.R. Jana, Y.F. Chen, X.G. Peng, *Chem. Mater.*, 16, 3931, 2004.
10. T. Hyeon, S.S. Lee, J. Park, Y. Chung, H.B. Na, *J. Am. Chem. Soc.*, 123, 12798, 2001.
11. J. Park, E. Lee, N.M. Hwang, M. Kang, S.C. Kim, Y. Hwang, J.G. Park, H.J. Noh, J.Y. Kim, J.H. Park, T. Hyeon, *Angew. Chem. Int. Ed.*, 44, 2872, 2005.
12. J. Ge, Y. Hu, M. Biasini, W.P. Beyermann, Y. Yin, *Angew. Chem. Int. Ed.*, 46, 4342, 2007.
13. L. Zhao, H. Zhang, Y. Xing, S. Song, S. Yu, W. Shi, X. Guo, J. Yang, Y. Lei, F. Cao, *Chem. Mater.*, 20, 198, 2008.
14. S. Peng, S. Sun, *Angew. Chem. Int. Ed.*, 46, 4155, 2007.
15. J. Huang, W. Chen, W. Zhao, Y. Li, X. Li, C. Chen, *J. Phys. Chem. C*, 113, 12067, 2009.
16. H.J. Fan, U. Gçsele, M. Zacharias, *Small*, 3, 1660, 2007.
17. C.M. Wang, D.R. Baer, L.E. Thomas, J.E. Amonette, J. Antony, Y. Qiang, G. Duscher, *J. Appl. Phys.*, 98, 094308, 2005.
18. L.P. Zhu, H.M. Xiao, W.D. Zhang, G. Yang, S.Y. Fu, *Cryst. Growth Des.*, 8, 957, 2008.
19. S. Liu, R. Xing, F. Lu, R.K. Rana, J.J. Zhu, *J. Phys. Chem. C*, 113, 21042, 2009.
20. P. Hu, L. Yu, A. Zuo, C. Guo, F. Yuan, *J. Phys. Chem. C*, 113, 900, 2009.
21. C. Cheng, F. Xu, H. Gu, *New J. Chem.*, 35, 1072, 2011.
22. X. Lin, G. Ji, Y. Liu, Q. Huang, Z. Yang, Y. Du, *Cryst. Eng. Comm.*, 14, 8658, 2012.
23. D.T. Nguyen, K.-S. Kim, *AIChE J.*, 59, 3594, 2013.
24. D.T. Nguyen, K.-S. Kim, *J. Nanosci. Nanotechnol.*, 13, 5773, 2013.
25. D.T. Nguyen, D.-W. Park, T. Kim, K.-S. Kim, *J. Nanosci. Nanotechnol.*, 15, 591, 2015.
26. J.-T. Jang, H. Nah, J.-H. Lee, S.H. Moon, M.G. Kim, J. Cheon, *Angew. Chem. Int. Ed.*, 48, 1234, 2009.
27. T.-J. Yoon, H. Lee, H. Shao, R. Weissleder, *Angew. Chem. Int. Ed.*, 50, 4663, 2011.
28. L.-M. Lacroix, N.F. Huls, D. Ho, X. Sun, K. Cheng, S. Sun, *Nano Lett.*, 11, 1641, 2011.
29. J.H. Lee, J.T. Jang, J.S. Choi, S.H. Moon, S.H. Noh, J.W. Kim, J.G. Kim, I.S. Kim, K.I. Park, J.W. Cheon, *Nat. Nanotechnol.*, 6, 418, 2011.
30. Q. Song, Z.J. Zhang, *J. Am. Chem. Soc.*, 134, 10182, 2012.

31. P.K. Manna, S.M. Yusuf, M. Basu, T. Pal, *J. Phys. Condens. Mat.*, 23, 506004, 2011.
32. A. López-Ortega, M. Estrader, G. Salazar-Alvarez, S. Estradé, I.V. Golosovsky, R.K. Dumas, D.J. Keavney, M. Vasilakaki, K.N. Trohidou, J. Sort, F. Peiró, S. Suriñach, M.D. Baró, J. Nogués, *Nanoscale*, 4, 5138, 2012.
33. A. Juhin, A. Lopez-Ortega, M. Sikora, C. Carvallo, M. Estrader, S. Estrade, F. Peiro, M.D. Baró, P. Sainctavit, P. Glatzel, J. Nogués, *Nanoscale*, 6, 11911, 2014.
34. M. Estrader, A. López-Ortega, S. Estradé, I. V Golosovsky, G. Salazar-Alvarez, M. Vasilakaki, K.N. Trohidou, M. Varela, D.C. Stanley, M. Sinko, M.J. Pechan, D.J. Keavney, F. Peiró, S. Suriñach, M.D. Baró, J. Nogués, *Nat. Commun.*, 4, 2960, 2013.
35. L. Josephson, C.H. Tung, A. Moore, R. Weissleder, *Bioconjugate Chem.*, 10, 186, 1999.
36. D. Hogemann, L. Josephson, R. Weissleder, J.P. Basilion, *Bioconjugate Chem.*, 11, 941, 2000.
37. H.W. Kang, L. Josephson, A. Petrovsky, R. Weissleder, A.J. Bogdanov, *Bioconjugate Chem.*, 13, 122, 2002.
38. E.A. Schellenberger, D.E. Sosnovik, R. Weissleder, L. Josephson, *Bioconjugate Chem.*, 15, 1062, 2004.
39. J.T. Li, K.D. Caldwell, N. Rapoport, *Langmuir*, 10, 4475, 1994.
40. S.M. Moghimi, *Biochem. Biophys. Acta*, 1336, 1, 1997.
41. S.M. Moghimi, A.C. Hunter, *Trends Biotechnol.*, 18, 412, 2000.
42. O. Veiseh, C. Sun, J. Gunn, N. Kohler, P. Gabikian, D. Lee, N. Bhattacharai, R. Ellenbogen, R. Sze, A. Hallahan, J. Olson, M.Q. Zhang, *Nano Lett.*, 5, 1003, 2005.
43. C. Sun, R. Sze, M.Q. Zhang, *J. Biomed. Mater. Res. A*, 78A, 550, 2006.
44. J.F. Lutz, S. Stiller, A. Hoth, L. Kaufner, U. Pison, R. Cartier, *Biomacromolecules*, 7, 3132, 2006.
45. T. Shen, R. Weissleder, M. Papisov, A. Bogdanov Jr., T.J. Brady, *Magn. Reson. Med.*, 29, 599, 1993.
46. L. Josephson, C.H. Tung, A. Moore, R. Weissleder, *Bioconjugate Chem.*, 10, 186, 1999.
47. P. Wunderbaldinger, L. Josephson, R. Weissleder, *Bioconjugate Chem.*, 13, 264, 2002.
48. E.A. Schellenberger, A. Bogdanov Jr., D. Hogemann, J. Tait, R. Weissleder, L. Josephson, *Mol. Imaging*, 1, 102, 2002.
49. E.H. Kim, H.S. Lee, B.K. Kwak, B.K. Kim, *J. Magn. Magn. Mater.*, 289, 328, 2005.
50. E.H. Kim, Y. Ahn, H.S. Lee, *J. Alloys Compd.*, 434, 633, 2007.
51. S. Santra, R. Tapec, N. Theodoropoulou, J. Dobson, A. Hebard, W. Tan, *Langmuir*, 17, 2900, 2001.
52. I.Y. Goon, L.M.H. Lai, M. Lim, P. Munroe, J.J. Gooding, R. Amal, *Chem. Mater.*, 21, 673, 2009.

53. D.T. Nguyen, D.-W. Park, K.-S. Kim, *J. Nanosci. Nanotechnol.*, 11, 7214, 2011.
54. D.T. Nguyen, D.-J. Kim, K.-S. Kim, *Micron*, 42, 207, 2011.
55. I. Robinson, L.D. Tung, S. Maenosono, C. Walti, N.T.K. Thanh, *Nanoscale*, 2, 2624, 2010.
56. S. Banerjee, S.O. Raja, M. Sardar, N. Gayathri, B. Ghosh, A. Dasgupta, *J. Appl. Phys.*, 109, 123902, 2011.
57. F. Mohammad, G. Balaji, A. Weber, R.M. Uppu, C.S.S.R. Kumar, *J. Phys. Chem. C*, 114, 19194, 2010.
58. E. Amstad, M. Textor, E. Reimhult, *Nanoscale*, 3, 2819, 2011.
59. S. Santra, C. Kaittanis, J. Grimm, J.M. Perez, *Small*, 5, 1862, 2009.
60. S. Majumdar, S.S. Zoghbi, J. C. Gore, *Invest. Radiol.*, 25, 771, 1990.
61. P. Varallyay, G. Nesbit, L.L. Muldoon, R.R. Nixon, J. Delashaw, J.I. Cohen, A. Petrillo, D. Rink, E.A. Neuwelt, *Am. J. Neuroradiol.*, 23, 510, 2002.
62. C. Fang, B. Shi, Y.Y. Pei, M.H. Hong, J. Wu, H.Z. Chen, *Eur. J. Pharm. Sci.*, 27, 27, 2006.
63. P. Bourrinet, H.H. Bengele, B. Bonnemain, A. Dencausse, J.M. Idee, P.M. Jacobs, J.M. Lewis, *Invest. Radiol.*, 41, 313, 2006.
64. M.M. Moghimi, A.C. Hunter, J.C. Murray, *Pharmacol. Rev.*, 53, 283, 2001.
65. V.I. Shubayev, T.R. Pisanić II, S. Jin, *Adv. Drug Deliv. Rev.*, 61, 467, 2009.
66. D.T. Margulies, F.T. Parker, F.E. Spada, R.S. Goldman, J. Li, R. Sinclair, A.E. Berkowitz, *Phys. Rev. B*, 53, 9175, 1996.
67. R.H. Kodama, *J. Magn. Magn. Mater.*, 200, 359, 1999.
68. Y. Yuan, D. Rende, C.L. Altan, S. Bucak, R. Ozisik, D.-A. Borca-Tasciuc, *Langmuir*, 28, 13051, 2012.
69. M.K. Yu, Y.Y. Jeong, J. Park, S. Park, J. W. Kim, J.J. Min, K. Kim, S. Jon, *Angew. Chem. Int. Ed.*, 47, 5362, 2008.
70. N. Kohler, C. Sun, J. Wang, M.Q. Zhang, *Langmuir*, 21, 8858, 2005.
71. R.K. Gilchrist, R. Medal, W.D. Shorey, R.C. Hanselman, J.C. Parott, C.B. Taylor, *Ann. Surg.*, 146, 596, 1957.
72. K. Overgaard, J. Overgaard, *Eur. J. Cancer*, 8, 65, 1972.
73. D.C.F. Chan, D.B. Kirpotin, P.A. Bunn, *J. Magn. Magn. Mater.*, 122, 374, 1993.
74. A. Jordan, P. Wust, H. Fahling, W. John, A. Hinz, R. Felix, *Int. J. Hyper.*, 9, 51, 1993.
75. A. Ito, M. Shinkai, H. Honda, K. Yoshikawa, S. Saga, T. Wakabayashi, J. Yoshida, T. Kobayashi, *Cancer Immunol. Immun.*, 52, 80, 2003.
76. M. Suzuki, M. Shinkai, H. Honda, T. Kobayashi, *Melanoma Res.*, 13, 129, 2003.
77. E. Kita, T. Oda, T. Kayano, S. Sato, M. Minagawa, H. Yanagihara, M. Kishimoto, C. Mitsumata, S. Hashimoto, K. Yamada, N. Ohkohchi, *J. Phys. D Appl. Phys.*, 43, 474011, 2010.
78. C. Rivière, C. Wilhelm, F. Cousin, V. Dupuis, F. Gazeau, R. Perzynski, *Eur. Phys. J. E*, 22, 1, 2007.
79. C. Wilhelm, J.P. Fortin, F. Gazeau, *J. Nanosci. Nanotechnol.*, 7, 2933, 2007.
80. J.P. Fortin, F. Gazeau, C. Wilhelm, *Eur. Biophys. J.*, 37, 223, 2008.

81. R.E. Rosensweig, *J. Magn. Magn. Mater.*, 252, 370, 2002.
82. M. Ma, Y. Wu, J. Zhou, Y. Sun, Y. Zhang, N. Gu, *J. Magn. Magn. Mater.*, 268, 33, 2004.
83. M. Gonzales-Weimuller, M. Zeisberger, K.M. Krishnan, *J. Magn. Magn. Mater.*, 321, 1947, 2009.
84. M.A. Gonzalez-Fernandez, T.E. Torres, M. Andrés-Vergés, R. Costo, P. de la Presa, C.J. Serna, M.P. Morales, C. Marquina, M.R. Ibarra, G.F. Goya, *J. Solid State Chem.*, 182 2779, 2009.
85. S. Larumbe, C. Gomez-Polo, J.I. Perez-Landazabal, J.M. Pastor, *J. Phys. Condens. Matter*, 24, 266007, 2012.
86. K.H. Bae, M. Park, M.J. Do, N. Lee, J.H. Ryu, G.W. Kim, C.G. Kim, T.G. Park, T. Hyeon, *ACS Nano*, 6, 5266, 2012.
87. S.H. Noh, W. Na, J.T. Jang, J.H. Lee, E.J. Lee, S.H. Moon, Y. Lim, J.S. Shin, J. Cheon, *Nano Lett.*, 12, 3716, 2012.
88. Y. Akin, I.M. Obaidat, B. Issa, Y. Haik, *Cryst. Res. Technol.*, 44, 386, 2009.
89. A.H. Yao, F.R. Ai, D.P. Wang, W.H. Huang, X.C. Zhang, *Mat. Sci. Eng. C: Mat.*, 29, 2525, 2009.
90. M.R. Barati, K. Suzuki, C. Selomulya, J.S. Garitaonandia, *IEEE T. Magn.*, 49, 3460, 2013.
91. G. Ferk, M. Drofenik, D. Lisjak, A. Hamler, Z. Jaglicic, D. Makovec, *J. Magn. Magn. Mater.*, 350, 124, 2014.
92. D.T. Nguyen, T. Charinpanitkul, D.-W. Park, K.-S. Kim, *J. Nanosci. Nanotechnol.*, 14 7995, 2014.
93. S. Liu, R. Xing, F. Lu, R.K. Rana. J.J. Zhu, *J. Phys. Chem. C*, 113, 21042, 2009.
94. X. Zhang, L. Clime, H. Roberge, F. Normandin, L'H. Yahia, E. Sacher, T. Veres, *J. Phys. Chem. C*, 115, 1436, 2011.
95. K. Cheng, S. Peng, C. Xu, S. Sun, *J. Am. Chem. Soc.*, 131, 10637, 2009.
96. T.Y. Liu, S.H. Hu, T.Y. Liu, D.M. Liu, S.Y. Chen, *Langmuir*, 22, 5974, 2006.
97. Hu S.-H., Liu T.-Y., Liu D.-M., Chen S.-Y., *J. Control. Release*, 121, 181, 2007.
98. T. Hoare, B.P. Timko, J. Santamaria, G.F. Goya, S. Irusta, S. Lau, C.F. Stefanescu., D. Lin, R. Langer, D.S. Kohane, *Nano Lett.*, 11, 1395, 2011.
99. W.-L. Chiang, C.-J. Ke, Z.-X. Liao, S.-Y. Chen, F.-R. Chen, C.-Y. Tsai, Y. Xia, H.-W. Sung, *Small*, 8, 3584, 2012.
100. C.R. Thomas, D.P. Ferris, J.H. Lee, E. Choi, M.H. Cho, E.S. Kim, J.F. Stoddart, J.S. Shin, J. Cheon, J.I. Zink, *J. Am. Chem. Soc.*, 132, 10623, 2010.
101. H. Huang, S. Delikanli, H. Zeng, D.M. Ferkey, A. Pralle, *Nat. Nanotechnol.*, 5, 602, 2010.
102. P. Kulshrestha, M. Gogoi, D. Bahadur, R. Banerjee, *Colloid Surface B*, 96, 1, 2012.



# Magnetic Nanomaterial-based Anticancer Therapy

Catalano Enrico

*Consorzio Interuniversitario Nazionale per la Scienza e Tecnologia dei Materiali (INSTM), FI, Italy*

---

## Abstract

Magnetic nanomaterials (MNMs) have the potential to solve cancer that is one of the biggest challenges facing modern medicine. Despite the multiple disease factors of cancer, meaningful diagnostic and therapeutic advances have been made in the past years, which are able to predict genetic, molecular, and nanoscale mechanisms of tumorigenesis. MNM-based systems possess several novel therapeutic opportunities for cancer therapy based merely on their unique physico-chemical and magnetic properties. Nanomedicine and nanotechnology may contribute to future developments through different strategies and initiatives from perspectives that are far removed from classical biological and medicinal aspects of cancer. Successful application of MNMs can revolutionize therapeutics, diagnostics, and imaging in anticancer therapy. MNMs have especially attracted considerable attention of researchers to address cancer diagnostics and chemotherapy. Recently, a new approach regarding production of MNMs was implemented. The most promising aspect of MNMs lies in their potential for “theranostic” applications. In this chapter, we report an overview of the key developments in recent years regarding MNMs as potential theranostic carriers for targeted cancer chemotherapy and hyperthermia. Emerging MNMs show considerable promise to realize cancer theranostic potential. In this context, functionalized MNMs can be designed to provide remarkable *in vivo* stability, and accompanying pharmacokinetics exhibit tumor localization that can be tailored for specific applications. Loading of anticancer chemotherapeutic drugs into magnetic nanoparticles (NPs) has shown to increase their circulation time, tumor localization, and therapeutic potential. In this context, even iron-based NPs show extended circulation as well

---

Corresponding author: enrico.catalano@med.uniupo.it

---

Ashutosh Tiwari *et al.* (eds.) Advanced Magnetic and Optical Materials, (141–164) © 2017  
Scrivener Publishing LLC

as diverse organ accumulation beyond the liver, which otherwise renders MNMs potentially toxic to liver function. MNMs, including those based on iron oxides, have entered a renaissance era where intelligent synthesis, functionalization, stabilization, and targeting provide ample evidence for applications in localized cancer theranostics and for the ablation of cancer cells. Through surface functionalization, MNMs can be specifically targeted to tumorous tissue allowing for an increase in therapeutic potential and reduction in side effects. Moreover, these features provide MNMs with a tunable surface which can be used to modify magnetic, thermal, and chemical properties. This chapter highlights and describes the different types of MNMs: maghemite (MGH) ( $\gamma\text{-Fe}_2\text{O}_3$ ), magnetite ( $\text{Fe}_3\text{O}_4$ ), co-ferrite ( $\text{CoFe}_2\text{O}_4$ ), MnZn-ferrite ( $\text{MnZnFe}_2\text{O}_4$ ), and emerging hybrids applied for cancer theranostics and thermolysis of cancer cells.

**Keywords:** Cancer therapy, drug delivery, drug targeting, hyperthermia, iron-oxide nanoparticles, magnetic nanomaterials, nanomedicine, oncology, theranostics

## 5.1 Introduction

Nanomaterials are defined as the production of matter with at least one dimension ranging between 1 and 100 nm (Figure 5.1). Due to the very small size and the resulting high surface/volume ratio, nanomaterials have physical-chemical properties that differ from those of macroscopic materials. Nowadays, nanomaterials are often applied in many industrial fields including electronics, optics, textile, and many others till to biomedicine [1].

The use of nanomaterials in medicine has expanded recently, especially in diagnostic and therapeutic applications [2]. Actually, nanomaterials could be designed as contrast agents or nanocarriers able to bind, specifically transport biomolecules and accumulate to the site to treat.

Cancer is one of the biggest challenges facing the medical research in our time. The goals are to improve not only the therapeutic outcome, even in the

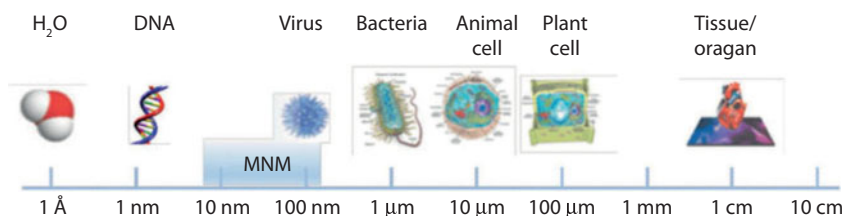


**Figure 5.1** Size scale of magnetic nanomaterials (MNMs) as compared to biomolecules. MNM can be adapted to include biomolecules, drugs, or targeting and imaging molecules to form targeted MNM theranostic agents.

cases of advanced and metastatic cancer, but also the methods of treatment, which often have considerable adverse effects. In addition, the current developments, such as demographic change, population growth, and increasing healthcare costs, have to be taken into consideration. In all likelihood, nanotechnology and, in particular, the use of magnetic nanoparticles (MNPs) consisting of the elements nickel, cobalt, and iron can make a significant contribution. In the past years, the production and applications of nanoparticles (NPs) based on iron oxides in the field of biomedicine presented a great interest due to their particular properties. Because of the expansion of the pharmaceutical industry numerous new systems for drugs delivery have appeared, and those centered on magnetic nanomaterials (MNMs) are in a particular attention and in different promising developmental stages.

The greatest potential can be ascribed to the drug delivery systems: MNPs are functionalized by binding them to various substances, including chemotherapeutic agents, radionuclides, nucleic acids, and antibodies. They can then be guided and accumulated using a magnetic field. The synthesis of these nanostructures with magnetic properties implies very simple assembling procedures and presents one of the lowest cytotoxic profiles. Magnetic nanostructures displayed possible appliance in a large diversity of biotechnological and medical fields, both for diagnose and therapy. Magnetic nanostructures are representative, interesting, and feasible for possible use in antitumor/anticancer therapy. Different types of magnetic nanocarriers loaded with different antitumor/anticancer agents and the cases tested *in vivo* were investigated in different studies. Hyperthermia can be induced with an alternating magnetic field, providing another therapeutic option. MNPs may be useful in overcoming cancer drug resistance. They also contribute to realizing a combination of diagnostic investigation and therapy in the field of “theranostics” (Figure 5.2). The multifaceted and promising results of research in the recent years offer the prospect of a real advance in cancer therapy in the near future.

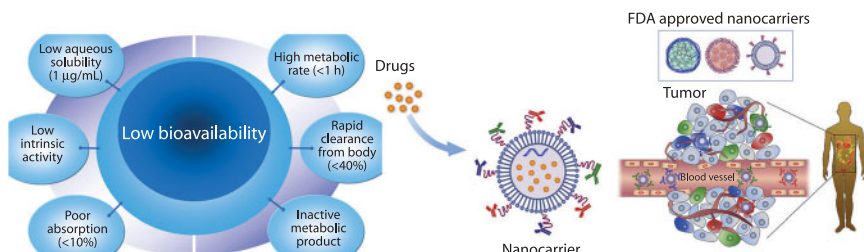


**Figure 5.2** Different types of drugs loaded/conjugated MNMs.

## 5.2 Magnetic Nanomaterials

Magnetic materials include various materials and are classified according to their chemical origin, crystallographic configuration, and magnetic properties. MNMs, consisting of magnetic elements (iron, cobalt, nickel oxides), are of great interest, particularly in biomedicine fields. The use of MNMs in biomedical research is progressively gaining a lot of importance, with the purpose to develop new types of functionalized and biocompatible MNPs. Different types of MNMs can be produced, such as cobalt ferrite ( $\text{CoFe}_2\text{O}_4$ ), manganese ferrite ( $\text{MnFe}_2\text{O}_4$ ), zinc-doped ferrites, hematite ( $\alpha\text{-Fe}_2\text{O}_3$ ), maghemite ( $\gamma\text{-Fe}_2\text{O}_3$ ), and magnetite ( $\text{Fe}_3\text{O}_4$ ), among which the latter could be very interesting for different biomedical applications [3].

Susceptibility to magnetic fields is a criterion to classify magnetic materials into diamagnetic materials which have a weak repulsion from an external magnetic field corresponding to a negative susceptibility, paramagnetic materials showing small and positive susceptibility, and ferromagnetic materials which have a large and positive susceptibility to magnetic fields [4].

Superparamagnetism of iron oxide particles is a prerequisite to MNP use, as well as an underlying reason for its limitations. Superparamagnetism gives the possibility to magnetize the NPs by an external magnetic field. This property is highly useful especially in biomedicine [5]. The limit volume to have superparamagnetic NPs at a certain temperature is related to the magnetocrystalline anisotropy. Iron oxide NPs have superparamagnetic properties, although they have larger dimensions compared to any other magnetic metal [5]. MNPs have the unique ability that can be directed under the influence of an external magnetic field. Each magnetic particle can be considered similar to a single magnetic domain that shows superparamagnetic behavior when its size is below 10–20 nm and when the temperature is above the so-called blocking temperature [6]. An important property of iron oxide NPs is the loss of their magnetization when the magnetic field is switched off.

### 5.2.1 Cobalt Ferrite

Cobalt ferrite NPs are used in hyperthermia treatment, since in nanosized state, cobalt magnetic moment relaxes much slower than in magnetite or maghemite NPs with similar size [7, 8]. Cobalt ferrite ( $\text{CoFe}_2\text{O}_4$ ) is a hard magnetic material with multiple properties: large magnetic anisotropy, high coercivity, high Curie temperature, large magnetostrictive coefficient, moderate saturation magnetization with good mechanical hardness,

and chemical stability [9, 10]. Moreover, the saturation magnetization of cobalt ferrite is almost the same as magnetite, but its crystalline anisotropy is one order of magnitude larger, making it suitable for hyperthermia treatment [11].

### 5.2.2 Manganese Ferrite

The  $\text{MnFe}_2\text{O}_4$  has a structure with excellent properties such as high resistivity, high saturation magnetization, and high initial permeability compared to the other ferrites [12]. The magnetic susceptibility of  $\text{MnFe}_2\text{O}_4$  NPs is higher respect to other ferrite NPs such as  $\text{Fe}_3\text{O}_4$ ,  $\text{CoFe}_2\text{O}_4$ , and  $\text{NiFe}_2\text{O}_4$  [13].  $\text{MnFe}_2\text{O}_4$  NPs could be used as novel magnetic resonance imaging (MRI) contrast agents [14].  $\text{MnFe}_2\text{O}_4$  MNPs have a greater biocompatibility and a strong phase contrast for MRI in comparison with  $\text{Fe}_3\text{O}_4$ ,  $\gamma\text{-Fe}_2\text{O}_3$ ,  $\text{CoFe}_2\text{O}_4$ , and  $\text{NiFe}_2\text{O}_4$  MNPs. Thus,  $\text{MnFe}_2\text{O}_4$  MNPs can provide the multiple functionalities of imaging, hyperthermia, and triggered drug release [15].

### 5.2.3 Zinc-doped Ferrites

Zinc oxide is commonly used as additive in ferrites. It can improve the properties and drive the medical applications of ferrite-based NPs [16, 17]. Zinc oxide increases the saturation of magnetization in small amounts [18].

## 5.3 Biomedical Applications of Magnetic Nanomaterials

MNMs can be used for a variety of biomedical applications: (1) transport and pharmacological release of drugs on specific sites, drug targeting, (2) gene delivery systems, (3) hyperthermia, (4) tissue engineering and repair, (5) diagnosis by MRI, (6) MRI-guided therapeutic cell replacement, (7) theranostics, (8) biochemical separations, (9) immunoassay platforms, (10) bioanalysis, and (11) magnetofection for target cancer gene therapy [19–22].

MNMs could play a key role in the treatment of tumors, using two different approaches: (1) targeted drug delivery in the cancer site and (2) cancer magnetic induction hyperthermia in which an alternating magnetic field is used to heat up MNMs and hereby destroy targeted cancer cells [23–25].

In this regard, iron oxide NPs with magnetic properties are one of the most suitable devices to achieve biomedical applications listed above.

## 5.4 Magnetic Nanomaterials for Cancer Therapies

Despite the intensive efforts within the past 50 years, it has only been possible to slightly, but not substantially, lower the mortality of cancer. On the other hand, considerable advances have been achieved for the other medical conditions, including the cardiovascular and cerebrovascular diseases and pneumonia [26]. At the present time, there are three basic approaches for treating cancer: surgery, radiotherapy, and chemotherapy. However, all of these procedures have considerable side effects and often are not sufficient for the curative treatment of metastatic cancer. The tumor-specific drugs, such as the tyrosine kinase inhibitors, have now been in use for several years with good results in certain types of cancer (e.g. Imatinib for chronic myeloid leukemia) [27]. The antibodies are also increasingly being used in oncology, although the antibody therapy sometimes has adverse systemic effects and often is expensive. For a subgroup of breast cancer patients, for example, the Her2-targeting antibodies are used successfully in treatment [28]. However, the approval of some previous indications for the antibody therapy has even been withdrawn recently [the British National Institute for Health and Clinical Excellence refused Avastin® (Bevacizumab) in colorectal carcinomas] [29]. There has not yet been a real breakthrough in cancer therapy, in general.

According to the estimates by the US National Cancer Institute, nanomedicine will prove to be trailblazing in the future prevention, diagnostic investigation, and treatment of cancer [30]. Nanotechnology has already found uses in many medical specialties, e.g. in otorhinolaryngology [31]. It is widely used in the different disciplines, from imaging to regenerative medicine. Before being used for medical purposes, however, those substances have to be investigated closely to determine their effects on the organism. This field of research is called nanotoxicology. It investigates the effects of both the NPs that occur naturally (in the environment) and those that are created by industry and traffic. Although a wide variety of materials are being used in medicine, the MNPs seem to hold the greatest potential of success. They are already established in clinical use as contrast media for MRI, e.g. Resovist® and Sinerem® [32]. In addition, these particles can be guided non-invasively (drug delivery) and have the ability to be heated (hyperthermia) by external magnetic fields [32]. A combination of diagnostic investigation and therapy, as “theranostics”, is, thus, possible.

Therefore, MNPs have excellent potential to improve the treatment of cancer.

## 5.5 Relevance of Nanotechnology to Cancer Therapy

Cancer is a huge burden not only to the healthcare system but also to the economy, in general. As the second most common cause of death in Europe, it generates annual costs of approximately 120 billion euro [33]. This does not merely include the direct costs of hospital treatment, nursing care, and medication; this also includes the expenses for information and loss of production. The costs for the treatment alone account for about 36% of the total, while the early mortality and morbidity are responsible for another 36% [33]. Considering the fact that the incidence of cancer increases with age, an escalation could be expected due to the present demographic trends. Irrespective of the dimension of the problem, the costs for healthcare per se are progressively increasing, which means that paying for the adequate treatment will become appreciably more difficult. The European Commission is assuming an increase in age-related public expenditure (healthcare and long-term nursing care, as well as pensions) by some five percentage points of the EU gross domestic product by the year 2060 [30]. Therefore, a considerable reduction in the costs of cancer therapy is needed. This reduction would also make it possible to provide better care in the poorer countries of the developing world, where only the upper echelons of society can afford the costly surgeries, radio- or chemotherapy at the moment. Besides infectious diseases, cancer is the second biggest challenge in healthcare that these countries have to face. Finally, the treatment of cancer should not be so time-consuming and complicated that it is only possible to be carried out in a few highly specialized centers, accessible to just a restricted circle of patients. The smaller facilities must be able to provide this care as well, as only in this way sufficient healthcare provision can be guaranteed to the population. The treatment in the local centers would also have the advantage of reducing the costs for transportation, which are sometimes considerable and often not covered by the health insurance (or only under very specific conditions). Apart from these structural problems, it is essential that the existing forms of treatment will be improved, not only in terms of outcome and expenditure but also in terms of tolerability. Surgery, radio- and chemotherapy often have considerable side effects. These adverse effects often affect the patients more than the disease itself. The initial approach certainly consists of improving the existing methods and/or supplementing and combining them with the new

procedures. The long-term goal has to be that everyone will have access to cancer therapy that is simple, cost-effective, and well tolerated. With the help of nanotechnology, nowadays, this seems to be possible to achieve.

A multitude of new potential is opening up. Efforts are being made to simultaneously measure a wide range of known laboratory parameters, like tumor markers and biomarkers *in vitro*, using simple and cheap methods, as well as to discover further parameters with novel techniques. The NPs are already being used as contrast agents in medical imaging, to visualize tumors more accurately, with respect not only to the margins and extent but also to distinguish between the active and inactive regions. Therewith, treatment such as radiotherapy can be planned and carried out more easily and efficiently. In addition, nanomedicine is being used to refine the monitoring of the disease progression so that the patient's management can be adjusted promptly, if necessary. This work focused more closely on the drug delivery, hyperthermia, and overcoming drug resistance as means of improvement of cancer therapy.

## 5.6 Cancer Therapy with Magnetic Nanoparticle Drug Delivery

As the conventional chemotherapy is administered systemically, it often causes considerable adverse reactions such as nausea, hair loss, and bone marrow suppression, as well as liver and kidney toxicity. These aspects determine the dose of the chemotherapeutic agents and limit their effects on the tumor. Therefore, in the recent years, it has been a trend in cancer pharmacotherapy to identify substances with higher specificity. Although considerable success has already been achieved (e.g. Herceptin<sup>®</sup>), the limits of this strategy have become clear. The targeted blockage of a specific signaling pathway has led to the emergence of genetically mutated cancer cells that are able to circumvent this blockage by upregulation of an effective parallel, alternative, or overlapping pathway [34]. That leads to broad-spectrum medicinal products being used again. The biodistribution of these substances is of particular relevance to targeted therapy. This is where nanotechnology comes in. It can be used to transport medicinal products very precisely to the intended site of action.

MNP drug delivery opens the possibility of using local enhancement methods so that the drug can accumulate and act in a previously determined area. This method was first described in 1978 [30]. It is based on the usage of three elements: iron (Fe), cobalt (Co), and nickel (Ni). All are ferromagnetic under physiological conditions, although they do not exhibit

the same magnetization: Ni 55 emu/g, Co 160 emu/g, and Fe 218 emu/g. Mostly, they are used as hybrids with other metal ions, oxygen, or carbon dioxide. There are innumerable possibilities for such combinations [35]. The iron compounds are predominantly used because of their biocompatibility. They show the lowest toxicity and are even used therapeutically for iron substitution [36]. The NPs are coated in order to prevent agglomeration, ensure stability, and provide a positive effect on biodistribution. A wide variety of materials, including fatty acids, polyethylene glycol (PEG), dextran, and chitosan may be used [37]. MNPs can transport various different substances and molecules, such as chemotherapeutic agents, antibodies, nuclear acids, and radionuclides. In principle, this approach can be used for any tumor, irrespective of its size, differentiation, or site.

## 5.7 Drug Delivery in the Cancer Therapy

MNPs appear to be very appropriate for drug delivery. Indeed, they can be synthesized in different sizes and can be functionalized (surface-coated) in order to carry various molecules. A number of issues need to be considered when using MNPs as carriers including colloidal stability and biocompatibility. It was recently described the properties of nanomaterials in the physiological environment and their specific properties used during the elaboration of these NP-based drug delivery systems [30]. Indeed, MNPs need to be coated with surfactants or polymers (e.g. dextran, PEG) to stabilize them and attach functional groups to their surfaces. The functionalisation is used to bind the appropriate molecules, such as anticancer drugs or antibodies, to the NPs. Surfactants and polymers increase also the biocompatibility of the NPs. Indeed, without this shield MNPs could not resist opsonization (i.e. the process by which an exogenous molecule is tagged for destruction by phagocytosis) when introduced *in vivo*. Another advantage of these NPs is that they are nontoxic and well tolerated *in vivo*, independently of the administration routes. NPs are already widely used in drug delivery, offering to transport various agents such as antimicrobial molecules, genes, proteins, and anticancer drugs. Many chemotherapeutic drugs and siRNA treatments have already been loaded in different NPs and have demonstrated a great efficacy against different types of cancers, some are even in phase I of drug development studies. While cancer drug delivery via MNPs is seen in its infancy (to date, only a few reports with *in vivo* results have been published), it has great potential due to the numerous advantages of MNPs. For example, recently, Maeng *et al.* have shown promising results MNPs loaded with doxorubicin (a potent anticancer

agent) against liver cancer in rat and rabbit cancer models. Gene therapy represents an alternative to anticancer drug treatment for cancer [38]. Indeed, this therapy could target directly genes and regulate the altered gene expression, which is involved in carcinogenesis. However, *in vivo*, the half-lives of DNA or RNA are very short which makes gene therapy delivery very challenging. NPs when used for drug delivery should, therefore, have a dual function, the first is to protect the therapeutic agent from degradation and the second is to deliver it to cancer cells. MNPs technology has one more advantage; it attracts NPs near the tumor and increases gene transfer into cells. This technique is called magnetofection and uses an external magnetic field (magnet) to concentrate and retain MNPs in a specific area. However, this approach is not applicable for non-accessible tumors.

### 5.7.1 Drug Targeting

The design of nanocarriers for drug delivery with selectivity to disease and anatomical sites has a great potential. For instance, NP-conjugated drug and gene delivery systems could be used to treat neurological diseases using MNP-conjugated drugs to cross the blood–brain barrier [39, 40]. Nanotechnology for drug delivery can be used to achieve (1) site-specific delivery of drugs in tissue and organs, (2) improved delivery of poorly water-soluble drugs, (3) transcytosis of drugs across tight epithelial and endothelial barriers, (4) co-delivery of two or more drugs for combination therapy, and (5) theranostic application of drug delivery by combining therapeutic agents with imaging modalities [30, 41]. The basic principles of magnetic targeting of MNP-conjugated drugs have been investigated experimentally. The surface hydrophilicity of MNPs plays a key role for drug delivery. Targeted therapy using MNPs assembled with drugs was already tested in clinical trials as a cancer therapy [25]. Various studies investigated the biodistribution of MNPs through intravenous injection directed by an external magnetic field to concentrate MNPs at a specific target site; this procedure has been well tolerated in cancer patients [24, 25].

### 5.7.2 Passive and Active Drug Targeting

There are two kinds of targeted drug delivery of nanocarriers: (1) active targeted drug delivery, that overcome the limitations of passive targeting by conjugation with affinity ligands (antibodies, peptides, aptamers, etc.) that recognize and bind to specific receptors on the target cell surface [42]; and (2) passive targeted drug delivery, such as the enhanced permeability and

retention effect [enhanced permeability and retention (EPR) effect] that allows migration of molecules up to 50–100 nm in diameter into the target site [43]. In fact, drug carriers are expected to stay in the blood for long time, accumulate in pathological sites with affected and leaky vasculature (tumors, inflammations, and infarcted areas) via the EPR effect and facilitate targeted delivery of specific ligand-modified drugs and drug carriers into poorly accessible areas [44]. The active drug targeting increases the selectivity of the delivery of drugs [43]. Passive and active drug targeting with nanocarriers to disease or tumor site reduce toxic side effects, increase efficacy, and enhance delivery of poorly soluble or sensitive therapeutic molecules [43].

## 5.8 Magnetic Hyperthermia

MNMs with superior magnetic properties and properly surface functionalized are being intensively investigated to achieve highly efficient carcinogenic cell destruction through hyperthermia treatments. In particular, it is difficult to find a definition for hyperthermia not linked to cancer therapy. Most definitions available of hyperthermia therapy come from health organizations or institutions. Here, we would like to cite one from the National Cancer Institute from United States of America, in which therapeutic hyperthermia is defined as: A type of treatment in which body tissue is exposed to high temperatures to damage and kill cancer cells or to make cancer cells more sensitive to the effects of radiation and certain anticancer drugs. This definition is not new. In fact, different approaches have been used to apply hyperthermia in tumor regions, but with harmful secondary effects in the healthy tissues [45]. This is the case of many techniques involving laser, ionizing radiation, and microwaves as tools to heat up malignant body tissues [45]. Although these techniques are able to increase the intracellular temperature up to the cellular death, additionally they can provoke harmful side effects such as ionization of the genetic material or lack of selectiveness in radiation and microwaves therapies, respectively, that affect the surrounding healthy tissues. This encouraged the search of new mechanisms capable of increasing the temperature of damaged areas while keeping the rest of tissues healthy. Nanotechnology has just provided a novel and original solution to this problem with the magnetic hyperthermia. Magnetic hyperthermia allows to remotely induce local heat by means of the magnetic energy losses of MNPs under an oscillating magnetic field. In other words, the ability of some MNPs to transform the electromagnetic energy into heat allows the temperature increase

in well-defined regions in the human body where the tumor cells and the NPs are located. Therefore, the activation of these NPs as nanoheaters can be controlled externally by applying or removing an oscillating magnetic field. The electromagnetic radiation used in magnetic hyperthermia is in the range of the radiofrequency (RF) (between several kHz and 1 MHz). This radiation is completely healthy and shows enough penetration depth to access inner organs or tissues in the body. The specificity of this technique is achieved by the higher sensitivity of the tumoral cells to temperature increases above 42 °C, temperatures at which the natural enzymatic processes that keep the cells alive are destroyed so that allowing their selective killing [46]. However, the apparent simplicity of the technique demands the fulfillment of several requirements to get the desired therapy effect. For biomedical applications, MNPs are preferred to show a superparamagnetic behavior, meaning that the magnetization drops to zero when the applied magnetic field is removed [47]. This fact implies that no coercive forces or remanence exist, preventing magnetic dipolar interactions between particles and, eventually, their aggregation, which could lead to serious adverse problems derived from the formation of clots in the blood circulation system. As previously indicated, the saturation magnetization should be also as high as possible in order to guarantee the efficient heating of the NPs under the oscillating magnetic field. And, this fact is very closely related to the particle size and distribution of the NPs. The superparamagnetic properties of MNPs are size dependent. An increase in the particle size will lead to higher saturation magnetization values and better performance for magnetic hyperthermia applications. The particle size is an issue of crucial interest in many biomedical applications in which the use of very small particles is highly desired to act as heat nanosources in tumoral regions of limited size access. The commonest barrier found in most tissues is the continuous blood capillaries type, so the separation between the endothelial cells along the basement membrane will determine the efficiency of the hyperthermia therapy.

### 5.8.1 Application of Hyperthermia for Cancer Therapy

Hyperthermia is a cancer therapy that relies on the localized heating of tumors above 43 °C for about 30 min. MNPs can generate heat under alternating magnetic fields due to energy losses in the traversing of the magnetic hysteresis loop [35]. Generation of different degrees of heat depends on the magnetization properties of specific MNP formulations and magnetic field parameters. Selectivity to tumors was considerably improved through the use of silane coatings and through functionalization approaches.

For example, MNPs conjugated with antibodies to cancer-specific antigens improved selectivity of MNP uptake by tumors during hyperthermia therapy. Magnetic hyperthermia using magnetic cationic liposomes has been used in a combination approach with TNF- $\alpha$  gene therapy and stress-inducible gadd153 promoter, resulting in a dramatic arrest in tumor growth [48].

### 5.8.2 Catabolism of Tumors by Hyperthermia

The possibility of treating cancer by artificially induced hyperthermia has led to the development of many different devices designed to heat malignant cells while sparing surrounding healthy tissue [49–51]. Experimental investigations of the application of magnetic materials for hyperthermia date back to 1957 when Gilchrist *et al.* heated various tissue samples with 20–100 nm size particles of  $\gamma\text{-Fe}_2\text{O}_3$  exposed to a 1.2 MHz magnetic field [52]. In broad terms, the procedure involves dispersing magnetic particles throughout the target tissue, and then applying a magnetic field of sufficient strength and frequency to cause the particles to heat. This heat conducts into the immediately surrounding diseased tissue whereby, if the temperature can be maintained above the therapeutic threshold of 42 °C for 30 min or more, the cancer is destroyed. Whereas the majority of hyperthermia devices are restricted in their utility because of unacceptable coincidental heating of healthy tissue, magnetic particle hyperthermia is appealing because it offers a way to ensure that only the intended target tissue is heated (Figure 5.3).

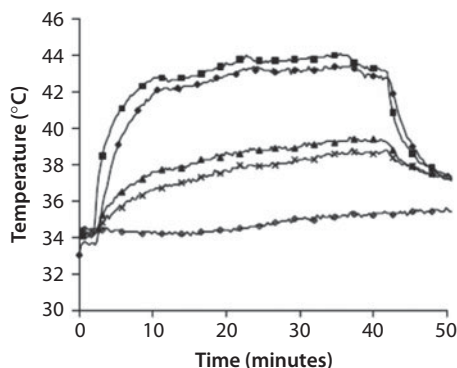


**Figure 5.3** Animal trial data on hyperthermia treatments, showing preferential heating of a tumor using intravascularly infused ferromagnetic microspheres; (■) tumor edge, (◊) tumor centre, (Δ) normal liver 1–2 cm from tumor, (x) alternative lobe, and (▽) core body temperature.

## 5.9 Role of Theranostic Nanomedicine in Cancer Treatment

Theranostic nanomedicine may be defined as nanomedicine that combines diagnostics with therapeutics [53] (Figure 5.4). Nanomedicine has applied nanotechnology in various medical fields such as imaging, diagnosis or therapy in human diseases. Theranostics combines the last two fields, while theranostic nanomedicine produces “NP-based drugs” simultaneously capable of the diagnosis and treatment of a disease. The goals of theranostic nanomedicine, therefore, are not only to improve the detection and to increase the efficacy of the treatment of cancers but also to limit the systemic toxicity associated with this treatment [54]. It is, therefore, important that the therapeutic agents reach and can be concentrated on the target sites. Indeed, the advanced theranostic nanomedicines conjugated with targeting moiety can recognize specific target, bind and be internalized via specific mechanism, e.g. receptor-mediated endocytosis [55].

Another important advantage of theranostic nanomedicine in the treatment of cancer is the potential for a rapid review of the outcome of a treatment in individual patient, in order to plan the next therapy or to decide to repeat the same therapeutic session (personalized medicine). We feel that the use of magnetic NPs in conjunction with MRI may advance the concept of personalized nanomedical theranostic treatment in cancer for an individual patient [55]. As MRI scanners are nowadays readily available

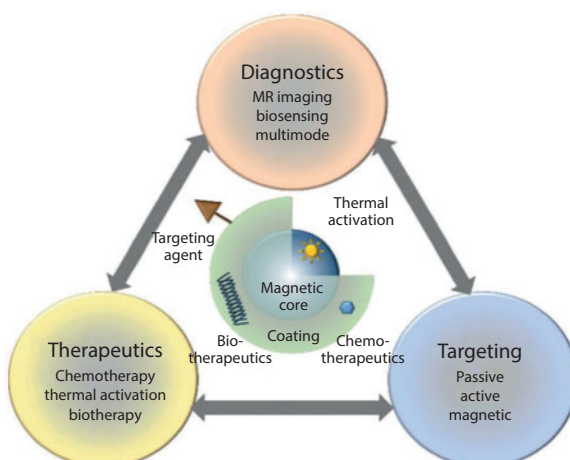


**Figure 5.4** Functional architecture of MNMs and theranostic modalities.

in hospitals this seems to be the most appropriate technique for monitoring the effects of cancer nanomedicine therapies. Moreover, magnetic NPs have an enormous advantage in this type of therapy, due to their paramagnetic propensity: they can be easily used as a contrast agent.

## 5.10 Magnetic Nanomaterials for Chemotherapy

Chemotherapy focuses on the treatment of disease through delivery of small molecule drug formulations [56]. Most of the drugs do not have cell-targeting capabilities which results in undesirable side effects when internalized by healthy cells. The success of MNMs in diagnostic imaging has generated considerable interest in their use as drug delivery vehicles. MNMs coatings provide anchor points to which drug molecules can be coupled. Integrating the drugs into MNMs improves their targeting abilities, limits their side effects, and allows increment of the drug dosage at the diseased tissue [57, 58]. Currently, several drugs have been combined with MNMs for cancer chemotherapy, including paclitaxel (PTX), doxorubicin (DOX), and methotrexate (MTX) [59, 60]. The therapeutic moieties can be covalently bonded to MNMs with cleavable linkages, encapsulated in the hydrophobic coating on MNMs, or physically absorbed on the surface of MNMs.

An ideal drug delivery vehicle should have efficient drug loading and controllable drug release. In applications where the drug has an affinity for the target cell, it can be advantageous to graft the drug to the surface of the MNMs.

The drug-loading capacity via direct conjugation can be found low due to the small number of functional groups on the surface of MNMs. Hollow MNMs can be used to increase chemotherapeutic efficacy due to higher drug-loading capacity [61]. Different studies found that MNMs loaded with both doxorubicin and paclitaxel in a 1:1 ratio demonstrated highly synergistic antiproliferative activity in MCF-7 breast cancer cells relative to MNMs loaded with only doxorubicin or paclitaxel [62]. The thermal energy from MNMs could be also used as an external trigger for controlled drug release.

In fact, MNMs coated with thermally responsive agents (e.g. hydrogels, thermosensitive polymers, lipids) were explored where temperature works as a trigger for drug release [63, 64].

An external RF field is able to release most of the drug from the MNMs. Drug release in the presence of RF field was found two times higher than in the absence of RF field due to thermal activation of MNMs.

## 5.11 Magnetic Nanomaterials as Carrier for Cancer Gene Therapeutics

Gene therapy is a technique that uses DNA and antisense RNA (siRNA) to treat and prevent disease via gene expression and gene silencing of defective genes [65, 66]. The coupling of nucleic acids with MNMs improves the plasma pharmacokinetics and plasma membrane penetration of nucleic acids necessary for internalization into cells [66]. MNMs designed for gene therapy can be coated with cationic polymers such as polyethylenimine (PEI), polyamidoamine, or chitosan in order to conjugate with negatively charged nucleic acids and potentiate the therapeutic effect. While the cationic MNMs have shown great success *in vitro*, their applicability *in vivo* has been limited because of toxicity and instability in biological media [67].

MNMs coated with a copolymer of PEI, PEG, and chitosan (NP-CP-PEI) demonstrated an innocuous toxic profile and a high level of expression of the delivered plasmid DNA in a C6 xenograft mouse model, while MNMs coated with only PEI or chitosan showed high toxicity or low gene transfection efficiency, respectively [68]. The attachment of the targeting ligand, chlorotoxin (CTX), to NP-CP-PEI can enhance the gene transfection efficiency [68].

One alternative to the cationic coatings was offered by conjugating siRNA to MNMs by covalent bonding. Medarova *et al.* developed a dual-purpose probe for the simultaneous noninvasive imaging and delivery of siRNAs to tumors. This probe consisted of MNMs labeled with Cy5.5 dye and conjugated to a synthetic siRNA duplex targeting a gene of interest. With use of model (green fluorescent protein, GFP) and therapeutic (surviving) genes, the authors demonstrated that the targeting and delivery of the probe could be monitored *in vivo* by MRI and optical imaging. In addition, they were able to follow the silencing process by optical imaging and to correlate it with histological data [69, 70].

## 5.12 Conclusions

MNMs truly represent a prototypical nanotechnology platform in the sense that their properties and phenomena are unquestionably size dependent in the nanoscale regime. Nominal ferrimagnetic behavior of MNM changes to superparamagnetism below  $\sim$ 10–15 nm size scale, which is essential for colloidal stability of MNM. The perturbations of protons in vicinity of the MNM provide the essential characteristics for contrast in MRI, while enthalpic contributions from external RF field generate localized thermal

energy for therapeutic purpose. Thus, the combined theranostic attributes of MNM arise from diagnostic imaging and thermal therapy combination.

Over and beyond the technical and scientific aspects of theranostic administration of cancer, MNM also embodies the other important attribute of nanotechnology in terms of complementarity, integration, and synergy of nominally disparate fields and subjects. For just MNM alone, these subjects and technical themes include physics of magnetism, chemistry of synthesis, materials science of structure–property relationship, surface science of functionalization, biomedical engineering in MRI protocols and RF activation parameters, and the core biology and medical themes of cancer targeting, diagnostics imaging, and therapy. As a result, this has brought together scientists, engineers, and clinical practitioners from diverse backgrounds for more than a decade to advance biomedical sensing, diagnostics, and therapeutics.

As demonstrated by the examples highlighted in this chapter, remarkable advances have been made in the recent decade to harness the size, composition, and size-dependent properties of MNM for cancer diagnostics, diagnostic imaging, and localized therapy. MNM continue to exhibit realistic potential to address diagnostic imaging by MRI and localized therapy via thermal activation and/or timed therapeutic cargo release. In particular, it has been shown that appropriate choice of composition, size, and surface functionalization has the potential for synergistic combination of diagnostics MR imaging and thermally activated therapy.

Despite some promising results obtained so far, including *in vivo* animal studies, there are specific challenges for effective use of MNM in humans; the final objective for any cancer theranostic platform. Regulatory approval for use in humans will require further and extensive safety and toxicology studies. Nevertheless, the clinical trials highlight numerous problems still to be resolved. If the principle of magnetic drug targeting is simple, the development of magnetic vectors is complex. The composition, surface properties, drug loading, biodistribution, and pharmacokinetics are the diverse factors that may affect the toxicity of the MNM in a direct or indirect manner and need to be understood thoroughly. The critical parameters to optimize are size, magnetization, biocompatibility, and drug loading and release. Although for the time being no preparation satisfies all requirements simultaneously, most research groups succeed to produce biocompatible magnetic vectors with controllable sizes in the nanometer range. Limitations also exist for targeting efficiency, the lack of homogeneous MNM penetration, and inadequate delivery of therapeutics into the tumor volume. Finally, magnetic drug targeting was investigated as a novel drug delivery system that has been proved feasible resulting in an increase

in local drug concentration and thus permitting a reduction of side effects [30]. This is a source of optimism for a real possibility of magnetically targeted chemotherapy.

### 5.13 Future Prospects

A tremendous amount of time and money has been invested in the development of iron oxide NPs and MNMs for their clinical application. Recent breakthrough within areas of magnetic hyperthermia is shadowed by the simultaneous withdrawal of several existing contrast agents. Toxicity concern or lack of clinical benefit is the main cause of removal. As scientific work with NPs has been attempted for approximately three decades and the already few accomplishments now are being second-guessed, it is natural to raise the concern that our resources allocated to medical research is being misplaced. MNMs truly represent a prototypical nanotechnology platform in the sense that their properties and phenomena are unquestionably size dependent in the nanoscale regime. Would the society benefit from iron oxide NPs as contrast agents for MR imaging? Although medical care continues to evolve, treatment-resistant diseases develop constantly throughout our population, with cancer representing a significant proportion of these. MNMs could become in future the gold standard tool in achieving appropriate diagnostic sensitivity. In addition, MNM could reduce human toxicity, and MNM could display reduced effects on the environment.

With growing incidence of cancer, contrast agents are necessary in order to provide the best sensitivity for tumor detection and early treatment options. Therefore, focusing research on contrast agent development can be of substantial benefit for the society long term. Furthermore, the theranostic potential of MNMs are showing promising results for further cancer treatment, as seen in the recent approval of NanoTherm for hyperthermia [35]. With the appropriate development, iron oxide NPs can provide new and effective treatment methods for cancers with previously limited treatment options, both as a contrast agent, and by improving drug delivery. Research is continuing in this regard; including development of new magnetic core materials with higher relaxivity and thermal activation properties, along with design of new coating materials to improve the pharmacokinetics, biodistribution, and biocompatibility. Success with MRI and progress over the past few years offer considerable prospects for eventual diagnostic and therapeutic translation of MNM technology. Indeed, several diagnostic clinical trials using MNM have been initiated over the past few years. The increasing trend toward *in vivo* studies in animals and

subsequent escalation to clinical trials are expected to help translate MNM from the laboratory to the clinic.

## References

- Zoraida P.A. *Nanomaterials for Medical Applications*. Springdale: Elsevier 1–32, 2013.
- Poon W., Zhang X., Nadeau J. Nanoparticle drug formulations for cancer diagnosis and treatment. *Crit. Rev. Oncog.* 19, 223–45, 2014.
- Gupta A.K., Gupta M. Synthesis and surface engineering of iron oxide nanoparticles for biomedical applications. *Biomaterials* 26, 3995–4021, 2005.
- Hofmann-Amtenbrink M., von Rechenberg B., Hofmann H. Nanostructured materials for biomedical applications. *Transworld Research Network* 5, 119–49, 2009.
- Huber D.L. Synthesis, properties, and applications of iron nanoparticles. *Small Weinh. Bergstr. Ger.* 1, 482–501, 2005.
- Lu C.W., Hung Y., Hsiao J.K., Yao M., Chung T.H., Lin Y.S., Wu S.H., Hsu S.C., Liu H.M., Mou C.Y., et al. Bifunctional magnetic silica nanoparticles for highly efficient human stem cell labeling. *Nano Lett.* 7, 149–54, 2007.
- Balakrishnan S., Bonder M. Particle size effect on phase and magnetic properties of polymer-coated magnetic nanoparticles. *J. Magn. Magn. Mater.* 321, 117–22, 2009.
- Peng S., Xie J., Sun S. Synthesis of Co/MFe(2)O(4) (M = Fe, Mn) Core/Shell nanocomposite particles. *J. Solid State Chem.* 181, 1560–64, 2008.
- Emad G., Mohamed W., Atef O., Lokeshwar B. Synthesis, magnetic and optical properties of core/shell  $\text{Co}_{1-x}\text{Zn}_x\text{Fe}_2\text{O}_4/\text{SiO}_2$  nanoparticles. *Nanoscale Res. Lett.* 6, 460–8, 2011.
- Rohilla S., Kumar S., Aghamkar P., Sunder S. Investigations on structural and magnetic properties of cobalt ferrite/silica nanocomposites prepared by the coprecipitation method. *J. Mag. Magn. Mater.* 323, 897–902, 2011.
- Baldi G., Bonacchi D., Innocenti C., Lorenzi G., Sangregorio C. Cobalt ferrite nanoparticles: the control of the particle size and surface state and their effects on magnetic properties. *J. Magn. Magn. Mater.* 311, 10–6, 2007.
- Soleimani R., Soleimani M., Godarzi M.G. Investigation of the thermal stability of Mn ferrite particles synthesized by a modified co-precipitation method. *J. Fusion. Energ.* 30, 338–41, 2011.
- Kim D.H., Nikles D.E., Brazel C.S. Synthesis and characterization of multi-functional chitosan –  $\text{MnFe}_2\text{O}_4$  nanoparticles for magnetic hyperthermia and drug delivery. *Materials* 3, 4051–65, 2010.
- Kim D.H., Zeng H., Ng T.C., Brazel C.S.  $T_1$  and  $T_2$  relaxivities of succimer-coated  $\text{MFe}_2^{3+}\text{O}_4$  ( $\text{M}=\text{Mn}^{2+}$ ,  $\text{Fe}^{2+}$  and  $\text{Co}^{2+}$ ) inverse spinel ferrites for potential use as phase-contrast agents in medical MRI. *J. Magn. Mater.* 321, 3899–904, 2009.

15. Batoo K.M. Study of dielectric and impedance properties of Mn ferrites. *Physica B* 406, 382–7, 2011.
16. Vaidyanathan G., Sendhilnathan S., Arulmurugan R. Structural and magnetic properties of  $\text{CoZnFe}_2\text{O}_4$  nanoparticles by co-precipitation method. *J. Magn. Magn. Mater.* 313, 293–9, 2007.
17. Rath C., Anand S., Das R.P., Sahu K.K., Kulkarni S.D., Date S.K., *et al.* Dependence on cation distribution of particle size, lattice parameter, and magnetic properties in nanosize Mn-Zn ferrite. *J. Appl. Phys.* 91, 2211–5, 2002.
18. Sharifi I., Shokrollahi H., Amiri S. Ferrite-based magnetic nanofluids used in hyperthermia applications. *J. Magn. Magn. Mater.* 324, 903–15, 2012.
19. Reddy L.H., Arias J.L., Nicolas J., Couvreur P. Magnetic nanoparticles: design and characterization, toxicity and biocompatibility, pharmaceutical and biomedical applications. *Chem. Rev.* 112, 5818–78, 2012.
20. Weissleder R., Moore A., Mahmood U., *et al.* *In vivo* magnetic resonance imaging of transgene expression. *Nat. Med.* 6, 351–5, 2000.
21. Bulte J.W., Douglas T., Witwer B., Zhang S.C., *et al.* Magnetodendrimers allow endosomal magnetic labeling and *in vivo* tracking of stem cells. *Nat. Biotechnol.* 19, 1141–7, 2001.
22. Kircher M.F., Allport J.R., Graves E.E., Love V., Josephson L., Lichtman A.H., Weissleder R. *In vivo* high resolution three-dimensional imaging of antigen specific cytotoxic T-lymphocyte trafficking to tumors. *Cancer. Res.* 63, 6838–46, 2003.
23. Farokhzad O.C., Langer R. Impact of nanotechnology on drug delivery. *ACS. Nano.* 3, 16–20, 2009.
24. Pankhurst Q.A., Connolly J., Jones S.K., Dobson J. Applications of magnetic nanoparticles in biomedicine. *J. Phys. Appl. Phys.* 36, r167–r181, 2003.
25. Duguet E., Vasseur S., Mornet S., *et al.* Magnetic nanoparticles and their applications in medicine. *Nanomed* 1, 157–68, 2006.
26. Violi F., Cangemi R., Calvieri C. Pneumonia, thrombosis and vascular disease. *J. Thromb. Haemost.* 12(9), 1391–400, 2014.
27. Ali M.A. Chronic myeloid leukemia in the era of tyrosine kinase inhibitors: an evolving paradigm of molecularly targeted therapy. *Mol. Diagn. Ther.* 20(4), 315–33, 2016.
28. Moasser M.M., Krop I.E. The evolving landscape of HER2 targeting in breast cancer. *JAMA. Oncol.* 1(8), 1154–61, 2015.
29. Esin E., Yalcin S. Maintenance strategy in metastatic colorectal cancer: a systematic review. *Cancer. Treat. Rev.* 42, 82–90, 2016.
30. Ferrari M. Cancer nanotechnology: opportunities and challenges. *Nat. Rev. Cancer.* 5, 161–71, 2005.
31. Ivan H. El-Sayed. Nanotechnology in head and neck cancer: the race is on. *Curr. Oncol. Rep.* 12(2), 121–8, 2010.
32. Mandal S., Chaudhuri K. Engineered magnetic core shell nanoprobes: synthesis and applications to cancer imaging and therapeutics. *World J. Biol. Chem.* 7(1), 158–67, 2016.

33. Piktel E., Niemirowicz K., Wątek M., Wollny T., Deptuła P., Bucki R. Recent insights in nanotechnology-based drugs and formulations designed for effective anti-cancer therapy. *J. Nanobiotechnol.* 14(1), 39, 2016.
34. Arvizo R.R., Saha S., Wang E., Robertson J.D., Bhattacharya R., Mukherjee P. Inhibition of tumor growth and metastasis by a self-therapeutic nanoparticle. *Proc. Natl. Acad. Sci. USA* 110(17), 6700–5, 2013.
35. Beik J., Abed Z., Ghoreishi F.S., Hosseini-Nami S., Mehrzadi S., Shakeri-Zadeh A., Kamrava S.K. Nanotechnology in hyperthermia cancer therapy: from fundamental principles to advanced applications. *J. Control. Release* 235, 205–21, 2016.
36. Radomska A., Leszczyszyn J., Radomski M.W. The nanopharmacology and nanotoxicology of nanomaterials: new opportunities and challenges. *Adv. Clin. Exp. Med.* 25(1), 151–62, 2016.
37. Muthu M.S., Leong D.T., Mei L., Feng S.S. Nanotheranostics – application and further development of nanomedicine strategies for advanced theranostics. *Theranostics* 4(6), 660–77, 2014.
38. Maeng J.H., Lee D.H., Jung K.H., Bae Y.H., Park I.S., Jeong S., Jeon Y.S., Shim C.K. et al. Multifunctional doxorubicin loaded superparamagnetic iron oxide nanoparticles for chemotherapy and magnetic resonance imaging in liver cancer. *Biomaterials* 31(18), 4995–5006, 2010.
39. Kreuter J. Nanoparticulate systems for brain delivery of drugs. *Adv. Drug. Deliv. Rev.* 47, 65–81, 2001.
40. Schroeder U., Sommerfeld P., Ulrich S., Sabel B.A. Nanoparticle technology for delivery of drugs across the blood-brain barrier. *J. Pharm. Sci.* 87, 1305–7, 1998.
41. Liong M., Lu J., Kovochich M., Xia T., Ruehm S.G., Nel A.E., Tamanoi F., Zink J.I. Multifunctional inorganic nanoparticles for imaging, targeting, and drug delivery. *ACS Nano* 2, 889–96, 2008.
42. Bamrungsap S., Zhao Z., Chen T., Wang L., Li C., Fu T., Tan W. Nanotechnology in therapeutics: a focus on nanoparticles as a drug delivery system. *Nanomedicine (Lond)* 7, 1253–71, 2012.
43. Torchilin V.P. Passive and active drug targeting: drug delivery to tumors as an example. *Handb. Exp. Pharmacol.* 197, 3–53, 2010.
44. Maeda H., Wu J., Sawa T., Matsumura Y., Hori K. Tumor vascular permeability and the EPR effect in macromolecular therapeutics: a review. *J. Control. Release* 65, 271–84, 2000.
45. Chicheł A., Skowronek J., Kubaszewska M., Kanikowski M. Hyperthermia – description of a method and a review of clinical applications. *Rep. Pract. Oncol. Radiother.* 12(5), 267.15, 2007.
46. Andra W., Nowak H. *Magnetism in Medicine: A Handbook*. First ed. Germany: Wiley-VCH; 1998.
47. Hofmann-Amtenbrink M., von Rechenberg B., Hofmann H. Superparamagnetic nanoparticles for biomedical applications. In: Tan MC, editor. *Nanostructured Materials for Biomedical Applications*. p. 119, 2009.

48. Veronica I. Shubayev, Thomas R. Pisanic, II, and Sungho Jin. Magnetic nanoparticles for theragnostics. *Adv. Drug. Deliv. Rev.* 61(6), 467–77, 2009.
49. Van der Zee J. Heating the patient: a promising approach? *Ann. Oncol.* 13, 1173–84, 2002.
50. Wust P., Hildebrandt B., Sreenivasa G., Rau B., Gellermann J., Riess H., Felix R. and Schlag P M. Hyperthermia in combined treatment of cancer. *Lancet. Oncol.* 3, 487–97, 2002.
51. Moroz P., Jones S.K. and Gray B.N. Status of hyperthermia in the treatment of advanced liver cancer. *J. Surg. Oncol.* 77, 259–69, 2001.
52. Gilchrist R.K., Medal R., Shorey W.D., Hanselman R.C., Parrott J.C. and Taylor C.B. Selective inductive heating of lymph nodes. *Ann. Surg.* 146, 596–606, 1957.
53. Janib S.M., Moses A.S., MacKay J.A. Imaging and drug delivery using theranostic nanoparticles. *Adv. Drug. Deliv. Rev.* 62(11), 1052–63, 2010.
54. Muthu M.S., Leong D.T., Mei L., Feng S.S. Nanotheranostics – application and further development of nanomedicine strategies for advanced theranostics. *Theranostics* 4(6), 660–77, 2014.
55. Choi K.Y., Liu G., Chen X. Theranostic nanoplatforms for simultaneous cancer imaging and therapy: current approaches and future perspectives. *Nanoscale* 4(2), 330–42, 2012.
56. DeVita V.T., Chu E. A history of cancer chemotherapy. *Cancer. Res.* 68(21), 8643–53, 2008.
57. Veiseh O., Gunn JW., Zhang M.Q. Design and fabrication of magnetic nanoparticles for targeted drug delivery and imaging. *Adv. Drug. Deliv. Rev.* 62(3), 284–304, 2010.
58. McCarthy J.R., Weissleder R. Multifunctional magnetic nanoparticles for targeted imaging and therapy. *Adv. Drug. Deliv. Rev.* 60(11), 1241–51, 2008.
59. Kohler N., et al. Methotrexate-immobilized poly(ethylene glycol) magnetic nanoparticles for MR imaging and drug delivery. *Small* 2(6), 785–92, 2006.
60. Sun C., et al. *In vivo* MRI detection of gliomas by chlorotoxin-conjugated superparamagnetic nanoprobe. *Small* 4(3), 372–9, 2008.
61. Shin J.M., et al. Hollow manganese oxide nanoparticles as multifunctional agents for magnetic resonance imaging and drug delivery. *Angew. Chem. Int. Ed.* 48(2), 321–4, 2009.
62. Jain T.K., et al. Magnetic nanoparticles with dual functional properties: drug delivery and magnetic resonance imaging. *Biomaterials* 29(29), 4012–21, 2008.
63. Pradhan P., et al. Targeted temperature sensitive magnetic liposomes for thermochemotherapy. *J. Controlled Release*. 142(1), 108–21, 2010.
64. Purushotham S., Ramanujan R.V. Thermoresponsive magnetic composite nanomaterials for multimodal cancer therapy. *Acta. Biomater.* 6(2), 502–10, 2010.
65. Mykhaylyk O., et al. siRNA delivery by magnetofection. *Curr. Opin. Mol. Ther.* 10(5), 493–505, 2008.

66. McBain S.C., *et al.* Magnetic nanoparticles as gene delivery agents: enhanced transfection in the presence of oscillating magnet arrays. *Nanotechnology* 19(40), 405102, 2008.
67. Petri-Fink A., *et al.* Effect of cell media on polymer coated superparamagnetic iron oxide nanoparticles (SPIONs): colloidal stability, cytotoxicity, and cellular uptake studies. *Eur. J. Pharm. Biopharm.* 68(1), 129–37, 2008.
68. Kievit F.M., *et al.* PEI-PEG-Chitosan-copolymer-coated iron oxide nanoparticles for safe gene delivery: synthesis, complexation, and transfection. *Adv. Funct. Mater.* 19(14), 2244–51, 2009.
69. Medarova Z., *et al.* *In vivo* imaging of siRNA delivery and silencing in tumors. *Nat. Med.* 13(3), 372–7, 2007.
70. Kumar M., *et al.* Image-guided breast tumor therapy using a small interfering RNA nanodrug. *Cancer Res.* 70(19), 7553–61, 2010.



# Theoretical Study of Strained Carbon-based Nanobelts: Structural, Energetic, Electronic, and Magnetic Properties of [n]Cyclacenes

E. San-Fabián, A. Pérez-Guardiola, M. Moral, A. J. Pérez-Jiménez and  
J. C. Sancho-García\*

*Department of Physical Chemistry, University of Alicante, Alicante, Spain*

---

## Abstract

Carbon nanohoops are sizeable structures formed upon bending a finite number of *para*-phenylene or benzene rings until a closed and bent structure is reached. These strained molecules are, respectively, named as [n]cycloparaphenylenes (or [n]CPP) and [n]cyclacenes (or [n]CC), where *n* represents the number of repeat units. They have recently attracted worldwide attention thanks to their unusual properties, as compared with their parent linear compounds (*oligo*)paraphenylenes and (*oligo*)acenes, respectively, as well as for their envisioned use as chemical templates for the fine-tuned and controlled synthesis of single-walled carbon nanotubes. Because of their particular geometry, with bent face-to-face benzene rings, noncovalent (i.e. dispersion) interactions are key to adequately predict their intramolecular properties, as well as their ground-state spin nature (i.e. singlet or triplet) and the energy difference between these low-lying spin states. Furthermore, their solid-state packing (driven by weak interactions) can lead to an emergence of unique yet challenging physical (including magnetic) properties, thus demanding the most to theoretical methods.

**Keywords:** [n]Cyclacenes, density functional theory, ground- and excited-state properties, strain energy, spin polarization, organic nanomagnets

---

\*Corresponding author: jc.sancho@ua.es

## 6.1 Introduction

Carbon nanoforms (e.g. fullerenes, nanotubes, or nanographenes) have attracted great interest in recent years, owing to their appealing mechanical, optical, electronic, and magnetic properties (to name just a few of them), which might pave the way toward the possible use of these tailor-made systems in nanoindustry applications, creating thus new nanotechnological revenues and platforms, and other emerging fields (e.g. organic electronics). However, their synthesis is not still fully controlled, despite these potential advantages, depending critically on (sometimes random) factors such as edges, environment, or chirality issues. Furthermore, the supramolecular organization of the samples has also revealed as a key ingredient driving the final efficiency or performance of any device based on these building blocks, and then underlying the subtle interplay between intra- and intermolecular electronic interactions and the need for an ultimate control of both effects, which would possibly challenge current synthetic approaches in their way from basic research to real applications.

This promising, yet challenging, context has prompted recent research at the nanoscale to find adequate precursors able to act as molecular templates [1], thus allowing the desired and fully controlled bottom-up synthesis of large 2D or 3D carbon nanoforms. The attention has been mostly focused up to now on olygophenylenes macrocycles, see Figure 6.1, which might, for instance, constitute an endless family for the template-driven synthesis of single-walled carbon nanotubes (SWCNTs). As a matter of example,  $[n]$ cycloparaphenylenes ( $[n]$ CPP) can be viewed as structural (sub)units of fullerenes and *armchair* (metallic) SWCNT, whereas  $[n]$  cyclacenes ( $[n]$ CC) might act as precursors for *zigzag* (semiconductor) SWCNT. These cyclic molecules are formed upon bending a finite number of subunits until a closed, and admittedly strained, structure is formed. Actually, the synthesis of the group of [5]–[16]CPP nanohoops has been accomplished successfully by several groups [2–5], which could thus give rise to the controlled (and thus fine-tuned) synthesis of the envisioned SWCNT as a function of the size of the molecule used as a template, if some experimental conditions were finally achieved [6]. Furthermore, the shape-persistent form of these nanobelts also allows hosting large molecules; for instance, the  $C_{60}$  molecule is known to form in solution a stable 1:1 complex with [10]CPP, and with a high binding constant, which represents the smallest fullerene-peapod discovered so far [7]. Note that the first set of cycloparaphenylen compounds ([9], [12], and [18]CPP) was synthesized in 2008 and that there is still a lot of opportunities concerning the rich chemistry of these compounds.

All these recent achievements allow one to speculate about the leading role of the systems shown in Figure 6.1 for future nanotechnological applications, although studies on  $[n]$ CC or other related nanorings are, however, still scarce. Furthermore, whereas some synthetic groups master the *gram*-scale synthesis of  $[n]$ CPP, the rest of forms are still experimentally elusive, which is particularly true for  $[n]$ CCs, despite a large number of specific attempts to synthesize these nanobelts [8]. This difficulty might be closely associated to the nature of their electronic ground-state (*i.e.* radicaloid), thus representing challenging targets to find out their potential (*i.e.* magnetic) applications and thus making further discoveries difficult [9]. However, this same pitfall might also become an opportunity since their (possible) magnetic properties might thus be exploited for building single-molecule nanomagnets or magnetic nanosensors, and thus shifting metal or inorganic devices to organic-based domains. Additionally, the versatility of materials through the myriads of possible synthetic routes demands a deeper understanding of the structure–property relationships of  $[n]$ CCs, before their synthesis can be accomplished in the near future.

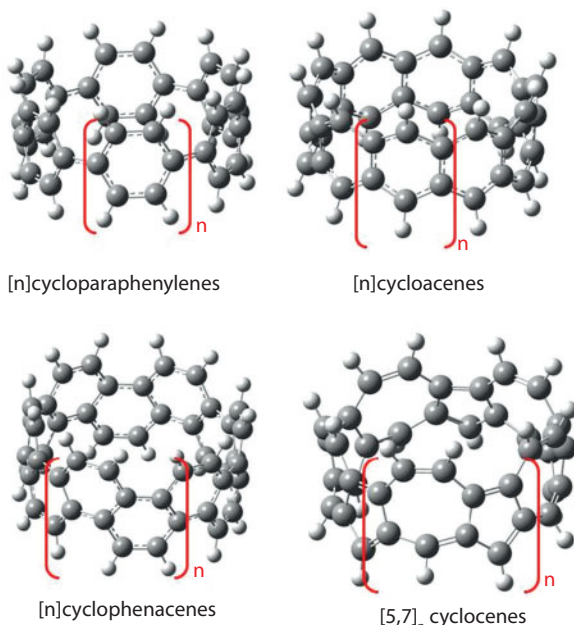


**Figure 6.1** Chemical structures of some carbon-based nanohoops used as model systems:  $n$  implies the number of constituting or fused benzene rings, for  $[n]$ CPP,  $[n]$ CC, or  $[n]$ cyclophenacenes ( $[n]$ CPC), while for  $[5,7]_n$  cyclocenes ( $[5,7]_n$ CC) means the number of fused azulene rings.

In absence of electron spin resonance measurements, or any other experimental information about these  $[n]$ CC systems, theoretical results can be viewed as a valuable tool for further advances within the field.

We will thus focus in the following mostly on these systems,  $[n]$ CC, and will compare their properties (when needed) with those of the parent  $[n]$ CPP compounds, trying to understand the origin of the different experimental behavior found, as well as with those of the parent linear forms, (*oligo*)acenes, to understand the effect of strain on the related properties. Note that, due to the increasing size of the systems tackled, very costly or sophisticated (first-principles) methods are prohibitive. On the other hand, semi-empirical or tight-binding approaches might not be accurate enough to calculate energy differences with the accuracy ( $\pm 0.1$  eV) demanded. Therefore, we will achieve these goals theoretically by carefully applying density functional theory (DFT), allowing reliable *in silico* predictions and comparisons with results from literature, paying particular attention to the interplay between covalent and (intramolecular) noncovalent interactions as well as to the multiplicity of the lowest-energy ground state found for these compounds.

## 6.2 Computational Strategy and Associated Details

The twisted and strained  $C_4H_2$  subunits of  $[n]$ CC compounds, which are closed to form the corresponding macrocycle contrarily to their linear, and vastly studied, parent systems known as (*oligo*)acenes, allow for radially oriented  $\pi$ -type electronic interactions and thus to face-to-face electronic interactions between  $\pi$ -electronic clouds. These closed configurations effectively induce a large set of new and interesting properties for individual molecules, such as the diameter of the nanohoop, the strain energy arising from closing these molecules into a ring, which renders them challenging synthetic targets, or the nature (i.e. the spin state) of their electronic ground state. Interestingly, the evolution of these properties with system size ( $n$ ) might disclosure some convergence pattern, and how they could manifest later when real samples (if any) are obtained in solution or while forming solid-state phases.

Thus, before explaining the computational strategy followed here, we will first briefly present in the following some literature calculations on  $[n]$ CC. Most modern investigations predicted an open-shell singlet ground state for these systems [10], which likely would explain their elusive synthesis, as well as their structural and electronic properties as a whole, although initial studies favored an open-shell triplet ground state [11], independently

of the system size. Geometry optimizations were carried out in previous studies mostly at the DFT-based B3LYP/6-31G\* level, with the energy further refined (but only for the smallest members of the family such as the [6]CC) at the more elaborated CASSCF/MRMP2 level with the same basis set. However, the electronic ground state of these compounds might be also strongly influenced by noncovalent effects, also known as weak interactions, which might affect the structure and thus the rest of derived properties concomitantly. These interactions are known to challenge application of theoretical methods since they are ubiquitous in all nanohoop systems due to their highly strained configuration. Note that the closed form of these compounds, with their diameters (a few Å) lying easily in the range of applications of weak interactions, induces an additional attractive component between laddered and/or opposite facets of the nanoring [12]. This energy contribution will be thus systematically included here, either by considering a well-trained density functional able to deal with these interactions in the medium-range (*i.e.* between 1.5 and 3.5 Å) regime (*e.g.* M06-2X) and/or by adding a specific correction for the long-range (*i.e.* beyond 3.5 Å) regime (*e.g.* M06-2X-D3) [13]. Note that the nature of the local minima found, after fully optimizing the geometries, is always verified by computing the corresponding Hessian matrix and obtaining real vibrational frequencies in all cases.

Strain, or deformation, energies will be also carefully investigated here by the aforesaid accurate DFT methods. These energies arise from closing the linear (strain-free) (*oligo*)acene molecules into a cyclic form, thus rendering these molecules as synthetically challenging. This energy is defined, see Eq. (6.1), as the difference between the standard enthalpy of the strained system and that of the (real or hypothetical) strain-free parent compound, keeping fixed the number of atoms and the bond types, which normally precludes their direct estimates:

$$E_{\text{strain}}([n]\text{CC}) = E([n]\text{CC}) - n E_{\text{strain-free}}(\text{C}_4\text{H}_2) \quad (6.1)$$

These energies are therefore usually evaluated by indirect ways, among which homodesmotic reactions have recently revealed as, probably, the best-suited method for them [14]. Additionally, we will systematically investigate the energy order among the set of the lowest-energy spin states considered [15], at their dispersion-corrected optimized geometries, employing for that the existing variants of closed-shell and open-shell Self-Consistent Field (SCF) methods (see Scheme 6.1). Two different electronic states, singlet ( $S = 0, M_s = 0$ ) and triplet ( $S = 1, M_s = 0, 1$ ), were investigated in agreement with previous evidences about the possible existence of a

Multiplicity ( $2S + 1$ )	Singlet	Singlet	Triplet
SCF method	Closed shell	Open shell	Open shell
Definition	Restricted Kohn–Sham	Broken-symmetry Kohn–Sham	Unrestricted Kohn–Sham
Acronym used herein	RKS	BS-KS	UKS
Specific keyword	–	Guess = Mix	–

**Scheme 6.1** Main characteristics of the self-consistent methods employed along the study. Note that only the relevant frontier MO and their occupation are shown.

triplet solution of lower energy; an issue which has been previously investigated for polyacene molecules too [16]. We remind here that: (i) the set of molecular orbitals (MOs) self-consistently obtained comprise both spatial and spin components, with their occupancy leading to closed-shell or open-shell solutions; and (ii) the spin of any state is given by the total spin of all electrons, occupying the set of MO of the lowest energy, contained in the molecule, although it normally suffices to consider if all electrons are paired (i.e. a singlet state) or if some are unpaired (i.e. a triplet state). Note also that one usually considers only the occupation of the frontier highest-occupied and lowest-unoccupied molecular orbitals (HOMO and LUMO, respectively) to determine the spin of any given state. In the simplest case, all  $\alpha$  and  $\beta$  electrons are paired and restricted to occupy the same spatial orbital, leading to a singlet state after self-consistently converging a closed-shell restricted Kohn–Sham (RKS) solution. A spin-polarized singlet state can, however, be also obtained within the KS theory by allowing the  $\alpha$  and  $\beta$  electrons to occupy different spatial orbitals, breaking the spatial-spin symmetry of the HOMO and LUMO. This situation is certainly useful to produce an open-shell wavefunction for singlet states. Finally, imposing a different multiplicity will lead to the lowest-energy triplet spin state.

The energy difference between the singlet and triplet states will be further investigated by means of time-dependent (TD-) DFT, and at the

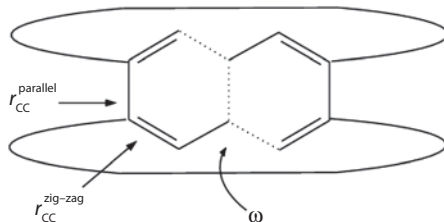
ground-state geometry, which allows to estimate the vertical excitation energy, helping to situate the relative position of the minima of the potential energy surfaces of both states. The Gaussian 09 package, Revision D.01 [17], was used for all the calculations reported here. The default numerical thresholds for convergence were kept fixed, although, however, a dense (ultrafine) integration grid was imposed to reduce numerical errors as much as possible. We have employed the 6-31+G\* basis sets, which represents a convenient trade-off between accuracy and computational cost, and allows also to compare our findings with previous results from the literature.

## 6.3 Results and Discussion

### 6.3.1 [6]CC as a Test Case

We start by discussing the main geometrical parameters of the [n]CC molecules, and their dependence with the method selected. To do that, we will preliminarily study the closed-shell (RKS) singlet state for the simplest [6]CC case and will inspect the characteristic parameters shown in Scheme 6.2; *i.e.*, the C-C bond length parallel to the axial axis, the corresponding peripherally distributed “zig-zag” C-C bond length, and the interannular dihedral angle reflecting the relative tilt of the inner benzene units upon formation of the nanoring.

Table 6.1 shows how these geometrical parameters change with the functional selected (M06-L, M06-2X, and M06-HF) according to the different weight (0%, 54%, and 100%, respectively) of the exact-like (*i.e.* Hartree-Fock) exchange introduced into them [18], and for the 6-31+G\* basis set. We have also incorporated the diameter of the nanoring to the data



**Scheme 6.2** Characteristic parameters for [n]CC systems, being  $r_{CC}^{\text{parallel}}$  and  $r_{CC}^{\text{zig-zag}}$  the bond length parallel to the axial axis and the peripherally distributed “zig-zag” bond length, respectively, and  $\omega$  the angle which shows the relative inclination of the inner benzene units.

**Table 6.1** Selected geometrical parameters (distances in Å, angle in °) for the [6] CC case, as calculated with the 6-31+G\* basis set.

Method	$r_{CC}^{\text{parallel}}$	$r_{CC}^{\text{zig-zag}}$	$\omega$	Diameter
M06-L	1.450	1.413	151.3	4.78
M06-2X	1.450	1.414	151.1	4.78
M06-HF	1.451	1.413	151.3	4.77

gathered in Table 6.1, which is defined as the distance between the opposite *peri*-carbon atoms for the even members, or as the distance between the *peri*-carbon atom and the center of mass of the opposite benzene ring for the odd members.

We can immediately observe how the main geometrical parameters seem to be almost independent of the method chosen, a result that is further corroborated with the (widely used) B3LYP functional, the latter providing bond lengths longer by 0.003 and 0.006 Å for the parallel and zig-zag distances, respectively, and with respect to the M06-type family of functionals, and a diameter of 4.80 Å. The above conclusions, as well as some previous claims about the quality of M06-2X to deal with medium-range noncovalent interactions [19], allow us to use solely this functional for the rest of this study.

Actually, to further assess (and then isolate) the effect of incorporating the attractive long-range noncovalent interactions, we will rely next on the -D3(BJ) correction [20] to the latter form, dubbing the method as M06-2X-D3(BJ). This correction was specifically devised for dealing with long-range effects, correctly scaling with the well-known decay of induced dipole-dipole ( $R^{-6}$ ) and dipole-quadrupole ( $R^{-8}$ ) interactions; we will thus for simplicity focus exclusively on the diameter of the nanoring, which should be the geometrical parameter influenced the most upon incorporation of this correction. However, the value obtained (see Table 6.1) at the M06-2X level is not altered upon inclusion of the -D3(BJ) correction, indicating that the original parameterization of the M06-2X functional includes implicitly these effects, at least for the range of intramolecular distances treated here. This prompted us to conveniently choose the M06-2X/6-31+G\* method for the rest of the systems. On the other hand, dispersionless B3LYP/6-311G calculations [21] provided a larger diameter of 5.18 Å, overestimating by 0.4 Å the M06-2X-D3(BJ) value. This range of overestimation has also been found previously for [n]CPP related

**Table 6.2** Selected geometrical parameters (distances in Å, angle in °) for the [6]CC case, and for the different spin states considered along the study, as calculated at the M06-2X/6+31G\* level.

State	$r_{CC}^{\text{parallel}}$	$r_{CC}^{\text{zig-zag}}$	$\omega$	Diameter
Singlet (RKS)	1.450	1.414	151.1	4.78
Singlet (BS-RKS)	1.450	1.416	150.9	4.79
Triplet (UKS)	1.453	1.416	150.6	4.78

compounds after comparing B3LYP and B3LYP-D3(BJ) results [12]. We would also like to remark from the results obtained that: (i) the edges present a completely delocalized structure, resembling thus a pair of polyacetylene chains bound by the trans-annular C–C bond acting as a linkage, and (ii) the bond length alternation between the two types of C–C bonds is 0.04 Å, and thus unusually small [22].

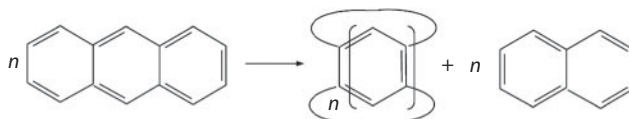
Furthermore, the studied bond lengths are only marginally affected by the spin state under consideration; for instance, the trans-annular C–C bond length changes only by 0.003 Å in the triplet with respect to the closed-shell singlet state, as it is shown in Table 6.2 for the [6]CC case taken again as benchmark systems. The change found in this bond length can be in principle attributed to the localization of spin densities along both edges of the nanoring, thus increasing electronic repulsion and lengthening the bond joining these edges. This is, however, not observed for the spin-polarized singlet state, showing the weak coupling between (one-electron) spin densities existing in this case (*vide infra*). Overall, the small geometrical changes found upon different wavefunctions, motivated us discussing (geometrically speaking) only the RKS solution in the following.

### 6.3.2 Geometries and Strain Energy Evolution with the Size of the Nanobelt

We explore next how these key geometrical parameters evolve with the size of the nanoring, with results included in Table 6.3 for the [6]CC-[11]CC set of studied compounds. Obviously, the diameter ( $d$ ) increases with the value of  $n$ , according to the function  $d = 0.741 n + 0.341$  ( $r^2 = 0.998$ ), with the concomitant increase of the dihedral angle  $\omega$ . Actually, in the limit of planarity the latter value should ideally equal 180°, with our data predicting 179.1° upon linear extrapolation of the results as a function of the

**Table 6.3** Selected geometrical parameters (distances in Å, angle in °) for the [n]CC compounds, as calculated at the M06-2X/6-31+G\* level.

	$r_{CC}^{\text{parallel}}$	$r_{CC}^{\text{zig-zag}}$	$\omega$	Diameter
[6]CC	1.450	1.414	151.1	4.78
[7]CC	1.468	1.409	154.5	5.54
[8]CC	1.458	1.407	158.3	6.31
[9]CC	1.466	1.407	160.1	6.88
[10]CC	1.462	1.404	162.5	7.86
[11]CC	1.465	1.405	163.6	8.46

**Scheme 6.3** Model reaction employed to calculate the strain energy of [n]CC systems.

inverse of the system size ( $\omega = 179.1 - 168.6 n^{-1}$ ), and thus indicating the (expectedly reasonable) convergence of the results.

We will turn next our attention to the strain energy, introducing here for the first time a suited and computationally affordable hyperhomodemistic chemical reaction (Scheme 6.3) to efficiently calculate this value. Note that this kind of reactions should likely have: (i) equal numbers of each type of C-C bond [C(sp<sup>3</sup>)–C(sp<sup>3</sup>), etc.] in reactants and in products, and (ii) equal number of each type of carbon atom (sp<sup>3</sup>, sp<sup>2</sup>, etc.) with one, two, or three hydrogen atoms attached.

Therefore, using this model reaction to adequately balance all kind of concurring stereoelectronic effects, the strain enthalpy per fragment for the set of [n]CC compounds can be calculated as follows:

$$\Delta_{\text{strain}} H ([n]\text{CC}) = \Delta_f H^\circ(\text{anthracene}) - [\Delta_f H^\circ([n]\text{CC}) + \Delta_f H^\circ(\text{naphtalene})] \quad (6.2)$$

where  $\Delta_f H^\circ$  refers to the enthalpy of formation (at 0 K and with the vibrational energy included) of the different compounds at their respective

**Table 6.4** Strain energies per fragment ( $\text{kJ mol}^{-1}$ ) for the  $[n]\text{CC}$  compounds, as calculated with the 6-31+G\* basis set.

	$\Delta_{\text{strain}} \text{H} ([n]\text{CC})$	
	M06-2X	M06-2X-D3(BJ)
[6]CC	157.7	157.6
[7]CC	122.2	121.6
[8]CC	93.6	93.0
[9]CC	81.2	80.7
[10]CC	65.5	65.0
[11]CC	60.2	59.8

optimized geometries. Note that the intrinsic error on reaction enthalpies calculated employing these hyperhomodesmotic (error-balanced) reactions is estimated to be as low as  $0.3 \text{ kcal mol}^{-1}$  [14]. Table 6.4 presents the results, employing both the dispersion-uncorrected M06-2X and the dispersion-corrected M06-2X-D3(BJ) methods, to also assess the influence of the latter term on the calculated values. Actually, we could infer how this expectedly small effect (as much as  $1 \text{ kJ mol}^{-1}$ ) decreases with the system size as it should be due to the long-range decay of these interactions, with the exception of [6]CC for which some double-counting of results might appear.

Evidently, following the chemical intuition, the strain energy of these compounds is expected to be large due to the geometrical constraints imposed, but one may always ask how large is it with respect to some related compounds. In fact, we compare in Figure 6.2 the strain energy per fragment of  $[n]\text{CC}$  and  $[n]\text{CPP}$  compounds, both calculated employing an equivalent hyperhomodesmotic chemical reaction and with a dispersion-corrected DFT method, as a function of diameter  $d$ . We also perform the fitting of the data to a previously used [12] function with the form  $\Delta_{\text{strain}} \text{H} = Ad^{-B}$ , where  $A = 1270 \text{ mol kJ}^{-1}$  and  $B = 2.106$  ( $r^2 = 0.996$ ), and  $A = 2536 \text{ mol kJ}^{-1}$  and  $B = 1.778$  ( $r^2 = 0.998$ ) for the  $[n]\text{CPP}$  and  $[n]\text{CC}$  family of compounds, respectively (see Figure 6.2). The release of strain energy thus decays very differently in both cases, not surprisingly, although it seems to progressively converge at large values of  $n$  which might help to anticipate some synthetic routes, doing some pre-screening of synthetic methodologies or sieving out non-promising candidates. Note that the

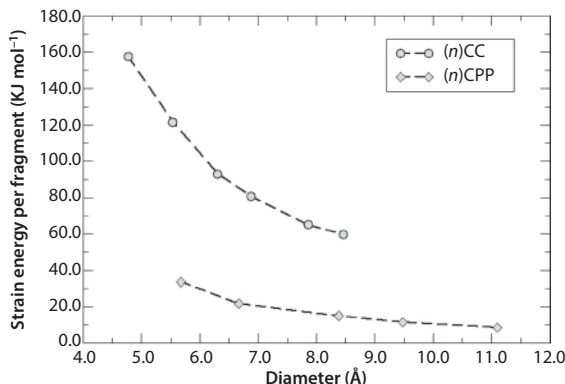


**Figure 6.2** Evolution of the calculated strain energy with the diameter of the nanobelt in  $[n]\text{CC}$  and  $[n]\text{CPP}$  compounds.

strain energy of related cyclacenes, with annelated six- and five-membered rings [10], has been recently calculated and compares well (at least semi-quantitatively) to that obtained through this work.

We have to remind that the whole set of  $[n]\text{CPP}$  compounds studied here has been successfully synthesized, which prompt us to drop some optimism about the future synthesis of the corresponding  $[n]\text{CC}$  molecules. This versatility has also a price, requiring first to theoretically explore the electronic properties of these molecules through robust and well-performing methods, as we will be done in the next section.

### 6.3.3 Electronic Structure Issues

The present calculations will also serve to ascertain the electronic structure of these compounds, be them of a singlet or triplet nature. We have now considered the adiabatic singlet–triplet splitting (energy change) achieved after performing RKS and UKS calculations for the singlet and triplet states, respectively, on the whole set of compounds. The results are presented in Figure 6.3 (UKS vs. RKS) and show a different pattern for even and odd systems, in agreement with previous calculations too [11]. Note that the relative order of these states has shown before to be fairly insensitive to basis set effects [15] and that a triplet state is favored for some of the compounds by around  $-0.2$  eV. However, spin contamination issues might overestimate the triplet state, as it was actually disclosed for polyacene molecules some time ago [23]. Thus, we have forced a broken-symmetry solution of the (spin-polarized) singlet ground state, by allowing the  $\alpha$  and  $\beta$  electrons to occupy different spatial orbitals, and compared this energy

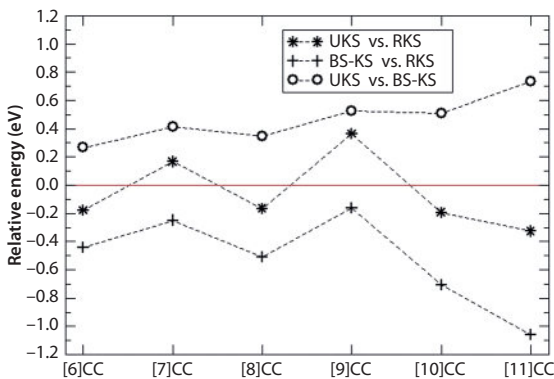


**Figure 6.3** Relative energy between spin states in  $[n]$ CC compounds, as calculated at the M06-2X/6-31+G\* level (see text for details). The dashed lines are a guide to the eye.

(open-shell singlet) with that of the closed-shell singlet ground state. The results shown in Figure 6.3 (BS-KS vs. RKS) clearly reveal a stable spin-polarized singlet ground state (open-shell singlet) whose stability grows with the system size, indicating thus a highly reactive character. If one assumes now that the ground state of  $[n]$ CC is a spin-polarized singlet, the triplet state is always found much higher in energy, and steadily increasing with the number of fused benzene rings, as it is also shown in Figure 6.3 (UKS vs. BS-KS).

Note that the question about the nature of the lowest-energy solution is of particular importance in organic electronics applications. The magnetic behavior of organic molecules relies on how the unpaired electrons couple, either on a triplet way (ferromagnetic) or on a singlet way (antiferromagnetic). To better illustrate these concepts, we closely look at the shape and distribution of the highest-occupied frontier MO for the spin-unpolarized (closed-shell) and spin-polarized (open-shell) singlet states (see Figure 6.4), with the latter case being energetically favored as mentioned before. Whereas the spin-unpolarized (closed-shell) singlet solution shows the expected behavior (the frontier HOMO resembles a delocalized orbital along the molecular backbone with contribution from each 2p orbital of the constituent carbon atoms) the spin-polarization localizes  $\alpha$  ( $\beta$ ) spin electron at the upper (lower) edge in an open-shell singlet state. This spin localization in two sublattices (one at each edge) might result in the antiferromagnetic behavior of  $[n]$ CC compounds, with the neighboring spins (neighboring sublattices) pointing in opposite directions and displaying a vanishing total magnetization. However, some ferrimagnetism might be further induced by applying an external magnetic field, thus resembling

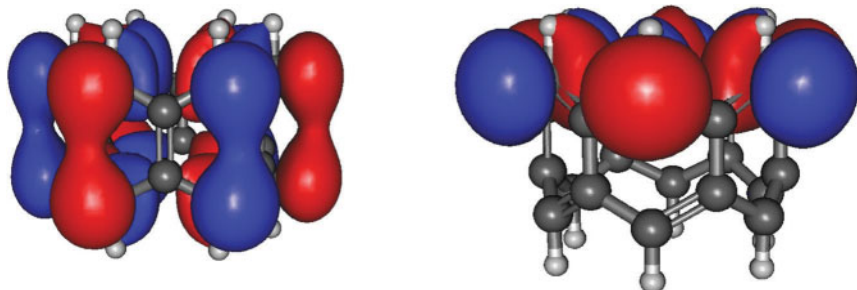


**Figure 6.4** Isocontour plots of the (left) HOMO and (right) single-occupied molecular orbitals (SOMO) for the [6]CC molecule, as obtained by a RKS and BS-KS solutions, respectively. The size and color describe the amplitude and sign, respectively, of the lobes of the orbitals.

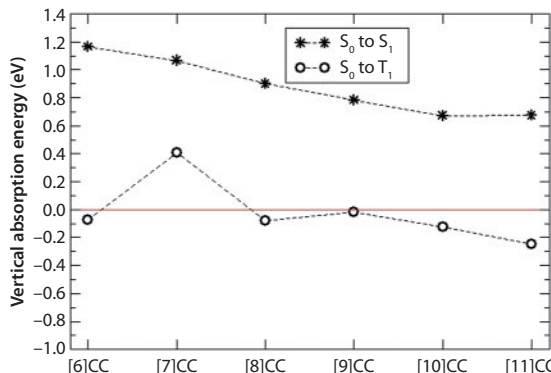
edge states found in graphene-like systems [24]. Note that multiple functionalization patterns are envisioned (i.e. introduction of heteroatoms like Si or Ge into the molecular backbone and/or replacement of hydrogen atoms by electroactive groups and/or complexation of the rings with transition metal complexes) that might reverse this behavior after favoring a closed-shell ground state [25].

We finally calculated, at the TD-DFT level with the same functional (M06-2X) and basis set (6-31+G\*) as those used previously, the lowest vertical absorption energy to the singlet and triplet states. Note that we are forced to start from a closed-shell ground state, due to some computational restrictions, and that this functional has been previously benchmarked for main-group electronic excitation energies, emerging as one of the most accurate expressions for it [26]. We also underline the use of the Tamm–Dancoff approximation (TDA) for all cases [27], which is known to only slightly alter the vertical singlet absorption energies but significantly improve the corresponding triplet ones [28]. The evolution of the excitonic properties for increasingly longer systems is gathered in Table 6.5, and graphically represented in Figure 6.5. We have also included results obtained with the B3LYP method, for the sake of comparison, in Table 6.5.

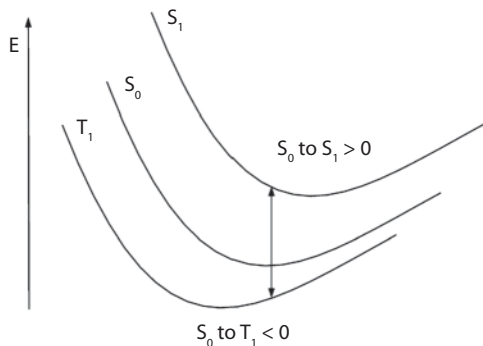
The evolution of excitonic properties of these compounds reveal so far several interesting features: (i) the lowest singlet–singlet (i.e. the  $S_0$  to  $S_1$ ) transition smoothly decreases with system size, a typical feature of conjugated systems [29] also shared by corresponding linear (*oligo*)acenes [30], reaching rapidly some saturation value; (ii) low oscillator strength values,

**Table 6.5** Calculated vertical absorption energies (eV) for the [n]CC compounds, as calculated with the 6-31+G\* basis set.

	B3LYP		M06-2X	
	S <sub>1</sub>	T <sub>1</sub>	S <sub>1</sub>	T <sub>1</sub>
[6]CC	1.33	0.11	1.16	-0.08
[7]CC	0.86	0.30	1.07	0.41
[8]CC	1.08	0.14	0.90	-0.08
[9]CC	0.49	-0.07	0.78	-0.02
[10]CC	0.88	0.14	0.67	-0.13
[11]CC	0.29	-0.28	0.67	-0.25

**Figure 6.5** Vertical absorption energies in [n]CC compounds to the lowest singlet and triplet state, as calculated at the TDA-M06-2X/6-31+G\* level (see text for details). The dashed lines are a guide to the eye.

which are directly related to absorption intensities, were always found for these [n]CC cyclic forms, although slightly larger for the odd with respect to the even molecules; and (iii) the corresponding singlet–triplet (i.e. the S<sub>0</sub> to T<sub>1</sub>) transition shows an irregular pattern, predicting the T<sub>1</sub> state slightly lower in energy for most of the compounds. Note that these results also predict an optically forbidden lowest-energy singlet state, displaying a vanishing or very low oscillator strength, and two degenerate states slightly higher in energy and dubbed as S<sub>2</sub> and S<sub>3</sub>, a pattern also found for the corresponding triplet ones. The emergence of a triplet state being lower in energy than any of the singlet states can be (qualitatively) understood



**Scheme 6.4** Relative (and simplified) position of the hypersurfaces of the low-lying energy states when an open-shell triplet state is energetically favored.

by looking at Scheme 6.4, where we displayed the relative (in a simplified manner) position of the curves for both states, which would lead to a singlet to triplet transition with a negative energy.

The singlet–singlet excitation energies ( $E_n$ ) can be fitted to some physical expressions, like that of the free-electron model (FEMO) or others, for a deeper understanding of their behavior with system size. We choose here an expression widely used before within the field of conjugated materials [31]:

$$E_n = a/(n + 1) + \beta(1 - 1/n) \quad (6.3)$$

showing a root mean-squared deviation (RMSD) of 0.04 eV for the set of TDA-M06-2X/6-31+G\* excitation energies included, and reproducing the slight nonlinear evolution found in Figure 6.4, with the value of  $a = 9.30$  eV (per monomer unit, and with  $\beta \ll a$ ) indicating the relative decay rate of excitation energies with increasing monomer length. Note how the irregular (somewhat unphysical) pattern of the B3LYP-based excitation energies (see Table 6.5) would preclude the above fitting. If we now fit separately the even and odd excitation energies, we obtain a better agreement (RSMD = 0.02 eV in both cases) and a finite and positive value of  $\beta$ , which indicates the excitation energy at the infinite limit, around 0.1–0.2 eV. Note that, with the exception of [7]CC, the singlet–triplet splitting, that is the energy difference between the  $S_1$  and  $T_1$  states, remains large (between 0.7 and 1.1 eV approximately) and does not significantly change with system size. On the other hand, the relaxation energy of the triplet state, that is the energy difference between the adiabatic (UKS) and vertical (TDA-DFT) singlet to triplet states, is found below 0.1 eV for even systems [6]CC, [8]CC, and

[10]CC, but 0.24, 0.35, and 0.08 eV for [5]CC, [7]CC, and [11]CC, respectively, showing a more marked effect for odd systems.

## 6.4 Conclusions

In summary, we have theoretically studied the geometrical, energetic, electronic, and magnetic properties of the set from [6]CC to [11]CC cyclic compounds, employing a particularly accurate exchange-correlation functional for it, and capturing efficiently the covalent and noncovalent interactions taking place within these nanorings. Interestingly, the (gas-phase) geometrical parameters do not appreciably change with the spin state, neither affect the diameter of the cavity. We have estimated, employing a hyperhomodesmotic reaction for it and thus allowing the direct comparison with closely related compounds, their strain energy, and how it evolves with system size too. This strain energy seems not to be the limiting factor for achieving the final synthesis of these compounds [32].

From an electronic point of view, the broken-symmetry (spin-polarized) singlet state has been unambiguously determined to be the lowest-energy ground state of  $[n]$ CC compounds of increasing size, with the triplet state being always higher in energy by a few tenths of eV. The stability of the open-shell singlet state increases with increasing  $n$ , which might manifest in an increase of the diradical character too. This issue should strongly influence the reactivity of these compounds, being for instance extremely prone to react with molecular oxygen, and be a decisive factor for elucidating synthetic reaction paths. Additionally, since these nanobelts can act as hosts for molecules or metal atoms, the latter would perceive inside the cavity of such cyclacenes challenging steric and magnetic effects. These systems, once synthesized, should be able to react upon external magnetic or conducting effects, as other interesting low-spin diradicals [33].

We have also reported how the optical properties (i.e. excitation energies) of these compounds evolve with system size, showing a very different pattern for the lowest-energy singlet and triplet states. A deeper understanding of this difference might allow its further manipulation, toward some applications in the field of organic electronics and/or photonics, and constitutes a topic of the most interest [34].

In summary, we have employed modern computational tools to accurately study even and odd members of the  $[n]$ CC family of compounds, hoping to establish some structure–property guidelines and providing insightful conclusions. Further computational efforts are, however, required to disclose how the supramolecular organization of these molecules might

influence the aforesaid stability of spin states, to shed light about the role of the guest system stabilized inside the cavity by host–guest interactions, or to alter electronic excitations when passing from an isolated single molecule to a pair of weakly bound interacting ones. This work is currently under progress in our group; nonetheless, further experimental studies will be concomitantly needed to convert these molecules from scratch to real samples.

## Acknowledgments

This work is supported by the “Ministerio de Economía y Competitividad” of Spain and the “European Regional Development Fund” through projects CTQ2014-55073-P and FIS2012-35880.

## References

1. M. Iyoda and H. Shimizu, *Chem. Soc. Rev.*, 44, 6411–6424, 2015.
2. Y. Nakanishi, H. Omachi, S. Matsuura, Y. Miyata, R. Kitaura, Y. Segawa, K. Itami, and H. Shinohara, *Angew. Chem., Int. Ed.*, 53, 3102–3106, 2014.
3. S. Yamago, E. Kayahara, and T. Iwamoto, *Chem. Rec.*, 14, 84–100, 2014.
4. P. J. Evans, E. R. Darzi, and R. Jasti, *Nat. Chem.*, 6, 404–408, 2014.
5. T. Nishiuchi, X. Feng, V. Enkelmann, M. Wagner, and K. Müllen, *Chem. – Eur. J.*, 18, 16621–16625, 2012.
6. E. S. Hirst and R. Jasti, *J. Org. Chem.*, 77, 10473–10478, 2012.
7. J. Xia, J. W. Bacon, and R. Jasti, *Chem. Sci.*, 3, 3018–3021, 2012.
8. Z. Chen, D.-E. Jiang, X. Lu, H. F. Bettinger, S. Dai, P. V. R. Schleyer, and K. N. Houk, *Org. Lett.*, 9, 5449–5452, 2007.
9. R. Gleiter, B. Esser, and S. C. Kornmayer, *Acc. Chem. Res.*, 42, 1108–1116, 2009.
10. B. Esser, *Phys. Chem. Chem. Phys.*, 17, 7366–7372, 2015.
11. H. S. Choi and K. S. Kim, *Angew. Chem. Int. Ed.*, 38, 2256–2258, 1999.
12. J. V. Climent-Medina, A. J. Pérez-Jiménez, M. Moral, E. San-Fabián, and J. C. Sancho-García, *ChemPhysChem*, 16, 1520–1528, 2015.
13. A. Karton, A. Tarnopolsky, J.-F. Lamère, G. C. Schatz, and Jan M. L. Martin, *J. Phys. Chem. A*, 112, 12868–12886, 2008.
14. S. E. Wheeler, *WIREs Comput. Mol. Sci.*, 2, 204–220, 2012.
15. D. Sadowsky, K. McNeill, and C. J. Cramer, *Faraday Discuss.*, 145, 507–521, 2010.
16. M. Das, *J. Chem. Phys.*, 143, 064704, 2015.

17. Gaussian 09, Revision D.01, M. J. Frisch, G. W. Trucks, H. B. Schlegel, *et al.*, Gaussian Inc. Wallingford, CT, 2009.
18. Y. Zhao and D. G. Truhlar, *Acc. Chem. Res.*, 41, 157–167, 2008.
19. Y. Zhao and D. G. Truhlar, *J. Phys. Chem. C*, 112, 4061–4067, 2008.
20. S. Grimme, J. Antony, S. Ehrlich, and H. Krieg, *J. Chem. Phys.*, 132, 132, 154104, 2010.
21. R. M. Kubba, H. N. Al-Ani, and M. Shanshai, *Jordan J. Chem.*, 6, 271–293, 2011.
22. J. C. Sancho-García and A. J. Pérez-Jiménez, *Phys. Chem. Chem. Phys.*, 9, 5874–5879, 2007.
23. E. San-Fabián and F. Moscardó, *Int. J. Quantum Chem.*, 113, 815–819, 2012.
24. J. L. Lado, N. García-Martínez, and J. Fernández-Rossier, *Synth. Metal*, doi:10.1016/j.synthmet.2015.06.026
25. M. Z. Kassaei, H. Zandi, H. Ar. Rad, and M. Ghambarian, *Monatsh. Chem.*, 144, 1783–1786, 2013.
26. D. Jacquemin, E. A. Perpète, I. Ciofini, C. Adamo, R. Valero, Y. Zhao, and D. G. Truhlar, *J. Chem. Theory Comput.*, 6, 2071–2085, 2010.
27. S. Hirata and M. Head-Gordon, *Chem. Phys. Lett.*, 314, 291–299, 1999.
28. M. Moral, L. Muccioli, W.-J. Son, Y. Olivier, and J. C. Sancho-García, *J. Chem. Theory Comput.*, 11, 168–177, 2015.
29. J. Gierschner, J. Cornil, and H.-J. Egelhaaf, *Adv. Mater.*, 19, 173–191, 2007.
30. K. Hummer and C. Ambrosch-Draxl, *Phys. Rev. B*, 72, 205205., 2005.
31. E. Fabiano, F. Della Sala, R. Cingolani, M. Weimer, and A. Görling, *J. Phys. Chem. A*, 108, 3078–3085, 2005.
32. G. J. Bodwell, *Nat. Chem.*, 6, 383–385, 2014.
33. G. Grynnova, M. L. Coote, and C. Corminboeuf, *WIREs Comput. Mol. Sci.*, 5, 440–459, 2015.
34. G. Chiappe, E. Louis, E. San-Fabián, and J. A. Vergés, *J. Phys.: Condens. Matt.*, 27, 463001, 2015.



# Room Temperature Molecular Magnets: Modeling and Applications

Mihai A. Gîrțu\* and Corneliu I. Oprea\*

*Department of Physics, Ovidius University of Constanța, Constanța, Romania*

---

## Abstract

The recent discovery of spin injection in hybrid organic-inorganic spin valves as well as in all-organic spin valves, and of spin-polarized transport in a light-emitting diode, all based on films of  $V[TCNE]_x$ , has brought back to the front line the first room temperature molecular magnet. We review recent studies on this family of semiconducting molecule-based magnets, focusing on the theoretical explanation of the magnetic behavior and emphasizing the potential spintronic applications. Density functional theory as well as multi-configurational calculations of the exchange interactions allowed for the explanation of the mechanism of antiferromagnetic spin coupling between  $V^{II}$  and  $[TCNE]^-$  spin carriers. We show how an analysis of the key sources of structural disorder may explain the amorphousness and non-stoichiometric nature of  $V[TCNE]_x$ . Calculations of the disordered structures reveal a rough energy landscape, but rule out not spin-glass-like behavior. Computations with additional spin-orbit interaction allow for the account of the single-ion anisotropy of the  $V^{II}$  ions in various environments, suggesting correlated sperimagnetic behavior, in agreement with puzzling experimental data. The review of the potential applications of this magnetic half-band organic-based semiconductor reveals how the separation between the electron bands responsible for magnetic and conducting properties along with the interaction between these bands has stirred interest in the use of  $V[TCNE]_x$  as a spin injector in spin valves and in spin-polarized light-emitting devices.

**Keywords:** Molecular magnetism, spintronics, spin valve, exchange coupling, magnetic anisotropy, random anisotropy magnets, *ab initio* calculations, density functional theory

---

\*Corresponding authors: mihai.girtu@univ-ovidius.ro, cornel.oprea@univ-ovidius.ro

## 7.1 Introduction

The goal of this review is to present some of the main recent theoretical and experimental results on a family of room temperature molecular magnets, with an emphasis on their physical properties and applications. Molecular magnets are systems in which electrons in molecular orbitals (MO), which consist of superpositions of *p* and even *s* atomic orbitals, play a crucial role in the magnetic ordering [1, 2]. In contrast, conventional atom-based magnets, well-known examples being iron, cobalt, nickel, and some of their oxides, rely on the coupling between metallic spins located in *d* atomic orbitals.

Molecular magnets are either purely organic or formed by assembling, at a molecular level, inorganic constituents and organic species, such that an extended structure, with interactions strong enough to cause bulk magnetic long-range order [3]. The critical temperature ( $T_c$ ) under which purely organic magnets display magnetic ordering is rather low, whereas the hybrid organic–inorganic magnets can order at temperatures significantly higher than 300 K [2, 4]. Prototypical examples of room temperature molecular magnets are the vanadium–chromium-based Prussian Blue analogues (such as  $V[Cr(CN)_6]_x \cdot nH_2O$ ), for which the organic part plays a passive role [5–7], and the  $V[TCNE]_x$  magnets, with the organic species playing an active role in the magnetic interactions, due to the net spin localized on the cyanocarbon ligand [8].

Of particular interest is the family of high-temperature molecular magnets having as prototype the first room temperature molecular magnet,  $V[TCNE]_x \cdot y(CH_2Cl_2)$  ( $x \sim 2$ , TCNE = tetracyanoethylene) discovered by Miller *et al.* in 1991 [9]. This family provides an unusual opportunity to study structure–property correlations, as it offers a wide range of controlling factors: the transition metal ion, the cyanocarbon acceptor, and the solvent [3]. The recent discovery by Epstein *et al.* of spin injection in hybrid organic–inorganic spin valves [10] as well as in an all-organic spin valve [11], and of spin-polarized transport in a light-emitting diode [12], all based on films of  $V[TCNE]_x$  ( $x \sim 2$ , TCNE = tetracyanoethylene), has brought back to the front line the first room temperature molecule-based magnet.

The amorphous and nonstoichiometric nature of the material, as well as its subtle synthesis, initially difficult to reproduce, also due to the high air sensitivity, has stirred both astonishment and controversy ever since [2]. The lack of knowledge concerning the structure made room for debates regarding the mechanism of ferrimagnetic ordering, the nature of the electronic spectrum and the corresponding electric properties, the origin and

role of single-ion anisotropy (SIA), the source of disorder, etc. The endeavor to answer fundamental questions has been complemented by attempts to find possible applications. Although the initial claims of applications in dc shielding [13] or other traditional magnetic devices [14] have run into difficulties due to the air sensitivity of the compound [15], more recently, better methods to obtain thin layers of air-stable  $V[TCNE]_x$  recommended this material for spintronic devices [16] culminating with the demonstration of its function as a spin injector in various types of spin valves and in light-emitting devices [10–12]. As it continues to stir interest from both fundamental and an applied science perspectives, the  $V[TCNE]_x$  system and its family of materials is worth a closer look.

The outline of the present review is as follows: The next section provides a background on the family of high-temperature molecular magnets based on TCNE, emphasizing the experimental work performed over the past two decades. The third section focuses on molecular modeling and simulations that revealed the ideal structure of the system and suggested the origins of structural disorder. The following two sections concentrate on recent theoretical work which succeeded in answering fundamental questions regarding the sources of structural disorder, the strength of the exchange interactions, and the origin and size of the magnetic anisotropy. The sixth section discusses the applications demonstrated for the room temperature systems, while the last describes trends and some open questions.

## 7.2 Experimental Background

Over the years, the progress in answering the multitude of open questions regarding  $V[TCNE]_x \cdot y(CH_2Cl_2)$  has been incremental. Despite intense synthetic efforts and X-ray diffraction studies, long after the initial report in 1991, the structure of the systems has not been resolved experimentally, due to its amorphous character. However, some basic information has been gathered through various other experiments. For instance, it was proposed [9, 17, 18] that the oxidation state is  $V^{II}$  and  $x \sim 2$ . Consequently, the spins involved in the magnetic interactions are  $3/2$ , located on the metal ion, and  $1/2$ , placed on the cyanocarbon radical anions. Although it was claimed that the compound has a three-dimensional (3D) network structure, and that each [TCNE] binds to up to four different vanadium ions [9] the suggestions regarding the structure remained unclear until late [8].

A key moment in the understanding of this system was in 2000, when two groups, independently, de Caro *et al.* in France [19] and Pokhodnya *et al.* in the USA [20], avoiding the elusive chemical synthesis, succeeded

in preparing  $V[TCNE]_x$  films without any solvent, by means of low-temperature chemical vapor deposition (CVD). The X-ray diffraction studies failed to reveal the structure, clearly indicating, despite the faceted morphology found in the scanning electron microscopy images of the CVD grown films, an amorphous structure, similar to the samples with solvent, only slightly more ordered [21]. A few years later, by means of X-ray absorption near-edge structure measurements performed on films of  $V[TCNE]_x$  prepared by CVD, Haskel *et al.* [22] provided new information regarding the local structure. The study showed that the vanadium ions are coordinated to six nitrogen atoms, in a slightly distorted octahedral environment. Moreover, it was suggested that there is strong binding between the vanadium ion and the nitrogen atoms of the [TCNE] radical anion. Another important advancement consisted of the estimation of the vanadium oxidation state, which indicated the presence of vanadium(II) ion, in agreement with a  $V[TCNE]_2$  stoichiometry [22].

Initial electric conductivity measurements by Epstein *et al.* [23] lead to the conclusion that the molecular magnets have semiconductor-like behavior, with values varying with preparation in the range  $10^{-2}$ – $10^{-4}$  S/cm. Later on, magneto-transport measurements of CVD-prepared  $V[TCNE]_x$  films [24] demonstrated positive magnetoresistance (increase in resistance with applied magnetic field). The magnetoresistance was explained by means of a charge transport model involving hopping of electrons in the  $\pi^*$  band of the [TCNE] anions. In that model, the half-filled  $\pi^*$  band, which was the highest-occupied band, was split by the strong on-site Coulomb repulsion in two subbands with opposite spin polarization, one occupied and one empty [24, 25].

The air sensitivity of the  $V[TCNE]_x$  material has been a major hindrance for obtaining direct measurements of the electronic structure using surface sensitive techniques such as photoelectron spectroscopy. As the first X-ray photoelectron spectroscopy (XPS) study of CVD-prepared  $V[TCNE]_x$  films showed, roughly half of the material in the surface region was oxidized due to the lack of ultra-high-vacuum conditions of the fabrication and sample transfer processes [20] an *in situ* CVD process for deposition of  $V[TCNE]_x$  films was subsequently developed by Fahlman *et al.* [26] and enabled the direct measurement of the occupied electronic structure. Virtually, oxygen-free thin films of  $V[TCNE]_x$  were studied by resonant photoemission measurements, to clarify the issue of the nature of the highest-occupied states in this compound. It was found [26] that the highest-occupied band is derived of  $V(3d)$  states, with rather strong covalent-type bonding between the vanadium(II) metal ion and the [TCNE] anionic radical [27–29]. The remaining frontier occupied bands were found to be derived from the singly occupied molecular orbital of [TCNE] with a considerable

wave function overlap of [TCNE]-derived states with the V(2p) core-hole, supporting the picture of hybridized orbitals in a covalently bonded network [28].

Over the years, extensive magnetic experimental studies of the  $V[TCNE]_x \cdot y(\text{solvent})$  systems, with various solvents, including dichloromethane ( $\text{CH}_2\text{Cl}_2$ ), tetrahydrofuran (THF), and acetonitrile (MeCN) were performed [9, 30–32]. The critical temperatures recorded for samples prepared using  $V(\text{C}_6\text{H}_6)_2$  showed extremely large variations, ~350, 215, and 138 K, for the three solvents, respectively. Static magnetic scaling analyses provided critical exponents typical not for pure magnets but to disordered ones, particularly to those with random anisotropy. It was speculated that the magnetic disorder is due to structural and substitutional disorder caused by the incorporation of the solvent and the random coordination of the vanadium ions [9, 30, 31].

Higher  $T_c$ s were obtained for  $V[TCNE]_x \cdot y(\text{solvent})$  when other solvents were used, as shown by Thorum *et al.* [33]. With  $V(\text{CO})_6$  as precursor, by using solvents such as dichloromethane ( $\text{CH}_2\text{Cl}_2$ ), hexane ( $\text{C}_6\text{H}_{14}$ ), toluene ( $\text{PhMe}$ ), and trifluoromethylbenzene ( $\text{PhCF}_3$ ), the critical temperature was slightly increased to 387, 388, 390, and 396 K, respectively (as shown in Figure 7.1).

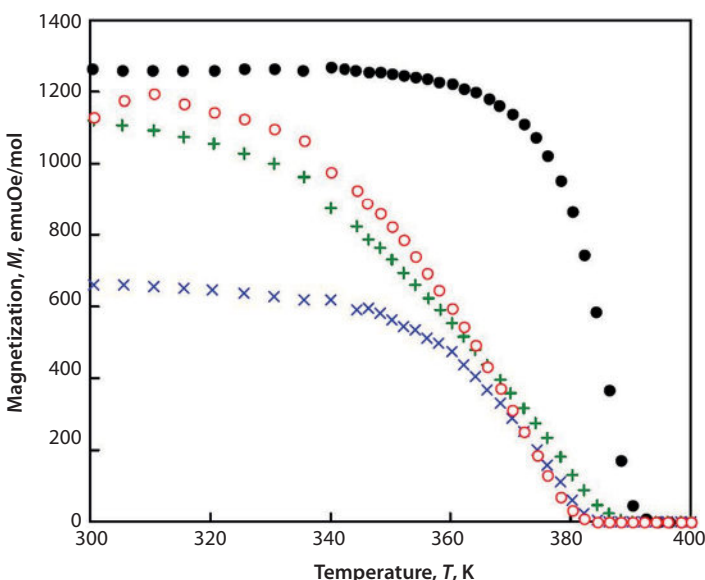


**Figure 7.1** Magnetization as a function of temperature for  $V[TCNE]_x \cdot y(\text{solvent})$  [solvent =  $\text{CH}_2\text{Cl}_2$  ( $\circ$ ), hexane ( $\times$ ), and  $\text{PhMe}$  (+), and  $\text{PhCF}_3$  ( $\bullet$ )] in an applied field of 5 Oe. From Ref. [33].

Various synthetic attempts have been made to replace TCNE with different organic acceptors, with the goal to discover new organic-based magnetically ordered materials. New high-temperature molecular magnets have been synthesized by Miller *et al.*, starting with the  $V[TCNQ]_2$  family [34], where  $TCNQ = 7,7,8,8$ -tetracyano-p-quinodimethane (Figure 7.2). The prototype of the family showed magnetic ordering below 52 K, whereas eight other members of the family, obtained by substituting hydrogen atoms of the aromatic, displayed critical temperatures in the range 7.5–106 K, significantly below room temperature. It was shown that the substitution of electron-donating groups (such as ethoxy) for H in TCNQ increased  $T_c$  to 106 K, whereas the substitution of less electron-donating alkyl groups (such as methyl) decreased  $T_c$  to 7.5 K [34]. Higher critical temperatures of about 220 K was obtained for  $V[TCNP]_2$  by Vickers *et al.* [35] and above room temperature, at about 330 K, for  $V[TCNB]_2$ , by Taliaferro *et al.* [36], where  $TCNP = \text{tetracyanopyrazine}$  and  $TCNB = \text{tetracyanobenzene}$ .

Given the experimental data available, it is interesting to note that by lengthening the distance between the  $V^{II}$  ions the critical temperature decreases. Worth noting is also that TCNB has hydrogen atoms that can be chemically substituted, which could open new opportunities for discovering new materials. However, so far, the experience gained by substituting TCNQ has not been extended to TCNB.

A search for TCNE substitutes that would allow an incremental and systematical variation of the steric and electronic properties of the resulting acceptors was reported by Harvey *et al.* [37] with the goal of uncovering the mechanism of magnetic ordering in these compounds and designing additional room temperature magnets. The goal was accomplished, as the five additional members of the family of high- $T_c$  molecule-based magnets,

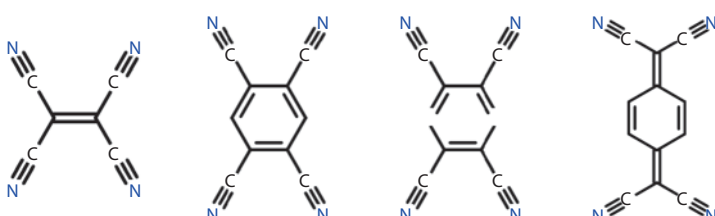


**Figure 7.2** Schematic structure of cyanocarbon acceptors used as building blocks in high-temperature molecular magnets. From left to right: tetracyanoethene (TCNE), tetracyanobenzene (TCNB), tetracyanopyrazene (TCNP), and 7,7,8,8-tetracyanoquinodimethane (TCNQ).

$V[acceptor]_2\text{CH}_2\text{Cl}_2$ , discovered (with the acceptor being a fluorophenyltricyanoethylene) displayed magnetic ordering temperatures ranging from 160 to 300 K (see Figure 7.3). Although successful in constructing a room temperature magnet, the authors admit that the key factors influencing the magnetic ordering of electronic remain elusive, with the electronic and steric effects, both playing a role [37].

After attempts to change the solvent and the cyanocarbon acceptor, other studies reported the change of the metal ion. Static and dynamic scaling studies completed on other members of the  $M[\text{TCNE}]_x \cdot y(\text{CH}_2\text{Cl}_2)$  family, with  $M = \text{Mn}$  [38] and  $\text{Fe}$  [39] indicated reentrant spin-glass and double-transition random anisotropy behaviors, for the two systems, respectively. Although the critical temperatures were also relatively high, 75 and 95 K, respectively, they were far below that of the record holder [20].

Noticing the large differences in the  $T_c$ s between the materials with other transition metal ions, Pokhodnya *et al.* synthesized two types of solid solutions:  $V_x\text{Co}_{1-x}[\text{TCNE}]_2 \cdot y(\text{CH}_2\text{Cl}_2)$  [40] and  $V_x\text{Fe}_{1-x}[\text{TCNE}]_2 \cdot y(\text{CH}_2\text{Cl}_2)$  [41], and Vickers *et al.* [42] reported a third solid solution,  $V_x\text{Ni}_{1-x}[\text{TCNE}]_2 \cdot y(\text{CH}_2\text{Cl}_2)$ . These studies showed that the

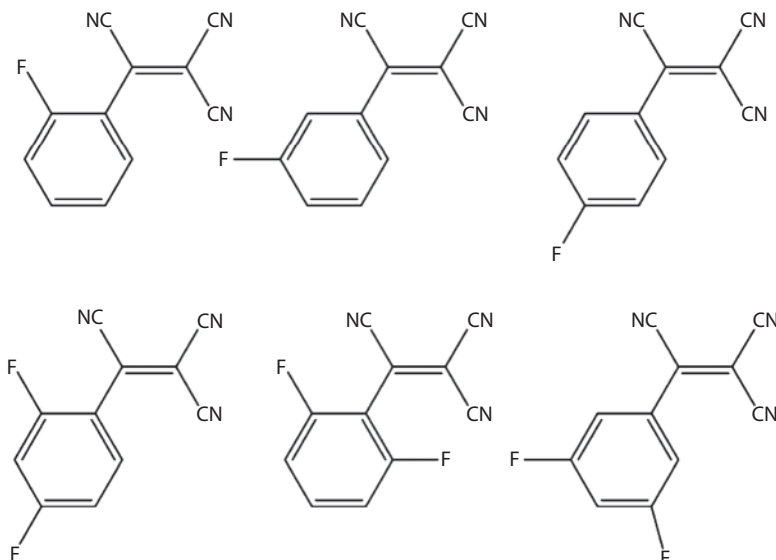


**Figure 7.3** Schematic structure of mono- and di-substituted cyanocarbon acceptors used as building blocks in high-temperature molecular magnets. From left to right and then top to bottom: 2-fluoro-, 3-fluoro-, 4-fluoro-, 2,4-difluoro-, 2,6-difluoro-, and 3,5-difluorophenyltricyanoethylene. From Ref. [37].

complete substitution of the vanadium ion with cobalt does not lead to a magnetically ordered material [40], whereas in the case of nickel the  $T_c$  is very low, about 13 K [42].

The key finding was that two important parameters describing the magnetic properties, the critical temperature and the coercive field, have a weak dependence on composition. For both solid solutions with Fe and Ni, the  $T_c$  drops below room temperature only when decreasing the V content to below  $x = 0.2$  (see Figure 7.4). Similarly, the coercive field,  $H_{cr}$ , varies by two orders of magnitude, but only below  $x = 0.2$ , likely correlated with a strong increase in magnetic anisotropy. It was argued that the control and fine-tuning of the critical temperature and the coercive field could open new opportunities for practical applications [40]; however, such possibilities have yet to be pursued.

In summary, despite extensive experimental studies performed over almost two decades many questions regarding the structure and mechanism of magnetic ordering of  $V[TCNE]_x$  still remained open. What is special about  $V^{II}$  that the critical temperature is so high compared to other magnetic ions? Why does TCNE outperform all other cyanocarbon ligands in terms of the  $T_c$ ? Where does the structural disorder actually come from? What is the source of random magnetic anisotropy? Answers to these questions are provided in the following two sections.

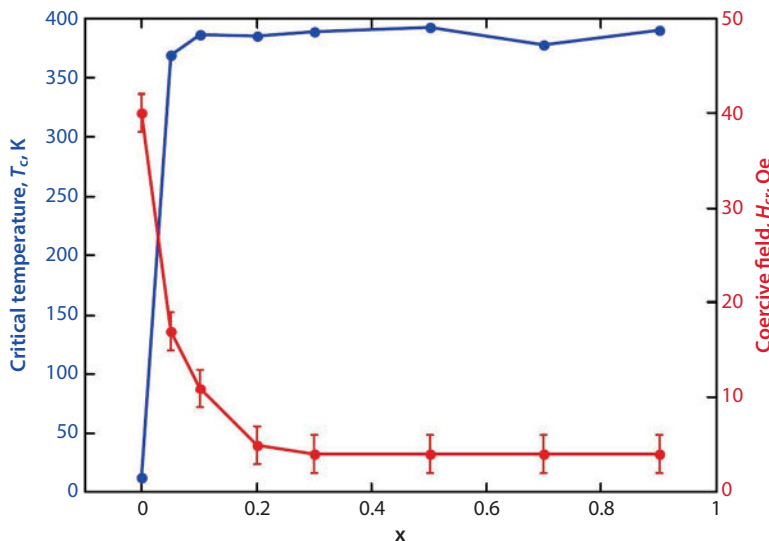


**Figure 7.4** Ordering temperature,  $T_c$ , and coercivity,  $H_{cr}$  as a function of  $x$  for  $V_xNi_{1-x}[TCNE]_2\cdot\gamma(CH_2Cl_2)$ . From Ref. [42].

### 7.3 Ideal Structure and Sources of Structural Disorder

Due to the amorphous character of  $V[TCNE]_x$ , experimentally it has been impossible to determine its structure. The suggestions regarding the structure were that the compound has a 3D network structure, and that each [TCNE] binds to up to four different vanadium ions [18] (as shown in Figure 7.5a). However, hypotheses regarding the presence of  $[TCNE]^{2-}$ , of the twist of its plane, as well as the lack of clarity regarding how on average  $[TCNE]^-$  binds to three vanadium(II) ions remained until late [8].

The early theoretical studies on the structure of the  $V[TCNE]_x$  system started from assuming a cubic structure of vanadium ions with planar TCNE molecules placed in the faces of the cubes [43]. According to such model, each  $V^{II}$  interacts with eight different cyanocarbon ligands. More than a decade later, based on density functional theory (DFT) [44] calculations on a modified structure attributed to the  $Fe[TCNE]_2$  system, it was claimed [45, 46] that the new model was compatible with the magnetization data and could serve as a prototype for the entire family of  $M[TCNE]_x$  magnets. However, that model was based on the assumption that the TCNE ligands would form dimers, the X-ray powder diffraction data being fitted in fact to  $Fe[TCNE]^- \cdot [C_4(CN)_8]_{1/2} \cdot zCH_2Cl_2$  and not to  $Fe[TCNE]_2 \cdot zCH_2Cl_2$  [47]. The claim was that undulating layers of  $[TCNE]^-$  tetra-coordinated to  $Fe^{II}$  ions are connected by tetra-coordinated  $[C_4(CN)_8]^{2-}$  species [47], although energetically such an artificial structure is unlikely. The high energy required to bind two [TCNE]s through the adjacent central carbons is due to both the strong distortion to the molecular plane and to the repulsion of the two negative charges which would be localized on such a dimer.

Other attempts, again using DFT calculations [48], were based on a model system allowing for an octahedral coordination of the vanadium(II)

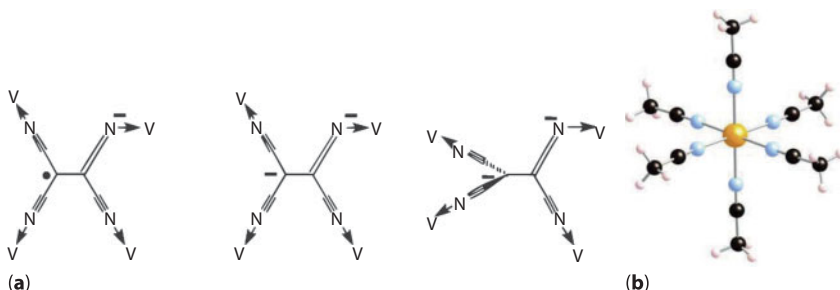


**Figure 7.5** (a) Illustration of the binding of  $[TCNE]^-$  and  $[TCNE]^{2-}$  to up to four  $V^{II}$  ions, based on Ref. [18]. (b) The environment around the  $V^{II}$  ion, indicating that the six N atoms surround the metal ion at an average distance of 2.084 Å, inspired by Refs [8, 22].

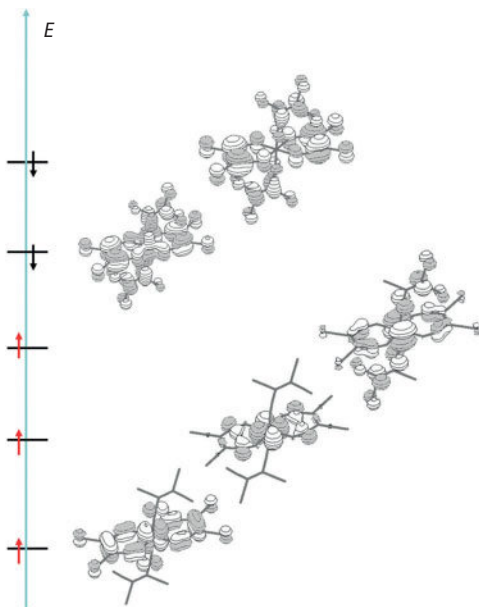


**Figure 7.6** Electron density drawn at  $0.025 \text{ e}/\text{bohr}^3$  of some key molecular orbitals of the  $\text{V}^{\text{II}}[\text{TCNE}]_4$  system, calculated by DFT and represented in the order of increasing energy. From Ref. [48].

ion by binding to four TCNE molecules. The calculations indicated anti-ferromagnetic (anti-FM) interactions between the spin of  $3/2$  on  $\text{V}^{\text{II}}$  and two spins  $1/2$  delocalized on the TCNEs, leading to a ferrimagnetic spin configuration. However, the electronic structure provided by such DFT calculations (see Figure 7.6) indicated as the highest-occupied molecular orbital an orbital with mostly  $\pi^*$  character, delocalized over the TCNEs, in contradiction with earlier photoelectron spectroscopy studies [26–28].

A detailed model structure was finally proposed and optimized using DFT calculations with periodic boundary conditions in 2009 by De Fusco *et al.* [49] and Cimpoesu *et al.* [50]. The ideal structure (see Figure 7.7) was in agreement with the earlier experimental results, but the calculated strength of the magnetic coupling was overestimated and the highest-occupied band was identified as a spin-down band with TCNE  $\pi^*$  character [49], in contradiction with the spectroscopic data [26–28].

In the following, we sketch the underlying principles which lead to the ideal structure. To be consistent with the available experimental data, the model structure should verify the  $\text{V}[\text{TCNE}]_2$  stoichiometry (the  $\text{V}^{\text{II}}$  binding on average to three TCNEs [8]) and a quasi-octahedral coordination sphere, with bond lengths of about  $2 \text{ \AA}$  [22].

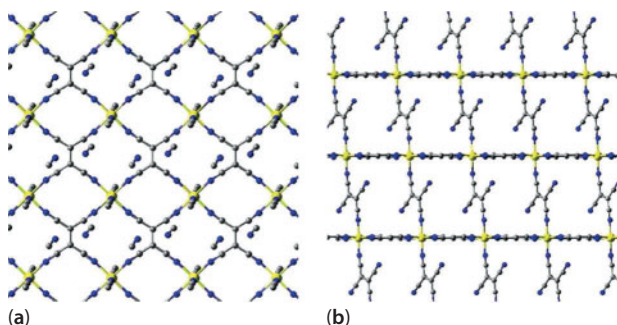


**Figure 7.7** Schematic representation of the optimized  $\text{V}[\text{TCNE}]_2$ , 3D structure displaying (a) a plane of tetra-coordinated and (b) bis-coordinated TCNE radical anions. The vanadium, carbon, and nitrogen atoms are represented as yellow, gray, and blue balls, respectively. From Ref. [49].

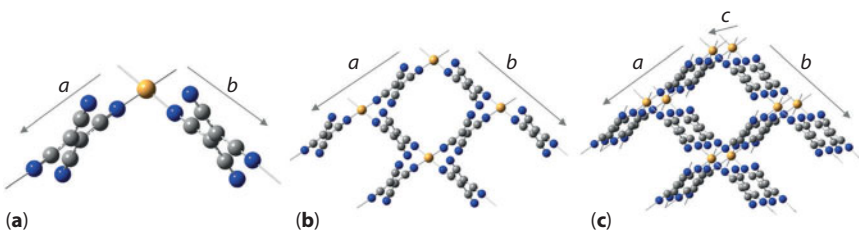


**Figure 7.8** Schematic representation of the ideal structure of  $\text{V}[\text{TCNE}]_2$ ; (a) molecular  $\text{V}[\text{TCNE}]_2$  unit, (b) 2D structure illustrating the 1:2 metal to ligand stoichiometry, and (c) 3D stacking along the  $c$  direction of the plains. The vanadium, carbon, and nitrogen atoms are represented in yellow, gray, and blue balls, respectively. From Ref. [57].

- (i) The most probable bridging mode for growing a network implies *trans* placement of the  $\text{V}^{\text{II}}$  ions near the N atoms of TCNE, as is the case for this ligand in other molecular magnets, such as the manganese porphyrin–TCNE chains [51, 52].
- (ii) The simplest 2D structure fulfilling the  $\text{V}[\text{TCNE}]_2$  stoichiometry and the *trans* V–TCNE–V bridging is a quasi-rectangular pattern with V placed at the tetra-coordinated nodes of the lattice and the TCNEs on the edges of the tetragonal wireframe (see Figure 7.8a for the unit cell and Figure 7.8b for the suggested 2D expansion). Note that the bridging TCNE ligands are equivalent at this step.
- (iii) The 3D lattice is finalized by the stacking of 2D planes along the  $c$  crystallographic axis (Figure 7.8c). Sliding along one

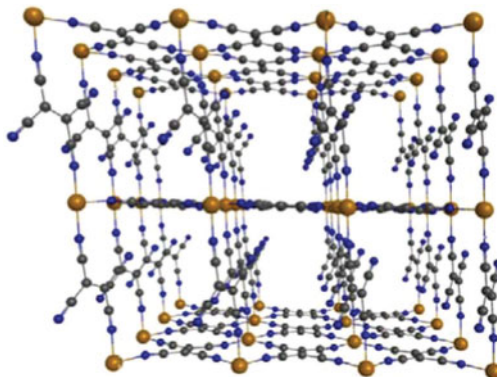


**Figure 7.9** Optimized structure of the ideal  $\text{V}[\text{TCNE}]_2$  lattice, viewed in perspective, along the  $c$  axis. The vanadium, carbon, and nitrogen atoms are represented in yellow, gray, and blue balls, respectively.

of the two directions, for instance,  $a$ , is required so that the upper and lower TCNEs can fulfill the axial coordination of  $\text{V}^{\text{II}}$  sites from adjacent planes. At this step, the ligands along the  $a$  and  $b$  crystallographic axes are no longer equivalent. The ligands in the  $a-c$  planes are tetra-coordinated, bridging along both  $a$  and  $c$  directions, whereas those along the  $b-c$  planes remain bi-coordinated, with  $-\text{CN}$  groups that are not coordinated along the  $c$  direction.

The DFT calculations with periodic boundary conditions were performed on a model structure initially idealized as a monoclinic cell, by taking orthogonal and identical  $a$  and  $b$  translation vectors. The DFT optimization used the BLYP functional [53, 54] and the 6-31G\* basis set [55]. The result for the ground state of the molecular unit was a triclinic structure with the following unit cell parameters:  $a = 10.191 \text{ \AA}$ ,  $b = 9.963 \text{ \AA}$ ,  $c = 7.213 \text{ \AA}$ ,  $\alpha = 81.57^\circ$ ,  $\beta = 135.22^\circ$ , and  $\gamma = 85.81^\circ$  (see Figure 7.9). The cell parameters are different from those reported in Ref. [49], due to another choice of the molecular orientation and cell definition. The volumes of the unit cells differ only slightly, from about  $493.8 \text{ \AA}^3$  [49] to our value of  $493.5 \text{ \AA}^3$  [56, 57]. We prefer our choice of lattice directions because it corresponds to the principles of stepwise construction established above.

In Figure 7.10, we illustrate various molecular fragments cut from the proposed  $\text{V}[\text{TCNE}]_2$  structure. For instance, the six coordination of the  $\text{V}^{\text{II}}$  ion is useful in the discussion of the SIA, whereas the illustration of the two types of TCNE bridges (tetra- and bis-connected) and their orientation

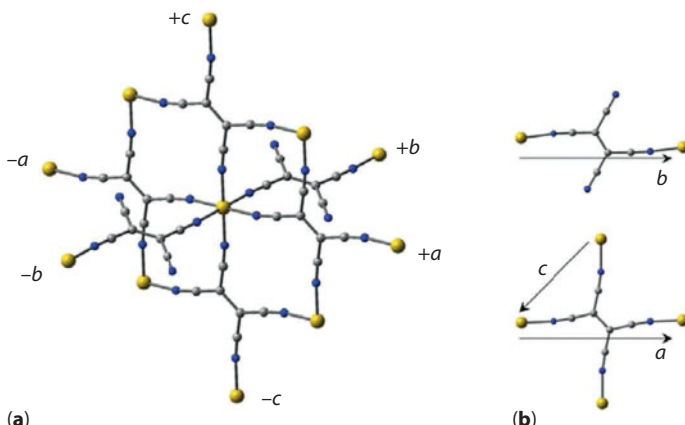


**Figure 7.10** Selected molecular fragments cut from the proposed  $\text{V}[\text{TCNE}]_2$  structure illustrating: (A) the six coordination of the  $\text{V}(\text{II})$  ion, (B) a tetra-connected moiety located in the  $a-c$  crystallographic plane, and (C) a bis-connected ligand along the  $b$  axis with the TCNE plane rotated by about  $20^\circ$  with respect to the  $b-c$  crystallographic plane. The vanadium, carbon, and nitrogen atoms are represented in yellow, gray, and blue balls, respectively.

with respect to the main crystallographic axes is used in the study of the various exchange coupling pathways.

The sources of disorder for the samples resulting from chemical syntheses include the ones found in CVD films as well as the additional defects due to the presence of the intercalated solvent. The main source of disorder is likely related to the equivalence of the  $a$  and  $b$  sliding directions when stacking the 2D layers to build the 3D network. As the usual synthesis routes, either chemical reactions in solution or CVD, are equally favorable to the two chiral structures (unless a deliberated asymmetry is induced in the environment by special procedures), a racemic mixture is globally probable. The resulting disordered structure is a combination of regions having the tetra-connected TCNE along the  $a$  and  $c$  axes intertwined with regions of tetra-coordinated cyanocarbon bridges along the  $b$  and  $c$  axes (see Figure 7.11). When the chirality is changed from one region to the next, lattice defects, such as TCNE vacancies are likely to occur. Therefore, likely, the main reason for the amorphousness observed experimentally is the damaged long-range order due to the random mixture of small enantiomeric regions [57].

Another important source of disorder is related to the different possible configurations of the TCNE ligands. Disorder due to the orientation of the TCNE anion radical has been previously observed [51] in the case of manganese-porphyrin-TCNE compounds [52]. The two possible

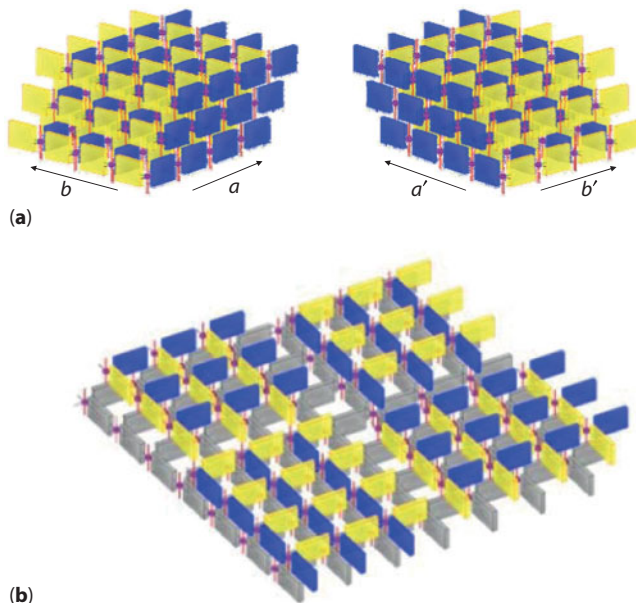


**Figure 7.11** Schematic drawings of the  $V[TCNE]_x$  structure illustrating the disorder caused by the chirality. The blue building blocks represent the tetra-connected TCNEs, whereas the yellow ones the bis-connected TCNEs. The 3D structure is the result of the combined vertical stacking and horizontal sliding of 2D layers. (a) The two mirror images represent enantiomeric networks, which differing only by the sliding direction performed to allow for tetra-coordination of the TCNEs. (b) The static disorder results from the racemic mixture of the two enantiomeric structures. A background reference layer is represented in grey. From Ref. [57].

orientations of TCNE discovered by X-ray diffraction studies are related by a rotation of about  $180^\circ$  around the diagonal axis which joins the *trans*-nitrogen atoms bound to the metal ion. The two forms have different probabilities to occur, the weight of the dominant orientation being 83.3%, compared to 16.7%, for the minor orientation [51, 52].

An extrapolation of the situation observed in quasi-1D systems is possible to the 3D network of  $V[TCNE]_x$ , only for the bis-connected *trans*- $\mu_2$ -TCNE ligands, the tetra-connected units remaining rigidly fixed. Three such possible configurations are shown in Figure 7.12, starting with the optimized geometry and continuing with a  $90^\circ$  and a  $180^\circ$  rotation of the upper bis-connected TCNEs around the *c* axis, the lower layer being kept fixed. Various other collective or individual movements of the  $\mu_2$ -TCNE units can be conceived, all leading to the disarray of crystal ordering, as a specific feature of this system.

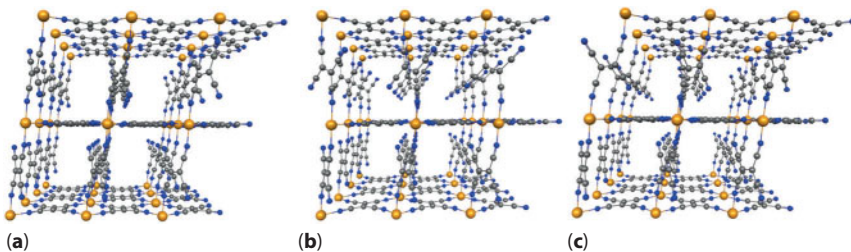


**Figure 7.12** Perspective view of the structures of  $\text{V}[\text{TCNE}]_2$  lattice along the  $c$  axis: (a) the DFT-optimized structure, (b) structure altered with a  $180^\circ$  rotation, and (c) a  $90^\circ$  rotation of the bis-connected  $\mu_2$ -TCNE units from the upper sheet around the  $b$  axis; the  $\mu_2$ -TCNE bridges from the lower sheet are kept fixed. The vanadium, carbon, and nitrogen atoms are represented in yellow, gray, and blue balls, respectively. From Ref. [57].

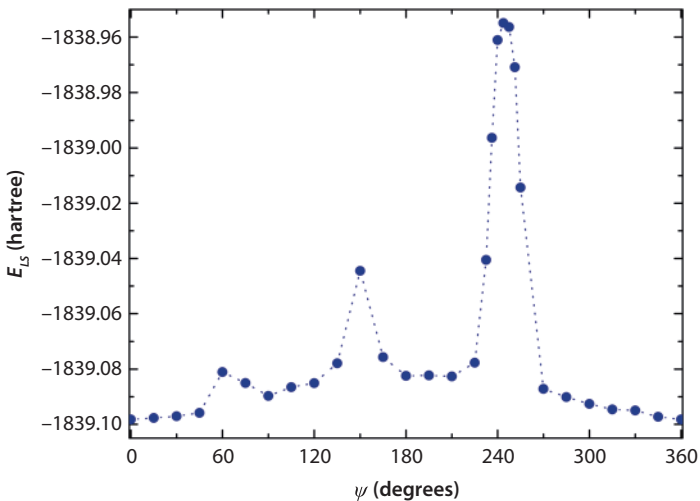


**Figure 7.13** Energy of the low-spin (ferrimagnetic) ground state as a function of the rotation angle,  $\psi$ , of the bi-connected TCNE, obtained by DFT band calculations of  $\text{V}[\text{TCNE}]_2$  structures. Note the following equivalences: 1 hartree  $\leftrightarrow$  27.2107 eV  $\leftrightarrow$  315777 K and  $1 \text{ cm}^{-1} \leftrightarrow 0.695 \text{ K}$ . From Ref. [57].

To better understand the likelihood of the rotation of the bi-connected TCNE molecule on the energy landscape, we performed calculations at DFT/BLYP/6-31G\* level with periodic boundary conditions (PBC) [57]. The energy of the low-spin state, with ferrimagnetic spin alignment as a function of the dihedral angle,  $\psi$ , which defines the rotation of the plane of the bi-connected TCNE around the line connecting the N-atoms bound to V(II), is displayed in Figure 7.13.

The energy landscape is relatively rough, with local minima at about 90° and 180°. The energy differences at these angles with respect to the optimized geometry ( $\psi = 0$ ) are of about 2693 and 4916 K, respectively (where the following equivalence was used: 1 hartree  $\leftrightarrow$  27.2107 eV  $\leftrightarrow$  315777 K). Reaching such geometries, however, requires passing over large barriers of more than 5420 K. In contrast, the dependence of the energy on the angle  $\psi$  is relatively weak, near 0° and 360°. For instance, rotations by 15°, 30°, or 45° require overcoming energy barriers of about 176, 369, and 751 K, respectively.

The large energy at  $\psi = 244^\circ$  is due to an unphysical situation, with two non-coordinated N atoms from neighboring cells getting too close, at 1.3408 Å. Such configuration is highly unlikely to occur experimentally.

In summary, the examination of the energy landscape suggests that small angle rotations can easily be thermally activated at room temperature, causing some dynamic disorder. Moreover, if during the CVD process the bis-connected cyanocarbon ligand binds with a deviation of 90° or 180–210° with respect to the optimal geometry, it may remain pinned into such position due to the large barrier to rotation. In this later case, quenched disorder is likely to occur.

## 7.4 Exchange Coupling Constants and Ferrimagnetic Ordering

### 7.4.1 Exchange Interactions

The main coupling mechanism that gives rise to magnetic ordering in solids is called Heisenberg exchange (sometimes Heisenberg–Dirac–Van Vleck exchange) [1, 2] and is a purely quantum effect due to the interplay of (i) the spin of the electron, (ii) Pauli's exclusion principle, (iii) Coulomb's electron–electron repulsion, and (iv) the kinetic energy of the electron. The exchange energy,  $J$ , for a system of two electrons is related to the difference between the energies of the two possible spin configurations (parallel and antiparallel). The result is an effective interaction, in the spin space, described by the Heisenberg exchange Hamiltonian for two electrons with total spin operators  $\hat{S}_1$  and  $\hat{S}_2$ :

$$\hat{H}_H = -2J_{12} \hat{S}_1 \cdot \hat{S}_2 \quad (7.1)$$

The ferromagnetic (FM) state, characterized by parallel alignment of the spins, occurs when the exchange constant is positive, while the anti-FM state, characterized by antiparallel spin alignment, arises when the

exchange integral is negative. The Heisenberg Hamiltonian can be generalized to a system of many localized electrons.

Superexchange is the crucial interaction in most molecular magnets and, therefore, the emphasis in the following discussion will be on this type of Heisenberg exchange. Superexchange occurs in insulators, between magnetic ions bridged by nonmagnetic atoms. As the wave functions of the magnetic ions tend to be well localized, the lack of orbital overlap would lead to weak magnetic interactions, if any. However, due to the covalent binding effects occurring between the  $d$  electrons of the magnetic ions and the  $p$ -electrons of the nonmagnetic bridges the overall magnetic wave functions spread over rather long distances. It is this overlap between such wave functions that is the determining factor for the sign and the strength of superexchange.

In the classical discussion of superexchange, Anderson [58] distinguishes four main contributions: potential, kinetic, polarization, and correlation exchange. We illustrate these effects with a [TCNE]-V-[TCNE] trinuclear model system, as shown in Figure 7.14. *Potential exchange*

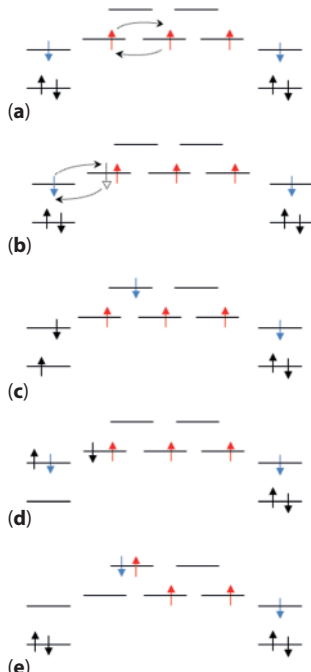


**Figure 7.14** Schematic representation of typical excitations in the case of the [TCNE]-V-[TCNE] model systems, illustrating the various contributions to superexchange: (a) potential exchange, (b) kinetic exchange, (c) spin polarization, and (d and e) correlation exchange. From Ref. [56].

occurs between electrons in singly occupied orthogonal orbitals and favors a parallel spin alignment, which keeps the electrons apart and lowers the Coulomb repulsion (Figure 7.14a). *Kinetic exchange* is important between antiparallel spins located in overlapping singly occupied orbitals. It lowers the kinetic energy when the electrons are delocalized (allowed to undergo a virtual transfer, back and forth, as in Figure 7.14b). *Spin polarization* involves also paired electrons and can be either FM or anti-FM. In this case, a spin from a singly occupied molecular orbital (SOMO) is excited into an empty orbital and one from a doubly occupied orbital is promoted into that SOMO (Figure 7.14c). *Correlation exchange* is anti-FM and requires the participation of either two spins from a doubly occupied orbital, which are excited to two different SOMOs, or two opposite spins from different SOMOs, which are promoted to an empty orbital.

Systems with strong magnetic anisotropy are described by the Ising Hamiltonian

$$\hat{H}_1 = -2J_{12} S_1^z \cdot S_2^z, \quad (7.2)$$

which is much simpler, dealing only with only the  $z$  component of the spin operators [2]. The Ising Hamiltonian considers only the two extreme spin orientations,  $S^z = \pm S$  without taking into account the intermediate  $S^z$  quantum numbers.

The connection between the exchange coupling parameters of two spins,  $S_1$  and  $S_2$ , and the critical temperature of a ferrimagnet is typically based on the expression derived by Néel in the mean field approximation [59, 60]:

$$T_c = |J_{12}| \frac{\sqrt{z_1 z_2} \sqrt{S_1(S_1+1)} \sqrt{S_2(S_2+1)}}{3k_B}, \quad (7.3)$$

where  $z_1$  and  $z_2$  are the number of nearest neighbors for each type of spin. Based on the experimental value of the critical temperature, estimated at 370 K, the mean-field exchange constant of  $\text{V}[\text{TCNE}]_2$ , with a spin of 3/2 on the hexa-coordinated  $\text{V}^{II}$  ion and a spin 1/2 on each of the cyanocarbon ligands (one bis-connected, the other tetra-coordinated), is estimated to be in the range  $135 \text{ K} < |J_{12}| < 190 \text{ K}$ .

#### 7.4.2 Broken-Symmetry DFT Band Calculations of Exchange Constants

Since the extended systems of interest are too large to be studied with elaborate multiconfiguration methods, as in principle demanded by the

physics of exchange coupled systems, the DFT approach is one of the few available alternatives [61]. The most common treatment of the open-shell states of the magnetic systems within the DFT methods is based on spin-polarized DFT calculations in combination with the broken-symmetry (BS) approach [62, 63], which has proved to be a powerful tool in the prediction and interpretation of magnetic properties of a large variety of magnetic systems, as well as for drawing magneto-structural correlations [64].

As the BS treatment results in solutions that are not the eigenstates of the  $\hat{S}^2$  operator, the careful mapping of the BS solutions onto the basis set of the spin Hamiltonian is required, in order to extract the values of exchange interaction parameters from the outcome of the quantum chemical calculations. Various possibilities to calculate the exchange constant have been proposed by several authors [65]. We mention here the approaches of Ginsberg [66] and Noddeman [67, 68], of Bencini [69] and Ruiz [70], and of Yamaguchi [71]. We concentrate on the later method as it reduces to the other two, in the limits of weak and strong orbital overlaps, respectively [65, 72, 73]. Another reason is that the approximate spin projection [65, 71] has been further generalized from dinuclears to systems with a large number of spins [74].

It has been shown [75] that the BS-DFT results interpreted via the Ising Hamiltonian provide a description consistent with the higher-spin (HS) and BS expectation values taken from a Heisenberg Hamiltonian only in the weak overlap limit. For the binuclear spin system, the resulting exchange constant is given by an expression identical to the one provided by Noodelman *et al.* [67, 68]. For periodic systems and band structure problems, the BS-DFT method has been less extensively applied. Yamaguchi *et al.* recently approached the problem of an  $(A-B)_n$  system, comparing the results obtained for finite systems, based on the so-called approximate projection (AP) method with those calculated for extended ones within the Ising model [76]. A similar approach was used to describe an extended system consisting of TCNE-bridged manganese porphyrin rings [77–79]. If we assume equal coupling parameters for all the V-TCNE contacts, for a system with a 3D topology, as in our case, the Ising-type formula used to interpret a couple of DFT calculations, for the extended system with periodic boundary conditions, at HS related with a ferro-type spin ordering and at a BS associated with complete ferrimagnetic spin alternation, reads as follows:

$$J_{12,\text{I-PBC}} = \frac{E_{\text{BS}} - E_{\text{HS}}}{24S_1S_2} \quad (7.4)$$

If compared with the formula for a simple dinuclear case (see Equation 7.7 in next section), we notice here a supplementary 1/6 factor, which appeared from topological reasons. Namely, the periodicity condition finds the same ion involved in different coupling effects, the topological factor amending the double count over the lattice, rescaling the estimated value per one V-TCNE contact.

The exchange coupling constant determined by means of BS DFT with periodic boundary conditions, based on Equation (7.4), is  $-718\text{ K}$  (with the equivalence  $1\text{ cm}^{-1} \leftrightarrow 0.695\text{ K}$ ), suggesting antiferromagnetic interactions and, thus, FM ordering [56]. The comparison between the results for the computed and the ideal expectation value of the square of the spin operator,  $\langle S^2 \rangle$ , for the corresponding configurations shows a good match for the HS case, for which the ideal result is 8.75 [56]. The ideal  $\langle S^2 \rangle$  expectation value for a BS-type unit cell with  $\{-1/2, 3/2, -1/2\}$  spins is 0.75, but the BS-DFT result is around 1.7, due to spin contamination [65].

The DFT study on  $\text{V}[\text{TCNE}]_2$  of De Fusco *et al.* [49] reported band calculations also using the Ising formalism and obtained large anti-FM exchange parameters of about  $-800$  and  $-840\text{ K}$ , for the two types of TCNEs. Our calculations of the  $J$  parameter [56] yielded similar values, yet sensibly overestimated with respect to the expected range based on the value of the experimental critical temperature. These results indicate the limits of the band DFT calculations, which account well for the bulk part of the bonding regime, providing reasonable bond lengths and optimized structural models, but underperform in the subtler balance of exchange coupling effects. The BS-DFT results qualitatively describe the anti-FM nature of the ground state, but severely overestimate the magnitude of the exchange coupling parameters, its absolute precision being in about the order of  $10^2\text{--}10^3\text{ cm}^{-1}$ , i.e. in the range of the estimated exchange coupling constants.

#### 7.4.3 Broken-Symmetry DFT Calculations of Exchange Constants of Finite Models

As DFT band calculations tend to overestimate the exchange coupling at a relatively heavy computation price [56, 77], it is worth attempting calculations of smaller systems, containing two or three spin carriers, derived from the geometry optimized with periodic boundary conditions. For this purpose,  $\{(\text{HCN})_5\text{V(II)}[\text{TCNE}]^-\}^+$  dinuclear as well as  $(\text{HCN})_4\text{V(II)}[\text{TCNE}]_2$  trinuclear systems were obtained by cutting V-[TCNE] blocks from the optimized geometry, along each of the three lattice directions (as shown in Figure 7.15) [56]. The coordination spheres around each VII ion

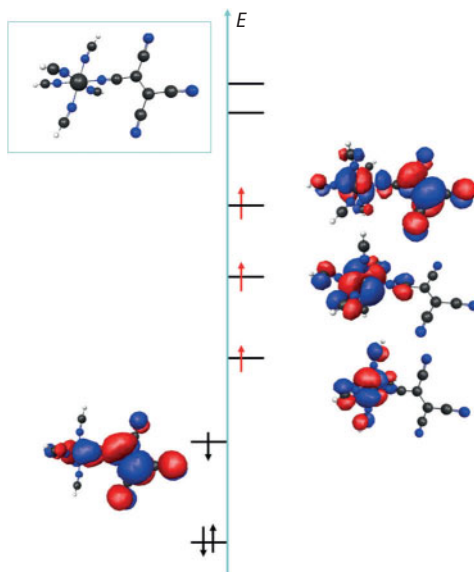


**Figure 7.15** Electron density drawn at 0.015 e/bohr<sup>3</sup> of some key molecular orbitals of the  $\{(HCN)_5V(\text{II})[\text{TCNE}]^-\}^+$  dinuclear, calculated by DFT and represented in the order of increasing energy. The structure of the  $\{(HCN)_5V(\text{II})[\text{TCNE}]^-\}^+$  dinuclear is represented in the inset. The vanadium, carbon, nitrogen, and hydrogen atoms are represented by a large black sphere, and yellow, gray, and blue balls, spheres, respectively.

were completed with NCH groups, up to the hexa-coordination. The NCH units were used as stoppers, mimicking the local coordination with the  $\text{N}\equiv\text{C}-$  groups of the TCNE molecules removed.

For the  $[(HCN)_5V(\text{II})-\text{TCNE}]^+$  fragments, there are three possible choices of the V(II)-[TCNE] dinuclears, due to slightly different configurations of ligands along the *a*, *b*, and *c* crystallographic axes. In these dinuclears, the TCNE is coordinating almost linearly, through one CN moiety. In the case of the V(II)-[TCNE] dinuclear [56], the AP method, starting from the Heisenberg Hamiltonian, determines the magnetic exchange interaction by means of the following relation [65]:

$$J_{12,H-d} = \frac{E_{BS} - E_{HS}}{\langle S^2 \rangle_{HS} - \langle S^2 \rangle_{BS}}. \quad (7.5)$$

This procedure, implying unrestricted DFT calculations for the system in both the BS state and the HS state, is based on the total energies and the expectation values of the square of the spin in the two states.

The Ising approach corresponds to the direct application of Equation (7.5), or equivalently, to the replacement in (7.6) of the expectation values obtained from the analytical treatment of the addition of two angular momenta,  $\langle S^2 \rangle_{HS} = S_1(S_1 + 1) + S_2(S_2 + 1) + 2S_1S_2$  and  $\langle S^2 \rangle_{BS} = S_1(S_1 + 1) + S_2(S_2 + 1) - 2S_1S_2$ , the exchange parameter being interpreted as [75]

$$J_{12,I-d} = \frac{E_{BS} - E_{HS}}{4S_1S_2}, \quad (7.6)$$

The above formula may differ by a factor of  $\pm 1/2$  with respect to the conventions where the Ising operator is equated by  $\mp J_{12}S_1^zS_2^z$  instead of the form used here,  $-2J_{12}S_1^zS_2^z$ .

The DFT calculations on dinuclear models were performed [56] with B3LYP/6-31G\* setting. The results displayed in Table 7.1 for three different V-TCNE dinuclear species show that the overestimation of the exchange coupling parameters observed after band calculations for extended systems, with periodic boundary conditions, persists in the case of finite models. Therefore, the drawback of exchange overestimation belongs to the DFT itself, and it is not a limitation specific just to band calculations.

As expected [77, 80], the results of the Ising approach overestimate the exchange constant with respect to the AP method [65, 71] as it relates to the approximation of orthogonal magnetic orbitals on the two spin centers. The differences between the corresponding estimations [56] come from spin contamination [65], which cause a departure of DFT-based expectation values of the square of the total spin,  $\langle S^2 \rangle_{HS} = 6.035$  and  $\langle S^2 \rangle_{BS} = 2.802$ , from the ideal ones, of 6 and 2, respectively.

The trinuclear systems considered were  $(HCN)_4V(II)[TCNE]_2$ , with various geometrical configurations, depending on the crystallographic axes

**Table 7.1** Calculated exchange parameters for the  $\{(HCN)_5V^{II}[TCNE]\}^+$  dinuclears cut from the unit lattice along each of the three crystallographic directions, determined by BS-DFT/B3LYP/6-31G\* calculations in the Heisenberg and Ising approximations and by CASSCF (Complete Active Space Self-Consistent Field) (6,7) calculations.

	$J_{12}(aa)$	$J_{12}(bb)$	$J_{12}(cc)$
BS-DFT H	-784.4	-791.5	-796.5
BS-DFT I	-845.8	-853.5	-859.0
CASSCF	-141.3	-166.6	-147.6

All quantities are expressed in K (1 K  $\leftrightarrow$  0.695 cm<sup>-1</sup>).

along which the moieties are cut (*a*, *b*, or *c*). The Heisenberg Hamiltonian takes the form

$$\hat{H}_{H-t} = -2J_{12} \hat{\mathbf{S}}_1 \cdot \hat{\mathbf{S}}_2 - 2J_{23} \hat{\mathbf{S}}_2 \cdot \hat{\mathbf{S}}_3 - 2J_{13} \hat{\mathbf{S}}_1 \cdot \hat{\mathbf{S}}_3, \quad (7.7)$$

where the subscript 2 labels the metal ion, with  $3/2$  spin, whereas 1 and 3 indices denote the  $1/2$  spins of the radicals. The TCNE(1)–TCNE(3) next-nearest-neighbor interaction is also taken into account, through  $J_{13}$ , as shown in Figure 7.16. The corresponding Ising Hamiltonian is

$$\hat{H}_{I-t} = -2J_{12} S_1^z \cdot S_2^z - 2J_{23} S_2^z \cdot S_3^z - 2J_{13} S_1^z \cdot S_3^z. \quad (7.8)$$

We use the above  $J_{ij}$  notations, corresponding to the topology suggested in Figure 7.16, adding also further labels defining the corresponding crystallographic species of TCNE. For instance, a model system denoted by TCNE(*a*)–V–TCNE(*a*) is made from the radical ligands along the *a* axis, and similarly TCNE(*b*)–V–TCNE(*b*) is the symmetric trinuclear made of the  $\mu_2$ -TCNE species along the *b* crystallographic axis. The asymmetric tri-nuclear TCNE(*a*)–V–TCNE(*b*) is analogous of the unit cell, realized picking the central V<sup>II</sup> and the ligands along the directions labeled +*a* and +*b*. The TCNE(*a*)–V–TCNE(*c*) and TCNE(*b*)–V–TCNE(*c*) angular conformations are obtained picking one of the axial ligands and an equatorial one, *a* or *b*, respectively. The exchange constants will be labeled correspondingly. For instance,  $J_{12}(aa)$  is the nearest-neighbor V<sup>II</sup>–TCNE interaction for the symmetric trimer along the *a* direction: TCNE(*a*)–V–TCNE(*a*), whereas  $J_{13}(ab)$  is the next-nearest-neighbor TCNE(*a*)–TCNE(*b*) interaction between the ligands oriented along the *a* and *b* directions.

In the case of a three-spin system, to access all three exchange interaction parameters, one has to construct four BS solutions corresponding

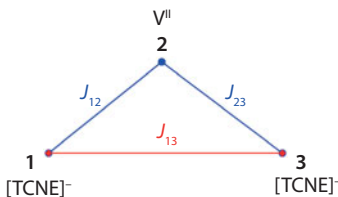


**Figure 7.16** Schematic representation of the interactions in a  $V[TCNE]_2$  trinuclear of  $3/1$ ,  $1/2$ , and  $1/2$  spin carriers. The exchange parameters  $J_{12}$  and  $J_{23}$  describe the  $V^{II}$ –[TCNE] interactions in various spatial configurations, whereas  $J_{13}$  stands for the next-nearest-neighbor interaction between the TCNEs. We represented here a general triangular conformation, but the same scheme holds for linear cases.

to states with the following  $\{S_1^z, S_2^z, S_3^z\}$  spin configurations: one high spin (HS)  $\{\alpha, 3\alpha, \alpha\}$ , two intermediate spin  $\{\alpha, 3\alpha, \beta\}$ ,  $\{\beta, 3\alpha, \alpha\}$ , and one low spin  $\{\beta, 3\alpha, \beta\}$ , picking from each output the total energy and the expectation value of the square of the spin, to be used for the generalized approximate spin-projection approach [74]. Since the configuration  $\{\beta, 3\alpha, \beta\}$  yields the minimal DFT energy, it is convenient to set its value to zero by subtracting from all the energies the value of the  $\{\beta, 3\alpha, \beta\}$  configuration [56].

The expressions of the energy in terms of the exchange coupling constants and the expectation values of  $S^2$  become (taking into account the full Heisenberg Hamiltonian and working in the approximate spin-projection approach [71]) were derived by Gorelik *et al.* [81].

The results of the global fits to the BS-DFT-calculated energies [56] are displayed in Table 7.2 for both AP and Ising approaches. Analyzing the results in Table 7.2, we note that the exchange parameters determined for the trinuclear systems are somewhat closer to the experimental estimation of the V-[TCNE] exchange. Comparing the magnitudes around  $\sim 500$  K obtained for the trinuclears with those around  $\sim 850$  K for the dinuclears and those above  $\sim 700$  K from the band calculations, it is obvious the improvement in the case of the trinuclear model systems. Despite the differences found in the various exchange constants (to within 15%), we note that the values of the  $J_{12}$  and  $J_{23}$  parameters, standing for the nearest-neighbor interactions, are always comparable and systematically stronger than  $J_{13}$  (assigned to next-nearest-neighbor interactions). Taking roughly the averages of over 500 and about 100 K for  $J_{12}$  and  $J_{13}$ , respectively, we obtain a ratio of about 1/5. As the magnitude of V-TCNE coupling ( $J_{12}$  and  $J_{23}$  series) seem rather large, the long-range radical-radical coupling may also be overestimated.

The electronic band structure of the geometrically relaxed V[TCNE]<sub>2</sub> model was computed by DFT by De Fusco *et al.* [49]. The one-electron bands for spin-up ( $\alpha$ ) and spin-down ( $\beta$ ) electrons are shown separately in Figure 7.17. A spin-polarized semiconducting behavior with an indirect spin-up band gap of 0.82 eV is revealed, in reasonable agreement with the activation energy of conductivity reported by Prigodin *et al.* [24] ( $\Delta E \approx 0.5$  eV). The three upper  $\alpha$  valence bands are dominated by the V 3d states,  $d_{xz}$ ,  $d_{yz}$ , and  $d_{x^2-y^2}$ , with some hybridization with 2p atomic orbitals localized on cyanocarbons. The two spin-up lower conduction states are dominated by the TCNEs  $\pi^*$  molecular orbitals. Although the two  $\beta$  upper valence bands lay higher ( $-1.20 \div -0.5$  eV) than the three spin-up upper valance bands ( $-1.60 \div -0.6$  eV), it was claimed [49] that the character of the computed crystalline orbitals was in excellent agreement with the experimental data. However, experimentally, it was shown that the upper

**Table 7.2** Calculated exchange parameters determined for [TCNE]–V–[TCNE] trinuclears, based on a global fitting of the BS-DFT values, using the AP approach or the Ising approach, and on the fitting of the CASSCF and MRPT2 results.

Notation	$J_a$	$J_b$	$J_c$	$j_{aa}$	$j_{bb}$	$j_{cc}$	$j_{ab}$	$j_{ac}$	$j_{bc}$
Topological equivalences	$J_{12}(aa)$	$J_{12}(bb)$	$J_{12}(cc)$	$J_{13}(aa)$	$J_{13}(bb)$	$J_{13}(cc)$	$J_{13}(ab)$	$J_{13}(ac)$	$J_{13}(bc)$
	$J_{23}(aa)$	$J_{23}(bb)$	$J_{23}(cc)$						
	$J_{12}(ab)$	$J_{23}(ab)$	$J_{23}(ac)$						
	$J_{12}(ac)$	$J_{12}(bc)$	$J_{23}(bc)$						
BS-DFT AP	-497.5	-522.1	-538.7	-89.9	-104.2	-95.4	-144.7	-96.1	-47.6
BS-DFT I	-516.2	-543.0	-561.7	-91.3	-106.1	-97.1	-148.1	-97.9	-48.1
CASSCF	-147.3	-166.2	-160.9	7.5	30.2	-9.9	-43.4	33.6	4.7
MRPT2	-338.0	-377.3	-392.4	32.4	26.0	20.7	-16.0	-61.0	21.2

The labels  $a$ ,  $b$ , and  $c$  denote the three directions of the lattice. The labeling and notations are according to Figure 7.16. All quantities are expressed in K. From Ref. [56].

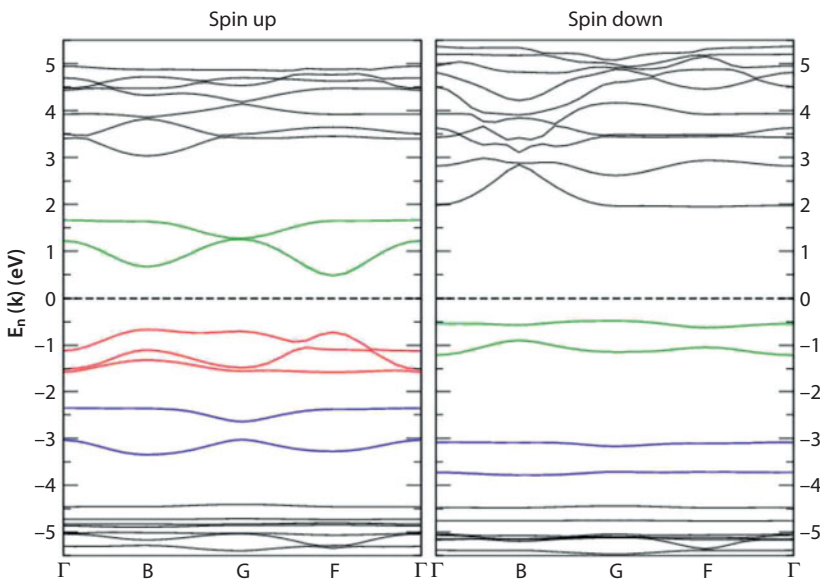


**Figure 7.17** The electronic structure of  $\text{V}[\text{TCNE}]_2$  in its ground-state anti-FM configuration. The energy scale (eV) has been normalized and expressed relatively to the Fermi energy,  $E_F$ . On the  $x$  axis the points labeled as  $\Gamma$ , B, G, and F correspond to the  $k$  points of the first Brillouin zone of the triclinic and monoclinic Bravais lattices whose absolute coordinates are  $(0,0,0)$ ,  $(1/2,0,0)$ ,  $(0,0,1/2)$ , and  $(0,1/2,0)$ , respectively. From Ref. [49]. From Ref. [49].

valence states are V ( $3d$ ) derived, exhibiting a significant hybridization between  $\text{V}^{II}$  and TCNE orbitals [26–28].

The density of states (DOS) resulted from the DFT band structure calculation of the low spin  $\text{V}[\text{TCNE}]_2$  system of Frecus *et al.* [56] is shown in Figure 7.18. The band structure obtained from computations of the extended system, with periodic boundary conditions, is correlated with the energy diagram and the molecular orbitals resulting from unrestricted DFT calculations of a finite model system, the TCNE(*a*)–V–TCNE(*b*) tri-nuclear. The molecular orbitals from the discrete system are in relatively good correspondence with the crystalline orbitals. It is to be noted that a certain shift in the energy scale is likely due to the presence of the terminating HCN groups in the tri-nuclear model. For instance, the three  $\alpha$  orbitals with energies between  $-5.5$  and  $-4.9$  eV correspond to the  $\alpha$  bands located between  $-4.7$  and  $-3.5$  eV. The  $\beta$  orbitals at  $-4.5$  to  $-4.2$  eV relate to the bands at  $-4.5$  to  $-3.5$  eV, but in the case of the crystal the  $\alpha$  and  $\beta$  bands are overlapping, suggesting an inversion between the lower  $\beta$  and the highest  $\alpha$  crystalline orbitals.

Important to note in Figure 7.18 is that the highest occupied molecular orbital (HOMO) clearly shows a mixture of  $d$  and  $\pi^*$  character, in agreement with the XPS experimental results [26, 27]. The DFT calculations for the tri-nuclear system, the electron densities located on the metal ion and TCNE bridges are distributed 15.1% and 84.9%, respectively. Correspondingly, the band calculations lead to similar results: 14.8% vs. 85.2%.

According to the DFT-PBC calculation, the highest-occupied  $\alpha$  band is filled only up to about -3.5 eV, whereas the  $b$  states are completed beyond this value, up to -3.35 eV. The DFT approach is known to have problems in describing the balance between the exchange and Coulomb effects in transition metal ions [82]. Consequently, a subtle imbalance of the exchange and correlation effects induced by density functional can affect the relative ordering of the  $\alpha$  and  $b$  states. On the other hand, the DFT calculations seem to certify a metal-ligand hybridized nature of the highest-occupied levels (in line with XPS experiments), in spite of the fact that they seem not to reproduce correctly their spin polarization.

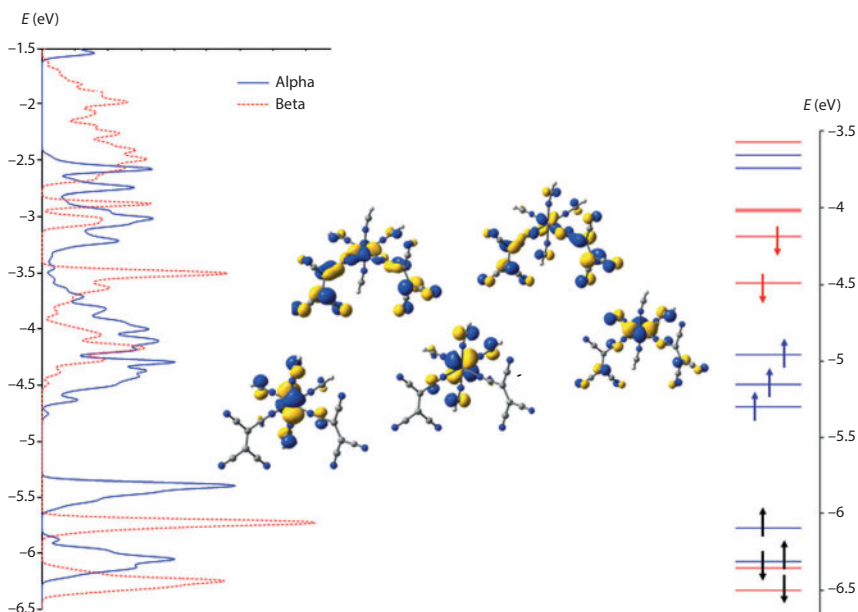


**Figure 7.18** DOS curves for  $\alpha$  and  $\beta$  bands (solid and dotted line respectively), as resulted from unrestricted DFT/BLYP/6-31G\* calculations on the optimized  $V[TCNE]_2$  crystal structure, in its ground-state anti-FM configuration (left). Electronic structure calculated by unrestricted DFT for the TCNE( $a$ )–V–TCNE( $b$ ) trinuclear cut from the optimized geometry (orbital shapes in the center and corresponding energies in the right). Electron densities of MOs determined for the trinuclear ( $0.03 \text{ e}/\text{bohr}^3$ ).

#### 7.4.4 CASSCF Calculations of Exchange Constants

Given the overestimation of the exchange coupling by BS-DFT methods, in order to obtain a more accurate description of the exchange parameters, we turned to the use of multiconfiguration *ab initio* calculations. Besides, the multiconfigurational approaches represent the best-suited methodology as the spin multiplet problems are naturally considered in this way. Being computationally prohibitive for large systems, advanced electron structure treatments can be applied only to systems with a small number of atoms. In this section, we present results of CASSCF [83] calculations of V-[TCNE] dinuclears and [TCNE]-V-[TCNE] trinuclears, practically the same systems as discussed in the previous DFT section.

The choice of the active space for both the di- and trinuclear model systems is not trivial as we noted after various computations that did not converge. A proper selection of the active space, able to provide the exchange coupling constants, should be based on an analysis of the types of excitations that need to be taken into account along with the ground state. Following the classical approach of Anderson [58], already mentioned in a previous section, we need to distinguish between the four main contributions to superexchange: potential, kinetic, polarization, and correlation exchange, taking as a case study the [TCNE]-V-[TCNE] trinuclear model system, shown in Figure 7.14. In order to account for all four types of contributions to superexchange, the ‘minimal’ active space formed from the valence electrons and the singly occupied orbitals is not sufficient. A more suitable description of superexchange requires also doubly occupied molecular orbitals, such as the  $\pi$  MOs that are localized on the ligand, and empty orbitals, such as the two MOs originating from the metal ion.

Consequently, for the V-[TCNE] dinuclear, we chose a (6,7) active space containing the interaction of all the configurations resulted distributing 6 electrons in 7 active molecular orbitals. The 6 electrons result from considering three  $d$ -type unpaired electrons on  $V^{II}$ , one electron in the  $\pi^*$  and the two electrons from the doubly occupied  $\pi$  system of the [TCNE]. The 7 active MOs include the 5 orbitals containing the above mentioned electrons plus two virtual  $d$ -type orbitals from the metal ion, considering the full  $d$  set.

In the case of the [TCNE]-V-[TCNE] trinuclear, we used a (9,9) active space. The nine electrons are the 3  $d$ -electrons from  $V^{II}$  and three electrons (two from  $\pi$  and one from  $\pi^*$ ) from each of the two TCNEs, as illustrated in Figure 7.14. The MOs are the ones derived from the 5  $d$  orbitals of  $V^{II}$  together with the  $\pi$  and  $\pi^*$  of each of the two TCNEs.

For a dinuclear of spins 3/2 and 1/2, the Heisenberg exchange interaction is analytically solvable, the two possible states being HS,  $S_{HS} = 2$ , and low spin,  $S_{LS} = 1$ . The coupling constant can be determined from the relation:

$$J_{12,H-d} = \frac{E_{LS} - E_{HS}}{S_{HS}(S_{HS} + 1) - S_{LS}(S_{LS} + 1)} = \frac{E_{LS} - E_{HS}}{4} \quad (7.9)$$

In the case of a symmetric trinuclear, the spin Hamiltonian of equation can be expressed in a simple manner with Kambe-type formulas [84] introducing for convenience along with the total spin  $S$ , an intermediate spin,  $S_{13}$  of the TCNE-TCNE moiety. The four possible states of the symmetric trinuclear with local (1/2, 3/2, 1/2) components, taking the low spin as ground state, are 0,  $-3J_{12}$ ,  $-5J_{12} + J_{13}$ , and  $-8J_{12}$  [56].

For the asymmetric trinuclear, the simple Kambe approach is not valid. Anticipating the anti-FM nature of the ground state, we take again as origin the energy of the  $S = 1/2$  state. With the appropriate shift in energy, we get for the upper three energy levels the expressions:

$$E(3/2)_{[\pm]} - E(1/2) = -2(J_{12} + J_{23}) + J_{13} \pm \sqrt{4(J_{12} - J_{23})^2 - J_{13}(J_{12} + J_{23}) + J_{12}J_{23} + J_{13}^2} \quad (7.10a)$$

$$E(5/2) - E(1/2) = -4(J_{12} + J_{23}) \quad (7.10b)$$

The two quartet states result from a nondiagonal  $2 \times 2$  interaction matrix. The matrix becomes diagonal only when the trinuclear is symmetric ( $J_{12} = J_{23}$ ), case in which the two quartet states become decoupled, with the energies coincident with those given in the previous paragraph.

For the  $[(\text{HCN})_5\text{V}(\text{II})-\text{TCNE}]^+$  dinuclear, CASSCF(6,7) calculations were performed [56], yielding low-spin ground states, which indicate anti-FM coupling between the spins on vanadium and [TCNE]. The values of the exchange coupling parameters are listed in Table 7.1. Despite the approximations made by considering the simplest fragments, the values obtained for the V-[TCNE] exchange are in relative agreement with the experimental estimations using the mean-field approach for the critical temperature of  $\text{V}[\text{TCNE}]_2$ .

For the  $[\text{TCNE}]^--\text{V}(\text{II})-[\text{TCNE}]^-$  symmetric trinuclears, the energy differences obtained by CASSCF(9,9) calculations [56] were used to fit the

$J_{12}, J_{23}$  main couplings, as well as the next-nearest-neighbor interaction,  $J_{13}$ . The three asymmetric trinuclears that we consider here involve TCNE-V-TCNE fragments oriented along the  $ab$ ,  $ac$ , and  $bc$  crystallographic axes. Just as for the symmetric trinuclears, we use CASSCF(9,9) calculations, with the same choice of electrons and orbitals.

The global fit of the exchange constants for all six sets of data, resulting from the calculations performed on the six types of trinuclear model systems ( $aa$ ,  $bb$ ,  $cc$ ,  $ab$ ,  $ac$ ,  $bc$ ), leads to the exchange values shown in Table 7.2.

As can be observed in Table 7.2, a convenient notation of the V-TCNE coupling parameters is introduced, describing by  $J_a$ ,  $J_b$ , and  $J_c$  the contacts developed along the  $a$ ,  $b$ , and  $c$  axes, respectively. Conversely, the long-range TCNE...TCNE next-neighbor effects (corresponding to  $J_{13}$  in the notation from Figure 7.16) are denoted by noncapitalized  $j$  symbols.

The  $J_a$ ,  $J_b$ , and  $J_c$  values for the trinuclears (Table 7.2) are in the same range and the same relative ordering,  $|J_a| < |J_c| < |J_b|$ , as those obtained in the case of the dinuclears (see Table 7.1). The relative order is different, however, from the DFT results reported in the previous section (which was  $|J_a| < |J_b| < |J_c|$ ). The value along the  $a$  direction remains systematically the smallest, whereas the values along the  $b$  and  $c$  directions are in reversed order. Despite the approximations made in chemical models and in the computations, the values obtained by means of CASSCF for the V-TCNE exchange seem to be in better agreement with the experimentally derived parameters than those provided by the BS-DFT methods.

Regarding the limitations of the chemical model, it should be noted that the NCH replacement groups are mimicking only the major part of the coordination effects, by the chemical composition of the immediate contacts V-NC. However, the other details due to charge and spin polarization are not that well reproduced. Therefore, the  $V^{II}$  sites suffer in dinuclears and asymmetrical trinuclears by an artificial polarization due to the negative charge in the TCNE parts that leads to an artificial asymmetrization in the lobes corresponding to the form of the  $d$ -type orbitals resulted from CASSCF estimation. This is due to the contribution of an artificial  $p-d$  mixing of AOs from the  $V^{II}$  site, which should not exist in the reality of the electronic structure, since the pseudo-octahedral centrosymmetric environment does not allow the orbital combinations that induce net polarity. However, when fitted in the discussed coupled manner, with all the trinuclears described by the same parameter set, the drawbacks resulted from each particular model are smoothed.

The CASSCF calculations of the symmetric and asymmetric trinuclears indicate that the long range effects are comparatively smaller than those predicted by BS-DFT methods. If the ratio between the average

next-nearest-neighbor and the average nearest-neighbor interactions ( $j/J$ ) was about 1/5 for the DFT results it is less than 1/10 for the corresponding CASSCF data. The small long range effects are yet significant, suggesting the important role of delocalization of the electron structure, which supports some distant spin-spin coupling and possibly, the charge transport throughout the lattice.

As noted in the previous section, a key theoretical question that has not been answered adequately yet regards the nature of the highest-occupied molecular orbital of  $V[TCNE]_x$ . Previous DFT calculations [49, 50] including our one, reported above [56], have provided a singly occupied spin-down highest solution with [TCNE] character, in contradiction with the experimental data [26, 27] which indicated a spin-up orbital with mixed  $3d$  and  $\pi^*$  character.

To address this issue, we analyzed the canonical orbitals from the CASSCF calculation on the symmetrical  $[TCNE](a)$ -V- $[TCNE](a)$  trinuclear. Although in a multiconfigurational frame [85] we cannot simply rely on the customary terminology of frontier orbitals, as matter of convenience, we will call the wavefunction with the highest canonical energy HOMO. Our CASSCF calculations, illustrated in Figure 7.19, show that

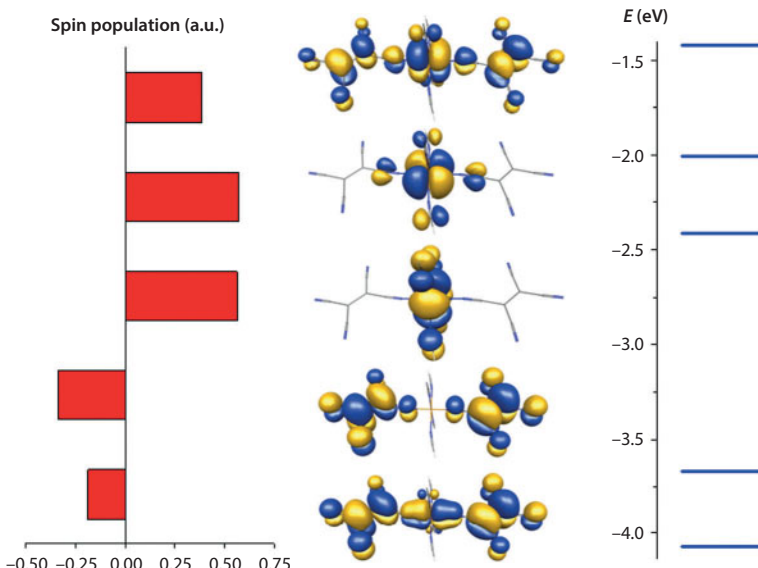


**Figure 7.19** Spin population (left), orbital shapes drawn at  $0.015 \text{ e}/\text{bohr}^3$  (center) and energies (right) of selected optimized MCSCF orbitals from the CASSCF(9,9) calculations of the  $[TCNE](a)$ -V- $[TCNE](a)$  trinuclear. From Ref. [56].

the HOMO of the trinuclear model system has a mixed,  $3d-\pi^*$  character, being delocalized over the whole system. In contrast, the HOMO-1 and HOMO-2 orbitals have strong  $3d$  character, being localized on the metal ion, whereas the HOMO-3 has a  $\pi^*$  nature, displaying high electron density on the two TCNEs.

The spin populations assigned to the CASSCF canonical orbitals displayed in the left panel of Figure 7.19 were determined from corresponding weights of all the configurations from the given active space, using + and - signs to account for the  $\alpha$  and  $\beta$  spin states, respectively. The value and, more importantly, the sign of the spin indicates that the highest-occupied orbitals HOMO, HOMO-1, and HOMO-2, with strong  $d$  contribution from V<sup>II</sup>, have the spin up, whereas the lower two, with strong  $\pi^*$  character from [TCNE], have the spin down. This result is important as it reproduces an experimental observation [26–28] that has not been explained by any of the calculations performed so far. Although the CASSCF optimized orbitals have only a conventional meaning and, therefore, the orbital energies should be considered in a semi-quantitative way [85], relationships between the orbital energies and their carried spin populations can be drawn.

#### 7.4.5 MRPT2 Calculations of Exchange Constants

Since CASSCF calculations usually account only for a small percentage of the dynamical correlation energy, it is believed that to obtain accurate results, subsequent correlation treatments should be performed [86, 87]. Consequently, multireference second-order perturbation theory (MRPT2) [88, 89] was carried out [56], starting from the CASSCF wave function. The exchange parameters obtained by a global fit of the MRPT2 results for the [TCNE]-V-[TCNE] trinuclears are reported in Table 7.2.

The MRPT2 values of the  $J$  constants are more than twice larger than the CASSCF ones, also larger than the estimations of the exchange constant based on the experimental value of the critical temperature. Moreover, in this case, the relative ordering is  $|J_a| < |J_b| < |J_c|$ , changed compared to CASSCF but the same with the DFT calculations. The ratio  $|J/j|$  between the absolute values of the average nearest-neighbor and the average next-nearest-neighbor interactions is larger than 5/1, consistent with both the DFT and CASSCF results mentioned above.

The increase in the magnitude of  $J$  is not surprising for the MRPT2 approach. Multireference PT2 calculations using the CASPT2 approach [90, 91] reported for NiO showed [92] that the superexchange coupling constant is enhanced almost three times in the CASPT2 calculations with

respect to the CASSCF results. Similarly, computations performed on a Cr-based dinuclear complex [93] lead to increases in the magnitude of the exchange coupling of at least four times, whereas for  $\text{La}_2\text{CuO}_4$  and some other cuprates increases of a factor 3–4 were observed [94].

Moreover, there are also some reports stating that the multiconfigurational second-order perturbation techniques have problems to describe the low-energy spectrum of systems with weak magnetic coupling [95, 96]. The method shows important deviations from the expected Heisenberg spectrum for couplings smaller than 15 K [96]. Also, there are cases when the method is unable to reproduce the expected Heisenberg spectrum, the perturbational results showing severe deviations in the values and even the sign of  $J$  [96].

In the case of V-TCNE, the coupling is much stronger than 15 K, the Heisenberg spectrum is well reproduced, and the strength of the magnetic exchange interaction increases only twice from the CASSCF to the MRPT2 calculations. We find here a significant increase in the absolute values of the coupling constants, beyond what would be expected from the estimations based on the critical temperature. Since for the nearest-neighbor  $\text{V}^{\text{II}}\text{-}[\text{TCNE}]$  coupling, this means an enhancement of the anti-FM effect, the PT2 corrections act toward the DFT results, but stopping in between.

#### 7.4.6 Mechanism of Ferrimagnetic Coupling

The understanding of the magnetic properties of  $\text{V}[\text{TCNE}]_x$  has been hindered by the missing structural information. In other systems, also relevant for their high critical temperature, such as the Prussian blue analogues [7], the mechanism of ferrimagnetic exchange was more readily understood, although they were discovered later because their structure was well known. Thus, it was explained qualitatively that when several electrons are present on each center, the exchange coupling constant can be described as the sum of the different orbital pathways weighted by the number of unpaired electrons [7, 97–100]. The magneto-structural rationalizations achieved for the Prussian blue analogues inspire similar correlations for the ideal  $\text{V}[\text{TCNE}]_2$  model employed to describe  $\text{V}[\text{TCNE}]_x$ . In the case of  $\text{V}[\text{TCNE}]_x$  magnets, however, the ligands are not only mediators of exchange effects, but also direct actors, as net spin carriers.

To facilitate the discussion, we make use of the symmetry notations for an idealized local  $O_h$  point group, as customary in coordination chemistry of hexa-coordinated complexes, even though the symmetry elements are only approximate. The vanadium(II) ion in an octahedral environment has each of the three  $t_{2g}$  orbitals singly occupied and the two  $e_g$  orbitals

empty, whereas the unpaired electron on [TCNE] is delocalized over the  $\pi^*$  orbital.

We turn again to the analysis of the canonical orbitals, optimized by CASSCF calculations on the TCNE-V-TCNE trinuclear model systems (see Figure 7.19) to better understand the magnetic interactions in V[TCNE]. Examining the results of the calculations on both di- and trinuclear model systems, as reported in Tables 7.1 and 7.2, respectively, we note that, regardless of the method used, all  $J$  values are systematically negative and, within each type of calculation, relatively close in value, indicating strong anti-FM interactions. Looking at Figure 7.19, we see that, regardless of the choice of directions, the overlap of the  $d$  orbitals on  $V^{II}$  and the  $\pi^*$  orbitals on the [TCNE] anion is strong for all HOMOs. In fact, all the HOMOs have a mixed,  $3d-\pi^*$  character, being delocalized and percolating through the whole system. Therefore, the main cause of the strong V-[TCNE] anti-FM interaction is the kinetic exchange through highly overlapping  $t_{2g}$  and  $\pi^*$  orbitals.

Further examination of the exchange parameters shows that the lowest absolute value of the  $J_a$  parameter, recorded for the fragment along the  $a$  axis, may be correlated with slightly longer  $V^{IV}N$  bond in this direction. It is known that exchange constants vanish extremely rapidly with increasing separation between spin centers, the  $r^{-n}$ , with  $n = 10$  or 12, behavior being proposed long ago [101–103].

For the  $b$  and  $c$  directions, with similar metal-ligand bond lengths, the DFT and MRPT2 calculations lead to  $|J_b|$  weaker than  $|J_c|$ , contrasting with the CASSCF results. One cause for the differentiation may be related to the  $V^{IV}N^oC$  bond angles. Along the  $b$  direction, we found a VNC bond angle closer to  $180^\circ$ , ensuring the best  $\sigma-\pi$  separation and the maximal  $d(\pi)-p(\pi)$  overlap, which strengthens the anti-FM contributions. On the other hand, for the tetra-connected ligand ( $\mu_4$ -TCNE), the proximity to four  $V^{II}$  ions may lead to an increased spin polarization of the cyanocarbon bridge, an effect more easily seen in the perturbational calculations.

The orbitals for the symmetric trinuclear model systems presented in Figure 7.20 illustrate that, out of the three  $t_{2g}$  orbitals, only one, the HOMO, overlaps with the  $p^*$  of the radicals. In contrast, the HOMO-1 and HOMO-2, with different  $t_{2g}$  character, are well localized on the metal ion. These two states can be involved mostly in potential exchange, leading to the parallel alignment of the spins on the metal. The contribution of the potential exchange to the overall superexchange,  $J$ , between  $V^{II}$  and [TCNE] is relatively small, only a partial compensation of the kinetic exchange. The last two orbitals are one located mostly on the organic ligands, HOMO-3, with no significant overlap, leading to weak potential exchange, and the other

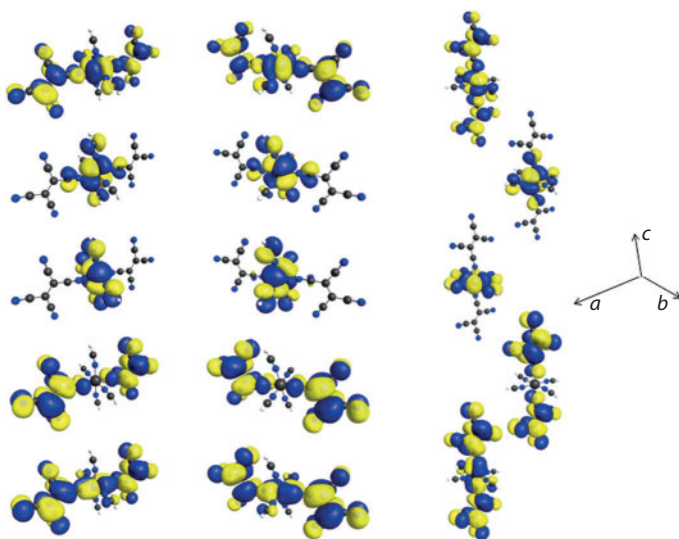


**Figure 7.20** Orbital shapes drawn at  $0.01 \text{ e/bohr}^3$  of the highest five singly occupied optimized MCSCF orbitals resulting from the CASSCF(9,9) calculations of the various symmetric trinuclears:  $[\text{TCNE}](a)\text{-V-}[\text{TCNE}](a)$  (left),  $[\text{TCNE}](b)\text{-V-}[\text{TCNE}](b)$  (center), and  $[\text{TCNE}](c)\text{-V-}[\text{TCNE}](c)$  (right). From top to bottom, displayed are the HOMO to HOMO-4, for each symmetric trinuclear system. From Ref. [56].

delocalized over the entire system, with possibilities for strong kinetic exchange.

In the case of the asymmetric trinuclears (see Figure 7.21), two  $t_{2g}$  orbitals, contributing to the HOMO and the HOMO-1, overlap with the  $p^*$  of the radicals and participate in kinetic exchange. In contrast, the HOMO-2 are well localized on the metal ion, being involved mostly in potential exchange. The last two orbitals have mixed  $t_{2g}$  and  $p^*$  character and contribute to the anti-FM coupling through kinetic exchange.

So far, we focused solely on the nearest-neighbor interaction,  $J$ , between  $\text{V}^{II}$  and  $[\text{TCNE}]$ . As we have already discussed, the next-nearest-neighbor TCNE...TCNE interaction,  $j$ , is about five times smaller. However, a discussion of the sign and magnitude is still important also for  $j$ . First of all, a more careful analysis of the data reported in Table 7.2 shows that in the case of the next-nearest-neighbor interaction the values obtained by DFT, CASSCF, and MRPT2 do not follow the same regularities observed for the nearest-neighbor coupling. For instance, the strongest  $j$  coupling is  $j_{ab}$  for DFT and CASSCF and  $j_{ac}$  for MRPT2 calculations, all three values being negative. The next strongest interaction is  $j_{bb}$  for DFT,  $j_{ac}$  for CASSCF, and

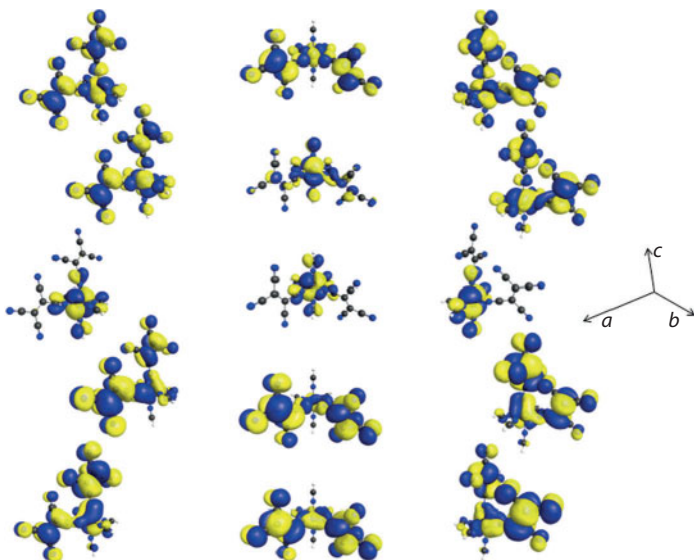


**Figure 7.21** Orbital shapes drawn at  $0.01 \text{ e/bohr}^3$  of the highest five singly occupied optimized MCSCF orbitals resulting from the CASSCF(9,9) calculations of the various asymmetric trinuclears: [TCNE](a)-V-[TCNE](c) (left), [TCNE](a)-V-[TCNE](b) (center), and [TCNE](b)-V-[TCNE](c) (right). From top to bottom, displayed are the HOMO to HOMO-4, for each asymmetric trinuclear system. From Ref. [56].

$j_{aa}$  for MRPT2, and the signs differ from one to the other. These apparently scattered values are more difficult to describe.

Worth noticing is that all  $js$  provided by DFT calculations are negative, which raises doubts that this method may systematically give exaggerated weight to the anti-FM interactions. In contrast, the results of CASSCF and MRPT2 calculations lead to four positive constants out of the total of six, which is more in line with our expectations for the [TCNE]...[TCNE] interactions. For this reason, in the following, we will focus on explaining the results of the multiconfigurational calculations

Looking at Figure 7.20, we note that for the symmetric trinuclears, the interaction channels are through spin polarization (exchange between one spin and the spin polarization of its neighbor) [58]. The strong kinetic exchange between [TCNE] and  $\text{V}^{II}$  and then between the metal ion and the next [TCNE] forces parallel orientation of the two spins on the ligands. Moreover, examining Figure 7.14c, the double excitation shown indicates the possibility for parallel spin orientation of the ligands through the polarization of the metal ion. This effect is revealed by the positive  $j_{aa}$ ,  $j_{bb}$ , and  $j_{cc}$  resulting from MRPT2 calculations, as perturbational methods take into

account such two excitation processes more so than other computational techniques.

In the case of the asymmetric trinuclears, we start with the  $j_{ac}$ , which registers the largest MRPT2 value. We note that the two [TCNE] radicals are in the same plane and the chance for exchange correlation is larger. The large orbital overlap seen in most MOs in Figure 7.21, favors for the *ac* trinuclear the double excitations of the spins, including the ligand to metal transfers, as illustrated in Figure 7.14d and e. The consequence is an antiparallel spin alignment, as indicated by the negative value of  $j_{ac}$ . The electron transfers are possible to a smaller extent in the case of the *ab* and *bc* trinuclears, where the ligands are no longer coplanar. On the contrary, the orientation approaching orthogonality hinders the electron transfer and favors potential exchange, leading also to some FM contributions. Under these circumstances,  $j_{ab}$  and  $j_{bc}$  show weak anti-FM and FM interactions, respectively.

In summary, adapting the method of counting the superexchange pathways [7] we find for all the symmetric trinuclears two very strong anti-FM channels (the HOMO and the HOMO-4) and three weak FM routes. In the case of the asymmetric trinuclears, there are four strong kinetic exchange pathways and only one weak potential exchange channel. Consequently, keeping in mind that the kinetic exchange is stronger by more than an order of magnitude than the potential exchange [58], our calculations indicate the clear dominance of the anti-FM interactions, which lead to antiparallel coupling between the spins on the vanadium(II) ion and the [TCNE] radical and an overall ferrimagnetic behavior, as observed experimentally.

#### 7.4.7 Role of the Transition Metal Ion

For comparison, we also analyze the corresponding manganese-based material, performing multiconfiguration calculations on Mn[TCNE]<sub>2</sub> fragments, to better understand the role played by the transition metal ion in the onset of magnetic ordering at high temperatures [104]. CASSCF calculations revealed the anti-FM nature of the Mn-[TCNE] interaction and lead to systematically smaller values of the exchange coupling parameters, as expected given the smaller experimental critical temperature,  $T_c \sim 75$  K for Mn[TCNE]<sub>2</sub> [38], compared to  $T_c \sim 370$  K for V[TCNE]<sub>2</sub> [20]. For Mn-TCNE dinuclears, our CASSCF(8,7) calculations, with the active space made of HOMO (doubly occupied) and SOMO from TCNE and  $d^5$  shell on Mn<sup>II</sup>, lead to exchange coupling varying between -81.5 and -69.6 K, sensibly smaller than for the V-TCNE analogues. For the TCNE-Mn-TCNE symmetrical trinuclears the CASSCF(11,9) simulations (active

space compatible with the  $2'(\text{HOMO}+\text{SOMO})$  from TCNE fragments and  $d^5$  from Mn<sup>II</sup>) provided values between  $-79.1$  and  $-59.5$  K [104].

In the case of the TCNE(*a*)–Mn–TCNE(*a*) system, the HOMO and the HOMO-1 are spin up and have strong  $3d$  character ( $e_g$ -type components), being well localized on the metal ion (see Figure 7.22). The following lower three orbitals are also spin up, corresponding to the  $t_{2g}$  symmetry, as in the case of vanadium. The HOMO-2 of the manganese trinuclears resembles very well with the HOMO of the vanadium analogue, being clearly delocalized. The lowest two MOs displayed in Figure 7.22 have  $\pi^*$  nature and are spin down orbitals, similar also to the vanadium congener [104].

The occupation of the  $e_g$  orbitals in the case of Mn<sup>II</sup>, in comparison with V<sup>II</sup>, where these functions are not occupied (or very weak population in CASSCF respects), brings FM pathways to the overall Mn–TCNE exchange. The positive terms are smaller than the large negative contributions due to the  $t_{2g}$  subsystem, which subsists in the Mn<sup>II</sup> system too, the overall balance being an effectively weaker antiferromagnetism [104], leading to a lower  $T_c$  for the Mn[TCNE]<sub>x</sub> system, in agreement with experimental observations [38].

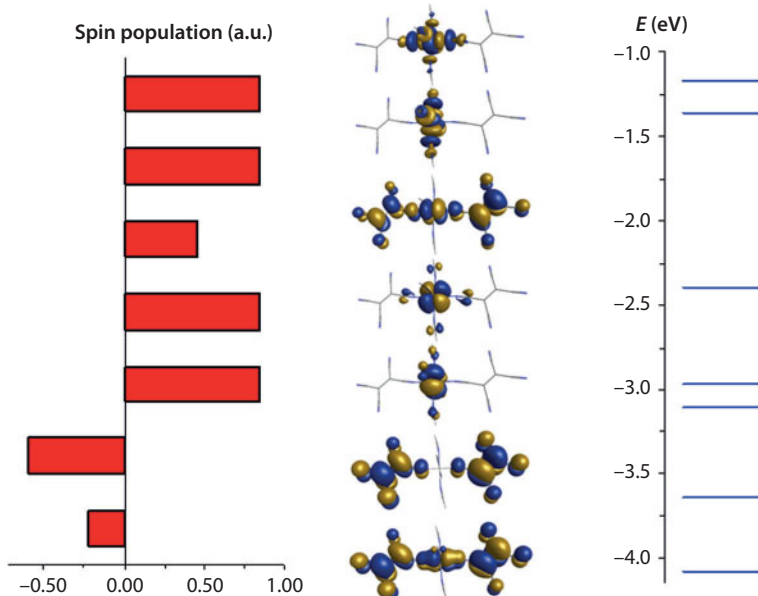


**Figure 7.22** Spin population (left), orbital shapes drawn at  $0.015 \text{ e}/\text{bohr}^3$  (center) and energies (right side) of selected canonical orbitals from the CASSCF(11, 9) calculations of the TCNE(*a*)–Mn–TCNE(*a*) trinuclear.

In summary, adapting the method of counting the orbital pathways [100], we found in the case of the TCNE(*a*)–V–TCNE(*a*) trinuclear that the HOMO is a delocalized orbital with strong 3d–π\* overlap and, consequently, strong anti-FM coupling. The next lower two molecular orbitals (HOMO-1 and HOMO-2) are localized, showing 3d–π\* orbital orthogonality against the considered TCNE spin carriers and therefore a weak FM contribution. In contrast, for the TCNE(*a*)–Mn–TCNE(*a*) trinuclear, we found that the HOMO is well localized and that there are three more orbital pathways for FM coupling, counterbalancing in part the single existing strong anti-FM pathway (HOMO-2). Therefore, a key factor determining the astonishing properties of V[TCNE]<sub>2</sub> consists the delocalized nature of the highest-occupied state and the smaller number of the FM orbital pathways. For Mn<sup>II</sup> the two extra electrons help in rising the  $T_c$  due to the larger value of the spin, but hinder through the lower overall exchange coupling due to the weak overlap of the HOMO and more numerous FM interaction pathways.

At the end of this section, it is worth presenting preliminary results of some unpublished work [104] which is focused on the role of the transition metal ion. CASSCF and BS-DFT calculations on the symmetrical M-[TCNE]–M trinuclears, with M = V, Fe, and Mn have been performed and the results are shown in Figure 7.23 and Table 7.3.

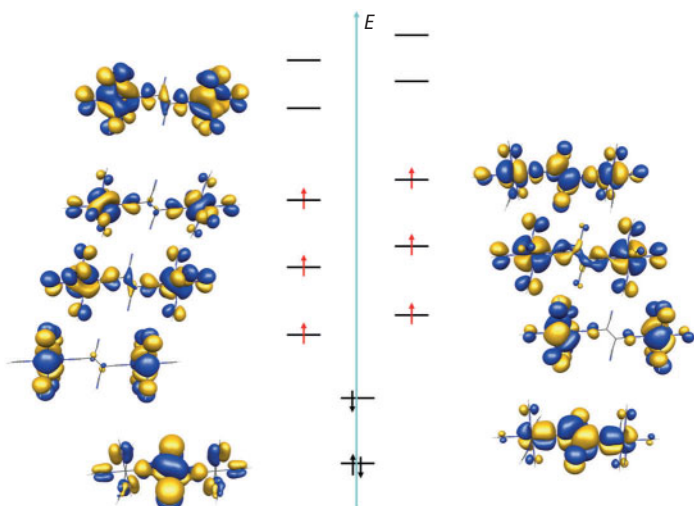


**Figure 7.23** Orbital shapes drawn at 0.015 e/bohr<sup>3</sup> of selected canonical orbitals from the CASSCF(9,11) calculations of the V-TCNE-V trinuclear, represented in the order of increasing energy.

**Table 7.3** Calculated exchange parameters determined for M-[TCNE]-M trinuclears, based on fitting of the BS-DFT values, using the AP approach [104].

Trinuclear system	$j$ (K)	$J$ (K)	$T_c$ (K)
V-[TCNE]-V	-5.06	-391.57	370
Mn-[TCNE]-Mn	-0.56	-75.96	75
Fe-[TCNE]-Fe	1.73	-224.40	95

For comparison, the critical temperatures are also presented based on values reported in Refs [20, 38, 39].

The key wavefunctions obtained from CASSCF(9,11) calculations of V-[TCNE]-V trinuclears are illustrated in Figure 7.23 [104]. The HOMO of the trinuclear model system is spin-up and has a mixed,  $3d-\pi^*$  character, being delocalized over the whole system. In contrast, the electron density of HOMO-1 to HOMO-5 wavefunctions, all spin-up, have mostly  $3d$  character and being strongly localized on the metal ion. In contrast, HOMO-6 has mixed character, with strong contribution from the  $\pi^*$  of TCNE, and is spin-down. HOMO-7 display high electron density on the TCNE and the ligands, with bonding,  $\pi$ , character.

The values of the exchange coupling constants shown in Table 7.3 are well correlated with the experimentally determined critical temperatures for magnetic ordering. The high  $T_c$  obtained for the vanadium(II) ion can be intuitively understood in terms of the delocalized nature of the highest-occupied state (strong kinetic exchange) and the small number of FM orbital pathways (weak potential exchange). Although they increase the total spin, the extra electrons in the Mn and Fe-based compounds hinder through the lower orbital overlap in the HOMO (lower kinetic exchange) and more numerous FM interaction pathways (larger potential exchange).

In addition to the work reported here, BS-DFT calculations of V-[TCNE]-M systems are underway to better understand the weak dependence on composition of the critical temperature of the  $V_xM_{1-x}[\text{TCNE}]_2 \cdot y(\text{CH}_2\text{Cl}_2)$  solid solutions [104].

## 7.5 Magnetic Anisotropy

### 7.5.1 Anisotropy in Pure and Disordered Magnets

The SIA arises if the symmetry of the environment is lower than cubic [2, 57]. In second order of perturbation theory, the additional spin-orbit

(SO) interaction leads to a zero-field splitting matrix which has different elements, even in the diagonal form. In the diagonal basis one gets a spin Hamiltonian that describes the SIA [105, 106]:

$$\hat{H}_{\text{SIA}} = D \left( S_z^2 - \frac{1}{3} S(S+1) \right) + E(S_x^2 - S_y^2) \quad (7.11)$$

If the environment is axially symmetric, than  $E = 0$  and the SIA reduces to  $\hat{H}_{\text{SIA}} = DS_z^2$  [105]. The anisotropy contribution to the spin Hamiltonian is related to the fact that, in the absence of an applied magnetic field the spins tend to orient along preferential directions, induced by the environment through the crystal field. In most cases of practical interest, the transition metal ions present in molecule-based magnets display some distortions from the ideal symmetry, which causes some anisotropy to arise [106]. The SIA constant,  $D$ , is proportional to the square of the SO coupling constant (which has typical values of the order of  $10^2 \text{ cm}^{-1}$ ) and inverse proportional to the crystal field splitting ( $\sim 10^4 \text{ cm}^{-1}$ ). Consequently,  $D$  is of the order of  $1 \text{ cm}^{-1}$  or even smaller for many transition metal ion systems [105, 106].

When combined with the Heisenberg exchange, the SIA can favor, in its two limiting cases, either Ising ( $D \rightarrow -\infty$ ) or XY ( $D \rightarrow \infty$ ) anisotropy of the spin systems. A Heisenberg spin is isotropic, such that the spin can be imagined like a classical vector that can point in any direction on a sphere, the spin-dimensionality being  $n = 3$ . In contrast, an XY spin can point anywhere on a circle ( $n = 2$ ) and an Ising spin can point along a single given direction either up or down ( $n = 1$ ) [2, 107].

Disorder can be quenched or annealed [2, 108–110]. Disorder is quenched in the magnetic systems in which the spatial distribution of magnetic exchange and/or anisotropy is frozen in, due to fixed magnetic moments. Disorder is considered annealed if the magnetic ions can diffuse in the solid and change the distribution of exchange and/or anisotropy. Experimentally, the main feature of the dynamic behavior of systems with disorder is the slower rate of relaxation processes. The thermodynamic equilibrium is regained very quickly after the perturbation is removed in pure magnetic systems. Consequently, even at phase transitions when the relaxation times are the largest, one can ignore nonequilibrium effects [110]. In contrast, in random magnetic systems, the relaxation is hindered by disorder and the evolution back to equilibrium is slower [110].

A magnetic system is frustrated if it cannot minimize the energy of each spin pair in the network, simultaneously [111]. Frustration is generated by competing interactions (competing FM and anti-FM interactions or competing nearest-neighbor and next-nearest-neighbor interactions, see

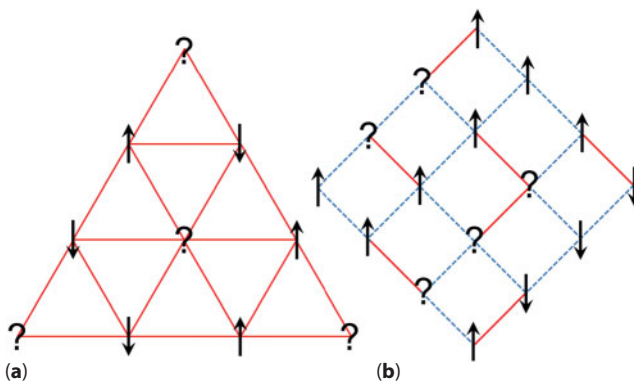


**Figure 7.24** Geometric frustration in Ising antiferromagnets on a triangular lattice (a) and random frustration in a random exchange Ising system on square lattice (b). The lines between adjacent spins are continuous for anti-FM exchange and dashed for FM exchange. The question marks suggest that those spins cannot minimize simultaneously the interactions with all the nearest neighbors.

Figure 7.24b) or induced by the lattice topology (e.g. triangular, kagomé, and pyrochlore lattices with anti-FM nearest-neighbor interactions, see Figure 7.24a) [112].

The dilute magnets [110] are systems with random exchange but with no frustration (see Figure 7.25). From a theoretical point of view, the dilute ferromagnet can be modeled by a random exchange coupling, such that the interaction varies only in strength, but not in sign. The equilibrium behavior of dilute ferromagnets is qualitatively the same as that of pure systems [110]. The dynamic properties of unfrustrated disordered systems are similar to the pure ones; however, the domain wall pinning at the disordered sites causes slower relaxation [113].

Spin glasses [108, 109, 114] are magnetic systems characterized by a random, yet cooperative freezing of spins below a well-defined temperature. Theoretically, a spin glass is a frustrated random exchange system [115, 116]. Unlike the dilute disordered systems discussed above, where the exchange was random in value but of the same sign, frustrated random exchange systems have both FM and anti-FM interactions. Such systems are described by the Hamiltonian:

$$\hat{H}_{SG} = -2 \sum_{i < j} J_{ij} \mathbf{S}_i \cdot \mathbf{S}_j, \quad (7.12)$$

where the exchange constants have both positive and negative values. For instance, one simple implementation of this model considers for

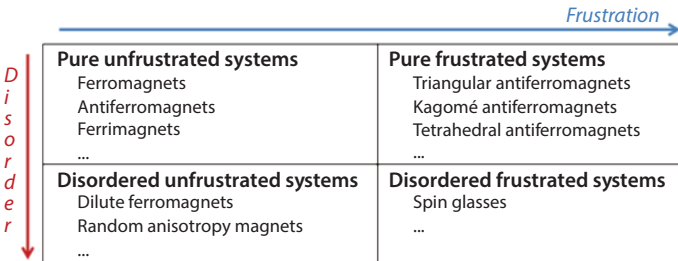


**Figure 7.25** Diagram illustrating a classification of disordered magnets based on both frustration and degree of disorder. For details see Ref. [2].

$J_{ij}$  only two values,  $\pm J_0$ , whereas the typical continuous distribution is a Gaussian centered in origin ( $J = 0$ ) [109]. The static response of a spin glass is dependent on the magnetic history, with different field-cooled and zero-field-cooled magnetization curves [108, 109]. The dynamics of the ac susceptibility close to the critical temperature are very slow. Due to the strong randomness present in the system, the domain wall has a fractal shape and is pinned longer and more often, causing strong irreversibilities in the magnetic behavior [117]. One indicator of such irreversibilities is the rough energy landscape [118].

The random anisotropy magnets (RAM) are systems with uniform exchange, while some kind of anisotropy is randomly distributed, determining the spins to orient along directions that vary randomly from site to site. The main model studied is the random uniaxial anisotropy model [119–121]:

$$\hat{H}_{RAM} = -2J \sum_{i < j} \mathbf{S}_i \cdot \mathbf{S}_j + D_r \sum_i (\hat{\mathbf{n}}_i \cdot \mathbf{S}_i)^2 + D_c \sum_i (\hat{\mathbf{N}} \cdot \mathbf{S}_i)^2 \quad (7.13)$$

The first term is the Heisenberg exchange of strength  $J$ , the second is a random uniaxial anisotropy term of strength  $D_r$ , and local orientation  $\hat{\mathbf{n}}_i$ , the third is a coherent (uniform, nonrandom) uniaxial anisotropy term of strength  $D_c$  and fixed orientation,  $\hat{\mathbf{N}}$ .

In the case of such systems, there is a competition between two energies: the exchange and the anisotropy. The random anisotropy, no matter how small, destroys the long-range FM order for systems with magnetic lattice dimensionality of three or less [122]. The random anisotropy model leads, depending on the strength of the anisotropy and of the external magnetic field, to various magnetic regimes, like speromagnet, correlated speromagnet, ferromagnet with wandering axis, etc. [123, 124]. We note that, at some point, similar terminology (in particular ‘spin glasses’) was

used for different types of systems. To avoid any confusion, the notion of a ‘spin glass’ is used in connection to the random frustrated exchange model, whereas ‘speromagnet’ and ‘correlated speromagnet’ are used regarding the states of random anisotropy systems [107, 109, 125].

When the random anisotropy is large compared to exchange and the coherent anisotropy is negligible, each spin tends to orient along the anisotropy axis at its site, the collective behavior being a secondary phenomenon. The resulting speromagnetic state [107, 123, 124] is described by only short-range FM order and the spin orientation may resemble that of a spin glass. When the random anisotropy is weak (and any uniform anisotropy and/or applied field are negligible), the system behaves cooperatively; however, it has no net magnetization [121]. The local FM magnetization changes direction significantly at distances on the order of the finite FM correlation length, leading to a correlated speromagnetic state [124].

In the presence of a moderate applied field, a magnetic moment is produced, leading to a field-induced new regime, called ferromagnet with wandering axis [123] or asperomagnet [124]. In the limit of high applied magnetic fields, the noncollinear structure aligns even further toward the applied magnetic field, the random anisotropy being able only to slightly tilt the spins from the direction of the applied field. A coherent uniaxial anisotropy can have the effect of an applied field, leading to either one of the states mentioned above, depending on its strength [123].

In all of the previous discussion of terminology, we assumed a FM exchange interaction between spins [2, 57]. If the exchange coupling constant is negative, in the case of two-subnetwork magnetic structures, the terminology changes accordingly. Continuing the parallel between ferro- and ferrimagnetism, in the case of random systems with strong anisotropy we contrast spero- and sperimagnetism [107, 124] as illustrated in Figure 7.26.

The term sperimagnet refers to a random ferrimagnet with strong anisotropy, a system with two subnetworks of spins, such that the moments

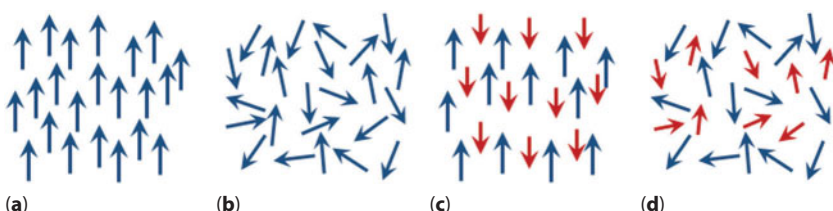


**Figure 7.26** Schematic representation of spin configurations in some disordered magnets: (a) dilute ferromagnet, (b) speromagnet, (c) dilute ferrimagnet, and (d) sperimagnet. For details, see Refs [2, 57, 107].

of one or both subnetworks are frozen in random orientations. Continuing the analogy, when the random anisotropy is weak compared to the exchange interaction, the system has no net magnetization but behaves cooperatively over larger distances, leading to a ‘correlated sperimagnetic’ state [2, 57].

### 7.5.2 Applicability of the Spin Glass Model

The results of DFT calculations providing the energy landscape due to various configurations of the TCNE ligand were presented in Section 7.3. In correspondence to the energy of the low-spin state,  $E_{LS}$ , shown in Figure 7.13, the magnetic exchange coupling constant,  $J$ , as a function of the dihedral angle,  $\psi$ , (which defines the rotation of the plane of the bi-connected TCNE around the line connecting the N-atobound to V<sup>II</sup>), is displayed in Figure 7.27. The exchange coupling constant was calculated following the BS-DFT approach with PBCs [74], based on a simple Ising Hamiltonian, also used for other TCNE-based systems [77]. The energy of the Ising spin system, assuming, regardless of the lattice direction, the same exchange coupling between V(II) and [TCNE], for the HS and BS states, is [56, 57]

$$E_{(\text{HS}/\text{BS})} = (+/-) 2 \cdot 3 \cdot (-2J) S_{z,V} \cdot S_{z,\text{TCNE}}. \quad (7.14)$$

A factor of 2 comes from the two V<sup>II</sup>–[TCNE] interactions per unit cell, a factor of 3 comes from the summation over the three crystallographic

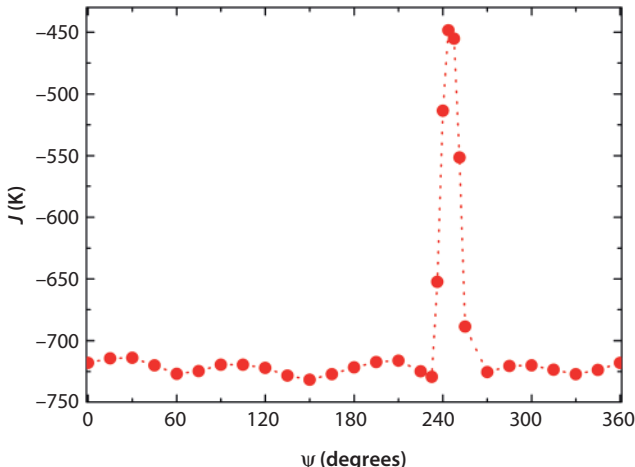


**Figure 7.27** Exchange coupling constant,  $J$ , as a function of  $\psi$ , determined for V[TCNE]<sub>2</sub> model structures by the BS-DFT approach through band structure calculations. From Ref. [57].

directions and the other factor of 2 comes from the expression of the Heisenberg interaction. Consequently, the magnetic exchange interaction strength can be determined based on the expression (7.4), where the energy difference in the numerator is between the BS and the HS states, 1/24 factor includes a 1/6 factor to account for the double counting when considering the PBCs [57].

The exchange constant is negative for all angles, indicating ferrimagnetic spin alignment of the spin  $S_v = 3/2$  on vanadium(II) with respect to the spin  $S_{\text{TCNE}} = 1/2$  on each of the two TCNEs. The absolute strengths of over 700 K, consistent with previous calculations [56], are significantly larger than the values expected given the critical temperature of 370 K. Such overestimations were found for other TCNE-based molecular magnets [79].

Regardless of the TCNE orientation, the exchange is always negative. With only anti-FM spin coupling, in the absence of competing exchange interactions, the applicability of the spin glass/random exchange model [109] is highly unlikely, in agreement with the experimental evidence [30–32].

### 7.5.3 Uniform and Random Magnetic Anisotropy in $\text{V}[\text{TCNE}]_x$

The magnetic anisotropy is caused by the asymmetry of the immediate coordination environment, through mechanisms interplaying the ligand field (LF) splitting and the SO coupling. The ground state of the V(II)  $d^3$  ion in an octahedral field is  ${}^4A_{2g}$ , and the excited states are lying higher in energy by amounts much larger than the SO coupling [106, 126]. The LF splitting parameter  $10Dq$  can be extracted [106] as the gap between the  ${}^4A_{2g}$  ground state and the first excited multiplet,  ${}^4T_{2g}$ . In lower symmetry, a conventional measure of the  $10Dq$  parameter can be obtained as the gap between the ground state and the average of the first three excited states, taken as a barycenter of the parent  $T_{2g}$  level (see Figure 7.28). In a distorted octahedral environment, the spin degeneracy of the  ${}^4A_{2g}$  state is partly removed into two doublets.

In the case of  $\text{V}[\text{TCNE}]_x$ , the magnetic anisotropy may be uniform, the same at each V(II) site, as well as random, because of lattice defects [30, 31, 39, 57]. To account for both the uniform and the random SIA, we considered [57] two simplified models, a hexa- and a penta-coordinated structure, respectively, shown in the background, in Figure 7.29. The two structures are obtained by cutting from the extended lattice  $\{\text{V}[\text{MCNE}]_6\}^{2+}$  and  $\{\text{V}[\text{MCNE}]_5\}^{2+}$  structures (MCNE = monocyanoethylene). The penta-coordinated fragments were created by removing a MCNE ligand placed along the  $c$  axis, on the assumption that the simplest and most relevant defect from the perspective of random anisotropy is the vacancy of one

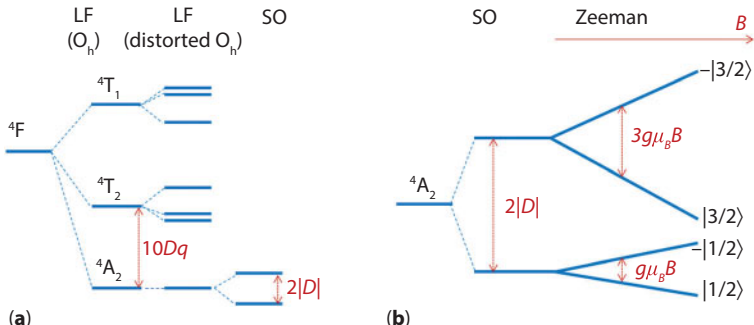


**Figure 7.28** (a) The  $^4F$  state is split by the octahedral LF into  $A_2$ ,  $T_1$  and  $T_2$  quartet states and distortions lead to further splittings. SO interactions in second order partially remove the degeneracy of the  $^4A_2$  leading to two Kramers' doublets. (b) Zeeman interactions cause a linear response to the applied field. From Ref. [57].

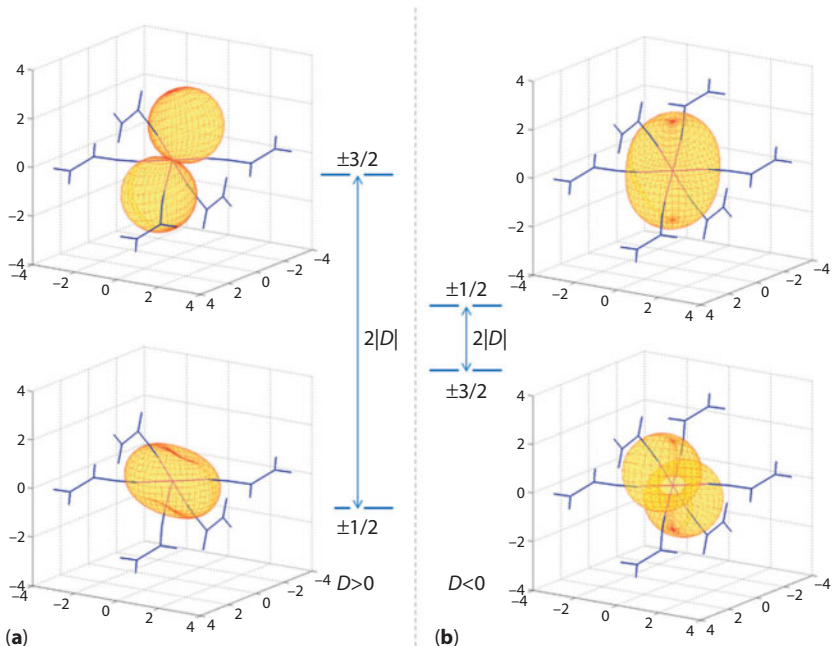


**Figure 7.29** Polar diagrams of the state-specific magnetization functions, for (a)  $\{V[MCNE]_5\}^{2+}$  and (b)  $\{V[MCNE]_6\}^{2+}$ , and the corresponding ZFS schemes, obtained via CASSCF+SO calculations. The  $M(\theta, \varphi)$  functions are represented in Cartesian frames, in Bohr magneton units. The molecular skeleton is immersed with arbitrary scaling. From Ref. [57].

TCNE ligand. Such vacancies occur in the trend of the system to achieve a nonchiral bulk status on the expense of local shifts resulting from the mutual sliding of planar substructure fragments, as already discussed in Section 7.3.

The CASSCF(3,5) calculations [57] considered 3 electrons in 5 orbitals, corresponding to the  $d^3$  configuration of V(II). With state averaging on the seven levels originating from the LF split of the  ${}^4F$  multiplet, we obtained for the  $10Dq$  parameter values of about  $11,900\text{ cm}^{-1}$  and  $18,875\text{ cm}^{-1}$  for the  $\{\text{V}[\text{MCNE}]_5\}^{2+}$  and  $\{\text{V}[\text{MCNE}]_6\}^{2+}$  molecular models, respectively [57]. The  $\{\text{V}[\text{MCNE}]_6\}^{2+}$  model yielded a value relatively close to that provided by experiments, of about  $20,000\text{ cm}^{-1}$  (2.3 eV) [27].

Adding the SO perturbation to the previous CASSCF calculations, we obtained [57] a full spectrum of 28 states, due to the degeneracy of the  ${}^4F_J$  multiplet ( $3/2 \leq |J| \leq 9/2$ ). The lowest four levels of the CASSCF+SO calculations, with  $|J| = 3/2$ , are of interest for the zero-field-splitting (ZFS) calculation of the spin-quartet ground state, as they lead to the two Kramers' doublets corresponding to the  $S_z = \pm 1/2$  and  $S_z = \pm 3/2$  components.

However, the output of the *ab initio* calculation does not offer direct information about the  $S_z$  values of the lowest two doublets. To completely describe the magnetic anisotropy, we numerically calculated [57] the state-specific magnetization functions, as the derivative of the energy of each CASSCF+SO state with respect to the applied field along various directions, defined by the polar angles  $\theta$  and  $\varphi$ , following the method developed by Cimpoesu *et al.* [127–129]. The dependence on the applied field,  $\mathbf{H}$ , is achieved by additionally considering the Zeeman Hamiltonian:  $\hat{H}_z = -g\mu_B\mathbf{H}\cdot\mathbf{J}$ , where  $g$  is the Landé factor and  $\mu_B$  the Bohr magneton.

The numerical derivative of the energy with respect to the magnetic field is represented as a polar diagram (see Figure 7.29), yielding the magnetization functions of the lowest doublet states of  $\{\text{V}[\text{MCNE}]_5\}^{2+}$  and  $\{\text{V}[\text{MCNE}]_6\}^{2+}$  model structures. The polar representations help identifying the  $S_z$  components of the ZFS multiplet as the maximal radial extension has approximately the  $gS_z$  value (in Bohr magnetons) [127–129]. In Figure 7.29, the lower state of  $\{\text{V}[\text{MCNE}]_5\}^{2+}$  has the  $M(\theta, \varphi)$  representation in the shape of a torus of radius  $gS_z \approx 1$ , corresponding to the  $S_z = \pm 1/2$  components, as the Landé factor is  $g \approx 2$ . The higher doublet shows a two-lobe shape and has maximal extension of the lobes amounting to  $gS_z \approx 3$ , in line with the  $S_z = \pm 3/2$  components. In the case of  $\{\text{V}[\text{MCNE}]_6\}^{2+}$ , the ZFS pattern is reversed.

The gap between the two doublet states is  $2|D|$ , providing the ZFS (or SIA) parameter,  $D$ , [57]. The  $D$  parameter is positive when the  $\pm 1/2$  doublet lays lower, indicating XY anisotropy, and negative when the  $\pm 3/2$  doublet is the ground state, corresponding to Ising anisotropy [2, 106]. For the  $\{\text{V}[\text{MCNE}]_5\}^{2+}$  unit, the SIA is  $0.388\text{ cm}^{-1}$  (about 0.56 K), whereas for  $\{\text{V}[\text{MCNE}]_6\}^{2+}$ , it is  $-0.019\text{ cm}^{-1}$  (about -0.03 K) [57].

The small value obtained for the SIA of the  $\{V[MCNE]_6\}^{2+}$  model mimicking the bulk of the material is consistent with the small uniform Ising anisotropy proposed based on experimental data [30–32]. The  $\{V[MCNE]_5\}^{2+}$  unit obtained by removal of one ligand along the *c* axis displays XY anisotropy. We note that the removal of the ligand along the other two axes, *a* or *b*, leads to similar angular distributions of the magnetization and values of the ZFS gaps ( $\sim 0.62$  K) [57].

The values of the exchange coupling ( $|J| \sim 700$  K), compared with the SIA parameters in the case of a perfect crystal, ( $|D_c| \sim 0.03$  K), and in the presence of disorder ( $D_r \sim 0.56$  K) [57], are consistent with the criteria that validate the RAM model [119, 123]. Following the standard RAM terminology [124], we argued that  $V[TCNE]_x$  can be considered a molecule-based correlated sperimagnet, as the spins interacting anti-FM ally are located in at least two sublattices and at least one sublattice has randomly frozen orientations [57].

## 7.6 Applications of $V[TCNE]_x$

When the first room temperature molecular magnet was reported in 1991 [9], with a critical temperature of about 100 °C, when most other molecular magnets displayed  $T_c$ s below 50 K [1, 2], the discovery leads to both astonishment and controversies. The initial claims of applications in magnetic shielding [13] or other traditional magnetic devices [14] have not been fulfilled. In the case of molecule-based magnets, the presence of large molecular units leads to a low spin density, a property that makes the competition with conventional atom-based magnets extremely difficult. Instead, more recently, better methods to obtain thin layers of air-stable  $V[TCNE]_x$  together with its semiconducting properties have recommended this material for spintronic devices [16, 24].

Spintronics (spin transport electronics or spin-based electronics) is a technology that uses not just the electron charge but also the electron spin to carry information [130]. Spintronics involves the study of active control and manipulation of spin degrees of freedom in solid-state systems [131]. Spin transport differs from charge transport in that spin is a nonconserved quantity in solids due to SO and hyperfine coupling. The basic physical principle underlying the operation of spintronic devices is the generation of carrier spin polarization and then the transport of such spin-polarized carriers in semiconductors and metals [132]. Injecting, manipulating, and detecting spins in molecular systems, particularly in organic materials, are the key issues addressed by molecular spintronics [133].

The strong superexchange interactions mentioned in the previous sections lead in the case of  $V[TCNE]_x$  to highly spin-polarized bands with a relatively narrow bandwidth [24]. Another important advantage is its unique electronic structure, of half-semiconductor, that is, fully spin-polarized valence and conduction bands. Figure 7.30 shows a schematic view of the proposed spin-resolved electronic structure of  $V[TCNE]_x$  [10]. Owing to on-site Coulomb repulsion ( $U_c$ ) within  $[TCNE]^-$  radical anions (estimated to  $\sim 2$  eV [26]), the  $\pi^*$  levels of  $[TCNE]^-$  split into two sublevels, one occupied ( $\pi^*$ ) and the other empty ( $\pi^* + U_c$ ), with opposite spin polarizations [10]. The occupied  $3d$  levels of  $V^{II}$  lie inside the gap  $1.5$  eV above the  $\pi^*$  levels and  $0.5$  eV below the  $\pi^* + U_c$  levels. The temperature dependence of the conductivity in  $V[TCNE]_x$  film was well described by an Arrhenius law with an activation energy of  $\sim 0.5$  eV at room temperature [24]. Magnetic circular dichroism and spin-polarized photoemission spectroscopy in metal-[TCNE] magnets support the presence of nonoverlapping spin-polarized bands in these materials [10].

The challenge that arises regarding the use of  $V[TCNE]_x$  in spintronic devices is related to whether these materials can be incorporated into conventional structures of magnetic multilayer devices. We stated in Section 7.2 that a key moment in the understanding of the  $V[TCNE]_x$  system was the preparation in 2000 by two independent groups [19, 20] of films without any solvent, by means of low-temperature CVD. The lack of solvent molecules cause slightly increased structural order and improved magnetic

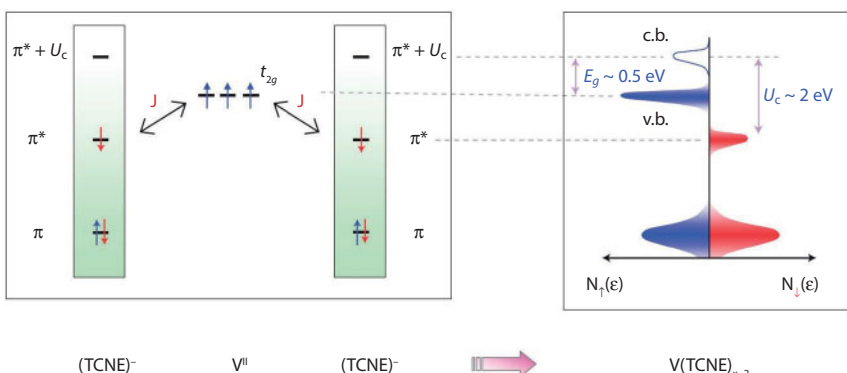


**Figure 7.30** Schematic view of a DOS in the organic-based magnetic semiconductor  $V[TCNE]_x$ . On the basis of X-ray, electron and neutron spectroscopies, it is determined that the valence band (v.b.) of  $V[TCNE]_x$  is derived from the  $3d(t_{2g})$  levels of vanadium and the conduction band (c.b.) stems from the  $\pi^* + U_c$  levels of TCNEs. The DOS in  $V[TCNE]_x$  features highly spin-polarized valence and conduction bands with the same spin orientation and nonoverlapping spin-polarized bands. From Ref. [10].

properties [21], but the remaining oxygen and the residual by-products [27, 28] degrade only a few minutes or, at most, hours in air, depending on the precursor used [19, 20]. Another important breakthrough was made in 2008 when Fahlman *et al.* reported [16] a physical vapor deposition (PVD) method resulting in films free of any residual solvent molecules and precursor-based by-products, which would retain their magnetic properties for at least several weeks in air. Instead of using precursor compounds such as  $V(C_6H_6)_2$  [9] or  $V(CO)_6$  [21], pure metal was utilized in ultra-high-vacuum conditions, which removed the oxygen from the thin films [16].

The PVD method had as a second advantage the possibility to prepare an unlimited number of other organic-based magnets in this family. Since the first report, several such studies have reported the PVD fabrication of thin films of  $M[TCNE]_x$  molecular magnets with  $M = Fe$  [134], Ni [135], and Co [136]. It was thus demonstrated that the PVD technique can facilitate the development of new organic-based magnets.

The next step, to prove that the PVD method enables the fabrication of spintronic devices, was made when Ni/V[TCNE]<sub>x</sub> interfaces were fabricated and characterized by Carlegrin *et al.* [137]. A new hybrid organic spin valve design, i.e. FM material/V[TCNE]<sub>x</sub>/FM material, was proposed (see Figure 7.31), where the semiconducting V[TCNE]<sub>x</sub> layer delivers both

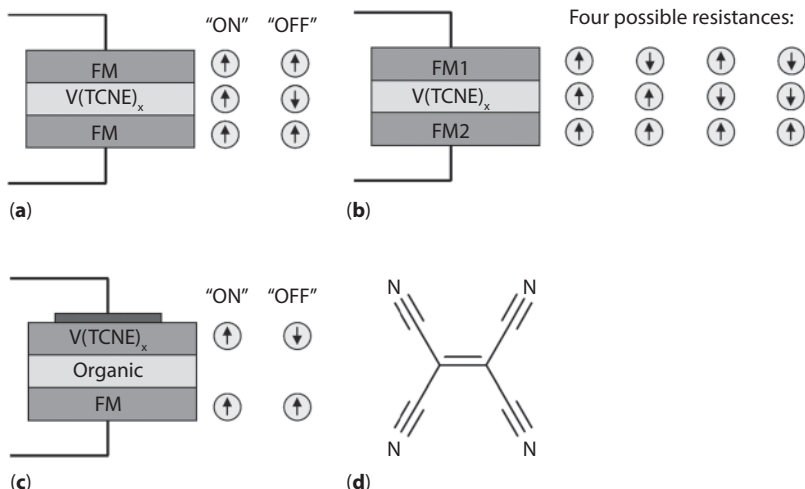


**Figure 7.31** Different spin valve designs and their possible resistances. (a)  $V[TCNE]_x$  sandwiched between two identical FM contacts. (b)  $V[TCNE]_x$  sandwiched between two different FM contacts. (c)  $V[TCNE]_x$  and a FM contact sandwiching an organic semiconductor. Since  $V[TCNE]_x$  is a semiconductor, a metallic contact on top of  $V[TCNE]_x$  is needed. (d) The chemical structure of TCNE. From Ref. [137].

spin-transporting and spin-filtering functionality. The electronic structure of the Ni/V[TCNE]<sub>x</sub> interface was investigated by means of photoelectron spectroscopy and near-edge X-ray absorption spectroscopy and the conclusion was that at the interface both the cyano groups that are not coordinated to V<sup>II</sup> and the vinyl groups participating in the reaction undergo chemical reactions with the underlying nickel atoms, whereas vanadium ions remain unaffected. The interface region was found to be fairly abrupt with no significant Ni diffusion into the V[TCNE]<sub>x</sub>, but the interface binding modifies significantly the former lowest unoccupied molecular orbital of V[TCNE]<sub>x</sub>, which could increase the electron injection barrier and degrade the magnetic network at the surface. Consequently, the need for a buffer layer between V[TCNE]<sub>x</sub> and Ni, and in extension most likely for any FM material/V[TCNE]<sub>x</sub> structure was suggested [137].

The next important development was the fabrication by Wegner *et al.* [138] of magnetic nanostructures that display variable molecule mediated spin–spin coupling using manipulation based on scanning tunneling microscopy (STM) of individual V atoms and TCNE molecules at the surface of Ag(100). Central to this technique is that V<sup>II</sup> and [TCNE]<sup>-</sup> can form a rigid chemical bond through STM manipulation.

Using a home built STM, V atoms were deposited onto the cold Ag(100) surface using electron beam evaporation. While isolated V adatoms cannot be moved on Ag(100), TCNE molecules can be slid with great precision along the surface using lateral STM manipulation and can thus be attached to individual V adatoms (see Figure 7.32). V–TCNE complexes formed in this way display an integration of V and TCNE. Once merged, the entire fused V–TCNE complex can be moved as a single unit along the surface by STM manipulation [138]. In all cases, the fused V atoms stay close to fourfold hollow sites on the Ag(100) surface, whereas the fused TCNE prefers bridge sites, thereby reducing the V–N distance. Spin-polarized DFT calculations suggested that V atoms are coupled through a TCNE molecule by a tunable magnetic interaction. These findings offered a new route for designing molecular spin nanostructures with atomic-scale precision [138].

The principal spintronics device, the ‘spin valve’, consists of two magnetic layers decoupled by a spin-transporting spacer, which allows parallel (on) and antiparallel (off) alignment of the magnetizations (spins) of the two magnetic layers [131, 133]. The device resistance then depends on the spin alignment controlled by the external magnetic field. In pursuit of semiconductor spintronics, there have been intensive efforts devoted to develop molecular semiconductors and carbon-based materials as the spin-transporting channels [132].

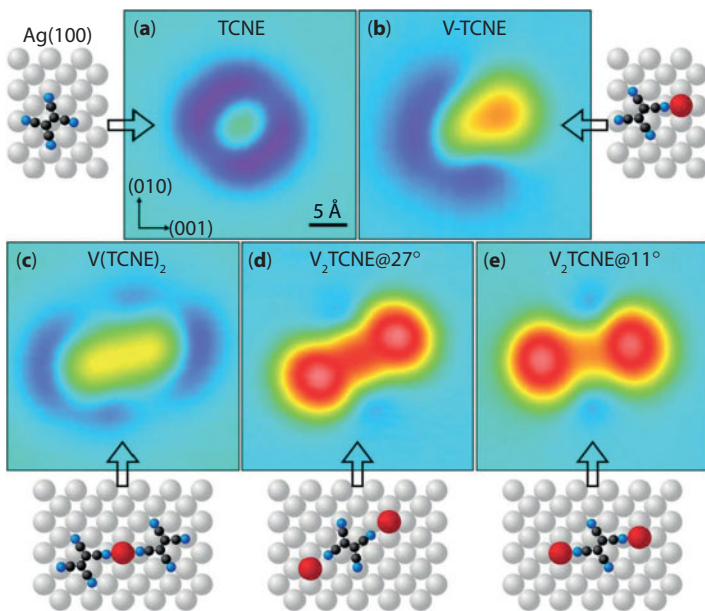


**Figure 7.32** Highly resolved STM images and structural models of (a) TCNE, (b) V-TCNE, (c) V[TCNE]<sub>x</sub>, (d) V<sub>2</sub>TCNE@27°, and (e) V<sub>2</sub>TCNE@11° on Ag(100). The models are derived from the STM images. Note that V<sub>2</sub>TCNE@11° has a shorter V-V distance compared to V2TCNE@27°. From Ref. [138].

Molecule/organic-based magnets, such as  $V[TCNE]_x$ , which allow chemical tuning of electronic and magnetic properties, are a promising new class of magnetic materials for future spintronic applications because of the coexistence of both semiconductor character and magnetic ordering at room temperature. Generally, the spins in carbon-based materials are perceived to have a long lifetime because of the extremely low SO coupling and weak hyperfine interaction [10]. The use of organic-based magnets in spintronics offers several advantages: unique spin-polarized semiconducting electronic structure, modulations of magnetic/electronic properties by chemical methodologies, and low-temperature processing. In addition, many of these materials,  $V[TCNE]_x$  included [139], exhibit magnetic bistabilities, which are often controlled by optical or magnetic excitations.

A true breakthrough in the field was accomplished by Yoo *et al.* [10] who reported in 2010 spin injection/detection using an organic-based magnetic semiconductor,  $V[TCNE]_x$ , which functions well as the FM layer in a hybrid magnetic tunnel junction device. A thin nonmagnetic organic

semiconductor layer and an epitaxial FM oxide film were employed to form a hybrid magnetic tunnel junction (see Figure 7.33) [10].

An epitaxial  $\text{La}_{2/3}\text{Sr}_{1/3}\text{MnO}_3$  (LSMO) thin film was employed as a second FM layer to detect spin-polarized tunnel current from  $\text{V}[\text{TCNE}]_x$ , as the LSMO films have been widely used in various organic/inorganic hybrid magnetic devices [140]. Three different types of barrier, a thin oxide (1.2 nm), a thin organic semiconductor layer (5 nm) and an oxide/organic semiconductor (1.2 nm/5 nm) hybrid barrier, were studied as tunneling barriers. A rubrene ( $\text{C}_{42}\text{H}_{28}$ ) small-molecule thin film was used for the organic semiconducting barrier for its highly efficient spin-polarized tunneling. A three-unit-cell layer of  $\text{LaAlO}_3$  (LAO) was used as the thin oxide barrier. Insertion of this ultrathin oxide insulating layer (1.2 nm) excluded the formation of a dipolar barrier at the metal/organic interface, to avoid interference with spin-conserved tunneling [10].

The resulting hybrid magnetic tunnel junction consisted of  $\text{V}(\text{TCNE})_x$ /rubrene/LAO/LSMO layers, such as the two FM layers of different coercivity  $H_{c1}$  and  $H_{c2}$  were decoupled by the hybrid barrier of rubrene/LAO. The 2% change in magnetoresistance demonstrates the spin-polarizing nature of the organic-based magnetic semiconductor,  $\text{V}[\text{TCNE}]_x$ , and its function as a spin injector/detector in hybrid magnetic multilayer devices [10].

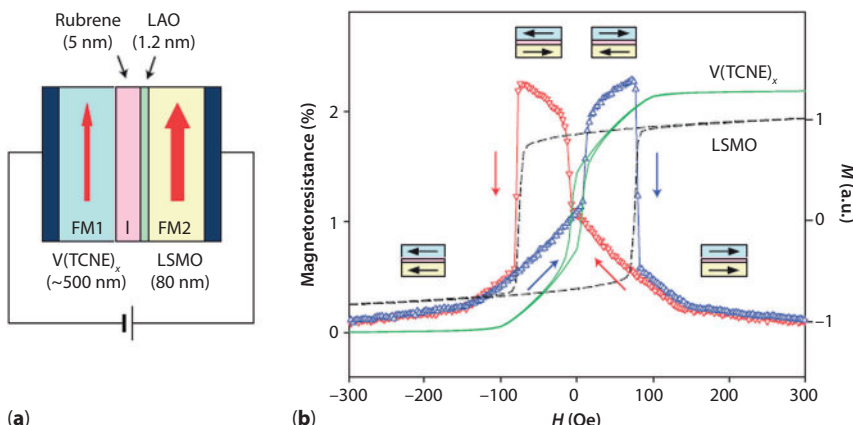


**Figure 7.33** (a) Schematic view of a hybrid magnetic tunnel junction of  $\text{V}[\text{TCNE}]_x$ /rubrene/LAO/LSMO. The two FM layers of different coercivity  $H_{c1}$  and  $H_{c2}$  are decoupled by the hybrid barrier of rubrene/LAO. (b) The magnetoresistance curves of a  $\text{V}[\text{TCNE}]_x$ /rubrene/LAO/LSMO junction measured at 100 K with a bias field of 0.5V. The line with up (down) triangles are the data collected with increasing (decreasing) field. The magnetizations of  $\text{V}(\text{TCNE})_x$  (500 nm) and LSMO (80 nm) on pseudo-cubic (001)  $\text{NdGaO}_3$  substrate are measured from individual films by SQUID magnetometry. From Ref. [10].

Extending further the study of spin valve effect in a ferromagnet/organic semiconductor/ferromagnet heterojunctions based on V[TCNE]<sub>x</sub> [141], Epstein *et al.* reported [142–144] the electrical bistability and bias-controlled spin valve effect in an organic device using rubrene, as an organic semiconductor spacer, and the half-metallic La<sub>0.7</sub>Sr<sub>0.3</sub>MnO<sub>3</sub> and Fe, as the two FM electrodes (see Figure 7.34). The epitaxial 50 nm film of LSMO was grown on lattice-matching (001) (LaAlO<sub>3</sub>)<sub>0.3</sub>(Sr<sub>2</sub>AlTaO<sub>6</sub>)<sub>0.7</sub> (LSAT) substrate by pulsed laser deposition. Three unit cells of LaAlO<sub>3</sub> (LAO) were deposited on top of LSMO to provide efficient spin injection into organic semiconductor spacer. The device showed reproducible switching between a low-impedance (ON) state and a high-impedance (OFF) state by applying different polarities of high biases. In the ON state, the device shows a spin valve effect with magnetoresistance values up to 3.75%. The observed spin valve effect disappears when the device recovers to the initial OFF state [142].

The next step was made by Li *et al.* [11] who demonstrated an all-organic-based spin valve, in which V[TCNE]<sub>x</sub> was used as both spin injector and analyzer. As shown in Figure 7.35, the overall structure of the device was, starting from the bottom: Al/V[TCNE]<sub>x</sub>/rubrene/V[TCNE]<sub>x</sub>/

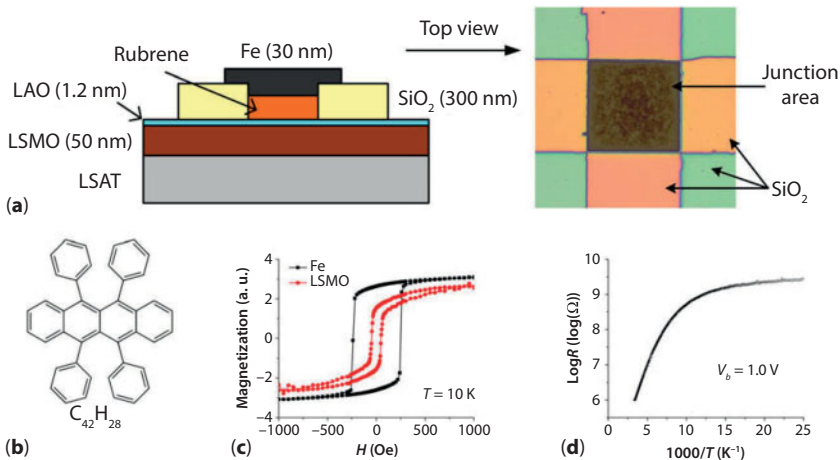


**Figure 7.34** (a) The schematic device structure. On the right side is the optical image of the cross-section. Rubrene (50 nm) is deposited in the center area of 0.2 mm by 0.2 mm surrounded by SiO<sub>2</sub>. Fe film (30 nm) will be deposited on top of the rubrene layer. (b) Chemical structure of rubrene (C<sub>42</sub>H<sub>28</sub>). (c) Magnetic hysteresis loops of LSMO (50 nm) on LSAT (0 0 1) substrate and Fe (30 nm) on glass substrate. (d) Temperature-dependent resistance (OFF state) of the LSMO (50 nm)/LAO/rubrene (50 nm)/Fe (30 nm) junction. From Ref. [142].

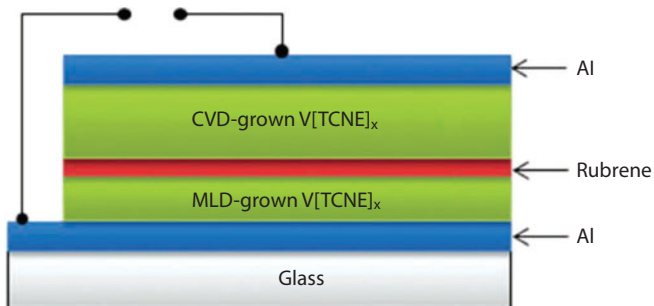


**Figure 7.35** Schematic view of an organic spin valve of Al/V[TCNE]<sub>x</sub>/rubrene/V[TCNE]<sub>x</sub>/Al. Based on Ref. [11].

Al. The V[TCNE]<sub>x</sub> films serve as two FM contacts with different coercive fields while the organic semiconductor rubrene is used as the spacer. Al (50 nm) is deposited on clean glass substrates as bottom electrode. The V[TCNE]<sub>x</sub> film grown by molecular layer deposition (MLD) [145, 146] (with a thickness of 40 layers,  $\approx$  50 nm) serves as the bottom FM layer. The 10 nm layer of rubrene (to insure the tunneling regime) is thermally evaporated on top of MLD grown V[TCNE]<sub>x</sub> using an effusion cell. The second V[TCNE]<sub>x</sub> film (300 nm) was grown by CVD as the top FM layer. Al (30 nm) is then deposited as the top electrode. The injected carriers are polarized by the first V[TCNE]<sub>x</sub> layer and then tunnel through the barrier, reaching the second V[TCNE]<sub>x</sub> which acts as the analyzer. Although negative magnetoresistance was demonstrated, the absolute magnetoresistance values remain small, optimization of the interfaces being needed to improve device performance [11].

Electrical spin injection in a hybrid organic–inorganic spin-resolved light-emitting diode (spin-LED) structure was reported by Fang *et al.* [12], opening the door to a new class of active, hybrid spintronic devices with multifunctional behavior defined by the optical, electronic, and chemical sensitivity of the organic layer. Spin-polarized carriers are extracted from a spin-polarized source, V[TCNE]<sub>x</sub>, and injected into the conduction band of the n-AlGaAs layer of an n-i-p diode with a GaAs quantum well (QW) embedded in the intrinsic region. The sign and magnitude of the spin-polarized charge injection are determined by the magnetization of the V[TCNE]<sub>x</sub> and can be analyzed through the polarization of the heavy-hole (HH) and light-hole (LH) electroluminescence from carriers that relax into the QW (see Figure 7.36). The optical polarization of the electroluminescence is directly proportional the spin-polarized current present in the V[TCNE]<sub>x</sub> [12].

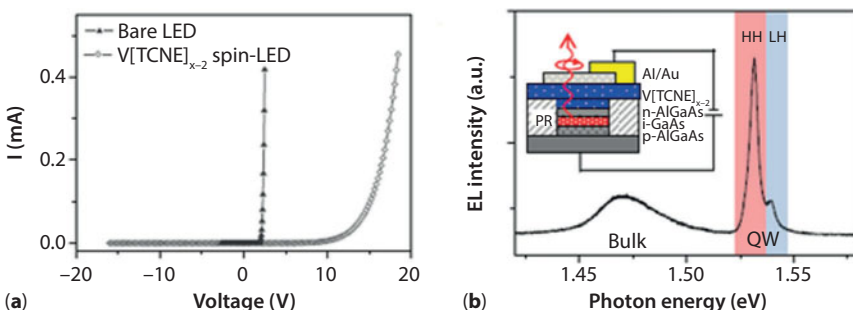


**Figure 7.36** (a) I-V curves for both bare LED (triangles) and  $V[TCNE]_x$  spin-LED (diamonds) devices at  $T = 60$  K. (b) Typical EL spectrum of a  $V[TCNE]_x$  spin-LED device ( $I = 0.5$  mA,  $V +18.5$  V) at  $T = 60$  K. The shaded areas in the spectrum indicate the region of polarization integration over the QW HH and LH peaks, respectively. Inset: A schematic of the  $V[TCNE]_x$  spin-LED device structure. From Ref. [12].

The inorganic and organic layers of the spin LED are synthesized using molecular beam epitaxy and CVD, respectively. The AlGaAs/GaAs heterostructure was grown on a p-doped GaAs (100) substrate, and the devices were fabricated using standard photolithography. The top electrical contact consists of an optically transparent aluminum layer and a high-conductivity gold layer. The measurements of the electroluminescence polarization lead to values for the injected electron spin polarization at the QW, of  $0.83 \pm 0.07\%$  at 60 K, comparable to results of similar studies performed on GaMnAs and Fe spin-LED structures [12].

## 7.7 Conclusions

In this chapter, we reviewed the recent studies on a family of room temperature molecular magnets, focusing on the theoretical explanation of the magnetic behavior and emphasizing the potential applications. Based on quantum chemical calculations, we discussed the structure, electronic spectrum, magnetic exchange couplings for nearest neighbor and next-nearest-neighbor interactions, as well as the SIA of the  $V[TCNE]_2$  system. Various numeric experiments were designed to provide answers to different questions and experimental facts. The DFT band structure calculations were valuable in retrieving a reasonable optimized lattice structure, but overestimated the value of the exchange coupling ( $|J| > 700$  K). BS-DFT calculations of finite systems cut from the ideal lattice improved the estimations (500–540 K). Multiconfigurational calculations provided values of

150–170 K calculations in the case of the CASSCF method and 330–390 K for the MRPT2 approach.

We were able to explain intuitively, the mechanism for anti-FM coupling in the  $M[TCNE]<sub>x</sub>$  family of molecular magnets, by analyzing the interplay of kinetic and potential exchange, through counting the various superexchange pathways and identifying their nature. Moreover, we clarified the influence of the transition metal ion on the strength of the exchange interaction by comparing  $V^{II}$  with  $Mn^{II}$  systems. In the latter case, the existence of two extra electrons leads to extra FM pathways, which diminish the overall strength of the overall anti-FM superexchange interactions.

CASSCF calculations for trinuclears, as well as DFT calculations for trinuclears and for extended periodic solids, showed that the HOMO exhibits a significant hybridization between  $V(3d)$  and TCNE  $\pi^*$  orbitals, in agreement with spectroscopy studies. However, the CASSCF and the DFT calculations provided opposite results for the spin of the HOMO-type function. Arguing against the reliability of the DFT results in this case, we showed that the more trustworthy CASSCF approach leads to a spin up polarization of higher molecular orbitals and to energy differences in semi-quantitative agreement with the experimental data.

By means of a CASSCF calculations on  $[V(MCNE)<sub>5</sub>]<sup>2+</sup>$  and  $[V(MCNE)<sub>6</sub>]<sup>2+</sup>$  molecular models, we obtained a LF parameter of  $18400\text{ cm}^{-1}$ , relatively close to that provided by experiments. Adding a subsequent SO treatment we also calculated the magnetic anisotropy of the system, in an attempt to explain the small uniform ZFS ( $D = -0.03\text{ K}$ ) and the random ZFS parameter ( $D_r = 0.45\text{ K}$ ). The relative values of the calculated parameters  $|J| \gg |D_r| \gg |D|$  were found to be consistent with the criteria that validate the random anisotropy magnet model proposed on experimental grounds. As the magnetic anisotropy is a key factor in achieving systems with a defined orientation of the local or bulk magnetization, our analysis offered a new insight for such structure–property correlations, by means of innovative methodologies, which provided suggestive representations of the state-specific magnetization functions.

We also reviewed the applications of these magnetic half-band semiconductors. Although the initial claims of applications in dc shielding or other traditional magnetic devices have run into difficulties due to the air sensitivity of the compound, better methods to obtain thin layers of air-stable  $V[TCNE]<sub>x</sub>$  recommended this material for spintronic devices. The separation between the electron bands responsible for magnetic ordering and conducting properties along with the interaction between these bands have stirred interest in the use of  $V[TCNE]<sub>x</sub>$  as a spin injector in various types of spin valves and in spin-polarized light-emitting devices.

One open question that has been pursued experimentally and still awaits for a theoretical answer regards the role of the cyanocarbon ligand. We mentioned the use of TCNB, TCNP, TCNQ, as well as other acceptors as building blocks for high- $T_c$  molecular magnets. Very recently, Johnston-Halperin *et al.* [147–149] have synthesized and characterized two new molecule-based magnets: vanadium[methyl tricyanoethylene carboxylate]<sub>x</sub> and vanadium[ethyl tricyanoethylene carboxylate]<sub>x</sub>, with critical temperatures of over 150 K. The fabrication of such thin films by CVD might open opportunities for spintronic applications.

Another question regards the stability of the critical temperatures to compositional changes in  $V_xM_{1-x}[TCNE]_2 \cdot y(CH_2Cl_2)$  solid solutions. An explanation for this slow variation of the  $T_c$  with  $x$  has not been offered yet, one possible way to approach the issue being by means of V-[TCNE]-M (M = Fe, Mn, Ni, etc.) DFT calculations.

Probably one of the most important questions is whether the better understanding of the interface phenomena observed in the case of the V[TCNE]<sub>x</sub> films used in spintronic applications could lead to actual commercial applications in a foreseeable future. This family of room temperature molecular magnets has proved to be very surprising, with some giant breakthroughs after years of slow accumulation. We believe that in the near future, the V[TCNE]<sub>x</sub> system will continue to stir interest from both fundamental and applied science perspectives, and we are eager to be, again, surprised.

## Acknowledgments

The authors are grateful to Dr Fanica Cimpoesu and Dr Bogdan Frecus for the fruitful collaboration that resulted in some of the work presented here. The financial support from the Romanian Ministry of Education and Research, through the CNCS-UEFISCDI research grant PN2-Idei-PCCE-239/2010, is acknowledged.

## References

1. Kahn, O., *Molecular Magnetism*, Wiley-VCH, Weinheim, 1993.
2. Girțu, M. A., Fahlman M., Hybrid organic-inorganic nanostructured magnets, in *Magnetic Nanostructures*, H.S. Nalwa, edt., American Scientific Publishers, Stevenson Ranch, California, pp. 359–433, 2009.
3. Miller, J. S., *Chem. Soc. Rev.* 40, 266, 2011.

4. Miller, J.S., *Adv. Mater.* 14, 1105, 2002.
5. Mallah, T., Thiebaut, S., Verdaguer, M., Veillet, P. *Science* 262, 1554, 1993.
6. Ferlay, S., Mallah, T., Ouahes, R., Veillet, P., Verdaguer, M. *Nature* 378, 701, 1995.
7. Verdaguer, M., Bleuzen, A., Marvaud, V., Vaissermann, J., Seuleiman, M., Desplanches, C., Scuiller, A., Train, C., Garde, R., Gelly, G., Lomenech, C., Rosenman, I., Veillet, P., Cartier, C., Villain, F. *Coord. Chem. Rev.* 190–192, 1023, 1999.
8. Miller, J. S., *Polyhedron* 28, 1596, 2009.
9. Manriquez, J. M., Yee, G. T., McLean, R. S., Epstein, A. J., Miller, J. S. *Science* 252, 1415, 1991.
10. Yoo, J.-W., Chen, C.-Y., Jang, H. W., Bark, C. W., Prigodin, V. N., Eom, C. B., Epstein, A. J., *Nat. Mat.* 9, 638, 2010.
11. Li, B., Kao, C.-Y., Yoo, J. W., Prigodin, V. N., Epstein, A. J., *Adv. Mater.* 23, 3382, 2011.
12. Fang, J., Deniz Bozdag, K., Chen, C.-Y., Truitt, P. A., Epstein, A. J., Johnston-Halperin, E., *Phys. Rev. Lett.* 106, 156602, 2011.
13. Morin, B. G., Zhou, P., Hahm, C., Epstein, A. J., *J. Appl. Phys.* 73, 5648, 1993.
14. Miller, J. S., Epstein, A. J., *Chem. Ind.* Jan 15, 49, 1996.
15. Pokhodnya, K. I., Bonner, M., Miller J. S., *Chem. Mater.* 16, 5114, 2004.
16. Carlegrim, E., Kanciurzewska, A., Nordblad, P., Fahlman, M., *Appl. Phys. Lett.* 92, 163308, 2008.
17. Miller, J. S., Epstein, A. J., *Chem. Commun.* 1319, 1998.
18. Miller, J. S., *Inorg. Chem.* 39, 4392, 2000.
19. de Caro, D., Basso-Bert, M., Sakah, J., Casellas, H., Legros, J. -P., Valade, L., Cassoux, P., *Chem. Mater.* 12, 587, 2000.
20. Pokhodnya, K. I., Epstein, A. J., Miller, J. S., *Adv. Mater.* 12, 410, 2000.
21. Pokhodnya, K.I., Pejakovic, D., Epstein, A. J., Miller, J. S., *Phys. Rev. B* 63, 174408, 2001.
22. Haskel, D., Islam, Z., Lang, J., Kmety, C., Srager, G., Pokhodnya, K. I., Epstein, A. J., Miller, J. S., *Phys. Rev. B* 70, 054422, 2004.
23. Du, G., Joo, J., Epstein, A. J., Miller J. S., *J. Appl. Phys.* 73, 6566, 1993.
24. Prigodin, V. N., Raju, N.P., Pokhodnya, K. I., Miller, J. S., Epstein, A. J., *Adv. Mater.* 14, 1230, 2002.
25. Yoo, J.-W., Edelstein, R. S., Lincoln, D. M., Raju, N. P., Xia, C., Pokhodnya, K. I., Miller, J. S., Epstein, A. J., *Phys. Rev. Lett.* 97, 247205, 2006.
26. Tengstedt, C., de Jong, M. P., Kanciurzewska, A., Carlegrim, E., Fahlman, M., *Phys. Rev. Lett.* 96, 057209, 2006.
27. de Jong, M. P., Tengstedt, C., Kanciurzewska, A., Carlegrim, E., Salaneck, W. R., Fahlman M., *Phys. Rev. B* 75, 064407, 2007.
28. Carlegrim, E., Gao, B., Kanciurzewska, A., de Jong, M. P., Wu, Z., Luo, Y., Fahlman, M. *Phys. Rev. B* 77, 054420, 2008.
29. Carlegrim, E., Kanciurzewska, A., de Jong, M.P., Tengstedt, C., Fahlman, M., *Chem. Phys. Lett.* 452, 173, 2008.

30. Zhou, P., Morin, B. G., Miller, J. S., Epstein, A. J., *Phys. Rev. B* 48, 1325, 1993.
31. Zhou, P., Long, S. M., Miller, J. S., Epstein, A. J., *Phys. Lett. A* 181, 71, 1993.
32. Yoo, J.-W., Edelstein, R.S., Lincoln, D.M., Raju, N.P., Epstein, A.J., *Phys. Rev. Lett.* 99, 157205, 2007.
33. Thorum, M.S., Pokhodnya, K.I., Miller, J.S., *Polyhedron*, 25, 1927, 2006.
34. Vickers *et al.*, *Inorg. Chem.* 43, 6414, 2004.
35. Vickers *et al.*, *J. Am. Chem. Soc.* 126, 3716, 2004.
36. Taliaferro *et al.*, *Angew. Chem. Int. Ed.* 45, 5326, 2006.
37. Harvey, M.D., Crawford, D., Yee, G.T., *Inorg. Chem.* 47, 5649, 2008.
38. Wynn, C. M., Gîrțu, M.A., Zhang, J., Miller, J. S., Epstein, A. J., *Phys. Rev. B* 58, 8508, 1998.
39. Gîrțu, M. A., Wynn, C. M., Zhang, J., Miller, J. S., Epstein, A. J., *Phys. Rev. B* 61, 492, 2000.
40. Pokhodnya, K.I., Burtman, V., Epstein, A.J., Raebiger, J.W., Miller, J.S., *Adv. Mater.* 15, 1211, 2003.
41. Pokhodnya, K.I., Vickers, E.B., Bonner, M., Epstein, A.J., Miller, J.S., *Chem. Mater.* 16, 3218, 2004.
42. Vickers, E.B., Senesi, A., Miller, J.S., *Inorg. Chim. Acta* 357, 3889, 2004.
43. Tchougréeff, A. L., Hoffmann, R., *J. Phys. Chem.* 97, 350, 1993.
44. R.G. Parr and W. Yang, *Density-Functional Theory of Atoms and Molecules*, Oxford University Press, New York, 1989.
45. Tchougréeff, A.L., Dronskowsky, R., *J. Comput. Chem.* 29, 2220, 2008.
46. Tchougréeff, A.L., Dronskowsky, R., *Int. J. Quant. Chem.* 111, 2490, 2011.
47. Her, J.-H., Stephens, P.S., Pohodnya, K.I., Bonner, M., Miller, J.S., *Angew. Chem. Int. Ed.* 46, 1521, 2007.
48. Oprea, C.I., Damian, A., Gîrțu, M.A., *AIP Conference Proceedings: Sixth International Conference of the Balkan Physical Union*, S.A. Cetin I. Hikmet, edt., AIP CP899, 716, 2007.
49. De Fusco, G. C., Pisani, L., Montanari, B., Harrison, N. M., *Phys. Rev. B* 79, 085201, 2009.
50. Cimpoesu, F., Frecus, B., Oprea, C.I., Gîrțu, M.A., *AIP Conference Proceedings: Seventh International Conference of the Balkan Physical Union*, Angelopoulos, A., Fildisis, T., edt., AIP CP1192, 2009, 1203.
51. Hibbs, W., Rittenberg, D. K., Sugiura, K.-I., Burkhardt, B. M., Morin, B. G., Arif, A. M., Liable-Sands, L., Rheingold, A. L., Sundaralingam, M., Epstein, A. J., Miller, J. S., *Inorg. Chem.* 40, 1915, 2001.
52. Wynn, C. M., Gîrțu, M. A., Brinckerhoff, W. B., Sugiura, K-I., Miller, J. S., Epstein, A., *J. Chem. Mater.* 9, 2156, 1997, Epstein, A. J., Wynn, C. M., Gîrțu, M. A., Brinckerhoff, W. B., Sugiura, K. -I., Miller, J. S., *Molec. Cryst. Liq. Cryst.* 305, 321, 1997.
53. Becke, A. D., *Phys. Rev. A* 1988, 38, 3098,
54. Lee, C., Yang, W, Parr, R. G., *Phys. Rev. B* 37, 785, 1988.
55. Jensen, F., *Introduction to Computational Chemistry*, 2nd edition, Wiley, New York, 2007.

56. Frecus, B., Oprea, C.I., Panait, Ferbinteanu, M., Cimpoesu, F., Gîrțu, M.A., *Theor. Chem. Acc.* 133, 1470, 2014.
57. Cimpoesu, F., Frecus, B., Oprea, C.I., Panait, P., Gîrțu, M.A., *Comput. Mater. Sci.* 91, 320, 2014.
58. Anderson, P.W., *Phys. Rev.* 115, 2, 1959, Anderson, P.W., *Solid State Phys.* 14, 99, 1963.
59. Neel, L., *Ann. Phys. (Paris)* 3, 137, 1948.
60. Ruiz, E., Rodriguez-Fortea A, Alvarez S, Verdaguer M., *Chem. A Eur. J.* 11, 2135, 2005.
61. Neese, F. *Coord. Chem. Rev.* 253, 526, 2009.
62. Daul, C. A., Ciofini, I., Bencini, A., in *Reviews of Modern Quantum Chemistry*, part II (Ed.: K. D. Sen), World Scientific, Singapore, 1247, 2002.
63. Noddleman, L., Peng, C. Y., Case, D. A., Mouesca, J. M. *Coord. Chem. Rev.* 144, 199, 1995.
64. Ruiz, E. *Struct. Bonding* 113, 71, 2004.
65. Nagao, H., Nishino, M., Shigeta, Y., Soda, T., Kitagawa, Y., Onishi, T., Yoshioka, Y., Yamaguchi, K. *Coord. Chem. Rev.* 198, 265, 2000.
66. Ginsberg, A. P., *J. Am. Chem. Soc.* 102, 111, 1980.
67. Noddleman, L., *J. Chem. Phys.* 74, 5737, 1981.
68. Noddleman, L., Davidson, E. R., *Chem. Phys.* 109, 131, 1985.
69. Bencini, A., Totti, F., Daul, C. A., Doclo, K., Fantucci, P., Barone, V., *Inorg. Chem.* 36, 5022, 1997.
70. Ruiz, E., Cano, J., Alvarez, S., Alemany, P., *J. Comp. Chem.* 20, 1391, 1999.
71. Yamaguchi, K., Takahara, Y., Fueno, T., in: V.H. Smith, et al. (edt.), *Applied Quantum Chemistry*, Reidel, Dordrecht, p. 155, 1986.
72. Nagao, H., Nishino, M., Shigeta, Y., Soda, T., Kitagawa, Y., Onishi, T., Yoshioka, Y., Yamaguchi, K., *Coord. Chem. Rev.* 198, 265, 2000.
73. Neese, F., *J. Phys. Chem. Solids* 65, 781, 2004.
74. Shoji, M., Koizumi, K., Kitagawa, Y., Kawakami, T., Yamanaka, S., Okumura, M., Yamaguchi, K., *Chem. Phys. Lett.* 432, 343, 2006.
75. Dai, D., Whangbo, M.-H., *J. Chem. Phys.* 118, 29, 2003.
76. Nakanishi, Y., Kitagawa, Y., Saito, T., Kataoka, Y., Matsui, T., Kawakami, K., Okumura, M., Yamaguchi, K., *Int. J. Quantum Chem.* 109, 3632, 2009.
77. Oprea, C.I., Cimpoesu, F., Panait, P., Frecuș, B., Ferbinteanu, M., Gîrțu, M.A., *Theor. Chem. Acc.* 129, 847, 2011.
78. Cimpoesu, F., Ferbinteanu, M., Frecuș, B., Gîrțu, M. A., *Polyhedron* 28, 2039, 2009.
79. Oprea, C.I., Panait, P., Cimpoesu, F., Humelnicu, I., Ferbinteanu, M., Gîrțu, M.A., *Theor. Chem. Acc.* 131, 1249, 2012.
80. Bencini, A., Totti, F., *J. Chem. Theory Comput.* 5, 144, 2009.
81. Gorelik, E. V., Ovcharenko, V. I., Baumgarten, M., *Eur. J. Inorg. Chem.* 2837, 2008.
82. Liechtenstein, A. I., Anisimov, V. I., Zaane, J., *Phys. Rev. B* 52, R5467, 1995; Anisimov, V. I., Lichtenstein, A. I., *LDA+U method: screened Coulomb*

- interaction in the mean-field approximation*, in *Strong Coulomb Correlations in Electronic Structure Calculations: Beyond the Local Density Approximation*, Anisimov, V. I., edt., Gordon and Breach Science Publishers, pp. 97–166, 2000.
83. Jensen, F. *Introduction to Quantum Chemistry*, Wiley, New York, 2002.
  84. Kambe, K., *J. Phys. Soc. Jpn.* 5, 48, 1950.
  85. Olsen, J., Yeager, D. L., Jorgensen, P., *Optimization and characterization of a MCSCF state*, in *Advances in Chemical Physics*, vol. 54, Prigogine, I., Rice, S. A., edt., Wiley Interscience, New York, pp. 1–176, 1983.
  86. Nakano H, Hirao K., *Chem. Phys. Lett.* 317, 90, 2000.
  87. Helgaker T, Jorgensen P, Olsen J., *Molecular Electronic-Structure Theory*, Wiley, New York, 2000.
  88. Hirao K., *Chem. Phys. Lett.* 190, 374, 1992.
  89. Nakano H., *J. Chem. Phys.* 99, 7983, 1993.
  90. Andersson, K., Malmqvist, P.-Å., Roos, B.O., Sadlej, A.J., Wolinski, K., *J. Phys. Chem.* 94, 5483, 1990.
  91. Andersson, K., Malmqvist, P.-Å., Roos, B.O., *J. Chem. Phys.* 96, 1218, 1992.
  92. de Graaf, C., Broer, R., Nieuwpoort, W.C., *Chem Phys Lett* 271, 372, 1997.
  93. de Graaf, C., Sousa, C., Moreira, I.P.R., Illas, F., *J Phys Chem A* 105, 11371, 2001.
  94. Munoz, D., de Graaf, C., Illas, F., *J Comput Chem* 25, 1234, 2004.
  95. Bordas, E., Caballol, R., de Graaf, C., *J Mol Struct (Theochem)* 727, 173, 2005.
  96. Queralt, N., Taratiel, D., de Graaf, C., Caballol, R., Cimiraglia, R., Angeli, C., *J Comput Chem* 29, 994, 2008.
  97. Hay, P. J., Thibeault, J. C., Hoffmann, R. *J. Am. Chem. Soc.* 97, 4884, 1975.
  98. Girerd, J. J., Journeaux, Y., Kahn, O., *Chem. Phys. Lett.* 82, 534, 1981.
  99. Ruiz, E., Rodriguez-Forteá, A., Alvarez, S., Verdauer, M., *Chem. Eur. J.* 11, 2135, 2005.
  100. Kahn, O., *Struct. Bonding* 68, 567, 1987.
  101. Bloch D., *J. Phys. Chem. Solids* 27, 881, 1963.
  102. Lowndes, D.H., Finegold, L., Rogers, R.N., Morosin, B., *Phys. Rev.* 186, 515, 1969.
  103. de Jongh, L.J., Block, R., *Physica B* 79, 568, 1975.
  104. Oprea, C.I., Trandafir, A., Frecus, B., Cimpoesu, F., Gîrțu, M.A. to be published.
  105. White, R.M., *Quantum Theory of Magnetism*, 3rd edition, Springer, Berlin, 2007.
  106. Figgis, B.N., and Hitchman, M.A., *Ligand Field Theory and Its Applications*, Wiley-VCH, New York, 2000.
  107. Coey, J.M.D., *Magnetism and Magnetic Materials*, Cambridge University Press, New York, 2009.
  108. Mydosh, J. A., *Spin Glasses: An Experimental Introduction*, Taylor and Francis, London, 1993.

109. Binder, K., Young, A.P., *Rev. Mod. Phys.* 58, 801, 1986.
110. Fisher, D. S., Grinstein, G. M., Khurana, A., *Phys. Today* 12, 56, 1988.
111. Aeppli, G., Chandra, P., *Science* 275, 177, 1997.
112. Diep, H.T., edt., *Magnetic Systems with Competing Interactions*, World Scientific, Singapore, 1994, Diep, H.T., edt., *Frustrated Spin Systems*, World Scientific, Singapore, 2004.
113. Huse, D. A., Fisher, D. S., *Phys. Rev. B* 35, 6841, 1987.
114. Fischer, K. H., Hertz, J. A., *Spin Glasses*, Cambridge University Press, Cambridge, 1991.
115. Edwards, S. F., Anderson, P. W., *J. Phys. F* 5, 965, 1975.
116. Edwards, S. F., Anderson, P. W., *J. Phys. F* 6, 1927, 1976.
117. Fisher, D. S., Huse, D. A., *Phys. Rev. B* 38, 386, 1988.
118. Fisher, D.S., *Physica D* 107, 204, 1997.
119. Harris, R., Plischke, M., Zuckermann, M.J., *Phys. Rev. Lett.* 31, 160, 1973.
120. Aharony, A., Pytte, E., *Phys. Rev. Lett.* 45, 1583, 1980.
121. Goldschmidt, Y.Y., Aharony, A., *Phys. Rev. B* 32, 264, 1985.
122. Alben, R., Becker, J. J., Chi, M., *J. Appl. Phys.* 49, 1653, 1978.
123. Chudnovsky, E. M., Saslow, W. M., Serota, R. A., *Phys. Rev. B* 33, 251, 1986.
124. Coey, J.M.D., *J. Appl. Phys.* 49, 1646, 1978.
125. Sellmyer, D. J., O'Shea, M. J., *Random anisotropy and phase transitions in magnetic glasses*, in *Recent Progress in Random Magnets*, D. H. Ryan, edt., World Scientific, Singapore, p. 71, 1992.
126. Abragam, A., Bleaney, B., *Electron Paramagnetic Resonance of Transition Ions*, Dover, New York, 1986.
127. Ferbinteanu, M., Cimpoesu, F., Kajiwara, T., Yamashita, M., *Solid State Sci.* 11, 760, 2009.
128. Tanase, S., Ferbinteanu, M., Cimpoesu, F., *Inorg. Chem.* 50, 9678, 9678.
129. Ferbinteanu, M., Cimpoesu, F., Gırmuş, M.A., Enachescu, C., Tanase, S., *Inorg. Chem.* 51, 40, 2012.
130. Wolf, S. A., Awschalom, D.D., Buhrman, R.A., Daughton, J.M., von Molnar, S., Roukes, M.L., Chtchelkanova, A.Y., Treger, D.M., *Science* 294, 1488, 2001.
131. Zutic, I., Fabian, J., Das Sarma, S., *Rev. Mod. Phys.* 76, 323, 2004.
132. Awschalom, D.D., Flatté, M.E., *Nat. Phys.* 3, 153, 2007.
133. Sanvito, S., *Chem. Soc. Rev.* 40, 3336, 2011.
134. Bhatt, P., Carlegrim, E., Kanciurzewska, A., de Jong, M.P., Fahlman, M., *Appl. Phys. A* 95, 131, 2009.
135. Bhatt, P., Kanciurzewska, A., Carlegrim, E., Kapilashrami, M., Belova, L., Rao, K.V., Fahlman, M., *J. Mater. Chem.* 19, 6610, 2009.
136. Carlegrin, E., Zhan, Y., de Jong, M.P., Fahlman, M., *Synth. Met.* 161, 1892, 2011.
137. Carlegrin, E., Zhan, Y., Li, F., Liu, X., Fahlman, M., *Organic Electr.* 11, 1020, 2010.
138. Wegner, D., Yamachika, R., Zhang, X., Wang, Y., Baruah, T., Pederson,, M.R., Bartlett, B.M., Long, J.R., Crommie, M.F., *Phys. Rev. Lett.* 103, 087205, 2009.

139. Yoo, J-W., Edelstein, R.S., Lincoln, D.M., Raju, N.P., Xia, C., Pokhodnya, K.I., Miller, J.S., Epstein, A.J., *Phys. Rev. Lett.* 97, 247205, 2006.
140. Yoo, J.-W., Jang, H. W., Prigodin, V. N., Kao, C., Eom, C.B., Epstein, A. J., *Phys. Rev. B* 80, 205207, 2009.
141. Prigodin, V.N., Yoo, J.-W., Jang, H.W., Kao, C.-Y., Eom, C.-B., Epstein, A.J., *J.Phys.: Conf. Series* 292, 012001, 2011.
142. Li, B., Yoo, J.-W., Kao, C.-Y., Jang, H.W., Eom, C.-B., Epstein, A.J., *Organic Electron.* 11, 1149, 2010.
143. Li, B., Zhou, M., Kao, C.-Y., Jang, H.W., Yoo, J.-W., Prigodin, V.N., Epstein, A.J., *Organic Electron.* 13, 1261, 2012.
144. Li, B., Kao, C.-Y., Lu, Y., Yoo, J.-W., Prigodin, V.N., Epstein, A.J., *Appl. Phys. Lett.* 99, 153503, 2011.
145. Kao, C.-Y., Yoo, J.-W., Min, Y., Epstein, A.J., *ACS Appl. Mater. Interfaces* 4, 137, 2012.
146. Kao, C.-Y., Li, B., Lu, Y., Yoo, J.-W., Epstein, A.J., *J. Mater. Chem. C* 2, 6171, 2014.
147. Lu, Y., Harberts, M., Kao, C. Y., Yu, H., Johnston-Halperin, E., Epstein, A. J., *Adv. Mater.* 26, 7632, 2014.
148. Lu, Y., Yu, H., Harberts, M., Epstein, A.J., Johnston-Halperin, E., *J. Mater. Chem. C* 3, 7363, 2015.
149. Lu, Y., Yu, H., Harberts, M., Epstein, A. J., Johnston-Halperin, E. *RSC Adv.* 5, 82271, 2015.



## **Part 2**

# **OPTICAL MATERIALS**



# Advances and Future of White LED Phosphors for Solid-State Lighting

Xianwen Zhang<sup>1\*</sup> and Xin Zhang<sup>2</sup>

<sup>1</sup>*Institute of Advanced Energy Technology and Equipment, Hefei University of Technology, Hefei, China*

<sup>2</sup>*Department of Chemical Engineering, Texas Tech University, Lubbock, TX, USA*

---

## Abstract

The industry of white light-emitting diodes (LEDs) has recently made significant progress due to its distinct advantages, such as high emission efficiencies, long life time, and small size. Major challenges in white LEDs have recently been focused on the achievement of high-performance LEDs device against fluorescent lamps. In this chapter, light generation mechanisms and history of LEDs chips, as well as the fabrication of white LEDs, are firstly presented. The evaluation system of white LEDs devices, including luminous efficacy, chromatic stability, color-rendering properties, and thermal quenching, is also discussed in the second section. Then, types of white LED phosphor materials, which critically determine the performance of white LEDs, are addressed. Finally, we introduce several synthetic strategies for white LEDs phosphors.

**Keywords:** White light-emitting diodes (WLEDs), device fabrication, phosphors, electroluminescence

## 8.1 Light Generation Mechanisms and History of LEDs Chips

### 8.1.1 Light Generation Mechanisms

Over centuries, artificial lighting technology has been remarkably developed from candles and gas and kerosene lamps to incandescent and

---

\*Corresponding author: xianwen.zhang@hfut.edu.cn

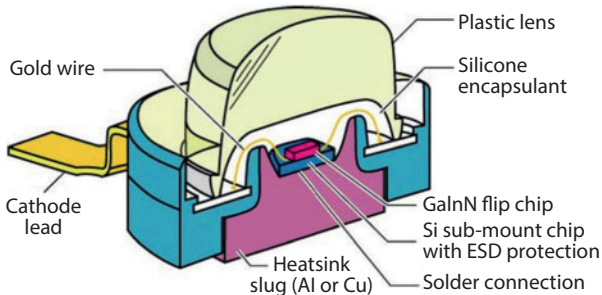


**Figure 8.1** Schematic structure of LEDs package. Adapted from Ref. [3], reproduced with permission.

fluorescent lighting. Today, we are on the bridge to the age of solid-state lighting. Light-emitting diodes (LEDs) as a cutting-edge technology in solid-state lighting are a semiconductor light source where electricity can be converted to visible light when a fitting voltage is applied to the leads and current flows through the p-n junction [1, 2]. The design of a typical LEDs device consists of a p-type semiconductor and an n-type semiconductor of the same kind. Either one or both of the conductive areas can take effect as radiative-recombination zone. Electrons are able to recombine with electron holes within the device, releasing energy in the form of photons. The color of the light (corresponding to the energy of the photon) is determined by the energy band gap of the semiconductor. On the other hand, the larger LEDs forward current comes through, the higher the luminous flux is. Figure 8.1 shows the setup of the commercial LEDs [3]. The LEDs consist of a semiconductor chip with two leads and plastic silicone lens that prevent the semiconductor from being forcefully pulled out from mechanical strain and give optical lens action.

### 8.1.2 History of LED Chips

The history of LEDs goes back to 1907, when electroluminescence was discovered by Round [4]. However, the efficiency of the light generated by passing current through silicon carbide junction diode is very low [5]. Much progress had been made through the investigation of current-voltage characteristics and led to the development of first practical visible spectrum LEDs in the 1960s with red/green-emitting GaP [6, 7]. However, LEDs with blue emission were still a challenge because it is difficult to make p type from n type and efficiency was as low as 1%. Only around 1995, the efficiency of high-brightness blue LEDs was improved by designing

double-heterostructure (Ga, In)N LEDs, which made it possible to use LEDs for general lighting [8].

To date, LEDs have extensively been used in numerical lighting, displays and signaling applications. LEDs can have longer life (up to 50,000 h) with better thermal management in comparison with conventional lighting sources, such as fluorescent lamps and incandescent lamps. LEDs also have other numerous advantages, such as ultra-high-speed response time (microsecond-level on-off switching), a wider range of controllable color temperatures (CTs) (4500–12000 K), a wider operating temperature range (20–85 °C), and no low-temperature startup problems. In addition, LEDs possess better mechanical impact resistance than traditional lighting. LEDs are also environmentally friendly products with no mercury and low health injury owing to low UV radiation. LEDs with a single color, such as red, yellow, green, or blue, are over ten times more efficient than traditional lamps [9, 10].

However, each single emitter in LEDs can provide only one single-color tone. Nowadays, a continuous progress has been made to produce white LEDs (WLEDs) covering the whole visible spectral range from blue to red. In comparison with currently employed incandescent and fluorescent tubes, the advantages of WLEDs include higher luminosity, emission efficiency, longer life time, and lower power consumption. It is well recognized that the widespread replacement of conventional incandescent, and mercury-based compact fluorescent lamps and will lead to a significant reduction in worldwide electricity consumption [11], thereby saving energy and reducing environmental contamination, shown in Figure 8.2 [12].

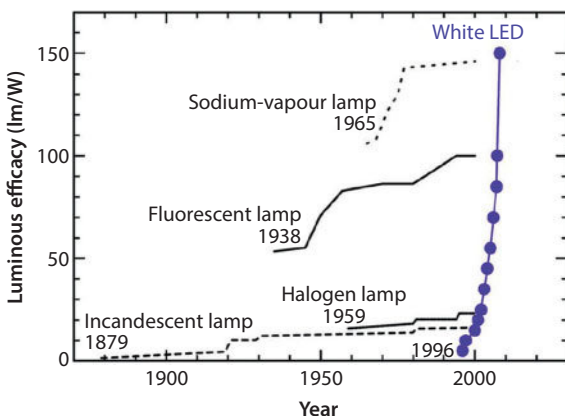


**Figure 8.2** The history of the luminous efficacy in incandescent, halogen, fluorescent, and sodium-vapour lamps and WLEDs. Adapted from Ref. [12], reproduced with permission.

As 2014 Nobel Prize committee said, one-fourth of world electricity consumption is used for lighting purposes, the LEDs contribute to saving the Earth's resources. According to a new report published by the US Department of Energy, it forecasts \$280 billion in energy costs would be saved by using LEDs over the next 20 years in residential and commercial buildings compared with conventional white-light sources, and this number is equal to the average annual per capita energy consumption of 10.9 million people in the USA [13].

By 2027, LEDs lighting could be an alternative light source like incandescent and fluorescent, which could lead to the decrease of national energy consumption for lighting by 33%. European and US companies are leading in the manufacture of LEDs, with three of the top four producers in Netherlands-based Philips, Germany's OSRAM, and USA's Cree in a gradually growing market.

## 8.2 Fabrication of WLEDs

There are three principal strategies for the realization of white LEDs, as illustrated in Figure 8.3. First, separate red, green, and blue LEDs are

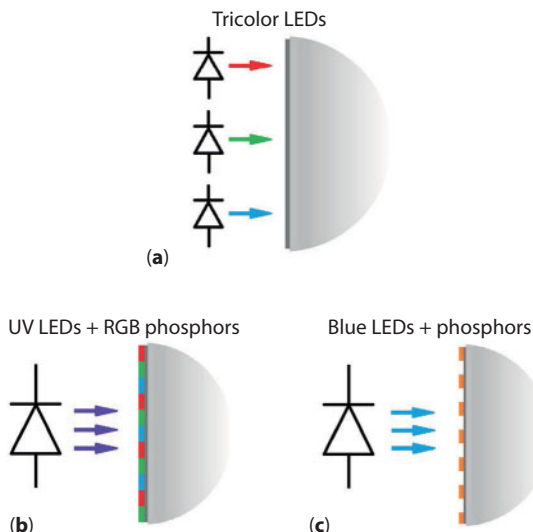


**Figure 8.3** Schematic diagram of the three main white-lighting strategies. (a) Tricolor LEDs combined by red, green, and blue (RGB) LED chips. (b) A three-phosphor strategy with a UV LED coated with RGB phosphors. (c) A blue LED with yellow or other phosphors.

combined to form a white light in a single device. The use of three LEDs is the best approach because there is no energy lost caused by the Stokes shift in phosphor-converted devices, but this technique requires complicated electronics and current low efficiency of yellow and green LEDs limits tricolor LEDs devices from gaining high efficiencies. Another drawback of the tricolor LEDs device is the CT is controlled by changing the power of the individual LEDs device, which would raise up the cost and complexity of circuitry. Moreover, this device has a low color rendering index (CRI) due to relatively narrow radiation components [14].

To realize WLED, most WLEDs manufacturers prepare a slurry of phosphors mixed with a thermoplastic resin. Polycarbonate and silicones are widely applied, with the polymer acting as a binder to fix the phosphors on the surface of LEDs chip. The second way is that, red, green, and blue light-emitting phosphors are employed to convert light from ultraviolet (UV) LEDs (300–410 nm) to broad-spectrum white light [15–17].

This approach also generate good color rendering and stable emission color because the color output of UV LED device on the basis of (Al, Ga)N will not be affected by the changes in the UV emission wavelength. Zhang *et al.* reported that under the excitation of 365 nm UV light, YBO<sub>3</sub>: Tb<sup>3+</sup>, Eu<sup>3+</sup> exhibits a white light, including three emissions: a blue band attributed to self-trapped exciton, a green band due to the Tb<sup>3+</sup> transition of <sup>5</sup>D<sub>4</sub> – <sup>7</sup>F<sub>j</sub> (j = 6, 5, 4, 3), and a red band due to the Eu<sup>3+</sup> transition of <sup>5</sup>D<sub>0</sub> – <sup>7</sup>F<sub>j</sub> (j = 0, 1, 2, 3, 4). Although these advantageous make this strategy seem a promising white light generation way, multiple phosphors can generate energy transfer by reabsorbing the emission of other phosphors and lead to energy loss and decrease of the efficiency of the device [17].

In the third approach, a blue LEDs chip is combined with the down-converting phosphors, which allow some of the blue radiation of LEDs to excite for the generation of white light [18].

These LEDs have been widely applied as long-life white light sources in outdoor and indoor lighting. In terms of the phosphors coated in blue LEDs, Figure 8.4 eliminates the third approach for making of white LEDs based on three types of phosphors. A blue light from LED chip is mixed with the yellow emission from phosphors, as shown in Figure 8.4a. Most commercially available single-phosphor LEDs have been based on Y<sub>3</sub>Al<sub>5</sub>O<sub>12</sub>: Ce<sup>3+</sup> (YAG: Ce) as the yellow-emitting phosphor material since it was firstly produced by Nichia Corporation. YAG: Ce possesses many favorable properties, such as broadband emission in the visible spectral region (500–700 nm), efficient absorption of blue light (420–480 nm), and excellent chemical and thermal stability. A major drawback of this material is the deficiency of the red component, which severely restrict their versatile

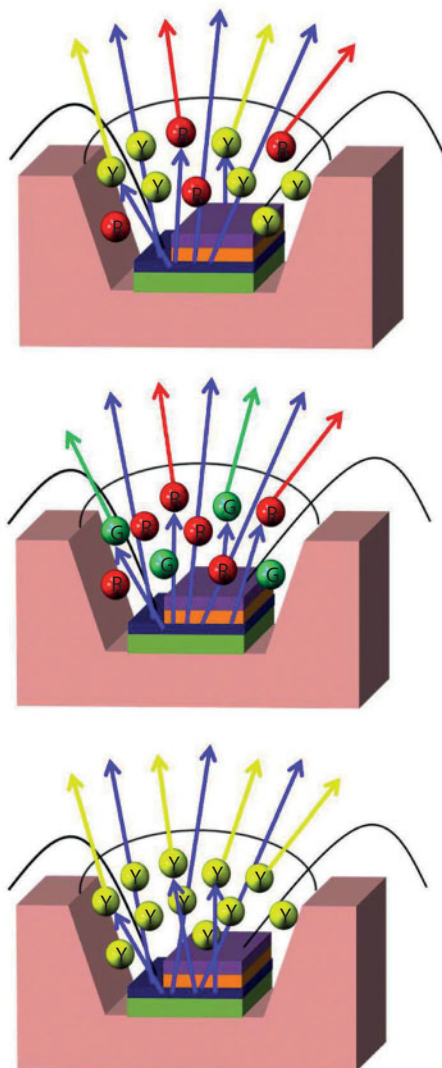


**Figure 8.4** Different methods of fabricating white light with blue LED and phosphors.  
Adapted from Ref. [1], reproduced with permission.

applications range to cool white light (correlated CT 4000–8000 K), and limited CRI (usually  $< 75$ ). To overcome this problem for the requirement of indoor lighting, proper red phosphor is added into the first type to compensate LEDs for the red deficiency of the output light and exhibit a lower CT, as shown in Figure 8.4b. The rendering index and luminous efficiency can be improved obviously. The third one is achieved by blending red and

green phosphors on a blue diode chip, as shown in Figure 8.4c. CRI in this way is high, but efficiency is rather low when lowering the correlated CT of the device.

## 8.3 Evaluation Criteria of WLEDs

To determine whether the spectrum of a light source is suitable for general lighting, the main evaluation criteria of physical requirements, optical requirements, and thermal requirements are described.

### 8.3.1 Physical Requirements

The important physical requirements as display phosphors include the morphology (phosphor particle size and shape), particle size distribution, body color, and rheology. The rheology of a paste or slurry is mainly affected by the size and shape of particles, binders and vehicles used in past formulations. To date, most of the LEDs are manufactured by depositing phosphor particles in the process of settling, slurry, dusting, screen printing, or ink jetting. The manufacturing and performance of the LEDs device depend on the morphology, particle size distribution, and phosphor thickness. Preparing phosphors in various synthetic methods, for example, can control its morphology and improve the optical characteristics [19].

### 8.3.2 Optical Requirements

#### 8.3.2.1 Color Temperature

CT and CRI are two most important parameters to classify white light sources. The CT of a white light source is the temperature of a Planckian black body radiator that has the same chromaticity coordinates as the white light considered [20, 21].

CT is a necessary way to characterize the emission spectral from phosphors. Higher CTs refer to higher brightness and color saturation. The color purity of a phosphors can be determined by the spectral energy distribution in form of (x, y) coordinates on a standard CIE color chart (Commission International de l'Eclairage). The Planckian locus is shown in a CIE diagram in Figure 8.5a. CIE diagram has been used to study the color purity of materials. The position of a color in the CIE diagram is called the chromaticity point of the color. Any color in the diagram can be formed by the color coordinates of suitable blue, green, and red primary

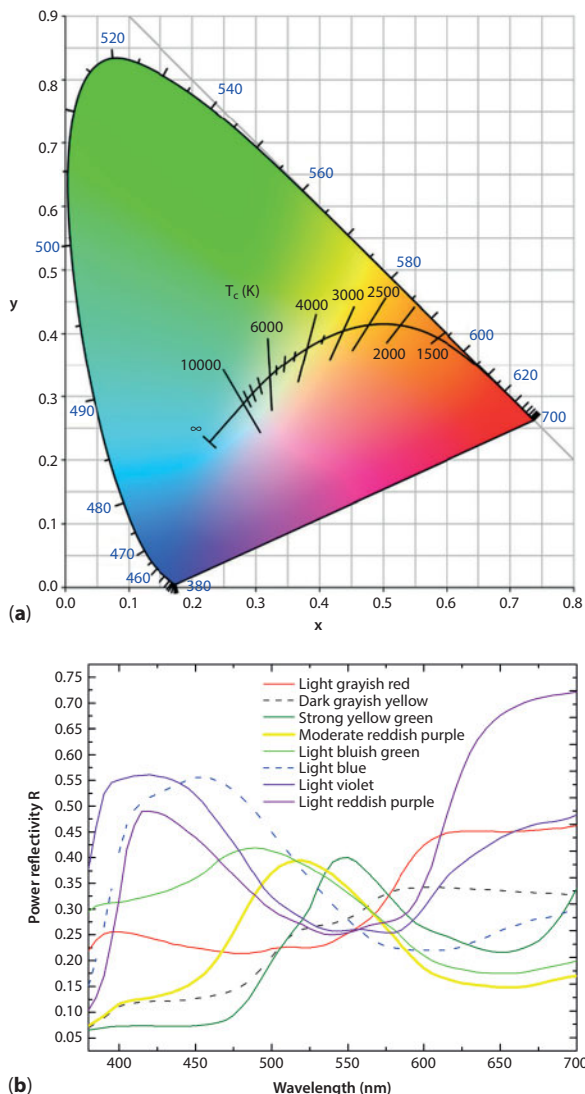


**Figure 8.5** (a) 1931 CIE diagram with Planckian locus. The lines on Planckian locus are known as isothermal lines. (b) Reflectivity spectra of eight test samples used for calculation of color rendering indices. Adapted from Ref. [3], reproduced with permission.

colors. If the color of white light source does not fall on Planckian locus, then CCT temperature defined instead of CT. Therefore, the CCT of white light source is defined as the temperature of a Planckian black body radiator, whose color is the closest to the color of the white light source. CCT can be calculated by method proposed by the McCamy [22].

McCamy proposed that we can calculate correlated CT of white light sources if we know the chromaticity coordinates of white light sources in CIE 1931 diagram.

### 8.3.2.2 Color Rendering Index

CRI is a quantitative measure of the ability of a light source under test to reproduce the colors of various objects in comparison with the colors of the samples illuminated by a reference source [24–26].

Thus, the choice of this reference source is very crucial because it defines what the ‘true’ colors of objects are. The light sources in the references can be incandescent, halogen lamp or daylight, etc. depends upon the correlated color temperature (CCT) of light source under test. A black body radiator acts as a reference for the comparison of test source, and the temperature of the black body that almost matches the spectrum of the test source is known as the CCT of the test source. CRI can be calculated by a procedure in which comparison of reflection spectra of eight color samples under the light source and a reference source has been made. The difference of appearance of eight samples illuminated under test light source and reference source can be calculated and subtraction of this difference number for each color from 100 will give CRI value of light source for that particular color. Then, averaging CRI values over eight color samples will give us general value of CRI.

The color rendering indices are given by [27]

$$\text{CRI}_{\text{general}} = \frac{1}{8} \sum_{i=1}^8 \text{CRI}_i$$

where  $\text{CRI}_i$  is special color-rendering indices.

$$\text{CRI}_i = 100 - 4.6\Delta E_i \quad (i = 1-8, \text{ eight colors})$$

where  $\Delta E_i$  is the difference in color that occurs when a sample object (means each one of 8-color object) is illuminated with reference source and the test illuminated source. The procedure is explained in the Ref. [28].

The procedure to calculate CRI is a matter of debate in lighting industry. There is a new procedure known as color quality scale (CQS) alternate to CRI in process of development. In future, it may replace current methods of calculating CRI [29].

### 8.3.2.3 Emission Spectrum

With the development of high-performance white LED, emission spectrum of phosphors needs to be paid attention because of the unique emission

properties. Broad-band emitting over a large part of the visible spectrum has been widely studied because it leads to good color rendering properties. Small Stokes shift is also required to allow excitation in the near UV or blue band of the spectrum.

#### 8.3.2.4 *Excitation Spectrum*

Another important criterion for the use of phosphors refers to the excitability of the phosphors, which should overlap with the emission of the pumping UV or blue LEDs. Phosphors with suitable excitation spectrum in the near UV to blue region are required to obtain high energy efficiency. On the other hand, the broad excitation spectrum has an advantage for the compensation of changes in the emission spectrum of the pumping LED, which is generated by the fluctuation in the driving current and the junction temperature.

#### 8.3.2.5 *Quantum Efficiency*

The quantum yield is the ratio between converted and absorbed photons. In an ideal situation, the quantum efficiency should approach unity and maximize the overall efficiency of the lighting sources. Besides the features of the excitation/emission spectra, equal attention should be paid to the efficiency of the entire conversion process of electrical power to the observed optical power in order to design suitable LEDs. The choice of good phosphors should meet the requirement of absorbing the excited light and emitting light afterward as efficiently as possible. It means the quantum efficiency should be maximized. Using phosphors with quantum efficiency close to unity plays role in the achievement of high efficiency. Unfortunately, the quantum efficiency of new LED conversion phosphors was not reported at all in some publications.

Generally, measuring the internal quantum yield is followed as below [22]:

$$n_{\text{exc}} = n_{\text{refl}} + n_{\text{conv}} + n_{\text{n-r}} = n_{\text{refl}} + Q n_{\text{abs}} + (1 - Q)n_{\text{abs}}$$

where  $n_{\text{exc}}$  stands for the number of photons excited from the phosphor,  $n_{\text{refl}}$  is the number of reflected photons,  $n_{\text{conv}}$  is the number of photons emitted from the phosphor, and  $n_{\text{n-r}}$  refers to all photons lost in nonradiative transitions.

The quantum yield can be illustrated as follows [30]:

$$Q = n_{\text{conv}} / n_{\text{abs}} = n_{\text{conv}} / (n_{\text{exc}} - n_{\text{refl}})$$

### 8.3.2.6 Luminous Efficiency ( $\eta$ )

The luminous efficiency of the source is a measurement of efficiency to describe how bright the visible light is perceived by the average human eye [31].

Not all wavelengths of light are equally visible at stimulating human vision, owing to the spectral sensitivity of the human eye. It is defined by the ratio of the luminous flux emitted by a light source ( $\Phi$ ) and the energy ( $P$ ) consumed by it in a time unit as follows:

$$\eta = \Phi/P$$

### 8.3.3 Thermal Requirements

The chip temperatures of today's high-power LEDs (>1 W power consumption) can be elevated up to 150 °C. Although high-power LEDs are required for many applications, the junction temperature of the chip will further increase with increasing power consumption [9].

Moreover, elevated temperatures due to the Stokes shift generate the phosphor's crystal lattice to relax. The phosphor electrons are allowed to decay to the ground state without emitting photons in the relaxed band structure, thereby it leads to reduce efficiency and raise the temperature still further, as shown in Figure 8.6. In brief, phosphor thermal quenching indicates that the efficiency of the phosphor is degraded when the temperature rises. So, there is a general demanding that phosphors for WLEDs possess low thermal quenching due to a small Stokes shift to avoid aberration in the chromaticity and brightness. Pust *et al.* [32] investigated a phosphor-converted LED, employing Sr[LiAl<sub>3</sub>N<sub>4</sub>]: Eu<sup>2+</sup> as the red-emitting component, which shows only very low thermal quenching (>95% relative to the quantum efficiency at 200 °C). Further research on thermal design of phosphor is required to enhance and maintain light extraction efficiency by optimizing the morphology, size, and geometry of phosphors to minimize temperature rise arising from the inside of LEDs packages.

## 8.4 Phosphors for WLEDs

Since the mid-1990s, phosphors have been widely investigated in emerging LEDs technologies that involve combining a nitride (III)-based near-ultraviolet (nUV) or blue solid-state light source with down conversion to longer wavelengths. An ideal phosphor should absorb the excitation

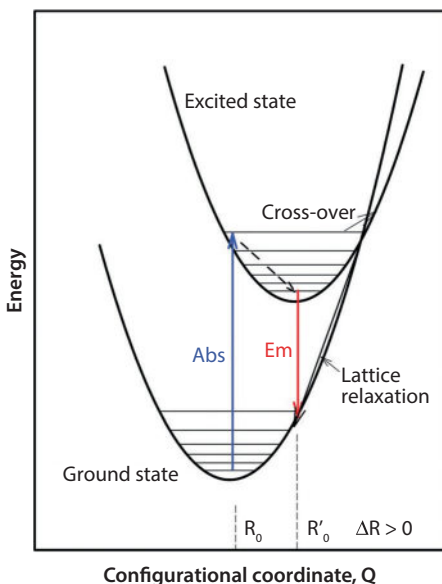


**Figure 8.6** At elevated temperatures, overlap between the ground state and excited state energy bands due to lattice relaxation allows electrons to dissipate absorbed energy without re-emission of a photon. Image courtesy Dow Electronic Materials.

energy and emit light afterward efficiently to maximize the quantum efficiency. Meanwhile, the elapsed or life time between excitation and emission should be as short as possible to avoid afterglow. Tables 8.1 and 8.2 present the intensity, width, durability, and thermal quenching of commercial phosphors for LEDs [33]. It includes two exciting approaches of UV LEDs chip (with the wavelength of 380–420 nm) and blue-LEDs chip (with the wavelength of 450–480 nm).

Rare-earth ions can efficiently absorb the excitation radiation from blue or UV LEDs and exhibit visible light (red, green, blue). Such property makes rare-earth-doped inorganic material promising as WLEDs phosphors. Besides dopants in LEDs phosphors almost all widely used phosphors consist of a crystalline host of garnets, orthosilicates, nitride, or oxynitride that are appropriately doped with either  $\text{Ce}^{3+}$  or  $\text{Eu}^{2+}$ . These rare-earth ions, with  $[\text{Xe}] 4f^n5d^0$  configurations ( $n = 1$  for  $\text{Ce}^{3+}$  and 7 for  $\text{Eu}^{2+}$ ) have proximal excited states of  $[\text{Xe}] 4f^n-15d^1$ . Although the rare-earth dopants have intrinsic characteristics that determine the optical properties, the host lattice characteristics finally contribute to optical properties of phosphors. In this section, the choice of the dopant ion and several families of host matrix will be introduced in brief.

**Table 8.1** Examples of WLEDs that incorporate UV LEDs excitable phosphors.

Led	Phosphor	Chemical composition	Emission characteristics			
			Intensity	Width	Durability	Thermal quenching
violet LED	blue phosphor	(Sr,Ca,Ba,Mg) <sub>10</sub> (PO <sub>4</sub> ) <sub>6</sub> Cl <sub>2</sub> /Eu	○	narrow	○	Δ
		(Ba,Sr)MgAl <sub>10</sub> O <sub>17</sub> /Eu	○	middle	○	○
		(Sr,Ba) <sub>3</sub> MgSi <sub>2</sub> O <sub>8</sub> /Eu	○	narrow	Δ	Δ
	green phosphor	SrGa <sub>2</sub> S <sub>4</sub> /Eu	○	middle	×	×
		$\beta$ -stilbon/Eu	○	middle	○	○
		SrSi <sub>2</sub> O <sub>2</sub> N <sub>2</sub> /Eu	○	middle	○	○
		Ba <sub>3</sub> Si <sub>6</sub> O <sub>12</sub> N <sub>2</sub> /Eu	○	middle	○	○
		BaMgAl <sub>10</sub> O <sub>17</sub> /Eu,Mn	○	narrow	○	○
		SrAl <sub>2</sub> O <sub>4</sub> /Eu	Δ	broad	Δ	Δ
		(Sr,Ca)S/Eu	○	broad	×	×
		(Ca,Sr) <sub>2</sub> Si <sub>5</sub> N <sub>8</sub> /Eu	Δ	broad	Δ	Δ
		CaAlSiN <sub>3</sub> /Eu	○	broad	○	○
red phosphor		La <sub>2</sub> O <sub>2</sub> S/Eu	Δ	narrow	Δ	Δ
		3.5MgO · 0.5MgF <sub>2</sub> · GeO <sub>2</sub> /Mn	Δ	narrow	○	○
		(Sr,Ca,Ba,Mg) <sub>10</sub> (PO <sub>4</sub> ) <sub>6</sub> Cl <sub>2</sub> /Eu,Mn	Δ	broad	○	○
		Ba <sub>3</sub> MgSi <sub>2</sub> O <sub>8</sub> /Eu,Mn	○	broad	Δ	Δ

○, good; Δ, medium; ×, bad.

**Table 8.2** Examples of WLEDs that incorporate blue-LEDs excitable phosphors.

Led	Phosphor	Chemical composition	Emission characteristics		
			Intensity	Width	Durability
blue LED	blue phosphor	(Sr,Ca,Ba,Mg) <sub>10</sub> (PO <sub>4</sub> ) <sub>6</sub> Cl <sub>2</sub> /Eu (Ba,Sr)MgAl <sub>10</sub> O <sub>17</sub> /Eu	○	narrow	○
		(Sr,Ba) <sub>3</sub> MgSi <sub>2</sub> O <sub>8</sub> /Eu	○	middle	○
	green phosphor	SrGa <sub>2</sub> S <sub>4</sub> /Eu	○	narrow	Δ
		SrGa <sub>2</sub> S <sub>4</sub> /Eu	○	middle	×
	β-sialon/Eu	○	middle	○	○
	SrSi <sub>2</sub> O <sub>2</sub> N <sub>2</sub> /Eu	○	middle	○	○
red phosphor	Ba <sub>3</sub> Si <sub>6</sub> O <sub>12</sub> N <sub>2</sub> /Eu	○	middle	○	○
	BaMgAl <sub>10</sub> O <sub>17</sub> /Eu,Mn	○	narrow	○	○
	SrAl <sub>2</sub> O <sub>4</sub> /Eu	Δ	broad	Δ	Δ
	(Sr,Ca)S/Eu	○	broad	×	×
	(Ca,Sr) <sub>2</sub> Si <sub>5</sub> N <sub>8</sub> /Eu	Δ	broad	Δ	Δ
	CaAlSiN <sub>3</sub> /Eu	○	broad	○	○
	La <sub>2</sub> O <sub>2</sub> S/Eu	Δ	narrow	Δ	Δ
	3.5 MgO · 0.5MgF <sub>2</sub> · GeO <sub>2</sub> /Mn	Δ	narrow	○	○
	(Sr,Ca,Ba,Mg) <sub>10</sub> (PO <sub>4</sub> ) <sub>6</sub> Cl <sub>2</sub> /Eu,Mn	Δ	broad	○	○
	Ba <sub>3</sub> MgSi <sub>2</sub> O <sub>8</sub> /Eu,Mn	○	broad	Δ	Δ

○, good; Δ, medium; ×, bad.

### 8.4.1 Dopants in WLEDs Phosphors

#### 8.4.1.1 Broad-band Emitting Rare-earth Ions as Dopants

The broad-band emitting rare-earth ions  $\text{Ce}^{3+}$  and  $\text{Eu}^{2+}$  have been widely investigated primarily due to their unique emission properties, including (1) a broad emission spectrum for a good color rendering, (2) small Stokes shift to allow excitation in the near UV or blue region, and (3) short decay lifetimes to avoid saturation. Moreover, the emission spectrum with a good thermal quenching behavior can be tuned under the nUV excitation. The energy level diagram of  $\text{Ce}^{3+}$  and  $\text{Eu}^{2+}$  was shown in Figure 8.7.

#### 8.4.1.2 Line Emitting Rare-Earth Ions as Dopants

A majority of trivalent rare-earth ions except  $\text{Ce}^{3+}$  can generate a series of relatively emissions with narrow lines [34].

It is due to the internal transitions of  $4f^n$ - $4f^n$  hardly influenced by the host matrix, which always determine the relative intensity of the emission lines, the crystal field splitting of the narrow lines and quantum yield through nonradiative and thermal quenching. Some of the rare-earth ions, such as  $\text{Tb}^{3+}$  and  $\text{Eu}^{3+}$ , have extensively attracted the attentions as they yield the green emission near 545 nm and red emission near 600 or 620 nm under the excitation below 350 nm, respectively, due to charge transfer process. Apparently, the lack of efficient, broad-band excitation in the nUV to blue region limits their application as LEDs phosphors. It is found that the appropriate addition of co-dopants, such as  $\text{Ce}^{3+}$  as sensitizer, can extend the excitation spectrum toward longer wavelength.

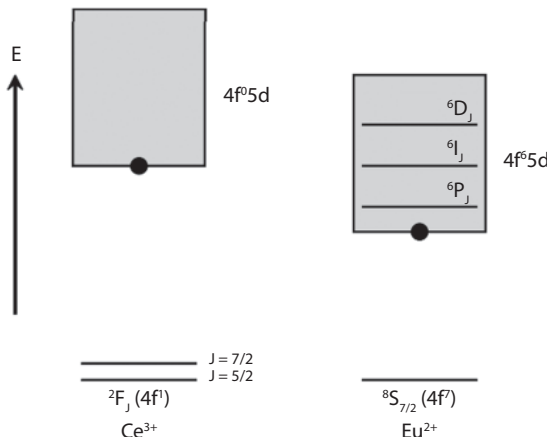


Figure 8.7 Energy level diagram of  $\text{Ce}^{3+}$  and  $\text{Eu}^{2+}$ .

### 8.4.1.3 Other Dopants

A class of transition elements, such as  $Mn^{2+}$ ,  $Cr^{3+}$ , and  $s_2$  ions, such as  $Pb^{2+}$ ,  $Bi^{3+}$ , and  $Sb^{3+}$ , have been reported to play role in the luminescence for the LEDs application, which is owing to the corresponding electron transitions.

## 8.4.2 Choice of Host Material in WLEDs Phosphors

Certain requirements should be fulfilled for the choice of host materials. As mentioned above, the host material has to be a thermally and chemically stable material to avoid thermal quenching due to the elevated temperatures on the pumping LED chip and to acquire the long lifetime. Secondly, the host material should meet the requirement of optical transparency for the emission of the pumping LED, except the presence of energy transfer from host to dopants. Finally, the phosphor production should also be considered as a cheap and environmentally friendly process, with respect to thermal input and the gasses and precursors used.

### 8.4.2.1 Garnet

YAG:Ce as one of the white-lighting phosphors used in industry has the garnet structure. In 1928, Menzer assigned the complex garnet structure to the space group  $Ia\bar{3}d$  [35]. The unit cell consists of four unique positions with a single type of Y-site. Two of  $Al^{3+}$  ions situated in octahedral positions and three remaining  $Al^{3+}$  ions are in tetrahedral sites. Eight oxygen atoms in a distorted dodecahedron coordinate the Y atom. The blue-to-yellow down-conversion of YAG:Ce was first reported by Blasse and Bril in 1967 for flying-spot cathode ray tubes [36]. Subsequently, this phosphor material has been widely commercialized combining with (Ga,In)N LEDs chip for the generation of white light since blue (Ga,In)N chip was made. YAG:Ce possesses advantages, such as convenient fabrication, low cost, broadband emission in the visible spectral region, efficient absorption of blue light, excellent chemical and thermal stability. Nevertheless, a major drawback of this phosphor is the light from YAG/Ce-based WLEDs is colder and bluer than that from a traditional incandescent lamp due to the red deficiency. Many researchers have sought to improve the color rendering property by adding  $Tb^{3+}$  [37],  $Gd^{3+}$  [38], Mg–Si [39], and Si–N [40].

Although a red-shift is found for  $Gd_3Al_5O_{12}:Ce$  compared with YAG:Ce, other garnet phosphors tend to have worse thermal quenching and quantum efficiency properties compared with YAG:Ce.  $Ca_3Sc_2Si_3O_{12}:Ce$  is

another phosphor with the garnet structure [41]. This phosphor has a broad excitation spectrum centered at 450 nm and broad emission with a maximum of 505 nm. The temperature quenching is less than that of YAG:Ce.

#### 8.4.2.2 Orthosilicates

The alkaline earth silicate-based host matrix has been widely used in the lighting and display industry because of their stable crystal structures and flexible application properties. Orthosilicate phosphors with the general composition of compositions are  $M_2SiO_4$ ,  $M_3SiO_5$ ,  $M_2MgSi_2O_7$ , and  $M_3MgSi_2O_8$  ( $M = Ca, Sr, or Ba$ ) doped with  $Eu^{2+}$  or  $Ce^{3+}$ , including the end members or intermediate compositions, have been investigated in the field of WLEDs. Park reported the  $Ce^{3+}/Mn^{2+}$ -codoped and  $Eu^{2+}$ -doped T-phase  $Ba_{1.2}Ca_{0.8}SiO_4$  phosphors for nUV WLEDs [42]. Subsequently, Park studied the effect of  $Ba^{2+}$  substitution in  $Sr_3SiO_5$  and proposed that low symmetry will be formed in the  $(Sr, Ba)_3SiO_5$  solid-solution phase, and it will produce slight changes in the stacking arrangement of the cations, which in turn change the luminescence behaviors [43]. A new intermediate phosphor of  $Ba_{1.55}Ca_{0.45}SiO_4$  serves as the host, and shows the interesting luminescence properties from the  $Eu^{2+}$  singly doped and/or  $Eu^{2+}/Mn^{2+}$ -codoped  $Ba_{1.55}Ca_{0.45}SiO_4$  phosphors. The phosphors can be excited by nUV light at wavelengths ranging from 200 to 450 nm matching well with the nUV LEDs chips. Fine-tuning the activators of different  $Eu^{2+}$  content and  $Eu^{2+}/Mn^{2+}$  couples with different ratios leads to tunable emission consisting of the blue emission (460 nm), green emission (520 nm) originating from  $Eu^{2+}$ , and the red emission (595 nm) [44].

#### 8.4.2.3 Sulfides and Oxysulfides

The combination of highly luminescent  $Eu^{2+}$  ions and a sulfide host allow the broad excitation and broad emission bands that are ideal for wavelength conversion in LEDs for solid-state white lighting. Meanwhile, emission of sulfide phosphors show apparent red-shift compared to their oxide counterparts.  $Ca_{1-x}Sr_xS:Eu^{2+}$  single crystal phosphors simultaneously have a broad excitation spectrum and a broad emission spectrum with saturated red, which makes it an ideal candidate for white light [45]. MZnOS-based phosphors with good thermal and chemical stability were reported ( $M = Ca, Ba$ ) [46, 47].  $CaZnOS:Eu^{2+}$  exhibits red emission region centered at 650 nm, with a thermal quenching slightly better than  $SrS:Eu^{2+}$ .  $CaZnOS:Mn^{2+}$  has a relatively narrow emission band centered at 614 nm and present intense  $Mn^{2+}$  excitation bands in the range of 350–500 nm.

#### 8.4.2.4 Nitrides and Oxynitrides

Most oxide-based phosphors make it impossible for them to be combined with blue LEDs owing to the low absorption in the visible-light spectrum. For sulfide-based phosphors, they are thermally unstable and very sensitive to moisture, so their luminescence degrades significantly under ambient atmosphere if lacking a protective coating layer. Consequently, it is crucial to modify existing phosphors or to explore new host materials for phosphors to solve these problems and develop high-performance phosphors for LEDs. Nitride and oxynitride phosphors have attracted significant attention in the past years due to their encouraging luminescent properties (excitability by blue light, high quantum efficiency, and the possibility of full color emission), as well as their low thermal quenching and high chemical stability. Although nitride and oxynitride materials had been studied for many years, these materials have only recently been explored as phosphor hosts with doped  $\text{Ce}^{3+}$  or  $\text{Eu}^{2+}$  ions.

Recently, Pust *et al.* reported that  $\text{Sr}[\text{LiAl}_3\text{N}_4]:\text{Eu}^{2+}$  can efficiently be excited by GaN-based blue LEDs and exhibit high-performance narrow-band red-emitting centered at 650 nm [32]. It also has low thermal quenching indicating the quantum efficiency is more than 95% at 200 °C. Subsequently, a prototype phosphor-converted LEDs, employing  $\text{Sr}[\text{LiAl}_3\text{N}_4]:\text{Eu}^{2+}$  as the red-emitting component, already shows an increase of 14% in luminous efficacy compared with a commercially available high CRI LEDs, together with an excellent color rendition.

Luminescent properties of oxynitride phosphors in the system of  $\text{Eu}^{2+}$ -doped M-Si-Al-O-N (M = Li, Ca, or Sr) were reported for white LEDs combining a GaN-based blue LEDs. The phosphors show high quantum efficiency of blue light, suitable emission colors and small thermal quenching. The bichromatic white LEDs exhibit high luminous efficacy at 55 lm W<sup>-1</sup> and the multi-phosphor converted white LEDs show high color rendering index of 82–95. Oxynitride phosphors are successfully proved to serve as down-conversion luminescent materials in WLEDs.

#### 8.4.2.5 Other Host Materials

Several other oxide phosphors also show unique luminescent properties optimal for WLEDs. A novel compound  $\text{Ca}_{0.5}\text{La}(\text{MoO}_4)_2:\text{Eu}^{3+}$  synthesized by solid-state reaction method shows an enhanced red emission at 615 nm originating from  $^5\text{D}_0 - ^7\text{F}_2$  transition of  $\text{Eu}^{3+}$ , which is 5.92 times higher than that of  $\text{CaMoO}_4:\text{Eu}^{3+}$ . Photoluminescent spectra, diffuse reflection spectra, and lifetime measurement indicate that the red emission enhancement is ascribed to the increase of the  $^7\text{F}_0 - ^5\text{L}_6$  absorption intensity of  $\text{Eu}^{3+}$ .

Enhanced red emission, stronger  ${}^7F_0 - {}^5L_6$  absorption intensity, and high color purity indicate that  $\text{Ca}_{0.5}\text{La}(\text{MoO}_4)_2:\text{Eu}^{3+}$  phosphor is a promising red phosphor for UV LEDs [48].  $\text{NaGd}(\text{WO}_4)_2:\text{Sm}^{3+}$  can efficiently absorb UV light and emit bright blue light from the host, and has yellow, orange, and red emissions from the f-f transitions of  $\text{Sm}^{3+}$ , due to the host sensitization effect. Under the excitation of 405 nm, this phosphor generates white and red lights, and the emission intensities reach a maximum at 0.015 equivalents of  $\text{Sm}^{3+}$ . In addition, under different UV radiation, the color-tunable emissions in  $\text{NaGd}(\text{WO}_4)_2:\text{Tb}^{3+}$ ,  $\text{Sm}^{3+}$  microcrystals are realized, and this could make them promising to be used as full-color phosphors for WLEDs [49]. Oxyfluorides phosphor  $\text{Ca}_2\text{Al}_3\text{O}_6\text{F}:\text{Eu}^{2+}$  shows good thermal stability and efficient absorption ranging from the UV to the blue region and a broad green emission band centered at 502 nm. Although the results of photoluminescence, CIE value, and quantum efficiency indicate that  $\text{Ca}_2\text{Al}_3\text{O}_6\text{F}:\text{Eu}^{2+}$  is a good candidate as a green component for nUV-excited WLEDs, poor chemical stability limits its development in future [50].

#### 8.4.3 Synthetic Approaches for WLEDs Phosphors

Different synthesis techniques have been developed all over the world for the important WLEDs phosphors. A major of industrial synthesis for almost all phosphors is still solid-state reactions at high temperature with long period of time. Such phosphor synthesis can be classified into two distinctly different types: (a) The first method involves adding the activator ions into an existing host material. (b) The second involves the simultaneous synthesis of the host compound and activator ions during firing. Usually, the high-purity precursor materials of the host materials, the activators (and/or co-activators), and the fluxes are blended together. Then, the mixture of three was co-fired in an unreactive crucible/container. The products after firing are usually sintered and require to be underwent a treatment of crushing and milling. Finally, products were often separated to sieve out the bigger particles and need surface treatments. Some of these processes were carried out several times if necessary. For example,  $\text{Ba}_3\text{WO}_6:\text{Eu}^{3+}$  nanowire phosphors were synthesized by the conventional solid-state method. The photoluminescence spectra demonstrate that the phosphors emit strong red light centered at 595 nm [51]. Yu *et al.* reported  $\text{Ba}_3\text{Si}_6\text{O}_9\text{N}_4:\text{Eu}^{2+}$  green-emitting phosphors for white LEDs. It could be efficiently excited by UV-blue light (280–500 nm) at the suitable excitation range and showed a single strong broad emission band (470–625 nm) [52].

Phosphors prepared by the solid-state reaction method have aggregated particles with irregular shape and large. Subsequent process of crushing and milling to reduce the particle size desired would affect the luminescent properties of phosphors for the industrial application. Recently, many new production approaches have been reported, involving spray pyrolysis route, sol-gel method, and hydrothermal method.

In the process of spray pyrolysis, a solution of the desired metal ion precursors is sprayed out from a nozzle with a carrier gas to generate small droplets. These droplets pass through a high-temperature furnace which facilitates the materials into spherical metal oxide particles.  $\text{La}_2\text{Si}_2\text{O}_7:\text{Eu}^{3+}$  phosphors with tetragonal phase were produced by spray pyrolysis synthesis to exhibit a strong orange-red luminescence, lifetime of 2.3 ms, and the quantum yield of 12% at 393-nm excitation. These experimental observations obtained from spray pyrolysis method make this material an excellent phosphor for optoelectronic applications [53].

Sol-gel methods involve the preparation of solution by formation of a gel produced from precursors, such as metal alkoxides, hydrolysis, and polycondensation reactions. It was reported that highly emissive broad-band phosphors were synthesized from a tetra-alkoxysilane sol-gel precursor and a variety of organic carboxylic acids, which exhibit an external quantum yield exceeding 35% at a 365-nm excitation wavelength. The air-stable phosphors were synthesized at low temperatures of less than 300 °C and showed broad visible photoluminescence spectra that appeared white to the eye. Water-soluble phosphors can be prepared by the substitution of 3-aminopropyltriethoxysilane for tetra-alkoxysilane in the similar synthesis [54].

In another case, YAG:Ce phosphors produced using sol-gel method exhibit intense broad green-yellow emission band in the range of 460–700 nm with a maximum intensity at around 530 nm assigned to the 5d–4f interconfigurationnelles transitions of Ce ion in YAG nanomaterial [55].

Hydrothermal synthesis is one of the solution-phase methods to make the reaction raw material form a solution under a certain temperature and pressure ( $T < 350$  °C,  $P < 100$  MPa) in the autoclave [56–58]. Hydrothermal method was initiated by geologists, who studied laboratory simulations of naturally hydrothermal phenomena in the middle of the 19th century. To date, hydrothermal synthesis is an important approach to synthesize inorganic materials including LEDs phosphors. It can control the particle size and morphology through the process of nucleation, growth and Oswald aging to meet the requirement of LEDs phosphors production. Uniform and well-dispersed  $\text{YBO}_3:\text{Eu}^{3+}$  with nine three-dimensional morphologies

were hydrothermally synthesized by tuning the reaction parameters and exhibit the high chromaticity values [56]. Subsequently,  $\text{YBO}_3:\text{Tb}^{3+}, \text{Eu}^{3+}$  phosphors with a morphology of uniform flower-like assembly are fabricated by a facile hydrothermal method.  $\text{YBO}_3:\text{Tb}^{3+}, \text{Eu}^{3+}$  exhibits a white light, including three emissions: a blue band attributed to self-trapped exciton, a green band due to the  $\text{Tb}^{3+}$  transition of  $^5\text{D}_4 - ^7\text{F}_j$  ( $j = 6, 5, 4, 3$ ), and a red band due to the  $\text{Eu}^{3+}$  transition of  $^5\text{D}_0 - ^7\text{F}_j$  ( $j = 0, 1, 2, 3, 4$ ) under the excitation of 365 nm UV light [17].

Other methods, such as wet process and thermal decomposition, have also been used to synthesis phosphor materials [59–61].

The rapid progress of synthesis methods has been made in recent years regarding the achievement of WLEDs phosphors with unique optical and thermal properties. Nevertheless, the number of phosphors effectively meeting all requirements is relatively small. It is apparent from the commercial importance of LEDs phosphor materials that existing methods of phosphor synthesis will continue to be improved, and new production approaches of phosphors will continue to attract the attention.

## 8.5 Conclusions

A careful review of the LEDs system is described here, given LEDs light generation mechanism and history, WLEDs fabrication, as well as WLEDs phosphors. The phosphors play a critical role in developing high-quality WLEDs because their performances directly determine the luminous efficacy, color quality, and reliability of the devices. A good phosphor candidate should fulfill all requirements simultaneously, including thermal, physical, and optical criteria identified in this chapter. Therefore, it is very worth of introducing a wide range of phosphors candidates and their synthetic methods. Although most phosphors fail on one or more criteria, some choices of phosphors with dopant–host combinations still encourage further in-depth research. Also, phosphor development largely depends on trial and error in screening suitable hosts and corresponding dopants. The development of LEDs and WLEDs phosphors has made a large step forward until now, but the story continues, especially for WLEDs based on diodes emitting in the UV region. In addition, the fine adjustment of overlap between diode emission and the excitation spectra of the phosphors deserve more attention to further increase quantum efficiency. The targeted market, including commercial, industrial, and retail regions, is very interested in the higher-efficiency products. Therefore, the future is bright for the development of WLEDs devices.

## References

- Chen, L., Lin, C. C., Yeh, C. W., Liu, R. S., Light converting inorganic phosphors for white light-emitting diodes. *Materials*, 3, 2172, 2010.
- Park, W. B., Singh, S. P., Sohn, K. S., Discovery of a phosphor for light emitting diode applications and its structural determination, Ba (Si, Al) 5 (O, N) 8: Eu<sup>2+</sup>. *J. Am. Chem. Soc.*, 136, 2363, 2014.
- Schubert, E. F, *Light-emitting Diodes*, Cambridge University, Cambridge, UK, 2006.
- Round, H. J., A note on carborundum. *Electr. World*, 49, 309, 1907.
- Chartier, C., Benalloul, P., Barthou, C., Frigerio, J. M., Mueller, G. O., Mueller-Mach, R., Trottier, T. Photoluminescence and cathodoluminescence properties of green emitting SrGa<sub>2</sub>S<sub>4</sub>: Eu<sup>2+</sup> thin film. *J. Phys. D: Appl. Phys.*, 35, 363, 2002.
- Xie, R. J., Hirosaki, N., Silicon-based oxynitride and nitride phosphors for white LEDs-A review. *Sci. Technol. Adv. Mater.*, 8, 588, 2007.
- Höppe, H. A., Lutz, H., Morys, P., Schnick, W., Seilmeier, A. Luminescence in Eu<sup>2+</sup>-doped Ba<sub>2</sub>Si<sub>5</sub>N<sub>8</sub>: fluorescence, thermoluminescence, and upconversion. *J. Phys. Chem. Solids.*, 61, 2001, 2000.
- Hoeppke, H. A., Stadler, F., Oeckler, O., Schnick, W., Ca [Si<sub>2</sub>O<sub>2</sub>N<sub>2</sub>]-A novel layer silicate. *Angew. Chem. Int. Ed.* 43, 5540, 2004.
- Chang, M. H., Das, D., Varde, P. V., Pecht, M., Light emitting diodes reliability review. *Microelectron. Reliab.*, 52, 762, 2012.
- Steranka, F. M., Bhat, J., Collins, D., Cook, L., Craford, M. G., Fletcher, R., Gardner, N., Grillot, P., Goetz, W., Keuper, M., Khare, R., Kim, A., Krames, M., Harbers, G., Ludowise, M., Martin, P.S., Misra, M., Mueller, G., Mueller-Mach, R., Rudaz, S., Shen, Y.-C., Steigerwald, D., Stockman, S., Subramanya, S., Trottier, T., Wierer, J. J., High power LEDs-Technology status and market applications. *Phys. Status. Solid. A*, 194, 380, 2002.
- Born, M., Justel, T., Umweltfreundliche Lichtquellen. *Phys. J.*, 2, 43, 2003.
- Narukawa, Y., Ichikawa, M., Sanga, D., Sano, M., Mukai, T., White light emitting diodes with super-high luminous efficacy. *J. Phys. D: Appl. Phys.*, 43, 354002, 2010.
- U.S. Dep. Energy. Build. Technol. Program, Off. Energy Effic. Renew. Energy, U.S. Dep. Energy, Washington, DC, 2012.
- Smet, P. F., Parmentier, A. B., Poelman, D. Selecting conversion phosphors for white light-emitting diodes. *J. Electrochem. Soc.*, 158, R37, 2011.
- Sandhu, A., The future of ultraviolet LEDs. *Nat. Photonics*, 1, 38, 2007.
- Höppe, H. A., Daub, M., Bröhmer, M. C., Coactivation of α-Sr(PO<sub>3</sub>)<sub>2</sub> and SrM (P<sub>2</sub>O<sub>7</sub>)(M= Zn, Sr) with Eu<sup>2+</sup> and Mn<sup>2+</sup>. *Chem. Mater.*, 19, 6358, 2007.
- Zhang, X., Zhao, Z., Zhang, X., Marathe, A., Cordes, D. B., Weeks, B., Chaudhuri, J., Tunable photoluminescence and energy transfer of YBO<sub>3</sub>: Tb<sup>3+</sup>, Eu<sup>3+</sup> for white light emitting diodes. *J. Mater. Chem. C*, 1, 7202, 2013.

18. Mueller-Mach, R., Mueller, G., Krames, M. R., Höppe, H. A., Stadler, F., Schnick, W., Juestel, T., Schmidt, P., Highly efficient all-nitride phosphor-converted white light emitting diode. *Phys. Status Solid. A*, 202, 1727, 2005.
19. Murthy, K. V. R., Nano phosphors for light emitting diodes (LEDs) syntheses and characterization. *Recent Res. Sci. Technol.*, 4, 8, 2012.
20. Jüstel, T., Nikol, H., Ronda, C. New developments in the field of luminescent materials for lighting and displays. *Angew. Chem. Int. Ed.*, 37, 3084, 1998.
21. Liu, R. S., Liu, Y. H., Bagkar, N. C., Hu, S. F., Enhanced luminescence of  $\text{SrSi}_2\text{O}_2\text{N}_2:\text{Eu}^{2+}$  phosphors by codoping with  $\text{Ce}^{3+}$ ,  $\text{Mn}^{2+}$ , and  $\text{Dy}^{3+}$  ions. *Appl. Phys. Lett.*, 91, 061119, 2007.
22. McCamy, C. S. Correlated color temperature as an explicit function of chromaticity coordinates. *Color Res. Appl.*, 17, 142, 1992.
23. Schubert, E. F. *Light Emitting Diodes*, Cambridge University, Cambridge, UK, 2003.
24. CIE, *CIE Publication*, TC-3.2, 1974.
25. CIE, *CIE Technical Report*, 13.3, 1995.
26. Schanda, J. E., *Colorimetry: Understanding the CIE system*, Wiley, Hoboken, New Jersey, 2007.
27. Zukauskas, A., Shur, M. S., Gaska, R., *Introduction to Solid State Lighting*, John Wiley & Sons, Inc., New York, 2002.
28. McColl, S. L., Veitch, J. A., Full-spectrum fluorescent lighting: a review of its effects on physiology and health. *Psychol. Med.*, 31, 949, 2001.
29. Davis, W., Ohno, Y. Color quality scale. *Opt. Eng.*, 2001, 49, 033602, 2010.
30. Khazova, M., O'Hagan, J. B. Optical radiation emissions from compact fluorescent lamps. *Radiat. Prot. Dosim.*, 131, 521, 2008.
31. Zheludev, N. The life and times of the LED-a 100-year history. *Nat. Photonics*, 1, 189, 2007.
32. Pust, P., Weiler, V., Hecht, C., Tücks, A., Wochnik, A. S., Henß, A. K., Wiechert, D., Scheu, C., Schmidt, P. J., Schnick, W. Narrow-band red-emitting  $\text{Sr}[\text{LiAl}_3\text{N}_4]:\text{Eu}^{2+}$  as a next-generation LED-phosphor material. *Nat. Mater.*, 13, 891, 2014.
33. Lin, C. C., Liu, R. S. Advances in phosphors for light-emitting diodes. *J. Phys. Chem. Lett.*, 2, 1268, 2011.
34. Lang, R. J., The spectrum of trebly ionized cerium. *Can. J. Res.*, 14a, 127, 1936.
35. Menzer, P. Die neue pestalozzi-ausgabe. *Kant-Studien*, 33, 239, 1928.
36. Blasse, G., Bril, A., A new phosphor for flying-spot cathode-ray tubes for color television: yellow-emitting  $\text{Y}_3\text{Al}_5\text{O}_{12}-\text{Ce}^{3+}$ . *Appl. Phys. Lett.* 11, 53, 1967.
37. Lin, Y. S., Liu, R. S., Cheng, B. M. Investigation of the luminescent properties of  $\text{Tb}^{3+}$ -substituted YAG: Ce, Gd phosphors. *J. Electrochem. Soc.*, 152, J41, 2005.
38. Fujita, S., Sakamoto, A., Tanabe, S. Luminescence characteristics of YAG glass-ceramic phosphor for white LED. *IEEE J. Sel. Top. Quant.*, 14, 1387, 2008.
39. Katelnikovas, A., Bettentrup, H., Uhlich, D., Sakirzanovas, S., Jüstel, T., Kareiva, A. Synthesis and optical properties of  $\text{Ce}^{3+}$ -doped  $\text{Y}_3\text{Mg}_2\text{AlSi}_2\text{O}_{12}$  phosphors. *J. Lumin.*, 129, 1356, 2009.

40. Setlur, A. A., Heward, W. J., Hannah, M. E., Happek, U. Incorporation of  $\text{Si}^{4+}$ - $\text{N}^{3-}$  into  $\text{Ce}^{3+}$ -doped garnets for warm white LED phosphors. *Chem. Mater.*, 20, 6277, 2008.
41. Im, W. B., George, N., Kurzman, J., Brinkley, S., Mikhailovsky, A., Hu, J., Chmelka, B. F., DenBaars, S. P., Seshadri, R. Efficient and color-tunable oxyfluoride solid solution phosphors for solid-state white lighting. *Adv. Mater.*, 23, 2300, 2011.
42. Park, K., Lee, J., Park, J., Kim, J., Kung, P., Kim, S. M., Kim, G. White-light generation through  $\text{Ce}^{3+}/\text{Mn}^{2+}$ -codoped and  $\text{Eu}^{2+}$ -doped  $\text{Ba}_{1.2}\text{Ca}_{0.8}\text{SiO}_4$  T-phase phosphors. *J. Lumin.*, 130, 2442, 2010.
43. Park, J. K., Choi, K. J., Yeon, J. H., Lee, S. J., Kim, C. H. Embodiment of the warm white-light-emitting diodes by using a  $\text{Ba}^{2+}$  codoped  $\text{Sr}_3\text{SiO}_5:\text{Eu}$  phosphor. *Appl. Phys. Lett.* 88, 043511, 2006.
44. Miao, S., Xia, Z., Zhang, J., Liu, Q. Increased  $\text{Eu}^{2+}$  content and codoping  $\text{Mn}^{2+}$  induced tunable full-color emitting phosphor  $\text{Ba}_{1.55}\text{Ca}_{0.45}\text{SiO}_4:\text{Eu}^{2+}, \text{Mn}^{2+}$ . *Inorg. Chem.*, 53, 10386, 2014.
45. Poelman, D., Van Haecke, J. E., Smet, P. F. Advances in sulfide phosphors for displays and lighting. *J. Mater. Sci. Mater. Electron.*, 20, S134, 2009.
46. Duan, C. J., Delsing, A. C. A., Hintzen, H. T. Photoluminescence properties of novel red-emitting  $\text{Mn}^{2+}$ -activated  $\text{M}\text{ZnOS}$  ( $\text{M} = \text{Ca}, \text{Ba}$ ) phosphors. *Chem. Mat.*, 21, 1010, 2009.
47. Kuo, T. W., Liu, W. R., Chen, T. M. High color rendering white light-emitting-diode illuminator using the red-emitting  $\text{Eu}^{2+}$ -activated  $\text{CaZnOS}$  phosphors excited by blue LED. *Opt. Express*, 18, 8187, 2010.
48. Shi, Y., Liu, B., Liu, B., Li, C., Wang, Z. Enhanced red emission in  $\text{Ca}_{0.5}\text{La}(\text{MoO}_4)_2:\text{Eu}^{3+}$  phosphors for UV LEDs. *RSC Adv.*, 5, 95953, 2015.
49. Liu, Y., Liu, G., Dong, X., Wang, J., Yu, W. Luminescence, energy-transfer and tunable color properties of single-component  $\text{Tb}^{3+}$  and/or  $\text{Sm}^{3+}$  doped  $\text{NaGd}(\text{WO}_4)_2$  phosphors with UV excitation for use as WLEDs. *RSC Adv.*, 4, 58708, 2014.
50. Xia, Z., Liu, R. S., Huang, K. W., Drozd, V.  $\text{Ca}_2\text{Al}_3\text{O}_6\text{F}:\text{Eu}^{2+}$ : a green-emitting oxyfluoride phosphor for white light-emitting diodes. *J. Mater. Chem.*, 22, 15183, 2012.
51. Li, Y., Liu, X. Structure and luminescence properties of  $\text{Ba}_3\text{WO}_6:\text{Eu}^{3+}$  nanowire phosphors obtained by conventional solid-state reaction method. *Opt. Mater.*, 38, 211, 2014.
52. Yu, L., Hua, Y., Chen, H., Deng, D., Wang, H., Ma, H., Xu, S. Luminescence properties of  $\text{Ba}_3\text{Si}_6\text{O}_9\text{N}_4:\text{Eu}^{2+}$  green-emitting phosphors for white LEDs. *Opt. Commun.*, 315, 83, 2014.
53. Fernández-Carrión, A. J., Ocaña, M., Florian, P., García-Sevillano, J., Cantelar, E., Fitch, A. N., Suchomel, M. R., Becerro, A. I. Crystal structure and luminescent properties of  $\text{Eu}^{3+}$ -doped  $\text{A}-\text{La}_2\text{Si}_2\text{O}_7$  tetragonal phase stabilized by spray pyrolysis synthesis. *J. Phys. Chem. C*, 117, 20876, 2013.

54. Green, W. H., Le, K. P., Grey, J., Au, T. T., Sailor, M. J. White phosphors from a silicate-carboxylate sol-gel precursor that lack metal activator ions. *Science*, 276, 1826, 1997.
55. Boukerika, A., Guerbous, L., Brihi, N. Ce-doped YAG phosphors prepared via sol-gel method: Effect of some modular parameters. *J. Alloy. Compd.*, 614, 383, 2014.
56. Zhang, X., Marathe, A., Sohal, S., Holtz, M., Davis, M., Hope-Weeks, L. J., Chaudhuri, J., Synthesis and photoluminescence properties of hierarchical architectures of  $\text{YBO}_3$ :  $\text{Eu}^{3+}$ . *J. Mater. Chem.*, 22, 6485, 2012.
57. Zhang, X., Zhang, X., Zhao, Z., Chaudhuri, J., *In-situ* crystal growth and photoluminescence properties of  $\text{YBO}_3$ :  $\text{Tb}^{3+}$  microstructures. *J. Mater. Sci.*, 50, 251, 2015.
58. Zhang, X., Zhao, Z., Zhang, X., Cordes, D. B., Weeks, B., Qiu, B., Madanan, K., Sardar, D., Chaudhuri, J., Magnetic and optical properties of  $\text{NaGdF}_4$ :  $\text{Nd}^{3+}$ ,  $\text{Yb}^{3+}$ ,  $\text{Tm}^{3+}$  nanocrystals with upconversion/downconversion luminescence from visible to the near-infrared second window. *Nano Res.*, 8, 636, 2014.
59. Wei, Z., Sun, L., Liao, C., Yan, C., Huang, S., Fluorescence intensity and color purity improvement in nanosized  $\text{YBO}_3$ : Eu. *Appl. Phys. Lett.*, 80, 1447, 2002.
60. Wei, Z. G., Sun, L. D., Liao, C. S., Jiang, X. C., Yan, C. H., Synthesis and size dependent luminescent properties of hexagonal (Y, Gd)  $\text{BO}_3$ :Eu nanocrystals. *J. Mater. Chem.*, 12, 3665, 2002.
61. Liu, L., Zhang, X., Chaudhuri, J., Synthesis of highly nanoporous  $\text{YBO}_3$  architecture via a co-precipitation approach and tunable luminescent properties. *Scanning*, 37, 277, 2015.



# Design of Luminescent Materials with “Turn-On/Off” Response for Anions and Cations

Serkan Erdemir<sup>1\*</sup> and Sait Malkondu<sup>2</sup>

<sup>1</sup>*Department of Chemistry, Selcuk University, Konya, Turkey*

<sup>2</sup>*Department of Environmental Engineering, Giresun University, Giresun, Turkey*

---

## Abstract

The detection of biologically important and environmentally pollutant anions and cations has become an essential task in many fields such as clinical, biomedical, and environmental monitoring, agriculture, and process controlling. The determination and control of them are of great interest to many scientists including chemists, biologists, clinical biochemists, and environmentalists since they play important roles. To date, a variety of analytical methods have been used in the detection of anions and cations. But, these methods require expensive analytical instruments and sophisticated experimental instrumentation and are time-consuming due to a sample collection, transportation, and pretreatment. In the past years, the development of luminescent materials for the detection of anions and cations has received great attention. Fluorescence detection provides several advantages such as high sensitivity, simple instrumentation, facile analysis, intrinsic selectivity, and the capacity for rapid, real-time monitoring over other mentioned methods and generally involves the design and synthesis of a lumino-ionophore containing more than one binding sites and a signaling unit. A number of selective luminescent probes on the basis of the nature of the luminophore including rhodamine, triphenylamine, coumarin, calixarene, pyrene, BODIPY, 8-hydroxy-quinoline, anthraquinone, BINOL, and salicylicnaphthaldehyde units have been reported. The present article does not, however, attempt to cover all of the different approaches to luminescent materials for anions and cations.

**Keywords:** Luminescence, optic, sensor, anion, cation

---

\*Corresponding author: serdemir82@gmail.com

## 9.1 Introduction

The presence of harmful cations and anions in the environment is a major concern due to their toxicity to many life forms. Their high levels in the environment may lead to long-term health risks to both humans and ecosystems. Therefore, the monitoring and controlling of their concentration levels in the biosphere are of current interest. Considerable efforts have been devoted to detecting anions and cations via different approaches such as ion selective electrodes [1, 2], voltammetry [3], atomic absorption spectrometry [4], and inductively coupled plasma mass spectrometry [5]. Most of these methods are different in performance, require high-cost instruments, show drawbacks such as low selectivity, low sensitivity, and delayed response to anions and cations, and are not convenient for on-line monitoring. Therefore, a simple, sensitive, and inexpensive method for quantitative detection of anions and cations is highly desirable for real-time monitoring of environmental, biological, and industrial samples. Recently, great attention has been paid to the development of luminescent chemosensors for the detection of anions and cations because they offer several advantages over other analytical methods in terms of high sensitivity, high selectivity, and fast response times, which can be used for real-time monitoring and nondestructive detection.

Many features of fluorescence to report the chemical recognition event make it one of the most powerful transmission mechanisms [6]. Fluorescence microscopy and spectroscopy techniques based on the lifetime, anisotropy, or intensity of the emission of luminescent probes have been developed over the years [7]. These are tremendously sensitive techniques that permit even the detection of single species. Fluorescence does not consume analytes and no need to reference. Light can travel without physical wave-guide, facilitating enormously the technical requirements [8]. Additionally with fluorescence method, it is possible to perform remote monitoring. For example, it is possible to monitor simultaneously concentrations of the target anions/cations in all regions of a living cell [9]. Fluorescence spectroscopy also enables the design of different assays based on different aspects of the fluorescence output (lifetime, intensity, anisotropy, and energy transfer). Laser fiber optics and detection technologies are also well established. Therefore, fluorescence techniques are considered as the most important detection method of the future for miniaturized ultra-high-throughput screening [8, 10].

A luminescent chemosensor usually includes two incorporated components in its structure (Figure 9.1). One of these components is a signaling luminophore, and another is a guest receptor that has recognition ability. Luminophore and guest receptor are linked through a spacer to produce a

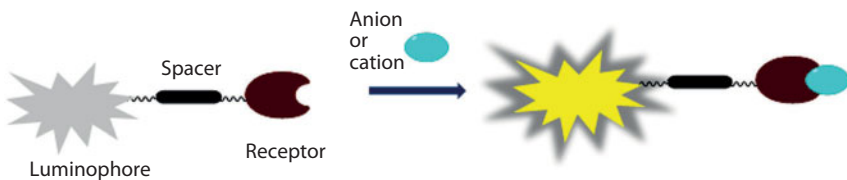


**Figure 9.1** Schematic representation of a luminescent sensor.

named luminophore-spacer-receptor scaffold [11]. Upon anion or cation are bound to the receptor, the photophysical features of the luminophore, such as emission intensity, lifetime and emission wavelength, will change via different mechanisms, and such a change produces a signal that shows binding to receptor of guest. Because luminescent sensors are applied to many disciplines such as food analysis, process control, environmental monitoring and medical diagnosis, a thorough understanding of constructions of these can help to clarify and to enhance the design of luminescent chemosensors to develop sophisticated sensing systems [12–14]. Up to now, a great variety of luminescent sensors for anions/cations have been derivatized from various chemical classes including rhodamine, triphenylamine, coumarin, calixarene, pyrene, perylene, boron-dipyrrromethene (BODIPY), 8-hydroxy-quinoline, anthraquinone, 1,1'-bi-2-naphthol (BINOL), and 2-hydroxy-naphthaldehyde (Figure 9.2).

To design new luminescent sensors, finding new interaction mechanisms between chemical species and chemosensors is still of increasing interest. Until now, a number of conventional signaling mechanisms have been developed and widely used for detection of different species. These involve photo-induced electron transfer (PET) [15–20], intramolecular charge transfer (ICT) [16–20], metal-ligand charge transfer (MLCT) [16, 18, 21], twisted intramolecular charge transfer (TICT) [16, 22], electronic energy transfer (EET) [16–18], C=N isomerization [23], excited-state intramolecular proton transfer (ESIPT), fluorescence resonance energy transfer (FRET) [24, 25], and excimer/exciplex formation [16–19, 20, 26]. The classification of these signal mechanisms has been simply summarized here. Among these signal mechanisms, PET is commonly utilized electron transfer process in this area. Generally, the emission of a luminophore is quenched owing to PET process, and could be recovered via the inhibition of PET by anions/cations. Charge transfer processes contain ICT, TICT, and MLCT. In the photo physics of donor-acceptor  $\pi$ -conjugated systems, ICT is one of the most widely studied phenomena. Otherwise, TICT is a strong ICT taking place in the excited state that includes solvent relaxation around the molecule. The luminescence

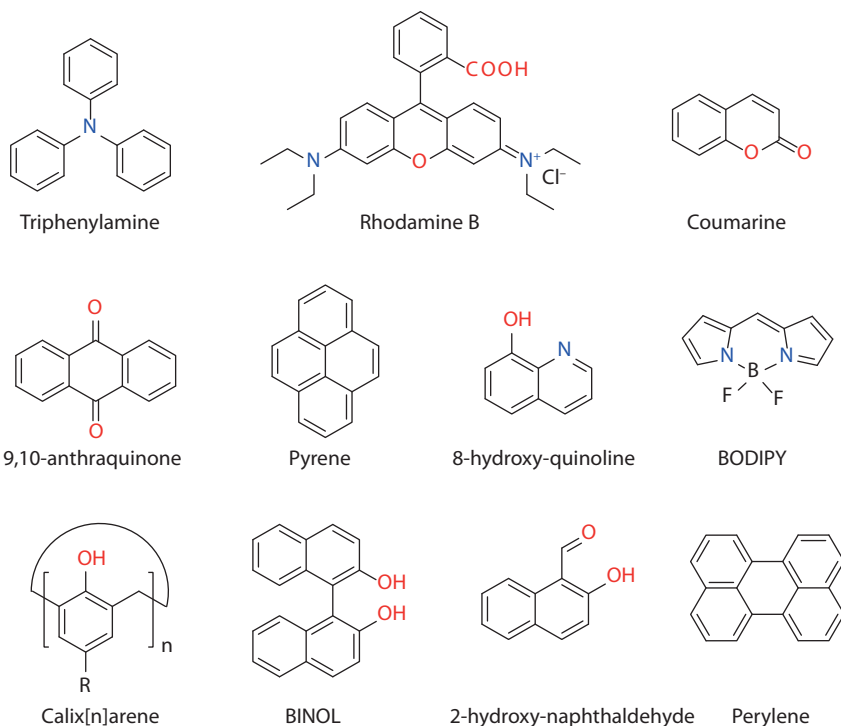


**Figure 9.2** The chemical structures of the different luminophores using in luminescent materials.

behavior is very sensitive to micropolarity and/or steric hindrance for molecular rotation because the intramolecular rotation and charge separation in the TICT state need the polar solvent relaxation. In addition, MLCT, in which charge transfer occurs from a ligand to a transition metal cation, is commonly observed in transition metal complexes. Also, it can be used for design of luminescent sensor through the influence of MLCT energy level by chemical species. FRET and EET are mechanisms describing energy transfer between two light-sensitive molecules. To be efficient of EET and FRET, the distance between the donor and acceptor should be 10 Å for EET and from 10 to 100 Å for FRET. ESIPT is of prime importance in luminescent materials. The most significant photophysical property of the ESIPT chromophores is the large Stokes shift, compared to other luminophores, and the large Stokes shift is a distinct characteristic for luminophores. C=N isomerization has been also used as a signaling mechanism for luminescent sensors. Compounds with an unbridged C=N structure are often nonluminescent due to the C=N isomerization in the excited

states. The C=N isomerization effect in compounds may be inhibited upon the coordination of imine derivative to a guest species. Above-mentioned signaling mechanisms are widely used for detection of anions and cations, and recently the amount of research in this field has increased considerably. Herein it is intended to provide an overview of luminescent materials for anions and cations.

## 9.2 Luminescent Materials for Sensing of Cations

The development of luminescent sensors for the detection of alkaline, alkaline earth, and transition metal ions has been attracted considerable attention because they play essential roles in physiological and environmental processes [27]. Among the various metal ions, Zn<sup>2+</sup> has attracted a great deal of attention ascribing to its biological significance. Minute quantity of Zn<sup>2+</sup> is necessary for the living organism, but excessive amount can have damaging effect to the organism [28–30]. On the contrary, a trace amount of Cd<sup>2+</sup> is known as toxic and carcinogenic for human body, which can cause serious disease such as prostate cancer, disorders of calcium metabolism, renal dysfunction, metal fume fever, pneumatics, and pulmonary edema [30, 31]. The unregulated Cu<sup>2+</sup> ion can lead to oxidative stress, and their concentration in the neuronal cytoplasm may cause the etiology of Alzheimer's or Parkinson's disease [32]. Cu<sup>2+</sup> ion plays a critical role as catalytic cofactor for a variety of metallo enzymes, involving superoxide dismutase, cytochrome oxidase, and tyrosinase. Among all metal ions, Hg<sup>2+</sup> and Pb<sup>2+</sup> are considered as most dangerous cations for their extreme toxicity may cause adverse effects on human health even at low concentration [33]. Hg<sup>2+</sup> also causes strong damage to the central nervous system. Accumulation of mercury in the human body may lead to various cognitive and motor disorders, and well known Minamata disease [34, 35]. Similarly, Pb<sup>2+</sup> exposure to the human body, especially in children may cause a variety of symptoms such as memory loss, irritability, anemia, and muscle paralysis [36]. Trivalent chromium (Cr<sup>3+</sup>) is not only an essential component of a balanced human and animal diet in amounts of 50–200 µg per day (WHO 1988), but also plays an important role in the metabolism of carbohydrates, lipids, proteins, and nucleic acids [37]. However, high levels of Cr<sup>3+</sup> can negatively affect cellular structures and damage cellular components by forming reactive oxygen species, thereby stimulating anti-oxidative enzyme activity [38, 39]. In addition to these prominent metal ions, there are advantages and disadvantages of other metal ions to humans and ecosystems. Consequently, the simple and inexpensive methods for

quantitative detection of them are highly desirable for real-time monitoring of environmental, biological, and industrial samples. Recently, luminescent sensors have shown great potential in the detection of metal ions. For convenience, luminescent materials for cations have been categorized according to the group of the element as below.

### 9.2.1 Luminescent Materials for Alkaline and Alkaline Earth Metals

Among the alkaline metal ions, lithium, sodium and potassium ions have very important functions in biological systems. In the group of alkaline earth metal ions, only  $Mg^{2+}$  and  $Ca^{2+}$  ions are ubiquitous and essential to all known living organisms and have proven biological functions. Luminescent materials are mostly used to detect alkaline and alkaline earth metal ions (Figure 9.3). In this context, Gunnlaugsson *et al.* (2002) designed and synthesized the chiral diaza-9-crown-3 derivative **1** which is the first example of a highly selective  $Li^+$  PET chemosensor. Sensor **1** showed “off-on” type response toward  $Li^+$  ion. The PET sensing ability of **1** was also examined in several organic solvents. The obtained results indicated that **1** was acting as a PET  $Li^+$  chemosensor in non-aqueous solutions. In  $CH_3CN$ , the addition of  $Li^+$  to **1** induced a ca. fivefold increase in emission intensity [40]. Kim *et al.* (2010) have reported a synthesis of the photostable two-photon (TP) luminescent probe **2**, which utilizes 1,7-diaza-15-crown-5 as the  $Na^+$  ion receptor, and 2-acetyl-6-(dimethylamino)-naphthalene (acedan) as the reporter luminophore. Probe **2** showed strong emission enhancement toward  $Na^+$  ion in the cell. The  $Na^+$  ions in live cells and living tissues can be selectively detected by this probe [41]. Huang *et al.* (2008) have prepared a new sensor complex (OG.Apt) using OliGreen and an ATP-binding aptamer. They investigated the selectivity of this sensor toward  $K^+$  over other ions ( $Na^+$ ,  $Li^+$ ,  $NH_4^+$ ,  $Mg^{2+}$ , and  $Ca^{2+}$ ) under the optimum conditions. It was found that the selectivity of this sensor for  $K^+$  over other ions in aqueous solution is remarkably high (>10,000-fold over  $Na^+$ ) and its detection limit is 75 nM [42]. To simultaneously detect  $Na^+$  and  $K^+$  at a single-cell level is significant. Li *et al.* (2015) have presented a novel method to discriminate and to quantify simultaneously  $Na^+$  and  $K^+$  in single cells using a new near-infrared luminescent probe associated with microchip electrophoresis. For this, they have synthesized a new probe **3** by reacting of acetophenone and 2,6-pyridinedicarboxaldehyde [43]. The results displayed that the luminescent probe **3** can simultaneously respond to both  $Na^+$  and  $K^+$  with near-infrared emission enhancement. As well as  $Li^+$ ,  $Na^+$ , and  $K^+$  ions, the detection of cesium is of great interest due to its intrinsic

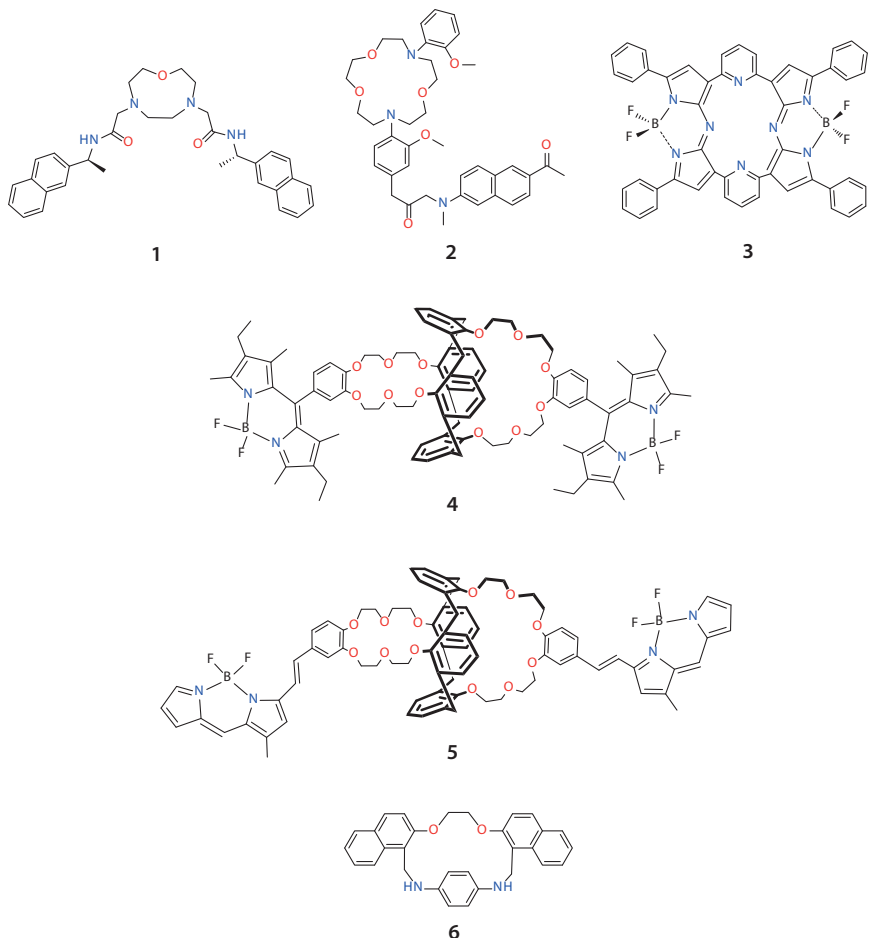


**Figure 9.3** Structures of luminescent sensor **1–6** for alkaline metal ions.

toxicity. Depauw *et al.* (2015) have improved two novel luminescent sensors (**4** and **5**) consisting of a calix[4]arene biscrown-6 ether as coordination site and a BODIPY derivative as signaling unit. The complexation behaviors of  $K^+$  and  $Cs^+$  with **4** and **5** were also investigated. While  $K^+$  and  $Cs^+$  ions cause a slight bathochromic shift in absorption and fluorescence spectra of **4**, cation complexation induces a more pronounced hypsochromic shift of absorption and fluorescence spectra of **5**. These sensors exhibited a high stability constant with cesium and a good selectivity toward the cesium ion versus the potassium ion [44]. In another study, a new macrocyclic nano-chemosensor based on 2-hydroxy-naphthalaldehyde **6** was reported by Azadbakht and Khanabadi (2015). The nano-chemosensors with size about

40 nm were synthesized by nanoprecipitation method. They have concluded that this nano-chemosensor shows a high affinity and selectivity for cesium ions over most other competitive metal ions such as  $\text{Na}^+$ ,  $\text{K}^+$ ,  $\text{Mg}^{2+}$ ,  $\text{Ba}^{2+}$ ,  $\text{Al}^{3+}$ ,  $\text{Pb}^{2+}$ ,  $\text{Mn}^{2+}$ ,  $\text{Fe}^{3+}$ ,  $\text{Fe}^{2+}$ ,  $\text{Co}^{2+}$ ,  $\text{Ni}^{2+}$ ,  $\text{Cu}^{2+}$ ,  $\text{Zn}^{2+}$ ,  $\text{Cd}^{2+}$ , and  $\text{Hg}^{2+}$  [45].

Some chemosensors working with different strategies have been developed for the selectively sensing of alkaline earth metal ions as illustrated in Figure 9.4. A simple quinolone derivative 7 showing a highly selective emission enhancement for  $\text{Mg}^{2+}$  ion over other metal ions has been reported by Kao *et al.* (2016). This selectivity was explained by C=N isomerization which is inhibited by the formation of a rigid structure between imine and  $\text{Mg}^{2+}$  ion. Also, the detection limit of 7 for  $\text{Mg}^{2+}$  ion and the association constant in 1:1 binding mode were determined as 19.1 ppb and  $1.91 \times 10^{-7} \text{ M}^{-1}$ , respectively [46]. Qin *et al.* (2015) have synthesized a naphthalene-based Schiff-base derivative containing rhodamine 8 which

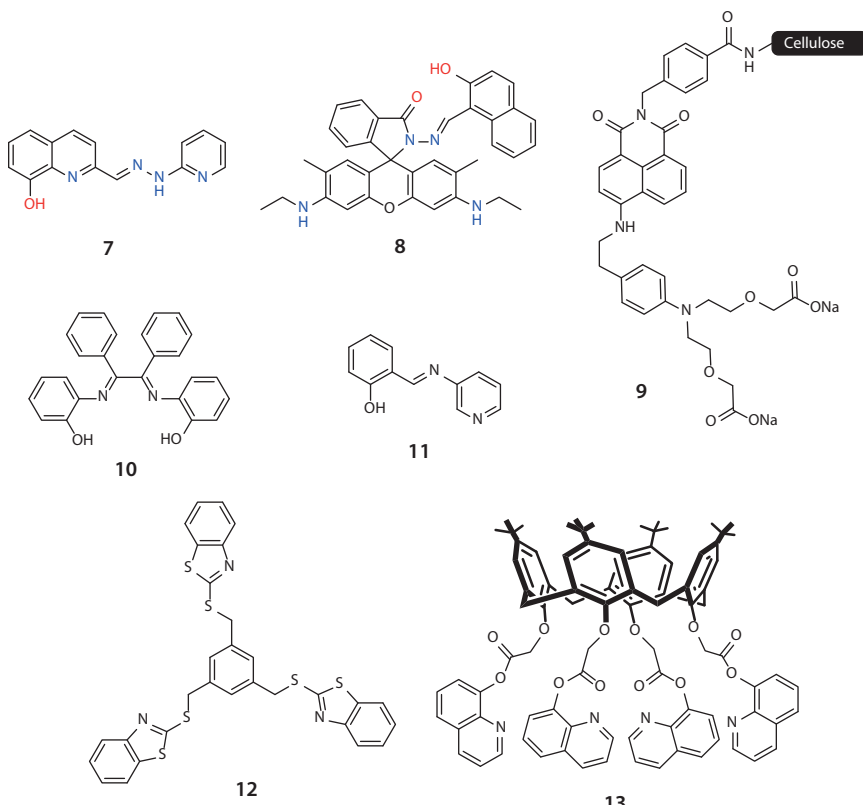
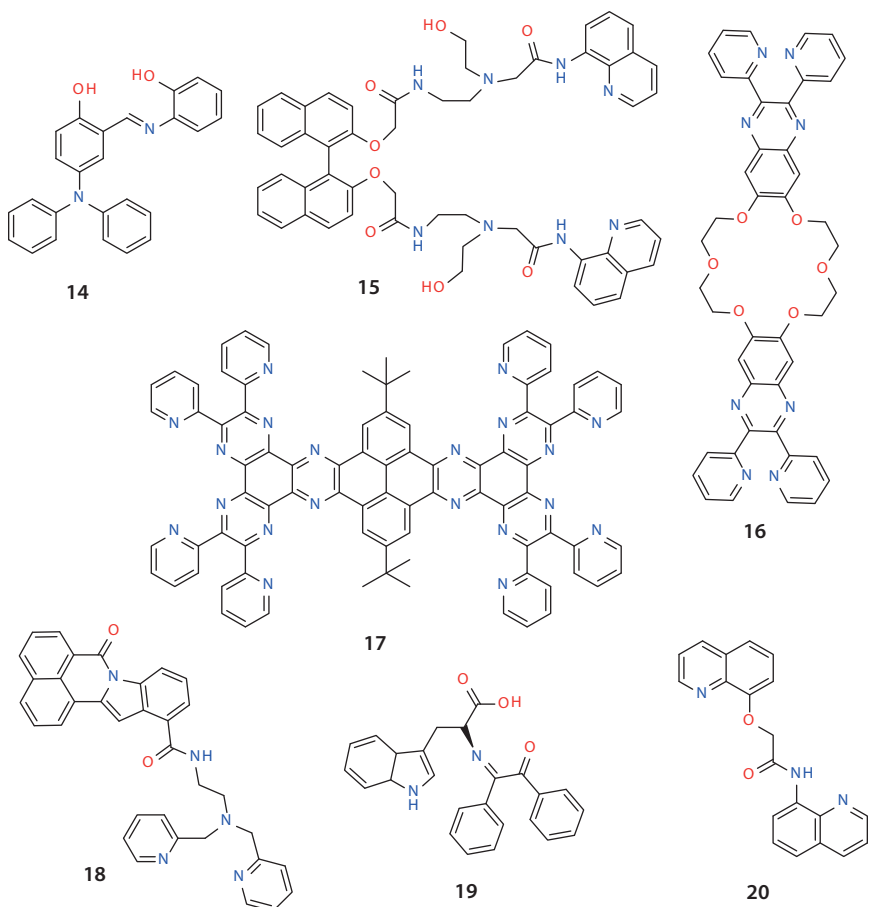


Figure 9.4 Structures of luminescent sensor 7–13 for alkaline earth metal ions.

serves as a dual analyte chemosensor for  $Mg^{2+}$  and  $Zn^{2+}$ . Chemosensor **8** displayed a weak emission due to the highly efficient PET process. PET process was inhibited by the coordination of the  $-C=N$  group in **8** with  $Mg^{2+}$  resulting in the emission enhancement [47]. To monitor of the calcium ion concentration in seawater, a novel 4-amino-1,8-naphthalimide-based luminescent sensor **9** bearing phenyliminodiethoxyacetic acid as receptor has been prepared by Liu *et al.* (2014). As known, the potential interfering species for the determination of calcium in seawater are magnesium and strontium ions. Also pH is one of the major factors affecting the sensing ability and sensitivity in the aqueous solutions. They reported that this sensor can be applied for the detection of calcium ion in fresh water and seawater in the presence of magnesium and strontium ions at optimum pH [48]. In another study performed for  $Ca^{2+}$  ion, Dutta *et al.* (2014) have synthesized a simple condensation product **10** containing benzyl and 2-aminophenol moieties. The spectroscopic studies showed that **9** act as "turn on" luminescence sensor for  $Ca^{2+}$  ion over other metal ions  $Na^+$ ,  $K^+$ ,  $Ba^{2+}$ ,  $Mg^{2+}$ ,  $Mn^{2+}$ ,  $Co^{2+}$ ,  $Ni^{2+}$ ,  $Zn^{2+}$ ,  $Cd^{2+}$ ,  $Ag^+$ ,  $Pb^{2+}$ , and  $Hg^{2+}$ . This emission enhancement was explained by higher planarity of the aromatic phenol rings in **10** based on DFT (density functional theory) calculations [49]. Due to the adverse effects of  $Ba^{2+}$  on the human body, development of a luminescent sensor for  $Ba^{2+}$  is currently of great importance. In this regard, an excellent luminescence sensor was designed and synthesized by Zhao *et al.* (2015). This sensor **11** was prepared by a simple condensation reaction between 3-aminopyridine and salicylaldehyde. The results displayed that **11** has high selectivity and sensitivity for  $Ba^{2+}$  over other metal ions through emission enhancement [50]. A benzothiazole-based tripodal chemosensor **12** showing a distinct luminescence response toward  $Ba^{2+}$  with high selectivity and sensitivity has presented by Saluja *et al.* (2011). Also, they have successfully used this sensor to monitor  $Ba^{2+}$  in biological samples [51]. Sutariya *et al.* have reported a quinolone-calix[4]arene-based "on-off-on" type PET sensor **13** for  $Sr^{2+}$  and  $Cd^{2+}$  ions. Moreover,  $Cd^{2+}$  and  $Sr^{2+}$  ions were detectable at levels as low as 0.94 and 1.04 pM, respectively, and their systems have been applied to detection of  $Cd^{2+}$  and  $Sr^{2+}$  with 101–115% recovery in industrial water samples [52].

### 9.2.2 Luminescent Materials for Transition Metal Ions

To develop luminescent sensors for transition metal ions among the different species, special interest is devoted by many scientists. Transition metal ions usually represent an environmental concern when present in uncontrolled amounts, but at the same time some of them are essential elements



**Figure 9.5** Luminescent probes **14–20** for  $Zn^{2+}$  and  $Cd^{2+}$  ions.

for biological systems. In our contribution, we will overview novel luminescent sensors for this class of metal ions (Figure 9.5).

The sensing of same group elements such as  $Zn^{2+}$  and  $Cd^{2+}$  ions with a single chemosensor by the emission enhancement at distinct wavelength is rare. Erdemir and Malkondu (2013) have presented a novel easily available turn-on luminescent sensor based on a triphenylamine-aminophenol conjugate **14**. Due to isomerization of the C=N double bond and ICT, **14** showed a weak emission band at 580 nm. The C=N isomerization and ICT effect in **14** are inhibited upon the coordination of **14** to  $Cd^{2+}$  or  $Zn^{2+}$ . In addition, it forms a rigid conjugation system, causing the CHEF (chelation-enhanced fluorescence) effect. They observed 8- or 10-fold emission enhancement upon the addition of  $Cd^{2+}$  or  $Zn^{2+}$ , respectively [53].

Tian *et al.* (2015) prepared a BINOL-derivative **15** for highly selective recognition of Zn<sup>2+</sup>. **15** showed a high selectivity toward Zn<sup>2+</sup> over other metal ions especially over Cd<sup>2+</sup> via the CHEF mechanism on a 1:1 binding stoichiometry. This sensor was also used in the determination of Zn<sup>2+</sup> in tap water. Recovery data showed that **15** has the appreciable practicality [54]. Li *et al.* (2012) have reported a Zn<sup>2+</sup> selective luminescent chemosensor **16** containing 2,3-bis(pyridin-2-yl)quinoxaline and crown ether moieties. The complexation studies were realized by single-crystal X-ray crystallography, mass spectrometry, and <sup>1</sup>H NMR (nuclear magnetic resonance) titration experiments. From the obtained results, they concluded that **16** can serve as both an INHIBIT logic gate and an "off-on-off" molecular switch triggered by Zn<sup>2+</sup> and K<sup>+</sup> [55]. Yang *et al.* (2014) have designed a hexaazatriphenylene derivative **17** including pyridyl and pyrene moieties serving as off-on type luminescent sensor for Cd<sup>2+</sup>. Also they investigated its performance in living cell and results showed that sensor **17** is suitable for the *in vivo* imaging of Cd<sup>2+</sup>. The detection limit of **17** toward Cd<sup>2+</sup> was calculated to be 0.02 μM, and this remarkably low detection limit was explained by the extending of the chromophoric group with pyrene in **17** exaggerates the emission response [56]. A luminescent sensor **18** based on the PET mechanism with a low detection limit ( $1.19 \times 10^{-12}$  M) for Cd<sup>2+</sup> has been designed and prepared by Liu *et al.* (2015). In addition, the reversibility and cycle ability properties of **18** were examined by testing a number of anions (Ac<sup>-</sup>, BF<sub>4</sub><sup>-</sup>, F<sup>-</sup>, Cl<sup>-</sup>, Br<sup>-</sup>, I<sup>-</sup>, NO<sub>3</sub><sup>-</sup>, NO<sub>2</sub><sup>-</sup>, S<sup>2-</sup>, HSO<sub>3</sub><sup>-</sup>, S<sub>2</sub>O<sub>3</sub><sup>2-</sup>, SO<sub>4</sub><sup>2-</sup>, PO<sub>4</sub><sup>3-</sup>, HPO<sub>4</sub><sup>2-</sup>, H<sub>2</sub>PO<sub>4</sub><sup>-</sup>, PPi, ATP, ADP, AMP). Only with the addition of PPi (pyrophosphate) to **18**-Cd<sup>2+</sup> complex, the obvious emission quenching was observed at 501 nm [57]. Dutta *et al.* (2014) have reported a Schiff base **19** obtained by condensation between benzil and L tryptophan. In CH<sub>3</sub>OH:H<sub>2</sub>O media, **19** induced a 10-fold the emission enhancement toward Zn<sup>2+</sup> with a detection limit in micromolar level. Also, they successively tested the ability of **19** in determination of Zn<sup>2+</sup> ion concentration in multi mineral tablet [58]. In another study, for distinguishing Cd<sup>2+</sup> from Zn<sup>2+</sup> ions, Zhao *et al.* (2012) have synthesized *N*-(quinolin-8-yl)-2-(quinolin-8-yloxy)acetamide **20** as an efficient sensor. Results showed that **20** can distinguish Cd<sup>2+</sup> from Zn<sup>2+</sup> via two different sensing mechanisms (PET for Cd<sup>2+</sup> and ICT for Zn<sup>2+</sup>) [59].

Some excellent luminescent chemosensors for Mn<sup>2+</sup> and Fe<sup>2+</sup> have been developed (Figure 9.6). Roy *et al.* (2015) have reported a Mn<sup>2+</sup> selective "turn on" luminescent chemosensor based on Schiff base **21**. Under similar conditions, the other common alkaline, alkaline earth and transition metal ions could not produce a considerable change in the emission spectra. They have confirmed 1:1 stoichiometry between **21** and Mn<sup>2+</sup> with association constant of  $3.1 \times 10^3$  M<sup>-1</sup> from the Benesi–Hildebrand equation.

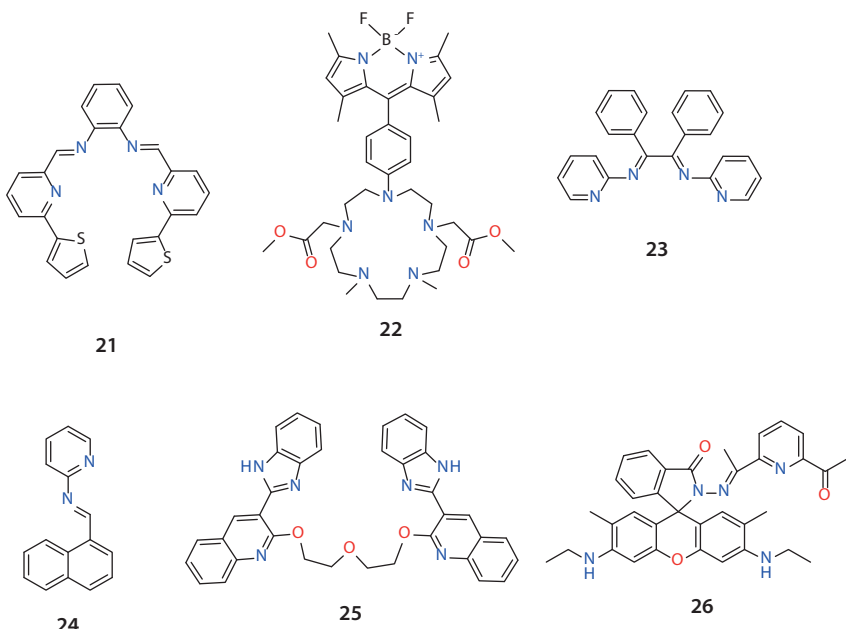


**Figure 9.6** Luminescent probes **21–26** for  $Mn^{2+}$  and  $Fe^{2+}$  ions.

To determine a suitable pH range for  $Mn^{2+}$  sensing, pH titration of **21** was also performed and the obtained results implied that **21** can be used to detect  $Mn^{2+}$  over a wide range of acidic pH of 3.0–7.0. [60]. The BODIPY-based luminescent sensor **22** for  $Mn^{2+}$  was developed by Bakthavatsalam *et al.* (2015). The addition of  $Mn^{2+}$  to **22** induced significant increase in emission intensity through PET mechanism. The selectivity and sensitivity of this sensor in determination of  $Mn^{2+}$  were tested within live cells [61]. Another study performed for  $Mn^{2+}$  has been presented by Dutta *et al.* (2013). They synthesized a “turn on” sensor **23** by using 2-Amino pyridine and benzil. Emission intensity of **23** enhanced distinguishingly on interaction with  $Mn^{2+}$  ion compared to other metal ions  $Na^+$ ,  $K^+$ ,  $Ca^{2+}$ ,  $Mg^{2+}$ ,  $Ba^{2+}$ ,  $Fe^{2+}$ ,  $Co^{2+}$ ,  $Ni^{2+}$ ,  $Cu^{2+}$ ,  $Zn^{2+}$ ,  $Cd^{2+}$ ,  $Hg^{2+}$ ,  $Pb^{2+}$ , and  $Ag^+$ . To understand better the complexation behavior of **23** with  $Mn^{2+}$ , DFT calculation was carried out, and the results displayed that  $Mn^{2+}$  ion binds to the chemosensor via the four N-atoms of the pyridine moiety. This binding was interrupted by the PET process leading to emission enhancement [62]. Among the transition metal ions, iron is one of the most essential metal ions in our living systems. Thus, the rapid detection and discrimination of  $Fe^{2+}$  from other ions including  $Fe^{3+}$  are significant. Santhoshkumar *et al.* (2015)

prepared a naphthalene pyridine Schiff base **24** as a luminescent sensor which exhibits high selectivity and sensitivity toward  $\text{Fe}^{2+}$  ions in  $\text{CH}_3\text{CN}-\text{H}_2\text{O}$  media with a low detection limit of  $1.5 \times 10^{-7}$  M. This selectivity was emerged from both ICT and C=N isomerization mechanisms. The practical applications also showed that **24** could potentially be used for the determination of  $\text{Fe}^{2+}$  ion in real samples [63]. A condensation reaction of 3-(1H-benzoimidazol-2-yl)-2-chloro-quinoline with diethylene glycol has carried out by Mahalingam *et al.* (2015). Metal binding properties of the synthesized Bisbenzimidazo quinoline **25** were examined by absorption, emission and electrochemical studies. **25** showed a "turn on" type response for  $\text{Fe}^{2+}$  ion [64]. Hou *et al.* (2013) have prepared a rhodamine derivative **26** bearing pyridine unit and examined its recognition behavior in presence of various metal ions. The results indicated high selectivity of **26** toward  $\text{Fe}^{2+}$  in PBS (phosphate-buffered saline) buffer. Selective emission enhancement of **26** upon interaction with  $\text{Fe}^{2+}$  was attributed to ring opening from the spirolactam (nonluminescent) to ring-opened amide (luminescent). In addition, they realized confocal laser scanning microscopy experiments showing that it can be used to monitor  $\text{Fe}^{2+}$  in living cells [65].

The construction and design of chemosensors exhibiting high selectivity and sensitivity for trace metal ions, such as  $\text{Ni}^{2+}$  and  $\text{Co}^{2+}$ , are of current interest as they allow prompt and nondestructive detection of metal ions through simple absorbance and emission responses (Figure 9.7). Bu *et al.* (2015) have reported a "turn on" luminescent sensor bearing Schiff base function **27** for  $\text{Co}^{2+}$  with a remarkably low detection limit of  $10^{-14}$  M. Chemosensor **27** showed high selectivity for  $\text{Co}^{2+}$  over other metal ions with 17-fold emission enhancement [66]. To determine  $\text{Co}^{2+}$  and  $\text{Ni}^{2+}$  ions in aqueous media, two novel luminescent and colorimetric sensor-based rhodamine **28** and **29** have been synthesized by Abebe *et al.* (2011). Chemosensors **28** and **29** showed high sensitivity and selectivity toward  $\text{Co}^{2+}$  and  $\text{Ni}^{2+}$  over other interfering cations through the spirolactam ring opening process. The 1:1 stoichiometry of **28** or **29** with  $\text{Co}^{2+}$  or  $\text{Ni}^{2+}$  was confirmed by Job's plot of the emission changes. Also, the association constants of **28** with  $\text{Co}^{2+}$  or  $\text{Ni}^{2+}$  were found to be  $2.1 \times 10^4$  and  $4.5 \times 10^3$  M<sup>-1</sup> from the fluorescence titration data, respectively [67]. A new terpyridine derivative ligand 4'-4-(1,2,4-triazol-1-yl)-phenyl-2,2':6',2"-terpyridine and its  $\text{Zn}^{2+}$  complex **30** were prepared by Wang *et al.* (2012) and the complex's structure was clarified by X-ray crystallography. The metal sensing studies revealed that complex **30** is a selective "turn-off" luminescent sensor for  $\text{Co}^{2+}$  and  $\text{Ni}^{2+}$  ions. Moreover, the diminished emission of **30+Co<sup>2+</sup>** could be restored by the addition of EDTA (ethylenediaminetetraacetic acid) into **30+Co<sup>2+</sup>** but not for **30+Ni<sup>2+</sup>**, indicating the strong coordination ability of

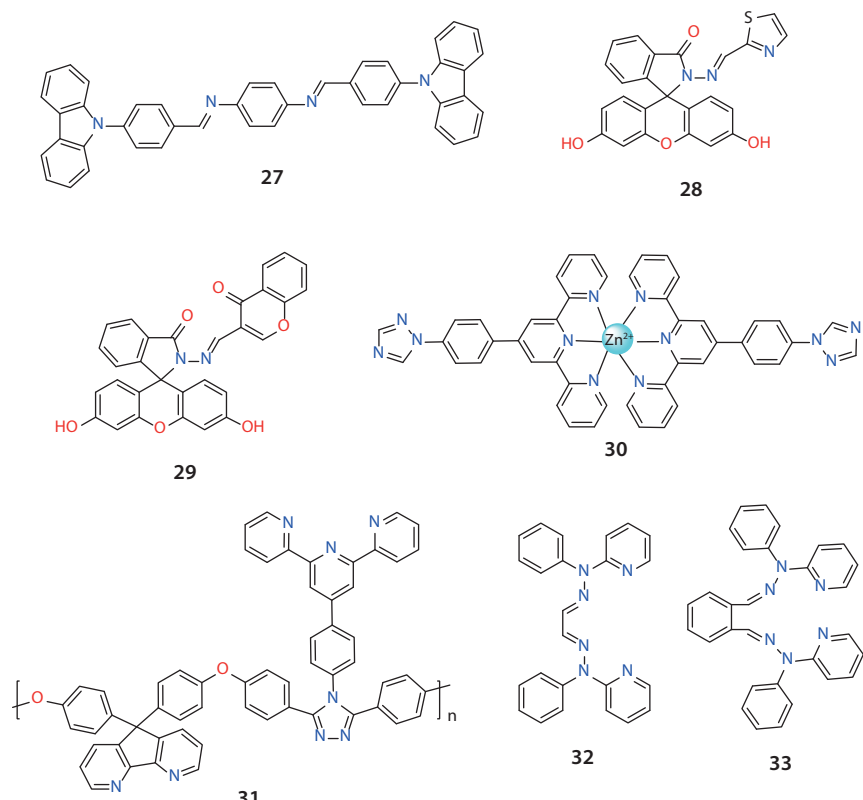


**Figure 9.7** Luminescent probes 27–33 for Ni<sup>2+</sup> and Co<sup>2+</sup> ions.

terpyridine to Ni<sup>2+</sup> [68]. Li *et al.* (2013) have interested conjugated polymers (CPs) acting as versatile sensory materials due to their ease of measurement and high sensitivity in transforming chemical signals into electronic signals when binding with metal ions as well as anionic species. They prepared a novel poly(arylene ether) (PAET) 31 substituted with terpyridine and investigated its cation sensing properties. The emission intensity of 31 is completely quenched by Ni<sup>2+</sup> ions. The results indicated that 31 can be used as a selective luminescent sensor for Ni<sup>2+</sup> in the presence of most competing metal ions [69]. Ghosh *et al.* have prepared two new tetradentate ligands 32 and 33 as luminescent probes for Ni<sup>2+</sup> ion. Fluorescence spectral studies displayed that Ni<sup>2+</sup> ions induce a significant emission enhancement, but not other metal ions. These data suggest that these molecules can be used as molecular probes to monitor Ni<sup>2+</sup> ion levels [70].

In addition, Cu<sup>2+</sup>, Hg<sup>2+</sup>, and Pb<sup>2+</sup> ions are significant environmental pollutants depending on their concentration. Owing to the advantages

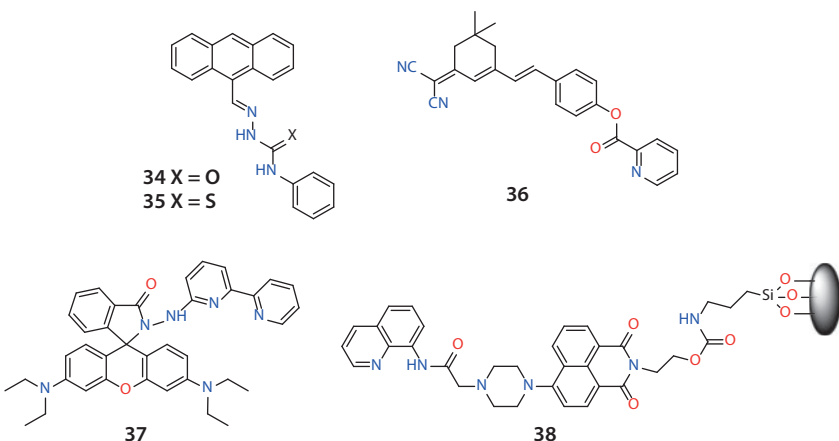


**Figure 9.8** Luminescent probes 34–38 for  $\text{Cu}^{2+}$  ion.

of simplicity, inexpensive instrumentation and suitability for real-time monitoring of these metals, novel luminescent sensors for the detection of  $\text{Cu}^{2+}$ ,  $\text{Hg}^{2+}$ , and  $\text{Pb}^{2+}$  in the environment have been designed in recent years (Figures 9.8–9.10). In 2015, Erdemir and Malkondu have designed and synthesized two novel anthracene-based receptors bearing Schiff base and urea groups 34 and 35. Also, they examined the optical properties of 34 and 35 in presence of various metal ions by UV-visible and fluorescence spectroscopy. Spectroscopic data indicated that 34 and 35 have high selective and sensitive behaviors toward  $\text{Cu}^{2+}$  ion over 17 metal ions. The addition of  $\text{Cu}^{2+}$  to 34 induced a 114-fold increase in emission intensity (blue emission), while the addition of  $\text{Cu}^{2+}$  to 35 led to a 15-fold increase (green emission) [71]. An *et al.* (2016) have reported a “turn-on” luminescent sensor based dicyanoisophorone 36 for detection of  $\text{Cu}^{2+}$  in aqueous media. 36 showed drastic emission enhancement with large Stokes shift to  $\text{Cu}^{2+}$  over other metal ions. The increased emission intensity resulted from the luminescent hydrolysis product of 36 catalyzed by  $\text{Cu}^{2+}$  in buffered water solution and hydrolysis mechanism was supported by  $^1\text{H}$  NMR data. Also, they successfully applied 36 to fluorescence imaging of  $\text{Cu}^{2+}$  in living cells [72]. In another study, Yuan *et al.* (2015) have synthesized a rhodamine B-based receptor 37 by reaction of 6-bromo-2,2'-bipyridine and rhodamine hydrazide in 2-propanol. This probe 37 presented fluorometric and colorimetric responses to  $\text{Cu}^{2+}$  ions with a detection limit of 0.739 nM, which is the lowest ever reported up to that time. Also, they developed the test papers of probe 37 to monitor  $\text{Cu}^{2+}$  ions in drinking water [73]. Bifunctional silica nanoparticle sensor bearing a naphthalimide

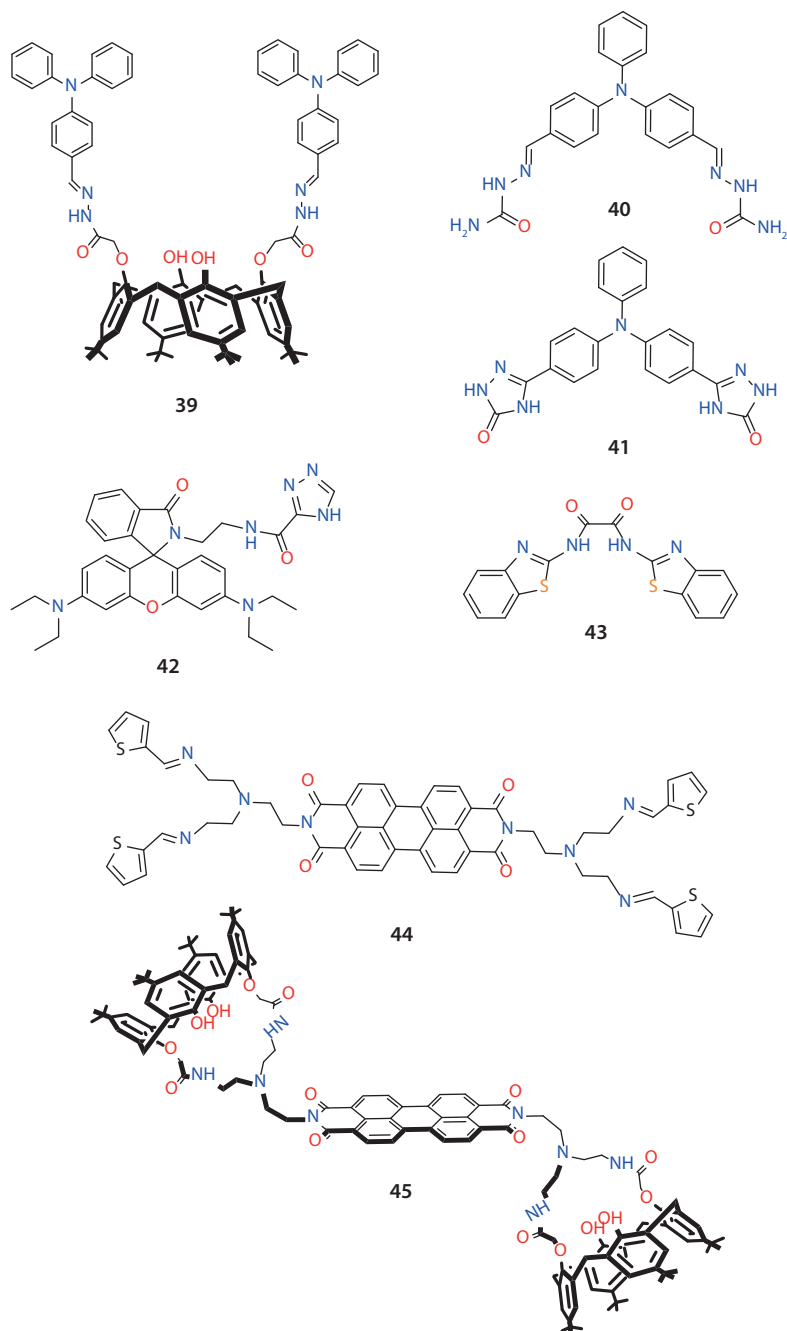
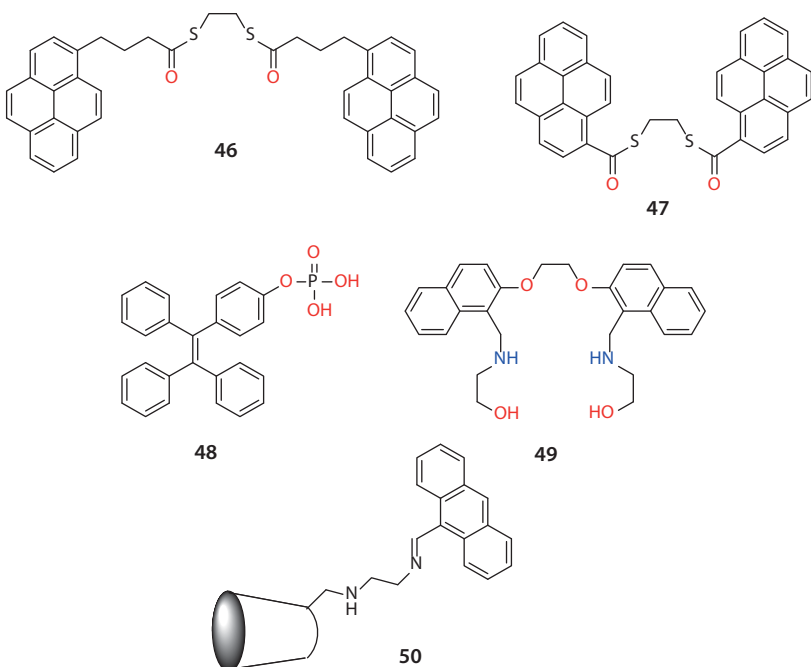


Figure 9.9 Luminescent probes 39–45 for  $\text{Hg}^{2+}$  ion.



**Figure 9.10** Luminescent probes **46–50** for  $\text{Pb}^{2+}$  ion.

group **38** has designed by Zhang *et al.* (2015). The prepared nanosensor was characterized by the combination of Fourier transform infrared spectroscopy (FTIR), scanning electron microscope (SEM), and thermogravimetric analysis (TGA). The selectivity of **38** was also tested in the presence of various metal ions by fluorescence and UV-vis techniques. Interaction of **38** with  $\text{Cu}^{2+}$  leads to the exclusive selectivity, and no obvious luminescent response to the other metal ions. Since the reversibility of a sensor is particularly attractive property for practical applications, they also tested the reversibility of **38** by the alternate addition of  $\text{Cu}^{2+}$  and EDTA [74].

Novel luminescent materials for  $\text{Hg}^{2+}$  considered as one of the most dangerous cation for its extreme toxicity have been reported by Erdemir's group. Calix[4]arene derivative appended triphenylamine moieties **39** was synthesized and its recognition process for anion and cation was monitored by luminescence UV-vis and  $^1\text{H}$  NMR spectral changes. Both selective fluorometric and colorimetric response for  $\text{Hg}^{2+}$  in  $\text{CH}_3\text{CN}$  were achieved with **39**. The quenching efficiency of **39** ( $I_0/I$ ) was found to be 31.2 for  $\text{Hg}^{2+}$ , showing strong complex formation with  $\text{Hg}^{2+}$  [75]. Another triphenylamine chemosensor bearing semicarbazide groups **40** have been reported by Malkondu

and Erdemir (2014). From the spectroscopic data, they found that **40** shows fluorogenic ‘turn-on’ response induced from Cu<sup>2+</sup> via a unique cyclization reaction. The radicalic cyclization reaction of **40** in the presence of Cu<sup>2+</sup> was proved by ESR (electron spin resonance) and diode-array UV-vis studies. The cyclization product **41** obtained from the reaction of **40** with Cu<sup>2+</sup> also displayed a selective luminescent sensing behavior toward Hg<sup>2+</sup> ions. They revealed that Hg<sup>2+</sup> ion coordinates with the nitrogen atoms of the imine group as well as oxygen atom of the carbazole moiety based on <sup>1</sup>H NMR titration studies [76]. To detection Hg<sup>2+</sup> in aqueous solutions, triazole moieties have been linked to rhodamine B hydrazide derivative **42** by Erdemir *et al.* (2015). The prepared rhodamine-based receptor was used to monitor Hg<sup>2+</sup> in a mixture of dimethylformamide (DMF) and water (v/v = 1/1, 5 mM, 4-(2-hydroxyethyl)-1-piperazineethanesulfonic acid (HEPES), pH 6.5). A weak and broad emission band were observed with a quantum yield of Φ<sub>**42**</sub> = 0.0039. Upon complexation with Hg<sup>2+</sup>, the quantum yield reached Φ<sub>**42-Hg**<sup>2+</sup></sub> = 0.0826 (about 22-fold). The spirolactam ring opening mechanism between **42** and Hg<sup>2+</sup> was proved by <sup>1</sup>H NMR, <sup>13</sup>C NMR and FTIR analysis. Particularly, FTIR spectra revealed that the complete disappearance of carbonyl band of the spirolactam ring in **42** with the addition of Hg<sup>2+</sup>. In addition, a signal of spiro C=O in <sup>13</sup>C NMR was disappeared upon addition of Hg<sup>2+</sup>, confirming clearly the spirolactam ring opening [77]. The same group (2015) has reported a synthesis of the benzothiazole-based sensor **43** in one step and its recognition ability toward metal ions. A significant emission change of **43** was observed upon the interaction of Hg<sup>2+</sup> ion within a pH range of 4.0–7.0, while only minor changes in emission intensity were observed with other metal ions. Moreover, the complexation behavior of **43** with Hg<sup>2+</sup> was explained by using <sup>1</sup>H NMR data [78].

Perylene-bisimide (PBI) dyes have been widely used as luminophore due to the good electron accepting ability and have generated great interest in the field of photonic materials because of their excellent light and thermal stabilities, high emission efficiency and good semiconducting properties. PBIs are also favorable luminophores for luminescent sensors in the detection of metal ions. For example, a highly efficient and selective PBI sensor bearing thiophene units **44** has been presented by Erdemir and Malkondu (2015). **44** exhibited a rapid and highly selective “turn on” response based on PET mechanism. A highly efficient PET process take places from di(2-thiophenylimino)ethylamine units (DTA) in **44** when DTA units are not involved in Hg<sup>2+</sup> binding. Once DTA units coordinated with Hg<sup>2+</sup> ions, PET process between DTA and PBI is inhibited and this case induces the strong emission enhancement. The formation of **44**-Hg<sup>2+</sup> complex in a 1:2 of stoichiometric ratio was confirmed by Job’s plot method. More importantly, **44**

also showed a similar response with other mercury compounds including  $\text{HgCl}_2$ ,  $\text{Hg}(\text{SCN})_2$ ,  $\text{Hg}(\text{AcO})_2$ , and  $\text{Hg}(\text{NO}_3)_2$ . The effect of the reaction time on the binding process of  $\text{Hg}^{2+}$  ion to **44** was also studied and the emission intensity of **44** was enhanced rapidly, reaching a stable value within 1 min [79]. Another probe with perylene core **45** have been designed and synthesized by Erdemir's group (2015). Firstly, *p*-tert-butylcalix[4]-aza-crown was linked to 3,4,9,10-perylenetetracarboxylicdianhydride in DMF. Secondly, **45** was successfully used to determine  $\text{Hg}^{2+}$  ions in the spiked tap water samples and living cells. Based on PET mechanism, the addition of  $\text{Hg}^{2+}$  to **45** induced a 14-fold increase in emission intensity. Also, a yellow colored visual emission change was developed upon addition of  $\text{Hg}^{2+}$  ion to a solution of **45**. The other metal ions did not produce a remarkable change in the emission spectra under similar conditions. They also performed the reversibility of **45** by the alternate addition of  $\text{Hg}^{2+}$  and tetrabutylammonium iodide (TBAI). Results demonstrated that this reversible process could be repeated several times with little emission efficiency loss [80].

Lead is recognized as one of the most hazardous metals to humans as well as mercury. In the past decade, considerable efforts have been devoted to designing and synthesizing luminescent chemosensors for  $\text{Pb}^{2+}$ . Two luminescent sensors **46** and **47** with high affinity to  $\text{Pb}^{2+}$  have been presented by Hou *et al.* (2011). **46** and **47** were synthesized in two steps by using 1-pyrenebutyric acid, 1-pyrenecarboxylic acid, and 1,2-ethanedithiol. **46** showed a significant pyrene excimer emission as well as the quenching of monomer in the presence of  $\text{Pb}^{2+}$ , while **47** indicated the emission quenching upon addition to  $\text{Pb}^{2+}$  but without emission of the pyrene excimer. From the measurements, they concluded that luminescent sensors requiring pyrene–pyrene interactions have to be sufficient flexibility [81]. An aggregation-induced emission (AIE) as signaling mechanism based "turn-on" luminescent sensor **48** (tetraphenylethylene phosphate monoester) for  $\text{Pb}^{2+}$  ions has been developed by Khandare *et al.* (2014).  $\text{Pb}^{2+}$  ions could be detected with **48** by the turn-on type fluorescence response. The formation of nanoscale aggregates was confirmed by the particle size analysis. After the addition of  $\text{Pb}^{2+}$  to **48**, the average particle size increased 16-fold. The capability of **48** for quantitative detection of  $\text{Pb}^{2+}$  ions was expressed as detection limit and it was found to be 10 ppb [82]. Azadbakht *et al.* (2015) have prepared a receptor **49** by condensation of 2-[2-(2-formyl-naphthoxy)ethoxy]naphthaldehyde with 2-aminoethanol in methanol, followed by reduction with  $\text{NaBH}_4$ . **49** showed a weak emission due to the PET quenching by the lone pair of electrons on the secondary N donor atoms. In presence of  $\text{Pb}^{2+}$ , since the lone pair of electrons on nitrogen gets involved in the coordination with the  $\text{Pb}^{2+}$  ion, significant emission

enhancement was observed. They also confirmed that the binding of L with  $\text{Pb}^{2+}$  is chemically reversible with EDTA [83]. An anthracene derivative of  $\beta$ -cyclodextrin **50** has been synthesized for sensing of  $\text{Pb}^{2+}$  ion by Antony *et al.* (2015). The emission intensity of **50** was quenched by all the metal ions, whereas only the  $\text{Pb}^{2+}$  ions enhanced it. The maximum emission intensity between **50** and  $\text{Pb}^{2+}$  was found when the molar fraction was 1.0. The emission enhancement might be due to the photoinduced charge transfer (PET) and the conformational restriction offered by the metal ion binding [84]

Trivalent ions such as  $\text{Al}^{3+}$ ,  $\text{Fe}^{3+}$ , and  $\text{Cr}^{3+}$  play important roles in living systems and show a pronounced impact on the environment and human health. Therefore, the design of ratiometric luminescent sensors capable of simultaneously detecting different trivalent cations is currently of great interest (Figure 9.11). Pathak *et al.* (2013) have designed and synthesized a triazole linked quinoline appended calix[4]arene derivative **51** to discriminate  $\text{Fe}^{3+}$  from  $\text{Fe}^{2+}$ . They used fluorescence spectroscopy to evaluating the receptor ability of **51** toward metal ions. Only  $\text{Fe}^{3+}$  induced an emission enhancement compared with other metal ions. The utility of **51**

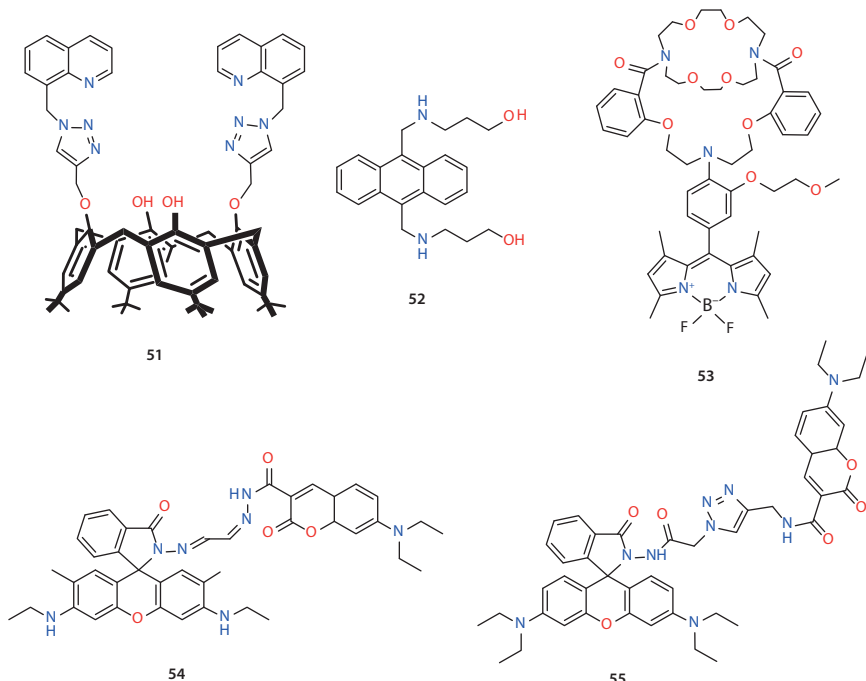
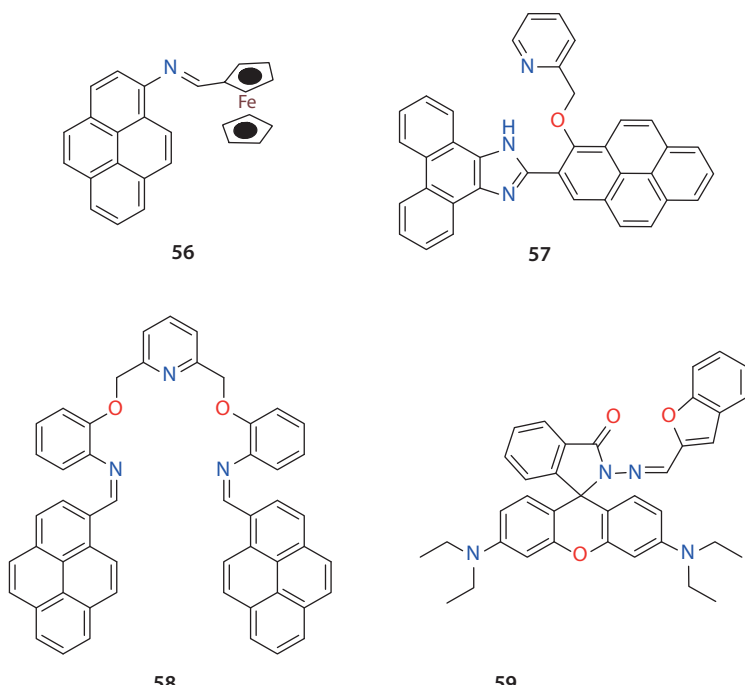


Figure 9.11 Luminescent probes **51–55** for  $\text{Fe}^{3+}$  ion.

was demonstrated by the combination logic gate system and detecting  $\text{Fe}^{3+}$  ions in cells [85]. A luminescent sensor **52** based on anthracene moiety of hydroxyalkylamine has prepared by An *et al.* (2014). Luminescent probe **52** indicated highly selective and sensitive luminescent "turn-on" response toward  $\text{Fe}^{3+}$  in acetonitrile solution. To evaluation the complexation between **52** and  $\text{Fe}^{3+}$ ,  $^1\text{H}$  NMR spectra of **52** was recorded in the absence and presence of  $\text{Fe}^{3+}$ . Results implied that the  $\text{Fe}^{3+}$  connects more strongly to the bridgehead nitrogen atoms than oxygen atoms [86]. A novel BODIPY-based luminescent turn-on sensor **53** for detecting  $\text{Fe}^{3+}$  in aqueous media has been designed by Sui *et al.* (2014).  $\text{Fe}^{3+}$  ions caused 23-fold emission enhancement over other metal ions. Also, they showed that **53** is efficient of sensing  $\text{Fe}^{3+}$  in living cells [87]. In another study, a rhodamine–coumarin conjugate **54** to detect  $\text{Fe}^{3+}$  ion through FRET mechanism in aqueous solution has been presented by Qin *et al.* (2015). **54** was synthesized by condensation reaction between rhodamine 6G hydrazide and coumarin's aldehyde derivative. In the presence of  $\text{Fe}^{3+}$  ions, **54** displayed significant emission enhancement which should be attributed to FRET mechanism from coumarin to Rhodamine 6G. Also, the detection limit of **54** reached a level of  $10^{-6}$  M which is sufficiently low to enable the detection of micromolar concentrations of  $\text{Fe}^{3+}$  in many systems [88]. A similar study has been reported by Yang *et al.* (2015). In this study, rhodamine and coumarin units were connected to each other via click chemistry leading to a new receptor **55**. Chemosensor **55** serves as multifunctional luminescent probe for ratiometric sensing of  $\text{Fe}^{3+}$ ,  $\text{Cr}^{3+}$ , and colorimetric sensing of  $\text{Cu}^{2+}$ . Also, **55** could sense  $\text{Fe}^{3+}$  in methanol and  $\text{Cr}^{3+}$  in acetonitrile by ratiometric emission change via FRET process.  $\text{Fe}^{3+}$  and  $\text{Cr}^{3+}$  ions induced 59-fold and 22-fold emission intensity change ratios, respectively [89].

Considerable efforts have been expended to developing luminescent chemosensors for  $\text{Cr}^{3+}$  over the recent few decades (Figure 9.12). Kaur *et al.* (2014) have developed a ferrocene–pyrene conjugate **56** as 'turn-on' chemodosimeter for  $\text{Cr}^{3+}$ . Chemodosimeter **56** showed a weak emission with low quantum yield ( $\Phi = 0.016$ ) due to PET process. Among a number of metal ions tested, only  $\text{Cr}^{3+}$  enhanced the emission intensity as well as quantum yield ( $\Phi = 0.528$ ) (33-fold). They revealed that the sensing mechanism proceeds via  $\text{Cr}^{3+}$ -promoted hydrolysis of imine functionality of **56**. The performance of **56** was determined by detecting intracellular  $\text{Cr}^{3+}$  in the human breast cancer cells [90]. For  $\text{Cr}^{3+}$  ion, an ICT-based luminescent sensor **57** containing the pyrene moiety has been reported by Huang *et al.* (2015). The emission intensity of **57** showed a decrease in the presence of only  $\text{Cr}^{3+}$ . Other competitive metals did not cause significant changes. They also determined the detection limit for  $\text{Cr}^{3+}$  from the fluorescence



**Figure 9.12** Luminescent probes **56–59** for Cr<sup>3+</sup> ion.

titration data and found to be 0.23 μM, which is almost 4-fold lower than total chromium level (0.96 μM) in drinking water permitted by the WHO [91]. For selective discrimination of Cr<sup>3+</sup> from Fe<sup>3+</sup> in aqueous media, a novel pyrene-based “turn-on” luminescent sensor **58** has been synthesized and reported its cation recognition properties by Rasheed *et al.* (2015). Spectroscopic data disclosed that **58** has high sensitivity and exceptional selectivity toward Cr<sup>3+</sup> through excimer formation between two pyrene moieties. Detecting of Cr<sup>3+</sup> in live cells with **58** was also investigated by confocal fluorescence microscopy [92]. A new study containing the synthesis of a rhodamine hydrazide derivative bearing a benzo[b]furan-2-carboxaldehyde **59** and its sensing behavior has been presented by Hu *et al.* (2016). While the addition of Cr<sup>3+</sup> to **59** induced a 10-fold emission enhancement, no obvious responses could be observed upon the addition of other metal ions except for Fe<sup>3+</sup> and Al<sup>3+</sup>. **59** was used to probe Cr<sup>3+</sup> which is reduced from Cr<sup>6+</sup>. They showed that **59** can be used to detect the reduction of chromate in cells using fluorescence spectroscopy [93].

Aluminum is the third most abundant element, behind oxygen and silicon, in the Earth's crust and has been widely used in modern life. Because

the toxicity of  $\text{Al}^{3+}$  induces damage of the central nervous system and is suspected in neuro degenerative diseases such as Alzheimer's and Parkinson's, the luminescent materials designed for  $\text{Al}^{3+}$  ion will be referred in this part (Figure 9.12). A novel 'turn-on' luminescent probe **60** consisting of perylene as the luminophore and di(2-(salicylideneamino))ethylamine as the metal ion receptor has been designed by Malkondu (2015). Chemosensor **60** displayed a considerable emission enhancement (110-fold) in the presence of  $\text{Al}^{3+}$  with high selectivity and sensitivity on the basis of PET mechanism. The stoichiometry between **60** and  $\text{Al}^{3+}$  was found to be 1:2 by Job's plot and mole-ratio methods. Also, the detection limit of **60** was calculated as 0.33  $\mu\text{M}$  showing that **60** possess a high sensitivity in detecting  $\text{Al}^{3+}$  ions [94]. Erdemir and Malkondu (2015) synthesized a triazole-based simple "turn-on" luminescent sensor **61** for  $\text{Al}^{3+}$  ion. Due to the C=N isomerization and effect of ICT in **61**, this probe displayed a weak emission intensity. These are inhibited upon the binding of  $\text{Al}^{3+}$  to **61**, resulting in a large increase in emission intensity (ca. 230-fold).  $^1\text{H}$  NMR studies demonstrated that phenolic-OH, amide NH and triazole groups are effective in formation of complex between **61** and  $\text{Al}^{3+}$  [95]. Aminophenol and cyanobiphenyl conjugate **62** as a different receptor for  $\text{Al}^{3+}$  ion has been designed by Alici and Erdemir (2015). Chemosensor **62** was obtained from the condensation reaction of 3'-formyl-4'-hydroxy-4-biphenylcarbonitrile and 2-aminophenol. **62** showed a 24-fold increase in emission intensity toward  $\text{Al}^{3+}$  over most other competitive metal ions in a mixture of acetonitrile and water. Moreover, complexation process was completed within 1 min, and the emission intensity did not display a considerable change after that time [96]. Sensing multiple analytes with a single chemosensor has found numerous applications in areas including food industry, air and water quality management, and chemical and biological sensors. It involves eliciting different responses by the chemosensor in the presence of different analytes. Within this context, Erdemir *et al.* (2015) have reported a bisphenol A-quinoline-based novel multianalyte sensor **63** for fluorogenic recognition of  $\text{Zn}^{2+}$ ,  $\text{Al}^{3+}$ , and  $\text{F}^-$  ions. Only  $\text{Zn}^{2+}$ ,  $\text{Al}^{3+}$ , and  $\text{F}^-$  among tested other cations and anions caused the enhanced yellow, green, and red emission, respectively. According to the quantum yield ( $\Phi$ ) measurements, **63-Zn<sup>2+</sup>**, **63-Al<sup>3+</sup>**, and **63-F<sup>-</sup>** complexes displayed 16, 22, and 30 times higher  $\Phi$  values than **63**, respectively. The nature of complexation between **63** and these species was also clarified by  $^1\text{H}$  NMR experiments [97]. Three N-stabilized rhodamine luminescent probes **64-66** for  $\text{Al}^{3+}$  working with the  $\text{Al}^{3+}$ -promoted hydrolysis have been reported by Ding *et al.* (2015). Due to the strong electron withdrawing group on benzene, **64** became stable and it showed the best sensing property compared with **65** and **66**. The addition of  $\text{Al}^{3+}$  to **64**, **65**, and **66** induced

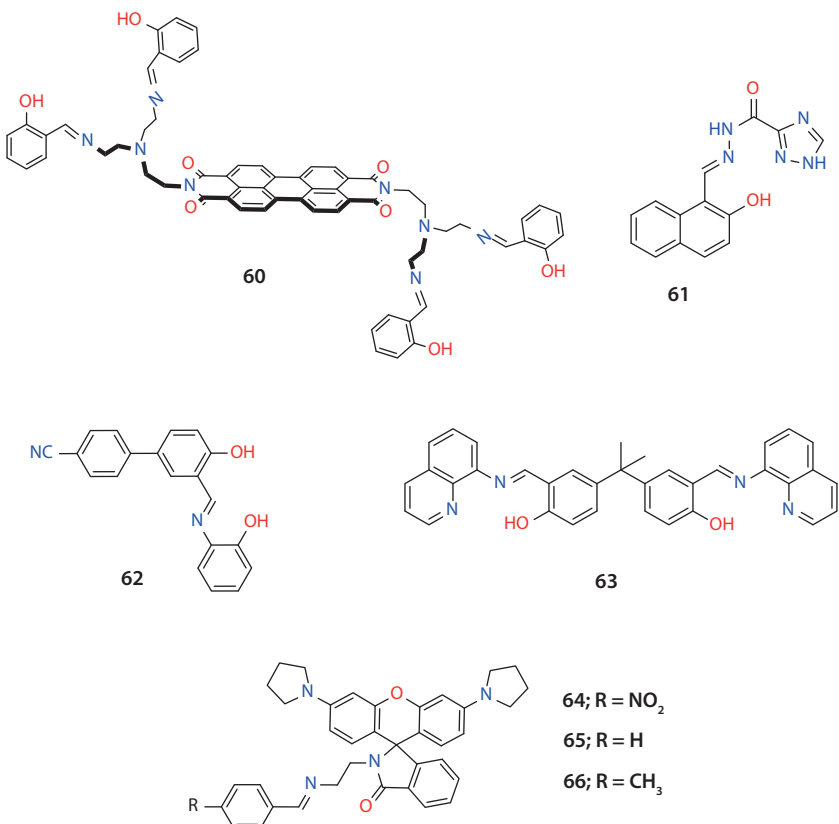


**Figure 9.13** Luminescent probes **60–66** for  $\text{Al}^{3+}$  ion.

190-, 120-, and 60-fold emission enhancement, respectively. FTIR and  $^1\text{H}$  NMR studies revealed that the interaction mechanism of  $\text{Al}^{3+}$  with probes based on Schiff base hydrolysis. The detection limit of  $\text{Al}^{3+}$  was measured to be 3.98  $\mu\text{M}$ . In addition, the test papers of **64** were prepared to show the practical application of **64**. It was concluded that these test kits may provide an easy way to detect  $\text{Al}^{3+}$  in environmental samples [98] (Figure 9.13).

### 9.3 Luminescent Materials for Sensing of Anions

As a result of the importance of anions in a number of chemical and biochemical processes, the search for effective luminescent materials for detecting of anions is the subject of a strong interest. Although conventional analytical methods such as ion chromatography and capillary

electrophoresis are used, fluorescence technique appears to be particularly important owing to its simplicity, high sensitivity, low detection limit, and low cost. Many fluorescent receptors for anions have been developed on the basis of a variety of signaling mechanisms such as ICT, PET, excimer or exciplex, FRET, excited-state proton transfer (ESPT), and MLCT.

Among the various important halide anions, as the most electronegative atom, and the smallest anion with high charge density, fluoride plays an important role in biological, medical, and chemical processes [99–101]. Proper ingestion of fluoride can prevent and cure dental problems and osteoporosis. Thus, it is necessary to add fluoride to toothpaste and drinking water [102]. Because fluoride is absorbed easily by the body and excreted slowly from the body [103], the presence of excess fluoride ions results in dental and skeletal fluorosis, bone diseases, mottling of teeth, and lesions of the thyroid, liver, and other organs [104–107]. Chloride is one of the important anions in biological fluids. Chloride sensing is also important in clinical diagnosis, environmental monitoring, and industrial applications [108]. Along with iodide, bromide is widely present in either the natural environment or in biological fluids such as saline, urine, serum, and saliva of the organism [109]. Bromide plays important roles in the areas of environmental, biological, and chemical systems [110]. Although chronic toxicity from bromide can cause bromism, bromide toxicity can also lead to a type of skin eruption [111]. Hence, novel probes for their powerful recognition and detection are necessary. Recently, Erdemir and Kocyigit (2015) have reported a novel Schiff base-based benzothiazole–bisphenol A **67**. This receptor displayed selective chromogenic as well as fluorescent sensor property toward fluoride by a 40-fold increase in the emission intensity upon binding with fluoride. However, other anions such as  $\text{Cl}^-$ ,  $\text{Br}^-$ ,  $\text{I}^-$ ,  $\text{NO}_3^-$ ,  $\text{ClO}_4^-$ ,  $\text{AcO}^-$ ,  $\text{HSO}_4^-$ , and  $\text{H}_2\text{PO}_4^-$  could not cause any color change. They also produced test strips based on **67**, which could act as a convenient and efficient fluoride test kit. Otherwise, an INHIBIT logic gate was proposed using the output obtained from spectroscopic data [112]. Bineci *et al.* (2016) have developed a novel sensing approach based on AIE phenomena for fluoride ion detection. This "turn-on" fluorescent approach was successively applied for analysis of fluoride ion in aqueous media. For this, probe **68** was synthesized by the palladium-catalyzed Suzuki–Miyaura coupling reaction, followed by substitution reaction with methyl iodide. The emission intensity of **68** increased 27-fold by addition of fluoride. They concluded that this increase is due to both the formation of less soluble amorphous aggregates and annihilation of deleterious heavy atom effect of iodide ion by displacement of fluoride ion with iodide ion [113]. Madhu *et al.* (2014) improved BODIPY based-optical sensors **69** and **70** that can

detect chloride ions in biological and environmental samples. **69** and **70** indicated “on-off” type fluorescence response toward  $\text{Hg}^{2+}$  with high selectivity. Once binding with  $\text{Hg}^{2+}$ , **69**– $\text{Hg}^{2+}$ , and **70**– $\text{Hg}^{2+}$  complexes displayed high selectivity for chloride. Among the various anions, only chloride anion induced the revival of fluorescence of **69** and **70**, resulting in “off-on” type sensing of chloride anion. They used these complexes for chloride sensing in living cells by fluorescence imaging [114]. Fully organic sensors for chloride in aqueous media typically undergo fluorescence quenching or suffer from competition with other anions. AIE-based “turn-on” fluorescent sensor containing urea groups **71** for chloride anion has been presented by Watt *et al.* (2015). Fluorescence intensity of **71** increased in the presence of chloride and the aggregates in samples formed. The formation of spherical aggregates was confirmed by SEM. Moreover,  $^1\text{H}$  NMR experiments indicated that **71** binds chloride more strongly than other anions [115]. To detect bromide and iodide ions, Xu *et al.* (2012) have reported a selective fluorescent probe **72** based on metal ion removal and anion ligand exchanging. Rhodamine derivative bearing 2-aminopyridine **72** showed high selectivity toward  $\text{Hg}(\text{ClO}_4)_2$  in 99% aqueous solution, while the other cations had almost no influence on the fluorescence spectra. Then, the selectivity of **72**– $\text{Hg}^{2+}$  toward various anions was studied. The addition of iodide to **72**– $\text{Hg}^{2+}$ – $\text{ClO}_4^-$  induced fluorescence quenching selectively by removing of  $\text{Hg}^{2+}$  from the **72**– $\text{Hg}^{2+}$ – $\text{ClO}_4^-$ ; however, the addition of bromide caused the fluorescence enhancing by exchanging the anion ligand from  $\text{ClO}_4^-$  to  $\text{Br}^-$ . They suggested that this sensing mechanism could serve as a novel approach for the design of a rhodamine-based probe [116] (Figure 9.14).

As well as halides, other anions, such as cyanide, sulfide, bisulfate, nitride, and phosphate, play a fundamental role in a wide range of chemical and biological processes. Accordingly, considerable effort has been paid to designing new luminescent materials for the detection of these anions. Chen *et al.* (2015) proposed a simple 7-azaindole-based fluorescent probe **73** for  $\text{CN}^-$  with specific selectivity in aqueous media based on excited-state intramolecular charge transfer (ESICT). The nucleophilic addition of  $\text{CN}^-$  ion to **73** caused a remarkable change, enabling fluorescent sensing of cyanide ions in aqueous media. Also, the absorption/emission spectrum of **73**– $\text{CN}^-$  was not substantially influenced by the addition of competing anions. The practical application of probe **73** was successively tested by using test strips [117]. In another study performed to sensing cyanide, coumarin–hemicyanine dye based on “turn-on” fluorescent probe **74** was prepared via the condensation reaction by Xiong *et al.* (2015). **74** indicated weak emission band due to an ICT. ICT blocked by nucleophilic addition of  $\text{CN}^-$  to **74** and  $\text{CN}^-$  enhanced the fluorescence intensity of **74**. Moreover, they revealed that **74** with low the

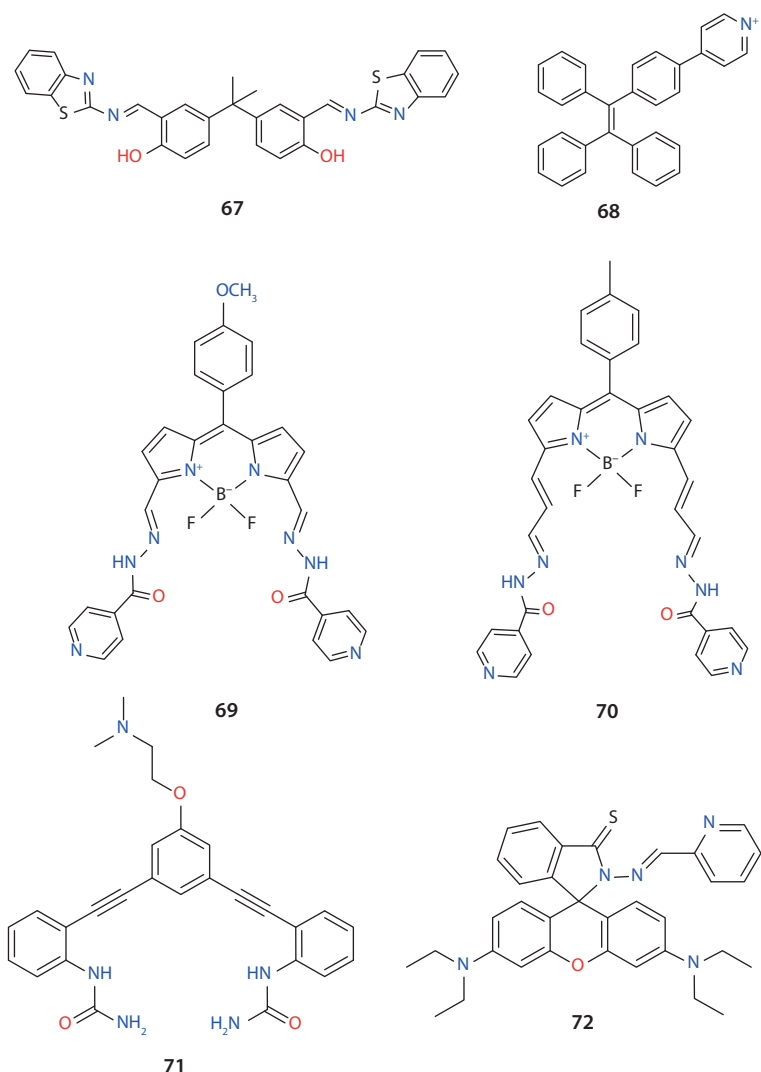
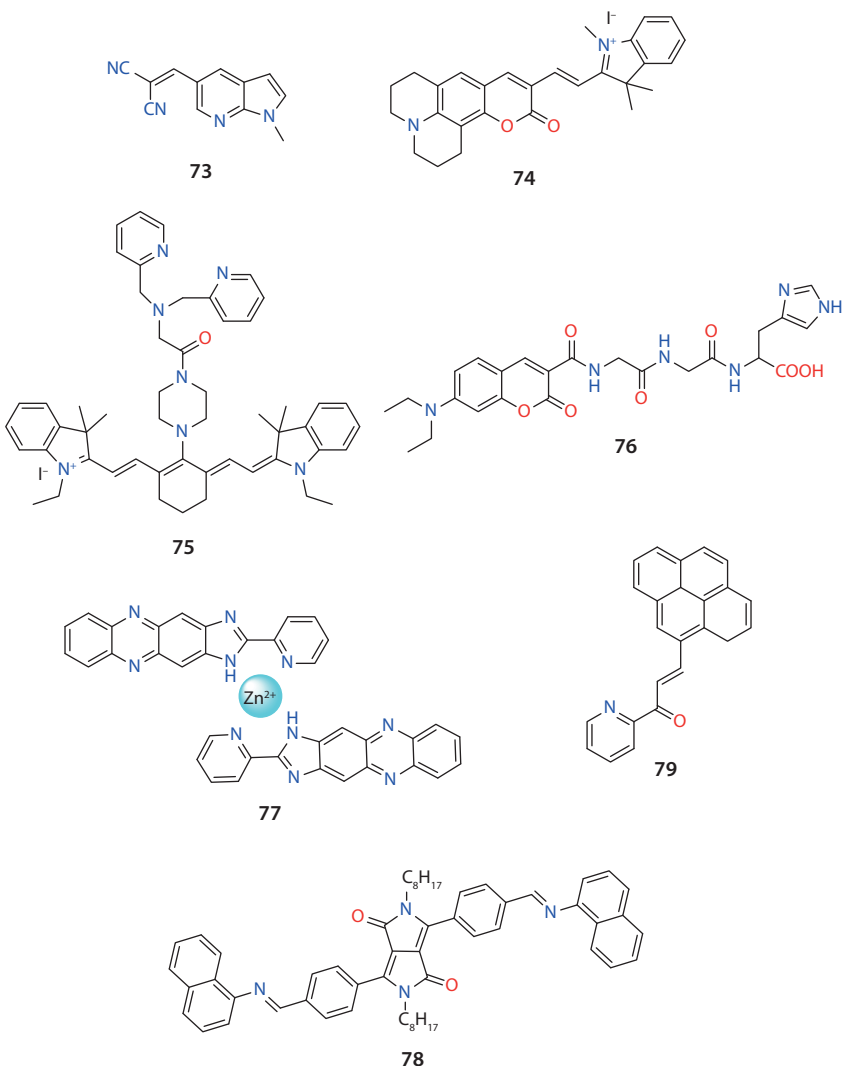


Figure 9.14 Luminescent probes 67–72 for halides.

detection limit ( $0.066 \mu\text{M}$ ) can be used to bioimaging [118]. As CN<sup>-</sup>, sulfide which is a toxic ion for living leads to various biochemical problems. Thus, sensing and tracing sulfide (S<sup>2-</sup>) ions are essential. Yang *et al.* (2015) have presented a probe based tricarbocyanine dyes 75 for sulfide ion via an “on-off-on” mode. Among the metal ions, Cu<sup>2+</sup> serves as an ideal probe for S<sup>2-</sup> recognition due to the formation of the very stable CuS ( $K_{\text{sp}} = 3.63 \times 10^{-36}$ ). This probe 75 served as an “on-off” sensor for Cu<sup>2+</sup>. The formed 75–Cu<sup>2+</sup>

complex selectively recognized to  $S^{2-}$  over other anions through a displacement mechanism. Also, bioimaging studies displayed that **75**– $Cu^{2+}$  complex was a promising candidate probe for  $S^{2-}$  in living cells [119]. A reusable and water-soluble fluorescent probe **76** based on the displacement mechanism for sulfide detection has been reported by Hao *et al.* (2015). The peptide based-probe **76** was obtained through incorporating of glycine, glycine, and histidine into a coumarin. In the presence of  $Cu^{2+}$  ions, **76** showed “on-off” type fluorescence response with high selectivity in 100% of aqueous solution. Then, **76**– $Cu^{2+}$  complex permitted detection of  $S^{2-}$  in aqueous buffer solution with low detection limit (0.44  $\mu M$ ). **76**– $Cu^{2+}$  complex for practical application was successively applied to monitor sulfide anion in water samples [120]. 2-pyridine-1H-imidazo[4,5-b]phenazine-Zn $^{2+}$  complex **77** as fluorescent probe for  $H_2PO_4^-$  based on TICT has synthesized by Shi *et al.* (2015). **77** showed yellow emission due to TICT. The interaction between Zn $^{2+}$  and **77** induced red emission owing to decreasing of the TICT ability. Upon the addition of  $H_2PO_4^-$  to the **77**–Zn $^{2+}$  complex, this complex was decomposed and the binding of  $H_2PO_4^-$  largely promoted the yellow fluorescence emission because of the conformational changes. In addition, test papers based on **77**–Zn $^{2+}$  were produced, which also shows a good selectivity to  $H_2PO_4^-$  as in solution [121]. Recently, a diketopyrrolopyrrole-derived Schiff base **78** as a novel fluorescent probe has presented by Wang *et al.* (2015). **78** displayed high selectivity for  $HSO_4^-$  over other anions via hydrolysis process with 10.6-fold fluorescence enhancement as well as color changing from red to orange. As known, Schiff bases tend to be hydrolyzed in acidic medium. The pKa value of  $HSO_4^-$  is 1.99 (in aqueous medium), and it is possible to act as a hydrogen (H $^+$ ) donor in aqueous/semaqueous medium. For these reasons, strong fluorescent hydrolysis products (aldehyde and amine) were generated from **78** +  $HSO_4^-$ . The hydrolysis mechanism was confirmed by  $^1H$  NMR and mass spectral studies [122]. The nitrite ( $NO_2^-$ ) which is other important anion, an inorganic contaminant, is found in drinking water and is a threat to human health. When present in high concentration in human blood, it can oxidize hemoglobin and myoglobin to methemoglobin and metmyoglobin, respectively. Thus, a selective probe to detect nitrite ion would be important from various angles. Rout *et al.* (2015) have prepared a chalcone derivative with pyrene fluorophore **79** and its Cu $^{2+}$  complex. The Cu $^{2+}$  center in the complex was found to be reduced by nitrite ion in presence of water in acetonitrile and methanol solution. During the reaction, oxidation of the nitrite to nitrate was observed. Other anions like nitrate, acetate, carbonate, perchlorate, sulfate, phosphate, and halides did not find to interfere with the detection of the nitrite using **79**–Cu $^{2+}$  complex.  $^1H$  NMR and X-band EPR studies also suggested the reduction of Cu $^{2+}$  to Cu $^+$  [123] (Figure 9.15).



**Figure 9.15** Luminescent probes 73–79 for cyanide, sulfide, bisulfate, nitride, and phosphate anions.

## 9.4 Conclusion

A large number of different approaches for the development of new luminescent materials for anion and cation sensing have been discussed in this chapter. This clearly shows that the chemistry community devotes strong attention to the development of systems able to detect of these species in

real time and real space. These types of highly sensitive and selective luminescent sensor will be useful for further investigation and developments. It is expected that more and more excellent luminescent sensors will be developed in the years to come.

## Acknowledgments

We thank to the Research Foundation of Selcuk University (BAP) and the Scientific and Technical Research Council of Turkey (TUBITAK).

## References

1. Gupta, V.K., Yola, M.L., Atar N, Solak, A.O., Uzun, L., Ustundag, Z., Electrochemically modified sulfisoxazolenano film on glassy carbon for determination of cadmium (II) in water samples. *Electrochim. Acta*, 105, 149, 2013.
2. Gupta, V.K., Singh, A.K., Singh, P., Upadhyay, A., Electrochemical determination of perchlorate ion by polymeric membrane and coated graphite electrodes based on zinc complexes of macrocyclic ligands. *Sensors Actuators B*, 199, 201, 2014.
3. Norouzi, P., Gupta, V.K., Larijani, B., Rasoolipour, S., Faridbod, F., Ganjali, M.R., Coulometric differential FFT admittance voltammetry determination of amlodipine in pharmaceutical formulation by nano-composite electrode. *Talanta*, 131, 577, 2015.
4. Iyengar, V., Wolttlez, J., Trace elements in human clinical specimens: evaluation of literature data to identify reference values, trace elements in human clinical specimens: evaluation of literature data to identify reference values. *Clin. Chem Wash DC*, 34, 474, 1988.
5. Townsend, A.T., Miller, K.A., McLean, S., Aldous, S., The determination of copper, zinc, cadmium and lead in urine by high resolution ICP-MS. *J. Anal. At Spectrom.*, 13, 1213, 1998.
6. Lakowicz, J. R., *Topics in Fluorescence Spectroscopy*, vol. 2, Principles, Plenum Press, New York, 1991.
7. Lakowicz, J. R., *Topics in Fluorescence Spectroscopy*, vol. 4, Techniques, Plenum Press, New York, 1991.
8. Lakowicz, J. R., *Topics in Fluorescence Spectroscopy*, vol. 3, Application, Plenum Press, New York, 1991.
9. Irvine, D. J., Purbhoo, M. A., Krogsgaard M., Davis, M. M., Direct observation of ligand recognition by T cells. *Nature*, 419, 845, 2002.
10. Pope, A. J., Haups, U. M. Moore, K. J. Homogenous fluorescence readouts for miniaturized high-throughput screening: theory and practice. *Drug Discovery Today*, 1999, 4, 350–362.

11. Zhaochao, X., Juyoung, Y., David, R. S., Fluorescent chemosensors for  $Zn^{2+}$ . *Chem. Soc. Rev.*, 39, 1996, 2010.
12. Gunnlaugsson, T., Glynn, M., Tocci, G. M., Kruger P. E., Pfeffer, F. M., Anion recognition in organic and aqueous media using luminescent and colorimetric sensors. *Coord. Chem. Rev.*, 250, 3094, 2006.
13. Jiang, P. J., Guo, Z. J., Fluorescent detection of zinc in biological systems: recent development on the design of chemosensors and biosensors. *Coord. Chem. Rev.*, 248, 205, 2004.
14. Bell, T. W., Hext, N. M., Supramolecular optical chemosensors for organic analytes. *Chem. Soc. Rev.*, 33, 589, 2004.
15. Gunnlaugsson, T., Ali, H. D. P., Glynn, M., Kruger, P. E., Hussey, G. M., Pfeffer, F. M., Santos, C. M. D., Tierney, J., Fluorescent photoinduced electron transfer (PET) sensors for anions; from design to potential application. *J. Fluoresc.*, 15, 287, 2005.
16. de Silva, A. P., Gunaratne, H. Q. N., Gunnlaugsson, T., Huxley, A. J. M., McCoy, C. P., Rademacher, J. T., Rice, T. E., Signaling Recognition Events with Fluorescent Sensors and Switches. *Chem. Rev.*, 97, 1515, 1997.
17. Callan, J. F., de Silva A. P., Magri, D. C., Luminescent sensors and switches in the early 21st century. *Tetrahedron*, 61, 8551, 2005.
18. Martinez-Manez, R., Sancenon, F., Fluorogenic and chromogenic chemosensors and reagents for anions. *Chem. Rev.*, 103, 4419, 2003.
19. Valeur, B., Leray, I., Design principles of fluorescent molecular sensors for cation recognition. *Coord. Chem. Rev.*, 205, 3, 2000.
20. Kim, J. S., Quang, D. T., Calixarene-derived fluorescent probes. *Chem. Rev.*, 107, 3780, 2007.
21. Zhao, Q., Li, F.Y., Huang, C. H., Phosphorescent chemosensors based on heavy-metal complexes. *Chem. Soc. Rev.*, 39, 3007, 2010.
22. Rettig, W., Lapouyade, R., Fluorescence probes based on twisted intramolecular charge transfer (TICT) states and other adiabatic photoreactions, in *Topics in Fluorescence Spectroscopy, Probe Design and Chemical Sensing*, J. R. Lakowicz (Ed.), pp. 109–149, Plenum Press, New York, 1994.
23. Wu, J. S., Liu, W. M., Zhuang, X. Q., Wang, F., Wang, P. F., Tao, S. L., Zhang, X. H., Wu, S. K., Lee, S. T., Fluorescence turn on of coumarin derivatives by metal cations: a new signaling mechanism based on C=N isomerization. *Org. Lett.*, 9, 33, 2007.
24. Sapsford, K. E., Berti, L., Medintz, I. L., Materials for fluorescence resonance energy transfer analysis: beyond traditional donor-acceptor combinations. *Angew. Chem. Int. Ed.*, 45, 4562, 2006.
25. Carlson, H. J., Campbell, R. E., Genetically encoded FRET-based biosensors for multiparameter fluorescence imaging. *Curr. Opin. Biotechnol.*, 20, 19, 2009.
26. Lodeiro, C., Pina, F., Luminescent and chromogenic molecular probes based on polyamines and related compounds. *Coord. Chem. Rev.*, 2009, 253, 1353.
27. (a) Bissell, R. A., de Silva, A. P., Gunaratne, H. Q. N., Lynch, P. L. M., Maguire, G. E. M., Sandanayake, K. R. A. S., Molecular fluorescent signalling

- with 'fluor-spacer-receptor' systems: approaches to sensing and switching devices via supramolecular photophysics. *Chem. Soc. Rev.*, 21, 187, 1992;
- (b) Desvergne, J. P., Czarnik, A. W., *Fluorescent Chemosensors for Ion and Molecule Recognition*. Kluwer Academic: Dordrecht, The Netherlands, 1997; (c) Prodi, L., Bolletta, F., Montalti, M., Zaccheroni, N., Luminescent chemosensors for transition metal ions. *Coord. Chem. Rev.*, 205, 59, 2000;
- (d) Quang, D. T., Kim, J. S., Fluoro- and chromogenic chemodosimeters for heavy metal ion detection in solution and biospecimens. *Chem. Rev.*, 110, 6280, 2010; (e) Kobayashi, H., Ogawa, M., Alford, R., Choyke, P. L., Urano, Y., New strategies for fluorescent probe design in medical diagnostic imaging. *Chem. Rev.*, 110, 2620, 2010.
28. Ahmad, M., Sundari, R., Heng, L.Y., Development of an optical fibre reflectancesensor for copper(II) detection based on immobilised salicylic acid. *Sensors Actuators B*, 113, 201, 2006.
29. Torrado, A., Walkup, G.K., Imperiali, B., Exploiting polypeptide motifs for the design of selective Cu(II) ion chemosensors, *J. Am. Chem. Soc.* 120, 609, 1998.
30. Jin, T., Lu, J., Nordberg, M., Toxicokinetics and biochemistry of cadmium with special emphasis on the role of metallothionein. *Neurotoxicology* 19, 529, 1998.
31. Satarug, S., Baker, J.R., Urbenjapol, S., Haswell-Elkins, M., Reilly, P.E.B., Williams, D.J., Moore, M.R., A global perspective on cadmium pollution and toxicity in non-occupationally exposed population. *Toxicol. Lett.* 137, 65, 2003.
32. (a) Barnham, K.J., Masters, C.L., Bush, A.L. Neurodegenerative diseases and oxidative stress. *Nat. Rev. Drug Discov.*, 3, 205, 2004; (b) Brown, D.R., Kozlowski, H., Biological inorganic and bioinorganic chemistry of neurodegeneration based on prion and Alzheimer diseases. *Dalton Trans.*, 13, 1907, 2004; (c) Deraeve, C., Boldron, C., Maraval, A., Mazarguil, H., Gornitzka, Vendier, H. L., Pitie, M., Meunier, B., Preparation and study of new poly-8-hydroxyquinoline chelators for an anti-Alzheimer strategy. *Chem. Eur. J.* 14, 682, 2008.
33. Zhan, S., Wu, Y., Luo, Y., Liu, L., He, L., Xing, H., Zhou P., Label-free fluorescent sensor for lead ion detection based on lead(II)-stabilized G-quadruplex formation. *Anal. Biochem.*, 462, 19, 2014.
34. Carvalho, C.M.L., Chew, E.H., Hashemy, S.I., Lu, J., Holmgren, A., Inhibition of the human thioredoxin system a molecular mechanism of mercury toxicity. *J. Biol. Chem.*, 283, 11913, 2008.
35. Clarkson, T.W., Magos, L., Myers, G.J., The toxicology of mercury e current exposures and clinical manifestations. *N. Engl. J. Med.*, 349, 1731, 2003.
36. Godwin, H.A., The biological chemistry of lead. *Curr. Opin. Chem. Biol.*, 5, 223, 2001.
37. Mcrae, R., Baqchi, P., Sumalekshmy, S., Fahrniv, C.J., *In situ* imaging of metal in cells and tissues. *Chem. Rev.*, 109, 4780, 2009.

38. Panda, S.K., Chromium-mediated oxidative stress and ultrastructural changes in root cells of developing rice seedlings. *J. Plant Physiol.*, 164, 1419, 2007.
39. Latva, S., Jokiniemi, J., Peraniemi, S., Ahlgren, M., Separation of picogram quantities of Cr(III) and Cr(VI) species in aqueous solutions and determination by graphite furnace atomic absorption spectrometry. *J. Anal. At. Spectrom.*, 18, 84, 2003.
40. Gunnlaugsson, T., Bichell, B., Nolan, C., A novel fluorescent photoinduced electron transfer (PET) sensor for lithium. *Tetrahedron Lett.*, 43, 4989, 2002.
41. Kim, M. K., Lim, C. S., Hong, J. T., Han, J. H., Jang, H.-Y., Kim H. M., Cho, B. R., Sodium-ion-selective two-photon fluorescent probe for *in vivo* imaging. *Angew. Chem., Int. Ed.*, 49, 364, 2010.
42. Huang, C.-C., Chang, H.-T., Aptamer-based fluorescence sensor for rapid detection of potassium ions in urine. *Chem. Commun.*, 1461, 1461, 2008
43. Li, L., Li, P., Fang, J., Li, Q., Xiao, H., Zhou, H., Tang, B., Simultaneous quantitation of Na<sup>+</sup> and K<sup>+</sup> in single normal and cancer cells using a new near-infrared fluorescent probe. *Anal. Chem.*, 87, 6057, 2015.
44. Depauw, A., Kumar, N., Ha-Thi, M.-H., Leray, I., Calixarene-based fluorescent sensors for cesium cations containing BODIPY fluorophore. *J. Phys. Chem. A.*, 119, 6065, 2015.
45. Azadbakht, R., Khanabadi, J., A novel fluorescent nano-chemosensor for cesium ions based on naphthalene macrocyclic derivative. *Spectrochim. Acta A.*, 139, 279, 2015.
46. Kao, M.-H., Chen, T.-Y., Cai, Y.-R., Hu, C.-H., Liu, Y.-W., Jhong, Y., Wu, A.-T., A turn-on Schiff-base fluorescence sensor for Mg<sup>2+</sup> ion and its practical application. *J. Lumin.*, 169, 156, 2016.
47. Qin, J.-C., Y., Z.-Y., Wang, G.-Q., Recognition of Mg<sup>2+</sup> and Zn<sup>2+</sup> based on a naphthalene-based fluorescent probe by regulating solvents. *Inorg. Chim. Acta*, 435, 194, 2015.
48. Liu, D., Qi, J., Yu, Z., Liu, X., Yang, R., Yang, H., Chang, H., He, H., Yang, G., A fluorescent sensor with high selectivity for Ca<sup>2+</sup> against Mg<sup>2+</sup> in seawater. *Anal. Methods*, 6, 3555, 2014.
49. Dutta, K., Deka, R. C., Das, D. K., The first enhanced ring planarity based fluorescent "off-on" sensor for Ca<sup>2+</sup> ion. *J. Lumin.*, 148, 325, 2014.
50. Zhaa, L., Sui, D., Wang, Y., Luminescent properties of N-salicylidene-3-amino pyridine and selective sensing behavior to Ba<sup>2+</sup>. *J. Lumin.*, 162, 81, 2015.
51. Saluja, P., Kaur, N., Singh, N., Jang, D.O., A benzthiazole-based tripodal chemosensor for Ba<sup>2+</sup> recognition under biological conditions. *Tetrahedron Lett.*, 52, 6705, 2011.
52. Sutariya, P. G., Pandya, A., Modi, N. R., Menon, S. K., A highly efficient PET switch on-off-on fluorescence receptor based on calix[4]arene for the selective recognition of Cd<sup>2+</sup> and Sr<sup>2+</sup>. *Analyst*, 138, 2244, 2013.
53. Erdemir, S., Malkondu, S., A novel "turn on" fluorescent sensor based on hydroxy-triphenylamine for Zn<sup>2+</sup> and Cd<sup>2+</sup> ions in MeCN. *Sensors Actuators B*, 188, 1225, 2013.

54. Tian, X., Guo, X., Jia, L., Yang, R., Cao, G., Liu, C., A fluorescent sensor based on bicarboxamidoquinoline for highly selective relay recognition of  $Zn^{2+}$  and citrate with ratiometric response. *Sensors Actuators B*, 221, 923, 2015.
55. Li, Y.-P., Yang, H.-R., Zhao, Q., Song, W.-C., Han, J., Bu, X.-H., Ratiometric and selective fluorescent sensor for  $Zn^{2+}$  as an “off-on-off” switch and logic gate. *Inorg. Chem.*, 51, 9642, 2012.
56. Yang, L.-L., Liu, X.-M., Liu, K., Liu, H., Zhao, F.-Y., Ruan, W.-J., Li, Y., Chang, Z., Bu, X.-H., A polypyridyl-pyrene based off-on  $Cd^{2+}$  fluorescent sensor for aqueous phase analysis and living cell imaging. *Inorg. Chem.*, 51, 9226, 2012.
57. Liu, Z., He, W., Pei, M., Zhang, G., A fluorescent sensor with a detection level of pM for  $Cd^{2+}$  and nM for  $Cu^{2+}$  based on different mechanisms. *Chem. Commun.*, 51, 14227, 2015.
58. Dutta, K., Deka, R.C., Das, D. K., A new fluorescent and electrochemical  $Zn^{2+}$  ion sensor based on Schiff base derived from benzil and L-tryptophan. *Spectrochim. Acta A*, 124, 124, 2014.
59. Zhou, X., Li, P., Shi, Z., Tang, X., Chen, C., Liu, W., A highly selective fluorescent sensor for distinguishing cadmium from zinc ions based on a quinoline platform. *Inorg. Chem.*, 51, 9226, 2012.
60. Roy, N., Dutta, A., Mondal, P., Paul, P.C., Singh, T.S., A new turn-on fluorescent chemosensor based on sensitive Schiff base for  $Mn^{2+}$  ion. *J. Lumin.*, 165, 167, 2015.
61. Bakthavatsalam, S., Sarkar, A., Rakshit, A., Jain, S., Kumar, A., Datta, A., Tuning macrocycles to design ‘turn-on’ fluorescence probes for manganese(II) sensing in live cells. *Chem. Commun.*, 51, 2605, 2015.
62. Dutta, K., Deka, R. C., Das, D. K., A new on-fluorescent probe for manganese (II) ion. *J. Fluoresc.*, 23, 1173, 2013.
63. Santhoshkumar, S., Velmurugan, K., Prabhu, J., Radhakrishnan, G., Nandhakumar R., A naphthalene derived Schiff base as a selective Fluorescent probe for  $Fe^{2+}$ . *Inorg. Chim. Acta.*, 439, 1, 2016.
64. Mahalingam, M., Irulappan, M., Kasirajan, G., Subramaniam, M. P., Ramasamy, S., Unnisa, N., Synthesis of bisbenzimidazo quinoline fluorescent receptor for  $Fe^{2+}$  ion in the aqueous medium – an experimental and theoretical approach. *J. Mol. Struct.*, 1099, 257, 2015.
65. Hou, G.-G., Wang, C.-H., Sun, J.-F., Yang, M.-Z., Lin, D., Li, H.-J., Rhodamine-based “turn-on” fluorescent probe with high selectivity for  $Fe^{2+}$  imaging in living cells. *Biochem. Biophys. Res. Commun.*, 439, 459, 2013.
66. Bu, J., Duan, H., Wang, X., Xu, T., Meng, X., Qin, D., New turn-on fluorescence sensors for  $Co^{2+}$  based on conjugated carbazole Schiff base. *Res. Chem. Intermed.*, 41, 2767, 2015.
67. Abebe, F.A., Eribal, C.S., Ramakrishna, G., Sinn, E., A ‘turn-on’ fluorescent sensor for the selective detection of cobalt and nickel ions in aqueous media. *Tetrahedron Lett.* 52, 5554, 2011.
68. Wang, P., Li, Z., Lv, G.-C., Zhou, H.-P., Hou, C., Sun, W.-Y., Tian, Y.-P., Zinc(II) complex with terpyridine derivative ligand as “on-off” type fluorescent probe for cobalt(II) and nickel(II) ions. *Inorg. Chem. Comm.*, 18, 87, 2012.

69. Li, H., Zhang, S.-J., Gong, C.-L., Li, Y.-F., Liang, Y., Qi, Z.-G., Chen, S., Highly sensitive and selective fluorescent chemosensor for  $\text{Ni}^{2+}$  based on a new poly(arylene ether) with terpyridine substituent groups. *Analyst*, 138, 7090, 2013.
70. Ghosh, K., Mohan, V., Kumar, P., Ng, S.W., Tiekink, E.R.T., Selective fluorescence sensing of  $\text{Ni}^{2+}$  by tetradentate ligands: Synthesis of nickel complexes and crystal structures. *Inorg. Chim. Acta*, 416, 76, 2014.
71. Erdemir, S., Malkondu, S., Novel "turn on" fluorescent sensors based on anthracene and carbazole units for  $\text{Cu}(\text{II})$  ion in  $\text{CH}_3\text{CN}-\text{H}_2\text{O}$ . *J. Lumin.*, 158, 86, 2015.
72. An, R., Zhang, D., Chen, Y., Cui, Y.-Z., A "turn-on" fluorescent and colorimetric sensor for selective detection of  $\text{Cu}^{2+}$  in aqueous media and living cells. *Sensors Actuators B*, 222, 48, 2016.
73. Yuan, Y., Sun, S., Liu, S., Song, X., Peng, X., Highly sensitive and selective turn-on fluorescent probes for  $\text{Cu}^{2+}$  based on rhodamine B. *J. Mater. Chem. B*, 3, 5261, 2015.
74. Zhang, X., Shen, Y., Zhang, H., Jin, J., Zhou, S., A new bifunctional fluorescent sensor based on naphthalimide-functionalized silica nanoparticles for detection and adsorption of  $\text{Cu}^{2+}$  in aqueous solution. *Anal. Methods*, 7, 8925, 2015.
75. Erdemir, S., Malkondu, S., Kocyigit, O., Alici, O., A novel colorimetric and fluorescent sensor based on calix[4]arene possessing triphenylamine units. *Spectrochim. Acta A*, 114 190, 2013.
76. Malkondu, S., Erdemir, S., A triphenylamine based multi-analyte chemosensor for  $\text{Hg}^{2+}$  and  $\text{Cu}^{2+}$  ions in  $\text{MeCN}/\text{H}_2\text{O}$ . *Tetrahedron*, 70, 5494, 2014.
77. Erdemir, S., Kocyigit, O., Malkondu, S., Detection of  $\text{Hg}^{2+}$  ion in aqueous media by new fluorometric and colorimetric sensor based on triazole-rhodamine. *J. Photochem. Photobiol. A Chem.*, 309, 15, 2015.
78. Erdemir, S., Malkondu, S., Alici, O., A highly selective and sensitive benzothiazole-based 'turn-on' fluorescent sensor for  $\text{Hg}^{2+}$  ion. *Color. Technol.*, 131, 1, 2015.
79. Malkondu, S., Erdemir, S., A novel perylene-bisimide dye as "turn on" fluorescent sensor for  $\text{Hg}^{2+}$  ion found in  $\text{DMF}/\text{H}_2\text{O}$ . *Dyes Pigm.*, 113, 763, 2015.
80. Erdemir, S., Kocyigit, O., Karakurt, S., A new perylene bisimide-armed calix[4]-aza-crown as "turn on"fluorescent sensor for  $\text{Hg}^{2+}$ ion and its application to living cells. *Sensors Actuators B*, 220, 381, 2015.
81. Hou, C., Xiong, Y., Fu, N., Jacquot, C.C., Squier, T.C., Cao, H., Turn-on ratiometric fluorescent sensor for  $\text{Pb}^{2+}$  detection. *Tetrahedron Lett.*, 52, 2692, 2011.
82. Khandare, D. G., Joshi, H., Banerjee, M., Majik, M.S., Chatterjee, A., An aggregation-induced emission based "turn-on" fluorescent chemodosimeter for the selective detection of  $\text{Pb}^{2+}$  ions. *RSC Adv.*, 4, 47076, 2014.
83. Azadbakht, R., Vaisi, H., Mohamadvand, H., Khanabadi, J., A new fluorescent chemosensor for  $\text{Pb}^{2+}$  ions based on naphthalene derivatives. *Spectrochim. Acta A*, 145, 575, 2015.

84. Antony, E. J., Raj, M., Paulpandi, R. Q., Paulraj, M. S., Enoch, I. V. M. V., A highly selective fluorescent sensor for  $\text{Pb}^{2+}$  based on a modified  $\beta$ -cyclodextrin. *J. Fluoresc.*, 25, 1031, 2015.
85. Pathak, R. K., Dessingou, J., Hinge, V. K., Thawari, A. G., Basu, S. K., Rao, C. P., Quinoline driven fluorescence turn on 1,3-bis-calix[4]arene conjugate-based receptor to discriminate  $\text{Fe}^{3+}$  from  $\text{Fe}^{2+}$ . *Anal. Chem.*, 85, 3707, 2013.
86. An, K.-L., Lee, S.-O., Koh, S. D., Shin, S.-R., Shin, J.I., Park, S.-Y., Son, Y.-A., Park, K.H., Jun, K., A new anthracene based fluorescent turn-on sensor for  $\text{Fe}^{3+}$ . *Bull. Korean Chem. Soc.*, 35, 277, 2014.
87. Sui, B., Tang, S., Liu, T., Kim, B., Belfield, K. D., Novel BODIPY-based fluorescence turn-on sensor for  $\text{Fe}^{3+}$  and its bioimaging application in living cells. *ACS Appl. Mater. Interfaces*, 6, 18408, 2014.
88. Qin, J.-C., Yang, Z.-Y., Wang, G.-Q., Li, C.-R., FRET-based rhodamine-coumarin conjugate as a  $\text{Fe}^{3+}$  selective ratiometric fluorescent sensor in aqueous media. *Tetrahedron Lett.*, 56, 5024, 2015.
89. Yang, Y., Yu, K., Yang, L., Liu, J., Li, K., Luo, S., One single molecule as a multifunctional fluorescent probe for ratiometric sensing of  $\text{Fe}^{3+}$ ,  $\text{Cr}^{3+}$  and colorimetric sensing of  $\text{Cu}^{2+}$ . *Sensors*, 15, 49, 2015.
90. Kaur, M., Kaur, P., Dhuna, V., Singh, S., Singh, K., A ferrocene-pyrene based ‘turn-on’ chemodosimeter for  $\text{Cr}^{3+}$ -application in bioimaging. *Dalton Trans.*, 43, 5707, 2014.
91. Huang, X., Fan, C., Wang, Z., Zhana, X., Pei, M., Lu, Z., A ratiometric and on-off fluorescent chemosensor for highly selective detection of  $\text{Cr}^{3+}$  ion based on an ICT mechanism. *Inorg. Chem. Comm.*, 57, 62, 2015.
92. Rasheed, L., Yousuf, M., Youn, S., Yoon, T., Kim, K.-Y., Seo, Y.-K., Shi, G., Saleh, M., Hur, J.-H., Kim, K.S., Turn-on ratiometric fluorescent probe for selective discrimination of  $\text{Cr}^{3+}$  from  $\text{Fe}^{3+}$  in aqueous media for living cell imaging. *Chem. Eur. J.*, 21, 1, 2015.
93. Hu, X., Chai, J., Liu, Y., Liu, B., Yang, B., Probing chromium(III) from chromium(VI) in cells by a fluorescent sensor. *Spectrochim. Acta A*, 153, 505, 2016.
94. Malkondu, S., A highly selective and sensitive perylenebisimide-based fluorescent PET sensor for  $\text{Al}^{3+}$  determination in MeCN. *Tetrahedron*, 70, 5580, 2014.
95. Erdemir, S., Malkondu, S., A simple triazole-based “turn on” fluorescent sensor for  $\text{Al}^{3+}$  ion in  $\text{MeCN}-\text{H}_2\text{O}$  and  $\text{F}^-$  ion in MeCN. *J. Lumin.*, 158, 401, 2015.
96. Alici, O., Erdemir, S., A cyanobiphenyl containing fluorescence “turn on” sensor for  $\text{Al}^{3+}$  ion in  $\text{CH}_3\text{CN}$ -water. *Sensors Actuators B*, 208, 159, 2015.
97. Erdemir, S., Kocyigit, O., Malkondu, S., Fluorogenic recognition of  $\text{Zn}^{2+}$ ,  $\text{Al}^{3+}$  and  $\text{F}^-$  ions by a new multi-analyte chemosensor based bisphenol A-quinoline. *J. Fluoresc.*, 25, 719, 2015.
98. Ding, P., Wang, J., Cheng, J., Zhao, Y., Ye, Y., Three N-stabilized rhodamine-based fluorescent probes for  $\text{Al}^{3+}$  via  $\text{Al}^{3+}$ -promoted hydrolysis of Schiff bases. *New J. Chem.*, 39, 342, 2015.

99. Zhang, G., Wang, L., Cai, X., Zhang, L., Yu, J., Wang, A., A new diketopyrrolopyrrole (DPP) derivative bearing boronate group as fluorescent probe for fluoride ion. *Dyes Pigm.*, 98, 232, 2013.
100. Ghosh, K., Kar, D., Fröhlich, R., Chattopadhyay, A.P., Samaddera, A., Khuda-Bukhsh, A.R., O-tert-Butyldiphenylsilyl coumarin and dicoumarol: a case toward selective sensing of F<sup>-</sup> ions in organic and aqueous environments. *Analyst*, 138, 3038, 2013.
101. Im, H.G., Kim, H.Y., Choia, M.G., Chang, S.K., Reaction-based dual signaling of fluoride ions by resorufin sulfonates. *Org. Biomol. Chem.*, 11, 2966, 2013.
102. J.S. Chen, P.W. Zhou, G.Y. Li, T.S. Chu, G.Z. He, Fluoride anion sensing mechanism of 2-ureido-4[1H]-pyrimidinone quadruple hydrogen-bonded supramolecular assembly: photoinduced electron transfer and partial configuration change. *J. Phys. Chem. B*, 117, 5212, 2013.
103. Mattiwala, N.M., Kamal, R., Sahoo, S.K., Schiff base bis(5-nitrosalicyl-aldehyde)ethylenediamine as colorimetric sensor for fluoride. *Res. Chem. Intermed.*, 41, 391, 2015.
104. Velmathi, S., Reena, V., Suganya, S., Anandan, S., Pyrrole based Schiff bases as colorimetric and fluorescent chemosensors for fluoride and hydroxide anions. *J. Fluoresc.* 22, 155, 2012.
105. Wang,C.,Li,G.,Zhang,Q.,A novel heteroacene, 2-(2,3,4,5-tetrafluorophenyl)-1H-imidazo[4,5-b]phenazine as a multi-response sensor for F<sup>-</sup> detection. *Tetrahedron Lett.*, 54, 2633, 2013.
106. Sharma, S., Hundal, M.S., Hundal, G., Selective recognition of fluoride ions through fluorimetric and colorimetric response of a first mesitylene based dipodal sensor employing thiosemicarbazones. *Tetrahedron Lett.*, 54, 2413, 2013.
107. Zang, L., Wei, D., Wang, S., Jiang, S., A phenolic Schiff base for highly selective sensing of fluoride and cyanide via different channels. *Tetrahedron*, 68, 636, 2012.
108. (a) Huber, C., Werner, T., Krause, C., Klimant, I., Wolfbeis, O. S., Energy transfer-based lifetime sensing of chloride using a luminescent transition metal complex. *Anal. Chim. Acta*, 364, 143, 1998; (b) Illsley, N. P., Verkman, A. S., Membrane chloride transport measured using a chloride-sensitive fluorescent probe. *Biochemistry*, 26, 1215, 1987.
109. Shao, J., Qiao, Y. H., Lin H., Lin, H. K., A novel switch-on fluorescent receptor for bromide based on an amide group. *J. Inclusion Phenom. Macrocyclic Chem.*, 62, 99, 2008.
110. Liao, J., Sihler, H., L. Huey, G., Neuman, J. A., Tanner, D. J., Friess, U., Platt, U., Flocke, F. M., Orlando, J. J., Shepson, P. B., Beine, H. J., Weinheimmer, A. J., Sjostedt, S. J., Nowak, J. B., Knapp, D. J., Staebler, R. M., Zheng, W., Sander, R., Hall, S. R., Ullmann, K., A comparison of Arctic BrO measurements by chemical ionization mass spectrometry and long path-differential optical absorption spectroscopy. *J. Geophys. Res.*, 116, 1, 2011.

111. Taylor, B. R., Sosa, R., Stone, W. J., Bromide toxicity from consumption of Dead Sea Salt. *Am. J. Med.*, 123, 11, 2010.
112. Erdemir, S., Kocyigit, O., Reversible “OFF-ON” fluorescent and colorimetric sensor basedbenzothiazole-bisphenol A for fluoride in MeCN. *Sensors Actuators B*, 221, 900, 2015.
113. Bineci, M., Baglan, M., Atilgan, S., AIE active pyridinium fused tetraphenylethene: rapid and selective fluorescent “turn-on” sensor for fluoride ion in aqueous media. *Sensors Actuators B*, 222, 315, 2016.
114. Madhu, S., Kalaiyarasi, R., Basu, S. K., Jadhav, S., Ravikanth, M., A boron-dipyrrin-mercury(II) complex as a fluorescence turn-on sensor for chloride and applications towards logic gates. *J. Mater. Chem. C*, 2, 2534, 2014.
115. Watt, M.M., Engle, J.M., Fairley, K.C., Robitshek, T.E., Haley, M.M., Johnson, D.W., “Off-on” aggregation-based fluorescent sensor for the detection of chloride in water. *Org. Biomol. Chem.*, 13, 4266, 2015.
116. Xu, L., Xu, Y., Zhu, W., Xu, Z., Chen, M., Qian, X., Fluorescence sensing of iodide and bromide in aqueous solution: anion ligand exchanging and metal ion removing. *New J. Chem.*, 36, 1435, 2012.
117. Chen, K.-Y., Lin, W.-C., A simple 7-azaindole-based ratiometric fluorescent sensor for detection of cyanide in aqueous media. *Dyes Pigm.*, 123, 1, 2015.
118. Xiong, K., Huo, F., Yin, C., Yang,Y., Chao, J., Zhang, Y., Xu, M., A off-on green fluorescent chemosensor for cyanide based on a hybridcoumarin-hemicyanine dye and its bioimaging. *Sensors Actuators B*, 220, 822, 2015.
119. Yanga, X., Shenc, L., Baoa, H., Fanga, X., Xua, J., Zhaoa, Y., Yanga, W., A tricarbocyanine near-infrared fluorescent probe for sulfide througha copper displacement mechanism. *Sensors Actuators B*, 220, 1361, 2015.
120. Hao, Y., Chen, W., Wang, L., Zhu, X., Zhang, Y., Qu, P., Liu, L., Zhou, B., Liu, Y.-N., Xu, M., A retrievable, water-soluble and biocompatible fluorescent probe for recognition of Cu(II) and sulfide based on a peptide receptor. *Talanta*, 143, 307, 2015.
121. Shia, B. B., Zhang, Y. M., Weia, T.B., Lina, Q., Yaoa, H., Zhang, P., Youa, X.M., A fluorescent and colorimetric chemosensor for dihydrogen phosphate ions based on 2-pyridine-1H-imidazo[4,5-b]phenazine-zinc ensemble. *Sensors Actuators B*, 190, 555, 2014.
122. Wang, L., Yang, L., Huang, L., Cao, D., Diketopyrrolopyrrole-derived Schiff base as colorimetric and fluoromeric probe for sequential detection of  $\text{HSO}_4^-$  and  $\text{Fe}^{3+}$  with “off-on-off” response. *Sensors Actuators B*, 209, 536, 2015.
123. Rout, K. C. Mondal, B., Copper(II) complex as selective turn-on fluorescent probe for nitrite ion. *Inorg. Chim. Acta*, 437, 54, 2015.

# Recent Advancements in Luminescent Materials and Their Potential Applications

Devender Singh\*, Vijeta Tanwar, Shri Bhagwan and Ishwar Singh

*Department of Chemistry, Maharshi Dayanand University,  
Rohtak, Haryana, India*

---

## **Abstract**

Phosphor or luminescent materials are the electronics materials of tomorrow. Besides their classical and extensive uses in lamp industries, T.V. tubes (cathode ray tubes), luminescent paints, and scintillators, these materials have recently appeared in electronic displays. Technologically, electroluminescent displays, vacuum fluorescent displays, and field emission displays are very important. Specialists in this field are now paying attention toward modifying newer synthetics methods. The current chapter focuses on the overview of research on luminescent materials based on phosphors, their synthesis techniques, and their promising applications.

**Keywords:** Phosphor, activators, rare-earth ions, display applications

## **10.1 Phosphor**

The word phosphor is also known as luminescent material, i.e. a material that converts absorbed energy into visible light, without undergoing incandescence. In current years, phosphor technology has evolved as a very dynamic research field. The emitted colors of phosphors vary with the variation in particle sizes. The nanosized phosphors demonstrate significant characteristics for example the bandgap is increased with decrease of particle size and superior quantum efficiency for luminescence. Phosphors with one dimension less than 100 nm are called nanophosphors that proficiently emit light on excitation with high-energy particle and electromagnetic

---

\*Corresponding author: devjakhar@gmail.com

radiation. Light emission from a phosphor is referred to as either fluorescence or phosphorescence. A phosphor compound is a powdered material from which emission of light occur upon excitation of radiation for example ultraviolet light, visible light, thermal radiation, or a beam of electrons or photons. A luminescent material or phosphor material basically works as a transducer because of emission of light via transferring one form of energy into another form. Phosphor may be composed of crystals or noncrystals. It is composed of a host lattice and one or more guest which are also known as activators, whose concentration ranges from few ppm to 10 mol%. Guest and host lattice are mutually liable for the luminescence characteristics of a phosphor. Average particle sizes of phosphors are generally ranges from micrometer to nanometer. Nanosized phosphors showed the blue shift of emission intensity, thus with decrease in the size of a particle the bandgap ( $E_g$ ) is blue-shifted owing to the consequence of quantum confinement [1].

Emission of light continues till an exciting radiation continues is known as fluorescence, while luminescence observed after the removal of an excitation sources is known as phosphorescence. However, in organic molecules, the two terms are differentiated by spin selection rules whether the transition is allowed or forbidden. Fluorescence is an allowed transition, while phosphorescence is a forbidden transition [2]. The term luminescence, which comprises both fluorescence and phosphorescence, is used to describe the nonequilibrium emission of radiation. Three processes are involved in the luminescence process: excitation, energy transfer, and radiative transition of the electrons. When light is absorbed as the excitation, the luminescence process is called photoluminescence (PL).

## 10.2 An Overview on the Past Research on Phosphor

The word phosphor was come into existence in the early 17th century. An alchemist, V. Casciarlo (Bologna), traced a crystalline stone near a volcano. Casciarlo observed that after absorption of sunlight sintered stone showed red color emission in the dark. This stone was named as 'Bolognian stone'. This Bolognian stone was found appears to have been barite ( $\text{BaSO}_4$ ) and after firing the obtained product being  $\text{BaS}$ , is used as a host for phosphor materials. It was this natural crystalline stone, which was studied for the light-emitting phenomena. Some other related discoveries were also marked in Europe, and these light-producing stones were known as 'phosphors'.

Though the preparation of  $\text{CaS}$  and  $\text{SrS}$  as a light-emitting material was developed in 1700 by Friedrich Hoffmann and 1817 by J. F. John,

respectively, French scientist Theodore Sidot in 1866 by coincidence synthesized a sample of the ZnS lattice based material, a vital material of television tubes. This manifested preparation and the foundation of technical study and preparation of phosphors. In earlier times, the optical properties of most vital luminescent hosts lattice ZnS were studied. The hexagonal ZnS also known as Sidot blend as was synthesized by Theodor Sidot. German scientist Philip E.A. Lenard and co-researchers carry out energetic and widespread investigation on phosphors which got remarkable consequences in the beginning of the 20<sup>th</sup> century. They synthesized a variety of phosphors based on sulfides, selenides, and chalcogenides. They also studied their luminescence characteristics. They found that phosphors could be prepared by incorporating metallic impurities into the host lattices by heating at higher temperature. Lenard and co-researchers worked on various rare-earth ions as potential activators along with heavy-metal ions for different lattices.

At the end of 1920s and 1930s, German scientist P. W. Pohl and co-researchers studied Tl<sup>+</sup>-doped alkali halide phosphors. They performed extensive spectroscopic studies and prepared single-crystal phosphors. P. W. Pohl with F. Seitz in the USA developed the configurational coordinate model of luminescence centre and established the foundation of modern luminescence physics. When the World War II was at end, research on these light-emitting materials explored spectacularly.

In 1888, Eilhard Wiedemann classified different types of the phosphors based on the type of excitation source. He introduced the terms luminescence, PL, thermoluminescence, electroluminescence, triboluminescence, crystalloluminescence, and chemiluminescence.

Nowadays, various industries (Samsung, LG, Kodak, Osram Sylvania, Philips, Oreva, Surya, Sony, etc.) are manufacturing these phosphor materials on large scale in all over the world (USA, S. Korea, China, Japan, France, India, etc) to meet out our daily technical requirements

### 10.3 Luminescence

Luminescence is a process in which electromagnetic radiation are emitted in visible region, by a physical system on excitation by thermal radiation or incandescence [3]. Luminescent materials transform some forms of energy into electromagnetic radiation. Most of the luminescent materials or phosphors emit radiation in the visible region. However, these materials may also emit in the ultraviolet and infrared regions upon tuning their luminescent properties with suitable dopants.

This physical system is a phosphor (luminescent materials) which essentially produces light by transferring one form of energy into another. These may be composed of crystals or noncrystals [4]. Luminescent characteristics of a phosphor depend on the host and activator. For example, ZnS:Ag or CdS:Ag can emit blue to red color with increasing Cd concentration. The particles sizes of phosphors are commonly observed in the range of micro- to nanometer [5].

According to the mode of excitation luminescence are classified into diverse types. Particularly, PL is the emission of light due to direct photo excitation of the emitting species [6]. Fluorescence, phosphorescence, and delayed fluorescence are well-recognized forms of PL. There are other types of luminescence that vary by the source of excitation (bioluminescence, chemiluminescence, crystaloluminescence, electroluminescence, cathodoluminescence, mechanoluminescence, radioluminescence, sonoluminescence, and thermoluminescence). There are two essentials for luminescence:

1. A semiconductor structure with a zero bandgap  $E_g$  is the prime requirement for a luminescent material, e.g. metals having no bandgap do not provide luminescence.
2. The energy must be provided to the phosphor materials for luminescence to take place.

#### **10.4 Mechanism of Emission of Light in Phosphor Particles**

Phosphor materials are powdered inorganic materials having a host lattice and trace of rare-earth ion impurities (dopant). When the phosphor is excited by an external photon sources, a phosphorescence process takes place in the material, as shown in Figure 10.1. The photon energy is absorbed either by the host lattice or is directly absorbed on impurity atom; the absorbed energy on host atom is transferred to the impurity atom (so-called activators). As a result of that, the activators emit visible light by relaxation of photo excited electron to lower energy state. In most cases, the emission of photon from phosphors is generated from impurities. The energy transfer mechanism in phosphor materials is described in Figure 10.1.

The luminescence process in phosphor materials is explained in details below [7–9], as depicted in Figure 10.1. When the excitation radiations

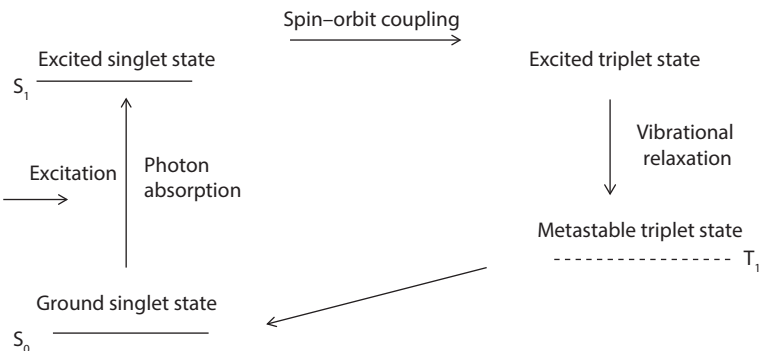


**Figure 10.1** Light emission mechanism in phosphor particles.

strike the phosphor material, it is absorbed by the activator. The metastable state is a triplet state, and the ground state is a single state. The ground state of the activator energy level represents the singlet ground state ( $S_0$ ). Upon excitation by an incident radiation, the activator energy level is raised to the singlet-excited state (higher than  $S_1$ ) on absorbing energy from the host lattice. Subsequent to the energy absorption, the initial excited states of energy level relax to an energy level  $S_1$  through radiationless transition by emitting phonons or lattice vibrations. The intersystem crossing from a singlet state ( $S_1$ ) to a triplet state (higher than  $T_1$ ) takes place by spin-orbit coupling. In a triplet state, it decays downward relatively quickly to the lowest energy level and once gets to the lowest triplet state, and stuck there, at least for a while. The excited triplet state ( $T_1$ ) of the lowest energy level returns back to its ground state ( $S_0$ ) by the photonic emission, which is emitted luminescent radiation. In the light emission (phosphorescence) process of the rare-earth-doped phosphor materials, the color of the emitting light from phosphor materials depends on the type of doping impurities in the host matrix. For example, red phosphor could be generated by adding europium to  $\text{Y}_2\text{O}_3$  cubic structure when UV or VUV is used as excitation source [10, 11].

## 10.5 How Luminescence Occur in Luminescent Materials?

In a luminescence process, system is composed of a host lattice and an activator showing excitation as well as radiative and nonradiative return to the ground state as shown in Figure 10.2. The activator absorb exciting

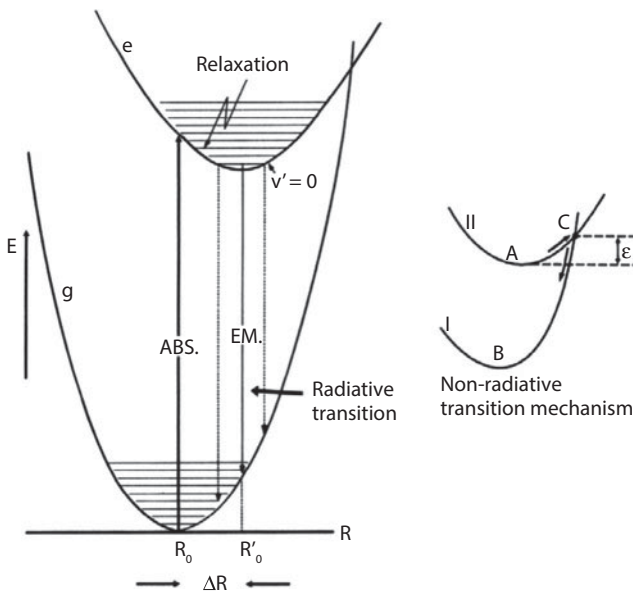


**Figure 10.2** Schematic energy level scheme of the luminescent ion.

radiation, raise up to an excited state, and then returns to ground state through the emission of radiative transition as available in Figure 10.2.

Each and every ion or material is not capable for producing luminescence and act as luminescent material as the rates of nonradiative emission to the ground state control the conversion efficiency of the luminescent material. So, it is necessary to overcome the nonradiative process. Enhancement of luminescence can also occur in several luminescent materials due to involvement of other ion beside activator in the host lattice called sensitizer, which absorbs the exciting radiation and transfer that absorbed energy to the activator as shown in the Figures 10.3 and 10.4. Halophosphate phosphors are examples of such type of luminescent materials. Some light-emitting materials involve energy transfer within the sensitizer system which may be the host lattice. Energy transport by migration through the lattice occurs, e.g.  $\text{Y}_2\text{O}_3:\text{Eu}^{3+}$ , the red-emitting phosphor. The ultraviolet radiation, electron beams, and X-rays excite the  $\text{O}^{2-}$  host lattice (sensitizer) which transfers this excitation energy rapidly to the  $\text{Eu}^{3+}$  (activator) ions. The phenomenon is shown in Figure 10.3.

In some cases, the host lattice gets excited by the X-ray or electron beam, e.g.  $\text{YVO}_4:\text{Eu}^{3+}$ . In this, the host lattice  $\text{VO}_4^{3-}$  is excited by the ultraviolet radiations, and this host lattice transfer its energy to  $\text{Eu}^{3+}$  ions, which emit red color.

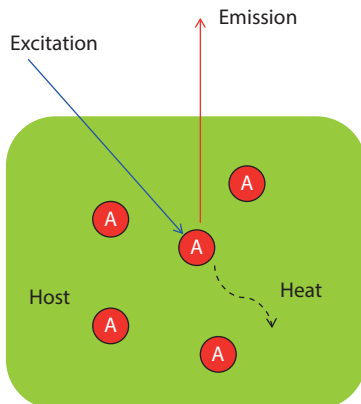


**Figure 10.3** Showing luminescent ion A in its host matrix.

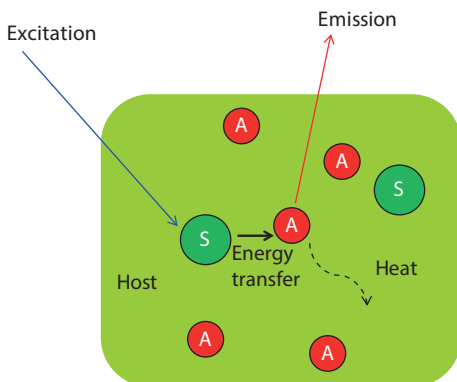
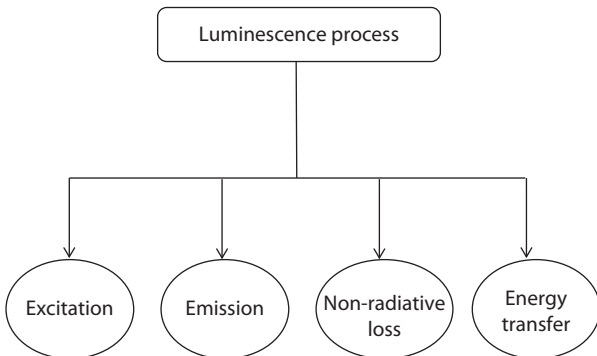


**Figure 10.4** Luminescent material showing energy transfer from sensitizer S to an activator A.

The significant physical processes which play a vital role in a luminescent material are detailed as follows:



### 10.5.1 Excitation

After excitation by ultraviolet or visible radiation, X-ray and  $\gamma$ -rays, etc., a luminescent material will emit radiation. The host lattice is excited by the high-energy fast electrons/X-rays/gamma-rays, whereas activator can be directly excited by ultraviolet/visible radiation.

The configurational coordinate diagram for this represents a plot of the energy versus the metal ligand distance. The metal ligand distance is the structural parameter, which varies during the vibration.

The configurational coordinate diagram is presented in Figure 10.5, where E is plotted versus R, the ground state is of parabolic shape as with a minimum at  $R_0$ , vibrational mode is supposed to be harmonic. The restoring force F is proportional to the displacement:

$$F = -k(R - R_0) \quad (10.1)$$

$$E = \frac{1}{2} k(R - R_0)^2 \quad (10.2)$$

The force analogous to a potential energy and depends on R, which is parabolic and the minimum  $R_0$  of the parabola is equal to the equilibrium distance in the ground state.

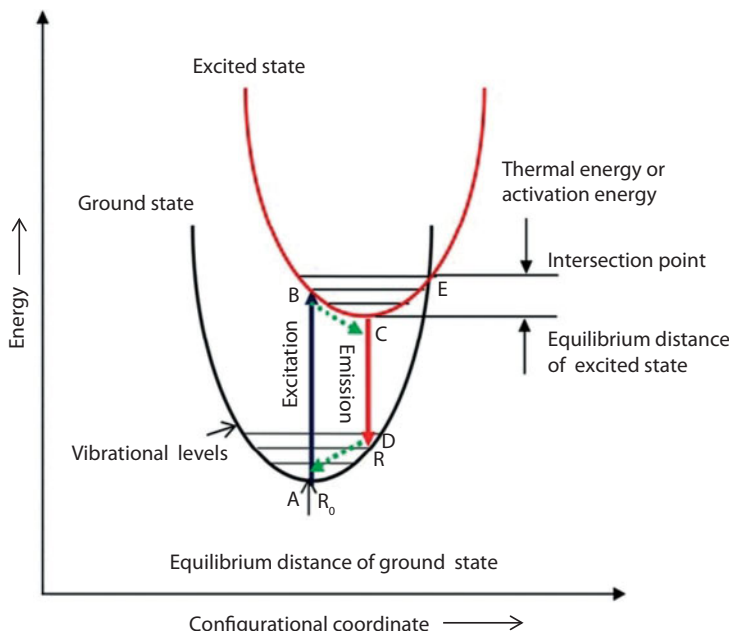


**Figure 10.5** Configuration coordinate graph showing the excited state and vibrational states. The ground state (g) has the equilibrium distance.

The centre is promoted from its ground state to an excited state in optical absorption. These are the electronic transitions, shown as vertical transition in coordinate diagram. The horizontal lines in this diagram (Figure 10.5) are representing nuclear and the internuclear distance. As the electrons are much lighter in weight than nuclei so move much faster than the nuclei, the electronic transition seen highly appropriate and in good estimation, place in static surroundings. The nuclei take their appropriate positions only later.

The optical excitation of absorption initiates from lower ( $v = 0$ ) vibrational level. Consequently most probable transition occurs at  $R_0$  where the vibrational wave function has its highest value as represents in Figure 10.5.

### 10.5.2 Emission

Emission from a luminescent centre is the radiative return to the ground state. The dopant centre attains high vibrational level of the excited state by the absorption process. Then, the luminescent centre returns first back to the lower vibrational level of the excited state giving up the excess energy to the surrounding environment. Instead, the nuclei adjust their positions according to the excited state so that the interatomic distances equal the equilibrium distances belonging to the excited state.

Then configurational coordinate changes by  $\Delta R$  ( $R - R_0$ ). This process is called relaxation. Emission of high intensity will not be there during relaxation process. A very fast emission has a rate  $10^8 \text{ s}^{-1}$ , the vibrational rate is about  $10^{-13} \text{ s}^{-1}$ . Then from the lowest vibrational level of the excited state, the system can return to the ground state instinctively emitting radiation. Rules for emission and absorption are same with a difference that emission occurs spontaneously but absorption occurs nonspontaneously. Absorption occurs only in the presence of radiation field. The reverse process of absorption is stimulated emission.

### 10.5.3 Nonradiative Transitions

A luminescent system on absorption of excitation energy can also go back to its ground state without radiative emission. This mode of returning to the ground state is known as nonradiative transition. This radiationless process always compete with the emission process, hence such processes must be suppressed to achieve high quantum efficiency of luminescent materials.

To have a technical importance, a luminescent material should have high quantum efficiency (ratio of the number of quanta emitted to the number of quanta absorbed). Phosphors used in fluorescent lamps, usually

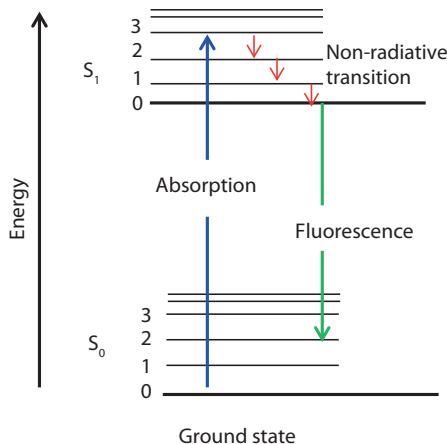


**Figure 10.6** Nonradiative transitions.

have quantum efficiency of at least 0.75. All the quanta absorbed would be remitted if there were no nonradiative losses. Figure 10.6 is showing nonradiative transitions.

#### 10.5.4 Energy Transfer

Energy transfer between two ions with the assistance of a multiphonon process can also be considered with respect to the sensitizer as a radiation-less process.

Many examples of luminescent materials are available in which an excited defect centre possibly transfer its energy to another centre either emitting a photon or decaying nonradiatively to its ground state. The ion is called a sensitizer which takes in the exciting radiation and consequently transfers it to the dopant ions. This procedure is elucidated by an example of  $\text{Ca}_{10}\text{K}(\text{PO}_4)_7\text{:Eu}^{2+}, \text{Mn}^{2+}$  where the CKP phosphor having  $\text{Eu}^{2+}$  ion act as sensitizer and  $\text{Mn}^{2+}$  as dopant.

### 10.6 Luminescence Is Broadly Classified within the Following Categories

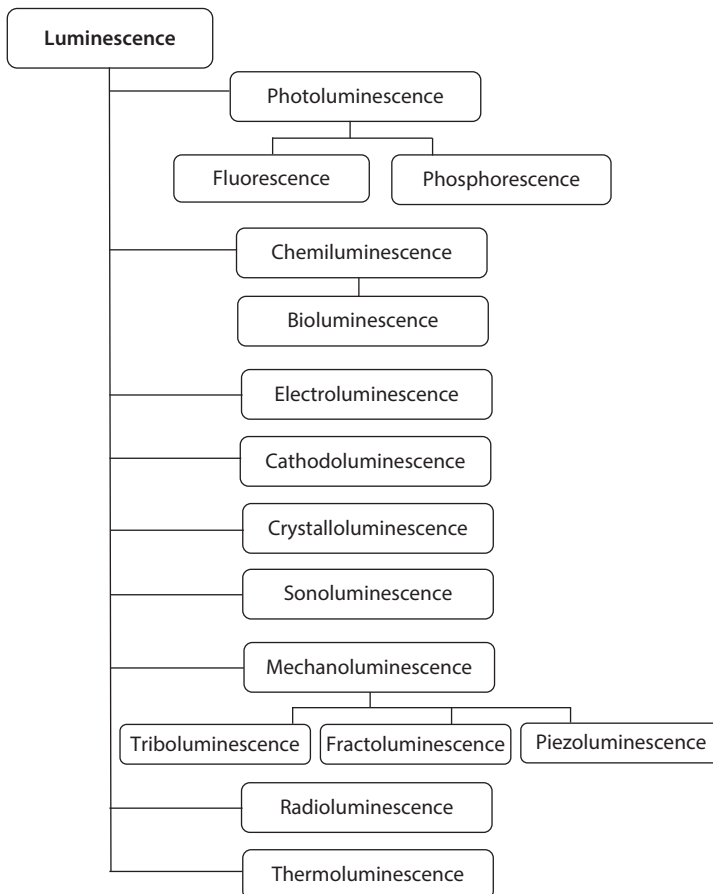
#### 10.6.1 Photoluminescence

Emission of light generated by the photo excitation of electrons under the action of electromagnetic radiation to energetically higher electronic state

by the absorbing photons which may take place through either phosphorescence or fluorescence, or both mechanisms. PL is a contactless, nondestructive technique of inquiring the electronic structure of molecules. PL is extensively used for material quality, level of impurity, detections of defect, mechanism of recombination as well as determination of bandgap.

PL may be divided into two kinds on the basis of emission [12]:

(i) Fluorescence (ii) Phosphorescence



#### 10.6.1.1 *Fluorescence*

Fluorescence is an instantaneous phenomenon in which emission of photons occurs on absorption of light or other variety of electromagnetic radiation. In fluorescence, emission of light occurs from excited singlet state to

the singlet ground state within a time of less than  $10^{-8}$  s without change in the spin of electron. Fluorescence is a temperature-independent process. The molecules in bulk subsist at lowest vibrational level of their ground state at room temperature. Upon absorption molecules get excited to a higher energy level and can reach to any of the vibrational sublevels associated with excited electronic state. The diverse vibrational energy levels are consisted of a series of rotational energy levels, which produce several absorption bands which are very difficult to resolve and consequently illustrate all the individual bands in the spectrum. When molecule excited to a higher vibrational energy level, the vibrational energy is wasted due to collision between the molecules and the molecules comes back to the lowest vibrational energy level of same excited state. Then, molecule can get back to the lowest vibrational level of the ground state by emitting of a photon of energy in the form of fluorescence. If all the excited molecules come back to the ground state, the quantum efficiency is said to be unity. Fluorescence has numerous practical applications, as chemicals sensors, fluorescent dyes, biological detectors, and fluorescent lamps.

#### 10.6.1.2 *Phosphorescence*

Phosphorescence is a process of generation of photon; it occurs when certain substances are irradiated by electromagnetic radiation and remains continue for some time even after the removal of an excitation source. Here, in this process, the transition is forbidden, consequently the time scale of re-emission is slow. When the photo-generated electrons and holes take considerable time to recombine in a luminescent material, then the light-emitting process is known as phosphorescence [13]. In phosphorescence, emission of light persists for a longer time in comparison to fluorescence. The decay time of phosphorescence after the removal of an excitation source can be enhanced by increasing the heating temperature but in fluorescence, this decay time does not change. One more difference between the two processes is that the phosphorescence is obtained at a longer wavelength than fluorescence. Common instances of phosphorescent materials are the paint, dark stickers, wristwatch, etc. that shine for some time after being charged in light. Phosphorescent materials are capable to accumulate light and liberate it gradually. Phosphorescence property can be used to analyze water, chemical pollutants, and drugs in pharmaceutical fields.

##### 10.6.1.2.1 Photoluminescence Mechanism (Franck–Condon Principle)

At normal temperature, an atom or molecule exists in its ground state without any exterior activation and can absorb only photons consequent

to the bandgap between the allowed energy levels. On absorption of light, whole energy of the photon is transferred to atoms or molecules. The light-absorbing species is thus excited, i.e. transition from its lowest-energy state (ground state) to energy-rich state (first singlet excited state). In a molecule, each electronic energy level consists of a series of vibrational and rotational levels which are superimposed to each other. When radiation is absorbed, the molecule is not easily shifted to high-energy state, but needs some additional vibrational energy to arrive at the highest vibrational level of excited state. After this, the molecule relaxes through radiationless transition to the lowest vibrational level of same state because of the time needed for this process, the nuclei rearrange themselves. Then molecule relaxes to its ground state through radiative transitions. It might be logical to expect that the optical transitions of a molecule undergoing absorption would take place at the equal energy as the emission. But similar to absorption, the relaxation to ground state can be possible to the lower vibrational levels rather than wholly undergoing emission back to the very lowest vibrational level directly. The result of this process is that the photons absorbed by the molecule are typically higher in energy than the photons that are emitted by the molecule due to the involvement of the vibrational levels. This energy change among the absorbed and emitted photons is known as Franck–Condon or Stoke shift [14, 15] as shown in Figure 10.7.

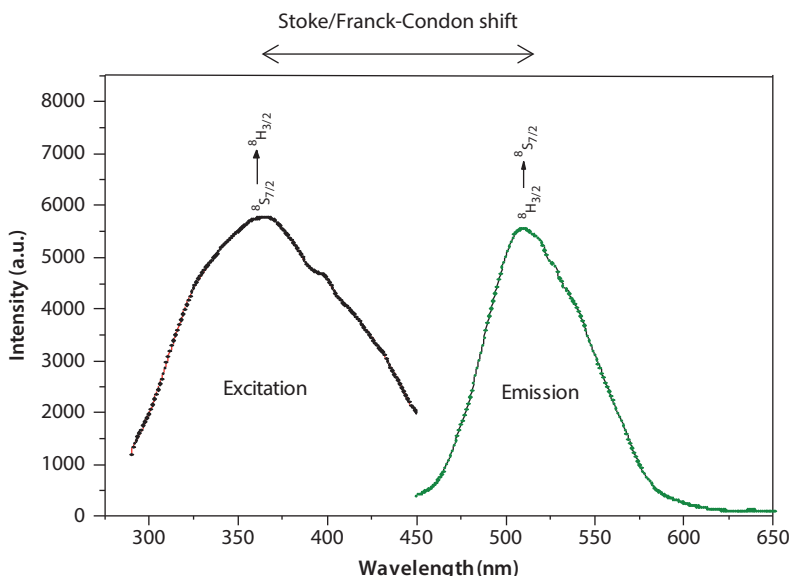


**Figure 10.7** Showing Franck–Condon or Stoke shift.

### 10.6.2 Bioluminescence

Luminescence produced by living organisms is called as bioluminescence. The light-producing molecules are excited via a chemical reaction; so, bioluminescence is associated to chemiluminescence. Few organisms, e.g. fireflies generate luciferin and luciferase chemicals. Light is produced by the catalytic oxidative reaction of luciferin pigment in the presence of air and luciferase acts as catalyst to promote the rate of reaction.

### 10.6.3 Chemiluminescence

Chemiluminescence is the process of emission of light resulted from either some chemicals or electrochemically redox reactions. The main drive energy to occur this type of luminescence comes from the enthalpy of the reaction. The chemical reaction produces few innovative molecules that can possess its electrons in an excited state just after creation, and after that decay to ground state producing visible light or liberate the energy in some other mode.

### 10.6.4 Crystalloluminescence

Luminescence occasionally produced during the process of crystallization is known as crystalloluminescence. This is special-type chemiluminescence in which light is produced by the formation of bonds between the atoms. This kind of luminescence is mainly used for determining the nuclear size.

### 10.6.5 Electroluminescence

It is an optoelectronic phenomenon in which materials produce the light by passing of electric current. The process of generation of luminescence is having different mechanism in both organic and inorganic materials. In general, luminescence is generated due to formation of excitons (electron-hole pair) in the recombination zone or at p-n junction and then followed by their radiative decay results in the emission of intense light.

### 10.6.6 Cathodoluminescence

Luminescence generated due to falling of an electron beam on a luminescent material. From many years, cathodoluminescence was used for constructing displays, flat screen displays like LCDs, examination of ceramics, glass, rocks, etc. in order to get information regarding growth, deformation, and quality of materials.

### 10.6.7 Mechanoluminescence

Luminescence generated due to mechanical action on a solid. This can be divided into three categories.

**(i) Triboluminescence**

If a solid substance emits light due to mechanical damage like scratching, crashing, or griding, the process is known as triboluminescence.

**(ii) Fractoluminescence**

Luminescence produced when bonds of crystals are ruptured.

**(iii) Piezoluminescence**

Light emitted by the some solids due to applying pressure on certain solids.

### 10.6.8 Radioluminescence

This type of luminescence is produced when certain substances are exposed to ionizing radiations like  $\alpha$ ,  $\beta$ , or  $\gamma$  rays. The emission of light by a substance under the bombardment with this ionizing radiation is known as radioluminescence. Radioluminescence was first reported by Pierre and Marie Curie. This type of luminescence plays a major role in night vision.

### 10.6.9 Sonoluminescence

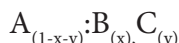
It is the emissions of short burst of light from the small bubbles in a solvent on excitation by ultrasonic waves. The exposure of sound waves in a solvent leads to the formation of bubbles which are filled with vapor and gas. Each one of these imploding bubbles can act as a microreactor. High temperature and pressure created during cavity formation cause the bubble to collapse quickly with a flash of light.

### 10.6.10 Thermoluminescence

It illustrates the phenomena that on heating some crystalline materials produce luminescence that is different from black body radiation or incandescence. Luminescence that produces on heating of a material and generally occurs below incandescence is known as thermoluminescence. Thermoluminescence is a significant technique for dating some archeological artifacts.

## 10.7 Inorganic Phosphors

The inorganic phosphor composed of two parts: one is the host lattice, and the other part is activators or luminescent center or dopant which is usually an impurity in a pure host lattice [16–18]. Activators are added in very low concentration levels varying from few ppm up to 1 or 2 mol% of the host lattice. Activators are chief localized centers for luminescence of the phosphor materials. The phosphor is represented in a formula as shown below:



Phosphors consisting host lattice represented as A and active center or dopant represented as B, in bracket its concentration in mole % is mentioned and C is the coactivator.

In brackets, their stoichiometry is mentioned. In a formula, the phosphor is represented as, for example:



here  $SrAl_2O_4$  is host lattice in which concentration of Sr is 97 mol%, Eu is activator whose concentration is 2 mol%, Dy is a coactivator whose concentration is 1 mol%.

## 10.8 Organic Phosphors

Organic luminescent materials are composed of basic element carbon with additional elements such as hydrogen (H), nitrogen (N), oxygen (O), phosphorous (P), and sulfur (S). The backbone of the organic materials is made up of strongly localized bonds between the carbon atoms that enable the conductivity through these bonds. Generally, metal-organic complexes and polymeric materials are used as organic luminescent materials. The design of active luminescent organic materials is one of the most significant considerations for the fabrication of organic light-emitting devices (OLEDs) as it determines stability, emission color and efficiency of the proposed device. The materials used for the fabrication of OLEDs are of organic origin and semi-conducting in nature. Since polymers and organic materials are not referred as conducting materials because of the large bandgap, a very high electrical field has to be applied. When applying an electrical field, the charge injections result in geometrical defects on the symmetric organic structure and exhibit a lower bandgap. The charge

carriers move along the structure and the attraction between the carrier results in an exciton with a possibility to emit light as photons. The exciton is either in singlet- or in triplet-state according to Pauli's principle. The exciton will form two new energy bands inside the bandgap. Upon relaxation of the exciton, heat and photons will be emitted with an energy set by the energy difference between the energy bands that represent the exciton. The singlet state is regarded as the light-forming state, while triplet state is not. In some special cases, the triplet state also produces light.

## 10.9 Optical Properties of Inorganic Phosphors

Inorganic phosphors are composed of a pure host lattice whose maximum concentration may be up to 99.98%, and another part is an impurity also called as activator or dopant or active centre whose concentration may vary from few ppm up to 10% of the host lattice. Activator ions contain mainly localized luminescence centers that exist in the phosphor materials.

Different types of localized luminescent centers which are having different electronic transitions are as follows [19, 20]:

(Here arrow to the left is indicating emission and to the right is indicating optical absorption)

1.  $4f^n \rightarrow 4f^{n-1}5d$  Sm<sup>2+</sup>, Eu<sup>2+</sup>, Ce<sup>3+</sup>, Tm<sup>2+</sup>, Yb<sup>2+</sup>, only absorption transition observed for Pr<sup>3+</sup> and Tb<sup>3+</sup>.
2.  $4f^n \rightarrow 4f^n$ ,  $5f^n \rightarrow 5f^n$  Rare-earth ions.
3.  $3d^n \rightarrow 3d^n$ ,  $4d^n \rightarrow 4d^n$  1<sup>st</sup> and 2<sup>nd</sup> row transition metals ions.
4.  $3d^{10} \rightarrow 3d^94s^1$  (for example, Ag<sup>+</sup>, Cu<sup>+</sup>, Au).
5.  $ns^2 \rightarrow ns^1 np^1$  Tl<sup>+</sup>, In<sup>+</sup>, Ga<sup>+</sup>, Pb<sup>2+</sup>, Sn<sup>2+</sup>, Ge<sup>2+</sup>, Bi<sup>3+</sup>, Sb<sup>3+</sup>, Cu<sup>+</sup>, Au<sup>+</sup>, Ag<sup>+</sup>, etc.
6.  $2s \rightarrow 2p$ ; It is an example of an F center.
7. Certain charge transfer-based transition involved between the p electron of anion and empty cation orbital. Intermolecular transition involved in the complexes of the MoO<sub>4</sub><sup>2-</sup>, WO<sub>4</sub><sup>2-</sup>, etc.

## 10.10 Role of Activator and Coactivator

The various metals which act as the active centre for the different host lattices (oxide, silicate, vanadates, aluminate oxysulfide, sulfide, etc.). These are used for making any host lattice as luminescent materials. These are

essential ions which are responsible for these electronic transitions which are necessary for phosphor material.  $\text{Tl}^+$ ,  $\text{In}^+$ ,  $\text{Ga}^+$ ,  $\text{Pb}^{2+}$ ,  $\text{Sn}^{2+}$ ,  $\text{Ge}^{2+}$ ,  $\text{Bi}^{3+}$ ,  $\text{Sb}^{3+}$ ,  $\text{Cu}^+$ ,  $\text{Au}^+$ ,  $\text{Ag}^+$ ,  $\text{Mn}^{2+}$ ,  $\text{Sm}^{2+}$ ,  $\text{Eu}^{2+}$ ,  $\text{Ce}^{3+}$ ,  $\text{Tm}^{2+}$ ,  $\text{Yb}^{2+}$ ,  $\text{Pr}^{3+}$ ,  $\text{Tb}^{3+}$ ,  $\text{Dy}^{3+}$ ,  $\text{Eu}^{3+}$ ,  $\text{Ce}^{4+}$ ,  $\text{Tb}^{4+}$ , etc.

Certain metal ions which help in the enhancement of the luminescent properties of the phosphor materials are called the codopants. These metal ions absorb the excitation energy and transfer it to the activator which improve the light-emitting properties of the dopants available in the host lattice.  $\text{Li}^+$ ,  $\text{Na}^+$ ,  $\text{K}^+$ ,  $\text{Cs}^+$ ,  $\text{Bi}^{3+}$ ,  $\text{Y}^{3+}$ ,  $\text{Pr}^{3+}$ ,  $\text{Nd}^{3+}$ ,  $\text{Gd}^{3+}$ ,  $\text{Dy}^{3+}$ ,  $\text{Er}^{3+}$ , and  $\text{Ho}^{3+}$  act as the coactivator in the various host lattice.

### **10.11 Role of Rare Earth as Activator and Coactivator in Phosphors**

The lanthanides play a vital role in recent optical technology as the vital components of materials. Rare-earth-activated materials have an astounding number of applications and today's optical technology and future improvements rely on their distinctive characteristics. There are 15 rare-earth elements from lanthanum to lutetium which act as activator and coactivators in the phosphor materials. Numerous phosphors having rare earth as activator and coactivator with different host lattices had been invented.

The phosphor compounds are broadly used for industrial as well as commercial use. The chemical technology for preparation and purification of these compounds has been improved significantly, providing reliable materials in purity levels required for efficient phosphor absorption and emission.

The lanthanides from Ce to Lu have 1–14 4f electrons in their inner shell configuration. Sc, Y, La, and Lu ions are without 4f electrons hence have no possible electronic levels for excitation and luminescence processes.

Lanthanide ions are the solid-state laser materials as  $\text{Nd}^{3+}$ , YAG lasers. These lasers are used in innumerable applications as in industrial equipment, surgical instrumentation, precision interferometry, and so many others. Some lanthanide ions-doped phosphors are energy-efficient luminescent materials and are used in various applications. Mercury-containing fluorescent lamps composed of rare-earth phosphor materials are more environmental safe alternatives such as xenon lamps. The energetic particles, gamma rays, or x-rays provide energy to these materials and convert the energy of these rays into visible or ultraviolet light that may be identified by usual resources, for example photomultiplier tubes or photodiodes.

The applications for rare-earth-activated optical materials are constantly increasing and more research on these materials will bring about improvements in optical technology.

The electronic structure of rare-earth ions has electron in unfilled 4f orbital which are greatly shielded from 5d and 5p orbitals. Due to shielding effect, the f-electrons preserve most of their atomic features, and their 4f<sup>n</sup> energy levels. The distinctive characteristics of lanthanides are responsible for their extensive variety of applications.

In most of the cases, luminescence developed due to lanthanide ions in phosphors because of multiple transitions inside f-electron. Due to having shielding effect, the 4f shell exhibits f-f emission spectra with typically sharp lines, but are orbitally forbidden transition as because of selection rule ( $\Delta L = \pm 1$ ) of electronic transitions. Many transitions are also spin forbidden ( $S = 0$ ) along with orbital forbidden transition, due to that less probable electronic transitions from micro- to milliseconds [21, 22]. Some lanthanide ions that demonstrate wide emission bands, particularly divalent europium and trivalent cerium, where the wide emission band is obtained due to 5d–4f optical transitions as these are spin allowed. The 5d electrons of lanthanide ions are strongly influenced by the surrounding environment. Thus in consequence, the band width and emission wavelength (e.g. Eu<sup>2+</sup>) are directly affected with the structure of host lattice.

Many of the lanthanides are used as activators in phosphors for using different lattices. The various probable transition of 4f electrons of lanthanides (III) ions have been specifically studied by Dieke and their research group, which is recognized as the “Dieke diagram” [23] as given in Figure 10.8. The transition spectra of rare-earth ions in host crystal levels are considered for determining energy levels experimentally. The measurements are relevant to rare-earth ions in different environment, of the order of several hundred cm<sup>-1</sup>.

### 10.11.1 Rare Earths as Activator

The use of rare earths as activators and coactivators is one of the advancements in phosphor materials. A number of phosphors based on rare earth as activators in different host lattices had been invented in the past few years. Preparation and purification chemical technology has been improved greatly due to huge demand in industries as well as for commercial purpose providing consistent and reliable materials in purity levels required for efficient phosphor absorption and emission.

From lanthanum to lutetium, there are 15 rare-earth elements. The electronic configurations of various rare-earth ions in trivalent oxidation state in their ground state are presented in the Table 10.1.

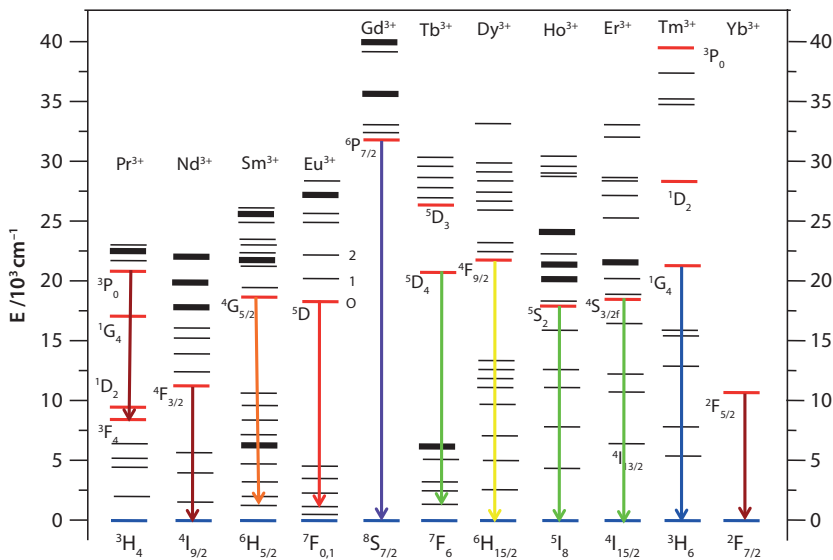


Figure 10.8 Showing different energy levels of lanthanides(III) ions.

Table 10.1 Electronic transitions in rare-earth ions.

Rare earth	Electronic configuration RE <sup>3+</sup>	Ground state terms	Excited state terms
Ce	$4f^1 5s^2 5p^6$	$^2F_{5/2}$	—
Pr	$4f^2 5s^2 5p^6$	$^3H_4$	$^3H_5, ^3F_2$
Nd	$4f^3 5s^2 5p^6$	$^4I_{9/2}$	$^4G_{5/2}, ^2G_{7/2}, ^4G_{7/2}$
Pm	$4f^4 5s^2 5p^6$	$^5I_4$	$^5G_{12}, ^5G_3$
Sm	$4f^5 5s^2 5p^6$	$^6H_{5/2}$	$^4H_{7/2}, ^6F_{1/2}, ^6F_{3/2}$
Eu	$4f^6 5s^2 5p^6$	$^7F_1, ^7F_0$	$^7F_2$
Gd	$4f^7 5s^2 5p^6$	$^8S_{7/2}$	$^6P, ^6I, ^6D, ^6G$
Tb	$4f^8 5s^2 5p^6$	$^7F_6$	$^7F_5$
Dy	$4f^9 5s^2 5p^6$	$^6H_{15/2}$	$^6F_{11/2}, ^6H_{13/2}, ^6H_{11/2}$
Ho	$4f^{10} 5s^2 5p^6$	$^5I_8$	$^5G_6, ^3H_6$
Er	$4f^{11} 5s^2 5p^6$	$^4I_{15/2}$	$^2H_{11/2}, ^4G_{11/2}$
Tm	$4f^{12} 5s^2 5p^6$	$^3H_6$	$^3F_4, ^3H_4, ^3H_5$
Yb	$4f^{13} 5s^2 5p^6$	$^2F_{7/2}$	$^2F_{5/2}$

The 4f electrons are serial wise put to their inner orbital configuration in lanthanides from Ce to Lu. Sc, Y, La, and Lu have no 4f electrons which can stimulate the excitation and luminescence in the visible range [24–26]. Ce to Yb ions has incompletely filled 4f orbitals, demonstrate the diversity of luminescence characteristics in the visible range. In phosphors host lattices, many of these ions can be used as activators and coactivators. Dieke *et al.* precisely studied the distinctive energy levels of electron available in 4f lanthanides(III) ions and gave a diagram for the energy levels of the rare-earth ions as shown in Figure 10.8.

The levels were experimentally established by taking into account the optical spectra of each ion in host crystal. There is no effect of environment on the Dieke diagram of rare-earth ions. The rare-earth ions show both charge transfer states and  $4f^{n-1}5d^1$  states [27]. Both states show allowed strong optical absorptions. Energy of these  $4f^{n-1}5d^1$  and charge transfer states are more directly reliant on their surrounding environments [28] than the energy of 4f energy levels. The comparative categorize of the energies of these states are established to be the same for the complete series of rare-earth ions in any of the host materials [29–31]. The  $4f^{n-1}5d$  transition in  $Ce^{3+}$ ,  $Pr^{3+}$ , and  $Tb^{3+}$  and the charge transfer state absorptions in  $Eu(III)$  and  $Yb(III)$  have energies less than ca  $40 \times 10^{-13} \text{ cm}^{-1}$ . Therefore, they interact with 4f levels, resulting in 4f-4f emissions. When the energy levels of these states are lower than those of 4f levels then direct luminescence from these levels are originated, such as 5d-4f energy transition in  $Ce(III)$ ,  $Pr(III)$ , and  $Eu(II)$ . Spectra of this type of luminescence differ due to crystal field splitting in the different host crystals. The tetravalent ions such as  $Ce^{4+}$  and  $Tb^{4+}$  show the same luminescence as in the  $La^{3+}$ ,  $Ce^{3+}$ , and  $Gd^{3+}$ .

### 10.11.2 Luminescence of Rare Earths

Rare-earth ions usually exist in II to IV oxidation state, but the trivalent oxidation state is the most stable in all their existing oxidation states. These rare-earth ions act as effective activator in various host lattices. The possible transitions of these ions in different oxidation are as follows:

#### 10.11.2.1 Tetravalent Ions

##### 1. $Dy^{4+}$

Luminescence lines at 525 nm due to  $^5D_4 \rightarrow ^7F_4$  transition and at 630 nm due to  $^5D_4 \rightarrow ^7F_3$  transition have been reported for example  $Cs_3Dy F_7:Dy^{4+}$  [32].

2. Nd<sup>4+</sup>

Luminescence at 415, 515, 550, and 705 nm has been accounted in Cs<sub>3</sub>NdF<sub>7</sub>:Nd<sup>4+</sup> [33].

#### 10.11.2.2 Trivalent Ions

1. Ce<sup>3+</sup>

Among all the rare earths, the 4f – 5d energy transition is less in Ce<sup>3+</sup>, but the energy gap between the 5d state to the adjoining energy level <sup>2</sup>F<sub>7/2</sub> is so huge that the 5d energy level acts as proficient light-producing state. PL energy depends strongly on the host lattice structure due to the CFT of 5d energy state. The Ce<sup>3+</sup>-activated phosphors show generally two types of the emission peaks are owing to two terminating energy levels <sup>2</sup>F<sub>5/2</sub> and <sup>2</sup>F<sub>7/2</sub>. The decay time of Ce<sup>3+</sup> emission exists in 10<sup>-7</sup>–10<sup>-8</sup> s. For example, in a phosphor with structural formula Y<sub>2</sub>SiO<sub>5</sub>:Ce<sup>3+</sup>, Tb<sup>3+</sup> is Ce<sup>3+</sup> activated which is used in flying spot scanners.

2. Pr<sup>3+</sup>

Luminescence of Pr<sup>3+</sup> comprises of several multiplets: 515 nm (<sup>3</sup>P<sub>0</sub> → <sup>3</sup>H<sub>4</sub>), ~670 nm (<sup>3</sup>P<sub>0</sub> → <sup>3</sup>F<sub>2</sub>), ~770 nm, (<sup>3</sup>P<sub>0</sub> <sup>3</sup>F<sub>4</sub>), ~630 nm (<sup>1</sup>D<sub>2</sub> <sup>3</sup>H<sub>4</sub>), ~410 nm (<sup>1</sup>S<sub>0</sub> <sup>1</sup>I<sub>6</sub>), and UV (5d4f) transitions. The comparative intensities of various transitions depend on the host matrix.

Y<sub>2</sub>O<sub>2</sub>S:Pr<sup>3+</sup> emits light at 670 nm which is due to emission from <sup>3</sup>P<sub>0</sub> to <sup>3</sup>F<sub>2</sub>.

3. Nd<sup>3+</sup>

The Nd<sup>3+</sup> ions give following transitions in infrared region when used as activator. These peaks are reported when Nd<sup>3+</sup> is used in Y<sub>3</sub>N<sub>5</sub>O<sub>12</sub>:Nd<sup>3+</sup>. Emission spectra are providing various peaks i.e. 870 – 950 nm due to 4F3/2 → 4I9/2, 1050–1120 nm due to 4F3/2 → 4I11/2 and at 1340 nm due to the transition 4F3/2 → 4I13/2.

4. Sm<sup>3+</sup>

Red luminescence at 610 nm (<sup>4</sup>G<sub>5/2</sub> → <sup>6</sup>H<sub>7/2</sub>) and 650 nm (<sup>4</sup>G<sub>5/2</sub> → <sup>6</sup>H<sub>9/2</sub>) are observed in Sm<sup>3+</sup>. Effective luminescence intensity in Sm<sup>3+</sup>, however, has not been accounted. Sm<sup>3+</sup> behaves as a supporting dopant in SrS:Eu<sup>2+</sup> (Mn<sup>2+</sup> or Ce<sup>3+</sup>) phosphors. Under excitation, Sm<sup>3+</sup> accepts an electron and converts to Sm<sup>2+</sup>, which sequentially shows an excitation at 1.0 μm.

5. Eu<sup>3+</sup>

Several luminescence peaks owing to  ${}^4D_5 \rightarrow {}^7F_s$  are shown by Eu<sup>3+</sup> when it is used as activator. The emission approximately at 610–630 nm is attributable to the hypersensitive transition of  ${}^5D_0 \rightarrow {}^7F_2$  of the trivalent europium site. The sharp emission due to the electric dipole transition is employed for practical relevances. The Y<sub>2</sub>O<sub>3</sub>:Eu<sup>3+</sup> phosphor in which Eu<sup>3+</sup> gives the red-emitting component at ~612 nm.

6. Gd<sup>3+</sup>

The lowest excited 4f level of Gd<sup>3+</sup> ( ${}^6P_{7/2}$ ) provides sharp line emission at ~315 nm [34]. Gd<sup>3+</sup> acts as sensitizer to the other lanthanide dopant ions [35]. The energy level of the charge transfer and the 4f<sup>6</sup>5d<sup>7</sup> states are the highest among the lanthanide so that Gd<sup>3+</sup> causes no quenching to the other lanthanide dopants.

7. Tb<sup>3+</sup>

Luminescence spectra lines attributable to  ${}^5D_5 \rightarrow {}^7F_{5J}$  are observed for Tb<sup>3+</sup>, but among all these, the  ${}^5D_4 \rightarrow {}^7F_5$  emission approximate at 550 nm is sharp and strongest [36]. An example of Tb<sup>3+</sup> activator phosphor is Ln<sub>2</sub>O<sub>2</sub>S:Tb<sup>3+</sup>.

8. Dy<sup>3+</sup>

Emission lines of Dy<sup>3+</sup> are existing from 470 to 500 nm because of ( ${}^4F_{9/2} \rightarrow {}^6H_{15/2}$ ) transition and in 570–600 nm range due to ( ${}^6F_{15/2} \rightarrow {}^6H_{11/2}$ ) transition. The color of luminescence Dy<sup>3+</sup> is very close to white.

9. Ho<sup>3+</sup>

Proficient luminescent emission of Ho<sup>3+</sup> has cross-relaxation among ( ${}^5S_2 \rightarrow {}^5I_4$ )  $\leftrightarrow$  ( ${}^5I_8 \rightarrow {}^5I_7$ ) at an interionic distance of 7.5 Å has been accounted. A green emission attributable to the  ${}^5F_4, {}^5S_2 \rightarrow {}^5I_8$  transition has been accounted in the infrared to visible up-convertor materials (LiYF<sub>4</sub>:Yb<sup>3+</sup>, Ho<sup>3+</sup>).

10. Er<sup>3+</sup>

The green luminescence due to ( ${}^4S_{3/2} \rightarrow {}^4I_{15/2}$ ) transition of Er<sup>3+</sup> has been observed in IR to visible up converter phosphors. Good examples of Er<sup>3+</sup> as activator are Y<sub>2</sub>O<sub>3</sub>:Er<sup>3+</sup> [37] and Y<sub>2</sub>O<sub>3</sub> S:Er<sup>3+</sup>.

11. Tm<sup>3+</sup>

The blue luminescence of Tm<sup>3+</sup> due to the ( ${}^1G_4 \rightarrow {}^3H_6$ ) transition has been reported in infra-red to visible upconvertor phosphors. ZnS:Tm<sup>3+</sup> [38] is the best example of the Tm<sup>3+</sup> when it is used as activator.

12. Yb<sup>3+</sup>

The Yb<sup>3+</sup> gives infrared absorption at 1000 nm due to the ( $^5F_{5/2} \rightarrow ^5F_{7/2}$ ) transition. The example of Yb<sup>3+</sup> as activator is La<sub>2</sub>O<sub>2</sub>S:Yb<sup>3+</sup>.

## 10.11.2.3 Bivalent Ions

1. Sm<sup>2+</sup>

Sm<sup>2+</sup> ions give transition at 550–850 nm due to ( $^4D_0 \rightarrow ^7F_{0-4}$ ). Example of this type is BaFCl:Sm<sup>2+</sup> phosphor [39] where Sm<sup>2+</sup> acts as an activator.

2. Eu<sup>2+</sup>

Eu<sup>2+</sup> generally shows the broad emission band attributable to f-d transition. The emission band depends enormously on host lattice structure, shifting from the near ultraviolet to the red color of visible range. Its reliance is deduced as because of the crystals field splitting of 5d levels [40]. With increasing crystal field strength, the emission peak shift to longer wavelength as shown in Figure 10.9. One of the best examples is the blue luminescence in BaMgAl<sub>10</sub>O<sub>17</sub>:Eu<sup>2+</sup>, used for tricolor fluorescent lamps.

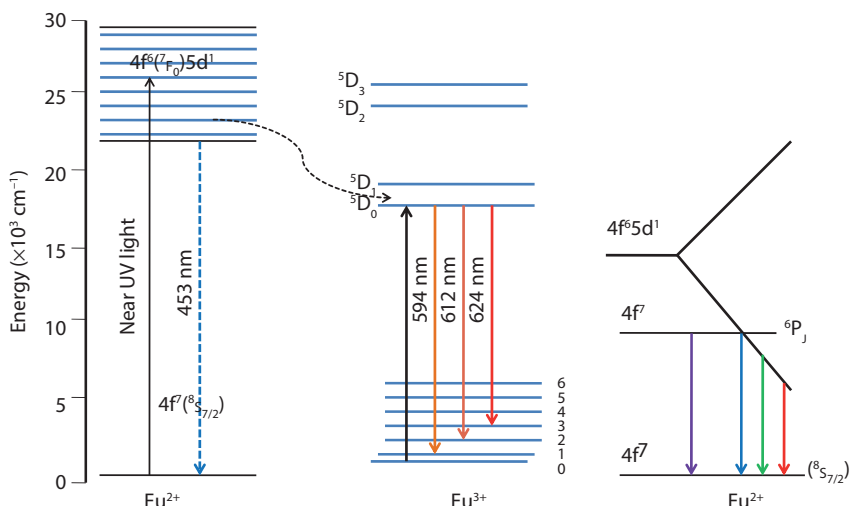


Figure 10.9 Mechanism of various transitions in Eu<sup>3+</sup> and Eu<sup>2+</sup> ions.

3.  $Dy^{2+}$ 

Luminescence of  $Dy^{2+}$  was reported in  $CaF_2$ ,  $SrF_2$ , and  $BaF_2$  having spectral line at 2.3–2.7  $\mu m$  at 77 and 4.2 K.  $Dy^{2+}$  in these hosts was synthesized through the reduction of  $Dy^{3+}$  with X-ray irradiation.

4.  $Ho^{2+}$ 

Infrared luminescence of  $Ho^{2+}$  in  $CaF_2$  showing approximately at 1.8  $\mu m$  at 77 K has been accounted [41].

5.  $Yb^{2+}$ 

The emission and absorption of  $Yb^{2+}$  due to the  $4f^{14} 4f^{13}5d^1$  transition have been reported [42].  $Sr_3(PO_4)_2:Yb^{2+}$  is an example which emits light at 432 nm.

### 10.11.3 Rare Earths as Coactivator

The rare-earth ions also act as the coactivator for the enhancement of the light-emitting properties of these materials. These ions are less efficient when present as alone but quite effective when these are present along with the dopant. These absorb and continuously provide their radiative energy directly to the activator which is quite efficient in the light emission of dopant as shown in Figure 10.10. Nd, Dy, Ho, Y, Pr, Er, etc. act as codopants along with the  $Eu^{2+}$  activator for the various aluminate or silicate based lattice used for the persistent phosphor materials [43–48]. Sometimes, combinations of these rare-earth ions are also used ( $Nd + Dy/Y/Pr/Er$ ) for making the best persistent phosphors.

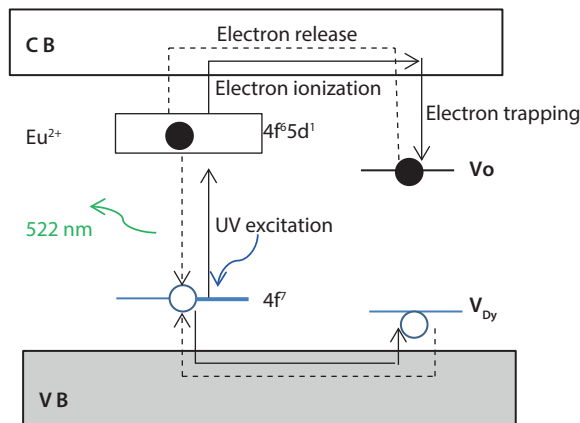


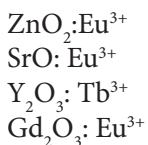
Figure 10.10 Showing the role of coactivator in the process of luminescence.

## 10.12 There are Different Classes of Phosphors, which May be Classified According to the Host Lattice

Inorganic luminescence materials absorb the high radiation energy and afterward emit the absorbed energy in the form radiative form. Luminescent materials are consisted of an inert host lattice and an optically active dopant. Various phosphors are given below based on their lattice type.

### 10.12.1 Oxide Lattice Phosphors

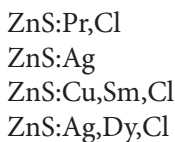
Oxide phosphors are originated appropriate for vacuum fluorescent display (VFD), electroluminescent (EL) devices, plasma panel display (PDP), and field emission display (FED). Luminescence efficiency increases with a decrease in the size of light-emitting materials. The experimental method for the synthesis of material is quite significant in technological process [49]. Some examples of oxide-based phosphors are



### 10.12.2 Sulphide Lattice Phosphors (ZnS)

Sulphide lattice phosphors are extensively used because of their commercial purposes. These phosphors are used in numerous fields of science and technology. Vital applications of these types of phosphor are that these are used in light sources, display devices and detector system. Researchers are continuously working on sulphide lattice phosphors due to their so wide use.

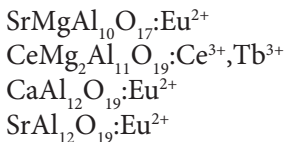
Some of important are given below [50–51]:



### 10.12.3 Aluminate Lattice Phosphors

Three band fluorescent lamps were prepared by the use of aluminate lattice phosphors by Verstegen *et al.* in 1974. Rare-earth ions-activated aluminate

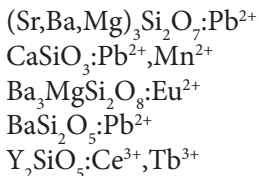
phosphors require high-temperature firing for synthesis. These materials are used in very overloading fluorescent lamps, for example compact fluorescent and photocopying lamps, etc. because of their extra stability. Some of important aluminate phosphor is given below [52–53];



#### 10.12.4 Silicate Lattice Phosphor

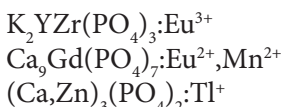
Silicate lattice phosphors were used as the most important fluorescent lamp phosphors until 1949. But the evolution started from 1957 to 1970, when  $\text{Pb}^{2+}$ -doped alkaline earth silicate phosphors were synthesized; these phosphors have proficient UV emissions.

Recently,  $\text{Eu}^{2+}$ -doped silicate phosphors have drawn much attention. Very complex silicates, halosilicates, and aluminosilicates phosphors have been developed. With the variation of the host materials, blue to blue/green-emitting phosphors can be obtained. Some important silicate lattice-based phosphors are listed below [54–55]:



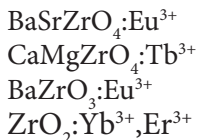
#### 10.12.5 Phosphate Lattice Phosphors

Phosphate compounds have low material cost, easy synthesis, and reasonable stability and have been utilized as host materials in many phosphors for many years. Due to these good properties, these types of phosphors are important to be used in industrial sectors. The synthesis of the first alkaline earth phosphate phosphor was done near 1938. These phosphors represented a milestone in the past of fluorescent lamp development. Some of the important phosphate lattice-based phosphors are shown below [56–59]:



### 10.12.6 Zirconates Lattice Phosphor

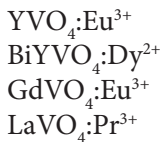
The zirconates phosphors are very important for fluorescent lamp. Rare-earth-doped green-emitting zirconates phosphors have sequentially been prepared for tricolor band lamps as competitive materials to aluminates and silicates phosphors. Some of zirconate phosphors are given below:



### 10.12.7 Vanadates Lattice Phosphors

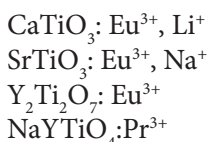
Inorganic luminous materials have significant practical consequences in approximately all devices, i.e. X-ray detectors lamps and CRT. In recent times, the advancement of flat or plasma or FEDs has enlarged the requirement of phosphor with gradually more superior properties of stability and luminescent qualities.

The yttrium vanadate ( $\text{YVO}_4$ ) in large demand applied as an efficient host for rare-earth ions in past some time [60]. Some of vanadate phosphors are given below:



### 10.12.8 Titanate Lattice Phosphors

Various researchers have made a lot of efforts recently for the improvement of highly developed displays applications. These modern technological demands can substitute the CRTs effectively. Consequently, the progress of light-emitting materials will make FED quite efficient. Some of titanate phosphors are given below:



### 10.12.9 Other Lattice Phosphors

For synthesizing good-quality phosphors for numerous uses, various types of host lattices have been used. Their enormous demands in industrial and commercial use require further more research on them. Some examples are given below:

	Types	Examples
i	Borate	$\text{SrB}_4\text{O}_7\text{F}:\text{Eu}^{2+}$
ii	Yttriate	$\text{SrY}_2\text{O}_4:\text{Eu}^{3+}$
iii	Tungstate	$\text{CaWO}_4:\text{Eu}^{3+}$
iv	Halosilicate	$\text{Ba}_2\text{Si}_3\text{O}_8 \cdot 2\text{SrCl}_2:\text{Eu}^{2+}$
v	Halophosphate	$\text{Ca}_{10}(\text{PO}_4)_6\text{Cl}_2:\text{Eu}^{2+}$
vi	Oxysulfide	$\text{La}_2\text{O}_2\text{S}:\text{Tb}^{3+}$
vii	Germinate	$4\text{MgO} \cdot \text{GeO}_2:\text{Mn}^{4+}$
viii	Sulfate	$\text{SrSO}_4:\text{Eu}^{2+}$

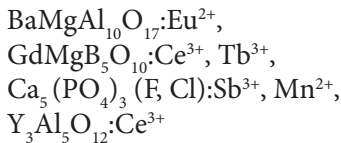
## 10.13 Applications of Phosphors

Nowadays, phosphors are widely used for commercial and industrial purposes. These have been utilized in many advanced prospective applications as described below.

### 10.13.1 Fluorescent Lamps

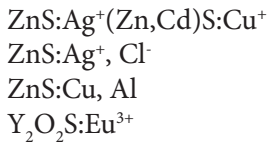
These lamps are consisting of a fluorescent tube wherein a phosphor material is coated on the inner wall and an electrode coil (cathode) is placed at both ends. The electrode is generally made of tungsten wire, so it can withstand at higher temperature. It is also coated with different metal oxides to increase its electron emission efficiency. The role of the electrode is to inject the flow of electrons into the discharge space. The lamp is closed with a little quantity of mercury and an inert gas at low pressure so that the vacuum has created inside the tube. In the discharge, mercury atoms undergo excitation and on returning to the ground state these will emit short wavelength UV radiation. Thus, a fluorescent lamp is a proficient source of ultraviolet radiation. Due to their long life time and high

luminous efficiency, these lamps are perfectly suited to lightning of large indoor and outdoor areas. Phosphors used in the fabrication of fluorescent lamps are given below:



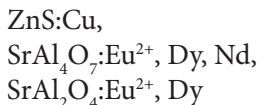
### 10.13.2 Cathode Ray Tubes

The cathode ray tubes (CRTs) were discovered by Professor Karl Ferdinand Braun in 1897, and therefore it is also recognized as the Braun tube in few countries. It is the extensively developed display device which has utilized in light-emitting devices, huge screens, computers, etc. A traditional colored CRTs transport different beam of electrons and have the consequential basic-colored phosphors (red, green, and blue). For the enhancement of the resolution of the image on the screens, an appropriate radiation absorbing graphite layer is positioned between the phosphors. Some of the phosphors used in CRTs making are given below:



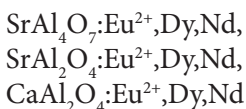
### 10.13.3 Luminescent Paints

These paints are prepared via adding a fluorescent pigment with a varnish. Paints prepared by this procedure have discrete brightness specifically as a minimum three times as the usual color under sunlight. Owing to their high visibility and color purity, fluorescent paints have an extensive range of uses such as in notice boards, in the fields of advertisement, bank notes, decoration, and also in warning signals for safety purpose. Phosphors used in the luminescent paints are as follows:



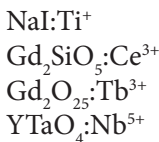
#### 10.13.4 Textiles

Fluorescent dyes are used in the application of textile printing. By the addition of a binder to the fluorescent color base, a mixture of fluorescent pigment is prepared. This mixture is subsequently used to create prints on the fabric. A reactive dye is frequently used along with the fluorescent color base. On dyeing cotton, reactive dyes produce distinctive and established colors. Phosphors used in textiles are given below:



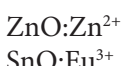
#### 10.13.5 X-ray Intensifying/Scintillation

Numerous phosphors are used in radiological diagnosis, nondestructive testing in industries, in X-ray computed tomography (XCT), positron emission tomography (PET) [61], and X-ray camera. Phosphors used for this purposes are given below:



#### 10.13.6 Vacuum Fluorescent Displays

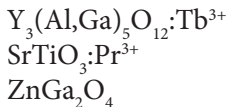
VFDs are the practical display devices. Its operation is similar to CRTs. Electrons emitted from one electrode are speeded up and bombarded on other electrode which is already covered with a luminescent materials; excited by the electron and them emit light. Various important phosphors used in VFD are the following:



#### 10.13.7 Field Emission Displays

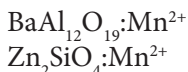
These devices are VFDs that employ field emission cathode. Up converter phosphors are useful in bioanalytical applications. The phosphor is applied

to the biological substrate and the interaction between substrate and the fundamental phosphor result in a detector color shift, this can be allied with the concentration of the initial bioactive molecules present in the sample. Many phosphors are used in them, some of which are listed below [62, 63]:



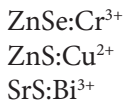
### 10.13.8 Plasma Display Panels

Plasma display panel can also be called as flat panel information display. In this type of devices, the luminating area is composed of gas-discharge cells that emit visible light directly. Many phosphors are used in PDPs, and some of them are given as follows:



### 10.13.9 Safety Indicators

Persistent phosphors can be used in safety purposes, e.g. in exit signs which still work in pass out. Further persistent phosphors used for this purposes are



## 10.14 Future Prospects of Phosphors

The emergent development on the light-emitting inorganic materials has provided an increasing command for new approaches to design more efficient materials for optoelectronic applications. From the scientific point of view, new synthetic methods such as combustion method, sol-gel method, and microwave-assisted method will take place to develop the highly efficient light-emitting materials. In the R&D scenario, new resourceful phosphor materials are being investigated than present. Detailed knowledge on the properties such as size and symmetry of appropriate host lattice,

energy level diagram of dopant and codopant, interactions among metal centers, interaction between the dopants and the host, as well as on energy transfer and quenching processes is a key for the successful development of novel phosphor. The development of highly efficient phosphor materials of the best device has surpassed that of fluorescent lamps, CRTs, and different types of display panels and one can anticipate that in the future we see more proficient luminescent materials with tunable properties which act as an alternate for the at present light sources.

## 10.15 Conclusions

In this chapter, certain attempts have been tried to explore brilliant investigation of inorganic luminescent materials for the improvement of highly efficient optoelectronic applications. The design and development of appropriate phosphors materials are very important reflection as these materials determine the stability, emission color quality, life time, and quantum efficiency of the projected device. We have described the basics properties and essential constituents of phosphor materials which have strong influence on the performance of the phosphor. Next, a brief overview about the luminescence processes and its various types and their mechanism is fully explained. The emphasis on optical transition in rare-earth-doped phosphor, role of rare-earth ions as activator and coactivator and different types of host lattice which are possible for the phosphor will be placed to illustrate the different type of phosphors in various efficient display applications. The potential applications of phosphor materials will have discussed in the subsequent section.

## References

1. Nanda, K.K., Kruis, F.E., Fissan, H., Acet, M., Band-gap tuning of PbS nanoparticles by in-flight sintering of size classified aerosols. *J. Appl. Phys.*, 91, 2315, 2002.
2. Yamamoto, H., *Fundamentals of Luminescence*, CRC Press, New York, 2007.
3. Leverenz, H. W., *An introduction to luminescence of solids*, John Wiley & Sons, New York, USA, 1950.
4. K. Compton, *Image Performance in CRT Displays*, The International Society for Optical Engineering, Washington, 2003.
5. Whitaker, J.C., *The Electronics Handbook*, CRC Press, USA, 2006.
6. Gribkovskii, V.P., Vij, D.R., *Luminescence of Solids*, Springer, US, 1998.
7. Kitai, A., *Luminescent Materials and Application*, John Wiley & Sons, 2008.

8. Jung, S., Kang, Y.C., Kim, J.H., Generation of phosphor particles for photoluminescence applications by spray pyrolysis. *J. Mater. Sci.*, 42, 9783, 2007.
9. Ropp, R.C., *Luminescence and the Solid State*, Academic Press, USA, 2004.
10. Ronda, C.R., Justel, T., Nikol, H., Rare earth phosphors: fundamentals and applications. *J. Alloys Compd.*, 275–277, 669, 1998.
11. He, C., Guan, Y., Yao, L., Cai, W., Li, X., Yao, Z., Synthesis and photoluminescence of nano-Y<sub>2</sub>O<sub>3</sub>: Eu<sup>3+</sup> phosphors. *Mater. Res. Bull.*, 38, 973, 2003.
12. Ronda, C.R., *Luminescence: From Theory to Applications*, John Wiley & Sons, New York, USA, 2008.
13. Yen, W.M., Shionoya, S., Yamamoto, H., *Phosphor Handbook*, CRC Press, Boca Raton, Florida, USA, 1995.
14. Franck, J., Elementary processes of photochemical reactions. *Trans. Farad. Soc.*, 21, 536, 1926.
15. Condon, E., A theory of intensity distribution in band systems, *Phy. Rev.*, 27, 640, 1926.
16. Isaacs, T.J., Fluorescence of alkaline-earth silicates activated with divalent europium. *J. Electrochem. Soc.*, 118, 1009, 1971.
17. Hoffman, M.V., Eu<sup>+2</sup> activation in some alkaline earth strontium phosphate compounds. *J. Electrochem. Soc.*, 115, 560, 1968.
18. Bless, P.W., Von Dreele, R.B., Kostiner, E., Hughes, R.E., Anion and cation defect structure in magnesium fluorogermanate. *J. Solid State Chem.*, 4, 262, 1972.
19. Shinde, K.N., Dhoble, S.J., Swart, H.C., Park, K., *Phosphate Phosphors for Solid-State Lighting*, Springer, Berlin, 2013
20. Shionoya, S., Yen, W.M., *Phosphor Handbook*, CRC Press, New York, 1998.
21. Grobelna, B., Bojarski, P., Red emission of Eu (III) ions doped gadolinium or lanthanum tungstate entrapped in silica xerogel. *J. Non-Cryst. Solids*, 355, 2309, 2009.
22. Blasse, G., Maier, B.C.G., *Luminescent Materials*, Springer, Berlin, 1994.
23. Dieke, G.H., *Spectra and Energy Levels of Rare Earth ions in Crystals*, Interscience, New Jersey, USA, 1968.
24. Blasse, G., *Handbook on the Physics and Chemistry of Rare Earth*, North-Holland, Amsterdam, Netherlands, 1979.
25. Hosina, T. *Luminescence of Rare Earth Ions*, Sony Research Center Rep. (Suppl.), Japan, 1983.
26. Adachi, G., *Rare Earths-Their Properties and Application*, Gihodo Publisher, Japan, 1980.
27. Martin, W.C., Zalubas, R., Hagan, L., *Atomic Energy Levels-The Rare Earth Elements*, NSRDS, Washington, 1978.
28. Kropp, J.L., Windsor, M., Luminescence and energy transfer in solutions of rare-earth complexes. I. Enhancement of fluorescence by deuterium substitution. *J. Chem. Phys.*, 42, 1599, 1965.
29. Judd, B.R., Optical absorption intensities of rare-earth ions. *Phys. Rev.*, 127, 750, 1962.

30. Ofelt, G.S., Intensities of crystal spectra of rare-earth ions. *J. Chem. Phys.*, 37, 511, 1962.
31. Barasch, G.E., Dieke, G.H., Fluorescence decay of rare-earth ions in crystals. *J. Chem. Phys.*, 43, 988, 1965.
32. Froelich, H.C., U.S. Patent 2,392,814, 1946.
33. Tanimizu, S., Shionoya, S., Yen, W.M., Yamamoto, H., *Principal Phosphor Materials and their Optical Properties*, CRC Press, Boca Raton, Florida, USA 1999.
34. Somerdijk, J.L., Stevels, A.L.N., Behavior of phosphors with aluminate host lattices. *Philips Tech. Rev.*, 37, 221, 1977.
35. Stevels, A.L.N., Verstegen, J.M.P.J.,  $\text{Eu}^{2+} \rightarrow \text{Mn}^{2+}$  energy transfer in hexagonal aluminates. *J. Lumin.*, 14, 207, 1976.
36. Apple, E.F., Ishler, W.E., *Luminescence of Organic and Inorganic Materials*, Proc. Int. Conf., New York, 576, 1962.
37. Somerdijk, J.L., Bril, A., Efficiency of  $\text{Dy}^{3+}$ -activated phosphors. *J. Electrochem. Soc.*, 122, 952, 1975.
38. De Hair, J., Vankemenade, J.T.C., *Science and Technology of Light Sources*, Proc. Int. Symp., Toulouse, 54, 1983,
39. Merrill, J.B., Shulman, J.H., The  $\text{CaSiO}_3$ ; ( $\text{Pb}+\text{Mn}$ ) phosphor *J. Opt. Soc. Am.*, 38, 471, 1948.
40. Verstegen, J.M.P.J., Radielovicand, D., Vrenken, L.E., A new generation of "deluxe" fluorescent lamps, combining an efficacy of 80 lumens/W or more with a color rendering index of approximately 85. *J. Electrochem. Soc.*, 121, 1627, 1974.
41. Weakliem, H.A., Kiss, Z.J., Energy levels and spectra of  $\text{Ho}^{2+}$  in  $\text{CaF}_2$ ,  $\text{SrF}_2$ ,  $\text{BaF}_2$ , and  $\text{SrCl}_2$ . *Phys. Rev.*, 157, 277, 1967.
42. Brown, J.J., Manganese-activated luminescence in the  $\text{MgO}-\text{Al}_2\text{O}_3-\text{Ga}_2\text{O}_3$  system. *J. Electrochem. Soc.*, 114, 245, 1967.
43. Singh, D., Tanwar, V., Simantilleke, A.P., Mari, B., Kadyan, P.S., Singh, I., Rapid synthesis and enhancement in down conversion emission properties of  $\text{BaAl}_2\text{O}_4:\text{Eu}^{2+}, \text{RE}^{3+}$  ( $\text{RE}^{3+}=\text{Y}, \text{Pr}$ ) nanophosphors. *J. Mater. Sci.: Mater. Electron.*, 2015 (DOI 10.1007/s10854-015-4020).
44. Singh, D., Tanwar, V., Simantilleke, A.P., Kadyan, P.S., Singh, I., Luminescent characterization of  $\text{Eu}^{2+}$  doped  $\text{BaMAl}_{10}\text{O}_{17}$  ( $\text{M} = \text{Ca}/\text{Mg}$  or both) blue nanophosphors for white light emitting applications *J. Mater. Sci.: Mater. Electron.*, 26, 9977, 2015
45. Luitel, H.N., Watari, T., Chand, R., Torikai, T., Yada, M., Giant improvement on the afterglow of  $\text{Sr}_4\text{Al}_{14}\text{O}_{25}:\text{Eu}^{2+}, \text{Dy}^{3+}$  phosphor by systematic investigation on various parameters. *J. Mat.*, 2013, 1, 2013.
46. Den Eeckhout, K.V., Smet, P.F., Poelman, D., Persistent luminescence in  $\text{Eu}^{2+}$ -doped compounds: a review. *Mater.*, 3, 2536, 2010.
47. He, Q., Qiu, G., Xu, X., Qiu, J., Yua, X., Photostimulated luminescence properties of  $\text{Eu}^{2+}$ -doped barium aluminate phosphor. *Luminescence*, 30, 235, 2015.

48. Zhang, L., Wang, L., Zhu, Y., Synthesis and performance of  $\text{BaAl}_2\text{O}_4$  with a wide spectral range of optical absorption. *Adv. Fun. Mater.*, 17, 3781, 2007.
49. Erdei, S., Roy, R., Harshe, G., Juwhari, H., Agrawal, D., Ainger, F.W., White, W.B., The effect of powder preparation processes on the luminescent properties of yttrium oxide based phosphor materials. *Mater. Res. Bull.*, 30, 745, 1995.
50. Takagi, K., Yamada, Y., *Optical Properties of Semiconductors Simplified*, Sanpo, Tokyo, 1965.
51. Anger, H.O., Scintillation camera. *Rev. Sci. Instr.*, 29, 27, 1958.
52. Mochel, V.D., Red emitting  $\text{Al}_2\text{O}_3$  based phosphors. *J. Electrochem. Soc.*, 113, 398, 1966.
53. Ohno, K., Abe, T., Effect of  $\text{BaF}_2$  on the synthesis of the single-phase cubic  $\text{Y}_3\text{Al}_5\text{O}_{12}\text{:Tb}$ . *J. Electrochem. Soc.*, 133, 638, 1986.
54. Peters, T.E., Cathodoluminescent  $\text{Ln}_y(\text{SiO}_2)_x\text{:Tb}$  phosphors. *J. Electrochem. Soc.*, 116, 986, 1969.
55. Froehlich, H.C., Manganese activated calcium silicate phosphors. *J. Trans. Electrochem. Soc.*, 93, 101, 1948.
56. Looney, J.R., Brown, J.J., Phase equilibria in the  $\text{Sr}_3(\text{PO}_4)_2\text{-Cd}_3(\text{PO}_4)_2$  system and  $\text{Eu}^{2+}$ -activated luminescence of  $\text{Sr}_3(\text{PO}_4)_2$  and related phases. *J. Electrochem. Soc.*, 118, 470, 1971.
57. Lagos, C.C., Luminescence of divalent europium in Ba-Ca, Ba-Sr, and Ca-Sr orthophosphate and pyrophosphate compositions. *J. Electrochem. Soc.*, 117, 1189, 1970.
58. Boucet, J.C., Fong, F.K., Quantum efficiency of diffusion limited energy transfer  $\text{La}_{1-x-y}\text{Ce}_x\text{Tb}_y\text{P}_0_4$ . *J. Chem. Phys.*, 60, 34, 1974.
59. Ropp, R.C., Phosphors based on rare earth phosphates fast decay phosphors. *J. Electrochem. Soc.*, 115, 531, 1968.
60. Song, D., Guo, C., Li, T., Luminescence of the self-activated vanadate phosphors  $\text{Na}_2\text{LnMg}_2\text{V}_3\text{O}_{12}$  ( $\text{Ln}=\text{Y}, \text{Gd}$ ). *Ceram. Inter.* 41, 6518, 2015.
61. Ter-Pogossian, M.N., Phelps, M.E., Hoffman, E.J., Mullani, N.A., A positron-emission transaxial tomograph for nuclear imaging (PETT). *Radiology*, 114, 89, 1975.
62. Johnson, L.F., Geusic, J.E., Guggenheim, H.J., Kushida, T., Singh, S., Van Uitert, L.G., Comments on materials for efficient infrared conversion. *Appl. Phys. Lett.*, 15, 48, 1969.
63. Mita, Y., Detection of 1.5- $\mu\text{m}$  wavelength laser light emission by infrared-excitable phosphors. *Appl. Phys. Lett.*, 39, 587, 1981.

# Strongly Confined PbS Quantum Dots: Emission Limiting, Photonic Doping, and Magneto-optical Effects

P. Barik<sup>1</sup>, A. K. Singh<sup>1</sup>, E. V. García-Ramírez<sup>2</sup>, J. A. Reyes-Esqueda<sup>2</sup>,  
J. S. Wang<sup>3</sup>, H. Xi<sup>4</sup> and B. Ullrich<sup>1,5\*</sup>

<sup>1</sup>*Instituto de Ciencias Físicas, Universidad Nacional Autónoma de México,  
Cuernavaca, Morelos, Mexico*

<sup>2</sup>*Instituto de Física, Universidad Nacional Autónoma de México, México, Mexico*

<sup>3</sup>*Air Force Research Laboratory, Materials & Manufacturing Directorate,  
Wright Patterson AFB, OH, USA*

<sup>4</sup>*Department of Physics and Astronomy, Bowling Green State University,  
Bowling Green, OH, USA*

<sup>5</sup>*Ullrich Photonics LLC, Wayne, OH, USA*

---

## Abstract

Quantum dots (QDs) have proved themselves to be an indispensable tool in various fields including biomedical research, fluorescence devices, drug delivery, light harvesting, alternative imaging techniques, and novel applications of soft materials. In this chapter, we review our work on the optical properties including transmission, reflection, and photoluminescence (PL) of oleic acid-capped colloidal 2–5 nm PbS QDs in toluene and deposited on glass and GaAs substrates formed by solvent deposition, and a supercritical fluid method, respectively. The experiments have been carried out in the temperature range from 5 to 300 K using monochromatic light and lasers as optical stimuli. The experiments reveal novel insights about QD PL intensity limiting, photonic doping of quantized soft matter, i.e. of QDs in solution, and magneto-optical effects achieved with magnetic flux densities below 1 T. We show that, as charge carrier transport in nanowires, the emission of QDs inherently possesses a square root limitation as a function of the impinging optical stimulus and that two-photon excitation of QDs can be

---

\*Corresponding author: bruno@fis.unam.mx; bruno.ullrich@yahoo.com

used for all-optical chemically inert quantized matter doping. Additionally, we reveal the potential of PbS QD thin films to be used for magneto-tunable mirrors, while the experiments demonstrate the influence of the experimental geometry on the fundamental transition in QDs and the impact of the stoichiometry on the diamagnetic properties of QDs in general. Most notably, from the practical point of view, we report here the discovery of emission amplitude tuning of QDs due to applied magnetic fields. The finding is considerably important for medical diagnostics applications such as magnetic resonance imaging.

**Keywords:** PbS, quantum dots, optical properties

## 11.1 Introduction

Nanostructured materials have gained great scientific and industrial interests, and market values, as they fill the gap between bulk and atoms or molecules, opening the path for novel hetero-paired materials, which can be employed in the important fields of optoelectronics and photonics [1, 2]. Consequently, the improvement of the understanding of the fundamental properties of nanosized matter is an imperative topic. During the past two decades, the field of semiconductor nanocrystals (NCs) has been one of the most rapidly growing areas of research stimulated by the expectation in devices with limited dimensions [1]. Almost the entire scientific community, i.e. physicists, chemists, biologists, and material scientists are trying to observe and manipulate the properties of nanosized matter by controlling its size/shape and/or their chemical compositions. For instance, in semiconductor NCs, also known as quantum dots (QDs), the three-dimensional quantum confinement of the electrons and holes leads to atomic-like energy levels, and therefore the electronic and optical properties of these materials are strongly size dependent [3]. The employment of colloidal QDs offers a number of advantages over nanostructures formed by lithographic processing or by self-assembly because of the flexibility in tailoring the functionality due to variations of the surface chemistry, relatively inexpensive synthesis methods adoptable for mass market production, and easily size selective synthesis [4–8]. The research in the field of colloidal semiconductor NCs has elucidated and disclosed many new concepts and mechanisms in optical physics, electronic structures, nanomagnetism, interfacial chemistry, redox chemistry, charge transport, crystal nucleation and growth, self-assembly, and has brought in new moves toward energy harvesting and conversion, electronics, catalysis, sensing, and imaging [9–14]. The latter moves the QDs

toward medical applications for tumor locations, whilst QDs might be also used for drug delivery [15].

Recently, narrow bandgap QDs operating in the near infrared (NIR) region receive much attention [1]. These QDs are of potential interest for applications in optoelectronics like infrared (IR) lasers, amplifiers, modulators, IR absorber in solar cells, field effect transistors (FETs), and fluorophores applications, to mention a few [7, 16]. In this context, one can find many reports of synthesis, and structural, electronic, and optical properties of chalcogenides including CdE, HgE, PbE, Ag<sub>2</sub>E, SnE, Bi<sub>2</sub>E<sub>3</sub>, and CuInE<sub>2</sub> (E = S, Se, or Te), which can be grown both in organic and aqueous media [7]. Among these lead chalcogenides are explicitly attractive for the fabrication of light-sensitive devices including light harvesting due to their tunable bandgap, large absorption coefficients, compatibility with liquid-phase processing [17–20]. Additionally, their NIR photo response pushing the envelope of applications toward bioimaging, telecommunications, light-emitting diodes (LEDs), lasers, photodetectors, and new-generation photovoltaic devices [9–13], while compared to the well-known II–VI (CdS or CdSe) QDs, lead chalcogenides QDs (PbS, PbSe, and PbTe) are the QDs of choice for studies in the strong-confinement regime [7, 21–25].

Herein, we report results of research carried out during 2010–2015 in three laboratories: Air Force Research Laboratory (AFRL), and institutions at the National Autonomous University of Mexico (UNAM), i.e. the Instituto de Ciencias Físicas (ICF), and the Instituto de Física (IF). We present an overview of our work revealing new achievements of research and results on PbS QDs such as, the limiting function of the PL intensity. This topic was never addressed in the literature and is of importance for dimensioning light-emitting devices based on QDs. By exploiting the Burstein–Moss effect [26, 27], we demonstrate photonic doping via two-photon absorption of PbS QDs in solution, i.e. all-optical soft-matter doping. The largest section of our presentation here is dedicated to magneto-optical effects. In fact, we report the realization of *magneto-smart mirror QD devices* responding to magnetic flux densities  $B$  below 1 T [28]. The functioning of the concept is demonstrated by reflectance (RE) and transmittance (TR) of monochromatic light impinging on PbS thin-film QDs, which are exposed to on-chip feasible magnetic fields. Additionally, these results demonstrate the influence of the experimental configuration on the optical properties of PbS QDs. Most notable, to the best of our knowledge never reported before, we show PL intensity tuning of PbS QDs in solution by the variation of low applied magnetic fields. This observation is of considerable interest for applications in the field of magnetic resonance imaging (MRI).

## 11.2 QDs Used and Sample Preparation

The majority of the presented experiments are carried out with QDs from the Center for Applied Nanotechnology (CAN) GmbH, Hamburg, Germany (lot numbers: SCR-0-058\_2 and SCR-0-061\_1 for the 3 and 5 nm QDs, respectively). These QDs are passivated by oleic acid organic ligands to avoid aggregations due to huge surface to volume ratio. We fabricated thin films by drop casting from the toluene solution on 1-mm-thick soda-lime glass (no. 2947 from Corning Glass Works) and GaAs substrates. The average film thickness was  $\sim$ 200 nm. In addition, oleic acid capped QDs with diameters of 2.0 nm on semi-insulating GaAs have been dispersed using a supercritical  $\text{CO}_2$  method [29, 30]. At this point, it is worthwhile to mention here an appealing technological application of PbS QDs. The deposition of PbS QDs on GaAs affects its absorption [25] and PL intensity [31]. As a result, PbS QDs can be used for bandgap and emission engineering of semiconductors. Currently, we are actively studying this subject and first outcomes have been presented [32], while further results of this topic will be addressed in a forthcoming paper. The samples used in the current work are listed in Table 11.1.

## 11.3 Basic Properties of PbS Quantum Dots

The IV–VI compound PbS is a direct narrow-gap semiconductor with a cubic crystal (Galena) structure. At room temperature (RT), the band-gap ( $E_g$ ) of PbS single crystals and polycrystalline coarse-grained PbS films is 0.41–0.42 eV, and the material has a relatively high dielectric

**Table 11.1** Parameters of the samples investigated.

Sample	Substrate	Preparation method	QD size (nm)	Characterization
A	Glass	Solvent deposition	$2.5 \pm 0.3$	Magneto-optical
B	Glass	Solvent deposition	$5.0 \pm 0.3$	Magneto-optical
C	N/A (solution)	N/A (Precursor for sample A)	$2.5 \pm 0.3$	Burstein–Moss doping, magneto-optical
D	GaAs	Supercritical $\text{CO}_2$	$2.0 \pm 0.4$	PL limiting

constant of 17.3, and relatively small electron and hole effective masses  $m_e^* = m_h^* = 0.08 \times m_e$  [33], resulting in the large exciton Bohr radius of  $\sim 18$  nm. Consequently, rather “big” QDs already enter the strong confinement limit and has been realized with PbS QDs below 5 nm diameter [34], i.e. with sizes investigated in the current work, as confirmed by the transmission electron microscopy (TEM) and scanning electron microscopy (SEM) images of samples A, B, and D, respectively, in Figure 11.1. We should stress that shrinking diameters influences the stoichiometry of PbS QDs [35] influencing the conductivity type. Typically, PbS QDs are presumed to be p-type because the oleic acid ligands preferentially bind to the lead atoms on the QD surface and leave the sulfur atoms unpassivated, being the origin of hole traps [36], while, on the other hand, n-type doping can be induced by the excess of Pb atoms. However, despite that our QDs possess a Pb surplus, for the highly confined QDs investigated here, we believe that the surface states define the electronic state. The spatial confinement of QDs in all three dimensions leads to appealing molecular-like optical properties, which arises from their limited dimensions only, while the QDs remain structurally similar to their bulk counterpart. Indeed, Figure 11.2, which shows X-ray diffraction patterns for PbS QDs in the diameter range of 2.1–14.4 nm, shows that the diffraction patterns of the PbS Galena structure are present for diameters as small as 2.1 nm, being – according to Ref. [35] – only 0.4 nm larger in diameter than the smallest structured PbS QD possible. Further important information used below is the PbS bulk exciton binding energy ( $R_x = 3.97$  meV) and the exciton cyclotron energy ( $\hbar\omega=2.2$  meV) at  $B = 1$  T.

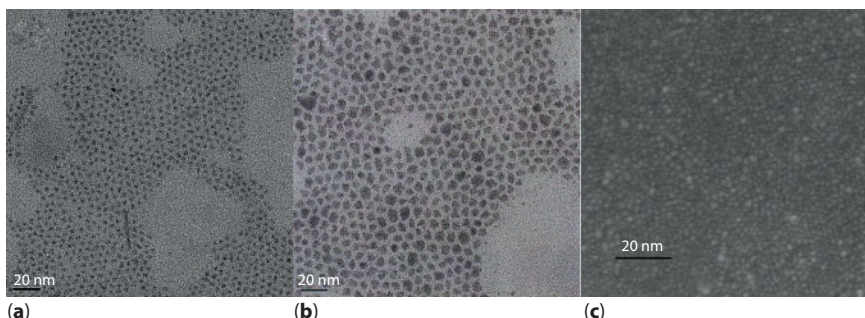


**Figure 11.1** TEM images of samples A and B: (a)  $2.5 \pm 0.3$  nm, (b)  $5.0 \pm 1.0$  nm oleic acid capped PbS QDs, and (c) SEM image of  $2.0 \pm 0.4$  nm PbS QDs (sample D).

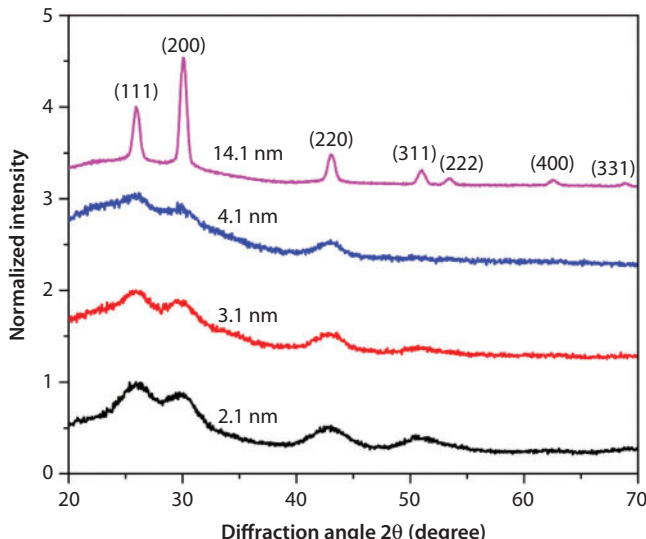


**Figure 11.2** X-ray patterns of PbS QDs of various sizes. The reflections of the Galena structure are observed for sizes as small as 2.1 nm. For clarity, the spectra are normalized and shifted.

## 11.4 Measuring Techniques and Equipment Employed

### 11.4.1 Fourier Transform Infrared Spectroscopy of PbS Quantum Dots

Sample D was investigated by Fourier Transform Infrared (FTIR) spectroscopy at cryogenic temperatures and RT with a BOMEM DA3 instrument [37, 38]. This spectrometer consists basically of an interferometer (beam-splitter, fixed mirror, and moving mirror) and a detector. In the actual case a nitrogen cooled InGaAs detector was used. The sample's PL, which was excited by the 532 nm continuous wave (cw) emission of a 2 W Coherent Verdi laser, was guided via gold mirrors into the spectrometer forming an interferogram that has all the IR frequencies “encoded”. In order to obtain the PL spectrum, the signal is translated from the time domain to the frequency (energy) domain by Fourier transformation. The advantage of the FTIR spectroscopy with respect to dispersive instruments is the dynamic calibration mechanism during scanning due to the generated harmonic modulation of the reference He-Ne laser beam and is referred to *Connes Advantage* [38]. The benefits of internal calibration are accuracy and

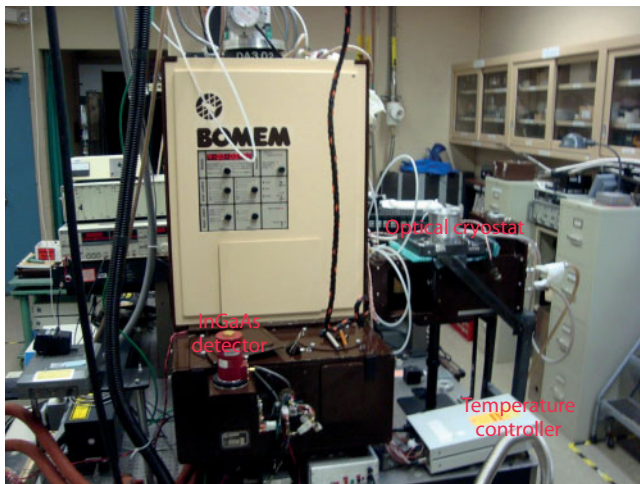


**Figure 11.3** BOMEM spectrometer with periphery able to measure the QD PL at various temperatures covering the range of 8–320 K.

precision of better than  $0.1\text{ cm}^{-1}$  by correcting mechanically caused errors. Figure 11.3 shows the spectrometer with the attached InGaAs detector. The measurements have been carried out by mounting the samples in an attached optical closed cycle cryostat from Janis (model SHI-4-1). In order to avoid transfer of the vibrations of the closed cycle equipment to the spectrometer, the optical cryostat was mounted on a specifically designed metal stand keeping a distance of about a quarter inch between the bodies of the cryostat and the BOMEM. The arrangement is shown in Figure 11.4.

#### 11.4.2 Two-photon Excited Emission in PbS Quantum Dots

Two-photon absorption stimulated PL, which excites the specimen with energies below the fundamental transition, abbreviated TPL hereafter, was carried out at RT using sample C. We kept the solution in a quartz vial with the dimensions of  $1\text{ cm} \times 2\text{ cm} \times 0.1\text{ cm}$ . The vial was irradiated with the unfocused (diameter  $\sim 1\text{ cm}$ )  $1064\text{ nm}$  ( $1.165\text{ eV}$ ) emission of a pulsed EKSPLA Nd:YAG laser (26 ps, 10 Hz). The PL spectra were recorded with the Ocean Optics USB 2000 fiber spectrometer detecting the signal emitted from the surface facing the incoming laser beam and behind the vial, referred to RE and TR geometry, respectively.



**Figure 11.4** Optical cryostat mounted on a metal stand keeping a distance of a quarter inch between the base of the cryostat and the BOMEM body.

### 11.4.3 Magneto-optical Measurements

For these measurements, the samples were mounted between the poles of an electromagnet from SVS labs (model EMU-50 V), which, depending on the air gap between the poles, is able to generate magnetic flux densities up to  $B \sim 1.0$  T, whereas the actual flux values were detected with a digital SVS labs Gauss meter (model DGM-102). The sample's optical excitation was provided by the emission of a 100 W tungsten-halogen lamp dispersed by the  $\frac{1}{4}$  m 260 Newport Cornerstone monochromator. Two Si photodiodes from Hamamatsu (models S1337-1010BQ and 1336-8BQ) were used to collect the TR and RE responses of sample A. The signal of the diodes was fed to computer-controlled lock-in amplifiers (SR830 and SR530). The setup was used for either individual data acquisition or as shown below in Figure 11.5 for simultaneous TR and RE recording. The required reference frequency of 2 kHz for the lock-in amplifiers was provided by an optical chopper from Edmund Optics (model 55-783). The measurements have been carried out with a gap of  $\sim 0.7$  cm between the electromagnet poles

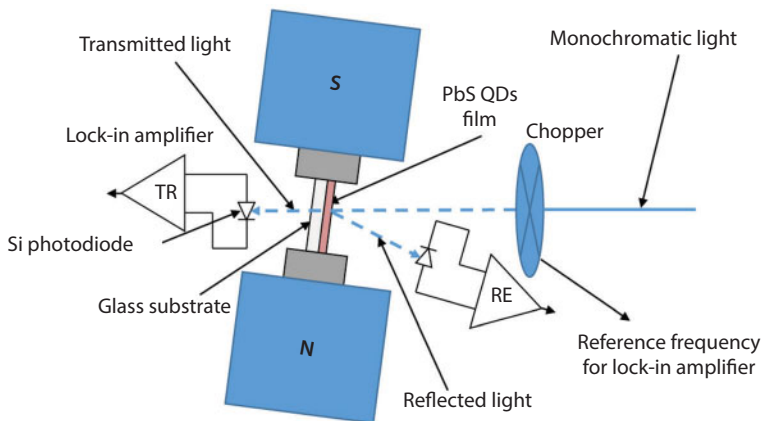


**Figure 11.5** Schematic diagram of magneto-optical TR and RE measurements.

at RT. The TR and RE spectra of sample B were measured in the same way, but the QD diameter increase with respect to sample A moves the fundamental transition deeper into the IR spectral range. Therefore, we used a ThorLabs Ge-photodiode (model FDG03).

Investigating the emission of sample C, we discovered PL intensity alterations evoked by *B* variations within the range of 0–0.56 T. For these experiments, the solution was kept in the same quartz vial used in section 11.4.2 and was mounted between the poles of the electromagnet mentioned above. The cw excitation at 532 nm was provided with diode-pumped solid-state lasers (DPSS) from LaserGlow exposing the sample to an intensity of about ~1 W/cm<sup>2</sup>, whilst the PL signal was recorded in RE and TR geometry with the fiber spectrometer from section 11.4.2.

## 11.5 Photoluminescence Limiting of Colloidal PbS Quantum Dots

During the past 10 years, the preparation methods of colloidal PbS QDs have considerably improved and enable now well-controlled size variations [21, 29]. The fine-tuning of the PL chromaticity of colloidal PbS QDs via diameter alterations has been vigorously studied [1, 8, 39–41]. Additionally, the influence of the Stokes shift and the dynamic Burstein–Moss shift (BMS), which will be also addressed in the next section, on the PL peak position ( $E_{PL}$ ) has been thoroughly investigated [2, 25, 42–44]. The important question, however, in what way the PL intensity ( $I_{PL}$ ) of

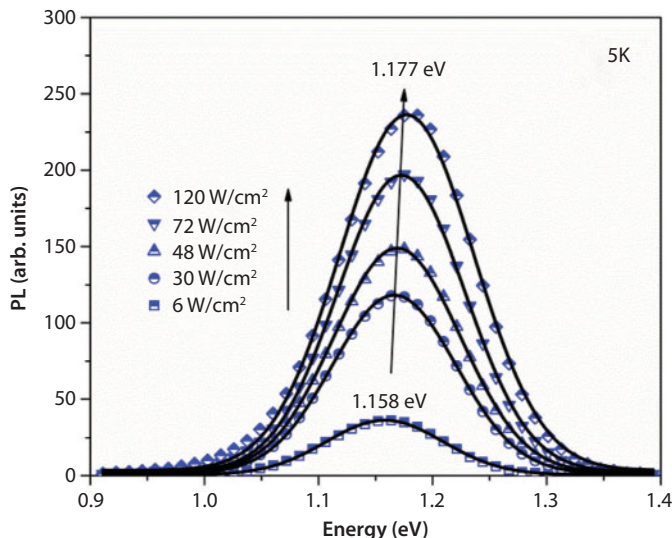


**Figure 11.6** PL spectra of sample D displayed for selected laser intensities at 5 K. The symbols represent the measurements and the lines Gaussian fits. The arrow indicates the blue shift of the spectra for increasing  $I_{\text{ex}}$ .

QDs scales with the strength of the exciting optical stimulus ( $I_{\text{ex}}$ ), i.e. possible PL intensity limitation, has not been discussed in the literature. Herein, we address this issue by presenting the nonlinearity of the function  $I_{\text{PL}} = f(I_{\text{ex}})$  of sample D shown in Figure 11.1c. The experiments have been carried out at 5 K according to section 11.4.1.

Figure 11.6 shows selected PL spectra. The BMS impact on  $E_{\text{PL}}$  can be clearly seen and is visualized with the arrow. The symbols represent the measurements and the lines Gaussian fits pointing toward inhomogeneous broadening of the PL spectra, which stems from excited QD ensembles [41]. The trend  $I_{\text{PL}} = f(I_{\text{ex}})$ , which was deduced from the Gaussian fit results in Figure 11.6, is displayed by symbols in Figure 11.7. The hardly differing trends depicted with (a) and (b) represent the peak and integral intensities, respectively. The data trends undergo at  $I_{\text{ex}} \sim 20 \text{ W/cm}^2$  the change from linear growth to a limiting square root function. Thus, the behavior is identical with the limiting characteristic found for the photocurrent (PC) limit of nanowires and we use [45]

$$I_{\text{PL}} = K \times [(1 + 4\sigma I_{\text{ex}})^{1/2} - 1], \quad (11.1)$$

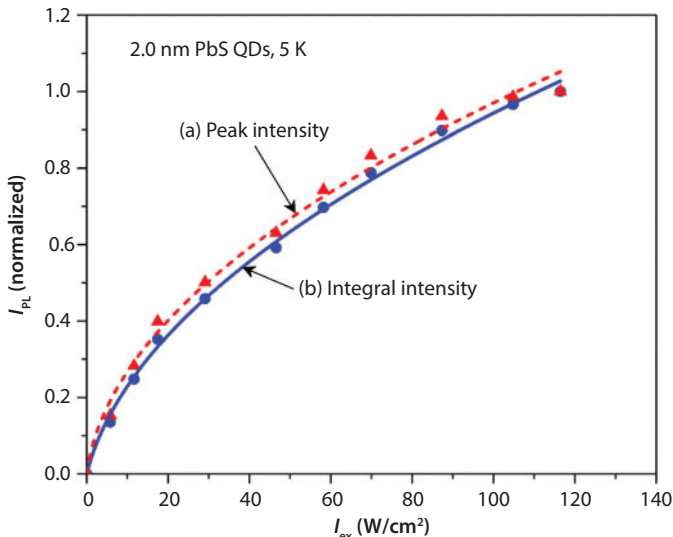


**Figure 11.7** (a) Peak and (b) integral PL intensity deduced from the Gaussian fits in Figure 11.6 versus  $I_{\text{ex}}$ . The symbols represent the measurements, while the lines are fits done with Eq. (11.1).

to fit the data, where  $K$  is a proportionality constant and  $\sigma$  is the slope parameter [45]. The closely matching fits for (a) and (b), i.e.  $\chi^2 = 0.997$  with  $\sigma = 0.60 \pm 0.5 \text{ cm}^2/\text{W}$  and  $\chi^2 = 0.999$  with  $\sigma = 0.15 \pm 0.055 \text{ cm}^2/\text{W}$ , respectively, are represented by the broken and solid lines. We should stress that the applicability of Eq. (11.1) implies that  $I_{\text{PL}}$  is proportional to the generated electron–hole pairs in the QDs and charge carrier diffusion processes are not of importance [46, 47].

Concluding, by laser excitation of PbS QDs at 532 nm with moderate intensities up to 120  $\text{W}/\text{cm}^2$ , we observed (i) the photoinduced dynamic BMS and (ii) a limiting  $I_{\text{PL}}$  trend revealing above  $\sim 20 \text{ W}/\text{cm}^2$  square root dependence on the optical stimulus. The first phenomenon was thoroughly discussed in Refs [25, 42, 44], while the second is not promoted in the literature. Based on Figure 11.8, which compares the PC trend of PbS nanowires [45, 48] with the  $I_{\text{PL}}$  behavior found here, and incorporating the conclusions in Ref. [45], we allocate Eq. (11.1) as the expression describing the limiting trend of PL and PC signals of optically excited semiconductors with suppressed diffusion capabilities, i.e. matter of limited dimensions.

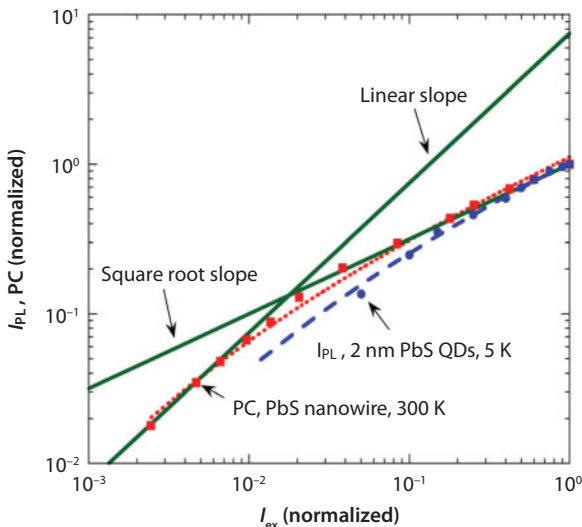


**Figure 11.8** Comparison of the PC trend of PbS nanowires and the  $I_{\text{PL}}$  trend in Figure 11.7. The PC data are deduced from Ref. [48]. The broken and dotted lines are fitted with Eq. (11.1). Both data sets show identical trends.

## 11.6 Photonic Doping of Soft Matter

The BMS [26, 27] can be defined as the shift of absorption onset to higher energies owing to the increase in the carrier density at the band bottoms [49]. This filling of the available states moves the Fermi energy ( $E_{\text{F}}$ ) into the conduction band (CB) for heavy n-type doping [or into the valence band (VB) for heavy p-type doping]. The effect is of importance in semiconductor device engineering because  $E_{\text{g}}$  determines many device characteristics and is essential for optimized performances [50]. In general, BMS is a consequence of heavy n-type doping in semiconductors, such as InSb [26] and GaAs [51]. In bulk semiconductors, the  $E_{\text{g}}$  shift due to n-type doping can be modeled with the following equation [26, 27]:

$$\Delta E_{\text{g}}^{\text{BM}} = \frac{\hbar^2}{2m_{\text{eh}}^*} (3\pi^2 n)^{2/3}, \quad (11.2)$$

where  $\Delta E_{\text{g}}^{\text{BM}}$  is the  $E_{\text{g}}$  increase with respect to the non-doped sample,  $m_{\text{eh}}^*$  is the reduced effective mass of the charge carriers ( $m_{\text{eh}}^{*-1} = m_e^{*-1} + m_h^{*-1}$ ),  $\hbar$  is the reduced Planck constant, and  $n$  is the free carrier density. As a result, the total optical transition energy becomes  $E_{\text{g}} = E_{\text{g}}^0 + \Delta E_{\text{g}}^{\text{BM}}$ , where  $E_{\text{g}}^0$  is

the semiconductor's intrinsic  $E_g$  value, i.e. 0.41 eV for PbS at RT, as mentioned above in section 11.3.

We discuss here doping by optical means only, i.e. the shift of  $E_g$  takes place due to sufficiently high light intensity. In the literature, the phenomenon is addressed as photo-dynamic BMS [44, 49]. According to Eq. (11.2), the dynamic BMS can generate nonlinear optical effects depending on the gain of the impinging optical stimulus. Of considerable importance for device engineering is the fact that the dynamic BMS represents a chemically inert doping method, which preserves stoichiometry and texture of the illuminated sample, whereas, equivalently to impurity doping, the material's electronic properties are changed, however in a reversible tunable way.

While in previous papers the BMS of thin-film QDs has been investigated [44, 49], in the current work the dynamic BMS of PL spectra at RT of *colloidal PbS QDs in solution* is reported. Thus, we demonstrate the all-optical doping of soft matter [42]. Presuming p-type conductivity of PbS QDs [36, 52], the concentration change of the minority carriers will define the type of the electronic state of the QDs under laser irradiation. Hence, the excited electrons by the impinging laser fill the CB edges resulting in n-type doping. In order to observe the BMS, one electron-hole pair per QD ought to be excited [44], whilst the generation of one electron-hole pair contributing actively to the PL signal leads to a nominal doping level of  $6 \times 10^{19} \text{ cm}^{-3}$ . In bulk, this number lies beyond the heavily doped "metallic" semiconductors [53]. Figure 11.9 schematically visualizes the photo-dynamic n-type doping of presumably p-type PbS QDs.

Figures 11.10 and 11.11 show the TPL spectra measured by collecting the PL intensities in RE and TR geometries. The tilted arrow visualizes the  $E_{\text{PL}}$  blue shift of ~4 meV, whilst the symbols in Figure 11.12 present the increase in  $E_{\text{PL}}$  versus  $I_{\text{ex}}$ . The  $E_{\text{PL}}$  values have been extracted from the Gaussian fits in Figures 11.10 and 11.11 and using Eq. (11.2) and  $n \propto I_{\text{ex}}$ , the  $E_{\text{PL}}$  blue shift is expressed by [44]

$$E_{\text{PL}}(n) = E_{\text{PL}}^0 + C \times I_{\text{ex}}^{2/3}, \quad (11.3)$$

where  $E_{\text{PL}}^0$  is  $E_{\text{PL}}$  without BMS influence and  $C$  is a constant. The broken lines in Figure 11.12 represent the fit for the RE and TR geometries by means of Eq. (11.3) with the parameters shown in Table 11.2. The results are in reasonable agreement with our former fit parameters reported in Ref. [42]. The slight increase in  $E_{\text{PL}}^0$  of 4–5 meV in comparison to the values in Ref. [42] is attributed to aging over more than 4 months during the

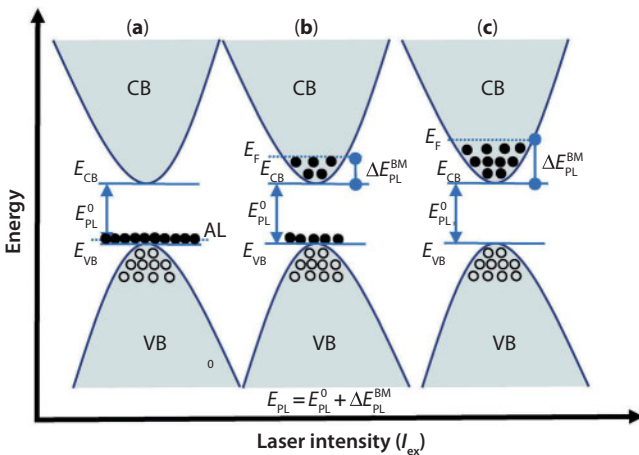


**Figure 11.9** Schematic of the BMS of p-type PbS QDs. The picture shows the change of the electronic state from (a) weak, (b) medium, and (c) intense optical excitations. The increasing optical stimulus empties the states at the acceptor level (AL) closely located to the VB by transferring the electrons to the CB. This transfer increases  $E_{PL}$  and successively moves the Fermi energy ( $E_F$ ) into the CB.

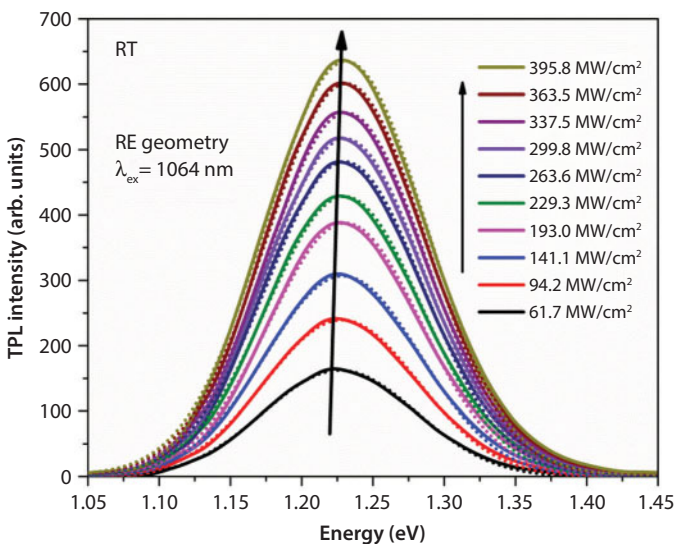


**Figure 11.10** Two-photon excited photoluminescence (TPL) of sample C measured with the corresponding impinging laser intensities noted to the right. The emission spectra were recorded according the description in section 11.4.2 in reflection (RE) geometry. The solid line represents the measurements and the dotted lines Gaussian fits. The oblique arrow following the peak emission indicates the blue shift of the spectra.

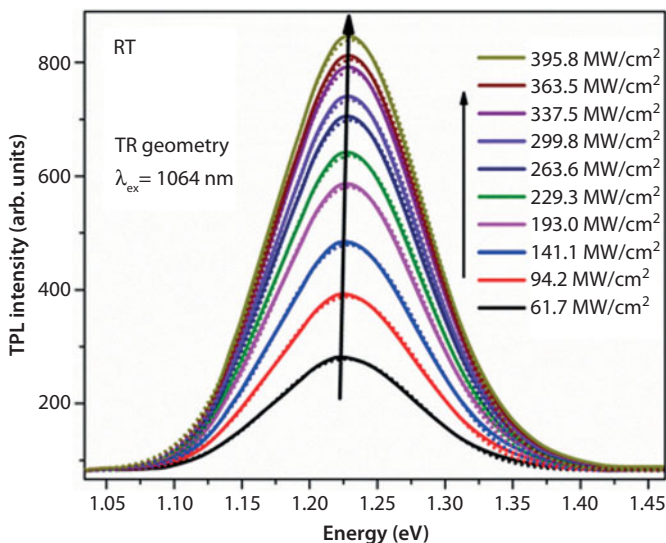


**Figure 11.11** TPL of sample C measured with the corresponding laser intensities noted to the right. The emission spectra were recorded in transmission (TR) geometry as described in section 11.4.2. The lines and arrow have the equivalent meaning as in Figure 11.10.

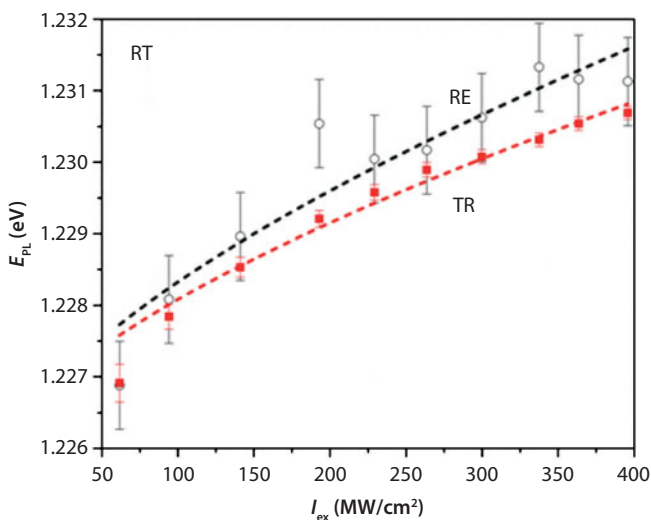


**Figure 11.12** The symbols represent  $E_{\text{PL}}$  versus  $I_{\text{ex}}$  measured in RE and TR geometries deduced from the fitted Gaussian profiles in Figures 11.10 and 11.11, and the lines are fits carried out with Eq. (11.3).

**Table 11.2** Fit parameters and the goodness of fit ( $\chi^2$ ).

TPL geometry	Fit parameters in Eqs (11.1) and (11.3)			
	$E_{\text{pl}}^0$ (eV)	$C$ (eV(MW/cm <sup>2</sup> ) <sup>-2/3</sup> )	$\chi^2$	$\sigma$ (cm <sup>2</sup> /MW)
$I_{\text{pl}} = K \times [(1 + 4\sigma I_{\text{ex}})^{1/2} - 1]$				$\chi^2$
RE	$1.2261 \pm 5.2805 \times 10^{-4}$	$1.0 \times 10^{-4} \pm 1 \times 10^{-5}$	0.999	$0.007 \pm 0.001$
TR	$1.2262 \pm 2.2083 \times 10^{-4}$	$8.4 \times 10^{-5} \pm 5 \times 10^{-6}$	0.968	$0.011 \pm 0.003$

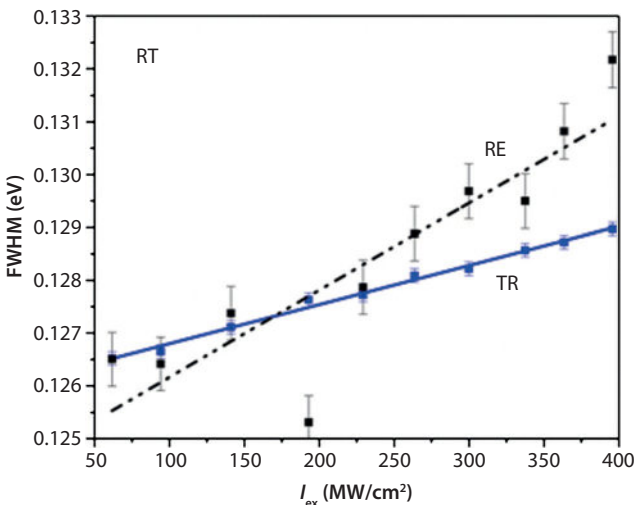


**Figure 11.13** FWHM versus  $I_{\text{ex}}$  measured in RE and TR geometry. The symbols represent the experimental data extracted from the fitted Gaussian profile in Figures 11.10 and 11.11, while the lines are linear fits.

measurements, corresponding roughly to an  $E_{\text{PL}}$  increase of  $\sim 1$  meV per month due to oxidation [54].

The increase in the full width at half maximum (FWHM) versus  $I_{\text{ex}}$  of the PL spectra in Figures 11.10 and 11.11 is displayed in Figure 11.13, showing the expected broadening because of band filling [55]. Due to the elevated intensity range starting above 50 MW/cm<sup>2</sup>, we do not observe a power law as in our previous works [42, 44], but a linear increase in the FWHM.

Figure 11.14 shows a notable result: Two-photon absorption induced effects, i.e.  $\chi(3)$  nonlinearities [56], cause in bulk semiconductors  $I_{\text{PL}} \propto I_{\text{ex}}^2$  [57]. However, here we get for the overall trend  $I_{\text{PL}} \propto I_{\text{ex}}^d$  with  $d \sim 0.7$ , whereas the lines in Figure 11.14 show the close fit of the data using Eq. (11.1). The fit parameters are displayed in Table 11.2. In other words, the TPL intensities reveal the same limiting behavior as the single-photon excited PL shown in Figure 11.7. We checked the result by exciting 2.5 nm QDs on GaAs under the same conditions, i.e. with the pulsed 1064 nm laser line, coincidentally observing the PL of GaAs substrate and the QDs. The  $I_{\text{PL}}$  of GaAs follows the expected square dependence on the impinging laser intensity, while the QD emission shows the same behavior as the ones revealed in Figure 11.14. We conclude therefore that PL intensity limiting in QDs follows different principles with respect to bulk matter, and apparently depends on the charge carriers available for excitation. Clearly, the observation merits further investigation.

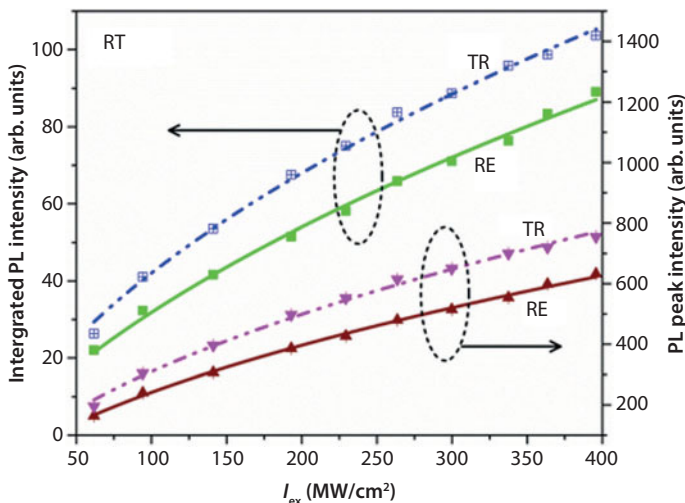


**Figure 11.14** Peak and integral PL intensities deduced from the Gaussian fits in Figures 11.10 and 11.11 versus  $I_{\text{ex}}$ . The symbols represent the measurements, while the solid and broken-dotted lines are fitted with Eq. (11.1). Error bars closely coincide with the symbol size.

## 11.7 Magneto-optical Properties

### 11.7.1 Quantum Dot Absorption

Parameters like static magnetic field, electric field, impurity concentrations, and size variations affect the optical properties of PbS QDs and have been intensively studied experimentally and theoretically [21, 35, 58, 59]. The fundamental absorptive transition, which defines  $E_g$  of the QD, takes place from the highest-occupied molecular orbital (HOMO) to the lowest-unoccupied molecular orbital (LUMO) and is decreasing with confinement weakening. We should stress that the location of  $E_g^{\text{PL}}$  is red-shifted with respect to  $E_g$  because of the Stokes shift [43, 60, 61]. The spectra of RE, TR, and PL are the basic phenomena usually studied to obtain information about the optical properties of semiconductors, in particular the location of  $E_g$ . In general, these experiments are the most straightforward and direct methods of spectroscopic analysis of materials due to the fairly easy accessibility of spectroscopic apparatuses in the wide wavelength region of interest.

### 11.7.2 Basics of the Magneto-optical Effects in Semiconductors

In this section, we present and discuss the magneto-optical properties of PbS QDs, i.e. the influence of external magnetic fields on the optical responses.

In general, in case the charge carriers undergo thermally activated movements, the exposition of matter to magnetic fields causes a force on the electrons and holes in semiconductors. The strength of this perturbation can be sensed by the “exciton cyclotron energy” ( $\hbar\omega_c = \hbar eB/\mu$ ), where  $e$ ,  $\omega_c$ , and  $\mu$  and are the elementary charge, the angular cyclotron frequency, and the reduced electron–hole effective mass, respectively. The excitonic Rydberg energy, also known as exciton binding energy, is defined with the relation

$$R_X = \left[ \frac{\mu}{m_0 \epsilon_r^2} \right] \times R, \text{ where } R \text{ is the atomic Rydberg energy (13.6 eV) and } \epsilon_r$$

is the relative dielectric constant of the material. Stronger confinement of excitons in QDs causes an increased reduced effective mass due to the squeezing effect according to the particle-in-the-box principle [62]. The behavior of the influence of external magnetic fields can be divided into weak and strong field regimes using the parameter  $\gamma = \hbar\omega_c/R_X$ . In weak field regime ( $\gamma \ll 1$ ), the Coulomb interaction rules and external magnetic fields can be treated as a perturbation causing a parabolic field dependence of the band energy levels (diamagnetic shift). Therefore, the Zeeman terms can be ignored and the diamagnetic shift is defined by the energy variation  $\Delta E_{dia} \propto B^2$  [63, 64]. We concentrate here on magneto-optical phenomena arising from interband effects. This magneto-optical effect can be classified further by the distinction whether it is of absorptive or dispersive origin, resonant or nonresonant, or whether it is dependent on the orientation of the magnetic field considering the direction of propagation of the electromagnetic radiation and its polarization components [65].

### 11.7.3 Reflection of Quantum Dots Under Low Magnetic Fields

The solid and broken-dotted lines in Figure 11.15 show the measured RE spectra and Gaussian fits, carried out for various  $B$  values. The spectra show a noticeable good signal-to-noise ratio. We conclude therefore that the investigated PbS QD ensemble possessed a decent homogeneity improving the quality of the diffuse RE spectra, i.e. narrow bandwidths and better relative intensities. The RE spectra are very well fitted using the following expression [28]:

$$I(E) = I(0) + k \times E + Ae^{-\frac{(E-E_{g,RE})^2}{2w^2}}, \quad (11.4)$$

where  $I(E)$  is the spectral intensity versus impinging photon energy  $E$  of the RE responses,  $k$ ,  $I(0)$ , and  $E_g$  are the corresponding slope, offset and

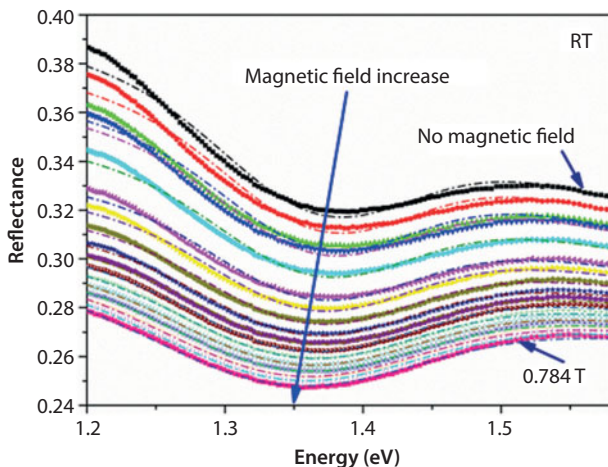


**Figure 11.15** The RE spectra of sample A, which divulge a clearly visible red shift of 23 meV with increasing B up to 0.784 T. The tilted arrow indicates the red shift of the spectra. The solid and broken-dotted lines represent the experimental results and Gaussian fits using Eq. (11.4), respectively.

bandgap parameters, respectively,  $A$  is the background free amplitude of  $I(E)$ ,  $E_{g,RE}$  is  $E_g$  of the RE spectra, and  $w$  is the width parameter, which, via  $\text{FWHM} = 2w\sqrt{\ln 4} = 2.3548 \times w$ , defines the spectral broadening (Table 11.3).

It can be seen that the impact on the amplitude is fairly small, whereas the  $E_{g,RE}$  shift is clearly visible. The trend of the latter induced by the magnetic field increase is fitted with the equation [64]

$$E_{g,RE}(B) = E_{g,RE}(0) - C_{RE} B^2, \quad (11.5)$$

where  $E_{g,RE}(0)$  is  $E_{g,RE}$  at zero magnetic field,  $C_{RE}$  represents the coupling strength of the QDs to the diamagnetic effects. Fitting with Eq. (11.5), we find  $E_{g,RE}(0) = 1.3664 \text{ eV}$  and  $C_{RE} = 0.0357 \pm 7.5 \times 10^{-4} \frac{\text{eV}}{\text{T}^2}$ , which we interpreted as a measure of stoichiometry deviations of the QDs [64], i.e.,  $C_{RE} = 0 \frac{\text{eV}}{\text{T}^2}$  would represent a perfect stoichiometry, while the QDs investigated possess a composition of 72 and 28 at.% of Pb and S, respectively [64]. It is not expected that PbS shows alterations of its optical properties because of low magnetic fields. Therefore, we proposed in Ref. [64] that the excess amount of lead in the QDs is the origin of the spectral shift

**Table 11.3** Parameters of Eq. (11.4) for the RE fits in Figure 11.15 and the goodness of fit ( $\chi^2$ ).

$B$ (T)	$k$ (eV) $^{-1}$	$I(0)$ (arb. units)	$A$ (arb. units)	$E_{\text{g,RE}}$ (eV)	FWHM (eV)	$\chi^2$
0.024	-0.1463 ± 0.0020	0.5562 ± 0.0027	-0.0377 ± 0.0009	1.3668 ± 0.0019	0.1568 ± 0.0021	0.977
0.072	-0.1319 ± 0.0019	0.5278 ± 0.0025	-0.0357 ± 0.0009	1.3674 ± 0.0018	0.1556 ± 0.0021	0.976
0.124	-0.1175 ± 0.0016	0.4991 ± 0.0021	-0.0342 ± 0.0007	1.3667 ± 0.0016	0.1568 ± 0.0019	0.978
0.181	-0.1149 ± 0.0014	0.4932 ± 0.0019	-0.0341 ± 0.0006	1.3656 ± 0.0015	0.1581 ± 0.0017	0.982
0.239	-0.0987 ± 0.0011	0.4603 ± 0.0014	-0.0324 ± 0.0005	1.3643 ± 0.0012	0.1601 ± 0.0013	0.987
0.301	-0.0804 ± 0.0008	0.4238 ± 0.0010	-0.0307 ± 0.0003	1.3624 ± 0.0009	0.1629 ± 0.0010	0.990
0.361	-0.0738 ± 0.0006	0.4099 ± 0.0009	-0.0304 ± 0.0003	1.3612 ± 0.0008	0.1641 ± 0.0009	0.992
0.418	-0.0666 ± 0.0005	0.3942 ± 0.0007	-0.0299 ± 0.0002	1.3601 ± 0.0006	0.1707 ± 0.0007	0.994
0.476	-0.0616 ± 0.0005	0.3823 ± 0.0006	-0.0297 ± 0.0002	1.3582 ± 0.0006	0.1747 ± 0.0007	0.995
0.530	-0.0579 ± 0.0005	0.3737 ± 0.0007	-0.0298 ± 0.0002	1.3565 ± 0.0006	0.1799 ± 0.0007	0.994
0.581	-0.0557 ± 0.0005	0.3678 ± 0.0007	-0.0299 ± 0.0002	1.3546 ± 0.0006	0.1843 ± 0.0008	0.994
0.628	-0.0541 ± 0.0006	0.3630 ± 0.0008	-0.0301 ± 0.0002	1.3530 ± 0.0007	0.1919 ± 0.0009	0.992
0.667	-0.0526 ± 0.0006	0.3584 ± 0.0009	-0.0305 ± 0.0002	1.3512 ± 0.0008	0.1970 ± 0.0010	0.990
0.703	-0.0528 ± 0.0006	0.3565 ± 0.0009	-0.0309 ± 0.0002	1.3491 ± 0.0008	0.2024 ± 0.0011	0.990
0.734	-0.0522 ± 0.0008	0.3542 ± 0.0011	-0.0316 ± 0.0003	1.3472 ± 0.0010	0.2096 ± 0.0013	0.988
0.761	-0.0530 ± 0.0008	0.3539 ± 0.0011	-0.0321 ± 0.0003	1.3451 ± 0.0010	0.2153 ± 0.0014	0.987
0.784	-0.0540 ± 0.0009	0.3541 ± 0.0012	-0.0331 ± 0.0003	1.3433 ± 0.0011	0.2218 ± 0.0014	0.986

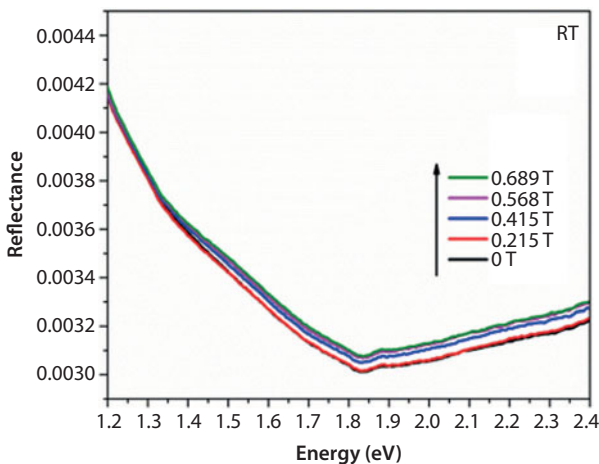


**Figure 11.16** RE spectra of industrial polished lead for various values of  $B$ .

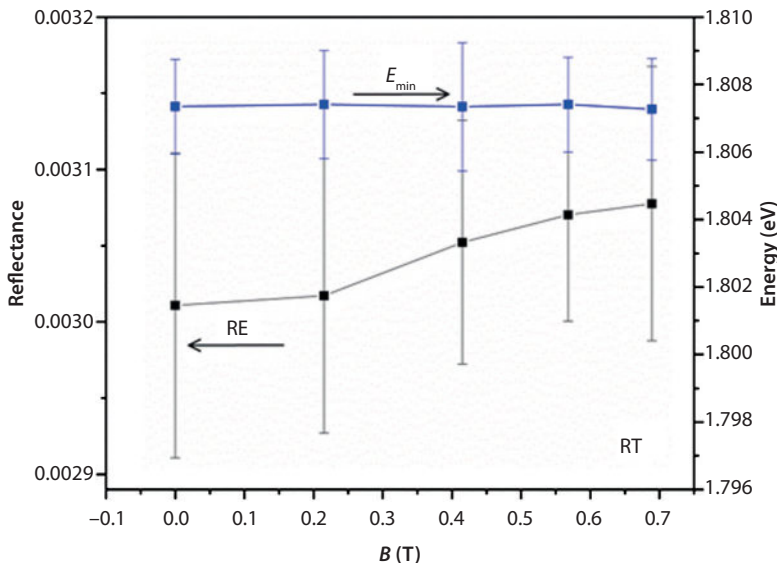
under the presence of magnetic fields. Indeed, as shown in Figure 11.16, the measurements of  $\text{RE}(B)$  of industrial lead from the automotive industry reveal that the spectra are altered by our employed low  $B$  values. Around  $1.8 \text{ eV}$  ( $E_{\min}$ ), the RE spectrum shows a pronounced minimum, which slightly increases with  $B$ . The increase in RE is shown in Figure 11.17, while, on the other hand,  $E_{\min}$  does not show a  $B$  dependence.

To further investigate the influence of the stoichiometry, we also measured the RE spectra of sample B, which has a more balanced stoichiometry (~60 at.% of Pb versus ~40 at.% of S) [28]. The results are shown in Figure 11.18 and, confirming our presumption in Ref. [64], we observed a reduced  $E_{g,\text{RE}}$  dependence on  $B$  alterations (~7 meV shift of  $E_{g,\text{RE}}$  at  $0.885 \text{ T}$  with respect to 23 meV in Figure 11.15). The fit with Eq. (11.5) of  $E_{g,\text{RE}}$  delivers the values  $E_{g,\text{RE}}(0) = 0.9355 \text{ eV}$  and  $C_{\text{RE}} = 0.0064 \pm 0.0021 \text{ eV/T}^2$  for sample B. The lower  $C_{\text{RE}}$  value points toward a more balanced stoichiometry.

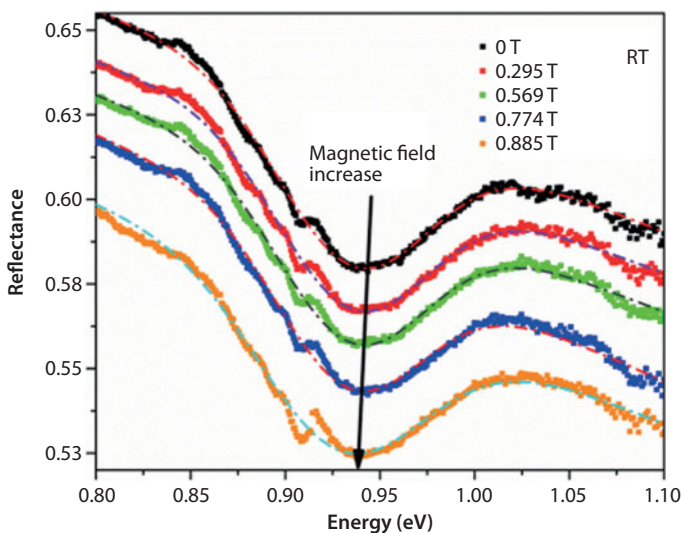
#### 11.7.4 Transmittance of Quantum Dots Under Low Magnetic Fields

Figure 11.19 shows the TR spectra of sample A. We express the spectral shift with the equation,

$$E_{g,\text{TR}}(B) = E_{g,\text{TR}}(0) - C_{\text{TR}} B^2, \quad (11.6)$$



**Figure 11.17** Plot of the  $B$  dependence of RE at  $E_{\min}$  and  $E_{\min}$  itself in Figure 11.16.



**Figure 11.18** The RE spectra of sample  $B$  showing a redshift of  $\sim 7$  meV (visualized by the arrow) with increasing  $B$  from 0.024 to 0.784 T. Symbols and broken-dotted lines represent the measurements and fits with Eq. (11.4), respectively. The dips in the spectra at 0.91 eV are caused by the Ge detector.

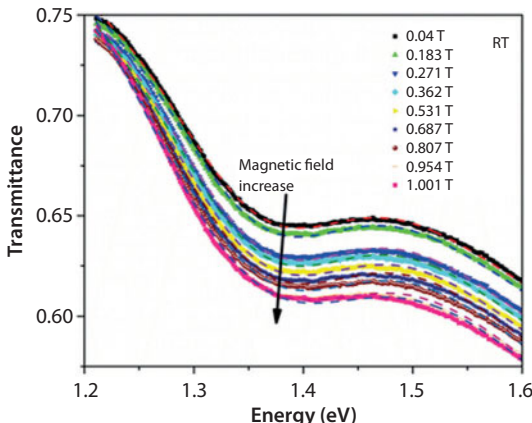


**Figure 11.19** The TR spectra of sample A. Visualized by the arrow, the spectra show a red shift of 9 meV with increasing  $B$  from 0.04 to 1 T. The broken lines represent the Gaussian fits using Eq. (11.4).

where the parameters have the equivalent meaning as in Eq. (11.5). Fitting with Eq. (11.6), the values of  $E_{g,TR}(0)=1.3592$  eV and  $C_{TR}=0.0083\pm 5.99\times 10^{-4}$  eV/T<sup>2</sup> are found. While  $C_{TR}$  is a factor ~4 smaller than  $C_{RE}$ , in agreement with the results published in [64], the TR spectra presented herein confirm the diamagnetic shift of the RE results in Figure 11.15. The differences between the C values, and the  $E_{g,RE}$  and  $E_{g,TR}$  shifts, i.e. 23 meV in Figure 11.15 and 9.2 meV in Figure 11.19, is subject of charge carrier recombination anisotropy within the QD films caused by the progressive addition of traps owing to the oxidation of the sections exposed to air [66]. Along with this statement goes our observation in Ref. [64] – recording the TR spectra from the glass/QD interface reveals a larger  $E_{g,TR}$  shift than from the QD film surface. Consequently, in harmony with Ref. [66], the shielding of QDs located closer to the glass substrate by the upper QD coating reduces oxidation [54]. Figure 11.20 displays the comparative plot of  $E_{g,RE}$  and  $E_{g,TR}$  as a function of  $B$ . The enhanced influence on  $E_g$  in RE geometry indicates probing of more “metallic” QDs at the surface. A more in depth analysis of the topic is presented in Ref. [28]. We further stress that we do not observe a distinguishable difference between the functions  $E_{g,RE}(B)$  and  $E_{g,TR}(B)$  of the QDs in solution (sample C). Two typical RE and TR spectra of sample C for various magnetic fields are shown in Figure 11.21. The flat response, which is caused by the high QD concentration, obstructs the observation of spectral shifts in the  $E_g$  region of the QDs. Therefore, highly concentrated QDs in solution are not very practicable for  $E_g$  determinations and stoichiometry analysis.

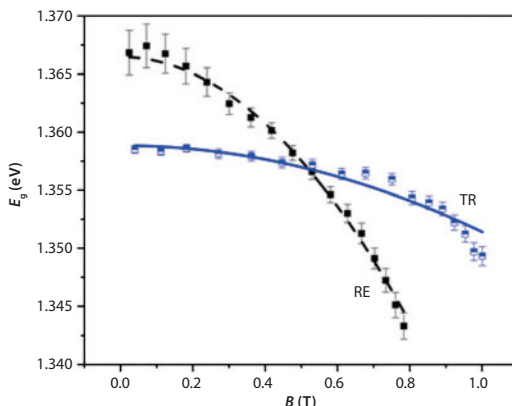


**Figure 11.20** Shift of  $E_g$  versus  $B$  of sample A in RE and TR geometries. The fit of the trends performed with Eqs (11.15) and (11.19) are visualized by the broken and solid lines.

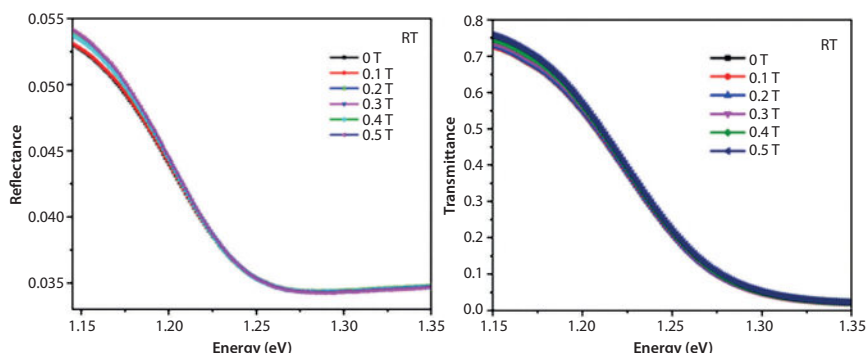


**Figure 11.21** The RE and TR spectra of sample C show hardly alterations with increasing  $B$  up to 0.5 T.

### 11.7.5 Magneto-photoluminescence of Colloidal PbS Quantum Dots at Room Temperature

The contact-free tuning of PL intensities of semiconducting matter is an intriguing subject. In the following, we reveal the possibility to control the emission intensity of PbS QDs via magnetic fields. We call the effect magneto-PL (MPL), which might find applications in the field of MRI. Bearing specifically bioimaging in mind, we investigated sample C and employed the experimental conditions and apparatuses described in section 11.4.3. We measured the PL spectra in RE and TR geometries

under exposure of various magnetic fields, i.e. 0.14, 0.29, 0.44, and 0.56 T. The experimental PL data are shown by symbols in Figure 11.22 and the lines are Gaussian fits with  $\chi^2 > 0.995$ .

In the absence of a magnetic field, the PL in RE geometry shows its peak at 1.2951 eV, which points to a Stokes shift of ~75 meV when compared to the TR spectra in Figure 11.19. The PL measured in TR geometry is further red shifted to 1.2211 eV because of the self-absorption process. Figure 11.23 shows the FWHM of the PL spectra versus  $B$  measured in RE and TR geometries. The FWHM linearly decreases with

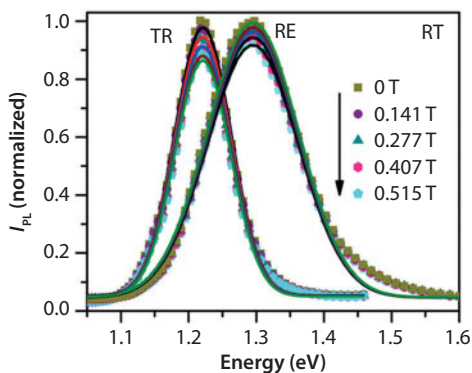


**Figure 11.22** PL intensity of sample C versus energy for different  $B$  values. Increasing  $B$  clearly reduces the emission intensity.

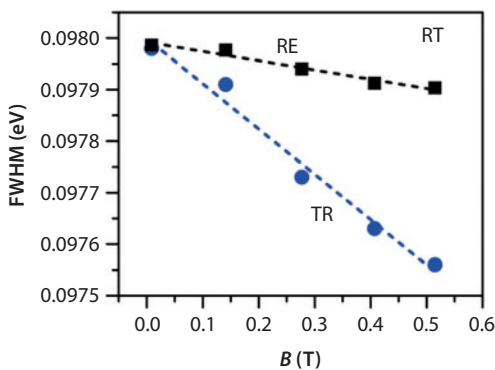


**Figure 11.23** FWHM versus  $B$  of the PL spectra in Figure 11.22. The symbols are extracted from the Gaussian fits in Figure 11.22, and the lines are linear fits. The error bars coincide with the symbol size.

increasing  $B$  values because of a possible slight increase in lifetime of the excited charge carriers or the decrease in electronic-vibrational coupling strength. The matrix element for cubic direct semiconductors such as PbS is [67]

$$|M^2| = \frac{m_0^2 \cdot E_g}{6 \cdot m_e^*}, \quad (11.7)$$

where  $m_0$  is the free electron mass. The remaining parameters have the same meaning as defined above. Considering the linear relationship between absorption coefficient and the matrix element, the above relation indicates that the PL intensity should be directly proportional to  $E_g$  of the semiconductor. We plotted in Figure 11.24,  $I_{PL}$  versus  $E_{PL}$  for the RE and TR geometries, and indeed it shows a linear relationship. Consequently, in order to explain the observed PL intensity decrease with increasing  $B$ , we tentatively suggest that the applied magnetic field, which subtle lowers  $E_{PL}$ , decreases the oscillator strength within the excited QD ensemble. This could be possible because of the reduction in solvent mobility in the presence of applied magnetic fields, which increase the electronic coupling between the PbS QDs [68].

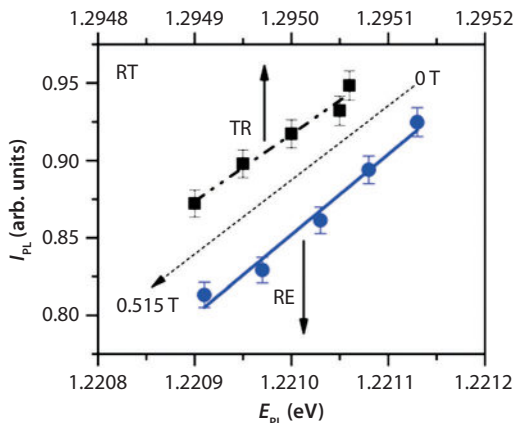


**Figure 11.24** Emission intensity decrease observed in RE and TR geometries. The symbols are extracted from the Gaussian fits in Figure 11.22, and the lines are linear fits. The dotted arrow indicates the increase in  $B$ .

## 11.8 Conclusions

The investigation of the dependence of the basic optical properties of PbS QDs on various optical stimulus intensities along with magnetic fields demonstrates the materials' suitability for changing markets. Emphasizing the works contribution to revealing the intensity limiting of QD PL, all-optical doping of soft quantized matter, and magneto-optical effects in QDs initiated with low magnetic fields, which are practicable for technological applications. Applying Eq. (11.1), we present the limiting function for charge carrier transport and PL in quantized matter and, during the course of all-optical doping of quantized soft matter via the BMS, we discovered that two-photon excited emission in QDs does not necessarily depend on the square of the exciting optical stimulus. This finding suggests the influence of quantization on the optical nonlinear effects in semiconductors. Additionally, magneto-optical results presented herein support the feasible application potential of PbS QD thin films to form novel magneto-optical smart device structures in conjunction with electromagnetic radiation. The observation of PL intensity tuning of PbS QDs in solution due to weak-applied magnetic fields lends this material to be strongly appealing in the employment of quantized soft matter for less invasive medical diagnostic applications.

## Acknowledgment

The work was partially supported by the DGAPA-UNAM PAPIIT projects TB100213-RR170213 (PI Bruno Ullrich) and IN117116 (PI J. A. Reyes-Esqueda) and the AFRL (PI Bruno Ullrich working for Universal Technology Corporation, subcontract agreement 11-S587-101-01-C1). PB and AKS acknowledge the DGAPA-UNAM program of postdoctoral fellowships. The authors acknowledge Robyn M. Duckworth for the critical reading of the manuscript and the technical support of R. Garcia and U. Amaya.

## References

1. H. Sargent, E. Infrared quantum dots. *Adv. Mater.*, 17(5), 512–22, 2005.
2. Ullrich, B., Wang, J.S., and Brown, G.J. (2011) Analysis of thermal band gap variations of PbS quantum dots by Fourier transform transmission and emission spectroscopy. *Appl. Phys. Lett.*, 99(8), 081901, 2005.

3. Olkhovets, A., Hsu, R.-C., Lipovskii, A., and Wise, F.W. Size-dependent temperature variation of the energy gap in lead-salt quantum dots. *Phys. Rev. Lett.*, 81(16), 3539–3542, 1998.
4. McDonald, S.A., Konstantatos, G., Zhang, S., et al. Solution-processed PbS quantum dot infrared photodetectors and photovoltaics. *Nat. Mater.*, 4(2), 138–42, 2005.
5. Bakueva, L., Musikhin, S., Hines, M.A., et al. Size-tunable infrared (1000–1600 nm) electroluminescence from PbS quantum-dot nanocrystals in a semiconducting polymer. *Appl. Phys. Lett.*, 82(17), 2895, 2003.
6. Moreels, I., Justo, Y., De Geyter, B., et al. Size-tunable, bright, and stable PbS quantum dots: a surface chemistry study. *ACS Nano*, 5, 2004–2012, 2011.
7. Kershaw, S. V., Susha, A.S., and Rogach, A.L. Narrow bandgap colloidal metal chalcogenide quantum dots: synthetic methods, heterostructures, assemblies, electronic and infrared optical properties. *Chem. Soc. Rev.*, 42(7), 3033–87, 2013.
8. Yue, F., Tomm, J.W., Kruschke, D., et al. Temperature dependence of the fundamental excitonic resonance in lead-salt quantum dots. *Appl. Phys. Lett.*, 107(2), 022106, 2015.
9. Shirasaki, Y., Supran, G.J., Bawendi, M.G., and Bulović, V. Emergence of colloidal quantum-dot light-emitting technologies. *Nat. Photonics*, 7(1), 13–23, 2012.
10. Frecker, T., Bailey, D., Arzeta-Ferrer, X., et al. Review—quantum dots and their application in lighting, displays, and biology. *ECS J. Solid State Sci. Technol.*, 5(1), R3019–R3031, 2016.
11. Carey, G.H., Abdelhady, A.L., Ning, Z., et al. Colloidal quantum dot solar cells. *Chem. Rev.*, 115 (23), 12732–63, 2015.
12. Jin, S., Hu, Y., Gu, Z., et al. Application of quantum dots in biological imaging. *J. Nanomater.*, 2011, 1–13, 2011.
13. Bera, D., Qian, L., Tseng, T.-K.K., and Holloway, P.H. Quantum dots and their multimodal applications: a review. *Materials (Basel.)*, 3, 2260–2345, 2010.
14. Deerinck, T.J. The application of fluorescent quantum dots to confocal, multiphoton, and electron microscopic imaging. *Toxicol. Pathol.*, 36(1), 112–6, 2008.
15. Qi, L., and Gao, X. Emerging application of quantum dots for drug delivery and therapy. *Expert Opin. Drug Deliv.*, 5(3), 263–7, 2008.
16. Eisler, H.-J., Sundar, V.C., Bawendi, M.G., et al. Color-selective semiconductor nanocrystal laser. *Appl. Phys. Lett.*, 80(24), 4614, 2002.
17. Konstantatos, G., Howard, I., Fischer, A., et al. Ultrasensitive solution-cast quantum dot photodetectors. *Nature*, 442, 180–183, 2006.
18. Jiang, X., Schaller, R.D., Lee, S.B., et al. PbSe nanocrystal/conducting polymer solar cells with an infrared response to 2 micron. *J. Mater. Res.*, 22(08), 2204–2210, 2011.
19. Luther, J.M., Law, M., Beard, M.C., et al. Schottky solar cells based on colloidal nanocrystal films. *Nano Lett.*, 8(10), 3488–92, 2008.

20. Talapin, D. V., Lee, J.S., Kovalenko, M. V., and Shevchenko, E. V. Prospects of colloidal nanocrystals for electronic and optoelectronic applications. *Chem. Rev.*, 110, 389–458, 2010.
21. Moreels, I., Lambert, K., Smeets, D., et al. Size-dependent optical properties of colloidal PbS quantum dots. *ACS Nano*, 3(10), 3023–30, 2009.
22. Neo, M.S., Venkatram, N., Li, G.S., et al. Size-dependent optical nonlinearities and scattering properties of PbS nanoparticles. *J. Phys. Chem. C*, 113(44), 19055–19060, 2009.
23. Rogach, A.L., Gaponik, N., Lupton, J.M., et al. Light-emitting diodes with semiconductor nanocrystals. *Angew. Chem. Int. Ed. Engl.*, 47 (35), 6538–49, 2008.
24. Steckel, J.S., Coe-Sullivan, S., Bulović, V., and Bawendi, M.G. 1.3  $\mu\text{m}$  to 1.55  $\mu\text{m}$  Tunable electroluminescence from PbSe quantum dots embedded within an organic device. *Adv. Mater.*, 15(21), 1862–1866, 2003.
25. Ullrich, B., Singh, A.K., Wang, J.S., and Xi, H. Colloidal PbS quantum dots on GaAs: optical properties and Urbach tail slope tuning, in *Nanotechnology for optics and sensors* (eds. Aliofkazraei, M.), One Central Press (OCP), Manchester, pp. 133–147, 2014. Comparing the results in this reference with the findings, it seems that the nature of the optical stimulus, i.e., continues wave vs. pulsed laser excitation, defines whether a blue or red EPL shift is observed for increasing optical stimuli.
26. Moss, T.S. The interpretation of the properties of indium antimonide. *Proc. Phys. Soc. Sect. B*, 67(10), 775–782, 1954
27. Burstein, E. Anomalous optical absorption limit in InSb. *Phys. Rev.*, 93(3), 632–633, 1954.
28. Barik, P., Singh, A.K., and Ullrich, B. Magneto-optical reflectance and absorbance of PbS quantum dots. *Phys. Scr.*, 90(9), 095501, 2015.
29. Wang, J.S., Ullrich, B., Brown, G.J., and Wai, C.M. Morphology and energy transfer in PbS quantum dot arrays formed with supercritical fluid deposition. *Mater. Chem. Phys.*, 141(1), 195–202, 2013.
30. Wang, J.S., Ullrich, B., and Brown, G.J. Lead sulfide quantum dot synthesis, deposition, and temperature dependence studies of the Stokes shift. *MRS Proc.*, 1409, mrsf11–1409–cc05–09, 2012.
31. Ullrich, B., Xiao, X.Y., and Brown, G.J. Photoluminescence of PbS quantum dots on semi-insulating GaAs. *J. Appl. Phys.*, 108(1), 013525, 2010.
32. Ullrich, B. GaAs band gap engineering by colloidal PbS quantum dots. *4th Int. Conf. Nanotek Expo*, Dec. 01–03, 2014, San Francisco, USA.
33. Kang, I., and Wise, F.W. Electronic structure and optical properties of PbS and PbSe quantum dots. *J. Opt. Soc. Am. B*, 14(7), 1632–46, 1997.
34. Wise, F.W. Lead salt quantum dots: The limit of strong quantum confinement. *Acc. Chem. Res.*, 33, 773–780, 2000.
35. Ullrich, B., Antillón, A., Bhowmick, M., et al. Atomic transition region at the cross-over between quantum dots to molecules. *Phys. Scr.*, 89(2), 025801, 2014.
36. Abel, K.A., Shan, J., Boyer, J.-C., et al. Highly photoluminescent PbS nanocrystals: the beneficial effect of trioctylphosphine. *Chem. Mater.*, 20(12), 3794–3796, 2008.

37. Ullrich, B., Wang, J.S., Xiao, X.Y., and Brown, G.J. Fourier spectroscopy on PbS quantum dots. *SPIE OPTO*, 8271, 82710A–82710A–6, 2012.
38. Ullrich, B., and Brown, G.J. Note: Phase sensitive detection of photoluminescence with Fourier transform spectroscopy. *Rev. Sci. Instrum.*, 83(1), 016105, 2012.
39. Bakueva, L., Gorelikov, I., Musikhin, S., *et al.* PbS quantum dots with stable efficient luminescence in the near-IR spectral range. *Adv. Mater.*, 16(11), 926–929, 2004.
40. Zhang, J., and Jiang, X. Steady state photoinduced absorption of PbS quantum dots film. *Appl. Phys. Lett.*, 92(14), 141108, 2008.
41. Ullrich, B., and Wang, J.S. Impact of laser excitation variations on the photoluminescence of PbS quantum dots on GaAs. *J. Lumin.*, 143, 645–648, 2013.
42. Ullrich, B., Barik, P., Singh, A.K., *et al.* Photo-dynamic Burstein-Moss doping of PbS quantum dots in solution by single and two-photon optical pumping. *Opt. Mater. Express*, 5(11), 2431–36, 2015.
43. Ullrich, B., and Wang, J.S. All-optical tuning of the Stokes shift in PbS quantum dots. *Appl. Phys. Lett.*, 102(7), 071905, 2013.
44. Ullrich, B., Xi, H., and Wang, J.S. Photoinduced band filling in strongly confined colloidal PbS quantum dots. *J. Appl. Phys.*, 115(23), 233503, 2014.
45. Ullrich, B., and Xi, H. Photocurrent limit in nanowires. *Opt. Lett.*, 38(22), 4698–700, 2013.
46. Moss, T.S. *Photoconductivity in the Elements*, Academic Press, New York, 1952.
47. Mooradian, A., and Fan, H. Recombination emission in InSb. *Phys. Rev.*, 148(2), 873–885, 1966.
48. Graham, R., Miller, C., Oh, E., and Yu, D. Electric field dependent photocurrent decay length in single lead sulfide nanowire field effect transistors. *Nano Lett.*, 11(2), 717–22, 2011.
49. Kamat, P. V., Dimitrijevic, N.M., and Nozik, A.J. Dynamic Burstein-Moss shift in semiconductor colloids. *J. Phys. Chem.*, 93(8), 2873–2875, 1989.
50. Sze, S.M., and Ng, K.K. *Physics of Semiconductor Devices*, 3rd Ed., John Wiley & Sons, Inc. NJ, 2007.
51. Schubert, E.F. *Doping in III-V Semiconductors*, Cambridge University Press, 1993.
52. Kramer, I.J., and Sargent, E.H. Colloidal quantum dot photovoltaics: a path forward. *ACS Nano*, 5(11), 8506–14, 2011.
53. Mocatta, D., Cohen, G., Schattner, J., *et al.* Heavily doped semiconductor nanocrystal quantum dots. *Science*, 332(6025), 77–81, 2011.
54. Wang, J.S., Steenbergen, E.H., Smith, H.E., *et al.* Stability studies of lead sulfide colloidal quantum dot films on glass and GaAs substrates. *SPIE OPTO*, 8634, 86340T–86340T-10, 2013.
55. Ekimov, A.I., Hache, F., Schanne-Klein, M.C., *et al.* Absorption and intensity-dependent photoluminescence measurements on CdSe quantum dots: assignment of the first electronic transitions. *J. Opt. Soc. Am. B*, 10 (1), 100–107, 1993.

56. Ironside, C.N. Optical nonlinear effects in semiconductors, in *Principles and Applications of Nonlinear Optical Materials* (eds. Munn, R.W., and Ironside, C.N.), Springer Netherlands, pp. 35–75, 1993.
57. Ullrich, B., Schroeder, R., Graupner, W., and Sakai, S. The influence of self-absorption on the photoluminescence of thin film CdS demonstrated by two-photon absorption. *Opt. Express*, 9(3), 116–20, 2001.
58. Sun, C.Q. Size dependence of nanostructures: impact of bond order deficiency. *Prog. Solid State Chem.*, 35, 1–159, 2007.
59. Nootz, G., Padilha, L. a., Levina, L., et al. Size dependence of carrier dynamics and carrier multiplication in PbS quantum dots. *Phys. Rev. B - Condens. Matter Mater. Phys.*, 83(15), 1–7, 2011.
60. Ullrich, B., Singh, A.K., Barik, P., et al. Inherent photoluminescence Stokes shift in GaAs. *Opt. Lett.*, 40(11), 2580–2583, 2015.
61. Ullrich, B., Ariza-Flores, D., and Bhowmick, M. Intrinsic photoluminescence Stokes shift in semiconductors demonstrated by thin-film CdS formed with pulsed-laser deposition. *Thin Solid Films*, 558, 24–26, 2014.
62. Verma, N.K. Nanophysics, in *Physics For Engineers*, PHI Learning Pvt. Ltd., Delhi, India, pp. 234–256, 2013.
63. Stephen, B., *Magnetism in Condensed Matter*, Oxford University Press, 2001.
64. Singh, A.K., Barik, P., and Ullrich, B. Magneto-optical controlled transmittance alteration of PbS quantum dots by moderately applied magnetic fields at room temperature. *Appl. Phys. Lett.*, 105(24), 242410, 2014.
65. Amirtharaj, P.M., and Seiler, D.G. Optical properties of semiconductors, in *Handbook of Optics, Volume II – Devices, Measurements, and Properties*, 2nd ed., McGraw-Hill, Inc., USA, pp. 1264–1359, 1995.
66. Terzis, A.F., and Baskoutas, S. Binding energy of donor states in a quantum dot with parabolic confinement, in *Quantum Dots: New Research* (ed. Ling, P.A.), Nova Science Publishers, pp. 125–151, 2008.
67. Bleicher, M. *Halbleiter-Optoelektronik*, Huethig, Heidelberg, 1986.
68. Moosavi, F., and Gholizadeh, M. Magnetic effects on the solvent properties investigated by molecular dynamics simulation. *J. Magn. Magn. Mater.*, 354, 239–247, 2014.

# Microstructure Characterization of Some Quantum Dots Synthesized by Mechanical Alloying

S. Sain and S. K. Pradhan\*

*Materials Science Division, Department of Physics, The University of Burdwan, Golapbag, Burdwan, West Bengal, India*

---

## Abstract

Zero-dimensional semiconductor nanocrystals, often termed as quantum dots (QDs), evoke a natural means of tuning the band gap by varying both the particle size and composition and have immense importance in multidisciplinary interests. QDs can be synthesized by several chemical and physical routes. Mechanical attrition/alloying (MA), one of the nonconventional physical routes of QD synthesis, is being recently used for their quick synthesis at room temperature using elemental powder precursors. Employing this easy, one-pot, one-step, and relatively inexpensive method, binary CdTe and ternary CdZnS are obtained, respectively, within 15 and 30 min of milling the elemental powders at room temperature. Other QDs such as ZnS, ZnTe, and CdZnS (with different Cd:Zn) have also been synthesized within record minimum time. Powder X-ray diffraction (XRD) patterns of most of these QDs are found to possess multiple phases with severely overlapped and broad reflections from the minor phase. Hence, it becomes very difficult, if not possible, to determine quantitative-phase analysis (QPA) and its associated microstructure parameters by any simple technique of XRD data analysis or even by high-resolution transmission electron microscopy. To redress this issue, a global approach in the form of Rietveld method is adopted. Optical properties of the materials are also analyzed.

**Keywords:** Quantum dots, nanocrystals, mechanical alloying, X-ray diffraction, Rietveld method, microstructure, HRTEM, optical properties

---

\*Corresponding author: skpradhan@phys.buruniv.ac.in

## 12.1 Introduction

In the past few decades, an enormous amount of research interests have been devoted in the field of nanoscience and technology primarily due to the quest to understand and discover the possibility and utility of promising nanostructured materials. Though many of the basic properties of materials were revealed by studying and observing the bulk structured materials, it is mostly with the advent of nanoscience, exotic quantum mechanical properties of materials in the nanoscale are being exposed. Materials in the nanometer regime play an important role in bridging the gap between the bulk and the molecular clusters that enables to pave the way forward in plethora of applications in the field of optoelectronics, electronics, biology, and so many [1–3]. As the particle size is reduced to the nanometer scale, three-dimensional electronic motion starts quenching. It is well known that all quantum structures have at least one dimension less than the de Broglie wavelength for an electron. Depending on the confinement of the electronic motion, nanostructured materials are broadly classified into three regimes: (i) two-dimensional structures: where electronic motion is quenched in one direction, such as quantum wells, and thin films; (ii) one-dimensional structures: where electronic motion is quenched in two directions, such as quantum wires; and (iii) zero-dimensional (dot) structures: where electronic motion is quenched in all three spatial directions, such as quantum dots (QDs).

The term ‘quantum dots (QDs)’ not only sounds elegant but the exotic properties it displays governing the laws of wave mechanics are also very important. QDs are basically semiconducting nanocrystals with dimension close to or smaller than the exciton Bohr radius associated for that materials which is found to be few nanometers in practical [4, 5]. In early 1980s, Ekimov *et al.* [6] and Henglein *et al.* [7] have pioneered in demonstrating the size dependence of the optical properties of QDs. Following this discovery, theoretical computations are started pouring in which is first enunciated by Brus [8] and Efros *et al.* [9] stating that the optical band gap (BG) of a semiconducting nanostructure can be shifted to a larger value if the crystallite size is reduced to nanoscale. The BG of a semiconductor is defined as the required energy to form excitons, far enough apart so as to neglect the coulomb attractive force, at rest with respect to the crystal lattice. The exciton Bohr radius ( $a_B$ ) for bulk semiconductors can be calculated by

$$a_B = \frac{h^2 k}{4\pi^2 \mu e^2} \text{ and } \mu = \frac{m_e m_h}{m_e + m_h} \quad (12.1)$$

where  $k$  is dielectric constant;  $h$  is Plank's constant,  $\mu$  is exciton reduced mass; and  $m_e$  and  $m_h$  are the effective mass of electron and hole, respectively. Depending upon the radius ( $a$ ) of the semiconducting nanocrystals, nature of confinement can be established, where  $a > a_B$ ,  $a \sim a_B$  and  $a < a_B$  represent weak, moderate and strong confinements, respectively [10].

## 12.2 Brief History of QDs

Though research on QDs started proliferating in the past few decades, use of QDs had started as early as 4000 years ago [11]. The ancient Egyptian used to prepare foundation cream and eye makeup from some minerals and various oils found profusely in nature. They had used synthetic white lead ( $2\text{PbCO}_3 \cdot \text{Pb}(\text{OH})_2$ ) and galena ( $\text{PbS}$ ) for this purpose which bears their knowledge in the field of lead based chemistry. In Greco-Roman era, people used to dye their grey hair by some natural resources such as henna along with some lead based compounds. It is surprising that some of those techniques are still being adopted in our modern society [11]. In early 1980s, discovery of QDs was pioneered by A. Efros and A.I. Ekimov from St. Petersburg, Russia and by Louis E. Brus from the Bell laboratories. They have synthesized QDs in different environment, Efros and Ekimov in a glass matrix [12, 13] and Brus [8] in colloidal solutions. Low-dimensional quantum structure in the form of quantum well appeared in existence in 1970. In 1971, Shklovskii *et al.* [14] described a thorough insight to the two-dimensional nanostructures. Reed *et al.* [15] showed that the excitation spectra of a semiconductor nanocrystal with three-dimensionally confinement of electrons can be measured. The change in properties in materials with the confinement of electrons such as blue shift of the absorption spectra was experimentally verified by Bayani *et al.* [16]. Efros *et al.* [12] postulated that quantum size confinement effect might be used to control the color of doped glass by either changing the size or atomic concentration of the dopant. Spanhel *et al.* [17] showed that different properties of synthesized monodispersed CdS nanocrystals (particle size  $\sim 4\text{--}5$  nm) strongly depended on the particle size. Hence, synthesis of good-quality semiconducting nanostructures employing different techniques becomes the fore-front challenge to the researchers worldwide. Murray *et al.* [18] synthesized CdE ( $E = \text{S, Se, Te}$ ) QDs achieving monodispersity by a single reaction. Grieser *et al.* [19] described the quantised-state (Q-state) particles of CdS, CdTe, CdSe,  $\text{Cd}_{x}\text{Se}_{1-x}$ ,  $\text{Cd}_{x}\text{Te}_{1-x}$  and  $\text{CdSe}_{x}\text{Te}_{1-x}$  in polymerized nonacosa-10, 12-diy-noic acid Langmuir–Blodgett (LB) films. In 1996, Paul Alivisatos [20] of

the University California, Berkley established that not only the optical properties but also the electrical properties of a material strongly depend on the quantum confinement appearing due to the small crystallite size. Research on both experimental and computational fronts has started divulging different exotic phenomena of QDs [21, 22] followed by different inevitable commercialization effects [23].

## 12.3 Theory of QDs

### 12.3.1 Band Gap and Quantization of Energy Levels

The most interesting characteristic of semiconductor is the presence of a BG between the valence and the conduction bands. QDs being semiconductors also possesses BG energies. For bulk semiconductors, the dispersion relation is parabolic in nature which holds good only for the electrons (holes) occupying the bottom (top) of the conduction (valence) band. This parabolic dispersion relation does not hold good as the dimensionality of the semiconductor is reduced. In case of three-dimensional structures the electrons can move in all three possible directions and the motion can be described by a linear combination of plane waves, the wave length of which is generally of the order of nanometers. With reducing in the dimensionality of the nanostructured materials, this electronic free motion is perturbed which is analogous to the situation of particle in a box [24]. The electronic states of the QDs face a discontinuity at the edge of the material just like the mechanism of an infinite potential well [25]. The quantum mechanical solutions of Schrödinger equation for such systems are standing waves having discrete energy values. The transition frequencies among these discrete quantum states are essentially different (higher) from that of a bulk semiconductor having continuous energy band giving rise to blue shift.

### 12.3.2 The Density of States

In case of bulk semiconductors where there is no effect of confinement of motion of the electrons, density of states (DOS) is continuous and varies proportional to,  $E^{1/2}$  where  $E$  denotes the energy of the state. For low-dimensional semiconductors, due to the confinement of motion of the electrons in one or more than one direction quantum mechanical effects begin to dominate and the energy levels become discrete. The DOS for a quantum well system looks like a 'staircase' due to confinement of one degree of freedom

of the electronic motion, whereas it looks like some sharp Lorentzian peaks for quantum wires due to two-dimensional confinement of electrons. In case of QDs, DOS are a series of discrete levels just like energy spectrum of an atom. Mathematically, DOS for low-dimensional semiconductors are proportional to  $E$ ,  $E^{-1}$ , and  $\delta E$  for quantum wells, quantum wires, and QDs, respectively [25]. Schematic representation of DOS for bulk and various low-dimensional nanostructures is shown in Figure 12.1 [26].

### 12.3.3 The Excitons

Exciton is the pair of an electron in the conduction band and a hole in the valence band [25]. If the electron and the hole approach toward each other, they may form a bound state analogous to hydrogen atom then they are termed as Wannier–Mott exciton [27]. With the analogy of hydrogen atom, concept of orbital motion of the electron and the hole around their center of mass gives rise to exciton Bohr radius. It is found that the energy gap between the lowest possible energy levels is greater than the BG energy of a bulk semiconductor [24, 28]. To evaluate the bang gap energy of QDs ( $E_g(QDs)$ ), infinite potential well model can be considered where the lowest energy state is

$$E_m = \frac{h^2}{2m^* R^2} \quad (12.2)$$

where  $h$  is Plank's constant,  $R$  is the width of the potential well, and  $m^*$  is the reduced mass of the excitons given by

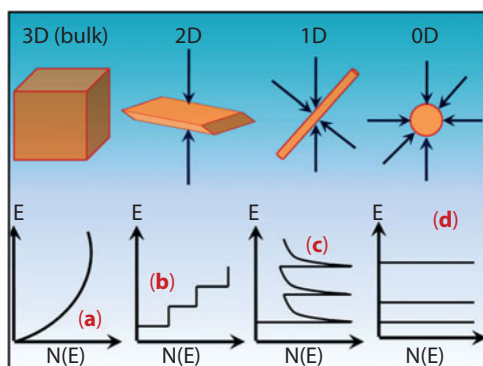


**Figure 12.1** Schematic diagram representing DOS ( $N(E)$ ) with respective energy ( $E$ ) for (a) 3D (three-dimensional) bulk semiconductor, (b) 2D (2-dimensional), (c) 1D (one-dimensional), and (d) 0D (zero-dimensional) nanostructures [26].

$$\frac{1}{m^*} = \frac{1}{m_e} + \frac{1}{m_h} \quad (12.3)$$

where  $m_e$  and  $m_h$  are the effective masses of electron and hole, respectively.

In case of excitons, the electron–hole pair remains in close vicinity. So, it is customary to consider the Coulomb interaction term ( $E_C$ ) into the calculation which is given by

$$E_C = -\frac{1.8e^2}{2\pi\epsilon\epsilon_0 R} \quad (12.4)$$

where  $e$  is the electronic charge,  $\epsilon_0$  is the permittivity of vacuum, and  $\epsilon$  is the relative dielectric constant of the semiconductor. Thus, considering these energies the BG of QDs is given by

$$E_g(QDs) = E_g(bulk) + \frac{\hbar^2}{2m^* R^2} - \frac{1.8e^2}{2\pi\epsilon\epsilon_0 R} \quad (12.5)$$

where  $E_g(bulk)$  is the band gap energy of the same semiconductor in its bulk form. However, this calculated value of the BG is not very much precise as several factors such as spin–orbit coupling and crystal anisotropy are not taken into consideration.

#### 12.3.4 The Effective Mass Theory

In 1983, L.E. Brus [29] first put forward the theoretical calculation to estimate the BG energy of quasi zero-dimensional QDs considering the effective masses of electrons and holes along with the electrostatic interaction between them. Electrons and holes follow the same quadratic dispersion relation on the wave vector  $k$  like that of free electrons, having effective masses  $0.1 m_e$  and  $0.3 m_h$  for electron and hole, respectively [13]. The concept of effective mass leads to the assumption that the relevant energy bands are parabolic near the BG. Using all these assumptions, Brus [29] derived the BG energy of QDs as

$$Eg(QDs) = Eg(bulk) + \frac{\hbar^2}{2R^2} \left( \frac{1}{m_e} + \frac{1}{m_h} \right) - \frac{1.8e^2}{2\pi\epsilon\epsilon_0 R} - 0.248 \left[ \frac{4\pi^2 e^4}{2(4\pi\epsilon\epsilon_0)(4\pi\epsilon\epsilon_0)^2 h^2 (1/m_e + 1/m_h)} \right] \quad (12.6)$$

Hence, the blue shift energy in case of QDs is

$$\Delta E_g (\text{QDs}) = \frac{\hbar^2}{2R^2} \left( \frac{1}{m_e} + \frac{1}{m_h} \right) - \frac{1.8e^2}{2\pi\epsilon\epsilon_0 R} - 0.248 \left[ \frac{4\pi^2 e^4}{2(4\pi\epsilon\epsilon_0)(4\pi\epsilon\epsilon_0)^2 \hbar^2 (1/m_e + 1/m_h)} \right] \quad (12.7)$$

The first term on the right hand side of Equation (12.7) is the most important kinetic energy term which varies as  $1/R^2$ . The second term represents screened Coulomb energy term arising due to the interaction between electron and hole and varies inversely to  $R$ . The last term does not have any spatial correlation and in general very small in magnitude. Assuming the hydrogenic model Bohr exciton radius ( $a_B$ ) can be obtained from Equations (12.6) and (12.7) as

$$a_B = \frac{4\pi\epsilon\epsilon_0 \hbar^2}{m^* e^2} = \frac{4\pi\epsilon\epsilon_0 \hbar^2}{e^2} \left( \frac{1}{m_e} + \frac{1}{m_h} \right) \quad (12.8)$$

where,  $\hbar$  is  $h/2\pi$ . This value ( $a_B$ ) is very helpful in determining the degree of confinement in QDs.

## 12.4 Different Processes of Synthesis of QDs

Nowadays, researchers are on the verge of finding fabrication techniques that can manipulate individual molecules and atoms. These fabrication techniques are aimed at achieving consistently and predictably creation of nanoscale structures with a high degree of control over size, shape, and distribution. The motivation for innovating different growth mechanism is to make 'tailor made' materials with desired properties. After the remarkable work at the beginning of 1980s [7, 12], there were unprecedented progress in the fabrication techniques of nanosemiconductors. In 1993, almost monodisperse nanostructures was obtained [18].

There are several techniques by which exotic QD nanostructures now can be synthesized. These methods are broadly classified into two categories: (i) bottom-up method and (ii) top-down method. Bottom-up approaches are primarily concerned with different chemical method of preparation.

### 12.4.1 Bottom-up Method

As the name suggests, this method primarily deals with fabrication of nano-materials starting with amorphous-like nanoparticles, atom or molecular species via self-assemble together due to some natural physical principle or some external driving force. There are different methods that fall into this category of synthesis. These methods may again be subdivided into two broad categories: (a) wet chemical method and (b) vapor-phase method [3]. Wet chemical method is constituted of hydrothermal method, hot-solution decomposition method, sol-gel method, microwave techniques, etc. Molecular beam epitaxy (MBE) method, sputtering techniques, etc. belong to the vapor-phase methods.

### 12.4.2 Top-down Method

In this method, a bulk material is broken into fine pieces by using mechanical, chemical or by some other energy. Some of the common methods in this category are: electron beam lithography, high-energy ball milling, laser ablation, reactive-ion etching, etc. It is often said that most of the top-down methods are very much prone to generate impurities and structural imperfections. However, if proper precautions are taken during material synthesis, then the possibility of inclusion of impurities in the processed samples can be removed or significantly reduced. Schematic diagram representing the synthesis of nanoparticles by top-down and bottom-up approaches is shown in Figure 12.2 [30].

## 12.5 Structure of QDs

It is found that most of the binary QDs crystallize either with cubic zinc blende (ZB) or in the hexagonal wurtzite (W) structure. Both of these structures are of four coordinates and the layer stacking sequences of most dense lattice planes for ZB and W are ABCABC... and ABAB..., respectively [31]. W-ZB polytypism may also be noticed in QDs for which there is minor difference in the total energies between ZB and W structures, i.e.  $E_{ZB} - E_W$  is small [32]. Depending upon the synthetic techniques which involve nucleation and growth mechanism, prepared QDs may exhibit either ZB or W or even simultaneous presence of ZB and W phases [31]. Figure 12.3 shows ZB (ICSD 77090; space group F43m) and W (ICSD 67453; space group P6<sub>3</sub>mc) structures of ZnS.

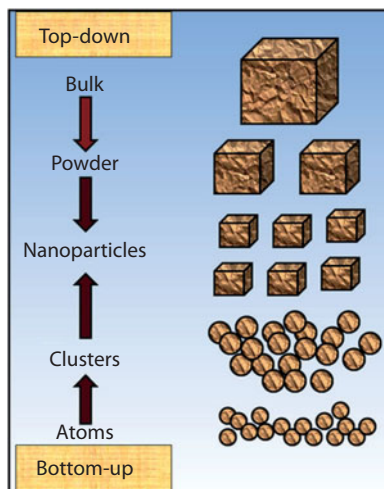


**Figure 12.2** Schematic representation of synthesis of nanoparticles by top-down and bottom-up approaches [29].

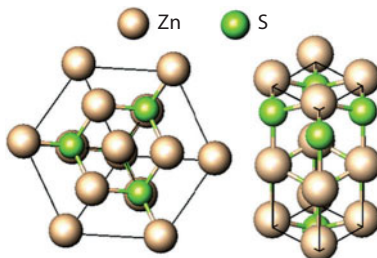


**Figure 12.3** Cubic zinc-blende (ICSD 77090) (left) and hexagonal wurtzite (ICSD 67453) (right) structures ZnS.

## 12.6 Applications of QDs

The study of different astonishing properties of zero-dimensional QDs has encouraged researchers to utilize it in various applications especially in the field of optoelectronics and biology.

### 12.6.1 Photovoltaic Devices

Improving the efficiency of the solar cell is one of the challenges to the researchers ever since its inception of by Chapin, Fuller, and Pearson [33]. The visible light emanating from the Sun is the primary source for converting the photon energy to electrical energy. The conversion efficiency is defined

as the ratio of maximum power out to the incident power. For a conventional solar cell of single-band-gap semiconductor the maximum efficiency become 31% [34]. This efficiency can be enhanced by employing multiple junction cells, but the practical problem lies in lattice mismatching of different materials used. In such cases, QDs with different sizes can be utilized as it provides different BGs with varying sizes. Though the experimental evidence of improving the efficiency to a greater extent by employing QDs in solar cell is still in its infancy, QDs have the potential to achieve the goal in near future.

### **12.6.2 Electroluminescence Devices**

There are several drawbacks in case of organic light-emitting diodes (OLED) [3], such as (i) the full width at half maximum (FWHM) values is quite broad, (ii) the display color generally changes with time due to different life time of the primary colors, (iii) organic materials generally display poorer thermal stability, and (iv) OLED does not produce infrared emission, etc. All the above-mentioned shortcomings can be overcome if it is replaced by QDs light-emitting diodes (QLED).

### **12.6.3 Infrared Photodetectors**

Infrared photodetector sensors are generally made up of materials with quantum well structures. The shortcoming of such type of detectors is the reduction of efficiency in the normal incidence [34]. It is predicted that by replacing quantum well by QDs would enhance the efficiency, since QDs being zero-dimensional structures are eligible to enhance the normal absorption of infrared light.

### **12.6.4 Downconversion of UV Light**

Recently, QDs are being used as phosphor materials to downconversion of higher-energy wave length to lower-energy wave length [3]. It has some obvious advantages over the traditional inorganic dyes, such as (i) QD dyes can be excited by a single excitation source eliminating the hassle of using multiple sources as required for traditional dyes, (ii) QDs are much bright and last longer, (iii) the emission range is broader, (iv) better stability, and (v) large absorption window.

### **12.6.5 QD Lasers**

In the past two decades, much attention has been paid to improve the efficiency of solid state laser devices using QDs. The DOS and discrete energy

levels of zero-dimensional QDs enable lasers to operate in a narrow, single excitation mode [34]. The variation of the BG energies with crystallite sizes in QDs makes the lasing wave length variable.

### 12.6.6 Cancer Diagnosis

Having excellent photo-physical properties, QDs-based probes have gained tremendous development in cellular and *in vivo* molecular imaging [35]. Cancer has evolved as the major public health concern globally and one in four deaths in the USA due to this fatal disease [36]. For medical sciences, it is of utmost importance to visualize the native processes occurring in living cells with respect to diagnosis and treatment [35]. It was not possible due to the unavailability of such type biological markers. But with the advent of QDs fluorophores for *in vivo* fluorescence imaging, treatment and diagnosis of different fatal diseases such as ovarian, breast, prostate, and pancreatic cancers have been facilitated [35].

## 12.7 Mechanical Alloying

Materials scientists around the world are always concerned with the synthesis of samples that can be obtained in a hassle free method and at the same time expect it to perform more efficiently and effectively. It is now well established that structure and properties of materials prepared through nonequilibrium methods (energizing and quenching) provide better control [37, 38]. The materials processed through these methods possess better physical and mechanical properties than those prepared by conventional ingot process [37]. There are many such methods among which mechanical attrition/milling (MA) is one of the simplest and inexpensive methods. MA is basically a dry (sometimes wet) ball milling of the blended powder mixtures to produce commercially viable and scientifically interesting materials. MA is generally carried by milling techniques capable of producing high-energy compressive impact forces such as planetary ball mills and vibrating ball mills [39].

### 12.7.1 Sample Preparation by MA

The process of MA starts with taking the elemental powders (commercially available highly pure powders having particle size  $\sim$ few  $\mu\text{m}$ ) that are to be ground in accurate proportion (stoichiometric ratio) into the vials containing the milling media (grinding balls). We have used Pulverisette-5 (P-5) (M/S Fritsch, GmbH, Germany) high-energy planetary ball mill

with chrome-steel vials of 80 ml volume. The grinding media consists of 30 chrome-steel balls having diameter 10 mm each. If the precursor powders are reactive in open air then the powders must be taken inside a glove bag under the inert atmosphere (such as Ar gas). This mixture of powers is then milled for a desired duration until desired homogeneity, particle size, etc. are attained.

The term ‘planetary ball mill’ is coined due to its similarity in kinetics to the planetary motion of our solar system. The grinding vessels that are stationed on the main rotating disc rotate in the opposite direction to that of the main rotating disc around an axis passing through the center of it, analogous to the motion of a planet. Due to such type of motion, the grinding balls feel not only the force due to gravity as happens in conventional milling, but centrifugal and coriolis forces further enhance the kinetic energy of the system. The analytical fineness and surface area minimization of the synthesized powders, which are required for various analytical methods, is achieved in very short time due to such a high-energy mechanism. In the present study, we have used successfully Fritsch Planetary pulversiette-5 classic line with four grinding bowl fasteners which is shown in Figure 12.4 [40].

### 12.7.2 Optimization of Different Parameters of MA

There are certain process variables that influence the milling process in effective ways [37]. Hence, optimization of these variables is crucial to obtain impurity free desired target materials. Some of such important parameters are as follows.

- (i) *Ball-to-powder mass ratio (BPMR)*: BPMR which is also termed as charge ratio (CR) is one of the most important parameters plays significant role in formation time of the material. In general, it is found that with increasing BPMR, formation time decreases [37]. The weight value of the milling media and the number of collisions per unit time increase with increasing BPMR and it imparts more energy to the sample, resulting in faster formation. Depending upon the volume of the grinding vial, this ratio can be optimized for better result.
- (ii) *Rotation speed*: It is evident that collision energy will increase with increasing speed of the rotating disc and range of rotation speed varies with model, manufacturer, and type of mills. The grinding balls get stuck to the inner



**Figure 12.4** High-energy planetary ball mill (Fritsch Planetary pulversiette-5 classic line with 4 grinding bowl fasteners) [40].

wall of the vial after an optimum rotation speed. This reduces the impact between the ball and the powder which lowers the efficiency of grinding. This optimum rotation is generally found to have value which is slightly less than the maximum attainable speed of the system [37].

- (iii) *Milling time:* Time of milling is also very important parameter which is so determined to achieve a steady state between the fracturing and cold welding of the powder particles [37]. This optimum time depends on some factors such as the type of mill, rotation (r.p.m) speed, BPMR, grinding media, and even the nature of powder sample. If the milling process is continued for a very long duration beyond the optimum time, there is every possibility of obtaining impurity from the milling media.

- (iv) *Grinding media:* Choosing of material for the grinding media is also very important. The grinding media is in general very hard and usually made up of hardened steel, hardened chrome steel, WC-lined steel, zirconia, agate, etc. It is customary that the grinding media should be harder than the sample to be grounded; else due to the high-impact collision between the grinding media and the sample, impurity may appear from the dislodged portion of the inner wall of the vial. In the present study, all samples are prepared using hardened chrome steel grinding media.
- (v) *Milling atmosphere:* Milling atmosphere in MA primarily deals with the contamination in the powders. To avoid the contamination in the milled sample, it is suggested to carry out the milling process under inert atmosphere. Ultra-high-pure argon gas is found to be the most ambient condition to avoid oxidation or contamination [37]. We have used highly pure argon gas atmosphere in synthesizing all the QDs reported here.

## 12.8 The Rietveld Refinement Method

This method was first reported by H. Rietveld himself at the seventh Congress of IUCr in Moscow in 1996. This method did not receive well acknowledgement until full implementation of it was published [41]. Rietveld method was at first applied on data obtained from fixed source of neutron diffraction for structure determination and structure refinement of almost 200 samples was carried in the subsequent three years. He proposed that this method can be extended for data obtained from X-ray sources and in 1977 ultimately this method was globally accepted for analysis of both X-ray and neutron data. Today, the Rietveld method is well recognized to be the most valuable for structure and microstructure analysis of all most all type of crystalline materials not available as single crystals [41].

### 12.8.1 The Rietveld Method: Mathematical Approach

Rietveld's powder structure refinement method [42, 43] is possibly the best-known method to obtain different structure/microstructure parameters and relative phase abundances in materials containing multiple phases. A powder diffraction pattern of a crystalline solid is supposed to be a summation of individual reflection profiles having individual peak

height, position, breadth, tail, etc. which diminishes gradually from the peak position [41]. In case of nanocrystalline solids, these profiles are not resolved but are severely overlapped. It is an important aspect of Rietveld method that no effort is made in prior to provide the observed intensity to a particular Bragg reflection or to resolve an overlapped reflection which demands a good structure model [crystallographic information file (cif), from ICSD] initially [41]. It is to be noted that the Rietveld method is not a structure solution method, but it is a structure refinement method which intern constitutes an important part for the structure solution. It is customary to obtain instrumental correction for the particular X-ray diffraction (XRD) set up usually by a Si standard [NIST Standard reference material (SRM) 640d] [44] where the peak broadening due to size and strain is negligible. For angle dispersive data, the dependence of the breadth ( $H$ ) of the reflection profiles (FWHM) is modeled by the following Caglioti formula [45].

$$H = [U \tan^2\theta + V \tan\theta + W]^{1/2} \quad (12.9)$$

where  $U$ ,  $V$ , and  $W$  are the refinable parameters. The simulation is carried out by refining different structure/microstructure parameters to fit the experimental XRD pattern using an analytical profile fitting function like pseudo-Voigt function which takes care of both size and strain broadening simultaneously by Marquardt least-square refinement procedure. The calculated intensity for the analysis is determined by the following equation [41]:

$$S_y = \sum_k L_k |F_k| 2\Phi(2\theta_i - 2\theta_k) P_k A + y_{bi} \quad (12.10)$$

where  $S$  is the scale factor,  $k$  represents the Miller indices ( $h, k, l$ ) for a Bragg reflection,  $L_k$  represents the Lorentz polarization and multiplicity factors,  $\Phi$  is the reflection profile function,  $P_k$  is the preferred orientation function,  $A$  is absorption function,  $F_k$  is the structure factor for the  $k^{\text{th}}$  Bragg reflection, and  $y_{bi}$  is the intensity of the background of the  $i^{\text{th}}$  step. The simulated pattern obtained by adding up the calculated intensities ( $y_{ci}$ ), quality of fitting is established by the residue,  $S_y$ , where

$$S_y = \sum_i w_i (I_{oi} - I_{ci})^2 \quad (12.11)$$

where  $w_i = 1/I_{oi}$  and  $I_{oi}$  are the observed intensity at  $i^{\text{th}}$  iteration [46].

### 12.8.2 Quantitative-phase Analysis by the Rietveld Method

A simple relationship exists between the individual scale factor and the phase concentration in a multiphase system [47]. The weight fraction of different phases is given by,

$$W_i = \frac{s_i(ZMV)_i}{\sum_j s_j(ZMV)_j} \quad (12.12)$$

where  $s_p$ ,  $Z_p$ ,  $M_p$ , and  $V_i$  are the scale factor, the number of molecules per unit cell, the molecular weight and unit cell volume of phase  $i$ , respectively. The summation is carried out over all the phases present. The density of each phase  $I$  is given by,

$$\rho_i = \frac{Z_i M_i}{N_A V_i} \quad (12.13)$$

where  $N_A$  is the Avogadro number.

Rietveld method is also efficient to quantify the amorphous phase even in a multiphase material treating the amorphous phase as a nanocrystalline phase without having long-range order. This method can produce almost similar result obtained from reverse Monte Carlo simulation (RMC) of a ceramic material mixed with glassy phase [48].

### 12.8.3 Coherently Diffracting Domain (Particle) Size and R.M.S. Strain

To determine the particle size and r.m.s. strain, Scherrer and Williamson-Hall plot equations can safely be used so long as the XRD peaks are well resolved and separated [49]. Pattern fitting or deconvolution must be taken into consideration when the peaks are considerably overlapped. It is known that broadening of peak occurs due to particle size and r.m.s. strain which are represented by Lorentzian and Gaussian functions, respectively. A convolution of both these functions termed as the pseudo-Voigt function [50, 51] is a good choice to determine the particle size and r.m.s. strain inside the lattice.

### 12.8.4 Lognormal Size Distribution

From the Fourier analysis of the XRD profiles, both area and volume weighted average grain size,  $D_A$  and  $D_V$  can be obtained. These parameters can facilitate to obtain grain size distribution which cannot be calculated directly from the Fourier coefficient [52]. Lognormal distribution for

spherical crystallites is characterized by average radius  $\bar{R}$  of the particles and the dispersion  $\sigma_{\bar{R}}^2$  [52, 53]. The dimensionless ratio C [54] is

$$c = \frac{\sigma_{\bar{R}}^2}{\bar{R}^2} \quad (12.14)$$

Then lognormal distribution can be written as

$$f(R) = R^{-1} [2\pi \ln(1+c)]^{-1/2} \exp\left\{ \frac{-\ln^2 \left[ R \bar{R}^{-1} (1+c)^{1/2} \right]}{[2 \ln(1+c)]} \right\} \quad (12.15)$$

The volume and area averaged dimensions are

$$D_V = \frac{3\bar{R}(1+c)^3}{2} \quad (12.16)$$

$$D_A = \frac{3\bar{R}(1+c)^2}{2} \quad (12.17)$$

$\bar{R}$  and  $c$  can be calculated using the value of  $D_V$  and  $D_A$  obtained from Fourier analysis of the line profile.

### 12.8.5 Planar Defects

There are three types of planar defects found in close packed fcc and hcp crystal lattices: (i) intrinsic ( $\alpha'$ ): when one or many lattice planes are missing in a normal stacking sequence ABCABC... of most dense (111) planes of fcc lattice, (ii) extrinsic ( $\alpha''$ ): when one or many lattice planes are inserted in a normal stacking sequence of lattices and (iii) twin ( $\beta$ ): when parallel lattice planes become twisted. During the formation of nanoparticles by high-energy methods such as planetary ball milling, planar defects are noticed, caused due to heavy plastic deformation during synthesis. Lutterotti and Gialanella [55] have introduced a novel method to quantify these crystal defects in terms probability by using Warren model [56].

### 12.8.6 Rietveld Refinement Software: MAUD

With the increasing demand for microstructure characterization by Rietveld method, several computer softwares have been developed with

special emphasis on either structure refinement or both structure and microstructure refinements simultaneously. Source codes of many of these programs are freely downloadable and distributed for modification and extension. There are some powerful Rietveld software such as GSAS, DBWS, RIETAN, Fullprof, and MAUD. In the present study, Rietveld software MAUD [57, 58] which has a special feature to refine simultaneously the structure/microstructure parameters has been used extensively.

## 12.9 Some Previous Work on Metal Chalcogenide QDs Prepared by Mechanical Alloying from Other Groups

There are very few reports on the synthesis of chalcogenide QDs by mechanical alloying. Tsuzuki and McCormick [59] in 1999 synthesized ZnS and CdS QDs by a long chain of mechanochemical reaction. Tan *et al.* [60] prepared single cubic phase CdTe nanocrystals by ball milling the elemental powders for more than 8h. With increasing milling time particle size decreased and reached ~2–6 nm after a long 50h of milling. Nano ZnTe was synthesized by Campos *et al.* [61] from elemental powders in equiatomic ratio by mechanical alloying and they found minority crystalline phases of Te and ZnO in the milled samples. CdS nanoparticles with particle size <8 nm were synthesized by Tsuzuki *et al.* [62]. They have varied the particle size in the range ~4–8 nm by varying the size of the grinding media. Dutkova *et al.* [63] synthesized nanocrystalline  $\text{Cd}_x\text{Zn}_{1-x}\text{S}$  (for  $x = 0, 0.5$ , and  $1.0$ ) by mechanochemical solid state method in a laboratory planetary ball mill (Pulverisette 6, Fritsch, Germany) in Argon atmosphere from the corresponding acetates and sodium sulfide. They indexed pure CdS as hawleyite (H) (JCPDS 10-454) and the pure ZnS as sphalerite (S) (JCPDS 5-566) phases, respectively. In case of  $\text{Cd}_{0.5}\text{Zn}_{0.5}\text{S}$ , they noticed a phase transformation from H→S with increasing Zn content.

## 12.10 Results and Discussion

### 12.10.1 Some Interesting Features Noticed in ZnS QDs Synthesized by MA

#### 12.10.1.1 Coexistence of Minor Wurtzite Phase with Major Zinc Blende Phase

XRD patterns of unmilled and ball-milled stoichiometric mixture of Zn (JCPDF 04-0831; hexagonal, Sp. Gr. P6<sub>3</sub>/mmc,  $a: 2.665\text{\AA}$ ,  $c: 4.947\text{\AA}$ ) and

S (ICSD- 412326, Sp. Gr. Fddd, orthorhombic,  $a: 10.393\text{\AA}$ ;  $b: 12.762\text{\AA}$ ;  $c: 24.436\text{\AA}$ ) powders with different milling time are shown in Figure 12.5 [64]. It is noticed that ZnS phase evolves just after 3.5h of milling and broadening of peaks is observed with increasing milling time up to 20h. It appears that the XRD patterns of all ZnS reflections are composed of only zinc blende (cubic) phase, but the Rietveld analysis confirms the coexistence of a minor wurtzite ZnS phase (shown in Figure 12.6a). Figure 12.6b confirms simultaneous presence of minor hexagonal with major cubic phase in 3.5 h milled sample. It is found that single cubic phase is sufficient to analyze the XRD pattern of 20 h milled sample, suggesting 20 h milled ZnS is composed only of single cubic phase. Rietveld analysis confirms that with increasing milling time the minor hexagonal phase gradually decreases and completely vanishes after 20 h of milling. The phase transformation kinetic with the formation of ZnS phase is shown in Figure 12.7. The presence of such minor phase is very difficult to ascertain unless the XRD patterns are properly analyzed by Rietveld method.

#### 12.10.1.2 Presence of Planar Defects in Ball-milled ZnS

The method of planetary ball milling is a high-energy method which produces nanomaterials by constant fracturing and rewelding mechanism. Such type of synthesis technique is expected to cause plastic deformation in the lattice. Hence, it is of utmost importance to characterize these

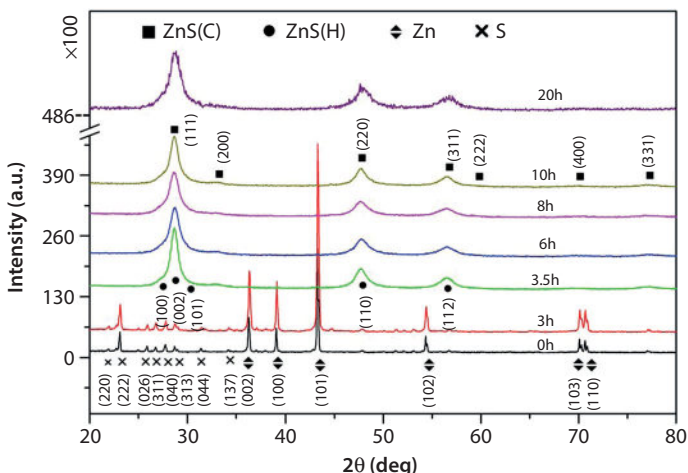


**Figure 12.5** XRD patterns of unmilled (0 h) and ball-milled Zn and S powders (Zn:S=1:1) for different durations. ZnS(C) and Zn(H) denote zinc blende and wurtzite structures respectively. [Reproduced with permission from [64] Copyright (2009) AIP Publication LLC.]

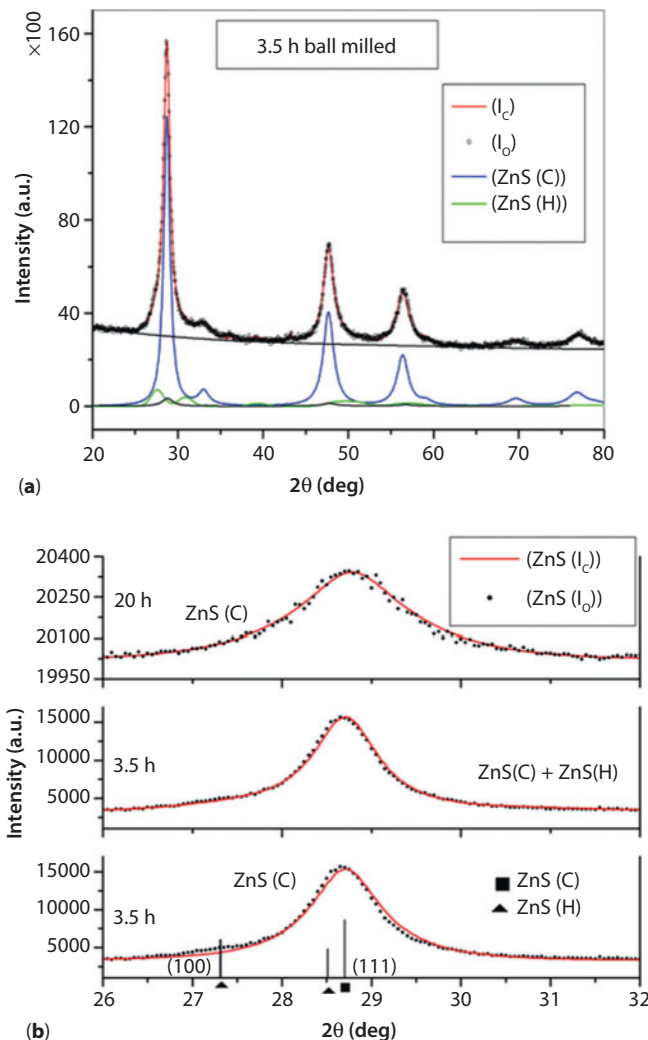


**Figure 12.6** (a) Coexistence of a minor hexagonal phase with a major cubic phase of ZnS, milled for 3.5 h as revealed from Rietveld analysis.  $I_c$  and  $I_o$  represent computed and observed (experimental) patterns respectively. (b) The presence of both cubic and hexagonal phases in 3.5 h milled ZnS and formation of single cubic phase ZnS in 20 h milled sample. [Reproduced with permission from [64] Copyright (2009) AIP Publication LLC.]

deformations in the lattice, since such type of change in microstructures brings in alteration in different physical, mechanical and chemical changes in the material. Reversely, it can be said that controlling these microstructure parameters ‘tailor-made’ materials with desired properties can be synthesized.

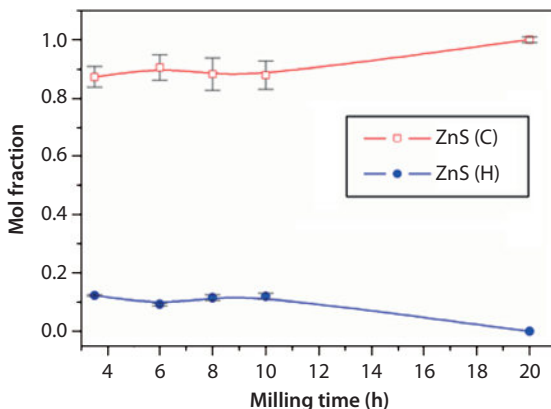


**Figure 12.7** Phase transformation kinetics of cubic (C) and hexagonal (H) ZnS with increasing milling time after the formation of ZnS phase. [Reproduced with permission from [64] Copyright (2009) AIP Publication LLC.]

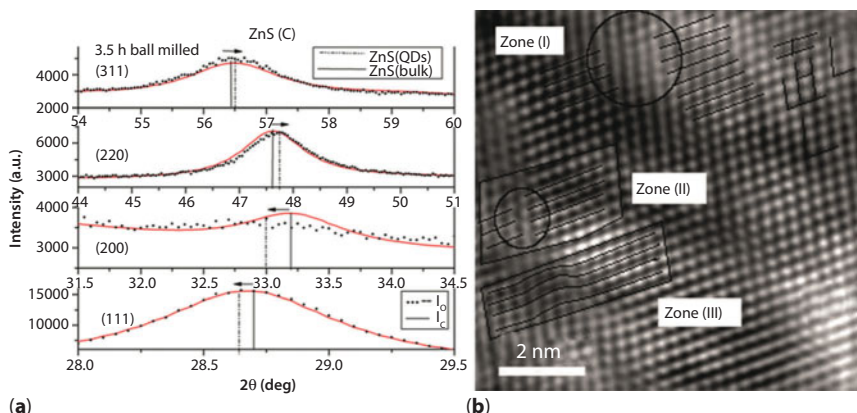


**Figure 12.8** (a) Shifting in peak positions of ZnS(C) in either side with respect to its bulk counterpart. Solid and dotted vertical lines represent the peak positions of bulk and milled ZnS(C) respectively. (b) HRTEM image of cubic (111) of ZnS showing different planar defects- (i) zone I: extrinsic stacking fault, (ii) zone II: intrinsic stacking fault and (iii) zone III: twin fault. [Reproduced with permission from [64] Copyright (2009) AIP Publication LLC.]

A close observation of the Rietveld analysis of 3.5 h milled ZnS (Figure 12.8a) reveals the shift in peak positions of cubic (111) and (200) toward the lower scattering angle with respect to bulk sample and those for (220) and (311) toward the higher scattering angle. Such type of peak shifting in either side cannot be accounted for the change in lattice parameter

only, instead due to the cumulative effect of change in lattice parameters, residual stress and more importantly stacking faults of the lattice. The presence of stacking fault (intrinsic, extrinsic, and twin faults) is also evidenced in the high-resolution transmission electron microscopy (HRTEM) images (Figure 12.8b).

### 12.10.1.3 Core–Shell ZnS

Core–shell formation in ZnS is noticed in the 10 h milled sample (Figure 12.9a). The HRTEM image (Figure 12.9b) suggests that the core is composed of cubic ZnS phase where the interplanar lattice spacing is 3.05 Å that corresponds to (111) plane of cubic lattice. The hexagonal phase on the shell does not show any lattice fringe and appears to be an amorphous like phase. With increasing milling time from 10 to 20 h, this amorphous like hexagonal phase diffuses gradually through the grain boundaries of the cubic core and transformation becomes complete after 20 h of milling.

## 12.10.2 Some Key Features in Mechanically Alloyed ZnTe QDs

### 12.10.2.1 Formation of ZnTe in Quickest Time by MA

Rietveld-analyzed XRD patterns of Zn (JCPDF 04-0831; hexagonal, Sp. Gr. P6<sub>3</sub>/mmc a: 2.665 Å, c: 4.947 Å) and Te (ICSD code 23058; Sp. Gr. P3<sub>1</sub>21; a: 4.411 Å; c: 5.934 Å) equimolar powder mixture is shown in Figure 12.10. It is noticed from the patterns that the unmilled mixture is composed only of the elemental powders. Just after 1 h of milling stoichiometric pristine ZnTe (ICSD code 653194, Sp. Gr. F43m, a = 6.1 Å) phase is formed

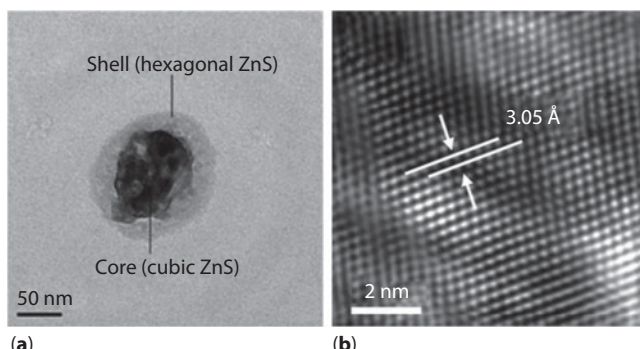


**Figure 12.9** (a) Bright field TEM showing core (cubic)–shell (hexagonal) ZnS in 10 h milled sample, (b) HRTEM image showing the presence of (111) plane of cubic ZnS in the lattice. [Reproduced with permission from [64] Copyright (2009) AIP Publication LLC.]

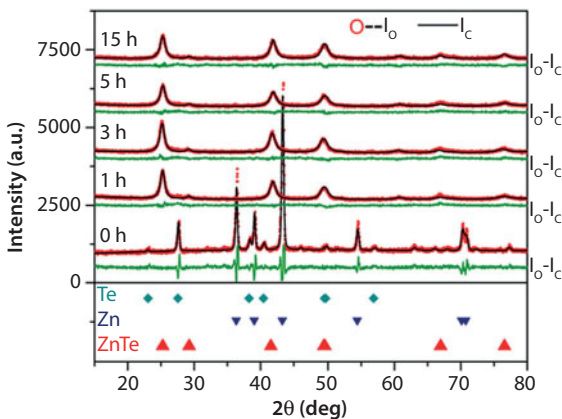


**Figure 12.10** Rietveld whole profile fitted output XRD patterns of unmilled and ball-milled equimolar powder mixture of Zn and Te. Dotted and solid lines represent observed ( $I_o$ ) and computed ( $I_c$ ) spectra respectively. Residue ( $I_o - I_c$ ) of each profile fitting is plotted corresponding to each pattern. Peak positions corresponding to each phase is marked at the bottom. [Reproduced with permission from Elsevier.]

and with increasing milling time FWHMs value of each peak gradually increases without appreciable change noticed in the patterns [65].

#### 12.10.2.2 Variation of Particle Size and R.M.S Lattice Strain

Particle size of ZnTe obtained after 1 h of milling gradually reduces from  $\sim 12.5$  to  $\sim 5.3$  nm due to the fracturing effect of ball milling (shown in Figure 12.11a). Distribution of particle sizes (Figure 12.11b) also follows similar way where the most probable values decrease gradually with increasing milling time. It is also interesting to note that with increasing milling time the width of the distribution becomes narrower which suggests that most of the particles are attaining the same size and monodispersity is gradually achieved at higher milling time.

ZnTe phase is formed with a significant amount of lattice strain. With increasing milling time, the r.m.s. lattice strain decreases gradually (Figure 12.12a). This decrease in lattice strain with increasing milling time is due to the fact that the excess lattice strain is released from the lattice due to the thermal energy developed during the milling. At the early stage of milling, this thermal energy is utilized to initiate the cubic ZnTe phase formation through solid state diffusion of Zn and Te particles. After formation, this energy has been utilized for diffusion of Zn and Te atoms to achieve its stability through release of excess lattice strain. The distribution of lattice strain is shown in Figure 12.12b. From the figure, it is evident

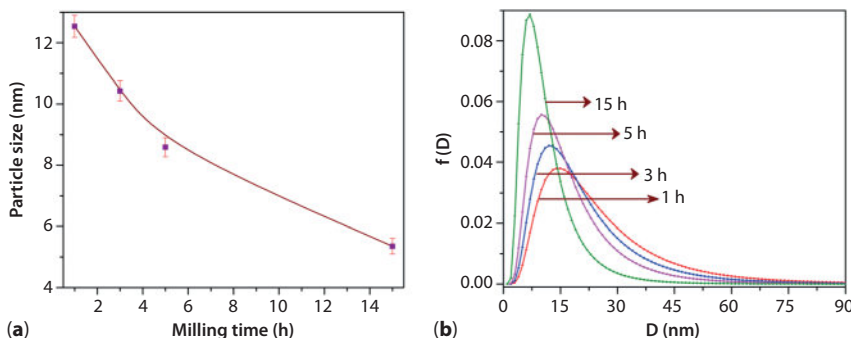


**Figure 12.11** (a) Variation and (b) distribution of particle size of ZnTe with respect to milling time. [Reproduced with permission from Elsevier.]

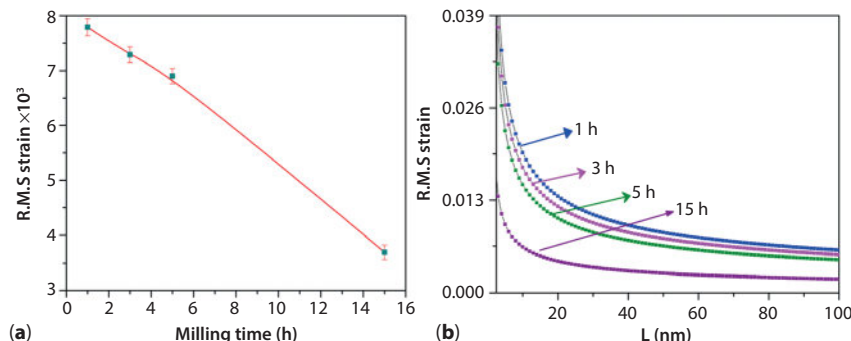


**Figure 12.12** (a) Variation and (b) distribution of r.m.s lattice strain for different hour milled ZnTe.  $L = n a_3$ ,  $n$  = harmonic number,  $a_3$  = lattice parameter. [Reproduced with permission from Elsevier.]

that the length available for strain distribution reduces as the particle size reduces with milling time. The value as well as the distribution of lattice strain gradually decreases to lower values with increasing milling time.

### 12.10.2.3 Quantitative and Qualitative Analysis of Stacking Faults

Just like the ZnS QDs [64], planar defects in ZnTe lattice have also been noticed. Quantitative analysis of these defects has been carried out by considering the Warren model [56] incorporated in the MAUD software, and it is expressed in term of stacking fault probabilities with increasing milling time (Figure 12.13a). It can be noted that intrinsic ( $a'$ ), extrinsic ( $a''$ ), and twin fault ( $\beta$ ) probabilities increase with increasing milling time. This suggests that with increasing milling time due to constant fracturing of

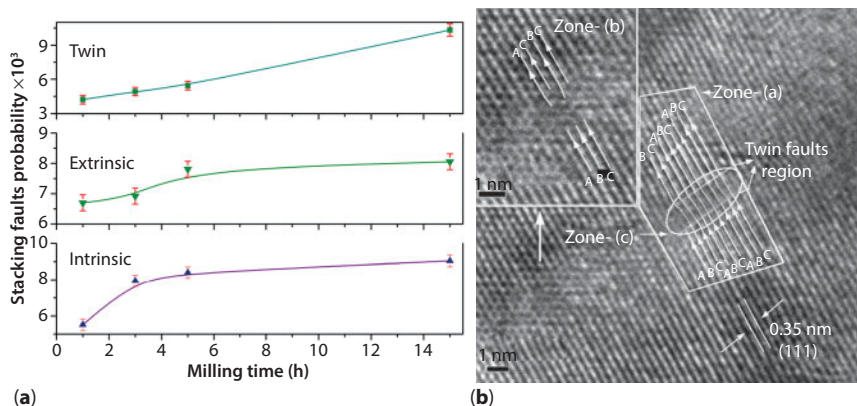


**Figure 12.13** (a) Variation of stacking fault probabilities of cubic ZnTe with changing milling time. (b) HRTEM images of 15h milled ZnTe QDs depicting the existence of different kinds of stacking and twin faults generated in the stacking sequence of (111) planes of cubic phase: (i) zone (a): intrinsic ( $a'$ ), (ii) zone (b): extrinsic stacking fault ( $a''$ ), and (iii) zone (c): twin fault ( $\beta$ ) is created. [Reproduced with permission from Elsevier.]

the crystal, lattice defects in the crystal lattice also increased. Qualitatively, these planar defects have also been evidenced in HRTEM image of 15 h milled sample (Figure 12.13b).

### 12.10.3 Few Special Features of CdTe QDs Synthesized by MA

#### 12.10.3.1 Formation of CdTe QDs in Quickest Time

Refined XRD patterns by Rietveld method of unmilled and ball-milled Cd and Te (1:1 ratio) powders are shown in Figure 12.14a. The unmilled pattern consists only of reflections from elemental powders Cd (JCPDF 05-0674; hexagonal, Sp. Gr. P6<sub>3</sub>/mmc;  $a = 2.9793 \text{ \AA}$ ,  $c = 5.6181 \text{ \AA}$ ) and Te (ICSD- 23058; trigonal; Sp. Gr. P3<sub>1</sub>21;  $a: 4.411 \text{ \AA}$ ;  $c: 5.934 \text{ \AA}$ ) and there is no trace of any reflection either from the milling media or from an impurity phase. XRD pattern of 5 min milled sample looks completely different from that of the unmilled sample. It is found that cubic CdTe phase (ICSD- 93944, Sp. Gr. F43m,  $a: 6.4894 \text{ \AA}$ ) has been initiated as the major phase just after 5 min of milling with insignificant amount of elemental powders. Additional milling for 10 min results in complete formation of CdTe phase. With increasing milling time, peak broadening of all reflections increases owing to gradual decrease in particle size. It is also observed that peak positions of cubic CdTe phase shift toward lower scattering angle which

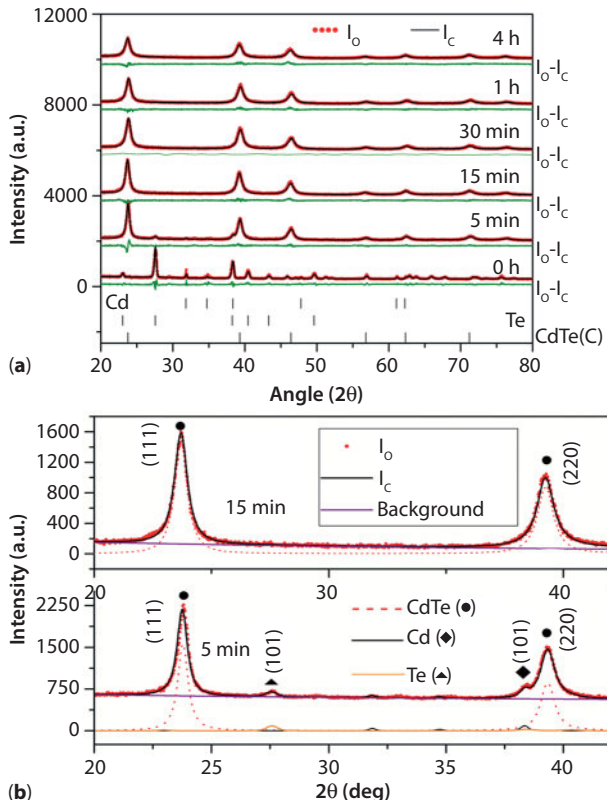


**Figure 12.14** (a) Output profile of Rietveld refinement of XRD data of unmilled and ball-milled stoichiometric powder mixture of Cd and Te for different durations. (b) Complete formation of stoichiometric CdTe nanocrystals after 15 min of milling. Dotted and continuous lines represent observed ( $I_o$ ) and computed ( $I_c$ ) patterns, respectively. ( $I_o - I_c$ ) represents residue of the refinement. [Reproduced with permission from [66] Copyright (2009) AIP Publication LLC.]

indicates that the lattice volume of cubic CdTe increases with increasing milling time [66].

It can be seen from Figure 12.14b that the cubic CdTe phase is formed just after 5 min of milling with (101) reflections from both the precursors—Cd and Te at  $2\theta \sim 38.0^\circ$  and  $\sim 27.5^\circ$ , respectively. It is found that these (101) reflections are the strongest ( $I/I_0 = 100$ ) for both Cd and Te, and they appear in very low intensity in the patterns which suggests that contributions of these phases are insignificant. After 15 min of milling, there is no trace of these peaks and stoichiometric cubic CdTe phase is formed without any contamination from either of the precursor powders.

### 12.10.3.2 Planar Defects Formed During the Synthesis of CdTe QDs

Shift in peak positions in XRD patterns governing primarily due to: (i) the presence of planar defects, (ii) change in lattice parameters, and (iii) long-range residual stresses [56, 67]. Very small change in peak positions may be overlooked if the XRD pattern is not analyzed properly. The Rietveld software MAUD [57] takes utmost care in determining different structure and microstructure parameters related to shifting in peak positions. As the crystallite size is very small the contribution of long-range residual parameters can be ignored. Change in lattice parameter of cubic CdTe phase would shift all peak positions either toward higher or lower scattering angle. In Figure 12.15a, it is noticed that (111) reflection of 4 h milled cubic CdTe phase shifts toward

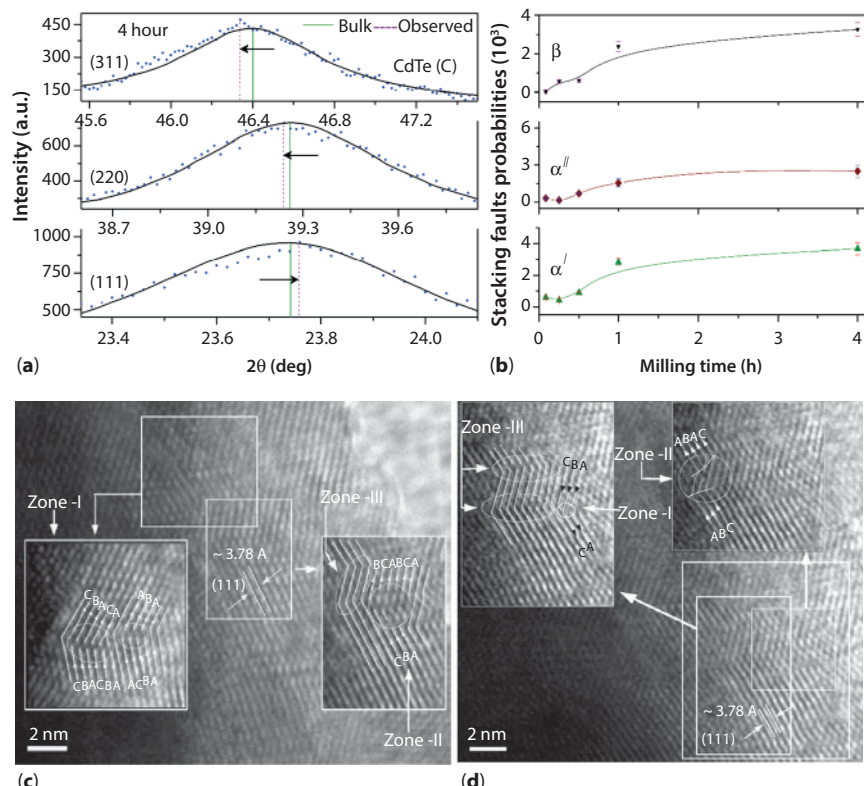


**Figure 12.15** (a) Shifting in peak positions of different lattice planes on either side of 4 h milled cubic CdTe nanocrystals with respect to its bulk counterpart. (b) Variation of intrinsic ( $\alpha'$ ), extrinsic ( $\alpha''$ ), and twin ( $\beta$ ) faults with increasing milling time in ball-milled CdTe. (c–d) HRTEM image showing the presence of planar defects in 4 h ball-milled cubic CdTe lattice. [Reproduced with permission from [66] Copyright (2009) AIP Publication LLC.]

higher Bragg angle, whereas (220) and (311) reflections shift toward lower Bragg angle compared to its bulk counterpart. Such type of peak shifting can only be accounted for only if the effect of intrinsic ( $\alpha'$ ), extrinsic ( $\alpha''$ ), and twin ( $\beta$ ) faults are taken care of. The quantitative analysis of such defects is analyzed in terms of stacking fault probabilities (occurring in 1000 lattice planes) with different milling time (shown in Figure 12.15b). It is evident from Figure 12.15b that initially values for all such faults are small and with increasing milling time increases gradually. Qualitative analysis of planar defects is verified in the HRTEM images (Figure 12.15c–d) by identifying the (111) plane of cubic CdTe phase. In zone I of Figure 12.15c, it is noticed that normal stacking sequence of lattice planes ABCA... is first twisted and thereafter the sequence is changed to A $\downarrow$ CA..., where  $\downarrow$  represents a fault in the normal stacking sequence. Hence, twin fault ( $\beta$ ) along with intrinsic fault ( $\alpha'$ ) occur at this zone. In zone II, normal stacking sequence ABCABC... becomes A $\downarrow$ C $\downarrow$ B $\downarrow$ A $\downarrow$ C $\downarrow$ B $\downarrow$ ... where three extra lattice layers are inserted in the normal stacking sequence and extrinsic ( $\alpha''$ ) stacking faults are generated. Multiple twin faults (twinning of lattice planes for more than once) are also noticed in zone III. In zone I of Figure 12.15d, normal stacking sequence ABCABC... changes to A $\downarrow$ CABC... by excluding a layer (say B) causing intrinsic stacking fault. In zone II, ABCABC... stacking sequence is twisted doubly and becomes AB $\downarrow$ A $\downarrow$ C.... causing thereby multiple extrinsic stacking faults.

#### *12.10.3.3 Variation in Coherently Diffracting Domain (Particle) Size and R.M.S Lattice Strain*

Variation in particle size and r.m.s. lattice strain are shown in Figure 12.16. Particle size of cubic CdTe decreases with increasing milling time due to the constant fracturing of grains by MA. From Figure 12.16, it is noticed that CdTe is formed with particle size  $\sim$ 20 nm and after 30 min of milling particle size reduces rapidly to 10 nm. Rate of reduction of particle size becomes slower after 30 min of milling and reaches  $\sim$ 5 nm after 4 h of milling. The variation in r.m.s lattice strain is completely reverse to that of the particle size. Initially, CdTe crystals are formed with minimum lattice strain and it rapidly increases till 30 min of milling. After this point the rate of increase in r.m.s. strain reduces up to 4 h of milling.

#### **12.10.4 Ternary CdZnS with Different Cd:Zn Ratio**

##### *12.10.4.1 X-ray Diffraction Study of $Cd_xZn_{1-x}S$ Nanocrystalline Semiconductors*

XRD patterns of  $Cd_xZn_{1-x}S$  with different Cd:Zn ratio just after their formation are shown in Figure 12.17. It is observed that all  $Cd_xZn_{1-x}S$  are

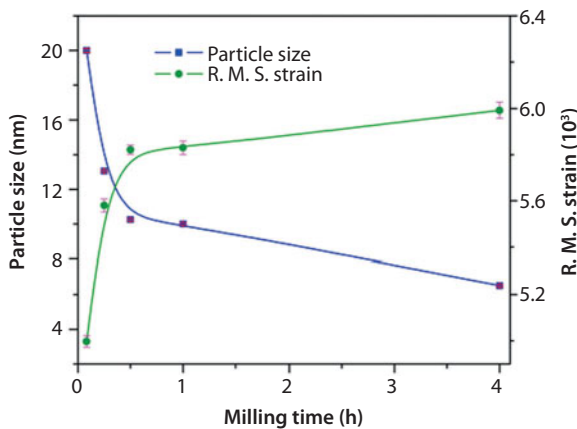


**Figure 12.16** Variations of particle size and r.m.s. lattice strain in ball-milled CdTe nanocrystals with time of milling. [Reproduced with permission from [66] Copyright (2009) AIP Publication LLC.]

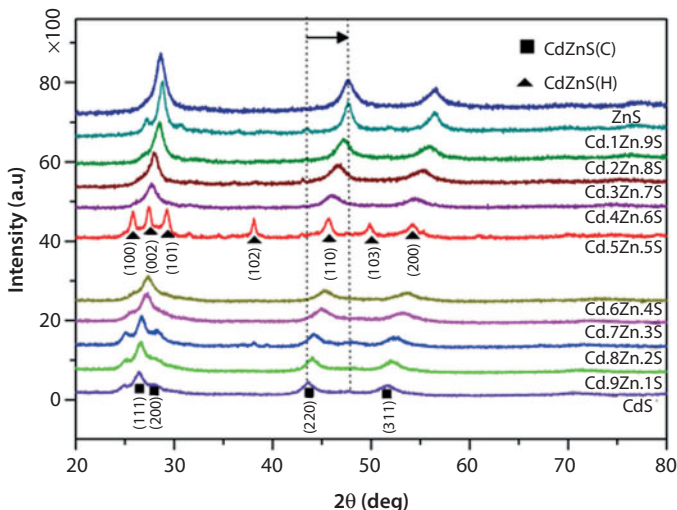


**Figure 12.17** XRD patterns of  $\text{Cd}_x\text{Zn}_{1-x}\text{S}$  (for different  $x$ ) just at their time of formation.  $\text{CdZnS(C)}$  and  $\text{CdZnS(H)}$  represent cubic and hexagonal phases, respectively. [Reproduced with permission from [68] © IOP Publishing. All rights reserved.]

formed through a mild explosive exothermal reaction inside the vial during mechanical alloying. Reflections of all the patterns are properly indexed using both zinc-blende (ZB) (620389-ICSD, Sp. Gr.  $F\bar{4}3m$ ,  $a: 5.434\text{\AA}$ ) and wurtzite (W) (ICSD 43598, Sp. Gr.  $P6_3mc$   $a = 3.95\text{\AA}$ ,  $c = 6.42\text{\AA}$ ) structures. Shifting in peak positions toward higher Bragg angle occurs with increasing Zn concentration. It suggests that with increasing Zn concentration

the lattice volume decreases. Relative phase abundances between ZB and W vary with varying  $x$ . The XRD pattern for  $x = 0.5$  looks somewhat different from the others, which is due to the maximum presence of wurtzite phase with larger crystallite size.  $\text{Cd}_{0.5}\text{Zn}_{0.5}\text{S}$  is formed in the smallest time of 25 min of milling having relatively larger crystallite size. It is very difficult, if not possible, to notice the presence of ZB and W phase in Cd rich and Zn-rich CdZnS, respectively, since almost all the reflections from these two phases are severely overlapped. It is indispensable to carry out the Rietveld refinement of the XRD patterns of ternary CdZnS alloys to quantitatively analyze the phase transformation kinetics between a major and a minor phase [68–71].

#### 12.10.4.2 Simultaneous Presence of Zinc-Blende and Wurtzite Phases

The XRD pattern of 0.5 h milled  $\text{Cd}_{0.5}\text{Zn}_{0.5}\text{S}$  appears to be consisted of solely hexagonal phase but Rietveld analysis confirms simultaneous presence of cubic phase also (Figure 12.18a). Intensity mismatch (shown in circles) is noticed when the pattern is tried to fit using only the hexagonal phase. The presence of minor cubic phase is thus ascertained in this sample.

Again, there is every possibility of overlooking the hexagonal phase in 15 h milled sample. It appears that single cubic phase is sufficient to fit the XRD pattern, but the intensity mismatch (shown in circles in Figure 12.18b) suggests simultaneous presence of minor hexagonal phase. Such small differences in the intensity may easily be overlooked unless the XRD pattern is analyzed properly by means of structure refinement procedure.

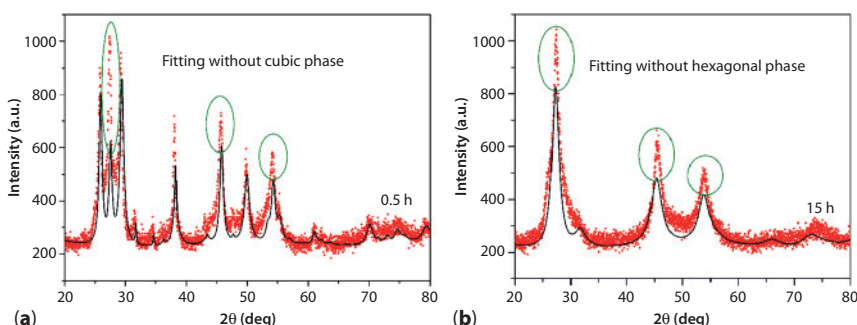


**Figure 12.18** Rietveld simulated XRD patterns of (a) 0.5h and (b) 15h milled  $\text{Cd}_{0.5}\text{Zn}_{0.5}\text{S}$  considering only hexagonal and cubic phases respectively. [Reproduced with permission from [68] © IOP Publishing. All rights reserved.]

#### 12.10.4.3 Variation in Lattice Parameters in $Cd_xZn_{1-x}S$

The lattice parameters of both cubic and hexagonal  $Cd_xZn_{1-x}S$  phases decrease almost linearly with same rate with increasing Zn concentrations (Figure 12.19). This decrease in lattice parameters is due to ionic radius mismatch of  $Cd^{2+}$  (ionic radius = 0.95 Å) and  $Zn^{2+}$  (ionic radius = 0.75 Å). This decrease in lattice parameters resembles with the substitutional solid solution alloy obeying Vegard's law.

#### 12.10.4.4 Variation of Formation Time in $Cd_xZn_{1-x}S$

The time of formation of  $Cd_xZn_{1-x}S$  with an exothermic reaction is found to vary with the concentration of Zn into the lattice. Figure 12.20 depicts that the time of formation of  $Cd_xZn_{1-x}S$  decreases linearly from 80 min. to a minimum of 25 min as the concentration of Zn increases from 0.1 to 0.5 mol fraction and afterward the formation time increases almost linearly up to 160 min when Zn concentration reaches up to 0.9. The lowest formation time for equimolar  $Cd_{0.5}Zn_{0.5}S$  may be ascribed to the most feasible substitutional solid solution with the lowest possible energy configuration since both  $Cd^{2+}$  and  $Zn^{2+}$  ions remain in equimolar ratio with same crystal structure (hcp), same valence state and same electron affinity just like an ideal 'Hume-Rothery' alloy [72].

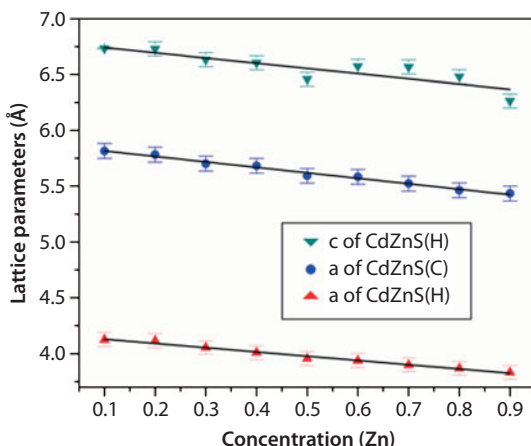


**Figure 12.19** Variation of lattice parameters of cubic and hexagonal ternary  $Cd_xZn_{1-x}S$  as a function of increasing Zn concentration. [Reproduced with permission from [68] © IOP Publishing. All rights reserved.]

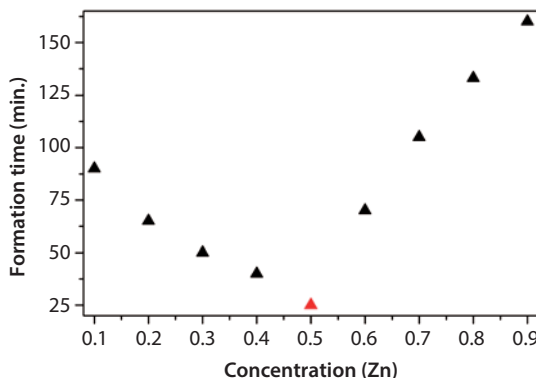


**Figure 12.20** Variation in time of formation of ternary  $\text{Cd}_x\text{Zn}_{1-x}\text{S}$  with different concentrations of Zn. [Reproduced with permission from [68] © IOP Publishing. All rights reserved.]

#### 12.10.4.5 Variation of Mol Fraction of Cubic and Hexagonal Phases

Variation of mol fraction obtained from Rietveld analysis of both cubic and hexagonal phases with different Cd concentrations is shown in Figure 12.21. This variation in mol fraction reflects that except at the equimolar ratio starting from 0.1 Cd concentration up to 0.7 Cd concentration, cubic phase always remains as the major phase but the situation becomes reverse for 0.8 and 0.9 Cd concentration. At the equimolar ratio, it is seen that the value of mol fraction of hexagonal phase is the maximum which suggests that the hexagonal phase is more stable in  $\text{Cd}_{0.5}\text{Zn}_{0.5}\text{S}$  and takes minimum time of formation.

#### 12.10.4.6 Presence of Planar Defects in $\text{Cd}_x\text{Zn}_{1-x}\text{S}$

The presence of different kinds of stacking faults is clearly evidenced in Figure 12.22a–b. Some zones in the lattice of these QDs contain high density of planar defects. One such zone is marked in HRTEM image of  $\text{Cd}_{0.5}\text{Zn}_{0.5}\text{S}$  QDs (shown in Figure 12.22a). Close observation into this zone reveals that the lattice planes are mutilated and distorted possessing high density of stacking faults. Figure 12.22b represents the HRTEM image of 15 h ball-milled  $\text{Cd}_{0.8}\text{Zn}_{0.2}\text{S}$  lattice. The atomic layers in this image are from (200) plane of cubic phase as identified from the interplanar spacing,  $d_{200} \sim 2.70\text{\AA}$ . Careful observation of this image confirms the presence of intrinsic ( $\alpha'$ ), extrinsic ( $\alpha''$ ) and twin ( $\beta$ ) faults even in a small area of the sample. In zones I and V, it is seen that the lattice planes are twinned multiple times along some imaginary mirror planes resulting in multiple twin fault in the region. In zone II, single twin fault is generated as the lattice planes there twisted for once along a mirror plane. In zone III, it

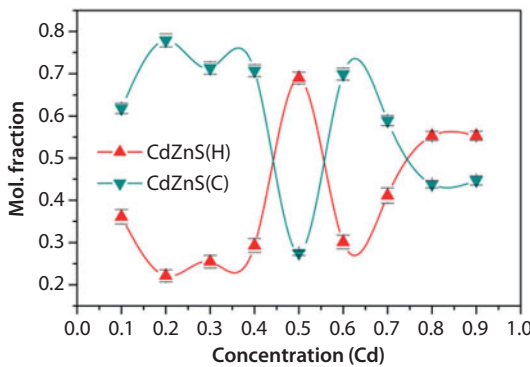


**Figure 12.21** Variation of mol fraction of cubic and hexagonal phases of ternary  $\text{Cd}_x\text{Zn}_{1-x}\text{S}$  at their time of formation with respect to concentration of Cd. [Reproduced with permission from [68] © IOP Publishing. All rights reserved.]

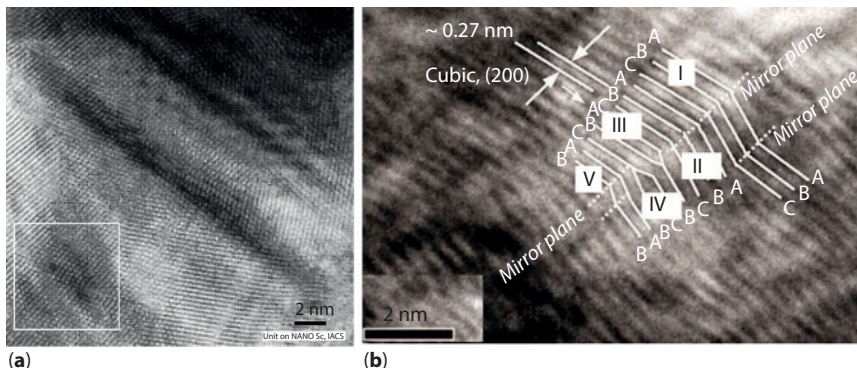
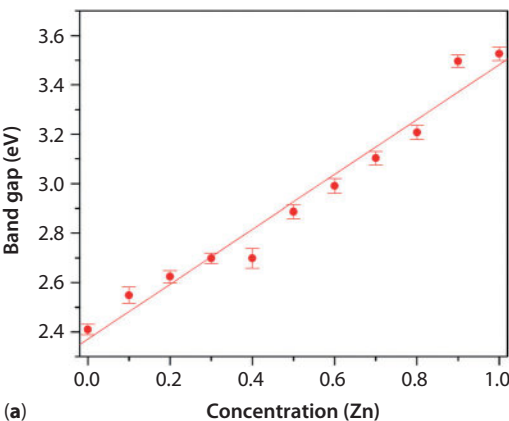


**Figure 12.22** HRTEM image revealing high density of planar defects in (a)  $\text{Cd}_{0.5}\text{Zn}_{0.5}\text{S}$  [Reproduced with permission from [68] © IOP Publishing. All rights reserved.] and (b) distorted lattice planes of cubic (200) of  $\text{Cd}_{0.8}\text{Zn}_{0.2}\text{S}$  forming intrinsic, extrinsic and twin faults. [Reproduced with permission from Elsevier.]

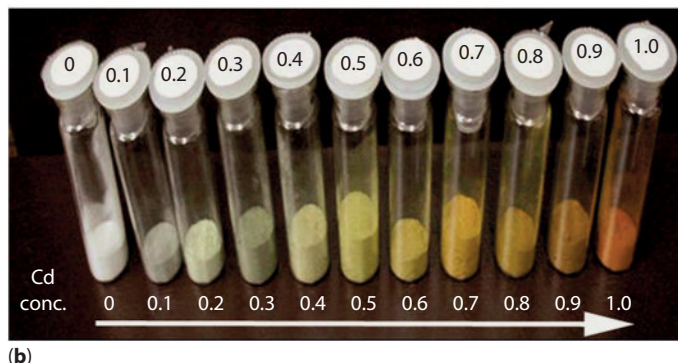
is noticed that two successive lattice planes are overlapped into a single plane which is analogous to the missing of a layer in the normal stacking sequence. Hence, it causes stacking fault of intrinsic in nature. This situation is completely reverse in zone IV, where it is observed that a single atomic layer is divided into two parallel planes which is similar to inclusion of a plane in the normal stacking sequence, termed as extrinsic stacking fault. Thus, it is observed that QDs synthesized by MA contain significant amount of stacking faults which may bring about changes in different properties of the materials. Therefore, it is of utmost importance to analyze these planar defects both qualitatively and quantitatively.

#### 12.10.4.7 Variation of Optical Band Gap in $Cd_xZn_{1-x}S$ with Different Cd:Zn Ratio

Variation of optical BG of  $Cd_xZn_{1-x}S$  as obtained from the absorption spectra of corresponding samples is shown in Figure 12.23a. Variation of optical BG of  $Cd_xZn_{1-x}S$  as a function of Zn concentration shows almost linear increase in BG with increase in Zn concentration from  $\sim 2.43$  eV (for Zn = 0, i.e., x = 1; which suggests pure CdS) up to 3.65 eV (for Zn = 1, i.e. x = 0; which suggests pure ZnS). This graph suggests that the optical BG can be adjusted by varying the molar ratio of Cd and Zn only and thus ‘tailor made’ materials can be synthesized having specific BG of such system. With this change in optical BG the color of the sample also changes (Figure 12.23b). This change in color shows to vary from whitish to reddish as Cd concentration is gradually increased [68].



(a)



(b)

**Figure 12.23** (a) Variation of BG as a function concentration of Zn and (b) change in color with increasing concentration of Cd in  $Cd_xZn_{1-x}S$ . [Reproduced with permission from [68] © IOP Publishing. All rights reserved.]

## 12.11 Conclusions

In the present study synthesis of some binary and ternary chalcogenide QDs by MA is discussed. Synthesis of nanomaterials by MA requires optimization of some important variables associated with the planetary ball mill for effective milling of the samples and also to reduce the possibility of contamination. ZnS, ZnTe, CdTe, and  $\text{Cd}_x\text{Zn}_{1-x}\text{S}$  (for different  $x$ ) QDs, without any impurity either from the milling media or from the atmosphere, have been successfully prepared by MA. To the best of our knowledge, reported time of formation for these nanocrystalline semiconductors are the quickest. To better understand a material, it is incumbent to analyze different structure/microstructure parameters of it as different physical, mechanical, chemical, etc. properties are strongly correlated with these parameters. Rietveld method of powder structure refinement plays a pivotal role in ascertaining these parameters. A successful application of this powerful technique has been well discussed in this chapter. It is found that Te-based QDs are formed in single cubic phase and S based QDs are formed in both cubic and hexagonal phases. In case of ZnS, the hexagonal phase transforms to cubic phase with increasing milling time and converts completely into cubic phase after 10 h of milling. However, in case of all  $\text{Cd}_x\text{Zn}_{1-x}\text{S}$ , coexistence of cubic and hexagonal phases persists (maintaining some phase transformation kinetics with changing milling time) for higher milling time also. Another salient feature noticed in all the QDs synthesized by MA is stacking fault of different kinds of the crystal lattices. Being a high-energy method of formation, planetary ball milling introduces heavy plastic deformation in the crystallites due to the grinding and rewelding mechanism. Therefore, the presence of planar defects is highly probable in the samples. Controlling these microstructure parameters materials with desired properties can be synthesized. Rietveld refinement method allows us to quantify the stacking faults generated inside the lattice in terms of probabilities which has been discussed in elaborative manner.

## References

1. Henglein, A., Small-particle research: physicochemical properties of extremely small colloidal metal and semiconductor particles. *Chem. Rev.*, 89, 1861, 1989.
2. Kuchibhatla, S., Karakoti, A.S., Bera, D., Seal, S., One dimensional nanostructured materials. *Prog. Mater. Sci.*, 52, 699, 2007.

3. Bera, D., Qian, L., Tseng, T.K., Holloway, P.H., Quantum dots and their multimodal applications: a review. *Materials*, 3, 2260, 2010.
4. Dyakonov, M. I. (Ed.), *Spin Physics in semiconductors*, Chap. 4, Springer, Berlin, 2008.
5. Warburton, R.J., Self-assembled semiconductor quantum dots. *Contemporary Phys.*, 43, 351, 2002.
6. Ekimov, A.I., Onushchenko, A.A., Tzehomskii, A.V., Exciton absorption by copper (I) chloride crystals in a glassy matrix. *Fiz. Khim. Stekla.*, 6, 511, 1980.
7. Henglein, A., Photo-degradation and fluorescence of colloidal-cadmium sulfide in aqueous solution. *Phy. Chem.*, 86, 301, 1982.
8. Nitzan, A., Brus, L.E., Theoretical model for enhanced photochemistry on rough surfaces. *J. Chem. Phys.*, 75, 2205, 1981.
9. Efros, A.L., Rosen, M., The electronic structure of semiconductor nanocrystals. *Annu. Rev. Mater Sci.*, 30, 475, 2000.
10. Stier, O., *Electronic and Optical Properties of Quantum Dots and Wires*, Wissenschaft & Technik Verlag, 2000.
11. Walter, P., Welcomme, E., Hallegot, P., Zaluzec, N.J., Deeb, C., Castaing, J., Veyssiere, P., Breniaux, R., Leveque, J.L., Tsoucaris, G., Early Use of PbS Nanotechnology for an ancient hair dyeing formula. *Nano Lett.*, 6, 2215, 2006.
12. Effros, A.L., Effros, A.L., Interband absorption of light in a semiconductor sphere. *Sov. Phys. Semicond.*, 16, 772, 1982.
13. Ekimov, A.I., Onushchenko, A.A., Quantum size-effect in the optical-spectra of semiconductor micro-crystals. *Sov. Phys. Semicond.*, 16, 775, 1982.
14. Shklovskii, B.I., Efros, A.L., Interband absorption of light in heavily doped semiconductors. *Sov. Phys.-JETP*, 59, 1343, 1970.
15. Reed, M.A., Randall, J.N., Luscombe, J.H., Frensel, W.R., Aggarwal, R.J., Matyi, R.J., Moore, T.M., Wetsel, A.E., Quantum dot resonant tunneling spectroscopy. *Adv. Solid State Phys.*, 29, 267, 1989.
16. Banyai, L., Asymptotic biexciton “binding energy” in quantum dots. *Phys. Rev. B*, 39, 8022, 1989.
17. Spanhel, L., Haase, M., Weller, H., Henglein, A., Photochemistry of colloidal semiconductors. 20. Surface modification and stability of strong luminescing CdS particles. *J. Am. Chem. Soc.*, 109, 5649, 1987.
18. Murray, C.B., Norris, D.J., Bawendi, M.G., Synthesis and characterization of nearly monodisperse CdE (E = sulfur, selenium, tellurium) semiconductor nanocrystallites. *J. Am. Chem. Soc.*, 115, 8706, 1993.
19. Grieser, F., Furlong, D.N., Scoberg, D., Ichinose, I., Kimizuka, N., Kunitake, T., Size-quantised semiconductor cadmium chalcogenide particles in Langmuir-Blodgett films. *J. Chem. Soc. Faraday Trans.*, 88, 2207, 1992.
20. Alivisatos, A.P., Semiconductor clusters, nanocrystals, and quantum dots. *Science*, 271, 933, 1996.
21. Klimov, V.I., Mikhailovsky, A.A., Xu, S., Malko, A., Hollingsworth, J.A., Leatherdale, C.A., Eisler, H.J., Bawendi, M.G., Optical gain and stimulated emission in nanocrystal quantum dots. *Science*, 290, 314, 2000.

22. Artemyev, M.V., Woggon, U., Wannemacher, R., Jaschinski, H., Langbein, W., Light trapped in a photonic dot: Microspheres act as a cavity for quantum dot emission. *Nano Lett.*, 1, 309, 2001.
23. Coe-Sullivan, S., Optoelectronics: quantum dot developments. *Nat. Photonics*, 3, 315, 2009.
24. Schmid, G. (Ed.) *Nanoparticles: From Theory to Application*, pp. 3–42, Second Edition, WILEY-VCH Verlag GmbH & Co. KGaA, Weinheim, 2010.
25. Pradeep, T., *NANO: The Essentials*, pp. 179–200, Tata Mc-Graw Hill Publishing Company Ltd, 2007.
26. Yoffe, A.D., Low-dimensional systems: quantum size effects and electronic properties of semiconductor microcrystallites (zero-dimensional systems) and quasi-two-dimensional systems. *Adv. Phys.*, 51, 799, 2002.
27. Yu, P.Y. and Cardona M., *Fundamentals of Semiconductors*, Springer-Verlag, 1999.
28. Tannoudji, C.C., Diu, B and Laloe F., *Quantum Mechanics*, 1<sup>st</sup> ed., John Wiley & Sons, 1997.
29. Brus, L. E., A simple model for the ionization potential, electron affinity, and aqueous redox potentials of small semiconductor crystallites. *J. Chem. Phys.*, 79, 5566, 1983.
30. Bottom-up and top-down approaches in nanotechnology, [www.gitam.edu/eresource/nano/NANOTECHNOLOGY/role\\_of\\_bottomup\\_and\\_topdown\\_a.htm](http://www.gitam.edu/eresource/nano/NANOTECHNOLOGY/role_of_bottomup_and_topdown_a.htm) 2015
31. Rogach, A.L. (Ed.), *Semiconductor Nanocrystal Quantum Dots*, pp. 35–77, SpringerWien, New York, 2008.
32. Yeh, C.Y., Lu, Z.W., Froyen, S., Zunger, A., Zinc-blende-wurtzite polytypism in semiconductors. *Phys. Rev. B*, 46, 10086, 1992.
33. Chapin, D.M., Fuller, C.S., Pearson, G.L., A new silicon p-n junction photocell for converting solar radiation into electrical power. *J. Appl. Phys.*, 25, 676, 1954.
34. Bukowski, T. J.; Simmons, J.H., Quantum dot research: current state and future prospects. Critical reviews in solid state and materials. *Sciences*, 27, 119, 2002.
35. Peng, C.W., Li, Y., Application of quantum dots-based biotechnology in cancer diagnosis: current status and future perspectives. *J. Nanomater.*, 2010, 1, 2010.
36. Jemal, A., Siegel, R., Ward, E., Hao, Y., Xu, J., Thun, M.J., Cancer statistics, 2009. *CA: A Cancer J. Clin.*, 59, 225, 2009.
37. Suryanarayana, C., Mechanical alloying and milling. *Prog. Mater. Sci.*, 46, 1, 2001.
38. Suryanarayana, C. (Ed.), *Non-equilibrium Processing of Materials*, Pergamon Press, Oxford, 1999.
39. Koch, C. C., The synthesis and structure of nanocrystalline materials produced by Mechanical attrition: A review. *Nanostruct. Mater.*, 2, 109, 1993.
40. Fritsch Planetary pulversiette-5 classic line with 4 grinding bowl fasteners <http://www.fritsch-milling.com/> 2015.

41. Young, R.A., *The Rietveld Method*, IUCr, Oxford University Press, 1996.
42. Rietveld, H.M., Line profiles of neutron powder-diffraction peaks for structure refinement. *Acta Crystallogr.*, 22, 151, 1967.
43. Rietveld, H.M., A profile refinement method for nuclear and magnetic structures. *J. Appl. Crystallogr.*, 2, 65, 1969.
44. Black, D.R., Windover, D., Henins, A., Gil, D., Filliben, J., Cline, J.P., Standard reference material 640d for x-ray metrology, *Proceedings of the 58th Denver x-ray conference*. 172–179, 2009.
45. Caglioti, G., Paoletti, A., Ricci, F.P., Choice of collimators for a crystal spectrometer for neutron diffraction. *Nucl. Instrum.*, 3, 223, 1958.
46. Young, R.A., Mackie, P.E., Von Dreele, R.B., Application of the pattern-fitting structure-refinement method of X-ray powder diffractometer patterns. *J. Appl. Cryst.*, 10, 262, 1977.
47. Hill, R.J., Howard, C.J., Hunter, B.A., A computer program for rietveld analysis of fixed wavelength x-ray and neutron powder diffraction patterns in austalian atomic energy commission (now ANSTO) Rept. No. M112 (Lucas Heights Research Laboratories, New South Wales, Australia, 1995).
48. Lutterotti, L., Ceccato, R., Maschio, R.D., Pagani, E., Quantitative analysis of silicate glass in ceramic materials by the Rietveld method. *Mater. Sci. Forum*, 278–281, 87, 1998.
49. Mittemeijer, E.J., Scardi, P. (Ed.), *Diffraction Analysis of the Microstructure of Materials*, Springer-Verlag, Germany, 2004.
50. Langford, J.I., Accuracy in powder diffraction. *NBS Special Publication*, 567, 255, 1980.
51. Balzar, D., Ledbetter, H., Voigt-function modeling in Fourier analysis of size- and strain-broadened X-ray diffraction peaks. *J. Appl. Crystallogr.*, 26, 97, 1993.
52. Krill, C.E., Birringer, R., Estimating grain-size distributions in nanocrystalline materials from X-ray diffraction profile analysis. *Philos. Mag. A*, 77, 621, 1998.
53. Scardi, P., Leoni, M., Diffraction line profiles from polydisperse crystalline systems. *Acta. Cryst. A*, 57, 604, 2001.
54. Popa, N.C., Balzar, D., An analytical approximation for a size-broadened profile given by the lognormal and gamma distributions. *J. Appl. Cryst.*, 35, 338, 2002.
55. Lutterotti, L., Gialanella, S., X-ray diffraction characterization of heavily deformed metallic specimens. *Acta. Mater.*, 46, 101, 1998.
56. Warren, B.E., *X-ray Diffraction*, Addison-Wesley, 1969.
57. Lutterotti, L., Program Maud, <http://maud.radiographema.com/> 2015.
58. Billinge, S.J.L., The atomic pair distribution function: past and present. *Z. Kristallogr.*, 219, 117, 2004.
59. Tsuzuki, T., McCormick, P.G., Mechanochemical synthesis of metal sulphide nanoparticles. *Nanostruct. Mater.*, 12, 75, 1999.

60. Tan, G.L., Hommerich, U., Temple, D., Wu, N.Q., Zheng, J.G., Loutts, G., Synthesis and optical characterization of CdTe nanocrystals prepared by ball milling process. *Scripta Mater.*, 48, 1469, 2003.
61. Campos, C.E.M., de Lima, J.C., Grandi, T.A., Höhn, H., Synthesis of nanocrystalline zinc blende ZnTe by mechanical alloying. *J. Non-Cryst. Solids*, 354, 3503, 2008.
62. Tsuzuki, T., McCormick, P.G., Synthesis of CdS quantum dots by mechano-chemical reaction. *Appl. Phys. A*, 65, 607, 1997.
63. Dutková, E., Baláž, P., Pourghahramani, P., Nguyen, A.V., Šepelák, V., Feldhoff, A., Kováč, J., Šatka, A., Mechanochemical solid state synthesis and characterization of  $\text{Cd}_x\text{Zn}_{1-x}\text{S}$  nanocrystals. *Solid State Ionics*, 179, 1242, 2008.
64. Patra, S., Satpati, B., Pradhan, S.K., Microstructure characterization of mechanically synthesized ZnS quantum dots. *J. Appl. Phys.*, 106, 034313, 2009.
65. Patra, S., Pradhan, S.K., Microstructural, optical and quantum confinement effect study of mechanically synthesized ZnTe quantum dots. *Acta Mater.*, 60, 131, 2012.
66. Patra, S., Pradhan, S.K., Micorstructure and optical characterization of CdTe quantum dots synthesized in record minimum time. *J. Appl. Phys.*, 108, 083515, 2010.
67. Cohen, J.B., Hilliard, J. E. (Ed.), *Local Atomic Arrangements Studied by X-Ray Diffraction*, Gordon and Breach, New York, 1966.
68. Sain, S., Patra, S., Pradhan, S.K., Microstructure and optical band-gap of mechano-synthesized  $\text{Cd}_x\text{Zn}_{1-x}\text{S}$  quantum dots. *J. Phys. D: Appl. Phys.*, 44, 075101, 2011.
69. Sain, S., Kar, A., Patra, A., Pradhan, S.K., Microstructure and photoluminescence properties of ternary  $\text{Cd}_{0.2}\text{Zn}_{0.8}\text{S}$  quantum dots synthesized by mechanical alloying. *J. Nanopart. Res.*, 16, 2673, 2014.
70. Sain, S., Patra, S., Pradhan, S.K., Quickest ever single-step mechanosynthesis of  $\text{Cd}_{0.5}\text{Zn}_{0.5}\text{S}$  quantum dots: Nanostructure and optical characterizations. *Mater. Res. Bull.*, 47, 1062, 2012.
71. Sain, S., Pradhan, S.K., Mechanochemical solid state synthesis of  $(\text{Cd}_{0.8}\text{Zn}_{0.2})\text{S}$  quantum dots: Microstructure and optical characterizations. *J. Alloys. Compd.*, 509, 4176, 2011.
72. Rothery, H.W., *Atomic Theory for Students of Metallurgy*, vol. 3, London: Institute of Metals, 1960.



# Advances in Functional Luminescent Materials and Phosphors

Radhaballabh Debnath

*School of Laser Science and Engineering, Jadavpur University, Kolkata, India*

---

## Abstract

Efficient luminescent materials are the fundamental component of all commercially used light-emitting devices like lasers, fluorescent lamps, display screens, imager, scintillators solar concentrators, etc. A luminescent material whether it is a bulk solid (CdS, CdSe) or luminescent ions/atoms or molecules doped guest–host structure, its luminescence efficiency largely depends on various physical and chemical factors, namely band structure, phonon structure of the material, particle size, crystal field strength surrounding the emitting species, purity of the ionic state in the case of ionic luminescent centers, presence of sensitizer, efficiency of energy transfer, etc. In this chapter, some of these basic concepts are discussed with special reference to preparation and characterization of a number of practical luminescent materials like: phosphors for X-ray imaging, CRT/plasma display, CFL/LED lamps, and others like luminescent solids for light energy upconversion, LEDs for display, and the materials for use as laser source.

**Keywords:** Luminescent materials, bulk solid, guest–host structure, crystal field strength, phonon structure, energy transfer, laser source

## 13.1 Introduction

Luminescent materials are those which emit light upon excitation by some external energy. Although in most of the cases, it is the radiation energy which is used for excitation, there are cases where thermal or electrical

---

*Corresponding author:* drdebnathr@gmail.com

---

Ashutosh Tiwari *et al.* (eds.) Advanced Magnetic and Optical Materials, (425–472) © 2017  
Scrivener Publishing LLC

energy is also used for such excitation. Depending on the nature of the emitting state of the luminescent center, duration of such light emission after cessation of excitation, may be very short (~few nanoseconds) or relatively longer (from few milli to micro seconds) and the emission is classified [1, 2] accordingly either as fluorescence or phosphorescence. Generally solid-state luminescent materials are referred to as phosphor. Luminescent bulk solids with suitable band gap structure, atoms/ions doped luminescent solids (crystals or glasses) and intrinsic defect related luminescent center containing solids, are normally the potential members of this group. A prototype band-gap transition phosphor is ZnS, which was first used as phosphor in early television picture tubes. Later a large number of chalcogenide band-gap transition phosphors (CdS, CdSe, GaAs, InGaAs, etc.) are developed and are being used for different applications. Various transition metal ions like  $\text{Cu}^+$ ,  $\text{Sn}^{2+}$ ,  $\text{Pb}^{2+}$ ,  $\text{Bi}^{2+}$ ,  $\text{Cr}^{3+}$  and rare earth ions like  $\text{Eu}^{2+}$ ,  $\text{Eu}^{3+}$ ,  $\text{Tb}^{3+}$ ,  $\text{Er}^{3+}$ ,  $\text{Ho}^{3+}$ ,  $\text{Tm}^{3+}$ ,  $\text{Sm}^{3+}$ , etc. when incorporated in appropriate solids are known to luminescence efficiently and hence they belong to a group of very efficient high quality visible light-emitting phosphors.

Luminescence efficiency of a phosphor depends, on various physical and chemical factors: namely phonon structure of the host [3–5], crystal field strength surrounding the emitting center [6–10] (for luminescent ion doped phosphor), purity of the ionic state of the activator [11–13], presence of sensitizer [14, 15] efficiency of energy transfer [9, 10, 16], particle size [17–19], presence of additives [20, 21], etc. Research on phosphors and their applications is thus an interdisciplinary subject of science and technology. While the science of development and synthesis of phosphors are the subjects of physical and inorganic chemistry, elucidations of mechanisms of their luminescence require knowledge of spectroscopy and solid-state physics.

Recently, many researchers have focused on preparation and studies of luminescent properties of nano-scale phosphors because of their expected better performance compared to those of their respective micron size counterparts.

As regards to the areas of applications of phosphors, they are numerous and diverse. Efficient phosphors are the central component of a number of functional devices such as fluorescent lamps, flat panel displays, and electroluminescent display panels, X-ray screens, scintillators, luminous paints, biomarkers, and many others.

In the present chapter, preparation and properties of some of these phosphors are discussed with special reference to some of the practical phosphors used for X-ray imaging, CFL/LED lamps, display screens, laser generation, light energy upconversion, and bio-labeling.

## 13.2 Some Theoretical Aspects of the Processes of Light Absorption/Emission by Matter

### 13.2.1 Electric Dipole Induced Electronic Transition Probability in a System

Electric/magnetic dipole mediated light absorption transition of an absorbing center, is induced due to the perturbation of the energy of the latter by the electromagnetic field of the incident radiation and the probability of such light absorption transition may be written as:

$$W_{nm} = \left( \frac{4\pi^3}{3\epsilon_0 h^2} \right) \rho(\nu_{nm}) |M_{nm}|^2 \quad (13.1)$$

where  $\epsilon_0$  is the dielectric constant of the medium,  $\rho(\nu_{nm})$  is the density of the incident photon of frequency  $\nu_{nm}$ , and  $M_{nm}$  is the integrated electric dipole moment of the system and is given by the expression  $M_{nm} = \int \Psi_n(\Sigma r_i) \Psi_m^* d\tau$ ;  $r_i$  being the position vector of the electron from the center of the system at different instant of time ( $d\tau$ );  $\Psi_n$  and  $\Psi_m^*$  are the wavefunctions of the ground (n) and the excited state (m) of the concerned absorption transition.

The energy of the photon absorbed or emitted due to the transition  $n \leftrightarrow m$  is  $(E_m - E_n) = hv$  where  $E_m > E_n$  and  $v$  is the frequency of light ( $v = c/\lambda$ ). The rate of absorption and emission of photons by an ensemble of 'N' number of active centers can be expressed in terms of transition probability per second. The rate of absorption in a radiation field of energy density  $\rho(\nu_{nm})$ , making the transition from  $n$  to  $m$ , is given by:

$$\text{Rate of absorption} = B_{n \rightarrow m} N_n \rho(\nu_{nm}) \quad (13.2)$$

Here  $N_n$  is the number of active centers in the state 'n' at any instant of time and  $B_{n \rightarrow m}$  is the transition probability or Einstein's  $B$ -coefficient for absorption.

So it is clear from the above that Einstein's  $B$ -coefficient of absorption has the value:

$$B_{n \rightarrow m} = \left( \frac{4\pi^3}{3\epsilon_0 h^2 N_n} \right) |M_{nm}|^2 \quad (13.3)$$

The rate of emission of light by the centers, on the other hand, is the sum of the rate of spontaneous emission and that of the stimulated emission, i.e.

$$\text{Rate of emission} = A_{m \rightarrow n} N_m + B_{m \rightarrow n} \rho(v_{nm}) N_m \quad (13.4)$$

Here  $N_m$  is the number of active centers in the excited state ' $m$ ' at any instant of time and  $A_{m \rightarrow n}$  is the Einstein's coefficient for spontaneous emission and  $B_{m \rightarrow n}$  is the Einstein's coefficient for stimulated emission. At equilibrium condition, the rate of absorption and the rate of emission by the active centers of the two states should be equal.

$$B_{n \rightarrow m} N_n \rho(v_{nm}) = A_{m \rightarrow n} N_m + B_{m \rightarrow n} \rho(v_{nm}) N_m \quad (13.5)$$

$B_{m \rightarrow n}$ , the Einstein's coefficient for stimulated emission being equal to  $B_{n \rightarrow m}$  the Einstein's coefficient of induced absorption, one can rewrite Equation (13.5) as:

$$A_{m \rightarrow n} N_m = B_{n \rightarrow m} \rho(v_{nm}) [N_n - N_m],$$

$$\text{therefore, } \rho(v_{nm}) = \frac{A_{m \rightarrow n} N_m}{B_{n \rightarrow m} [N_n - N_m]} = \frac{A_{m \rightarrow n}}{B_{n \rightarrow m} \left[ \frac{N_n}{N_m} - 1 \right]} \quad (13.6)$$

Taking Boltzmann distribution function of the system into consideration, one has,  $N_m = N_n e^{-hv/kT}$  or  $(N_n/N_m) = e^{hv/kT}$ , comparing Equation (13.6) with the Plank's equation for distribution of energy density of emission of radiation by the system at temperature T,

$$\rho(v) = 8\pi h v^3 / c^3 [1/(e^{hv/kT} - 1)] \quad (13.7)$$

it can be easily shown that

$$A_{m \rightarrow n} = [8\pi h v^3 / c^3] B_{n \rightarrow m} \quad (13.8)$$

Therefore, the probability of optical absorption, and that of the spontaneous emission between the states  $m$  and  $n$  are interrelated. Putting the value of  $B_{n \rightarrow m} = (\pi/3\varepsilon_0 c h^2) \rho(v_{nm}) |M_{nm}|^2$ , in Equation (13.8),  $A_{m \rightarrow n}$ , can be expressed in terms of integrated electric dipole moment of the system:

$$\begin{aligned}
 A_{m \rightarrow n} &= \left( \frac{8\pi h\nu^3}{c^3} \right) \left( \frac{4\pi^3}{3\epsilon_0 h^2 N_n} \right) |M_{nm}|^2 \\
 &= \left( \frac{32\pi^4 \nu^3}{3\epsilon_0 h c^3 N_n} \right) |M_{nm}|^2
 \end{aligned} \tag{13.9}$$

The oscillator strength of an optical center is often used in order to represent the strength of light absorption and emission of a center. It is defined by the following equation as a dimensionless quantity.

$$f_m = (8\pi^2 m \nu / 3 h e^2) |M_{nm}|^2$$

The other emission parameter namely the radiative lifetime  $\tau_{mn}$ , which is defined as the inverse of the spontaneous emission probability ( $A_{m \rightarrow n}$ ), can be written as:

$$\tau_{mn}^{-1} = A_{m \rightarrow n} \tag{13.10}$$

If there are several terminal states of the emission transition and the relaxation is controlled only by spontaneous emission processes, the decay rate of the emitting level is determined by the sum of the transition probabilities to all the states involved, i.e.

$$\tau_{mn}^{-1} = \sum A_{m \rightarrow n} \tag{13.11}$$

### 13.2.2 Optical Parameters of an Optical Center Doped in a Host

So far we have discussed the light absorption and emission properties of an optical center (atom or ion or molecule) when it is in its free state, i.e. when it is not under the influence of any electric or magnetic field. In the case of an optical center doped in a solid/ liquid host, the former is influenced by the surrounding electric or magnetic field of the host that is generated in the medium due to polarization of the host's structure. As a result, the optical properties of the optical centers (particularly in case of molecular and ionic centers) suffer changes from those of the centre in its free state. The velocity of light propagating through the host also gets reduced to  $c/n$ , where 'n' is the refractive index of the medium.

The Hamiltonian for such a system of active centre -host combination, is represented by:

$$H = H_0 + H_{CF} \tag{13.12}$$

where  $H_0$  is the total Hamiltonian of centre in free state and  $H_{CF}$  is the energy of interaction between the center and the crystal field of the host. In the case of a transition metal ion center, the value of  $H_{CF}$  in some cases may be so high that it can alter even the energy level scheme of the centre. However, in the case of an atom which is electrically neutral or a rare earth ion in which the optically active 4f electrons are shielded by the electrons of its outer 5p and 6s orbitals, the energy of interaction between the center and the surrounding field of the host is very weak and  $H_{CF}$  in that case is taken as a perturbation term. Judd and Ofelt [6, 7] for the first time, independently developed theoretical expression for electric dipole mediated absorption strength of such rare earth ion in a host. For an electric dipole transition from an initial  $(S, L)J$  state to the final  $(S', L')J'$  state of a rare-earth ion in a host, the electric dipole absorption strength is given by the expression:

$$S_{Cal}^{Ed}(J \rightarrow J') = \sum_{t=2,4,6} \Omega_t \left| \langle (S, L)J | U^t | (S', L')J' \rangle \right|^2 \quad (3.13)$$

where,  $\langle (S, L)J | U^t | (S', L')J' \rangle$  is the reduced matrix element of the irreducible tensor operator of rank 't' calculated in the intermediate coupling approximation and depends only on the  $\text{Ln}^{3+}$  ion under consideration.  $(\Omega_t)$ , the Judd–Ofelt intensity parameters (t runs over 2, 4, and 6) actually represent the crystal field properties of the host. Similarly, the strength of a magnetic dipole mediated transition is given by the expression:

$$S_{md}(J \rightarrow J') = \left( \frac{e\hbar}{4\pi mc} \right)^2 \left| \langle (S, L)J | L + 2S | (S', L')J' \rangle \right|^2 \quad (13.14)$$

Here, e = electronic charge; h = Planck's constant; c = velocity of light; m = mass of electron.

The value of magnetic dipole line strength  $S_{md}(J \rightarrow J')$  does not depend on the nature of the host and it is an exclusive property of the rare-earth ion itself. The contribution of magnetic dipole transitions is generally much lower than that of electric dipole one.

The corresponding expression based on experimentally determined parameters of an electric dipole mediated transition may be written as:

$$\begin{aligned} S_{ed}^{meas}(J \rightarrow J') \\ = \frac{9n}{(n^2 + 2)^2} \left[ \frac{3hc(2J+1)2.303}{8\pi^3 e^2 N \lambda_{max} d} \right] x \int_J^{J'} OD(\lambda) d\lambda - nS_{md} \end{aligned} \quad (13.15)$$

where,  $S_{ed}^{meas}(J \rightarrow J')$  is the measured electric dipole line strength,  $\lambda_{max}$  is the mean wavelength of the absorption band,  $n$  is the refractive index of the host with respect to  $\lambda_{max}$ ,  $d$  is the thickness of the sample under study,  $N$  is the concentration of lanthanide ions (in terms of number of ions/cc) in the host,  $\int O.D(\lambda)d\lambda$  represents the experimental integrated optical density in the wavelength range of the band and  $nS_{md}$  is the magnetic dipole mediated line strength. Similar expressions for calculated and experimental oscillator strengths of a transition can be derived, which are as follows:

$$f_{cal}(J - J') = \frac{8\pi^2 mc}{3h(2J+1)\lambda_{max}} \left[ \frac{(n^2 + 2)^2}{9n} S_{ed}^{cal} + nS_{md} \right] \quad (13.16)$$

$$f_{exp}(J - J') = \frac{2.303 mc^2}{\pi e^2 N d \lambda^2} \int O.D.(\lambda) d\lambda \quad (13.17)$$

### 13.2.3 Experimentally Measurable Parameters and Their Correlation with Theoretical Expressions

The rate of decrease of intensity of the light propagating through a medium containing the light absorbing centers of definite concentration is given by Lambert's law:

$$I = I_0 e^{-\alpha d} \quad (13.18)$$

where  $I_0$  is the intensity of the incident light minus reflection losses at the surface, and  $\alpha(cm^{-1})$  is the absorption coefficient of the absorber and  $d$  is the path length the light has traversed through the medium. For different concentration of the absorber in the medium, light intensity also decreases with the change in concentration of the absorber even if the path length  $d$  remains unchanged. Such decrease in intensity is governed by a similar law proposed by Beer:

$$I = I_0 e^{-ac}, \text{ when 'd' the path length is constant} \quad (13.19)$$

So for variation of both the parameters ( $c$  and  $d$ ) the combine equation can be expressed as:

$$I = I_0 e^{-acd} \quad (13.20)$$

Different methods are used in literature to represent the absorption of light by a medium, which are as follows:

1. Optical density or absorbance,

$$O.D. = \log(I_0/I) = \alpha cd/2.303 = (\alpha/2.303)cd = \varepsilon cd, \quad (13.21)$$

$\varepsilon = O.D./cd$ , is known as the molar extinction coefficient of the absorber, when concentration ( $c$ ) of the absorber is expressed in (mol/l),

2. Optical constant,

$$\kappa \text{ (cm}^{-1}\text{)} = \varepsilon c = O.D./d \quad (13.22)$$

3. Absorption cross-section per absorbing center [ $\sigma_{abs}(\text{cm}^2)$ ] defined as the probability that an absorbing species absorbs a photon when light befitting to its absorption transition energy is incident upon its unit area. It is related to the experimental O.D. of the system as follows:

$$\sigma_{abs}(\text{cm}^2) = 2.303 \times (OD)/N.d \quad (13.23)$$

Here,  $N$  is the concentration of the absorbing center in number ( $N$ ) of species per cubic centimeter. The absorption cross-section  $\sigma_{abs}(\text{cm}^2)$  actually represents the absorption strength of the concerned transition.

4. Emission cross-section per emitting center  $\sigma_{em}(\text{cm}^2)$  is also defined in a similar way. Emission cross-section per emitting center can be determined with the help of McCumber equation [22] using the experimental absorption cross-sectional data. According to McCumber theory the emission cross-section of an emitting center at any particular wavelength is related to its absorption cross-section at the same wavelength by the following eqn.

$$\sigma_{em}(\lambda) = \sigma_{abs}(\lambda) \frac{Z_i}{Z_u} \exp\left(\frac{E_{Z_i} - hc\lambda^{-1}}{k_B T}\right) \quad (13.24)$$

Here  $\sigma_{ab}(\lambda)$  and  $\sigma_{em}(\lambda)$  denote the absorption and the emission cross-sections, respectively, of the transition at the wavelength  $\lambda$ . The terms  $Z_l$  and  $Z_u$  are the partition functions of the lower and the upper states involved in the emission, while  $E_{zl}$  is the energy of the zero-zero line of the absorption and  $k_B$  is the Boltzmann's constant.

### 13.3 Sensitization/Energy Transfer Phenomenon in Luminescence Process

#### 13.3.1 Resonant Energy Transfer

To enhance the excitation of a luminescent centre of which efficiency of light absorption transition is weak, some time, assistance of a second strong absorber (having absorption band in the near higher energy region of the absorption band of the center) is utilized. This is done either by incorporating the centre in a host having the desired absorption properties, e.g.  $\text{Y}_2\text{O}_3$  host in the case of commercial red phosphor,  $\text{Y}_2\text{O}_3:\text{Eu}^{3+}$ ; (Here the charge-transfer band [21] of  $\text{Y}_2\text{O}_3$  is utilized to efficiently excite the doped  $\text{Eu}^{3+}$  centers) or by co-doping a second centre [9, 10, 14] in the host, which have a strong absorption band matching with the energy of the excitation source and can produce efficient luminescence of energy equal/bit above the absorption energy of the acceptor.

In a host-guest energy transfer process, the host is first efficiently excited through its absorption transition which then efficiently transfers its excited state energy to the guest ions. In the case of donor-acceptor co-doped system, donor is first excited so that it can produce strong luminescence which is subsequently absorbed by the acceptor and is raised to its excited state. Rate of such an energy transfer is mediated by the dipole-dipole, dipole-quadrupole interactions between the initial and final states of the transfer process and is largely dependent on the extent of overlap between the emission and the absorption bands of the donor and the acceptor ions, respectively. The rate of such energy transfer can be given by the Forster relation [23] as follows:

$$W_{DA} = \frac{2\pi}{\hbar} |H_{DA}|^2 \int f_D(E) f_A(E) dE \quad (13.25)$$

Here  $|H_{DA}|$  is the ‘interaction Hamiltonian’ which coherently connects the excited and the groundstates of the donor ( $D$ ) and the acceptor ( $A$ ), respectively, over a range of distance ( $r_{DA}$ ) between the donor and the acceptor.  $fD(E)$  and  $fA(E)$  are the line functions of the emission and absorption cross-sections of the donor and the acceptor, respectively.

### 13.3.2 Phonon-assisted Non-resonant Energy Transfer

Although Forster equation suggests that for an energy transfer to occur from a donor to an acceptor in a medium overlapping of donor’s emission and acceptor’s absorption spectra is required, in the case of solid host, on many occasions it is observed that the energy transfer takes place even when donor’s emission and acceptor’s absorption spectra are far apart energetically. To explain the phenomenon, Miyakawa and Dexter [24] proposed that the phonons of the host structure play a significant role in such energy transfer process. Actually phonon assisted non-resonant energy transfer (PAET) is based on the premises that the donor’s emission sacrifices part of its energy to the host’s phonons which are coupled with the donor’s emitting state and hence becomes matching with the energy of the excited state of the acceptor (which may be a pure excited state or a coupled phonon side band state after absorbing the generated phonons) and makes the energy transfer possible. The expression for the rate of PAET per unit time ( $W_{DA}$ ) between a donor ( $D$ ) and an acceptor ( $A$ ) in the case of a non-resonant energy transfer is given by Miyakawa and Dexter introducing a term for host’s phonons contribution in the Foster’s equation which can be written as:

$$W_{DA} = \frac{2\pi}{\hbar} |H_{DA}|^2 \int f_D(E - E_{ph}) f_A(E) dE \quad (13.26)$$

Here  $E_{ph}$  is the energy of the phonon involved in meeting the energy gap. More precisely the ( $E_{ph}$ ) represents the combine energy of the phonons created at the donor’s site and annihilated at the acceptor’s site. Because the distribution of Phonon’s density of states at any temperature ( $T$ ) is dependent on their energies and is governed by Bose–Einstein statistics, Orbach [25] modified the rate expression (13.26) as follows:

$$W_{DA} \propto I_{Overlap} = \frac{\frac{E_{ph}}{k_B T}}{\frac{E_{ph}}{k_B T} - 1} \int_{E1}^{E2} \frac{f_D(E - E_{ph}) f_A(E)}{E^2} dE \quad (13.27)$$

where  $E1$  and  $E2$  are the two extremes of energy of the overlapping region.

## 13.4 Functional Phosphors

Functional phosphors are synthesized on the basis of their areas of applications, namely desired wavelength range of the emitted light for application, intensity of emission needed, source to be used for excitation and the application temperature. Apart from its inherent transition strength, a luminescent center doped in a host, experiences profound influence on the transition by the crystal field of the host. So choice of appropriate activator-host combination is an important task for developing a functional phosphor. Moreover, for direct excitation of the activator in a host, the latter should not have any absorption property in the wavelength region of the excitation light. It should not also have any absorption property in the wavelength region of the emission light of the phosphor. However, when the excitation of the activator is mediated through the host, the host should have strong absorption band in the wavelength region of the excitation light. As mentioned before, that various transition metal/rare earth ions in their different valence states are used as good luminescent centers in functional phosphors. Of course the efficiency of the ultimate phosphor product depends on many tricky factors namely choice of appropriate host, phonon structure of the host, choice of starting materials, purity of the materials, methods of preparations, presence of sensitizer, presence of appropriate additives and finally the phase purity and optimum particle size of the product.

### 13.4.1 Preparation of Functional Phosphors

Most of the functional phosphors are synthesized by solid-state reactions at high temperature. A batch containing highly pure precursors, respectively, of the host, the activators, sensitizer, additives, etc. is first prepared by mixing well in a mixer. It is then taken in a crucible (silica or alumina or carbon) and then subjected to solid-state reactions at high temperature in a furnace. In some cases small quantity of certain flux materials are added to lower the reaction-temperature as well as to make the reaction efficient. In some cases, certain additives that can increase the plaque brightness of the phosphor are also added. After complete chemical reaction the entire batch material becomes a floppy sintered mass. The product is then crushed and milled. It is very important to note that presence of trace undesired impurity in the phosphor can drastically reduce the luminescence efficiency of the phosphor. For example, the luminescence efficiency of calcium halophosphate phosphor  $[\text{Ca}_5(\text{PO}_4)_3\text{F}, \text{Cl}: \text{Sb}^{3+}, \text{Mn}^{2+}]$ , which is used in common fluorescent lamps for white light generation, is drastically reduced in

**Table 13.1** Influence of impurities on the plaque brightness of a 3000 K calcium halophosphate phosphor [20].

Addition of 100 ppm of additives	
Impurities	Plaque brightness*
Al <sup>3+</sup>	100.9
Na <sup>+</sup>	100.8
Ga <sup>2+</sup>	100.1
S <sup>2-</sup>	100.2
Si <sup>4+</sup>	100.2
Sn <sup>2+</sup>	98.9

\*Normalized to the brightness for 1 ppm addition of each impurity.

presence of any heavy metal ions [26]. A list of additives [20] that influence the Plaque Brightness of 3000 K (color temperature) Calcium halophosphate phosphor is given in Table 13.1.

Rare earth ions of the lanthanide series have very similar chemical properties so contamination of other rare earth ions with the desired one is highly likely. But contamination of trace amount of other rare earth ion may affect the luminescence spectrum making the product unusable. So purification of the ingredients is a must for achieving efficient product. As mentioned earlier that achieving the correct crystal phase of the host with the activator ions in the appropriate sites [27] is a primary criterion for obtaining a successful product. The phase structure of the product can be checked by the X-ray diffraction and microscopic studies. It is observed that in the case of synthesis of Y<sub>2</sub>O<sub>3</sub>: Eu<sup>3+</sup> (a well known commercial red phosphor) mere bringing about solid-state reaction between its reactants namely, Y<sub>2</sub>O<sub>3</sub> and Eu<sub>2</sub>O<sub>3</sub>, does not yield a phase pure product but requires tricky chemical conversion to make the reaction effective. Actually one needs first to make an intimate mixture of the oxalates of the respective ions by co-precipitation from a mixed solution of their oxides in nitric acid and then carrying out the solid-state reaction of the oxalate mixture. Maintaining the temperature of the reaction is also very important. For phosphate phosphors reaction temperatures normally range from 900 to 1200 °C, for silicates it is 1000 to 1300 °C, while for aluminate phosphors temperature range as high as 1200 to 1500 °C, may be required. It is possible to follow the progress of a phosphor reaction by DTA studies of the products of different stages of the reaction. For example, studies on the reaction of formation of Zn<sub>2</sub>SiO<sub>4</sub>: Mn<sup>2+</sup>, a green phosphor, using a

mixture of  $ZnO$ ,  $SiO_2$ , and  $MnCO_3$  as reactants revealed that the reaction between the host ingredients ( $ZnO$ ,  $SiO_2$ ) occurs at about  $770^\circ C$  and the  $Mn^{2+}$  ions enter into the lattice according to the proportion of the  $Zn_2SiO_4$  produced and occupy the substitutional sites of  $Zn^{2+}$ . Site selective incorporation of activators is very important because each has definite role at the specific site, e.g. in  $ZnS$ :  $Cu^+$ ,  $Cl^-$  green-emitting phosphor, copper ions occupy  $Zn$  sites and chlorine ions occupy sulfur sites to maintain the charge compensation. Atmosphere during the time of high temperature chemical reactions is another important parameter needed to be seriously taken care of. Depending on the nature of the host and the valence state of the activator ions, reactions are carried out either in air or in a controlled atmosphere. For example, phosphors activated with  $Tl^+$ ,  $Pb^{2+}$ ,  $Mn^{2+}$ ,  $Sb^{3+}$ , or  $Eu^{3+}$  ions can be fired in air, while phosphors activated with  $Sn^{2+}$ ,  $Eu^{2+}$ ,  $Ce^{3+}$ , or  $Tb^{3+}$  ions are needed to be synthesized in a reducing atmosphere. Normally argon/nitrogen gas mixed with few percentage of hydrogen is used for maintaining reducing atmosphere.

### 13.4.2 Functional Nanophosphors and Their Preparation

Phosphors material prepared in the form of particles of sizes within  $\sim 100$  nm is called nanophosphors. Objective of reducing the particle's size of the phosphor to the nanometer dimension is to make their diameter approach to the Bohr diameter and increase the surface area of the particle so that more and more nonbonded electrons remain dangling on the surface. The optical properties of the particles at this stage begin to change and quantum confinement effect starts to play a significant role in determining the luminescence energy and the efficiency of luminescence of the phosphor. In fact, the dangling cloud of electrons on the surface of the particle, which is called surface plasmon, creates an electromagnetic field surrounding the Nanoparticle which can interact with the electric dipole of the emission transition of the phosphor and hence increase the efficiency of the emission significantly. For this reason, scientists are at present very much interested in preparing core-shell nanophosphors with particles sizes of nanometer dimensions. In most of the cases noble metal nanoparticles (Au, Ag etc) are used as the core and the luminescent material is used as the shell in the core-shell nanostructure. Objective is to use the electromagnetic field of the highly dense surface plasmon of the metal nanoparticle to enhance the luminescence efficiency of the shell material. However, it is necessary to consider at the same time the possible detrimental effects of reducing the particle size on the properties of a phosphor. Not always the reduction of particle size yields better results. This is because, as the

particle size decreases the surface area as well as non bonded electrons on the surface increase making the system unstable and prone to chemical reactions with the atmosphere and others materials in contact. These sometimes make the phosphor even worse compared to the luminescence efficiency of its micron size version. Luminescence properties of a series of  $\text{Y}_2\text{O}_3$ ;  $\text{Eu}^{3+}$  red phosphor of particle sizes ranging from 50 to 300 nm were investigated by the author's group [4] as a function of time. The samples were found to lose luminescence efficiency and suffer a change in the excitation profile with time. Infrared studies showed that although the samples at their freshly prepared stage were almost free from contaminated water, on aging in air at room temperature, they become hydrated. A phenomenon of hydration-induced coupling of the excitonic state of  $\text{Y}_2\text{O}_3$  with one of its Fu modes has been detected in the case of the hydrated sample, which is shown to be instrumental in introducing newer nonradiative relaxation channels in the system. Because of larger surface-to-volume ratio, the effect was most pronounced in the case of Nanocrystalline samples.

Nanophosphors can be synthesized by a variety of chemical methods: (1) solid-state combustion reaction, (2) co-precipitation, (3) encapsulation in micelle medium, (4) sol-gel processing, (5) growing in a template, etc. In a combustion reaction, the reactants are taken as mixture of nitrates to which a fuel like urea or carbohydrazide or oxalic acid, is added and the combustion reaction is initiated at low temperature. The reaction is highly exothermic, resulting in a flame with a temperature in excess of 1200 °C. The phosphor is produced in the form of Nanocrystalline powder. In co-precipitation method, a basic solution is added to an acidic aqueous solution of atomically mixed constituent elements. Precipitation of hydrous oxides takes place. The precipitate is initially heated at low temperatures to drive out the residual organic bye products and water, then at high temperatures to have well-crystallized nanoparticles. Core-shell nanostructure formation is a technique used to stabilize Nanoparticles and some time also to enhance their optical, catalytic and magnetic properties.

### 13.5 Classifications of Functional Phosphors

Functional phosphors, as discussed above, are classified either on the basis of the area of their applications or on the basis of energy source required for their excitation. Here we categorize them considering their field of applications, e.g. phosphors for X-ray imaging, phosphors for fluorescent display, phosphors for fluorescent lamps, etc. In each class, again a large variety of phosphors are used. Some of the representative phosphors of each category are discussed below.

### 13.5.1 Phosphors for X-ray Fluorescence Imaging

The fundamental process of X-ray fluorescent imaging is the generation of fluorescence by excitation of a phosphor by X- radiation. In this technique, the X-ray is passed through the object to be imaged before shining the phosphor plate. Intensity of the X-ray emanating out of the object varies point to point depending on the point to point absorption/reflection of X-ray by the object and hence excites the phosphor plate at different point at different intensity generating fluorescence of different intensity. On projecting the fluorescence on a TV screen the image of the object can be viewed. An X-ray fluorescent screen as shown in Figure 13.1 consists of a high-quality paper or plastic as base over which a reflective layer is deposited then the top of reflective layer is coated with a 200- to 300- $\mu\text{m}$ -thick X-ray phosphor layer. Phosphors used in the fluorescent screens of such a radiological imaging device are  $(\text{Zn}, \text{Cd})\text{S:Ag}$  phosphors. Such phosphors have emission peak at 525 nm, providing a spectral luminous efficacy that allows the X-ray image to be seen by the human eye. Since point to point brightness of luminescence is very important for generation of good image, sensitivity of the phosphor to X-ray radiation is a very important. For this purpose, a large-grain phosphor (average size 20 to 40  $\mu\text{m}$ ) is normally used.  $\text{Gd}_2\text{O}_2\text{S:Tb}^{3+}$  phosphor is at present being used instead of  $(\text{Zn}, \text{Cd})\text{S: Ag}$  phosphor. The  $\text{Gd}_2\text{O}_2\text{S:Tb}^{3+}$  phosphor-based fluorescent screens are superior to that of a  $(\text{Zn}, \text{Cd})\text{S:Ag}$ -based ones in respect of properties like, X-ray absorption coefficient, the emission efficiency and sharpness of the emission band, etc.  $\text{Gd}_2\text{O}_2\text{S:Tb}^{3+}$  phosphor can be synthesized as follows. An intimate mixture of oxalates of Gd and Tb is first prepared by co-precipitating from a nitric acid solution of their oxides ( $\text{Gd}_2\text{O}_3$  and  $\text{Tb}_2\text{O}_7$ ). Mixture of oxalates is then thermally decomposed to get mixed oxides.  $\text{Na}_2\text{CO}_3$  and sulfur are then added to the oxide mixture and fired at a high temperature in an atmosphere of sulfuric vapor to produce the oxysulfide

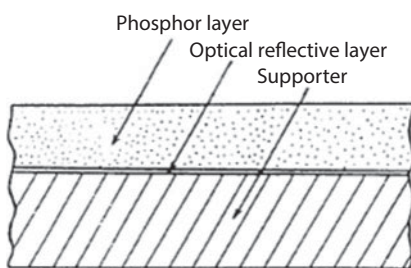
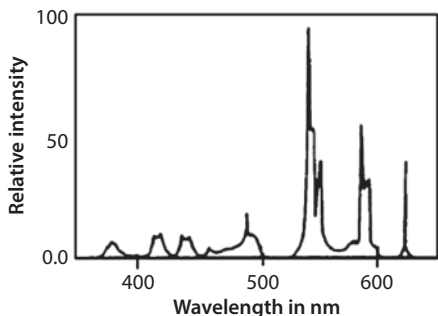


Figure 13.1 X-ray fluorescent screen.



**Figure 13.2** Emission spectrum of X-ray imaging Gd<sub>2</sub>O<sub>3</sub>: Tb<sup>3+</sup> phosphor [after Ref. 28].

product. An excess amount of sulfur over the stoichiometry is required for successful reaction. Emission spectrum of Gd<sub>2</sub>O<sub>3</sub>: Tb<sup>3+</sup> phosphor is shown in Figure 13.2 [28].

### 13.5.2 Phosphors for Fluorescent Display

Depending on the nature of the energy source used for the excitation of the phosphor, display phosphors are further subdivided into groups like CRT (cathode ray tube) display phosphors, plasma display phosphors, electroluminescent display phosphors, etc. Some representative members of these phosphors are discussed in this section.

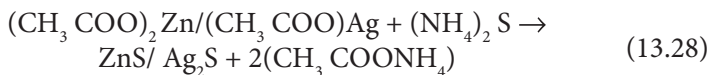
#### 13.5.2.1 CRT-display Phosphors

CRT-display technology is based on the principle that the phosphors deposited on the pixels of the display screen are excited by modulated cathode ray to generate luminescence and thereby create the picture on the screen. The technology is used in black-and-white/color television, giant display screens, computers monitors, etc.

##### 13.5.2.1.1 Black-and-white CRT-display Phosphors

The pixels of a black and white display screen of a CRT -TV are normally loaded with a mixture of blue-emitting silver-activated zinc sulfide phosphor and a yellow-emitting copper- and aluminum-activated zinc-cadmium sulfide phosphor [ZnS:Ag + (Zn,Cd)S:Cu,Al]. In some cases a mixture of [ZnS: Ag and (Zn,Cd)S: Ag] or a mixture of [ZnS:Ag + ZnS:Cu,Al+ Y<sub>2</sub>O<sub>3</sub>:Eu<sup>3+</sup>] phosphors is also used. All these phosphor mixtures are designed to emit white light upon cathode ray excitation. Since for achieving higher luminescence efficiency purity of the final phosphor

product is very important, the best method of preparing the blue-emitting silver-activated zinc sulfide ( $\text{ZnS}: \text{Ag}$ ) phosphor is by co-precipitating the sulfides of both Zn and Ag from a mixed acetate solution of the two metals by adding ammonium sulfide  $[(\text{NH}_4)_2\text{S}]$  and then filtering and repeatedly washing the precipitate and finally making it dry.



The yellow-emitting copper and aluminum-activated zinc-cadmium sulfide phosphor ( $\text{Zn}, \text{Cd}\text{S}: \text{Cu}, \text{Al}$ ) can also be prepared by a similar method of co-precipitation, i.e. first make a solution of zinc and cadmium salts containing the respective ions in the required stoichiometry and then co-precipitate their sulfides by passing hydrogen sulfide. Copper and aluminum ions are, respectively, introduced in the lattices of  $(\text{Zn}, \text{Cd})\text{S}$  as the activator and co-activator by diffusion on firing a mixture of  $(\text{Zn}, \text{Cd})\text{S}$  and appropriate salts of copper and aluminum at high temperature under a controlled atmosphere. The emission spectra of  $\text{ZnS}: \text{Ag}$  phosphor and that of  $[\text{ZnS}: \text{Ag} (0.01\text{--}0.03 \text{ wt\%}) + (\text{Zn}, \text{Cd})\text{S}: \text{Cu}(0.002\text{--}0.03 \text{ wt\%}), \text{Al}]$  mixed phosphor are shown [29] in Figures 13.3 and 13.4, respectively.

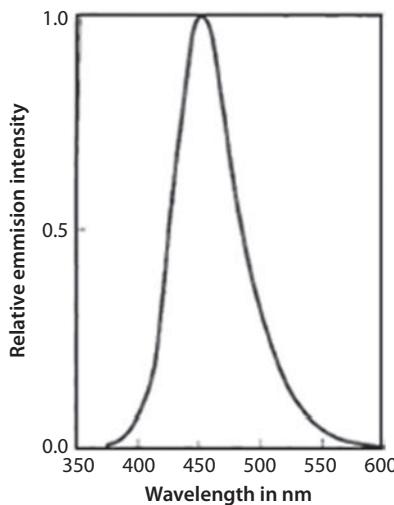


**Figure 13.3** Emission spectrum of the blue-emitting ( $\text{ZnS}: \text{Ag}$ ) phosphor [after Ref. 29].

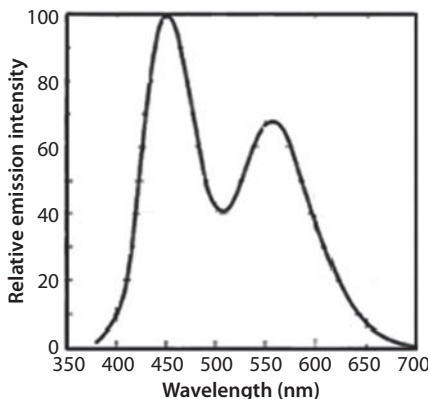


**Figure 13.4** Emission spectrum of [ZnS: Ag + (Zn, Cd)S: Cu, Al] phosphor [after Ref. 29].

### 13.5.2.1.2 Color CRT-display Phosphors

For color display of pictures on a CRT screen, the pixels of the screen are loaded with three different phosphors emitting, respectively, in three primary colors (red, green, and blue) and the emission intensities of the phosphors in these three kinds of pixels are controlled independently. Most common three phosphors used for color CRT screens are ZnS:Ag (blue emitting), ZnS:Cu,Al (green emitting) and  $\text{Y}_2\text{O}_2\text{S}: \text{Eu}^{3+}$  (red emitting). Some of the essential characteristics needed to be met by the phosphors for use in color CRT screen are as follows: (1) high color purity of emission, (2) high emission efficiency, and (3) high chemical stability.

The method of preparation of Blue emitting ZnS: Ag phosphor has already been described. The green phosphor, ZnS:Cu,Al can be prepared following the same method described earlier for the preparation of (Zn,Cd) S:Cu,Al phosphor, just without the addition of cadmium. An emission spectrum of a (ZnS: Cu, Al) phosphor sample is shown in Figure 13.5.

The starting ingredients for synthesis of  $\text{Y}_2\text{O}_2\text{S}: \text{Eu}^{3+}$  red phosphor are the high pure  $\text{Y}_2\text{O}_3$  and  $\text{Eu}_2\text{O}_3$ . The oxides are first dissolved in nitric acid solution. The PH of the solution is brought to a desired level by dilution with distilled water then the ( $\text{Y}^{3+}$  and  $\text{Eu}^{3+}$ ) ions are co-precipitated as oxalates by ammonium oxalate. Since the chromaticity coordinates of the emission varies with the  $\text{Eu}^{3+}$  concentration, it is necessary to add appropriate proportion of  $\text{Eu}^{3+}$ . The residue is then thermally decomposed to mixed oxides. To convert the mixed oxides into oxysulfide the former is fired at 1100 °C in a hydrogen sulfide atmosphere for 1 hour. The emission and excitation

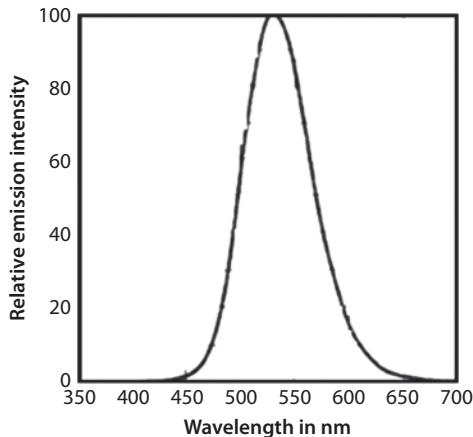


Figure 13.5 Emission spectrum of the ZnS: Cu, Al phosphor [after Ref. 29].

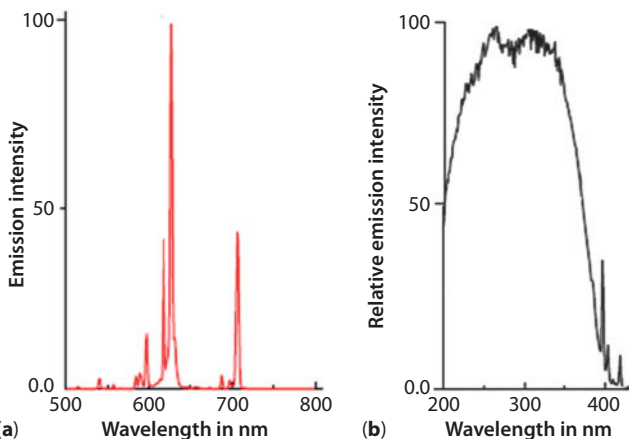


Figure 13.6 (a) Emission spectrum of the  $\text{Y}_2\text{O}_2\text{S}: \text{Eu}^{3+}$  phosphor [after Ref. 30].  
(b) Excitation spectrum of  $\text{Y}_2\text{O}_2\text{S}: \text{Eu}^{3+}$  phosphor [after Ref. 30].

spectra of  $\text{Y}_2\text{O}_2\text{S}: \text{Eu}^{3+}$  phosphor are shown in Figure 13.6(a) and (b) [30], respectively.

### 13.5.2.2 Color Plasma Display Phosphors

In a plasma display screen, the pixels consist of small gas-discharge cells those are loaded with blue, green and red phosphors. The phosphors emit color light upon excitation by the gas discharge plasma VUV emission (147 and 173 nm when the gas is Xenon). The discharge in each cell is individually controlled to generate a picture. Since energy of the

excitation source lies in the VUV region, the phosphors for such applications should have strong absorption in the wavelength region of the emission of the plasma (e.g. 147 and 173 nm for xenon plasma). Another essential requirement is that the phosphors should be robust enough to sustain continuous exposure to the VUV light. The phosphors which are found to be suitable for such applications are: (1) divalent europium activated barium magnesium aluminate ( $\text{BaMgAl}_{10}\text{O}_{17}$ :  $\text{Eu}^{2+}$ ), also known as BAM as the blue emitting component, (2)  $\text{Mn}^{2+}$ -activated zinc silicate ( $\text{Zn}_2\text{SiO}_4$ :  $\text{Mn}^{2+}$ ) or  $\text{Mn}^{2+}$ -activated barium magnesium aluminate ( $\text{BaMgAl}_{10}\text{O}_{17}$ :  $\text{Mn}^{2+}$ ) as the green emitting component, and (3) any one from ( $\text{Y}, \text{Gd}$ ) $\text{BO}_3$ :  $\text{Eu}^{3+}$ ,  $\text{Y}_2\text{O}_3$ :  $\text{Eu}^{3+}$ , and  $\text{GdBO}_3$ :  $\text{Eu}^{3+}$  phosphors as the red component. The quantum efficiency of conversion of the VUV excitation light to red by the [( $\text{Y}, \text{Gd}$ ) $\text{BO}_3$ :  $\text{Eu}^{3+}$ ] is relatively higher compared to those of the others, so this material is chosen as the red emitting component in most of the cases.

The blue emitting phosphor,  $\text{BaMgAl}_{10}\text{O}_{17}$ :  $\text{Eu}^{2+}$ , is prepared by solid-state reactions using a proportionate mixture of high pure  $\text{BaCO}_3$ ,  $\text{Mg}_4(\text{CO}_3)_3(\text{OH})_2 \cdot 3\text{H}_2\text{O}$ , and  $\text{Eu}_2\text{O}_3$  at about 1200 °C under reducing atmosphere for several hours. Some amount of flux material (like  $\text{AlF}_3$  and  $\text{BaCl}_2$ ) is needed to be added to facilitate the reaction. The sintered mass obtained in the form of cake is then crushed to powder and sieved. The sieved powder is once again fired under the similar conditions. To achieve optimum luminescence the recommended concentration of  $\text{Eu}^{2+}$  is 0.1–0.2 mol per 2 mole of  $\text{MgO}$ . The Emission and excitation spectra [31] of the phosphor are shown in Figure 13.7(a) and (b).

The starting materials for synthesis of green emitting ( $\text{Zn}_2\text{SiO}_4$ :  $\text{Mn}^{2+}$ ) phosphor are:  $\text{ZnO}$ ,  $\text{SiO}_2$ , and  $\text{MnCO}_3$ . These are uniformly mixed in a ratio of 1.5  $\text{ZnO}$ :  $\text{SiO}_2$ : 0.08  $\text{MnCO}_3$ , and then the mixture is fired at 1200 °C in air for several hours. The sintered cake is milled and fired again in air at 1200–1300 °C for several hours.

The green emission in these  $\text{Mn}^{2+}$  activated phosphors occurs due to the spin forbidden  ${}^4\text{T}_1 \rightarrow {}^6\text{A}$  transition of the  $\text{Mn}^{2+}$  ion and hence exhibits a long decay time (tens of milliseconds) which causes overlapping of pictures on the TV screen. However, by doping the phosphor with relatively higher concentration of  $\text{Mn}^{2+}$  ion (up to 10%), the decay time of the emission can be reduced to ~10 ms making the material usable. At higher concentration,  $\text{Mn}^{2+}$  ion pairs are formed in the host. Magnetic interaction between  $\text{Mn}^{2+}$  ions of the pairs greatly increases the transition probability of the spin forbidden  ${}^4\text{T}_1 \rightarrow {}^6\text{A}$  transition of the  $\text{Mn}^{2+}$  ions thereby reducing the decay time. Excitation and emission spectra of  $\text{Zn}_2\text{SiO}_4$ :  $\text{Mn}^{2+}$  [32], are shown in Figure 13.8(a) and (b).

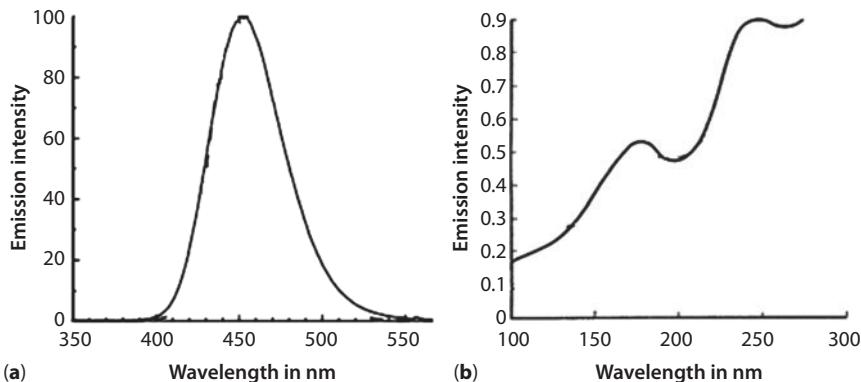


**Figure 13.7** (a) Emission spectrum of  $\text{BaMgAl}_{10}\text{O}_{17}:\text{Eu}^{2+}$  phosphor [after Ref. 31].  
 (b) Excitation spectrum of  $\text{BaMgAl}_{10}\text{O}_{17}:\text{Eu}^{2+}$  phosphor [after Ref. 31].

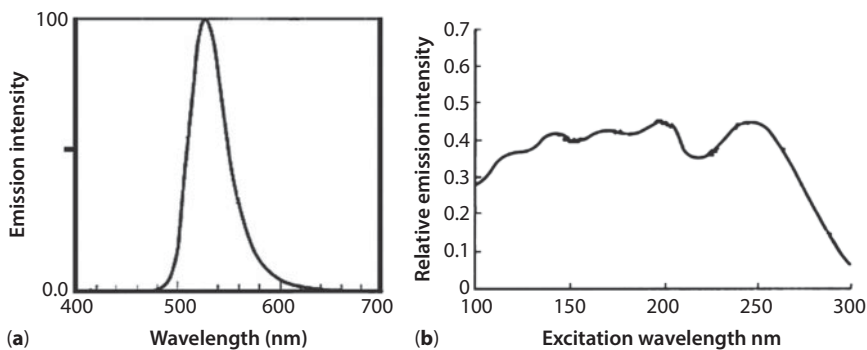


**Figure 13.8** (a) Emission spectrum of  $\text{Zn}_2\text{SiO}_4:\text{Mn}^{2+}$  [after Ref. 32]. (b) Excitation spectrum of  $\text{Zn}_2\text{SiO}_4:\text{Mn}^{2+}$  [after Ref. 32].

The red emitting  $[(\text{Y},\text{Gd})\text{BO}_3:\text{Eu}^{3+}]$  phosphor can be prepared by the co-precipitation method. The method is very useful for preparation of submicron size and spherical-shaped phosphors required for display applications [33–35]. The oxides of Y, Gd, and Eu are first dissolved in nitric acid to get a mixed solution of the ions. The ions are then co-precipitated as their oxalates under suitable PH. The mixed precipitate is filtered off and dried. To get the borate salt it is mixed with required amount of high pure boric acid and fired at designated temperature. Excitation and emission spectra of  $[(\text{Y},\text{Gd})\text{BO}_3:\text{Eu}^{3+}]$  phosphor [33] are shown in Figure 13.9(a) and (b). It is clear from the emission spectrum that the color of the phosphor is bit orange rather than perfect red because of the presence of strong 590 nm band. For this reason, in some cases,  $\text{Y}_2\text{O}_3:\text{Eu}^{3+}$  phosphor is also used [36].

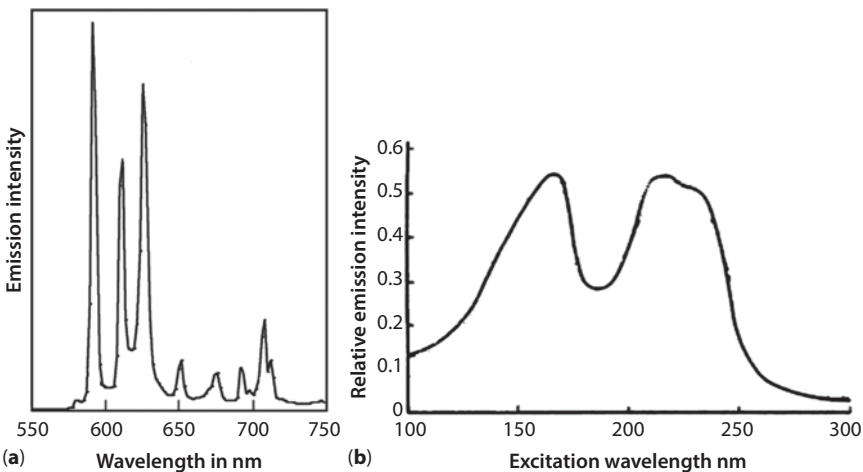


**Figure 13.9** (a) Emission spectrum of  $[(Y, Gd)BO_3: Eu^{3+}]$  phosphor [after Ref. 33].  
(b) Excitation spectrum of  $[(Y, Gd)BO_3: Eu^{3+}]$  phosphor [after Ref. 33].

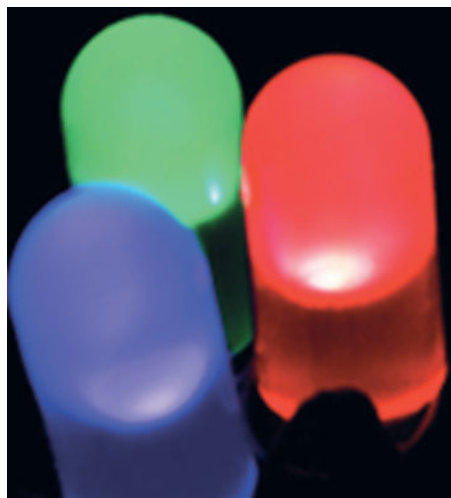
### 13.5.2.3 Luminescent Diode Materials for Display

Semiconductor diodes are p-n junction semiconductors of which electrons and holes on the two sides of the junction can be made to overcome the junction-barrier and recombine by applying a small DC bias (typically less than 10 V). In many cases recombination of the electrons and holes of these diodes results in emission of light and hence such diodes are called light-emitting diodes or in short LED. Depending on the energy of the junction-barrier, the emitted light of the LEDs may lie in the visible or in the NIR region of the spectrum. Of course at present diodes emitting in the UV and near UV are also known [37]. Although most of the conventional LEDs are of inorganic origin, there are also a large numbers of LEDs which are organic in nature (OLEDs). OLEDs are rapidly capturing the market of the inorganic LEDs because of their higher luminescence efficiency. Table 13.2 shows some of the LED materials emitting in the different wavelength of the radiation spectrum, while Figure 13.10 shows three color LEDs emitting in the blue, green, and red.

The LEDs/OLEDs which emit blue, green and red light are presently being used for lighting as well as for visual display. In a LED display panel, an array of miniaturized color LEDs functions as pixel. These LEDs are made 'on and off' by the modulated digitized signals of a picture to display the picture on the screen. Since LEDs are themselves light source of

**Table 13.2** Some of the LED materials emitting in the different wavelengths of the spectrum.

LED materials	Spectral region of emission	Wavelength range (nm)	Emission color
(AlN), (AlGaN), (AlGaInN)	UV	$\lambda < 400$	Violet
(ZnSe), (InGaN)	Near visible	$450 < \lambda < 500$	Blue
(InGaN)/(GaN),(GaP), (AlGaInP), (AlGaP)	Visible	$500 < \lambda < 570$	Green
(AlGaAs), (GaAsP), (GaP), (AlGaInP)	Visible	$610 < \lambda < 760$	Red

**Figure 13.10** Color LEDs emitting in the blue, green, and red.

different colors, no extra light source or phosphor is required for display of the picture. However LED technology for display of a motion picture is still a subject of further research, because for display of a motion picture, 'on and off' process of the LEDs must be done at a very high speed which is yet to be achieved.

### 13.5.3 Phosphors for Fluorescent Lamps

In a fluorescent lamp visible (white/color) light is generated by excitation of a suitable phosphor or a mixture of phosphors with the UV emission

from rare-gas/mercury discharge plasma. In most of the common fluorescent lamps Hg discharge plasma emission of 185 and 254 nm UV light is used to excite the phosphors coated inside the wall of the lamp bulb/ tube. So it is essential that phosphors proposed to be used in an Hg-discharge fluorescent lamp must have strong UV absorption property in the wavelength around 254 and 185 nm.

### 13.5.3.1 *Sb<sup>3+</sup> and Mn<sup>2+</sup>-based Lamp Phosphor*

McKeag *et al.* [38] first developed a ( $\text{Sb}^{3+} + \text{Mn}^{2+}$ ) ions co-activated calcium halophosphate-based phosphor [ $3\text{Ca}_3(\text{PO}_4)_2 \cdot \text{Ca}(\text{F}, \text{Cl})_2; \text{Sb}^{3+}, \text{Mn}^{2+}$ ] which was found to be suitable for white light generation by Hg-discharge excitation. The halophosphate host can absorb efficiently the 254 nm light of Hg plasma and transfer its excitation energy to the incorporated  $\text{Sb}^{3+}$ . The excited  $\text{Sb}^{3+}$  ion emits a broad blue emission peaking at 480 nm.  $\text{Mn}^{2+}$  ion, which gets excited by absorbing a part of  $\text{Sb}^{3+}$  emission via Forster's resonance energy transfer mechanism, emits yellow light peaking at around 580 nm. Mixing of the two emissions ultimately gives a white emission. The ratio of the blue to orange emission can be adjusted by adjusting  $\text{Mn}^{2+}$  content of the phosphor. Color rendering index (CRI) values of such a fluorescent lamp ranges from 50 to 60. The phosphor can be prepared by solid-state reaction of a batch mixture of  $\text{CaHPO}_4$ ,  $\text{CaCO}_3$ ,  $\text{CaF}_2$ ,  $\text{CaCl}_2$ ,  $\text{Sb}_2\text{O}_3$ , and  $\text{MnCO}_3$  along with additional halogen sources  $\text{NH}_4\text{F}$  and  $\text{NH}_4\text{Cl}$ , at a temperature at around 1100–1150 °C under  $\text{N}_2$ -atmosphere. Mixing ratio of the ingredients is taken bit excess of the stoichiometry. A slight excess of  $\text{PO}_4$  gives favorable results. The preferred ratio of Metal:  $\text{PO}_4$ ; F, Cl lies in between 9.8:6.0:1.6 and 9.95:6.0:1.9 [39]. To achieve optimum efficiency of luminescence, additive ions like  $\text{Al}^{3+}$ ,  $\text{Mg}^{2+}$ ,  $\text{Cd}^{2+}$ ,  $\text{Sr}^{2+}$ ,  $[\text{BO}_3]^{3-}$  in appropriate proportions are also added in the batch mixture. The emission and excitation spectra [40] of a sample of such phosphor emitting day light, are given in Figure 13.11(I) and (II). The phosphor has a hexagonal structure and crystal shape identical with natural apatite. The Ca ions occupy two different sites, the ions in Ca(I) sites are surrounded by six oxygen atoms and those in Ca (II) sites are contiguous with halogen atoms. The Sb (III) and the Mn (II) are capable of occupying both these sites. While manganese ions are generally found to be distributed uniformly, antimony ions mostly remain on the surface region of the crystal. To maintain charge compensation in the system addition of some alkali cation ( $\text{Na}^+$ ) is required. Two different types of mechanism of charge compensation are reported:  $\text{Mn}^{+3} + \text{Na}^{+1} = 2\text{Ca}^{+2}$  and  $\text{Ca}^{+2} + \text{X}^- = \text{M}^{+3} + \text{O}^{-2}$  ( $\text{X}^-$  = halide ion). Our group for the first time, showed [27] that

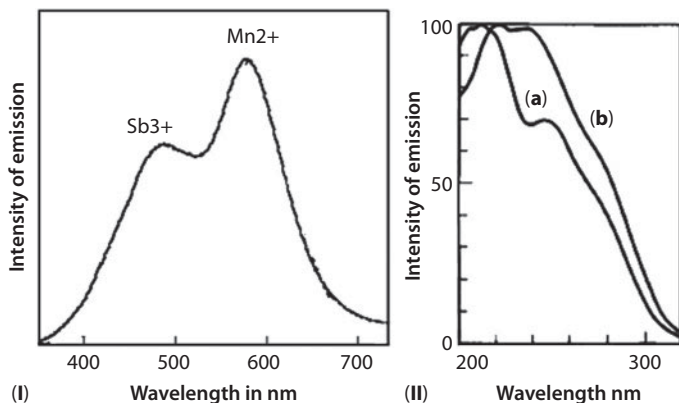


**Figure 13.11** (I) Emission spectrum of the Halophosphate phosphor [after Ref. 40]. (II) Excitation spectrum of  $\text{Sb}^{3+}$  emission (a), and that of  $\text{Mn}^{2+}$  emission (b), of the phosphor [after Ref. 40].

in case of a halo-apatite phosphor, a third type of charge compensation, e.g.  $\text{Ca}^{+2} = \text{Mn}^{+3} + (\text{F}_{2n})^-$  also becomes active in the substitution process which greatly influences the luminescence efficiency. We also showed [13] that the presence of aluminum impurity in the batch mixture of a fluoroapatite helps growth of a new phase namely calcium fluoroaluminate ( $\text{Ca}_2\text{AlO}_6\text{F}$ ) along with the main fluoroapatite phase. This new phase sometime, gives additional luminescence property to the phosphor. The lamp efficacy was also found to depend on the ratio of the metals present and M/phosphate ratio of the phosphor, where M stands for amount of metal Ca, Sr, and Mn in total.

### 13.5.3.2 Rare Earth-based Lamp Phosphors

Being encouraged with the results of a theoretical modeling in around 1970s, that an appropriate combination of rare earth narrow emissions of three fundamental colors (blue, green, and red), a white emission can be generated, scientists started research to use the narrow band visible emissions of the lanthanide ions for lighting purposes. Absorptions and emissions in a lanthanide ion occur due the f-f transitions of their 4f-electrons. The 4f electrons in a lanthanide ion ( $\text{Ln}^{3+}$ ) is shielded by its 5p and 6s electrons, so its energy levels structure remains more or less unaffected by the crystal field when incorporated in a host and for this reason the absorption and emission bands involving f-f transitions are narrow in nature. Unfortunately, f-f transitions are parity forbidden and hence intensity of both absorption and emission of such transitions

are weak. So, it is difficult to efficiently excite the rare earth ions to the desired excited levels in a direct mode. This initially posed a concern in using lanthanide emissions for lighting purposes. However, it was later revealed both from experiment and theoretical calculations that although the energy level structure of the ion remains unaffected, the electric dipole transition strengths of electronic transitions of a rare earth ion get greatly enhanced by the influence of the crystal field of the host [6, 7]. Side by side a general strategy to excite the  $\text{Ln}^{3+}$  ions through the charge transfer band of the host was adopted. With all these information in view scientists initiated intensive research to develop rare earth doped efficient phosphors through right choice of host-ion combinations; and a number of rare earth-based phosphors like red emitting  $\text{Eu}^{3+}$  activated  $\text{Y}_2\text{O}_3$ , blue emitting  $\text{Eu}^{2+}$  activated  $\text{BaMgAl}_{10}\text{O}_{17}$  or  $\text{Eu}^{2+}$  activated calcium halophosphate and green emitting  $\text{Tb}^{3+}$  activated  $\text{CeMgAl}_{11}\text{O}_{19}$  were synthesized. In the case of  $\text{Ce}^{3+}$  ion, absorption and emission occur due to transitions between  $4f \leftrightarrow 5d$  levels which are open to the crystal field of the host resulting broad bands. Fluorescent lamps based on a blend of blue, green and red emitting rare earth-based phosphors were developed and introduced in the market in subsequent year. Actually, with the invention of rare earth-based phosphors construction of compact fancy fluorescent lamps with high-efficacy and high-color-rendering has become possible. More over these phosphors are being photo-stable and rugged they can withstand higher wall temperature and higher ultraviolet Hg plasma flux in side of a CFL lamp. Preparation and emission properties of some of the commonly used rare earth-based lamp phosphors are discussed in the subsequent sections.

### 13.5.3.2.1 $\text{Eu}^{2+}$ Doped Blue Emitting (Sr, Ba, Ca) Halophosphate Phosphor

The most commonly used blue emitting lamp phosphor is  $\text{Eu}^{2+}$  activated halophosphate phosphor  $(\text{Sr, Ba, Ca})_{10}(\text{PO}_4)_6\text{Cl}_2$ :  $\text{Eu}^{2+}$ . It has apatite structure. The phosphor displays strong ultraviolet absorption in the 260–270 nm region and emits a blue emission band peaking at 450 nm. It can be synthesized by solid-state reaction of a mixture of  $\text{SrCO}_3$ ,  $\text{CaCO}_3$ ,  $\text{SrCl}_2$ ,  $\text{BaCO}_3$ ,  $\text{BaCl}_2$ ,  $\text{NH}_4\text{Cl}$ ,  $\text{SrHPO}_4$  and  $\text{Eu}_2\text{O}_3$  in their appropriate proportion at a temperature of  $\sim 1050^\circ\text{C}$  for 2–3 h under a strong reducing atmosphere. To achieve optimum performance of the phosphor some additives in small proportions are also added to the mixture. Its emission and the excitation spectra [12] are shown in Figure 13.12. The phosphor is used as the blue emitter in a tri-band compact fluorescent lamp (CFL).

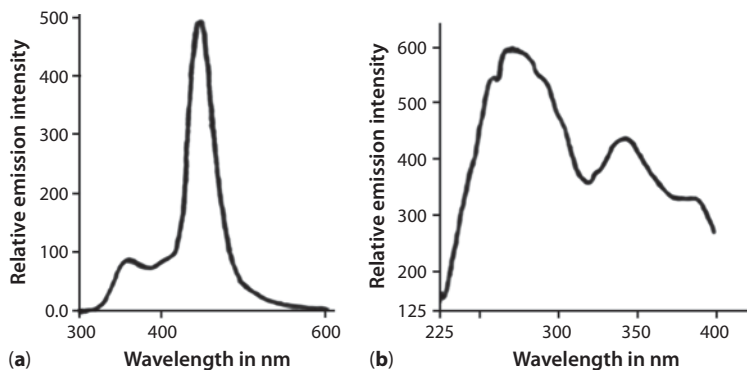


**Figure 13.12** (a) Emission spectrum of  $[(\text{Sr}, \text{Ba}, \text{Ca})_{10}(\text{PO}_4)_6\text{Cl}_2; \text{Eu}^{2+}]$  [after Ref. 12].  
(b) Excitation spectrum of  $[(\text{Sr}, \text{Ba}, \text{Ca})_{10}(\text{PO}_4)_6\text{Cl}_2; \text{Eu}^{2+}]$  [after Ref. 12].

**13.5.3.2.2 Ce<sup>3+</sup>, Tb<sup>3+</sup> Ions Co-doped Green Emitting LaPO<sub>4</sub> Phosphor**  
Green emitting [LaPO<sub>4</sub>: Ce<sup>3+</sup>, Tb<sup>3+</sup>] phosphor is normally used as the green component of a tri-band CFL. The main advantage of this phosphor is that it can be synthesized at relatively lower temperatures (about 1000 °C) compared to the other materials like Tb<sup>3+</sup> activated CeMgAl<sub>11</sub>O<sub>19</sub>. Optimum performance can also be achieved with relatively lower concentration of Tb<sup>3+</sup> ions. The phosphor can be synthesized by firing an homogeneous reaction mixture of cerium oxide, terbium oxide, lanthanum oxide and di-ammonium hydrogen phosphate in an alumina crucible initially for 2–3 h at 1180 °C and then for 1–2 h at 900 °C in a reduced atmosphere. Co-activation of Ce<sup>3+</sup> ion actually results in remarkable increase in the emission intensity, because Ce<sup>3+</sup> ions act as an effective sensitizer to Tb<sup>3+</sup>. The phosphor displays excellent lumen output and maintenance during lamp operation. Figure 13.13 exhibits the emission and excitation spectra of the phosphor [12].

#### 13.5.3.2.3 Eu<sup>3+</sup> Doped Yttrium Oxide Red Emitting Phosphor

Eu<sup>3+</sup> doped yttrium oxide phosphor (Y<sub>2</sub>O<sub>3</sub>: Eu<sup>3+</sup>) strongly emits in the red with a peak at around 612 nm. The color purity of the red emission of the material made it most demanding both to the manufacturers of CFL lamp and color display screen. It can be prepared by firing a reaction mixture of oxalates of europium and yttrium along with a small proportion of flux materials in an electric furnace at around 1200–1400 °C under ambient atmosphere. Incorporation of trace Al<sup>3+</sup> and B<sup>3+</sup> ion in the Y<sub>2</sub>O<sub>3</sub>-lattice has been found to enhance greatly [21] the efficiency of both red emitting  $^5\text{D}_0 \rightarrow ^7\text{F}_2$  transition of Eu<sup>3+</sup> as well as its excitation. The emission and the excitation spectra of the phosphor [12] are shown in Figures 13.14(a) and (b). It is established [21] that enhancement of excitation remains

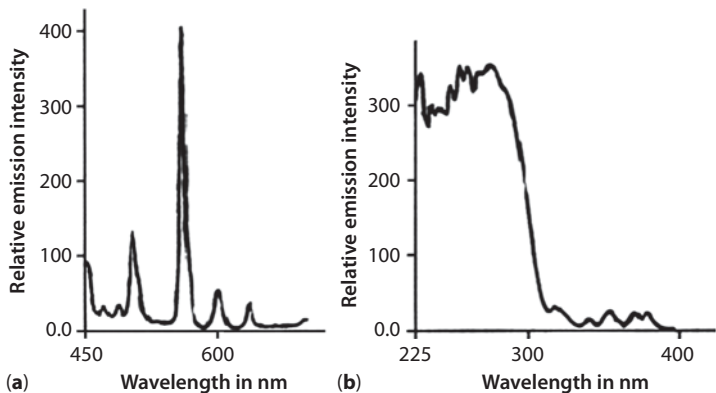


**Figure 13.13** (a) Emission spectrum of the  $\text{LaPO}_4: \text{Ce}^{3+}, \text{Tb}^{3+}$ [after Ref. 12].  
 (b) Excitation spectrum of  $\text{LaPO}_4: \text{Ce}^{3+}, \text{Tb}^{3+}$  [after Ref. 12].

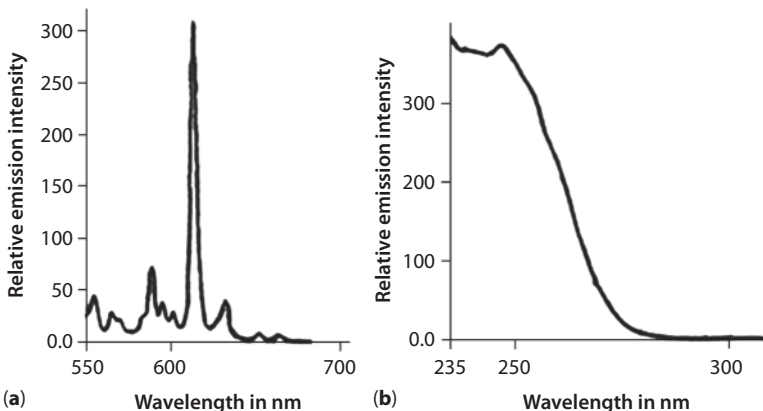


**Figure 13.14** (a) Emission spectrum of  $\text{Y}_2\text{O}_3: \text{Eu}^{3+}$  red phosphor[after Ref. 12].  
 (b) Excitation spectrum of  $\text{Y}_2\text{O}_3: \text{Eu}^{3+}$  red phosphor [after Ref. 12].

restricted around the  $(\text{Eu}^{3+}-\text{O}^{2-})$  C-T band. The  ${}^5\text{D}_0 \rightarrow {}^7\text{F}_2$  decay characteristics and the build-up time of the  ${}^5\text{D}_0$  excited state of  $\text{Eu}^{3+}$  are also shown to change due to such incorporation. The results have been interpreted in terms of change in polarity of the host rather than a change in site symmetry of  $\text{Eu}^{3+}$  due to incorporation of the hetero-cations. Calculation of Judd–Ofelt parameters supported our view.

### 13.5.3.3 Phosphors for LED Lamps

The LED lighting is based on the technique, which uses luminescence from a LED or a combination of LEDs for lighting purposes. Although

compact fluorescent lamps (CFLs) are at present meeting most part of the market demand for household lamps, LED lamps, which do not contain mercury, are capturing the market very fast because of their energy efficiency as well as their nontoxic nature. Unfortunately all most all of the LEDs developed so far have color luminescence rather than a bright white luminescence. So, two different strategies are generally adopted to generate white light using LEDs. (1) Luminescence from three appropriate LEDs emitting in the blue, green and red are focused on a spot to superpose on each other and thus create white light for general lighting. (2) A LED is coated with a complementary color-emitting efficient phosphor/phosphor blend of which excitation band matches with the emission of the LED. The complementary emission from the phosphor together with the transmitted part of the LED emission generates the desired white light. All the existing phosphors which are used in Hg-discharge fluorescent lamps have their effective excitation band in the UV region of the spectrum as they are designed to absorb 254 nm emission of the Hg-plasma. Most of the commonly available LEDs, on the other hand, have emission bands in the visible or NIR region. Existing lamp phosphors are therefore not useful to design phosphor coated LED lamps. Intensive research have therefore, been initiated to develop a new class of phosphors having excitation band in the emission wavelength regions of the available LEDs like zinc selenide (ZnSe), Indium gallium nitride (InGaN), etc. (emission ranges  $450 < \lambda < 500$  nm). Synthesis of a number of such phosphors has already been reported. Some of them, e.g. Ce<sup>3+</sup> doped yttrium aluminum garnet [41–45] (YAG: Ce<sup>3+</sup>; excitation =  $455 \pm 5$  nm, yellow emission =  $550 \pm 5$  nm), Ce<sup>3+</sup> doped yttrium, gadolinium aluminum garnet [46] [(Y,Gd)<sub>3</sub>Al<sub>5</sub>O<sub>12</sub>:Ce<sup>3+</sup>; excitation =  $470 \pm 5$  nm, yellow emission =  $560 \pm 5$  nm], Eu<sup>2+</sup> doped barium aluminate [47] (BaAl<sub>2</sub>O<sub>4</sub>:Eu<sup>2+</sup>; excitation = 470–480 nm, yellow emission =  $590 \pm 5$  nm), have already been shown to be prospective for commercial exploitation coupling with blue emitting LEDs.

#### 13.5.3.3.1 Ce<sup>3+</sup> Ion Doped Yttrium Aluminum Garnet (YAG: Ce<sup>3+</sup>)

The YAG: Ce<sup>3+</sup> phosphor emits a broad luminescence peaking around  $550 \pm 5$  nm and has excitation band around  $455 \pm 5$  nm. It can be prepared by solid-state reaction of a mixture of submicron sized powders of Y<sub>2</sub>O<sub>3</sub>,  $\alpha$ -Al<sub>2</sub>O<sub>3</sub>, and CeO<sub>2</sub> at a temperature of 1500 °C under a vacuum of about  $10^{-3}$  Pa. Emission and excitation spectra [44] of the phosphor are shown in Figure 13.15(a) and (b), respectively. Spectrum of the lamp [41] made by using YAG: Ce<sup>3+</sup> phosphor and a blue LED is shown in Figure 13.16.

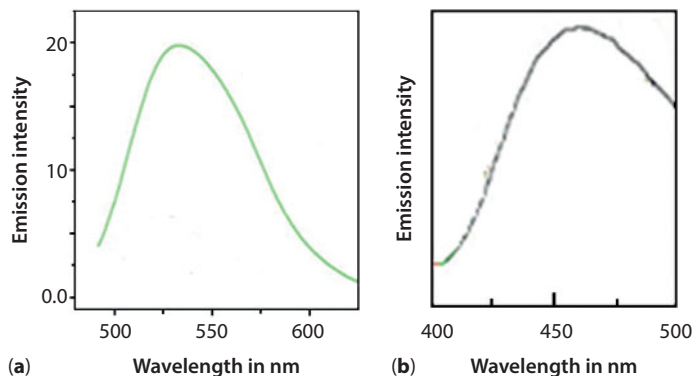


**Figure 13.15** (a) Emission spectrum of YAG: Ce<sup>3+</sup> phosphor [after Ref. 44]. (b) Excitation spectrum of YAG: Ce<sup>3+</sup> phosphor [after Ref. 44].

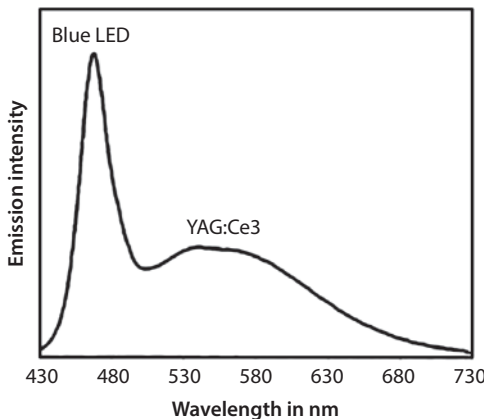


**Figure 13.16** Spectrum of the lamp made by coating a blue LED with YAG: Ce<sup>3+</sup> phosphor [after Ref. 41].

### 13.5.3.3.2 Eu<sup>2+</sup> Ion Doped Barium Aluminate ( $\text{BaAl}_2\text{O}_4$ : Eu<sup>2+</sup>)

The phosphor can be synthesized [46] by firing a mixture of high-purity powders of BaO, Eu<sub>2</sub>O<sub>3</sub>, and Al<sub>2</sub>O<sub>3</sub> mixed with charcoal powder in a molar ratio of BaO/Eu<sub>2</sub>O<sub>3</sub>/Al<sub>2</sub>O<sub>3</sub>/charcoal, 1:0.05:0.2:10, under reducing atmosphere and vapor-phase deposition of the product on alumina plate. The Figure 13.17(a) shows the emission and excitation spectra of the BaAl<sub>2</sub>O<sub>4</sub>: Eu<sup>2+</sup> phosphor [47], while Figure 13.17(b) shows the emission spectrum of the lamp constructed using the phosphor and a 480 nm emitting blue LED. The lamp is shown in the Inset.

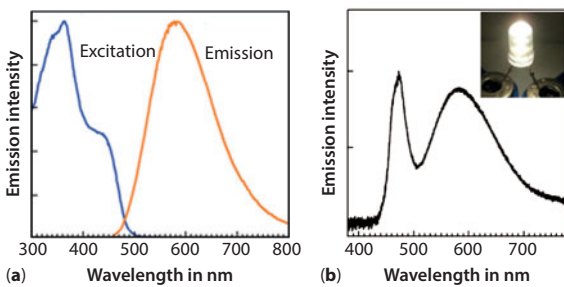


**Figure 13.17** (a) Emission and excitation spectra of  $\text{BaAl}_2\text{O}_4:\text{Eu}^{2+}$  LED phosphor [after Ref. 47]. (b) Emission spectrum of the lamp made by coating the phosphor on a 480 nm blue LED. Inset: The lamp [after Ref. 47].

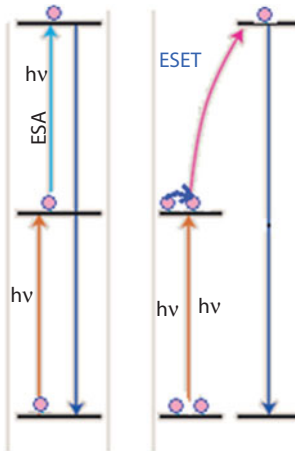


**Figure 13.18** Photo physical scheme of the ESA and ESET.

### 13.5.4 Phosphors for Upconversion Luminescence

Upconversion luminescence (UC) is a photo-physical process by which an activator can emit a higher energy photon after being excited with photons of lower energy. It is in fact, a sequential multi photon absorption process in which the activator by sequential excited state absorption (ESA) of the excitation photons or by excited state co-operative energy transfer (ESET), is raised step by step to the second and some time, to a third excited state and then come down from the higher excited state directly to the ground state by emitting a high energy photon. Thus it is called an upconversion emission. It should be noted that the energy conversion is strongly dominated by ESA and ESET processes and the latter occurs in a donor acceptor (D-A) mode and its energy transfer probability  $W_{\text{D-A}}$  follows the Forster's like equation [23] discussed earlier. Figure 13.18 shows

the photo-physical schemes of the UC luminescence process. Since the process involves absorption of photons by the active centers at the excited state/co-operative energy transfer amongst the active centers at the excited state, the population of which is only a fraction of that of the center in the ground state, a light source of very high photon density like laser, is necessary so that sufficient number of activators can be raised to the first excited state facilitating both ESA and ESET. Moreover, since the excitation source is photons of single energy, for sequential absorption of photons at different steps, the activator should have energy level disposition such that the energy gaps between the two consecutive higher excited states be more or less matching with the energy of the excitation photon. Most of the rare earth ions have energy levels spread over from UV to NIR spectral region, this is why the upconversion luminescence phenomenon is prevalent in rare earth activated materials. Of course there are reports of observations of upconversion luminescence in the cases of several organic dyes. In case of an upconversion luminescence, upconversion luminescence intensity  $I_{\text{upc}}$  is related to the intensity of the excitation source  $I_{\text{exc}}$  by the following relation.

$$I_{\text{upc}} = (I_{\text{exc}})^m \quad (13.30)$$

where 'm' is the number of IR photons absorbed per UC photon emission. So by plotting  $\log(I_{\text{upc}})$  against  $\log(I_{\text{exc}})$ , it is possible to know from the slope the number of photons (m) required to be absorbed by the ion/activator to reach the upconversion state.

There has been a vast body of research during the last decades on the UC-luminescence properties of lanthanide ions in various crystalline and glassy hosts [48–62]. Amongst these materials,  $\text{NaYF}_4$  crystal [50–52, 54, 57] singly doped with  $\text{Er}^{3+}$  or  $\text{Tm}^{3+}$ , and co-doped with  $(\text{Yb}^{3+} + \text{Er}^{3+})$  or  $(\text{Yb}^{3+} + \text{Tm}^{3+})$  and their glassy counter parts: similarly doped high barium containing tellurite glasses [16, 18, 19] or Pb-germanate glasses [59, 60] are found to be relatively more efficient. In the cases of  $\text{Yb}^{3+}$ -co-doped systems,  $\text{Yb}^{3+}$  acts as sensitizer and transfers its excitation energy to the UC activator by the mechanism of phonon assisted energy transfer [5]. Strong crystal field and favorable phonon structure of both of these category of hosts, help efficient energy transfer to occur from  $\text{Yb}^{3+}$  to the respective UC-activator ( $\text{Er}^{3+}/\text{Tm}^{3+}$ ). Upconversion phosphors have potential prospect of use in various applications. It can be used for hazard free biological labeling [48–53], NIR solar concentration [54, 55], solid-state lighting [57–60] and optical data storage [18, 19, 61], upconversion display [62], etc. Here, preparation and optical properties of some of the potential upconversion phosphors are discussed.

### 13.5.4.1 Sodium Yttrium Fluoride Co-doped with $\text{Yb}^{3+}$ and $\text{Tm}^{3+}$

$\text{NaYF}_4 : \text{Yb}^{3+}, \text{Tm}^{3+}$  can be prepared [51] in the form of Nanocrystals by making first a solution mixture of stoichiometric amounts of  $\text{YCl}_3$ ,  $\text{YbCl}_3$ , and  $\text{TmCl}_3$  in a mixture of oleic acid (OA) and octadecene (ODE). The mixture is then heated at  $160^\circ\text{C}$  for 30 min, when a clear solution is obtained. A methanol solution of mixture of required amount of  $\text{NH}_4\text{F}$  and  $\text{Na(OH)}$  is then injected into the mother solution by a syringe at a flow rate of  $200 \text{ L/min}$ . The mixed solution thus obtained is first slowly heated to evaporate the methanol and then degassed at  $100^\circ\text{C}$ . Solution is then further heated at  $300^\circ\text{C}$  for 1.5 h under argon atmosphere. Concentrated solution on cooling to room temperature causes precipitation of  $\text{Yb}^{3+}$  and  $\text{Tm}^{3+}$  co-doped  $\text{NaYF}_4$  Nanoparticles. The precipitate is then washed with ethanol/water mixture (1:1 v/v) and finally centrifuged. Figure 13.19(a) shows the

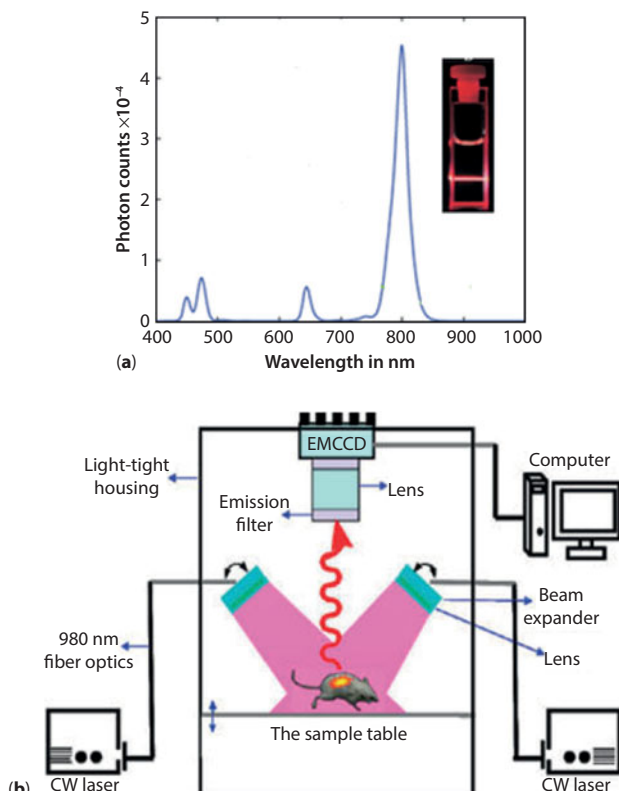


**Figure 13.19** (a) UC emission spectrum of a sample of  $\text{NaYF}_4 : \text{Yb}^{3+}, \text{Tm}^{3+}$  under  $\lambda_{\text{exc}} = 985 \text{ nm}$ . Inset:  $800 \text{ nm}$  emission of a  $\text{NaYF}_4 : \text{Yb}^{3+}, \text{Tm}^{3+}$  dispersed solution. (b) Scheme of a set up for diagnosis of affected biological cells/tissues inside a living body with the help of UC nanoparticles.

UC emission spectrum of a sample of  $\text{NaYF}_4$ :  $\text{Yb}^{3+}$ ,  $\text{Tm}^{3+}$ phosphor upon excitation of 985 nm laser. The spectrum shows a strong UC emission band at 800 nm along with two other UC emission bands at 470 and 650 nm, respectively. The inset of Figure 13.19(a) shows the 800 nm blood red emission of a ( $\text{NaYF}_4$ :  $\text{Yb}^{3+}$ ,  $\text{Tm}^{3+}$ ) nanoparticles dispersed solution.

Figure 13.19(b) shows a scheme how( $\text{NaYF}_4$ :  $\text{Yb}^{3+}$ ,  $\text{Tm}^{3+}$ )Nanoparticles can be used for diagnosis of an affected cells/ tissues inside a living body. The affected location is labeled by injecting the probe with a Nanoparticle dispersed solution of the material then illuminated the affected area with 980 nm NIR laser.

#### 13.5.4.2 $\text{Er}^{3+}$ and $\text{Yb}^{3+}$ Co-doped Barium Fluorotellurite Glass

The UC emitting  $\text{Er}^{3+}$  and  $\text{Yb}^{3+}$  co-doped barium fluorotellurite glass can be prepared [16] by melting a well mixed and grinded batch of composition (mol%) 80 $\text{TeO}_2$ -15( $\text{BaF}_2$ ,  $\text{BaO}$ )-3 $\text{La}_2\text{O}_3$ -1 $\text{Er}_2\text{O}_3$ -1 $\text{Yb}_2\text{O}_3$ , in a platinum crucible at 750 °C for 2 h with intermittent stirring in an electric furnace. The melt is then cast on to a preheated (250 °C) carbon mold. The glass obtained in the shape of a disk is annealed at 250 °C for 12 h to make the material free from any stress. Upconversion emission spectra of the  $\text{Er}^{3+}$  and  $\text{Yb}^{3+}$  co-doped glass [16] under different excitation powers of a 980 nm diode laser are shown in Figure 13.20. The spectra show three upconversion

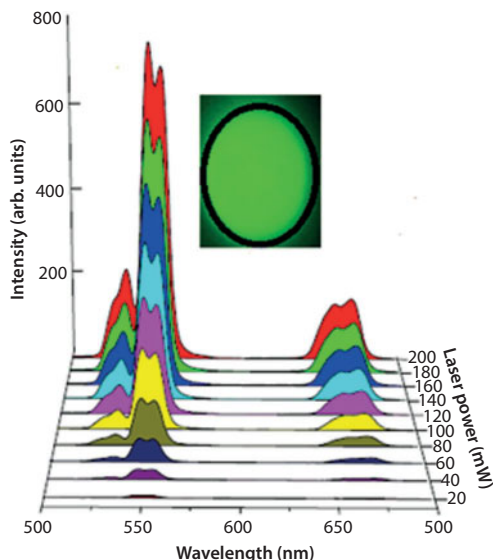


**Figure 13.20** Upconversion emission spectrum of a ( $\text{Er}^{3+}$  +  $\text{Yb}^{3+}$ ) co-doped barium fluorotellurite glass under 980 nm excitation. Inset: strong green upconversion emission of  $\text{Er}^{3+}$  under 60 mw laser [after Ref. 16].

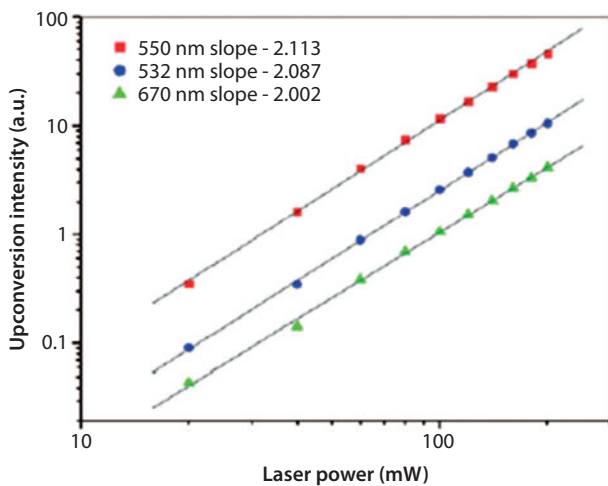


**Figure 13.21** Log-log plots of different UC luminescence of  $\text{Er}^{3+}$  vs. laser power [after Ref. 16].

emission bands, respectively, at 532, 550, and 670 nm of which the 550 nm green UC emission band is the strongest. Strong green upconversion emission from a card coated with the powdered glass under excitation of 60 mw power of the laser is shown in the inset. Figure 13.21 shows the log-log plots [16] of luminescence intensities vs. excitation power of the 980 nm laser for different UC luminescence of  $\text{Er}^{3+}$  of the glass. It is clear from the value of the slope of each of the plots that all the UC emission processes of  $\text{Er}^{3+}$  in this system involve two photons absorption.

#### 13.5.4.3 ( $\text{Tm}^{3+}$ , $\text{Ho}^{3+}$ , and $\text{Yb}^{3+}$ )-tridoped Fluorolead Germanate Glass

To prepare the glass,  $\text{PbGeO}_3$  is used as one of the principal ingredients. The other ingredients are  $\text{PbF}_2$  and  $\text{CdF}_2$ . First  $\text{PbGeO}_3$  component of the batch is separately prepared in the form of glass [61] by melting a 1:1 mixture of  $\text{PbO}$  and  $\text{GeO}_2$  at 800 °C for 30 min and then quenching to room temperature in between two copper plates. A batch is then prepared after appropriately adjusting the composition [(mol%) 70 $\text{PbGeO}_3$ -15 $\text{PbF}_2$ -15 $\text{CdF}_2$ ] for addition of (mol %) x $\text{Ho}^{3+}$ , y $\text{Tm}^{3+}$ , and z $\text{Yb}^{3+}$  of three rare earth ions. The batch mixture is then dispersed in n-heptane taken in an agate mortar and is homogenously mixed with a pestle. Finally, the glass is prepared by melting the batch in a Pt-Au crucible at 800 °C for 30 min in an ambient atmosphere. The glassy melt is then cast on a graphite mold. The glass slab obtained is then annealed at a temperature near its glass transition point for about 30 min when it is partially ceramiced.

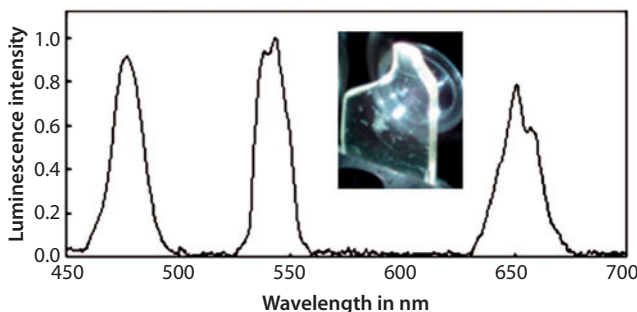


**Figure 13.22** UC luminescence spectrum of the ( $\text{Ho}^{3+}$ ,  $\text{Tm}^{3+}$ ,  $\text{Yb}^{3+}$ ) – tri-doped fluoro-lead germanate glass ceramic under 975 nm laser excitation. Inset: white light of the mixed blue, green and red emissions [after Ref. 58].

The UC luminescence spectrum of the ( $\text{Ho}^{3+}$ ,  $\text{Tm}^{3+}$ , and  $\text{Yb}^{3+}$ ) – tridoped glass-ceramic under 975 nm laser excitation [58] is shown in Figure 13.22. The white light generated as a result of mixing of blue, green and red emission of the glass is shown in the Inset. The material may be prospective for use for solid-state lighting.

### 13.6 Solid-state Luminescent Materials for Laser

Laser is basically a light source. But the light emanating from such a source differs from the light of an ordinary source mainly in three special features which are: (1) monochromatic, i.e. light rays emanating out of such a source have uniform wavelength; (2) coherent, i.e. the emanated light rays have propagation waves which are super imposable over each other making the amplitude of the resultant beam very high; and (3) unidirectional, i.e. it is directed in one direction. Figure 13.23 shows (a) a cavity of a laser source; (b) coherent nature of the light; and (c) high amplitude laser beam.

However, to achieve these special features in the emitted light from a source, we need a light emitter where the emission process involves a quantum system like atom, ion, or molecule. So luminescent materials of which absorption and emission processes meet the criteria required for achieving laser action in the emission, can be considered as laser source. The term LASER originates from an optical phenomenon of light amplification by stimulation of emission process of an emitter. In fact the concept of stimulated emission was first introduced theoretically by A. Einstein in 1917. He actually extended, the concept of mechanism of

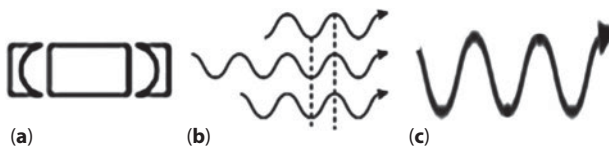


**Figure 13.23** (a) Cavity of a LASER source. (b) Coherent emission. (c) Amplified beam.

absorption of light by an atom or ion or a molecule in its ground state, to the process of emission of light by an atom or ion or molecule in an excited state. He proposed that the atoms or ions or molecules of an emitter in the excited state can emit in two processes: (1) mostly by spontaneous emission because they are in an excited state which is unstable, and (2) an additional emission due to stimulation of the excited state atoms or ions or molecules by the electromagnetic field of the light of the spontaneous emission. He argued that similar to the process of absorption, where a ground state atom or ion or molecule of an absorber get stimulated by the electromagnetic field of the incident radiation to absorb photon energy and jump to its excited state, the electromagnetic field of the light of emission of the activators, which have already partially emitted spontaneously, should stimulate the remaining excited state activators to come down to the ground state by emitting photon. This second type of emission is termed as stimulated emission. Unfortunately in a normal luminescence process fraction of stimulated emission compared to spontaneous emission, is so low that it is not detectable. So two main requirements for achieving sufficient stimulated emission in a quantum system are: (1) the system of choice, should have such an energy levels disposition so that an inversion of population of the atoms/ ions/ molecules can be easily created in the upper laser level with respect to population of the species in the terminal level; (2) designing of a suitable cavity configuration where the light of the emission can have maximum interaction with number of atoms/ions/molecules still left in the excited state to generate stimulated emission. Mathematically it can be easily shown that for a quantum emitting system having only two energy levels (the ground and an excited state), it is not possible [63] to create population inversion. It is possible to create the same in the case of systems having three or more energy levels disposition. The life time of the emitting state of the system is also an important factor. It should not be very short or very long. In other words, the emitting state should be a meta-stable one so that in spite of spontaneous emission process a sufficient number of activators are left in the excited state to get stimulated by the emitted light.

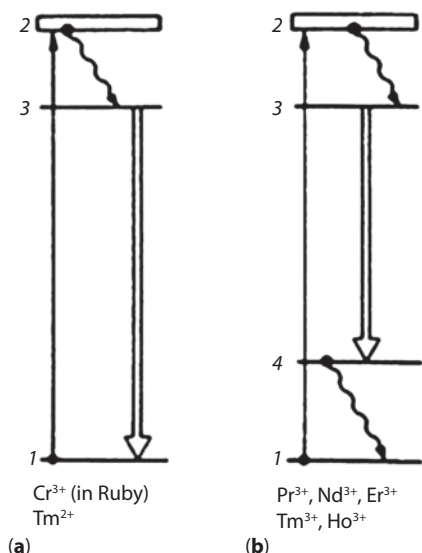


**Figure 13.24** (a and b) Energy level schemes normally observed in the process of laser action of an emitter.

Energy levels scheme of some ions which exhibit laser action are shown in Figure 13.24(a) and (b).

Theodore Maiman in 1960 first succeeded in designing a cavity configuration (Figure 13.25) which facilitated interaction of the spontaneously emitted light with the activators still left in the excited state and thus achieved considerable stimulated emission in the luminescence process of the activator  $\text{Cr}^{+3}$  of a ruby crystal ( $\text{Al}_2\text{O}_3$ ;  $\text{Cr}^{+3}$ ). The laser action in this system operates in three levels scheme shown in diagram (a) of Figure 13.24. Immediate after the successful demonstration of laser action in Ruby crystal, laser action was also achieved in different lanthanide and actinide ions activated crystals [64–67] and glasses [68]. Subsequently intense research for deeper understandings of optical spectroscopy of various luminescent ions like (3d) transition metal ions  $\text{Ti}^{3+}$ ,  $\text{Cr}^{2+}$ ,  $\text{Cr}^{4+}$ ,  $\text{Ni}^{2+}$  and (4f) rare earth ions  $\text{Ce}^{3+}$ ,  $\text{Pr}^{3+}$ ,  $\text{Nd}^{3+}$ ,  $\text{Dy}^{3+}$ ,  $\text{Ho}^{3+}$ ,  $\text{Er}^{3+}$ ,  $\text{Tm}^{3+}$ ,  $\text{Yb}^{3+}$  doped in both crystals and glasses was initiated worldwide to see the feasibility of use of their luminescent properties for laser action. Emission bands/lines of some of these ions in oxide hosts, which are potential for laser action, are shown in Figure 13.26(a) and (b).

To develop an efficient solid-state laser material, the host should be more or less optically and chemically inert. The crystal or glass containing the active ions/centers should be transparent to the generated laser

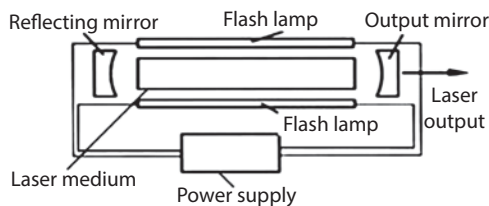


**Figure 13.25** Cavity configuration of a solid-state laser.

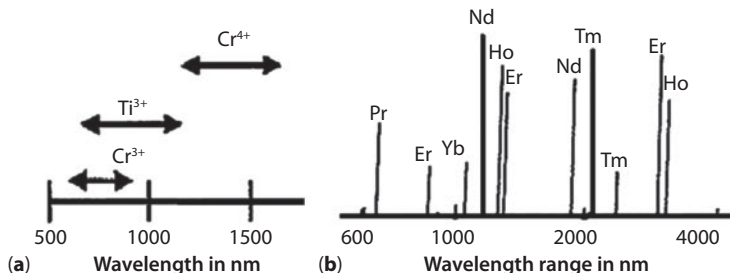


**Figure 13.26** (a) Emission bands/lines of some of the transition metal ions which are proved potential for efficient laser action [after Ref. 66]. (b) Emission lines of some of the rare earth ions potential for efficient laser action [after Ref. 66].

radiation. The laser radiation should not create light induced color centers and defect centers in the host matrix on multiple transits through the latter. The host should also not interact chemically with the activator/center so that the chemical state of the activator [11] remains unaltered even after repeated use.

Development of new crystal growth techniques, improvement of known techniques and development of newer glass compositions and technologies for their preparation have resulted birth of various newer laser crystals and glasses. The selection of the best laser crystals/glass judging the figure-of-merit [69–72] is very important. We will discuss here optical properties of some of the best known laser crystals/glasses.

### 13.6.1 Nd<sup>3+</sup>-YAG/Nd<sup>3+</sup>-glass Laser

The laser medium is Nd<sup>3+</sup> doped yttrium aluminum garnet(YAG) crystal where activator is Nd<sup>3+</sup> ions. Since the ionic sizes of Nd<sup>3+</sup> and Y<sup>3+</sup>, are similar, the dopant Nd<sup>3+</sup> ions when incorporated in to the host, occupy substitutional Y<sup>3+</sup> positions of the host's (YAG) structure. Laser operation of YAG: Nd<sup>3+</sup> was first demonstrated by J.E. Geusic *et al.* [65] at Bell Laboratories

in 1964. YAG: Nd<sup>3+</sup> absorbs mostly in the bands between 730–760 nm and 790–820 nm. So it is pumped optically either by using krypton/xenon flashtubes or appropriate laser diode array. Main emission occurs in the NIR region with a maximum at 1064 nm. The lasing process follows a four level scheme as shown in Figure 13.24(b). Nd<sup>3+</sup> ion has other emissions also, e.g. bands with maxima at 940, 1120, 1320, and 1440 nm, respectively. Figure 13.27(a) shows picture of samples of Nd<sup>3+</sup> doped YAG crystals, while Figure 13.27(b) shows a sample of Nd<sup>3+</sup> doped polished laser glass rod.

YAG:Nd<sup>3+</sup> lasers operate in both pulsed and continuous mode. The concentration of Nd<sup>3+</sup> ions in the host can be increased up to a certain level to increase the laser power. The laser performance [67] of a Nd-YAG single crystal rod resonator is shown in Figure 13.28. Nd-crystal laser is used in materials processing, medical surgery, target designation, etc. Nd<sup>3+</sup>-glass

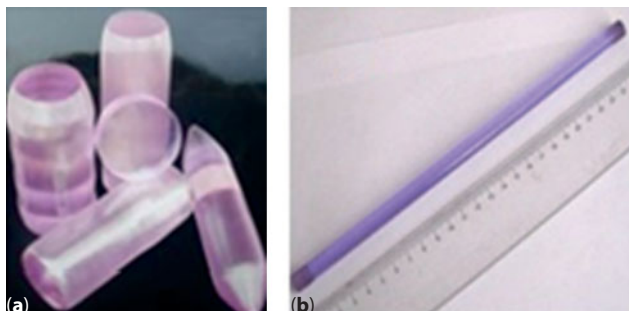


**Figure 13.27** (a) Nd<sup>3+</sup>-doped single crystals. (b) A sample of polished Nd<sup>3+</sup>-doped laser glass rod.

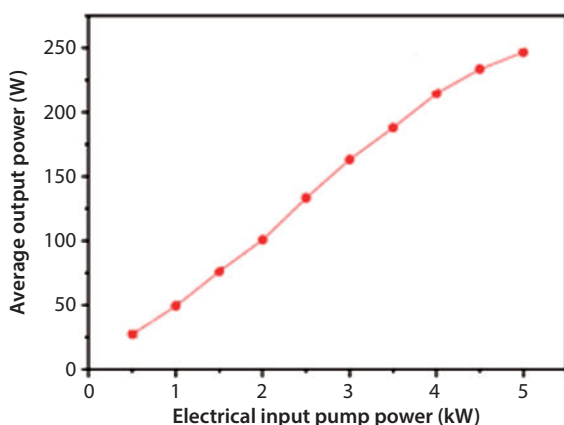


**Figure 13.28** Plot of average output power vs. average input pump power of a Nd:YAG single crystal rod resonator (Nd<sup>3+</sup>-concentration = 1.1 at.%) [after Ref. 67].

laser [68], on the other hand, finds application in fusion research where a very high power is required.

### 13.6.2 Yb<sup>3+</sup>-YAG Laser

Here again the host is yttrium aluminum garnet (YAG) and the luminescent center is Yb<sup>3+</sup>. The Yb<sup>3+</sup> ion exhibit a broad emission peaking at 1015 nm which is an average of its all possible inter stark level transitions. Its strong absorption band lies at ~ 983 nm and hence can be pumped by using a diode array. The crystal is grown by Czochralski method. The batch is melted in an iridium crucible using induction coil. The growth process starts on a seed rod. Variation of experimental decay time of the  $^2F_{5/2}$  emitting state of Yb<sup>3+</sup> as a function of its concentration in the crystal has been studied [73, 74] in order to understand the mechanism of concentration quenching of its luminescence and estimate parameters those can indicate the prospect of use of the crystal as laser medium. It has been reported [73] that to achieve optimum gain, the concentration of Yb<sup>3+</sup> in a YAG: Yb<sup>3+</sup> laser crystal should be around  $N = 1.98 \times 10^{21} \text{ cm}^{-3}$  (i.e. 14.3%). Figure 13.29 shows the picture of a sample of as grown Yb<sup>3+</sup>doped YAG crystal [66].

### 13.6.3 Ho<sup>3+</sup>/Yb<sup>3+</sup> Co-doped Tellurite-based Laser Glass

In this glassy laser medium Ho<sup>3+</sup> ion is the luminescent center of which NIR emission due to the  $^5I_7 \rightarrow ^5I_8$  transition is utilized for laser action. The host is a (Ba, La)-tellurite glass. Yb<sup>3+</sup> is co-activated as sensitizer for efficient excitation of Ho<sup>3+</sup>. The material can be prepared [9] by melting a batch of the glass composition (mol%) TeO<sub>2</sub> (70–65), ZnO (15–10), MO (20–15); [M = Ba, Sr] and LaO<sub>3</sub>/2 (10–5) doped with 2 mol% Yb<sup>3+</sup>and 0.5 mol% Ho<sup>3+</sup>, at a temperature 800–850 °C for an hour in a Pt crucible. The co-activator Yb<sup>3+</sup> ion is first excited through its  $^2F_{7/2} \rightarrow ^2F_{5/2}$  transition using 983



**Figure 13.29** Picture of a Yb<sup>3+</sup>-doped YAG crystal <111> grown by Czochralski method [after Ref. 66].

nm diode laser, which subsequently makes a phonon assisted energy transfer [5] of its emission energy to the activator  $\text{Ho}^{3+}$  ion raising the latter to the 1153 nm  ${}^5\text{I}_6$  excited state. The excited state  $\text{Ho}^{3+}$  ion then emits through  ${}^5\text{I}_7 \rightarrow {}^5\text{I}_8$  transition covering wavelength range 1900–2100 nm. The absorption and emission cross-section spectra of  $\text{Ho}^{3+}$  of the glass [9] are shown in Figure 13.30. A study on the gain spectrum (Figure 13.31) of the  ${}^5\text{I}_7 \rightarrow {}^5\text{I}_8$

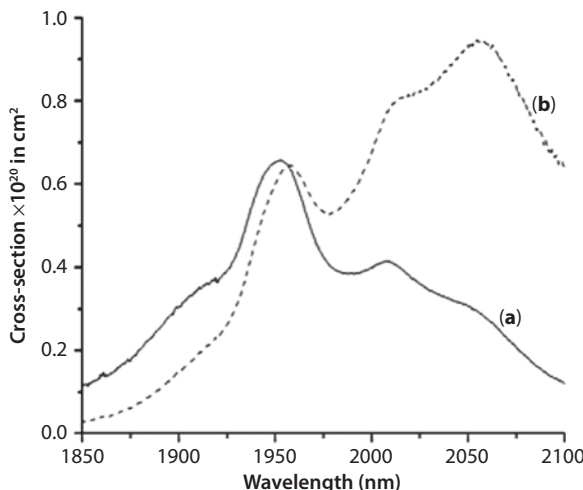


**Figure 13.30** Absorption (a) and emission cross-section (b) spectra of  $\text{Ho}^{3+}$  of the glass [after Ref. 9].

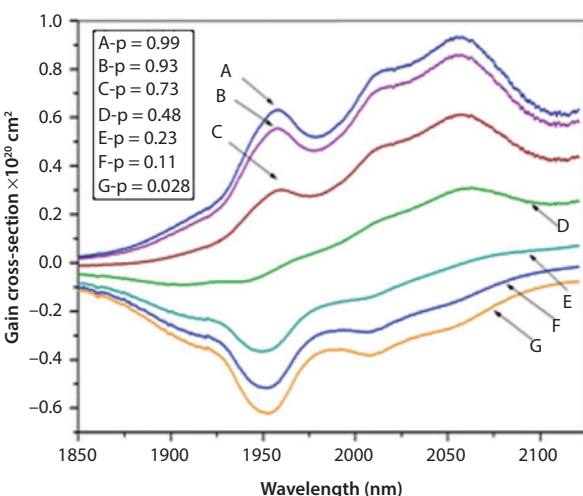


**Figure 13.31** Gain spectrum of the  ${}^5\text{I}_7 \rightarrow {}^5\text{I}_8$  NIR emission of  $\text{Ho}^{3+}$  of the glass [after Ref. 9].

emission cross-section of  $\text{Ho}^{3+}$  showed that the laser operation in the wavelength range 2000–2075 nm can be achieved in this system [9]. The laser operation in this system follows the energy level scheme (a) of Figure 13.24.

## Acknowledgments

The author expresses his sincere thanks to all his PhD students (Dr J. Chowdhuri, Dr R. Sahoo, Dr A. Nayak, S. Balaji, and Dr S. Bose) who did some of the research work presented in this chapter during their PhD theses work and now after receiving their PhD degree have gone to the outer world.

## References

1. Becker, R. S., *Theory and Interpretation of Fluorescence and Phosphorescence*, pp 157–158, Wiley-Interscience, New York, 1969
2. Debnath, R., On the excitation of  ${}^3\text{E}$  luminescent state of copper ions in glass, *J. Lumin.*, 43, 375, 1989.
3. Pfau, C., Miclea, P.-T., Bohley, C., Schweizer, S., Phonon spectra of barium halide nanocrystals in fluorozirconate glasses, *IOP Conf. Series: Mater. Sci. Eng.*, 15, 012021, 2010.
4. Nayak, A., Sahoo, R., Debnath, R., Hydration induced coupling of the excitonic state of  $\text{Y}_2\text{O}_3$  with its phonon: Negative effect on the luminescence efficiency of  $\text{Eu}_2\text{O}_3$ :  $\text{Eu}^{+3}$  nanophosphor, *J. Mater. Res.*, 22, 35, 2007.
5. Debnath, R., Bose, S., A comprehensive phononics of phonon assisted energy transfer in the  $\text{Yb}^{3+}$  aided upconversion luminescence of  $\text{Tm}^{3+}$  and  $\text{Ho}^{3+}$  in solids, *J. Lumin.*, 161, 103, 2015.
6. Judd, B. R., Optical absorption intensities of rare-earth ions, *Phys. Rev.*, 127, 750, 1962.
7. Ofelt, G. S., *J. Chem. Phys.*, 37, 511, 1962.
8. Ghosh, A.; Debnath, R.; Judd-Ofelt analysis of  $\text{Er}^{+3}$  ion in a fluoro-barium tellurite glass, *Opt. Mater.*, 31, 604, 2009.
9. Bose, S., Misra, D., Debnath, R.,  $\text{Ho}^{3+}$  ion in a (Ba, La)-tellurite glass: Strong  $2.0\mu\text{m}$  NIR emission and  $\text{Yb}^{3+}$  aided efficient NIR to Vis upconversion, *Optical. Mater.*, 2013, 36, 221.
10. Bose, S., Debnath, R., Strong crystal-field effect and efficient phonon assisted  $\text{Yb}^{3+} \rightarrow \text{Tm}^{3+}$  energy transfer in a ( $\text{Yb}^{3+}/\text{Tm}^{3+}$ ) co-doped high barium-tellurite glass, *J. Lumin.*, 155, 210, 2014.
11. Debnath, R., Das S. K., Site dependent luminescence of Cu(I) in silica glass, *Chem. Phys. Letts.*, 155, 52, 1989.
12. Sahoo, R., Debnath, R., Phosphor for lamps, *unpublished work*, 2001 – 2004

13. Sahoo, R., Bhattacharya, S. K., Debnath, R., Strong green and red emission from a newly developed calcium fluoro-aluminate: Eu<sup>3+</sup> phosphor, *J. Mater. Res.*, 18, 609, 2003.
14. Yu, M., Wang, H., Lin, C. K., Li, G. Z., Lin, J., Sol-gel synthesis and photoluminescence properties of spherical SiO<sub>2</sub>@LaPO<sub>4</sub>:Ce<sup>3+</sup>/Tb<sup>3+</sup> particles with a core-shell structure, *Nanotechnology*, 17, 3245, 2006.
15. Bose, S., Debnath, R., Optical Characterization of Tm<sup>3+</sup> ion in a high Barium-tellurite glass in absence and presence of Yb<sup>3+</sup>: Evidence of Strong Crystal-field effect and Efficient Yb<sup>3+</sup>→Tm<sup>3+</sup> energy transfer, *J. Lumin.*, 169, 782, 2016.
16. Pokhrel, M., Kumar, G.A., Balaji, S., Debnath, R., Sardar, D. K., Optical characterization of Er<sup>3+</sup> and Yb<sup>3+</sup> co-doped barium fluorotellurite glass, *J. Lumin.*, 132, 1910, 2012.
17. Saboktakin, M., Ye, X.; Ju Oh, S., Hong, S-H., Fafarman, A. T., Chettiar, U.K., Engheta, N., Murray, Christopher B., Kagan, Cherie R., Metal-enhanced upconversion luminescence tunable through metal nanoparticle-nanophosphor separation, *ACS Nano*, 6, 8758, 2012.
18. Ghosh, A., Balaji, S., Debnath, R., Synthesis and optical properties of (Er<sub>2</sub>Te<sub>4</sub>O<sub>11</sub>) nanocrystals dispersed upconverting tellurite glass for use as NIR sensor and solar concentrator, *Chem. Phys. Lett.*, 474, 331, 2009.
19. Balaji, S., Debnath, R., Enhanced green emission from Er<sub>2</sub>WO<sub>6</sub> nanocrystals embedded composite tellurite glasses, *J. Fluoresc.*, 21, 1053, 2011.
20. Wachtel, A., The effect of impurities on the plaque brightness of a 3000°K calcium halophosphate phosphor, *J. Electrochem. Soc.*, 105, 256, 1958.
21. Debnath, R., Nayak, A., Ghosh, A., On the enhancement of luminescence efficiency of Y<sub>2</sub>O<sub>3</sub>: Eu<sup>3+</sup> red phosphor by incorporating (Al<sup>3+</sup>, B<sup>3+</sup>) in the host lattice, *Chem. Phys. Lett.*, 444, 324, 2007.
22. McCumber, D. E., Einstein relations connecting broad band emission and absorption spectra, *Phys. Rev.*, 136, A954, 1964.
23. Forster, Th., Excitation transfer, in *Comparative Effects of Radiation*, Burton, M., Kirby-Smith J. S. and Magee, J. L. (eds), Wiley, New York, 1960.
24. Miyakawa, T., Dexter, D. L., Phonon Sidebands, Multiphonon Relaxation of Excited States, and Phonon-Assisted Energy Transfer between Ions in Solids, *Phys. Rev. B*, 1, 2961, 1970.
25. Orbach, R. L.; Relaxation and Energy Transfer, in *Optical Properties of Ions in Solids*; Plenum, New York, 1975.
26. Kamiya, S., Mizuno, H., Phosphors for lamps in *Phosphor Handbook*, (2<sup>nd</sup> Edition), Yen, W. M.; Shionoya, S.; Yamamoto, H. (Eds) CRC Press, Boca Raton, 2007.
27. Sahoo, R., Bhattacharya, S. K., Debnath, R., A new type of charge compensating mechanism in Ca<sub>5</sub>(PO<sub>4</sub>)<sub>3</sub>F:Eu<sup>3+</sup> phosphor. *J. Sol. Stat. Chem.*, 175, 218, 2003.
28. Miura, N., Phosphors for X-ray and ionizing radiation, in *Phosphor Handbook* (2<sup>nd</sup> Edition), Yen, W. M.; Shionoya, S.; Yamamoto, H. (Eds) CRC Press, Boca Raton, 2007.

29. Inaho S., Hase, T., Phosphors for cathode-ray tubes, in *Phosphor Handbook* (2<sup>nd</sup> Edition), Yen, W. M.; Shionoya, S.; Yamamoto, H. (Eds) CRC Press, Boca Raton, 2007.
30. *Phosphor\_Information\_Leaflet\_L-O2-02*; <https://www.fh-muenster.de>
31. Koike, J., Kojima, T., Toyonaga, R., Takahashi, K., Kagami, A., Hase, T., *Tech. G., Electron Device*, Inst. TV Eng. Jpn., ED317, 1977.
32. Kojima T., Hisamune, T., Phosphors for plasma display, in *Phosphor Handbook* (2<sup>nd</sup> Edition), Yen, W. M.; Shionoya, S.; Yamamoto, H. (Eds) CRC Press, Boca Raton, 2007.
33. Kim, K. N., Jung, H. K., Park, H. D., Synthesis and characterization of red phosphor (Y,Gd)BO<sub>3</sub>:Eu by the coprecipitation method, *J. Mater. Res.*, 17, 907, 2002.
34. Rao, P. R., Eu<sup>3+</sup> activated red emitting phosphors for PDP applications, *SID 03 Digest*, 1219, 2003.
35. Justel, T.; Krupa, J. C., Wiechert, D. U., VUV spectroscopy of luminescent materials for plasma display panels and Xe- discharge lamps, *J. Lumin.*, 93, 179, 2001.
36. Takei, M.; Tamura, A.; Takahashi, K.; Wani, K.; *Tech. Report*, Inst. TV Eng. Jpn., 16, 43, 1992.
37. Masui, H., Yamada, H., Iso, K., Nakamura, S., DenBaars, S. P., Optical polarization characteristics of *m*-oriented InGaN/GaN light-emitting diodes with various indium compositions in single-quantum-well structure, *J. Phys. D: Appl. Phys.* 41, 225104, 2008.
38. McKeag, A.H. and Steward, E.G., *Br. J. Appl. Phys.*, Suppl. 4, S16, 1955,
39. Ouweltjes, J. L., Wanmaker, W. L., Contribution to the problem of nonstoichiometry in oxygen-dominated phosphors, *J. Electrochem. Soc.*, 103, 160, 1956.
40. Tamaki H., Murazaki, Y., Phosphors for lamps, in *Phosphor Handbook* (2<sup>nd</sup> Edition), Yen, W. M.; Shionoya, S.; Yamamoto, H. (Eds) CRC Press, Boca Raton, 2007.
41. Shimizu, Y., Sakano, K., Noguchi, Y., Moriguchi, T., Light emitting device having a nitride compound semiconductor and a phosphor containing a garnet fluorescent material, US. Pat. No. 5,998,925, assigned to Nichia Kagaku Kogyo Kabushiki Kaisha (JP), 1997.
42. Pan, Y. X., Wu, M. M., Su, Q., Tailored photoluminescence of YAG: Ce phosphor through various methods, *Phys. Chem. Solids*, 65, 845, 2004.
43. Schubert, E. F.; Kim, J. K., Solid-state light sources getting smart, *Science*, 308, 5726, 1274, 2005.
44. Xiaa, G., Zhoua, S., Zhang, J., Xua, J., Structural and optical properties of YAG:Ce<sup>3+</sup> phosphors by sol-gel combustion method, *J. Cryst. Growth*, 279, 357, 2005.
45. Shi, H., Z<sup>hu</sup>, C., Huang, J., Chen, J.; Chen, D., Wang, W., Wang, F., Cao, Y., Yuan, X., Luminescen<sup>ce</sup> properties of YAG: Ce, Gd phosphors synthesized under vacuum condition and their white LED performances, *Opt. Mater. Express*, 4, 649, 2014.

46. Li, X., Budai, John D., Liu, F., Howe, Jane Y., Zhang, J., Wang, Xiao-J., Gu, Z., Sun, C., Meltzer, R. S., Pan, Z., New yellow  $\text{Ba}_{0.93}\text{Eu}_{0.07}\text{Al}_2\text{O}_4$  phosphor for warm-white light-emitting diodes through single-emitting-center conversion, *Light Sci. Applis.*, 2, e50, 2013.
47. Svetlana V. E.; Jean-Claude G. B., Lanthanide luminescence for functional materials and bio-sciences, *Chem. Soc. Rev.*, 39, 189, 2010.
48. Zhou, B., Shi, B., Jin, D.; Liu, X., Controlling upconversion nanocrystals for emerging applications, *Nat. Nanotech.*, 10, 924, 2015.
49. Chatterjee, D. K., Rufaihah, A. J., Zhang, Y., Upconversion fluorescence imaging of cells and small animals using lanthanide doped nanocrystals, *Biomaterials*, 29, 937, 2008.
50. Xu, Can T., Svenmarker, P., Liu, H., Wu, Xia., Messing, Maria E., Wallenberg, L. R., Andersson-Engels, S., High-resolution fluorescence diffuse optical tomography developed with nonlinear upconverting nanoparticles, *ACS Nano*, 6, 4788, 2012.
51. Wilhelm, S., Hirsch, T., Patterson, W. M., Scheucher, E., Mayr, T., Wolfbeis, Otto, S., Multicolor upconversion nanoparticles for protein conjugation, *Theranostics*, 3, 239, 2013.
52. Chen, G., Shen, J., Ohulchanskyy, T. Y., Patel, N. J., Kutikov, A., Li, Z., Song, J., Pandey, R. K., Ågren, H., Prasad, P. N., Han, G., ( $\alpha$ -NaYbF<sub>4</sub>:Tm<sup>3+</sup>)/CaF<sub>2</sub> Core/shell nanoparticles with efficient near-infrared to near-infrared upconversion for high-contrast deep tissue bioimaging, *ACS Nano*, 6, 8280, 2012.
53. Shalav, A., Richards, B. S., Trupke, T., Krämer, K. W., Güdel, H. U., Application of NaYF<sub>4</sub>: Er<sup>3+</sup> up-converting phosphors for enhanced near-infrared silicon solar cell response, *Appl. Phys. Letts.* 86, 013505, 2005.
54. Van der Ende, B. M., Aarts, L., Meijerink, A., Lanthanide ions as spectral converters for solar cells, *Phys. Chem. Chem. Phys.*, 11, 11081, 2009.
55. Wang, H-Q., Batentschuk, M., Osvet, A., Pinna, L., Brabec, C. J., Rare-earth ion doped up-conversion materials for photovoltaic applications, *Adv. Mater.* 23, 2675, 2011.
56. Chen, D., Wang, Y., Zheng, K., Guo, T., Yu, Y., Huang, P., Bright upconversion white light emission in transparent glass ceramic embedding Tm<sup>3+</sup>/Er<sup>3+</sup>/Yb<sup>3+</sup>: beta-YF<sub>3</sub> nanocrystals, *Appl. Phys. Letts.*, 91, 1903, 2007.
57. Mahalingam, V., Mangiarini, F., Vetrone, F., Venkatramu, V., Bettinelli, M., Speghini, A., Capobianco, John A., Bright white upconversion emission from Tm<sup>3+</sup>/Yb<sup>3+</sup>/Er<sup>3+</sup>-doped Lu<sub>3</sub>Ga<sub>5</sub>O<sub>12</sub> nanocrystals, *J. Phys. Chem. C*, 112, 2008.
58. Gouveia-Netoa, A. S.; Bueno, L. A., do Nascimento, R. F., da Silva, E. A. Jr., da Costaa, E. B., White light generation by frequency upconversion in Tm<sup>3+</sup>/Ho<sup>3+</sup>/Yb<sup>3+</sup>codoped fluorolead germanate glass, *Appl. Phys. Letts.*, 91, 091114, 2007.
59. Yang, J.; Zhang, C., Peng, C., Li, C.; Wang, L., Chai, R., Lin, J., Controllable red, green, blue (RGB) and bright white upconversion luminescence of Lu<sub>2</sub>O<sub>3</sub>:Yb<sup>3+</sup>/Er<sup>3+</sup>/Tm<sup>3+</sup> nanocrystals through single laser excitation at 980 nm, *Chem. Eur. J.*, 15, 4649, 2009.

60. Li, Z. Q., Li, X. D., Liu, Q. Q., Chen, X. H., Sun, Z., Liu, C., Ye, X. J., Huang, S.M., Core/shell structured  $\text{NaYF}_4\text{:Yb}^{3+}/\text{Er}^{3+}/\text{Gd}^{3+}$  Nanorods with Au Nanoparticles or shells for flexible amorphous silicon solar cells, *Nanotechnology*, 23, 025402, 2012.
61. Rapaport, A., Milliez, J., Bass, M., Fellow, L., Cassanho, A., Review of the properties of up-conversion phosphors for new emissive displays, *J. Disp. Technol.*, 2, 68, 2006.
62. Gouveia-Neto, A. S., da Costaa, E. B., Ribeirob, B. S., Intense red upconversion emission in infrared excited holmium-doped  $\text{PbGeO}_3\text{-PbF}_2\text{-CdF}_2$  transparent glass ceramic, *J. Lumin.*, 110, 79, 2004.
63. Kaminskii, A., *Laser Crystal: Their Physics and Properties*, Springer, Verlag, Berlin, 1990
64. Sorokin, P., Stevenson, M. J., Stimulated infrared emission from trivalent uranium, *Phys. Rev. Lett.*, 5, 557, 1960.
65. Geusic, J. E., Marcos, H. M., Van Uitert, L. G., Laser oscillations in Nd-doped aluminum yttrium gallium and gadolinium garnets, *Appl. Phys. Lett.*, 4, 182, 1964.
66. Boulon, G., Fifty years of advances in solid-state laser materials, *Opt. Mater.*, 34, 499, 2012.
67. Choubey, A., Vishwakarma, S. C., Ali, S., Jain, R. K., Upadhyaya, B. N., Oak, S. M., Performance study of highly efficient 520 W average power long pulse ceramic Nd:YAG rod laser, *Optics Laser Tech.*, 51, 98, 2013.
68. Snitzer, E., Optical Maser action of Nd in a barium crown glass, *Phys. Rev. Lett.*, 7, 444, 1961.
69. De Loach, L. D., Payne, S. A., Chase, L. L., Smith, L. K., Kway, W. L., Krupke, W. F., Evaluation of absorption and emission properties of  $\text{Yb}^{3+}$  doped crystals for laser applications, *IEEE J. Quant. Electron.*, 29, 1179, 1993.
70. Brenier, A., Boulon, G., New criteria to choose the best  $\text{Yb}^{3+}$ -doped laser crystals, *Europhys. Lett.*, 55, 647, 2001.
71. Brenier, A., Boulon, G., Overview of the Best  $\text{Yb}^{3+}$ -Doped Laser Crystals, *J. Alloys Compds.*, 210, 323, 2001.
72. Tsunekane, M., Taira, T., High-power operation of diode edge-pumped, glue-bonded, composite  $\text{Yb:Y}_3\text{Al}_5\text{O}_{12}$  microchip laser with ceramic, undoped YAG pump light-guide, *Jpn. J. Appl. Phys.*, 44, L 1164, 2005.
73. Taira, T., Sato, Y., Saikawa, J., Ikesue, A., Spectroscopic properties and laser operation of  $\text{RE}^{3+}$ -ion doped garnet materials, *Proc. SPIE*, 6216, 621607, 2006.
74. Moulton, P. F., in: *Proceedings CLEO(Paper WA2)*, Anaheim, CA, 1984.  $\text{Yb}^{3+}$  ion is first excited through its  $^2\text{F}_{7/2} \rightarrow ^2\text{F}_{5/2}$  transition using 983 nm diode laser, which subsequently makes a phonon assisted energy transfer [5] of its emission energy to the activator  $\text{Ho}^{3+}$  ion raising the latter to the 1153 nm  $^5\text{I}_6$  excited state. The excited state  $\text{Ho}^{3+}$  ion then emits through  $^5\text{I}_7 \rightarrow ^5\text{I}_8$  transition covering wavelength range 1900–2100 nm. The absorption and emission cross-section spectra of  $\text{Ho}^{3+}$  of the glass [9] are shown in Figure 13.30. A study on the gain spectrum (Figure 13.31) of the  $^5\text{I}_7 \rightarrow ^5\text{I}_8$



# Development in Organic Light-emitting Materials and Their Potential Applications

Devender Singh\*, Shri Bhagwan, Raman Kumar Saini,  
Vandna Nishal and Ishwar Singh

*Department of Chemistry, Maharshi Dayanand University, Rohtak,  
Haryana, India*

---

## Abstract

Research in the design and development of organic/polymeric electronic and photonic materials for optoelectronic applications is proceeding very rapidly as these are potential applicants that could promote the future prospect of highly emissive organic light-emitting devices (OLEDs). The scientific society considers organic electroluminescent materials and devices as the next generation of light emitters which may lead to future applications such as heads-up displays, automotive dashboards, billboard-type displays, home and office lighting, cell phones, digital cameras, and flexible displays. Developing sufficiently durable and flexible OLEDs will require better materials and further development of manufacturing tools and processes. To reach high luminescence, metal complexes and especially transition metal complexes have been widely investigated as exemplified by the numerous devices fabricated with Pt, Os, and Ir complexes. Other metal complexes based on lanthanides and rare-earth complexes have been also studied.

**Keywords:** Light emitters, OLEDs, metal complexes, display devices

## 14.1 Luminescence in Organic Molecules

Luminescence is the emission of electromagnetic radiation by the relaxation of an electron from the highest energy level to the lowest energy level. Emission occurs when an excitation source causes an electron of an atom or molecule to become excited, but unstable. As electron jumps back

---

\*Corresponding author: devjakhar@gmail.com

to its ground state, the extra amount of energy is released in the form of light (photon). Luminescence is not purely thermal in origin as it occurs at room temperature, so it is also called as cold light. Luminescence differs from incandescence (emission of light due to the high temperature of an object). Materials that generate the luminescence are known as phosphors. Most of the luminescent materials emit light in the visible region but may also emit in ultraviolet and infrared regions. The luminescence efficiency of these materials depends on their capacity to transform excitation energy into visible light. Luminescence can be possible in different kinds of material. Thus, small molecule, polymeric materials, organic or organometallic complexes, other crystalline, and amorphous material emits light under suitable circumstances. Commercially phosphors are mostly inorganic compounds prepared in very large scale than the organic luminescent materials. Besides inorganic light-emitting devices (LEDs), there is a strong interest in electroluminescence originating from organic or polymeric devices because they have following distinguishing features as compared to their inorganic analogues:

- (i) The structure of organic molecule is made up of strongly localized carbon–carbon bond which enables the conductivity through these bonds. The length of conjugation sets the band gap of molecules. Larger conjugation length results in small band gap, which produces red light, whereas smaller conjugation length results in generation of blue light.
- (ii) Organic molecules have well-defined spin state either singlet or triplet as luminescence processes in organic molecules are typically associated with excited state of material, while luminescence in inorganic materials is considerably due to either defects or impurities available in host lattice.
- (iii) Size of exciton tends to be small in organic molecules and remains at single molecule owing to electrostatic force of attraction among dissimilar charge carriers, resulting into emission of photon.

According to the mode of excitation, luminescence is classified into various types. Particularly, photoluminescence is the emission of light due to direct photo excitation of the emitting species [1]. Fluorescence, phosphorescence, and delayed fluorescence are well-recognized forms of photoluminescence. There are other types of luminescence that vary by the source of excitation (bioluminescence, chemiluminescence, crystalloluminescence,

electroluminescence, cathodoluminescence, mechanoluminescence, radio-luminescence, sonoluminescence, and thermoluminescence).

There are two main requirements for luminescence:

- (i) A semiconductor structure with a non-zero band gap ( $E_g$ ) is the most prime requirement for a luminescent material, e.g. metals having no band gap do not provide luminescence.
- (ii) Energy must be given to the organic materials for executing the process of luminescence.

## 14.2 Types of Luminescence

The different types of luminescence on the basis of mode of initiation and the source of excitation are explained as below:

**(i) Cathodoluminescence:** Cathodoluminescence is the emission of light of specific wavelength due to irradiation of a high-energy electron beam on a luminescent material. When a luminescent material such as quartz or calcite with small energy gap is bombarded by electrons of appropriate energy, electrons from lower-energy valence band are shifted to the high-energy conduction band, leaving behind a hole. The recombination of electron and hole results in luminescence. The nature of cathodoluminescence in materials depends on its purity, lattice structure, composition, and defect state. From many years, cathodoluminescence was used for constructing displays, flat screen displays like liquid crystal displays (LCDs) and classical cathode ray tube. Cathodoluminescence is most commonly used to examine the internal structure of semiconductor, ceramics, glass, rocks, etc. in order to get information regarding growth, deformation, and quality of materials.

**(ii) Bioluminescence:** Bioluminescence is the process of generation of light by living organisms. Certain luminescent materials in these living organisms are excited via an oxidation reaction, catalyzed by enzyme in the presence of air which results in luminescence. Hence, bioluminescence is associated to chemiluminescence. This is the most effective way of producing light as it converts almost all absorbed energy into light without wasting any energy in producing heat. It is very beneficial in deep sea as it may provide survival advantage in the darkness of the deep sea and allow them to attract their mate, find food, communicate, and assist the self-defensive

mechanism. Few organisms, e.g. fireflies generate light-producing protein (luciferin) and enzyme (luciferase). Luciferin pigment produces light by the reaction with oxygen and luciferase works as a catalyst for the catalytic reaction. However, some bioluminescent members do not produce luciferin and luciferase chemicals. As an alternate, they take it through other members either by eating it or through a symbiotic relationship. This means that an organism may be bioluminescent if it does not initially produce bioluminescence at earlier stage of life cycle.

**(iii) Chemiluminescence:** Luminescence resulted from chemicals or electrochemical reaction concerning an oxidation-reduction process. The energy required for chemiluminescence comes from the enthalpy in a highly exothermic reaction. The chemical reaction creates few pioneering molecules that can shift its electrons in an excited state just after creation. After that these electrons decay to ground state producing light energy in the visible region or liberate the energy in some other useful form. 5-Aminophthalhydrazide (Luminol) is the most commonly available artificial chemoluminescent product. Luminol is used by detectives at crime scenes in forensics laboratories as it reacts with very small amount of iron present in blood and produce luminescence.

**(iv) Thermoluminescence:** Thermoluminescence is a temperature-dependent phenomenon which illustrates that some crystalline materials on heating produce luminescence that is different from black body radiation or incandescence. Mechanism of thermoluminescence first involves the alteration of system from equilibrium state to intermediate state as consequences of absorbing the light and then relaxed the system back to the equilibrium by release of energy due to thermal stimulation. Thermoluminescence is a significant technique for dating some ancient pottery samples, mineralization, growth rate of sand dunes, and sedimentation.

**(v) Crystalloluminescence:** This type of luminescence occasionally generated in duration of crystallization. This is some other type of chemiluminescence as the energy is produced critically from bonding between the atoms. Crystalloluminescence emerges through separation of electrical charges on the microfractures developed on the surface of growing crystallites. The main purpose of studying this luminescence as it is used determines the critical size of the crystalline nucleus.

**(vi) Radioluminescence:** Radioluminescence is produced when appropriate materials are bombardment with radioactive particles and photons

like  $\alpha$ ,  $\beta$ , or  $\gamma$  rays emitted from radioactive substance. Radio luminescent paints are commonly used as low-level light source for dial marking in watches and other instruments, enabling them to read even in the dark.

(vii) **Sonoluminescence:** It is the emissions of short burst of photons generating due to collapse of gas-filled bubbles in a solvent on excitation by ultrasound waves. The exposure of sound waves in liquid leads to the production of small bubbles which are filled with vapor and gas. Each one of these imploding bubbles can act as microreactor. High temperature and pressure created during cavitation cause the bubble to collapse quickly with a flash of light.

(viii) **Mechanoluminescence:** Luminescence generated due to action of external mechanical energy on a solid. This can be divided into three parts.

- (i) **Triboluminescence:** Emission of light generate when solid substance emits light due to mechanical deformation like cutting, scratching, rubbing, or griding, the process is known as triboluminescence.
- (ii) **Piezoluminescence:** Light emitted by applying when high pressure on certain solids.
- (iii) **Fractoluminescence:** Luminescence produced when bonds of all crystals are breakdown.

(ix) **Ionoluminescence:** Luminescence is produced in the visible region when fast-moving energetic ions are colliding with organic or crystalline compounds. This spectroscopy technique is very useful for explaining material phenomena such as presence of impurity, symmetry of molecules, production of internal defects, and interaction of ions with matter.

(x) **Electroluminescence:** It is a light generation phenomenon in which certain crystals produce light by passing of electric current. Electroluminescence occurs under the action of passing electric current is known as Lossev effect. Luminescence is generated due to formation of excitons (electron-hole pair) and then followed by their radiative decay. The process of generation of luminescence has different mechanisms in both organic and inorganic compounds.

Mechanism of electroluminescence is illustrates as

- (i) Electroluminescence is due to radiative recombination of excitons in a semiconductor material. Electrons after

excitation liberate energy in the form of photons in the visible region. Before recombination, electrons and holes are possibly separated via a barrier (i.e. p-n junction) in semiconductor organic light-emitting devices (OLEDs).

- (ii) Electroluminescence also can occur due to collision of high-frequency electrons under the influence of electrical field which is known as Destriau effect.
- (xi) Photoluminescence:** Emission of light generated by the photo excitation of electrons under the action of electromagnetic radiation to energetically higher electronic state by the absorbing photons which may takes place through either phosphorescence or fluorescence, or both mechanisms. Energy of emitted light is usually equal or lesser than that of irradiating light as some part of exciting energy is used to transform the nonradiating vibration of atoms or ions. Photoluminescence spectroscopy is a contactless, nondestructive technique of inquiring the electronic structure of molecules. Photoluminescence is extensively used for material quality, level of impurity, detections of defect, mechanism of recombination, as well as determination of band gap.

Photoluminescence may be divided into two kinds on the basis of emission [2]:

- (i) Fluorescence,
- (ii) Phosphorescence.

**(i) Fluorescence:** Fluorescence is an instant method in which photons are generated from appropriate luminescent materials as a consequence of absorbing electromagnetic radiation. This phenomenon stops as soon as the exciting source is removed. In fluorescence, light emission takes from excited triplet state within a time of less than  $10^{-8}$  s without change in the spin of electron. Fluorescence is a temperature-independent process, and light emission is nearly not dependant on incident radiation. Most of the molecules exist at the lowest vibrational level of their ground state at room temperature. Upon excitation by electromagnetic radiation, the molecules get excited to a higher-energy state by absorbing energy. Due to excitation, the molecule can reach to any of the vibrational sublevels associated with each electronic state. A series of absorption bands in the absorption spectrum is obtained on absorbing energy in distinct photon. The diverse vibrational energy levels are consisted of a series of rotational energy levels, which produce several absorption bands which are very difficult to resolve and consequently illustrate all the individual bands in the spectrum.

Fluorescence has numerous practical applications, as chemicals sensors, fluorescent screens, biological detectors, chemical analyzer, and fluorescent lamps.

**(ii) Phosphorescence:** Phosphorescence is a process of emission of light when certain substances are irradiated with electromagnetic radiation. The materials which show this type of luminescence are called persistent luminescent materials. These materials do not instantly re-emit the light as it absorbed because of flipping of an electron spin in excited state as it takes some time. Luminescence remains continuous for noticeable time ( $10^{-4}$ – $10^{-2}$  s) even after excitation source is removed. If the time interval is short for luminescence, then material is short-persistent phosphor. If time lasts for longer duration, it is called long-persistent phosphor. There is a strong dependence of temperature on phosphorescence decay rate which is usually increased with increase in temperature. Phosphorescence property is used to analyze water, chemical pollutants, and drugs in pharmaceutical field.

### 14.3 Mechanism of Luminescence

The distinct energy level of a luminescent material involved in the absorption and emission of photons are explained by Jablonski energy diagram as shown in Figure 14.1. This diagram features the electronic states within a molecule and different de-excitation processes occurring during the transitions between these electronic states. The main processes involves are light absorption, fluorescence (radiative transitions among the energy level of identical multiplicity), internal conversion (radiationless transitions between the level of similar multiplicity), phosphorescence (radiative transitions among the energy levels of different multiplicity), intersystem crossing (radiationless transitions between the states of different multiplicity), vibrational relaxation, etc. Generally, electronic transitions between the states of same multiplicity are allowed, whereas transitions with different multiplicity are spin forbidden. However, spin-forbidden transitions may also be possible due to spin-orbit coupling.

On absorption of electromagnetic radiation of appropriate frequency, an electron from low-lying vibrational level of the singlet ground state ( $S_0$ ) of a molecule is moved to the different vibrational level in the second singlet excited state ( $S_2$ ). The process of absorption of light and then excitation of molecules occurs very rapidly ( $10^{-15}$  s), without any change in the electronic spin. Excited state are short-lived, in the order of nanoseconds

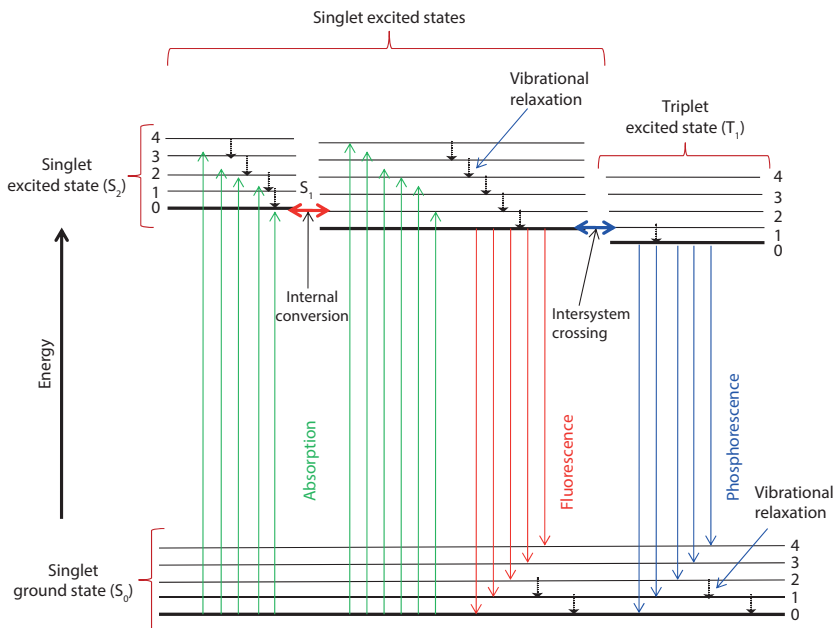


**Figure 14.1** Jablonski energy diagram showing mechanism of luminescence.

( $1 \text{ ns} = 10^{-9} \text{ s}$ ). So, an electron comes to lower-energy state by loosing extra amount of energy, either through nonradiative transitions or through generation of light. Different de-excitation processes occur with varying possibilities. The most common pathway will be relaxation to the low-lying vibrational level of the first singlet excited state ( $S_1$ ), called as vibrational relaxation or internal conversion ( $1 \text{ ps} = 10^{-12} \text{ s}$ ). Singlet excited state is the initial centre for fluorescence emission to the lowest vibrational level of the singlet ground state ( $S_0$ ), radiationless transitions to ground state (internal conversion), and decay to the lowest vibrational level of excited triplet state (intersystem crossing). The triplet state is long-lived and molecule remains for a long time before it will relax to ground state ( $S_0$ ). This spin-forbidden transition ( $T_1 \rightarrow S_0$ ) is known as phosphorescence.

#### 14.4 Organic Compounds as Luminescent Material

Generally the materials used for the fabrication of OLEDs are of organic origin and semiconducting in nature. The design and characterization of active luminescent organic materials are one of the most significant considerations for the fabrication of OLEDs as it determines stability, emission

color, and efficiency of the proposed device. In the current years, organic molecules as electroluminescent materials have sought much consideration owing to their prospective applications in smart lightning panels, ultra-thin displays [3–6], etc. The organic compounds that emit light under the action of electric current or UV light are called organic phosphor. Different types of organic materials used for this purpose are as follows.

#### 14.4.1 Small Organic Materials

These organic materials are usually low-molecular-weight complexes of organic molecules. The prerequisites for a small molecule to be used as organic emissive layer in the device are that

1. It should possess thin-film forming capability.
2. It should be highly luminescent.
3. It should be thermally stable.
4. It should also be able to transport electrons with the desired efficiency.

These materials are generally deposited onto the appropriate substrate by physical vacuum deposition technique in form of thin amorphous film or used as blender into a polymer backbone. Different classes of small organic materials are classified below.

##### *(i) Metal chelates*

Luminescent metal chelates have paying incredible attention because of their prospective utility in organic electronics. In metal chelates, ligand-centered  $\pi-\pi^*$  electronic transitions are dominant and responsible for emission of color [7]. Their properties can be tuned by both, change of the central metal ion as well as modification of complexing organic ligands. The choice of the metal ions for luminescent metal chelates is very crucial and limited to only those metals which do not exhibit d-d transition that may interfere with the luminescence of the ligand. Therefore,  $\text{Li}^+$ ,  $\text{Be}^{2+}$ ,  $\text{Mg}^{2+}$ ,  $\text{Zn}^{2+}$ ,  $\text{Al}^{3+}$ , and  $\text{B}^{3+}$  have been ideal metal ions for their application in color emission. These do not contain d-electrons, for zinc d-shell is completely filled and no d-d transition is possible. The transitions in these metal chelates are ligand centered, and metal ions are used to stabilize the structure of the luminescent ligand. Metal complexes are placed in the categories of organic materials known as organic semiconductors. Due to their extremely low intrinsic conductivity, most organic semiconductors

are designated as insulators. The use of the name semiconductors is based on the extrinsic semiconducting properties of organic systems such as transport of charge generated by light.

Numerous metal-organic complexes have been used as luminescent materials. Among these, tris(8-hydroxyquinoline)aluminum ( $\text{Alq}_3$ ) is one of the most efficient light-emitting materials.  $\text{Alq}_3$  is thermally and morphologically stable, forming thin amorphous films.  $\text{Alq}_3$  complex has been used in emissive layer as well as in electron transport layer (ETL) during the fabrication of electroluminescent devices.

Metal chelates of bivalent and trivalent metal ions (Mg, Be, Zn, Eu, Tb, Er, Dy, B, Al, Ga, In, Ru, Os, Pt, etc.) have been used as Electroluminescence (EL) materials for fabrication of OLEDs [8–19]. OLEDs with trivalent europium [20], terbium [21], and thulium [22] complexes emit monochromatic red, green, and blue lights, respectively. Trivalent samarium complex emits orange color light [23], while neodymium and erbium complexes are used to obtain yellow and orange lights [24] respectively. Within group III metals, Al (III) is the most important metal which emits green light in  $\text{Alq}_3$ . Boron also belongs to Group III like aluminum and having both metallic and non-metallic characters. It forms complexes with coordination number 3–4 to give efficient blue emission [25]. Be and Zn metals of Group II emit green light. Divalent  $\text{Eu}^{2+}$  has been used to demonstrate orange emission [26].

Trivalent rare-earth ions particularly  $\text{Sm}^{3+}$ ,  $\text{Eu}^{3+}$ ,  $\text{Tb}^{3+}$ , and  $\text{Dy}^{3+}$  form complexes that frequently emit the light in visible region owing to the intraconfigurational  $f \rightarrow f$  transitions of central ion when irradiated by near-ultraviolet radiations.

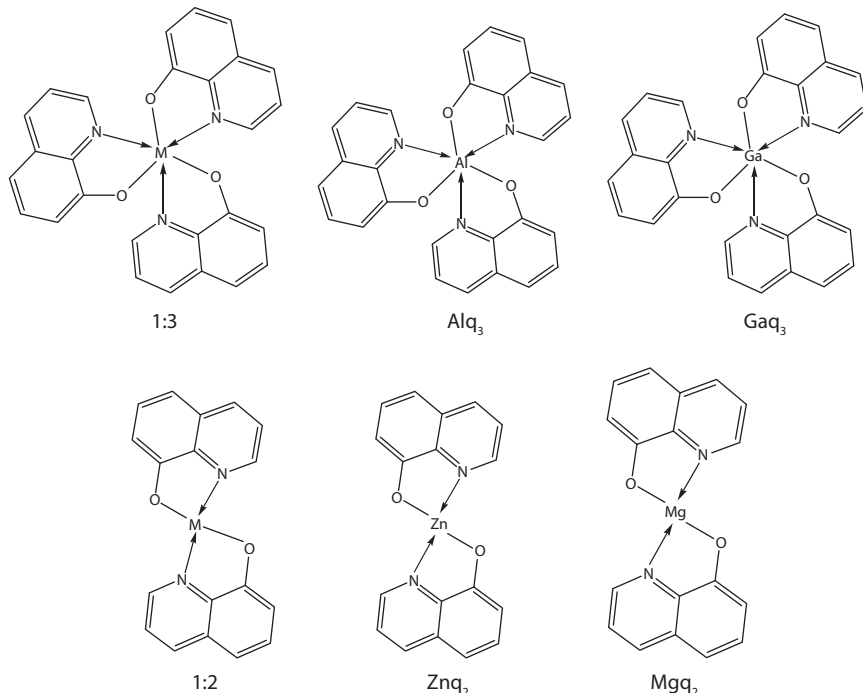
The metal ions that form complexes mainly with organic ligands 8-hydroxyquinoline derivatives, diketones, porphyrines, poly aromatics, cryptands [27, 28], podands [29, 30], carboxylic acid derivatives [31], and calixarenes [32, 33] are luminescent materials. Azomethine, 2-(2-hydroxy-phenyl)benzothiazole and porphyrin complexes and  $\beta$ -diketones complexes belong to class of organic materials for use as organic electroluminescent materials. In small molecules, many classes of complexes like complexes of 8-hydroxyquinoline and its derivatives with different metals like aluminum, gallium, indium, zinc, and rare-earth complexes with  $\beta$ -diketones are well known [34, 35].  $\text{Alq}_3$  was the first metal complex which was used as light-emitting material in OLEDs [4]. Some important classes of such materials are discussed in the proceeding section.

#### *(a) Quinoline-based metal complexes*

The most common material that is used as light-emitting material is  $\text{Alq}_3$  (1:3 complexes of aluminum with 8-hydroxyquinoline) which is first of all

reported by Tang and Van Slyke [4].  $\text{Alq}_3$  is low molecular weight, simply prepared, easily purified, keep away from exciplex formation, and green fluorescent to be a good emitter. Ga and In complexes with 8-hydroxyquinoline in 3:1 ratio as  $\text{Gaq}_3$  and  $\text{Inq}_3$  are also reported having good luminescence.

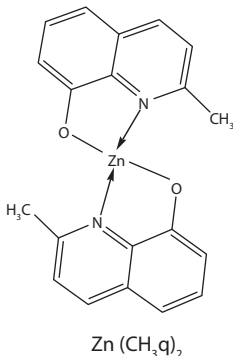
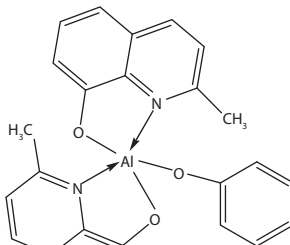
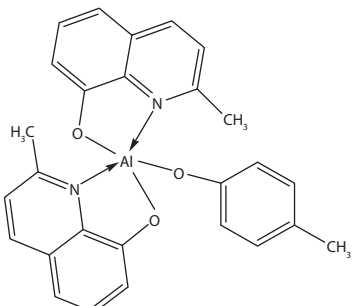
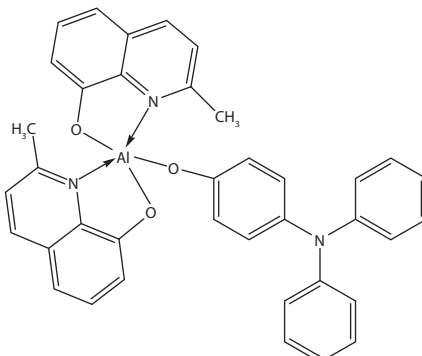
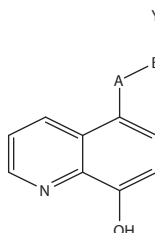
1:2 Complexes of different central ions, such as Be(II), Mg(II), Ca(II), Sr(II), Cu(II), or Zn(II), with 8-hydroxyquinoline have been synthesized.  $\text{Beq}_2$  are found to be the most fluorescent among these. Complex with metals like Cu complex are less fluorescent. However, the  $\text{Znq}_2$  complex had a strong yellow fluorescence, even though beryllium is a comparatively lighter metal than zinc. These metal complexes can be used both as an electron transport material as well as an emissive layer.



#### (b) Derivatives of 8-hydroxyquinoline-based metal complexes

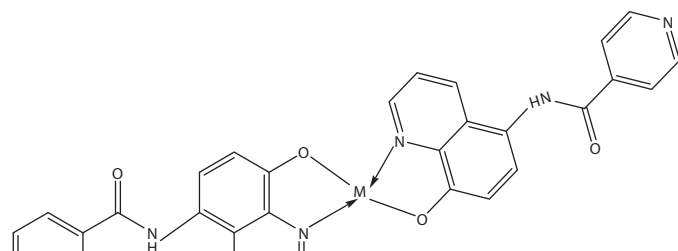
Different derivatives of 8-hydroxyquinoline as methyl substitution at C-2 position leads to the synthesis of an oxo-bridged complex,  $(\text{qAl})_2\text{O}$ , which emits a blue color but not very stable while zinc forms a bis complex  $\text{Zn}(\text{CH}_3\text{q})_2$ . Penta-coordinated bis(2-methyl-8-hydroxyquinoline) phenolate-aluminum is more stable blue light-emitting complex having formula  $(\text{q}_2\text{Al-L})$  where q is “2-methyl-8-hydroxyquinoline” and L is a phenolic or an aryl derivative of carboxylate ion.

5-Substituted-8-hydroxyquinolines having formula HQ'A—BY with aliphatic or aromatic groups are used as light-emitting material in which A-B is a connection between the HQ' (quinoline portion) to a Y (any group) which produces diverse electronic and/or steric effects.

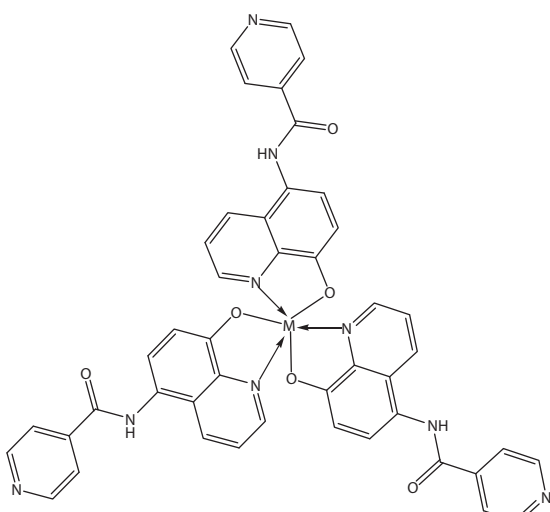
 $\text{Zn}(\text{CH}_3\text{q})_2$  $\text{Al}(\text{CH}_3\text{q})_2 \text{ (phenol)}$  $\text{Al}(\text{CH}_3\text{q})_2(4\text{-methyl-phenol})$  $\text{Al}(\text{CH}_3\text{q})_2(4\text{-diphenylamino-phenol})$ 

$\text{A-B; -N = N-; -CH = N-; -NH-CO-; -CH}_2\text{-NH-}$

Other derivatives of 8-hydroxyquinoline have also been used as light-emissive materials, among these C-5 substituted are the well known. Emission of



M = Be, Zn.2H<sub>2</sub>O, Cd.2H<sub>2</sub>O

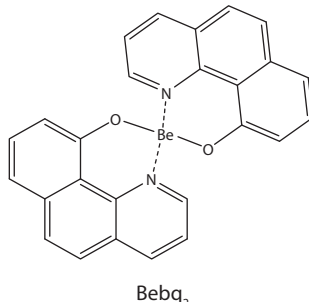


M = Al, Ga, In

light in Alq<sub>3</sub> complexes occurs from  $\pi-\pi^*$  electronic transitions localized on the quinolinolate ligands. HOMOs are positioned on the phenolate ring and LUMOs are positioned at the pyridyl ring of the ligands. According to molecular modeling predictions, attachment of electron-donating substituents at phenolate side results in a red-shift emission, while the attachment of electron-donating substituent to the pyridyl ring will cause a blue-shift emission from Alq<sub>3</sub>. If the electron-withdrawing groups are attached at the respective sites, the direction of spectral response will be reversed. Additionally, the nature of the metal ion has been shown to have a profound effect on the quinolinolate photoluminescence and electroluminescence. With increased covalent nature of the metal-ligand bonding (primarily metal-nitrogen bond), the emission is red-shifted, while the more ionic bond in strongly electropositive metal ions results in a blue shift [36, 37].

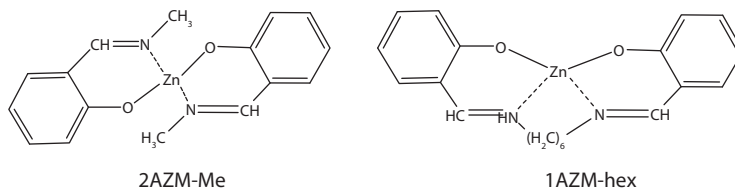
(c) Benzoquinoline-based metal complexes

Beryllium complex with 10-hydroxybenzo[h] quinoline ( $\text{Bebq}_2$ ) has been found to have a very strong green fluorescence and thermally stable which are useful as electroluminescent material.

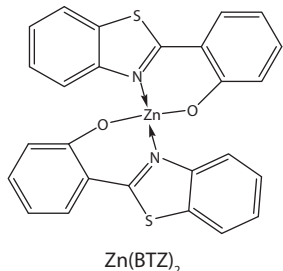


(d) Azomethine metal complexes

Metal complexes with azomethine ligands are used as blue electroluminescent materials. For example, 1:2 and 1:1 metal complexes of Zn(II) ion and *N*-methylsalicylidene amine [2AZM-Me] and *N,N'*-disalicylidenehexane-1,6-diamine [1AZM-hex], respectively [38]. The complex bis(2-(2-hydroxyphenyl)benzothiazolato)zinc [ $\text{Zn(BTZ)}_2$ ] is also a bright greenish white color-emitting material [85].

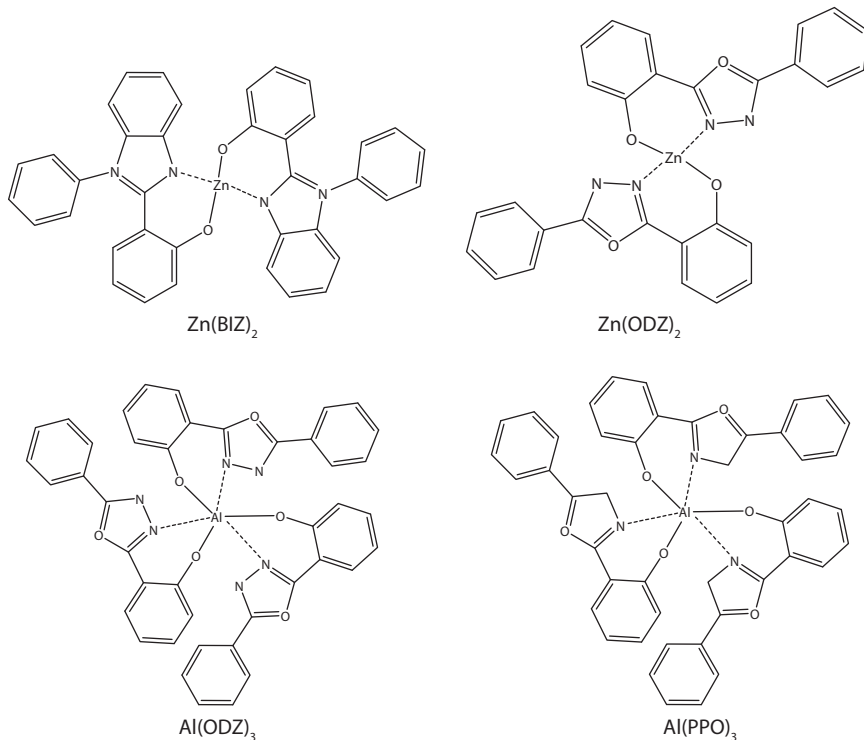


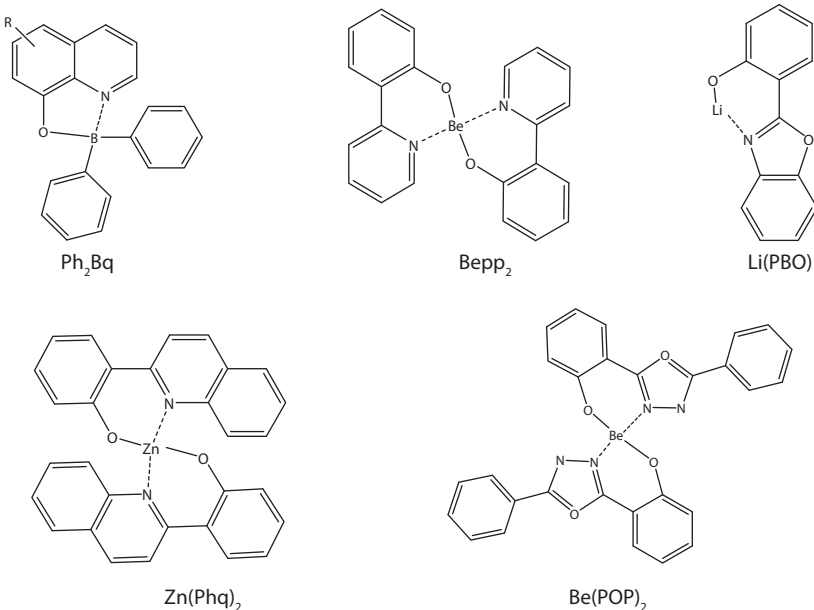
Metal chelate complexes like bis(2-(2-hydroxyphenyl)benzothiazolate) zinc [ $\text{Zn(BTZ)}_2$ ], bis(2-(2-hydroxyphenyl)benzoxazololate)zinc [ $\text{Zn(BOX)}_2$ ], and tri(4-phenanthridinolate) aluminum ( $\text{Alph}_3$ ) are also used as light-emitting materials. These complexes chelate through phenolic oxygen which is doubly bound to nitrogen to Zn or Al.



(e) Metal complexes of polycyclic aromatic or fused ring ligand

The oxadiazole, thiadiazole, phenylpyridine, benzimidazole groups, and phenyl-substituted quinoline polycyclic ligands are also used as the fused ring ligand for metal complex formation. These complexes are used as light-emitting materials for display applications. 2-(2-Hydroxyphenyl)-5-phenyloxadiazole (ODZ) and 1-phenyl-2-(2-hydroxyphenyl)benzimidazole (BIZ) chelates such as  $[\text{Zn}(\text{ODZ})_2]$ ,  $[\text{Al}(\text{ODZ})_3]$ , and  $[\text{Zn}(\text{BIZ})_2]$  are very useful blue electron-transport materials [39]. Bis[2-(2-hydroxyphenyl) pyridine]beryllium ( $\text{Bepp}_2$ ) and bis(10-hydroxybenzo[h] quinolinato) beryllium ( $\text{Bebq}_2$ ) are reported as strong green fluorescence emitter [40]. The diphenyl boron analogs of  $\text{Alq}_3$  ( $\text{Ph}_2\text{Bq}$ ) have also been used as light-emitting materials. Lithium(8-hydroxyquinolinolato) ( $\text{LiQ}$ ) and lithium(2-methyl-8-hydroxyquinolinolato) ( $\text{LiMeQ}$ ) are also found to be functional luminescent materials [41]. Metal complexes of POP = 2-(5-phenyl-1,3,4-oxadiazol-yl)phenonate; PBO = 2-(2-hydroxyphenyl) benzoxazolato; 2-(2-hydroxyphenyl)-5-phenyl-1, 3-oxazole; (PPO) and NOP = 2-(5-naphthyl-1,3,4-oxadiazolyl)phenonate ligands  $\text{Al}(\text{POP})_3$ ,  $\text{Al}(\text{PPO})_3$ ,  $\text{Li}(\text{PBO})$ ,  $\text{Be}(\text{POP})_2$ , and  $\text{Be}(\text{NOP})_2$  have been found to be blue light-emitting materials [42, 43].



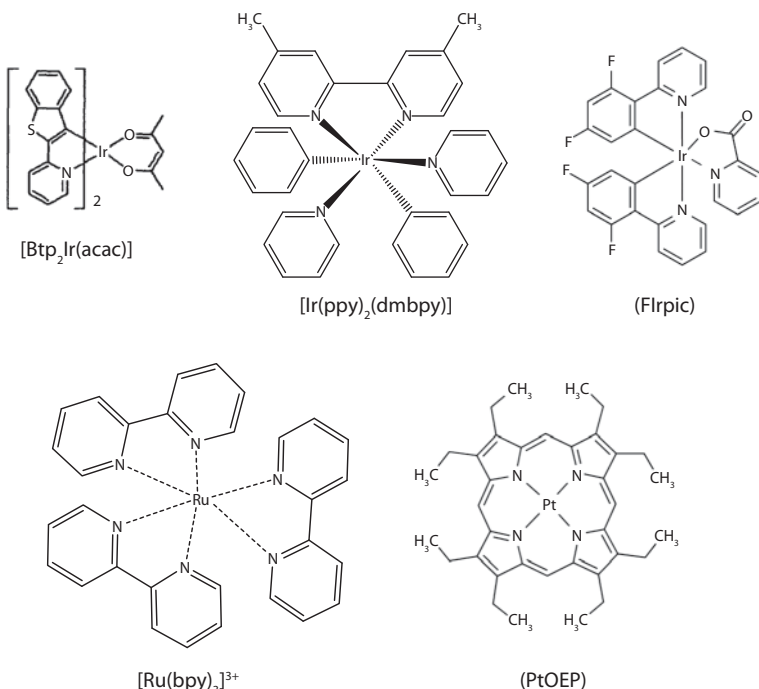


### (f) Phosphorescent materials

The materials which show phosphorescence are called phosphorescent materials or triplet-light emitter as they can produce light from both triplet- and singlet-excited states. However, confinement of triplet excitons in the organic emissive layer plays a major role for proficient phosphorescence in optoelectronic devices. Synthesis of triplet-emitting material including heavy-metal complexes is very useful in order to achieve high effectiveness in phosphorescent emission, where strong spin-orbit coupling directs to mixing of singlet- and triplet-excited states which eliminate the spin-forbidden nature of the radiative relaxation of triplet state.

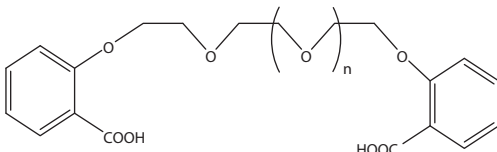
Iridium (III) chelate complexes such as bis[2-(2'-benzothienyldpyridinato-N,C<sup>3'</sup>) (acetylacetonato)iridium(III) [Btp<sub>2</sub>Ir(acac)] (44, 45), fac-tris2-phenylpyridinatodiridium(III) [Ir(ppy)<sub>3</sub>] (45), and bis[(4,6-difluorophenyl)pyridinato-N,C<sup>2'</sup>](picolinato)iridium(III) (FIrpic) (45,46) are also used as red-, green-, and blue-light-emitting materials, respectively.

Ruthenium, osmium, and platinum metal complexes like 2,3,7,8,12,13,17,18-octaethyl-12H,23H-porphine platinum(II) (PtOEP) [47], [Os(bpy)<sub>2</sub>L]<sup>2+</sup>(PF<sub>6</sub>)<sup>2-</sup>, and [Ru(bpy)<sub>3</sub>]<sup>3+</sup> where L is *cis*-1,2-bis(diphenylphosphino)ethylene and bpy is 2,2'-dipyridyl are used as light-emitting metal chelate complexes.

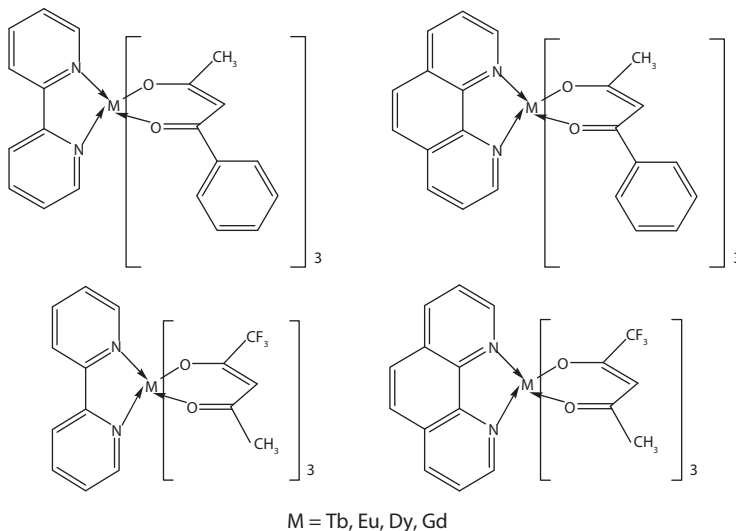


*(g) Lanthanide metal complexes*

Open-chain crown ether molecules are having a series of numerous oxygen atoms linked by methine groups. Compounds 1,7-(bis(2'-carboxylphenyl)1,4,7-triaoxaheptane ( $L'$ ,  $n = 0$ ) and 1,10-bis(2'carboxylphenyl)-1,4,7,10-tetraoxadecane ( $L''$ ,  $n = 1$ ) with europium and terbium emit strong red and green colors, respectively.



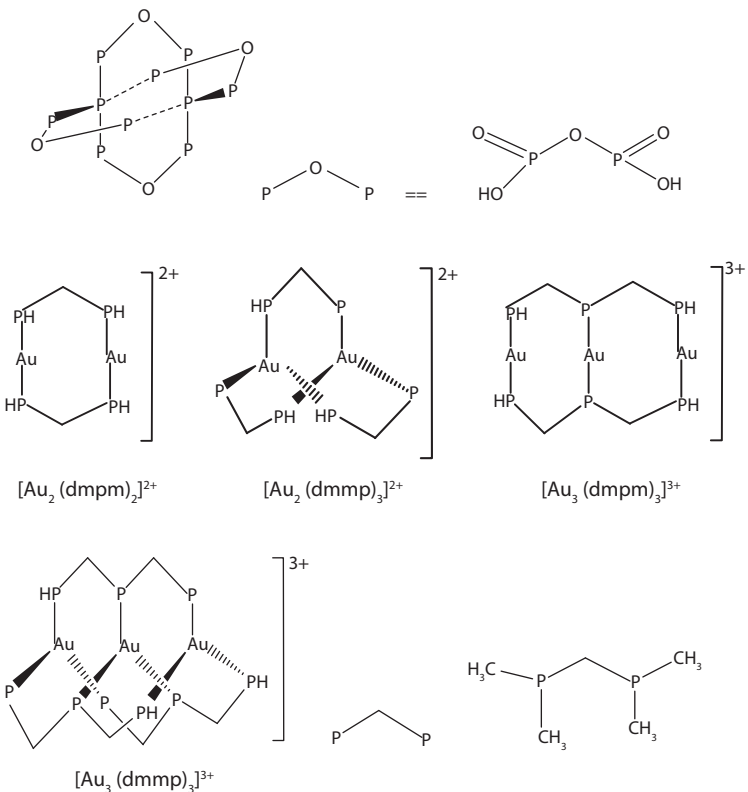
Europium complexes of 3-aminopyridine-2-carboxylic acid and mono hexadecylphthalic acid are used as red light-emitting material, whereas terbium complexes of mono hexadecyl p-aminobenzoic acid and pyridine-2,6-dicarboxylate dianion are used as green color light-emitting materials.



Lanthanide metals form light-emitting complexes with  $\beta$ -diketone. These types of complexes are denoted by formula  $[\text{Ln}(\text{L})_3\text{B}]$  where  $\text{Ln}$  is lanthanide ion,  $\text{L}$  is a  $\beta$ -diketone ligand and  $\text{B}$  is a lewis base such as 1,10-phenanthroline (phen), 2,2'-bipyridiyl (bipy). A few important lanthanide complexes are  $\text{Eu}(\text{Btfa})_3 \cdot 2\text{H}_2\text{O}$ ;  $\text{Eu}(\text{Btfa})_3 \cdot o\text{-phenNO}$ ;  $\text{Eu}(\text{Bzac})_3 \cdot 2\text{H}_2\text{O}$   $\text{Eu}(\text{DBM})_3 \cdot o\text{-phen}$ ;  $\text{Eu}(\text{DPM})_3 \cdot o\text{-phen}$ ;  $\text{Eu}(\text{TTA})_3 \cdot 2\text{H}_2\text{O}$ ; and  $\text{Eu}(\text{TTA})_3 \cdot \text{DBSO}$ , where TTA = 2-thenoyltrifluoroacetone; DBSO = dibenzylsulfoxide; 3-NH<sub>2</sub>pic = 3-aminopyridine-2-carboxylic acid; DPM = 2,2,6,6-tetramethyl-3,5-heptanedione; Bzac = benzoylacetone; Btfa = benzoyltrifluoroacetone; DBM = Dibenzoylmethane; o-phen = 1,10-phenanthroline; DB-bpy = 4,4'-Di-tertbutyl-2,2'-dipyridyl; DN-bpy = 4,4'-Dinonyl-2,2'-dipyridyl; biq = 2,2'-Biquinoline; terpyridine (terpy). Compounds of  $\text{Eu}^{3+}$  and  $\text{Tb}^{3+}$  with pyridine carboxylic acids and their N-oxides have exposed to be dominant antennas for lanthanide(III) luminescence than the parent complexes [48–53].

#### (h) Polynuclear $d^{10}$ metal complexes

Di- and tri-phosphines as bridging ligands are also used as light-emitting materials. The triphosphine ligand bis(dimethylphosphinomethyl)methylphosphine, dmmp complexes with three Au(I) centers and the dinuclear  $[\text{Au}_2(\text{dmppm})_2]^{2+}$  [ $\text{dmppm} = \text{bis(dimethylphosphino)methane}$ ] and tri-nuclear  $[\text{Au}_3(\text{dmmp})_3]^{3+}$  have been reported. These polynuclear gold (I) phosphine complexes are strongly luminescent [54].

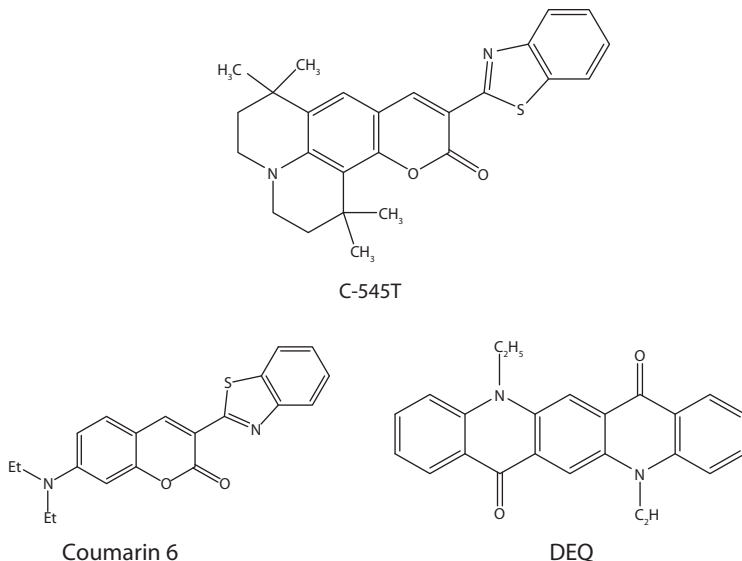


### (ii) Organic dyes

The small molecules organic dyes and dopant emitters like triphenyl diamines (TPDs), oligothiophenes, rubrene, oxadiazoles, triazoles, porphyrines, perylenes, coumarines, Nile red, etc. having high luminous efficiency [55, 56]. These are agitated by transfer of energy from the host lattice to give rise to tunable color of light.

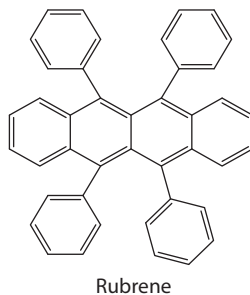
#### (a) Green dye

Coumarin 6 was first used as host emitter with high fluorescence. One of the most suitable green doping agents is 10-(2-benzothiazolyl)-1,1,7,7-tetramethyl-2,3,6,7-tetrahydro-1H,5H,11H-[1]benzo-pyrano[6,7,8-ij]quinolizin-11-one, recognized as C-545T [57, 58]. Another example of green dopant used is *N,N'*-diethyl quinacridone (DEQ) [59, 60].



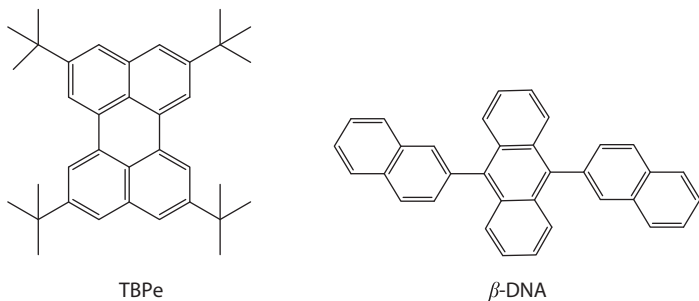
*(b) Yellow dye*

Rubrene dye is commonly used as yellow dopant [61, 62].



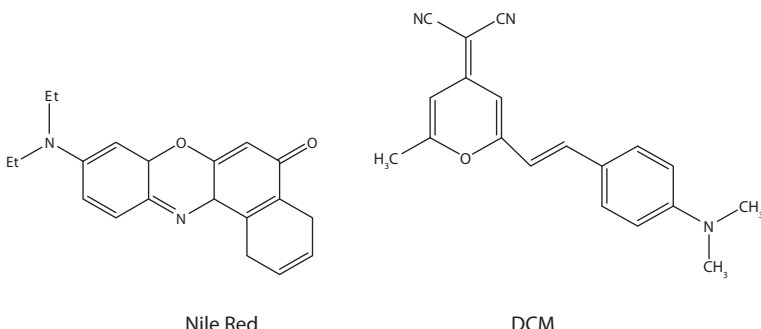
*(c) Blue dye*

$\beta$ -DNA and tetrakis(t-butyl)perylene (TBPe) are used as doped blue emitters [63, 64]. Another good blue emitter dopant is amino substituted distyrylarulene (DSA) doping agent doped with host DSA.



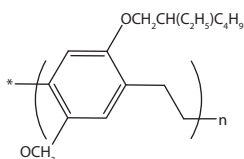
*(d) Red dye*

Red dye (4-dicyanomethylene-2-methyl-6-(p-dimethylaminostyryl)H-pyran (DCM) was reported initially as a doping agent in the tris(8-hydroxyquinolinato)aluminum ( $\text{Alq}_3$ ) layer. Nile Red, perylene dicarboxyimide, Eu(III) compounds, phorphyrin, and other materials have been used as red emitter dopants [41, 65–67].



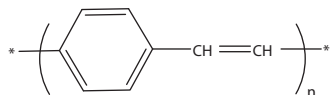
#### 14.4.2 Polymers

Polymers mainly used as electroluminescent materials are guest-host polymers, side-chain polymers, and  $\pi$ -conjugated polymers. The main advantages of using polymer over small molecule are that polymers have high glass transition temperature, better thin-film forming properties, and longer  $\pi$ -conjugation lengths which can be easily processed by low-cost conventional techniques such as ink-jet printing and roll-to-roll processing. As a result of these qualities, polymer LEDs are preferably appropriate to applications as they can produce full-color display, highly resolved images at low operating voltages, screens with wide-viewing angles and increases the operational life-time of the electroluminescent devices.  $\Pi$ -Conjugated polymers are the most studied materials both from the chemical and the physical point of view [68–71]. Different types of conjugated polymers are as follows:

*(i) Orange-red-emitting polymers*

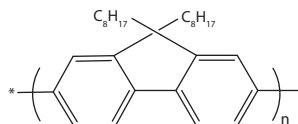
Poly (2-methoxy-5-(2'-ethylhexoxy)-p-phenylene vinylene)  
(MEH-PPV)

## (ii) Green-emitting polymers



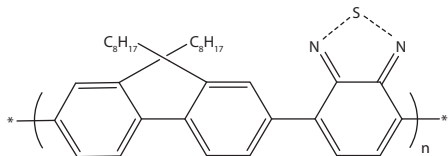
Poly(paraphenylenevinylene) (PPV)

### (iii) Blue-emitting polymers



### Polyfluorene (PF)

#### **(iv) Yellow-emitting polymers**



Poly[(9,9-dioctylfluorenyl-2,7-diyl)-alt-co-(1,4-benzo-[2,1',3]-thiadiazole)]  
(F8BT)

## 14.5 Possible Transitions in Organic Molecules

Organic molecules with optimum energy difference between the lowest unoccupied and the highest occupied molecular orbitals act as organic semiconductor and transition between these energy levels results in emission of photons. The probability of transition increases with increase in the square of the spin-orbit coupling of the substituent atom. Indium tin oxide (ITO) is often used as the anode partly because it is transparent (suitable for bringing out the light) and partly because it has a high-work function. It serves to inject holes into the HOMO levels. The cathode is made of aluminum, magnesium, or calcium, low-work function materials, suitable to inject electrons into the LUMO levels. When the electrons and holes meet at the junction, there is formation of exciton intermediates of two kinds. When the electron-hole pair has opposite spins it is a singlet exciton if they have parallel spins then it is triplet exciton. Singlets decay fast (order of ns) and emit a photon, triplets decay slowly (order of ms) and generate heat. Thus, normally an OLED cannot have higher than 25% efficiency.

There are though hopes that, by including heavy-metal elements into the compound, the triplets can also be persuaded to help the radiative process.

## 14.6 OLED's Structure and Composition

OLEDs cover a simple structure, having biodegradable compounds. These consist of semiconducting organic small molecules or polymers mounted on a glass substrate or flexible substrate as polythene [72] between two electrodes cathode and anode. Application of voltage generates electrons and holes at their respective electrodes. Pair of electron and hole forms exciton which emits light. The molecular structure of semiconductor materials used determines the color of emitted light. In order to achieve high luminescence efficiency and long life-time, an optoelectronic device must possess the low-energy barrier for the balanced injection of charge carriers at the interface between the metal electrodes which results in the alignment of charge carrier density in the recombination zone of an optoelectronic device. A hierarchy in the development of different types of structures of OLED is broadly explained below.

### 14.6.1 Mono-layered OLED Devices

The simplified OLED architecture is a mono-layered device structure. The first report on single-layer OLED device was made by *Pope et al.* in 1963 using large-sized anthracene crystal as emissive material [73]. ITO is used as anode and sublimed metal is used as cathode. Under the influence of electric field, injected charge carriers recombine in the organic emissive layer to produce light. A basic schematic diagram of a mono-layered OLED is shown in Figure 14.2. The first polymeric single-layer OLED was

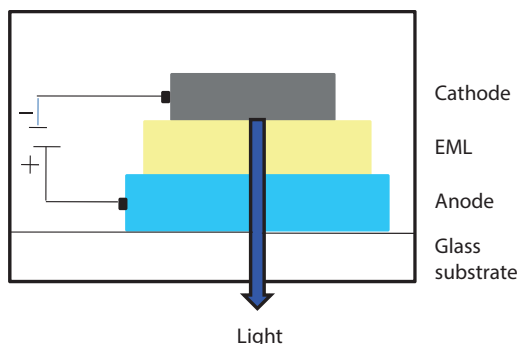


**Figure 14.2** Schematic cross-section of a typical mono-layer OLED.

fabricated by Burroughs *et al.* involving poly(p-phenylene vinylene) (PPV) as emissive layer.

### 14.6.2 Double-layered OLED Devices

In the 1980s, Tang and Van Slyke made a breakthrough in the history of OLEDs [4]. For the first time, they fabricated double-layer OLED device with two organic layers placed between two electrodes (Figure 14.3). The device consists of a conductive ITO mounted on a substrate as transparent anode. The device also having a diamine layer as a hole transport layer (HTL), Alq<sub>3</sub> as an ETL as well as an emitting layer and a Mg–Ag alloy as a cathode.

Figure 14.3 shows the structure of double layer OLED. The difference in energy levels between the two organic layers creates a potential barrier at the interface. The barrier confines the holes and electrons in emissive layer and contributes to an increased recombination probability.

In comparison to mono-layer device, the double-layer device was highly efficient due to three main factors:

- (i) Work function of the specific electrode used in the device match with the energy level of the ETL and HTL, resulting in improved injection of charge carriers.
- (ii) HTL and ETL used in the device have high mobilities for their respective charge carriers, leading to a balanced carrier's transport and results in improved device efficiency.
- (iii) The operating voltage in the double-layer device is low as the total thickness of a bilayer device is less than that of a mono-layer device.

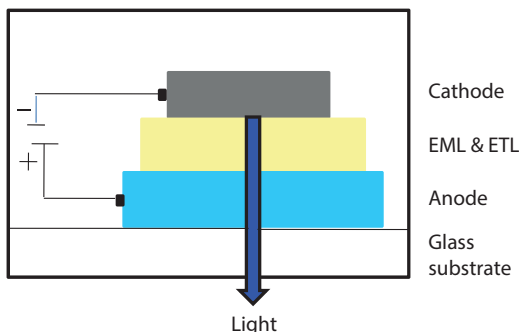


**Figure 14.3** Cross-section of a typical double-layer OLED.

### 14.6.3 Multi-layered OLED Devices

It was found that the single-layer devices and even the double-layer devices are not as efficient as the commercially available inorganic LEDs. In case of single-layer devices unmatched energy levels of cathode and anode with organic layer, holes and electrons injection from electrodes respectively are found difficult due to the potential barrier at interface results in a poor recombination of charge carriers in the emissive layer. Problem cannot be sorted out just looking into myopically. Some problems like charge injection, carrier mobility, band gap, and blocking of holes and electrons from seeping out of emitting layer should be given importance. For better performance of the devices, multilayered device could be fabricated using some useful layers like electron injection layer (EIL), ETL, HTL, hole injection layer (HIL), and anode and cathode of appropriate band gap. The complete device structure is shown in Figure 14.4.

The constituents of multilayer devices are explained as follows.

#### (i) Substrate

This provides support to the whole layers structure, all material layers are deposited on the substrate. It may be a rigid glass or flexible plastic surface which protects the organic layers from eventual degradation by moisture or air. Rigid materials are more helpful in keeping the organic compounds safer than flexible substrate. Light is emitted from the top substrate of a device.

#### (ii) Anode

A transparent anode is the most suited material so that the radiated light can leave the device. It removes electrons from deposited organic molecule

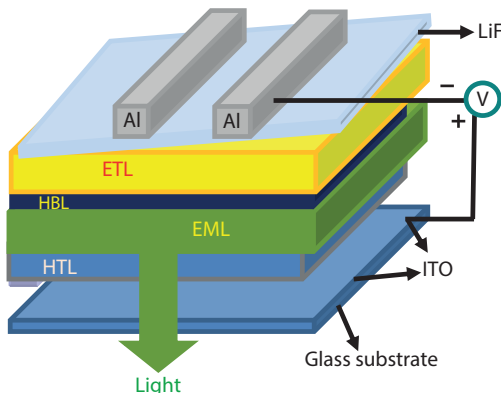
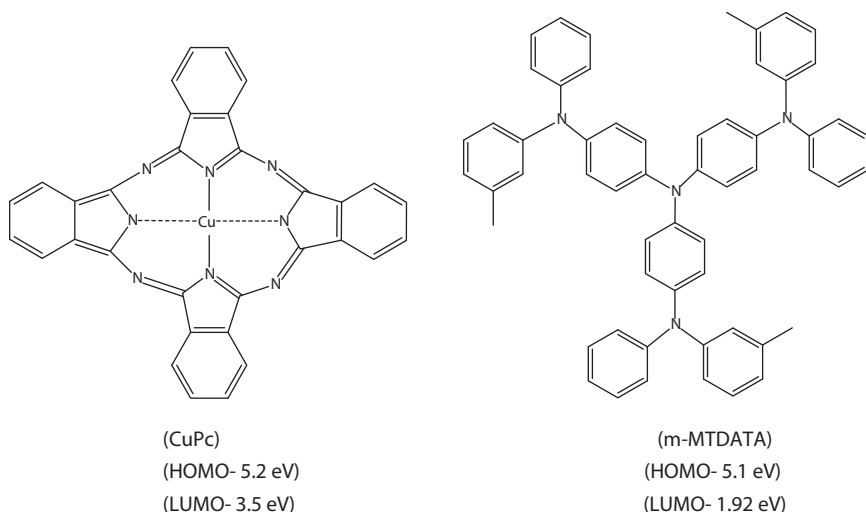


**Figure 14.4** Multilayer device structure.

layers when electric current is passed through the circuit. Anode material should have high work function which gives barrier to electron ejection from this, and holes are created in the adjacent layers. Tin oxide, indium oxide and zinc oxide combinations are mainly used as anode. Mostly anode of a thin layer of mixed indium oxide and tin-oxide is used due to its good transparency, low electrical resistivity, easy processability, and large work function (4–5 eV). The thin layer of conducting metal oxide on glass or plastic substrate can be deposited by high-energy sputtering or electron beam evaporation method. For efficient injection of holes, the work function of the anode (ITO) should closely match with the ionization energy ( $I_E$ ) of the HTL. In order to improve the device performance, the ITO-coated substrate should be cleaned properly as it enhances the work function of surface.

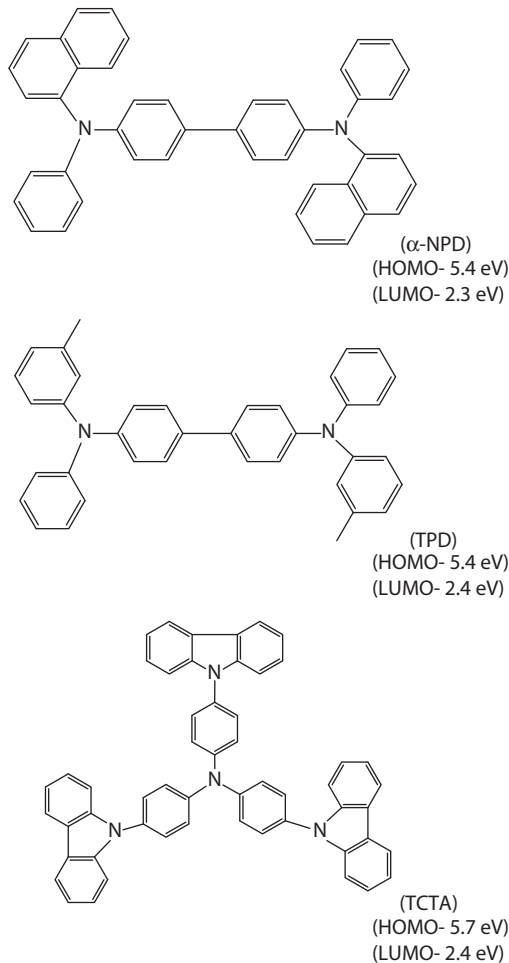
### *(iii) Hole injection layer*

It is an electron acceptor or p-type-doped organic layer which is inserted between anode and HTL which enhances the injection of holes from the anode. This concentrates the holes to the HTL and thereby efficiency of the optical device is increased [75]. For efficient charge carrier injection efficiency, HOMO level of the injection layer should be between work function of anode and HOMO level of HTL. Some of the materials used for the purpose are copper phthalocyanine (CuPc), perylene tetracarboxylic diamine (PTCDA), 4,4',4''-tris(3-methylphenyl(phenyl)amino)triphenylamine (m-MTDATA), and poly ethylenedioxy thiophene (PEDOT: PSS) [76, 77].



**(iv) Hole transport layer**

An effective organic HTL having high mobility for holes and low electron mobility is used to transport hole effectively to the light-emitting zone. This layer also acts as electron blocker and limits the electron within the emissive layer. Poly-9-vinylcarbozole (PVK), *N,N'*-bis(3-methylphenyl)-*N,N'*-diphenyl-[1,1-biphenyl]-4,4-diamine (TPD), *N,N'*-diphenyl-*N,N*-bis(1-naphthyl)-1,1-biphenyl-4,4-diamine ( $\alpha$ -NPD), poly(phenylenevinylene) (PPV), and 4,4',4''-tris(N-carbazolyl)triphenylamine (TCTA) are the commonly used materials for the purpose of HTL [78–84]. The properties of the device are also improved by using proper HTL material [85]. Hole transport materials should have small ionization potentials and wide optical band gap.

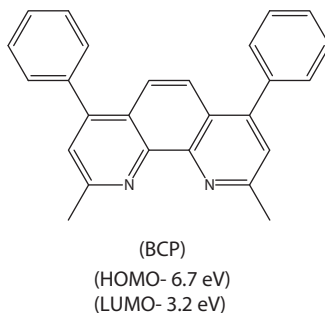


**(v) Emitting layer (EML)**

The emitting layer provides the levels for hole, injected from anode and electron, injected from cathode to recombine, and decay radiatively. The excitation energy of the emissive layer should be higher than that of the HTL and the ETL. Materials used for this are PPVs, polyfluorene, ladder polymers, dendrimer, and small molecules like metal chelates and oligomers.

**(vi) Hole blocking layer (HBL)**

This layer confines the holes within the emitting layer and helps in improving the device efficiency by reducing operating voltage. BCP (2,9-dimethyl-4,7-diphenyl-1,10-phenanthroline) is most commonly used as hole blocking layer [79, 86–88].

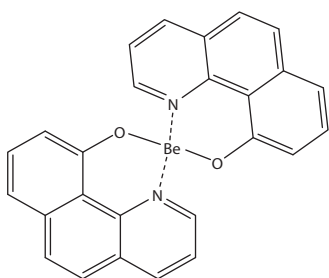


**(vii) Electron transport layer**

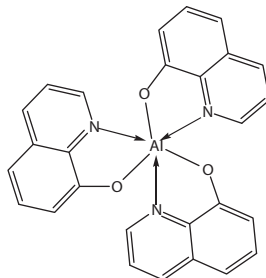
The ETL is an n-type-doped organic material that transports the electron. An effective material has high LUMO and high ionization energy. The electron affinity of electron transport material should match with the work function of the cathode for efficient transport of electrons. Both quinoxalines and quinolines are major electron transport materials and used as emissive layers in the optoelectronic devices [87–91]. Zinc and beryllium quinolates are also used as electron transport materials with better efficiency. Alq<sub>3</sub> is the most suitable material as ETL.

**(viii) Electron injection layer**

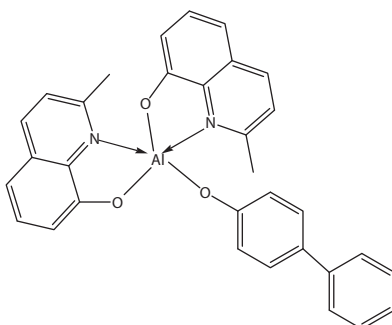
Like holes, for the electrons an organic injection layer as EIL is used to help the electron to move from the cathode to the ETL. For a high mobility, a high HOMO and low LUMO is required. Better transport of the charge carriers accomplish a lower required electric field, which leads to a more



Bis(10-hydroxybenzo quinolinato)beryllium  
( $\text{BebQ}_2$ )  
(HOMO- 5.5 eV)  
(LUMO- 2.9 eV)



Tris(8-hydroxyquinolinato)aluminum  
( $\text{AlQ}_3$ )  
(HOMO- 5.8 eV)  
(LUMO- 3.0 eV)



Bis(8-hydroxy-2-methylquinolinato)-(4-phenylphenolato)aluminum  
(HOMO- 5.7 eV)  
(LUMO- 3.2 eV)

power efficient OLED device.  $\text{Alq}_3$  is the most suitable material used for the purpose.

### **(ix) Cathode**

For cathode low-work function metals are generally used, as energy barrier for electron injection is decreased so that electrons can be ejected easily into the LUMO of the EIL. Some of the widely used metals as cathode are lithium (Li, 2.90 eV), cesium (Cs, 2.14 eV), silver (Ag, 4.26 eV), calcium (Ca, 2.87 eV), magnesium (Mg, 3.66 eV), aluminum (Al, 4.28 eV), composite cathode ( $\text{LiF-CsF}$ ), etc. is often used to inject electrons in the organic layer. An effective cathode injects a large number of electrons in the light-emitting layer. For efficient injection of charge carriers, the work function of cathode or anode should be compatible with either the HOMO or the LUMO level of the transport layer.

## 14.7 Basic Principle of OLEDs

Device operates only if voltage is applied in such a way that cathode is made at more negative potential with respect to anode. Application of voltage across the electrode produces charge carriers and then under field gradient these start moving in opposite direction as shown in Figure 14.5. Electrostatic force of attraction between oppositely charged carriers bring electron and hole toward each other. The recombination of electron and hole take place in emitting layer. In semiconductor material, holes are more mobile than electrons, which leads to radiative emission of photon with an energy equivalent to band gap ( $E = h\nu$ ) of emissive material. Here, the electrical energy is transformed into visible colored light. Various light-emitting materials with different dopants are applied to produce different colors and their mixing can develop white light for their emission.

## 14.8 Working of OLEDs

OLEDs operate on a phenomenon known as electroluminescence in which light is generated on application of electric current supply. Since in general polymers and organic materials are not referred as conducting materials because of their large band gap, a very high electrical field has to be applied to conduct electricity. The application of voltage across the electrode creates charge injection (electrons and holes) that results in geometrical defects on the symmetric organic molecular structure and exhibit a lower band gap ( $E_g$ ). The recombination of electron and hole take place at emitting layer molecules result in formation of excitons with a possibility to emit light as photons. The excitons are either in singlet or in triplet-states according to the Pauli's principle. The exciton will form two new energy bands inside the band gap. Upon relaxation of the exciton, heat and

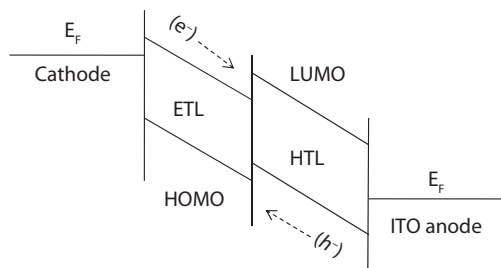


**Figure 14.5** Basic operation of LED.

photons are emitted with an energy set by the energy difference between the energy bands that represent the exciton. The singlet-state is regarded as the light forming state, while triplet state is non-allowed transition and decay thermally. In some special cases, the triplet state produces light as well. The color of the light developed in electroluminescence is determined through the energy gap of the electron–hole pair whereas intensity of light on voltage or current applied to the device. Light emission increases with increase in voltage.

The process of electroluminescence in an OLED device takes place into four steps (Figure 14.6):

(i) Introduction of carriers into device

The electrodes upon application of an electric field from battery or power supply of OLED inject charge carriers into the emissive material.

(ii) Movement of the carriers

Once electrons are injected, they drift to the electrode of more positive potential. Holes are inserted by anode to the valence band ( $E_v$ ) in the semiconductors. Injection of holes corresponds to the removal of electrons from electroactive material, i.e. oxidation of the electroactive material.

(iii) Excitation of the radiative material

Holes and electrons recombine in the active material producing an excited state called exciton on the emitting material which decays radiatively to emit light. A collective state of electron with hole forms an uncharged exciton particle.

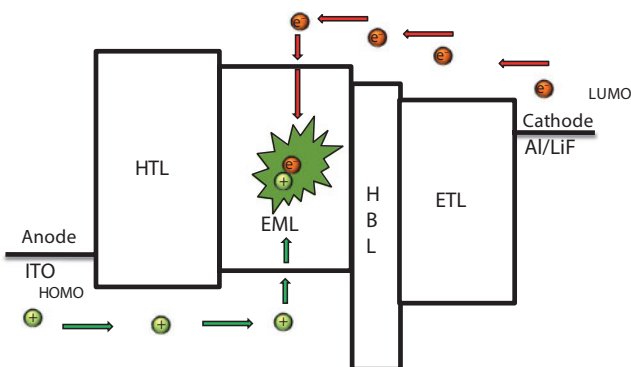


**Figure 14.6** Working of OLED.

## (iv) Radiative relaxation of the excited material

The exciton's electron comes to the hole of an atom from which electron is removed. As it takes place, there is release of energy in the form of light from emissive layer.

## 14.9 Light Emission in OLEDs

Light is emitted by radiative relaxation of exciton particle as shown in Figure 14.7. Each exciton formed is quasi-degenerate in state having three triplets and one singlet state. All these states are equally populated. There may be emission from both singlet and triplet excitons. When there is small spin-orbit coupling, the emission takes place by combination of electron and hole in same spin state that is called as fluorescence emission. Here, only 25% of the injected electron results in light emission and triplet exciton come to ground state by nonradiative transition. However, when there is large spin-orbit coupling, the singlet exciton may couple with triplet exciton by intersystem crossing. Hence, emission can be obtained by

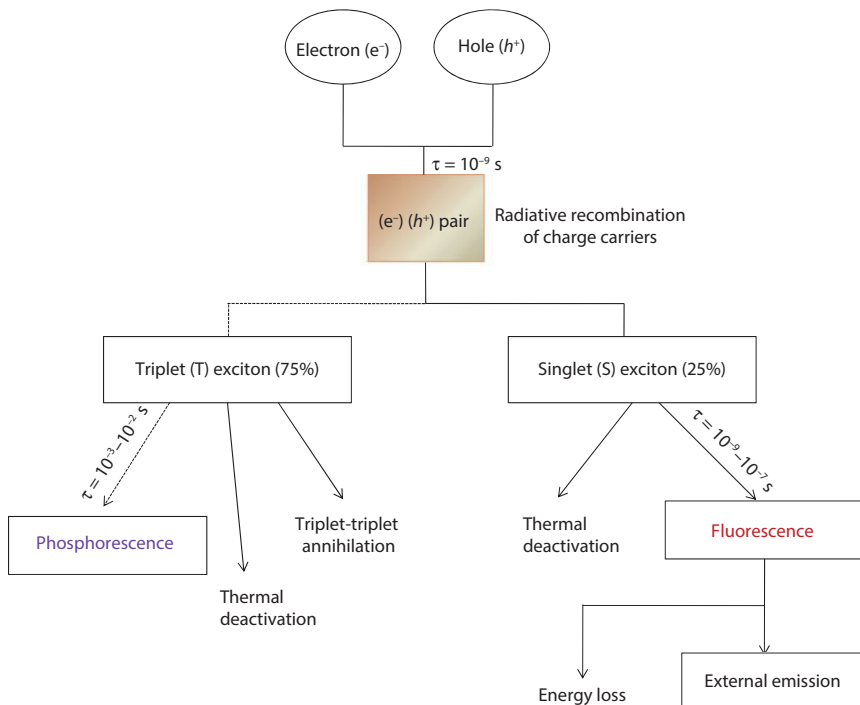


**Figure 14.7** A schematic diagram representing the emission of light in OLEDs.

triplet states also, which may lead to 100% efficiency as compared to singlet emission with 25% light energy output [13, 92]. Emission from triplet spin state exciton is phosphorescent emission, it is found in organic molecules containing heavy metals where strong spin-orbit coupling can take place.

## 14.10 Types of OLED Displays

There currently are six types of OLED displays, each designed for a different type of use. The types are as follows.

### *(i) Passive-matrix OLED (PMOLED)*

The passive-matrix OLEDs have stack layers of cathode, organic and anode like strips. Columns of organic materials and cathode are superimposed on rows of anode to form a two-dimensional array of pixels. Pixel is the intersecting point of cathode and anode where light is emitted from organic material which is sandwiched between the electrodes. Electric voltage is applied to the selected strips of anode and cathode, which switches on the required pixel. These OLEDs are suitable for small screen displays as in cell phones and small gadgets. PMOLEDs are easily constructed but consume more power but better than LCDs and have low life-time than other OLEDs.

### *(ii) Active-matrix OLED Displays (AMOLED)*

Active matrix OLEDs have full layers of all component layers incorporated on a thin-film transistor (TFT) array. TFT has a capacitor in back plane which maintains the circuitry of current flow for pixels to work as requirement. This technology is suitable for large-area display and because it requires less power for each pixel to turn on. AMOLEDs are used in computer monitors and large-screen displays, etc.

### *(iii) Transparent OLEDs*

Transparent OLEDs (TOLEDs) have only transparent components, i.e. substrate, cathode, and anode. These appear very much transparent when switched off and gives off light in both directions when turned on. TOLEDs can be of both types as active-matrix and passive-matrix displays. These devices have applications in head-up displays, cell phones, smart windows, etc.

### *(iv) Top-emitting OLEDs*

Top-emitting OLEDs display can be like TOLEDs or active-matrix OLEDs (AMOLEDs). In AMOLEDs, they have opaque substrates and displays

light away from the TFT backplane so can improve power consumption. These devices are used in smart card applications.

**(v) Flexible or Foldable OLEDs**

Flexible OLEDs are made up on flexible substrates like metallic or plastic foils. These are used in cell phones and portable personal gadgets. There are less chances of breakage so these are more durable.

**(vi) White OLEDs**

These devices emit light in whole spectral coverage and can be made on large sheets. White LEDs can give light energy at low cost as compared to fluorescent lights. These can be used as source for lightning in homes and buildings. These devices create the brightest light of all. The best approach to achieve this is through the stacked OLED in which red, green, and blue emitting layers are placed on one another.

### 14.11 Techniques of Fabrication of OLEDs Devices

Fabrication of OLEDs requires the deposition of thin layer of a pure organic material on a cleaned glass or plastic substrate which is already coated with ITO. Moisture and UV light may degrade mechanism of the device during manufacturing; hence, care has to be taken during manufacturing [93].

Following techniques are used for fabrication of the OLED devices.

**(i) Vacuum thermal evaporation or physical vapor deposition**

Vacuum deposition technique is broadly used for the deposition of small organic molecules on the surface of suitable substrate. Organic material is either sputtered by bombardment of ions which ejects atoms and molecules from the sample or these are evaporated by slow heating and form thin layer on the substrate placed into vacuum chamber. The low vapor pressure of  $10^{-6}$  or  $10^{-5}$  Torr is used, to avoid the reaction between vapor and atmosphere and particles move towards the substrate and get adhere. The evaporation process results in parallel surface, important for life-time of device. Good uniformity and purity is achieved by sputtering process. The atoms and molecules form a thin film at the substrate. Full color displays are manufactured using particular RGB materials by this deposition process. This method is complicated, expensive and materials also deposit on undesired space.

**(ii) *Organic vapor phase depositions***

In organic vapor phase deposition (OVPD), an inert gas carrier is used to transfer organic films on a cooled substrate at less pressure in hot-walled reactor chamber. Nitrogen is used as carrier gas at controlled flow rate, temperature, and pressure. Thin film prepared by this process are highly pure, good quality, better performance, and at reliable cost than other fabrication methods.

**(iii) *Inkjet printing***

In this technique, solution of polymeric organic material is dispensed on the substrate as ink through inkjet nozzles. Once dispensed, the sample is dried, the solvent is evaporated, and the thin film is formed. This is accompanied by very low manufacturing cost and can be used for preparation of large films for big displays. However, the major limitations of this technique are that pixels are not filled uniformly and difficulty arising in patterning the substrates.

**(iv) *Dip coating***

In dip-coating method, the substrate is slowly dipped into the polymeric material solution resulting in a cover of polymer layer at both sides. The substrate is immersed in coating material solution, and allowed for coating. Finally, substrate is withdrawn and solvent is evaporated then dried. Although it is very simple and popular way of deposition, there are limitations for coating on light substrates and varying thickness of film on top and bottom parts of the substrate.

**(v) *Spin coating***

In spin-coating method, a drop of organic material (polymer) solution is placed on a rotating late. The coating solution is spread out to form a uniform thin film by centrifugal force at room temperature. This technique is one of the most commonly used techniques for deposition, and it is widely used for thin-film preparation in organic electronics, nanotechnology, and industrial field. Drops formed may result in non smooth and nonparallel surfaces and causing degradation of device because of different distances between the electrodes.

## **14.12 Advantages of OLEDs**

The demand for flat, lightweight televisions, and computer screens has given rise to many different flat-panel display technologies. Recently, a

large-scale production has been occurred on the development of OLEDs for both researchers and industrialist, motivated by the assurance of light-emitting plastics for the fabrication of huge, bendable, low-priced and proficient display to be used in various applications. The large sizes of OLEDs display can be fabricated easily. OLEDs are fundamentally plastics which can be developed into large sheets easily as compared to LCDs. Some of the most important advantages that have led to the development of the OLEDs as one of the feasible conventional display technologies are as follows.

#### *(i) Better contrast ratio*

Contrast ratio is one of the most significant forms of image quality. OLED screens appear extraordinarily bright due to their remarkably high contrast ratio (1,000,000:1) than that reachable with an LCD (350-450:1) and each pixel illuminates like a luminescent bulb. The ratio is simply calculated by contrast ratio formula as

$$\text{Contrast Ratio (CR)} = \text{Luminance}_{(\text{white})}/\text{Luminance}_{(\text{black})}$$

#### *(ii) Improved color quality*

OLEDs have a stable color rendering performance and luminance levels, which is not the case with inorganic LED used to illuminate the LCD. It is easy to fabricate the OLED displays in all bright saturated pure native colors including red, green and blue color. A mass production of display from small monochrome to large full color displays (Figure 14.8) can be marked with improved color gamut and resolution.

#### *(iii) Wide viewing angles*

Viewing angle is the maximum angular distance at which an OLED screen can be sighted without losing clarity or color shifts. In several display panels, increase in viewing angle certainly distorted the color and image quality. OLEDs have a wide field of view ( $\geq 170^\circ$ ) compared to LCDs because



**Figure 14.8** Full color display having primary colors.

OLED pixels are self-illuminated whereas liquid crystals work via blocking the light, as these materials have an intrinsic performance barrier through define angles. OLED displays provide consistent clear and quality images even in intense light from almost any angle and allowing reading a message clearly even when wearing Polaroid glasses.

**(iv) Fast response time**

The response time of an OLED is much faster than their inorganic counterpart. The response time for OLEDs is shorter than 1  $\mu$ s as compared to 25 ms for active matrix LCDs and 300 ms for passive addressed LCDs [94]. The fast response time for OLEDs makes them possible for use in video application even in passive matrix addressing, which is not possible for LCDs.

**(v) Economical**

Although fabrication of an OLED requires higher price, the use of OLED lighting considerably lowers the expenses in a number of ways. High power efficiency and long life-time reduces the maintenance cost and energy required for lightening. Roll-to-roll vapor deposition methods such as inkjet printing and screen printing for optoelectronic devices do permit for huge construction of displays which makes the OLEDs up to 20–50% cheaper than LCDs or plasma displays so effectively could be affordable to general public. LCD manufacturing is more costly due to need of luxurious components like color filters, polarizers, diffuser, and backlight.

**(vi) Low power consumption**

OLED technology is power efficient than conventional LCD and VFD as construction of organic devices does not require any polarizer and back-light which reduces the efficiency of emitted light like in other display technologies. OLEDs take less power to run (in the low voltage range of 2–15 volts) and fast switching speed because the pixel is turned on only when emission of light is required. But in LCD the backlight always emit light over the whole surface regardless whether the pixels are active or not. OLEDs consume very less energy than standard light bulbs, leading to greatly reduced energy costs. These have already surpassed the efficiency of halogen, and are expected to reach up to 150 lm/W.

**(vii) Wide temperature range**

LCDs are badly affected by high temperature, by destroying the twisting properties of the liquid at temperature higher than 90 °C [95]. The temperature also affects AMLCDs, causing a higher response time at low

temperature, but not affects OLEDs. Brightness and chromaticity are also dependent on temperature to some extent [98]. The OLEDs has an operating temperature range from –40 to 85 °C compared to 10 to 60 °C of LCDs. Planar thin-film EL screens (TFEL) have the wide temperature range (–100 °C) of any commercially existing technology.

**(viii) Thinness and flexibility**

OLEDs panels are exceedingly thin and bendable. It is achievable to bend, even roll up the membrane that forms an OLED TV. OLED is a self-illuminated device so no need of backlight. The OLED displays consist of substrate deposited with light weight organic emissive layer which can be made very thinner and flexible than other existing displays technologies.

**(ix) Better durability and lighter weight**

Ultra-light weight OLED displays are free from the added bulk and weight of backlighting, making them ideal for compact devices and thus are easy to incorporate. Additionally, the OLED displays themselves are quite durable and can withstand a wide operating temperature range.

**(x) Eco-friendly**

The reduced emission of CO<sub>2</sub> gas by OLED lighting due to low energy consumption can be beneficial for the environment in times when global warming is a huge concern. In addition to this, they do not discharge toxic mercury vapors which are commonly found in fluorescent lamps.

**(xi) Robust design**

OLEDs are sufficient to be used in transportable devices such as mobile phones, video cameras, vehicle audio components, and personal digital assistant.

**(xii) Inherent ruggedness**

OLED posses a much more rugged structure because no liquid or gases are part of technology as compared to LCD contrary to OLED, contact pressure and vibrations affects the LCD.

**(xiii) Video capabilities**

OLEDs grasp the capability to hold digital video, which could modernize the PDA's and cell phones market.

**(xiv) High resolution**

Active matrix OLEDs, videos and graphics are used for high information applications. OLEDs are much intense than LEDs. The emissive layer of an

OLED is very thin and conductive in comparison to LCDs. Also, LEDs and LCDs require glass for support which absorbs some light. OLEDs do not require glass.

**(xv) Better safety and security**

The less production of heat, no poisonous fumes and low operating voltages used by OLEDs makes them a safe source of light. Due to durability of light sources, they are used even you need in an urgent situation, thereby enhances the user's level of personal safety and security.

## 14.13 Potential Applications of OLEDs

OLEDs are emissive displays which emit their own light, i.e. they are self illuminated. They do not need backlighting, polarizers, and diffusers unlike LCDs. These will allow in diverse mounting option because of their flexibility and thinness. OLEDs consume very less power which minimizes thermal and electrical intervention in optoelectronic devices. Because of robust design, OLED displays are best suited for different applications which are summarized as below:

### 14.13.1 Conventional Applications

- (i) **Monochrome applications**
  - (a) Heads-up instrumentation for aircraft and automobiles
  - (b) Small display for hand held electronic screens (mobile phone, wristwatch PDAs, video cameras, global positioning systems, portable entertainment devices, etc.).
- (ii) **Two or multicolor applications**
  - (a) In car electronics such as audio components, navigation systems, locating maps, warning indicators, etc.
  - (b) Full-motion video camcorders
- (iii) **Full color applications**
  - (a) High resolution, full color, personal communicators.
  - (b) Fabrication of white organic light-emitting devices (WOLEDs).
- (iv) **Nearly achievable applications**
  - (a) Large flat panel screens.
  - (b) Wall-hanging television displays.
  - (c) Large-screen laptop and desktop computers.
  - (d) Large-area illumination.

### **14.13.2 Applications Convertible to OLEDs (Which Can Boost Their Commercial Development)**

- Color changing display for lighting of residential and commercial buildings,
- Large display panels for advertising signs boards and warning signals, etc.,
- Ultra-lightweight wall-size television monitors, office windows, walls and partitions that double as computer screens,
- Applications dominating on head wearable displays in the field of defense,
- High quantum yield and power efficiency.

## **14.14 Future Prospects of OLEDs**

The growing attention toward the benefit of metallic chelates or polymeric materials for optoelectronic devices has provided an increasing demand for new approaches to design more molecular structures with tunable optical and electronic properties. In the research and development centers, new luminescent materials are being reported everyday which are far more efficient than those which are present already. From the technological point of view, new device configurations and fabrication technologies, such as roll-to-roll technology, will take place in developing stretchable and biocompatible optoelectronic devices. The efficiency of the best device has surpassed that of fluorescent lamps and one can expect that in the coming years we see more efficient devices which replaces the existing lighting concepts.

## **14.15 Conclusions**

In this chapter, efforts have been devoted to the research of proficient organic materials for development of highly efficient optoelectronic devices. The design and development of appropriate light-emitting materials are very useful reflection for the fabrication of OLEDs as it determines durability, emission color, life-time, and efficiency of the projected device. We begin by describing the basic properties of organic materials which have a strong influence on the performance of the device. Next, a brief overview about the luminescence processes in organic molecule will be presented, followed by throughout description of mechanism of the

luminescence. The emphasis will be placed on the illustration of different type of fluorescent and phosphorescent emitters and on the discussion of recent efforts in device architecture for high-efficiency OLEDs as well as introduce with different display technologies. The advantages and potential applications of OLEDs will discuss in the subsequent section.

## References

1. Takeuchi, Y., Amao, Y., Materials for luminescent pressure-sensitive paint. *Front. Chem. Sens.*, 3, 303, 2005.
2. Ronda, C.R., *Luminescence: From Theory to Applications*, John Wiley & Sons, 2008.
3. Malliaras, G.G., Friend, R.H., An organic electronics primer. *Physics Today*, 58, 53, 2005.
4. Tang, C.W., Van Slyke, S.A., Organic electroluminescent diodes. *Appl. Phys. Lett.*, 51, 913, 1987.
5. Hamada, Y., The development of Chelate metal complexes as an organic electroluminescent material, *IEEE Trans. Electron Dev.*, 44, 1208, 1997.
6. Tang, C.W., Van Slyke, S.A., Chen, C.H., Electroluminescence of doped organic thin films. *J. Appl. Phys.*, 65, 3611, 1989.
7. Shunmungam, R., Tew, G.N., White-light emission from mixing blue and red-emitting metal complexes. *Polym. Adv. Technol.*, 19, 596, 2008.
8. Kumar, A., Palai, A.K., Srivastava, R., Kadyan, P.S., Kamalasan, M.N., Singh, I., n-Type ternary zinc complexes: Synthesis, physicochemical properties and organic light emitting diodes application. *J. Org. Chem.*, 756, 38, 2014.
9. Nishal, V., Kumar, A., Kadyan, P.S., Singh, D., Srivastava, R., Singh, I., Kamalasan, M.N., Synthesis, characterization, and electroluminescent characteristics of mixed-ligand zinc(II) complexes. *J. Elect. Mater.*, 42, 973, 2013.
10. Nishal, V., Singh, D., Kumar, A., Tanwar, V., Singh, I., Srivastava, R., Kadyan, P.S., A new zinc-Schiff base complex as an electroluminescent material. *J. Org. Semi.*, 2, 15, 2014.
11. Yan, B., Zhao, L.M., Construction of luminescent terbium inorganic/organic molecular-based hybrids from modified functional bridge ligand. *Mater. Lett.*, 59, 795, 2005.
12. Wang, Q.M., Yan, B., From molecules to materials: a new way to construct luminescent chemical bonded hybrid systems based with ternary lanthanide complexes of 1,10-phenanthroline. *Inorg. Chem. Commun.*, 7, 1124, 2004.
13. Wang, Q.M., Yan, B., Optically hybrid lanthanide ions ( $\text{Eu}^{3+}$ ,  $\text{Tb}^{3+}$ )-centered materials with novel functional di-urea linkages. *Appl. Organomet. Chem.*, 19, 952, 2005.
14. Dumur, F., Zinc complexes in OLEDs: An overview. *Synth. Met.*, 195, 241, 2014.

15. Deun, R.V., Fias, P., Nockemann, P., Schepers, A., Parac-Vogt, T.N., Hecke, K.V., Meervelt, L.V., Binnemans, K., Rare-earth quinolinates: infrared-emitting molecular materials with a rich structural chemistry. *Inorg. Chem.*, 43, 8461, 2004.
16. Yu, J., Zhou, L., Zhang, H., Zheng, Y., Li, H., Deng, R., Peng, Z., Li, Z., Efficient electroluminescence from new lanthanide ( $\text{Eu}^{3+}$ ,  $\text{Sm}^{3+}$ ) complexes. *Inorg. Chem.*, 44, 1611, 2005.
17. Kido, J., Okamoto, Y., Organo lanthanide metal complexes for electroluminescent materials. *Chem. Rev.*, 102, 2357, 2002.
18. Wu, A., Yoo, D., Lee, J.K., Rubner, M.F., Solid-state light-emitting devices based on the tris-chelated ruthenium(II) complex: 3. high efficiency devices via a layer-by-layer molecular-level blending approach. *J. Am. Chem. Soc.*, 121, 4883, 2000.
19. Singh, D., Singh, K., Bhagwan, S., Saini, R.K., Kadyan, P.S., Singh, I., Bis(5,7-dimethyl-8-hydroxyquinolinato)beryllium(II) complex as optoelectronic material. *J. Lumin.*, 169, 9, 2016.
20. Adachi, C., Baldo, M.A., Forrest, S.R., Electroluminescence mechanisms in organic light emitting devices employing a europium chelate doped in a wide energy gap bipolar conducting host. *J. Appl. Phys.*, 87, 8049, 2000.
21. Moon, D.G., Salata, O.V., Etchells, M., Dobson, P.J., Christou, V., Efficient single layer organic light emitting diodes based on a terbium pyrazolone complex. *Synth. Met.*, 123, 355, 2001.
22. Hong, Z., Li, W., Zhao, D., Liang, C., Liu, X., Peng, J., Zhao, D., Spectrally-narrow blue light-emitting organic electroluminescent devices utilizing thulium complexes. *Synth. Met.*, 104, 165, 1999.
23. Reyes, R., Hering, E.N., Cremona, M., Silva, C.F.B., Brito, H.F., Achete, C.A., Growth and characterization of OLED with samarium complex as emitting and electron transporting layer. *Thin Solid Films*, 420, 23, 2002.
24. Wang, G., Ding, Y., Wei, Y., Relationship between organic thin film uniformity and its electroluminescence. *Appl. Surf. Sci.*, 93, 281, 1996.
25. Wu, Q., Esteghamatian, M., Hu, N.X., Popovic, Z.D., Enright, G., Breeze, S.R., Wang, S., Isomerism and blue electroluminescence of a novel organoboron compound:  $\text{B}_2^{\text{III}}(\text{O})(7\text{-azain})_2\text{Ph}_2$ . *Angew. Chem. Int. Ed.*, 38, 985, 1999.
26. Shipley, C.P., Capecchi, S., Salata, O.V., Etchells, M., Dobson, P.J., Christou, V., Orange electroluminescence from a divalent europium complex. *Adv. Mater.*, 11, 533, 1999.
27. Sabbatini, N., Guardigli, M., Lehn, J.M., Luminescent lanthanide complexes as photochemical supramolecular devices. *Coord. Chem. Rev.*, 123, 201, 1993.
28. Blasse, G., Dirksen, G.J., Sabbatini, N., Perathoner, S., Photophysics of  $\text{Ce}^{3+}$  cryptates. *Inorg. Chim. Acta*, 133, 167, 1987.
29. Sabbatini, N., Guardigli, M., Manet, I., Ungaro, R., Casnati, A., Ziessel, R., Ulrich, G., Asfari, Z., Lehn, J.M., Lanthanide complexes of encapsulating ligands: Luminescent devices at the molecular level. *Pure Appl. Chem.*, 67, 135, 1995.

30. Jones, P.L., Amoroso, A.J., Jeffery, J.C., Mc Cleverty, J.A., Psillakis, E., Rees, L.H., Ward, M.D., Lanthanide complexes of the hexadentate n-donor podand tris[3-(2-pyridyl)pyrazolyl]hydroborate: solid-state and solution properties. *Inorg. Chem.*, 10, 36, 1997.
31. De Sa', G.F., Nunes, L.H.A., Wang, Z.M., Choppin, G.R., Synthesis, characterization, spectroscopic and photophysical studies of ternary complexes of Eu(III) with 3-aminopyrazine-2-carboxylic acid (HL) and heterobiaryl ligands (2,2'-bipyridine and 1,10-phenanthroline). *J. Alloys Comp.*, 196, 17, 1993.
32. Bunzli, J.C.G., Moret, E., Foiret, V., Schenk, K.J., Mingzhao, W., Linpei, J., Structural and photophysical properties of europium(III) mixed complexes with  $\beta$ -diketonates and o-phenanthroline. *J. Alloys Comp.*, 207, 107, 1994.
33. Bunzli, J.C.G., Froidevaux, P., Harrowfield, J.M., Complexes of lanthanoid salts with macrocyclic ligands. 41. Photophysical properties of lanthanide dinuclear complexes with p-tert-butylcalix[8]arene. *Inorg. Chem.*, 32, 3306, 1993.
34. Nishal, V., Singh, D., Saini, R.K., Bhagwan, S., Tanwar, V., Sonika, Srivastava, R., Kadyan, P.S., Optoelectronic characterization of zinc complexes for display device applications. *J. Mater. Sci. Mater. Electron.* 26, 6762, 2015.
35. Nishal, V., Singh, D., Saini, R.K., Tanwar, V., Bhagwan, S., Sonika, Singh, I., Kadyan, P.S., Synthesis and optical characterization of mixed ligands beryllium complexes for display device applications. *Inter. J. Opt.*, 2015, 7, 2015.
36. Singh, K., Kumar, A., Srivastava, R., Kadyan, P.S., Kamalasan, M.N., Singh, I., Synthesis and characterization of 5,7-dimethyl-8-hydroxyquinoline and 2-(2-pyridyl)benzimidazole complexes of zinc(II) for optoelectronic application. *Opt. Mater.*, 34, 221, 2011.
37. Duvenhage, M.M., Visser, H.G., Ntwaeborwa, O.M., Swart, H.C., The effect of electron donating and withdrawing groups on the morphology and optical properties of Alq<sub>3</sub>. *Physica B*, 439, 46, 2014.
38. Hamada, Y., Sano, T., Fujita, M., Fujii, T., Nishio, Y., Shibata, K., Blue electroluminescence in thin films of azomethin-zinc complexes. *Jpn. J. Appl. Phys.*, 32, L511, 1993.
39. Tokito, S., Noda, K., Tanaka, H., Taga, Y., Tsutsui, T., Organic light-emitting diodes using novel metal-chelate complexes. *Synth. Met.*, 111, 393, 2000.
40. Schmitz, C., Schmidt, H.W., Thelakkat, M., Lithium-quinolate complexes as emitter and interface materials in organic light-emitting diodes. *Chem. Mater.*, 12, 3012, 2000.
41. Kumar, A., Srivastava, R., Bawa, S.S., Singh, D., Singh, K., Chauhan, G., Singh, I., Kamalasan, M.N., White organic light emitting diodes based on DCM dye sandwiched in 2-methyl-8-hydroxyquinolinolatolithium. *J. Lumin.*, 130, 1516, 2010.
42. Blasse, G., Grabmaier, B.C., *Luminescent Materials*, Springer, Berlin, 1994.
43. Pope, M., Swenberg, C.E., *Electronic Processes in Organic Crystals and Polymers*. 2<sup>nd</sup> Ed., Oxford University Press, 1999.

44. Ho, P.K.H., Granstrom, M., Friend, R. H., Greenham, N. C., Ultrathin self-assembled layers at the ITO interface to control charge injection and electroluminescence efficiency in polymer light-emitting diodes. *Adv. Mater.*, 10, 769, 1998.
45. Burn, P.L., Holmes, A.B., Kraft, A., Bradley, D.D.C., Brown, A.R., Friend, R.H., Synthesis of a segmented conjugated polymer chain giving a blue-shifted electroluminescence and improved efficiency. *J. Chem. Soc.*, 1, 32, 1992.
46. Kanabara, T., Inoue, T., Sugiyama, K., Yamamoto, T., Preparation of poly(quinoxaline-5,8-diyl) derivatives by using zero-valent nickel complexes. Electrical and optical properties and light-emitting diodes. *Synth. Met.*, 71, 2207, 1995.
47. Greiner, A., Design and synthesis of polymers for light-emitting diodes. *Polym. Adv. Technol.*, 9, 371, 1998.
48. Binnemans, K., *Rare-earth b-diketonates, Handbook on the Physics and Chemistry of Rare Earths*, Elsevier, 2005.
49. Vicentini, G., Zinner, L.B., Zukerman-Schpector, J., Zinner, K., Luminescence and structure of europium compounds. *Coord. Chem. Rev.*, 196, 353, 2000.
50. Yoneda, H., Choppin, G.R., Bear, J.L., Graffeo, A.J., Complexes of the lanthanide elements with  $\alpha$ -picolinate and  $\alpha$ -picolinate N-oxide ions. *Inorg. Chem.*, 4, 244, 1965.
51. [51]De Sa, G.F., Synthesis and spectroscopic studies of europium chelate complexes. *Polyhedron*, 2, 1057, 1983.
52. Alencar, F.L., Matos, J. R., Zinner, L.B., Pyrazine-N-oxide (pyzNO) complexes of lanthanide(III) trifluoroacetates (TFA). *J. Alloys Comp.*, 207–208, 461, 1994.
53. Binnemans, K., Interpretation of europium(III) spectra. *Coord. Chem. Rev.* 295, 1, 2015.
54. Yam, V.W.W., Lo, K.K.W., Luminescent polynuclear  $d^{10}$  metal complexes. *J. Chem. Soc., Dalton Trans.*, 28, 323, 1999.
55. Mc Gehee, M.D., Bergstedt, T., Zhang, C., Saab, A.P., Regan, M.B.O', Bazan, G.C., Srdanov, V.I., Heeger, A., Narrow bandwidth luminescence from blends with energy transfer from semiconducting conjugated polymers to europium complexes. *J. Adv. Mater.*, 11, 1349, 1999.
56. Liang, C.J., Zhao, D., Hong, Z.R., Zhao, D.X., Liu, X.Y., Li, W.L., Peng, J.B., Yu, J.Q., Lee, C.S., Lee, S.T., Improved performance of electroluminescent devices based on an europium complex. *Appl. Phys. Lett.*, 76, 67, 2000.
57. Uddin, A., Lee, C.B., Wong, J., Emission properties of dopants rubrene and coumarin 6 in  $\text{Alq}_3$  films. *J. Lumin.*, 131, 1037, 2011.
58. Okumoto, K., Kanno, H., Hamada, Y., Takahashi, H., Shibata, K., Organic light-emitting devices using polyacene derivatives as a hole-transporting layer. *Appl. Phy. Lett.*, 89, 63504, 2006.
59. Fatemi, D.J., Murata, H., Merritt, C.D., Kafafi, Z.H., Highly fluorescent molecular organic composites for light-emitting diodes. *Synth. Met.*, 85, 1225, 1997.

60. Murata, H., Merritt, C.D., Inada, H., Shirota, Y., Kafafi, Z.H., Molecular organic light-emitting diodes with temperature-independent quantum efficiency and improved thermal durability. *Appl. Phys. Lett.*, 75, 3252, 1999.
61. Huang, H.H., Chu, S.Y., Kao, P.C., Chen, Y.C., High efficiency white organic light emitting diodes using Rubrene doped N,N'-bis-(1-naphthyl)-N,N'-diphenyl-1,1'-biphenyl-4,4'-diamine as an emitting layer. *Thin Solid Films*, 516, 5669, 2006.
62. Saxena, K., Mehta, D.S., Rai, V.K., Srivastava, R., Chauhan, G., Kamalasanan, M.N., Jain, V.K., Studies on organic light-emitting diodes based on rubrene-doped zinc quinolate. *Phys. Status Solidi A*, 206, 1660, 2009.
63. Hung, L.S., C.H. Chen, Recent progress of molecular organic electroluminescent materials and devices. *Mater. Sci. Engin. R: Reports*, 39, 143, 2002.
64. Nakanotani, H., Higuchi, T., Furukawa, T., Masui, K., Morimoto, K., Numata, M., Tanaka, H., Sagara, Y., Yasuda, T., Adachi, C., High-efficiency organic light-emitting diodes with fluorescent emitters. *Nature*, 5, 1, 2014.
65. Jung, B.J., Lee, J.I., Chu, H.Y., Do, L.M., Lee, J., Shim, H.K., A new family of bis-DCM based dopants for red OLEDs. *J. Mater. Chem.*, 15, 2470, 2005.
66. Petrova, P. K., Ivanov, P.I., Tomova, R.L., Color tunability in multilayer OLED based on DCM doped in a PVK matrix. *J. Phys. Conf. Ser.*, 558, 012028, 2014.
67. Kido, J., Hayase, H., Hongawa, K., Nagai, K., Okuyama, K., Bright red light-emitting organic electroluminescent devices having a europium complex as an emitter. *Appl. Phys. Lett.*, 65, 2124, 1994.
68. Chen, C.H., Tang, C.W., Shi, J., Klubek, K.P., Improved red dopants for organic electroluminescent devices. *Macromol. Symp.*, 125, 49, 1998.
69. Friend, R.H., Gymer, R.W., Holmes, A.B., Burroughes, J.H., Marks, R.N., Taliani, C., Bradley, D.D.C., Dos Santos, D.A., Bredas, J.L., Loegdlund, M., Salaneck, W.R., Electroluminescence in conjugated polymers. *Nature*, 397, 121, 1999.
70. Mitschke, U., Bäuerle, P.J., The electroluminescence of organic materials. *Mater. Chem.*, 10, 1471, 2000.
71. Shirota, Y., Organic materials for electronic and optoelectronic devices. *J. Mater. Chem.*, 10, 1, 2000.
72. Gustaffson, G., Cao, Y., Treacy, G.M., Klavetter, F., Colaneri, N., Heeger, A.J., Flexible light-emitting diodes made from soluble conducting polymers. *Nature*, 357, 477, 1992.
73. Pope, M., Kallmann, H.P., Magnante, P., Electroluminescence in organic crystals. *J. Chem. Phys.*, 38, 2042, 1963.
74. Cho, H.Y., Park, E.J., Kim, J.H., Park, L.S., Effect of hole injection layer/hole transport layer polymer and device structure on the properties of white OLED. *J. Nanosci. Nanotechnol.*, 10, 4916, 2008.
75. Lee, H., Hwang, Y., Won, T., Effect of inserting a hole injection layer in organic light-emitting diodes: a numerical approach. *J. Korean Phys. Soc.*, 66, 100, 2015.

76. Thelakkat, I., Schmidt, H.W., Low molecular weight and polymeric heterocyclics as electron transport/hole-blocking materials in organic light-emitting diodes. *Polym. Adv. Technol.*, 9, 429, 1998.
77. Zheng, D., Gao, Z., He, X., Zhang, F., Liu, L., Surface and interface analysis for copper phthalocyanine (CuPc) and indium-tin-oxide (ITO) using X-ray photoelectron spectroscopy (XPS). *Appl. Surf. Sci.*, 211, 24, 2003.
78. Gao, Z.Q., Luo, M., Sun, X.H., Tam, H.L., Wong, M.S., Mi, B.X., Xia, P.F., Cheah, K.W., Chen, C.H., New host containing bipolar carrier transport moiety for high-efficiency electrophosphorescence at low voltages. *Adv. Mater.*, 21, 688, 2009.
79. Strohrigl, P., Grazulevicius, J.V., Charge-transporting molecular glasses. *Adv. Mater.*, 14, 1439, 2002.
80. Lee, D.H., Liu, Y.P., Lee, K.H., Chae, H., Cho, S.M., Effect of hole transporting materials in phosphorescent white polymer light-emitting diodes. *Org. Electron.*, 11, 427, 2010.
81. Goushi, K., Kwong, R., Brown, J.J., Sasabe, H., Adachi, C., Triplet exciton confinement and unconfinement by adjacent hole-transport layers. *J. Appl. Phys.*, 95, 7798, 2004.
82. Su, S.J., Gonnori, E., Sasabe, H., Kido, J., Highly efficient organic blue-and white-light-emitting devices having a carrier- and exciton-confining structure for reduced efficiency roll-off. *Adv. Mater.*, 20, 4189, 2008.
83. Kim, S.H., Jang, J., Yook, K.S., Lee, J.Y., Gong, M.S., Ryu, S., Chang, G.K., Chang, H.J., Triplet host engineering for triplet exciton management in phosphorescent organic light-emitting diodes. *J. Appl. Phys.*, 103, 054502, 2008.
84. Kim, S.H., Jang, J., Lee, J.Y., Relationship between host energy levels and device performances of phosphorescent organic light-emitting diodes with triplet mixed host emitting structure. *Appl. Phys. Lett.*, 91, 083511, 2007.
85. Kim, E., Jung, S., Effects of polymeric hole transporting layer on the stability of organic light emitting device. *J. Korean Phys. Soc.*, 45, 1361, 2004.
86. Li, Y.Q., Fung, M.K., Xie, Z., Lee, S.T., Hung, L.S., Shi, J., An efficient pure blue organic light-emitting device with low driving voltages. *Adv. Mater.*, 14, 1317, 2002.
87. Adamovich, V.I., Cordero, S.R., Djurovich, P.I., Tamayo, A., Thompson, M.E., D'Andrade, B.W., Forrest, S.R., New charge-carrier blocking materials for high efficiency OLEDs. *Org. Electron.*, 4, 77, 2003.
88. Wu, M.H., Lee, J.H., Leung, M.K., Liao, C.C., Chang, Y., Low-power-consumption and long-lifetime OLED with a high Tg n-type organic transport material. *Proc. SPIE-Int. Soc. Opt. Eng.*, 5519, 263, 2004.
89. Kido, J., Hongawa, K., Okuyama, K., Nagai, K., White light-emitting organic electroluminescent devices using the poly(N-vinylcarbazole) emitter layer doped with three fluorescent dyes. *Appl. Phys. Lett.*, 64, 815, 1994.
90. O'Brien, D.F., Weaver, M.S., Lidzey, D.G., Bradley, D.D.C., Use of poly(phenyl quinoxaline) as an electron transport material in polymer light-emitting diodes. *Appl. Phys. Lett.*, 69, 881, 1996.

91. Baldo, M.A., Forrest, S.R., Transient analysis of organic electrophosphorescence: I. Transient analysis of triplet energy transfer. *Phys. Rev. B Condens. Matter Mater. Phys.*, 62, 10958, 2000.
92. Kim, J.J., Han, M.K., Noh, Y.Y., Flexible OLEDs and organic electronics. *Semicond. Sci. Technol.*, 26, 1, 2011.
93. Yamashita, K., Mori, T., Mizutani, T., Encapsulation of organic light-emitting diode using thermal chemical-vapour-deposition polymer film. *J. Phys. D Appl. Phys.*, 34, 740, 2001.
94. Melzer, J.E., Moffitt, K., *Head Mounted Displays: Designing for the User*, McGraw-Hill, 1997.
95. Sato, Y., Ichinosewa, S., Kania, H., Mauch, R.H., Gumlich, H.E., (Eds.), *Inorganic and Organic Electroluminescence*. Wissenschaft und Technik Verlag, Berlin, 1996.



# Index

- [n]cyclacenes ([n]CC), 166–181
- Activator, 318–321
- Aggregation-induced emission (AIE), 297, 303–304
- Alkaline earth metal ions, 283–284, 286, 289
- Alkaline metal ions, 283–286, 289
- Andreev reflection, 12
- Anisotropy
- coherent, 228
  - random, 189, 191, 227–230, 242
  - Single ion, 185, 187, 196, 224–225, 230, 232–233, 241
- Anthraquinone, 279, 281–282
- Antibodies, 143, 146, 149, 150, 153
- Antiferromagnetism, 178
- Antiresonance, 47
- Band gap, 318, 320, 327, 332–335
- BINOL, 279, 281–282, 289
- Biocompatibility, 122, 125
- Biomedical applications, 145, 146
- Blood-brain barrier, 150
- Blue-shift, 485–486
- BODIPY, 279, 281–282, 285, 290, 299, 303
- Bond length alternation, 173
- Bond lengths, 170–173
- Bone tumor,
- chemokine, 82, 83
  - metalloproteinase, 82, 83
- osteopontin, 82, 83
- pre-metastatic niche, 83
- Born approximation, 19–20
- Broken symmetry, 202–204
- C=N Isomerization, 281–283, 286, 288, 291, 301
- Calculations,
- ab initio*, 212, 231
  - broken symmetry DFT, 203–206, 208–209, 212, 214, 223–224, 229–230, 241
- CASSCF, 206, 209, 212–219, 221–224, 231–232, 242
- DFT, 193–194, 196, 199, 202–206, 208–212, 214–220, 223–224, 229–230, 236, 241, 242
- MRPT2, 209, 216–221
- Calixarene, 279, 281–282, 285, 287, 295, 297–298
- Cancer gene therapeutics, 156
- Cancer therapy, 146–152
- Carbon nanoforms, 166–168
- Catabolism of tumors, 153
- Chalcogenide QDs,
- CdTe, 409
  - CdZnS, 412
  - ZnS, 402
  - ZnTe, 406
- Chelation-enhanced fluorescence (CHEF), 288–289

- Chemotherapy, 141, 146–148, 154, 155, 158  
 CIE diagram, 257  
 Clean limit, 20  
 Coactivator, 332–335  
 Cobalt ferrite, 144, 145  
 Coercive field, 192, 240  
 Coherently diffracting domain (particle) size, 400, 407–408, 412  
 Color rendering index, 255, 259  
 Color temperature, 253, 257  
 Component control, 121  
 Conductance, 27  
 Configuration, 262  
 Core-shell structure, 119, 121  
 Core-Shell ZnS, 406  
 Correlated sperimagnet, 229, 233  
 Correlated speromagnet, 227–228  
 Coumarine, 279, 281–282, 299, 304, 306  
 Critical size, 126  
 Critical temperature, 5, 7, 11, 14, 15, 30, 31, 34, 35  
 Crystal field, 225  
 Curie temperature, 131  
 Density functional theory (DFT), 168, 169, 198, 201–202, 204, 206, 208, 210–212, 215–217, 221, 287, 290  
 Dieke diagram, 335, 337  
 Dirty limit, 21  
 Display, 473, 475, 481, 505  
 Dopant, 121  
 Dopants, 265  
 Drug delivery, 132, 148, 149  
 Drug release, 132  
 Drug targeting,  
     active, 150, 151  
     passive, 150, 151  
 Dynamic Burstein–Moss shift (BMS), 361, 364  
 Electron donating group (EDG), 485  
 Electron withdrawing group (EWG), 485  
 Electronic energy transfer (EET), 281–282  
 Emission spectrum, 259  
 Energy level, 265  
 Energy transfer, 326  
 Exchange Hamiltonian, Heisenberg, 200–201, 203, 205–208, 213, 217, 225, 227, 229  
 Ising, 202–204, 206–209, 216, 223, 225–226, 229, 232–233  
 Exchange internations, antiferromagnetic, 193, 222, 226–227  
 ferromagnetic, 194, 200, 226–228, 239  
 nearest-neighbor, 202, 216–217, 219, 225–226, 241  
 next-nearest-neighbor, 207, 214–216, 220, 225  
 Excimer, 281, 297, 300, 303  
 Excitation spectrum, 260  
 Excited-state intramolecular charge transfer (ESICT), 304  
 Excited-state intramolecular proton transfer (ESIPT), 281–282  
 Exciton, 488, 494–495, 502–504  
 Fatty acids, 149  
 Ferrimagnet, 186, 194, 199–200, 202–203, 217, 221, 227–229  
 Ferrimagnetism, 178  
 Ferromagnet, 200, 222, 226–228, 239  
 Ferromagnet with wandering axis, 227  
 Ferromagnetic antiresonance (FMAR)  
     conditions of observation, 63, 64  
     definition, 48  
     frequency, 48, 67  
     giant, 72  
     orientation of magnetic field, 74–76

- Ferromagnetic resonance  
(FMR) frequency  
frequency, 67  
orientation of magnetic field, 74–76
- Ferromagnetism, 126, 129
- Fluorescence resonance energy  
transfer (FRET),  
281–282, 299, 303
- Fourier Transform Infrared  
Spectroscopy, 358
- Gap, 6–9
- Garnet, 266
- Gradient approximation, 20
- Heterogeneity, 75, 76
- Highest occupied molecular  
orbital (HOMO),  
170, 177, 178
- Highest occupied molecular  
orbitals (HOMOs),  
485, 494, 498
- Hollow structure, 119, 120
- Host lattice, 318–319, 322, 332
- Host materials, 266
- HRTEM, 405–406, 409, 411–412,  
416–417
- Hydrothermal, 270
- Hyperhomodesmotic reaction, 174
- Hyperthermia, 145, 151–153, 156  
DNA repair, 90  
exosomes, 91, 93, 94  
heat shock proteins, 91–93, 95  
hot-water bath, 88  
local hyperthermia, 86, 87, 92,  
93, 97  
lymphocytes, 95  
magnetic induction, 88, 98  
microwaves, 89, 95  
NK cells, 91, 93–95  
perfusion, 87  
regional hyperthermia, 87  
T cells, 82, 85, 91–95  
ultrasound, 89
- vasculature, 91, 93  
whole-body hyperthermia, 87
- Hysteresis, 127
- Internal transition, 265
- Intramolecular charge transfer  
(ICT), 281, 288–289,  
291, 299, 301, 303–304
- Iron-oxide nanoparticles, 142–144,  
146, 148, 149, 158
- Josephson effect, 12–14, 27, 29, 30,  
35, 36
- Junction temperature, 261
- Ligand field, 230–232, 236–238, 240
- Light-emitting diodes, 252
- Logic gate, 289, 298, 303
- Lognormal size distribution, 400
- Lowest unoccupied molecular  
orbitals (LUMOs), 485
- Luminescence, 319–321, 326,  
bioluminescence, 474–475  
cathodoluminescence, 475  
chemiluminescence, 475–476  
crystalloluminescence, 474, 476  
electroluminescence, 474–475,  
477–478, 485, 502–503  
fluorescence, 478–480  
ionoluminescence, 477  
mechanoluminescence, 475, 477  
phosphorescence, 488, 504  
radioluminescence, 475–476  
sonoluminescence, 477  
thermoluminescence, 476
- Luminous efficiency, 261
- Magnetic anisotropy, 202, 205,  
210, 213
- Magnetic behavior, 177
- Magnetic composites,  
antibacterial, 102  
bioactive glass, 89, 96, 97, 99–103  
calcium phosphate, 82, 97

- cytocompatibility, 98
- hydroxyapatite, 82, 98, 99
- ISO, 97, 98
- magnetite, 96, 97, 99–101
- nanoparticles, 82, 89, 96, 97
- polymethyl methacrylate, 96, 97
- Magnetic frustration, 225–227
- Magnetic hyperthermia, 128, 130
- Magnetic nanomaterials, 143–146, 155
- Magnetization, 116, 127
- Magnetofection, 145, 150
- Magneto-optical effects in semiconductors, 370
- Manganese ferrite, 144, 145
- Mean-field, 202, 213
- Mean-field approximation, 20
- Mechanical alloying, 395, 402
- Meissner effect, 5, 38
- Metal chelates, 481–482, 500
- Metal-ligand charge transfer (MLCT), 281–282, 303
- Metastatic bone disease, arthroplasty, 86 intramedullary nailing, 86 open reduction internal fixation, 86 radiotherapy, 86, 89, 96
- Molecular magnet, 186–195, 201, 229, 233, 235, 241–243
- Multidomain, 126, 129
- Nanocomposites, ferrite garnet particles, 61, 62 lanthanum-strontium manganite particles, 62, 63 metallic particles, 60, 61
- Nanoring diameter, 171–174
- Nanotechnology, 143, 146–148, 150, 151, 154, 156–158
- Naphthaldehyde, 279, 281–282, 297
- Nitrides, 268
- Non-covalent interactions, 169, 172
- Non-radiative transitions, 325
- Odd-frequency symmetry, 7, 14, 30, 31
- Opal matrix electron microscopy, 55 obtaining, 54 parameters, 54 X-ray diffraction, 56, 57
- Optical band gap, 499
- Optical materials, 425
- Laser materials, 460–467 Nd-YAG laser crystal/glass, 464–465 Yb-YAG laser crystal, 465–466 (Yb,Tm)- codoped laser glass, 466–467
- Phosphors, 435–455 phosphors for X-ray imaging, 439–440 phosphors for display, 440–447 CRT display, 442–443 plasma display, 443–446 LED display, 446–447 phosphor for lamps, 447–455 normal flourescent lamps, 448–449 compact fluorescent lamps, 449–452 LED lamps, 452–455
- Upconversion luminescence (UCL) Materials, 455–460
- UCL materials for biolabeling, 457–458
- UCL materials for white light generation, 458–460
- Organic light-emitting devices (OLEDs)
- anode, 495
- cathode, 496–497, 500–501
- electron injecting layer (EIL), 497, 500–501
- electron transport layer (ETL), 482, 500

- emitting layer (EML), 502, 506  
 hole blocking layer (HBL), 500  
 hole injecting layer (HIL), 498  
 hole transport layer (HTL),  
     496, 499  
 indium tin oxide (ITO), 493,  
     495–496  
 Orthosilicates, 267  
 Ostwald ripening, 120  
 Oxynitrides, 268  
 Oxysulfides, 267
- Particle synthesis,  
     co-precipitation, 115  
     gas-phase, 115  
     hydrothermal, 115  
     microemulsion, 115  
     sol-gel, 115  
     solvothermal, 115
- PbS quantum dots, 356  
     basic properties, 356  
     magneto-optical properties, 370  
     magneto-photoluminescence, 377  
     photoluminescence limiting, 361  
     photonic doping, 364  
     reflection in magnetic field, 371  
     transmittance in magnetic  
         field, 374
- Permeability, 65–67
- Permittivity, 65
- Persistent phosphors, 341, 348
- $\Phi_0(\phi_0)$  junction, 34
- Phosphor, 317–320  
     aluminate lattice phosphors, 342  
     oxide lattice phosphors, 342  
     phosphate lattice phosphors, 343  
     silicate lattice phosphor, 343  
     sulphide lattice phosphors, 342  
     titanate lattice phosphors, 344  
     vanadates lattice phosphors, 344  
     zirconates lattice phosphor, 344
- Photo-induced electron transfer  
     (PET), 281, 284, 289–290,  
     296–299, 301, 303
- Photoluminescence,  
     fluorescence, 318, 320, 327–328  
     phosphorescence, 318, 320,  
     327–328
- Planar defects/stacking faults, 401,  
     403, 408, 411, 416
- p-n junction, 252
- Polyethylene glycol (PEG), 149
- Porous structure, 119, 120
- Proximity effect, 5, 6, 9–15
- Pyrene, 279, 281–282, 289, 297,  
     299–300, 306
- Quantitative-phase analysis, 400
- Quantum dots (QDs),  
     applications, 393  
     band gap, 388, 390, 418  
     density of states, 389  
     effective mass theory, 390  
     exciton Bohr radius, 386, 391  
     excitons, 389  
     structure, 392
- Quantum efficiency, 260
- Quasiclassical theory, 16–23
- Quinoline, 279, 281–282, 291,  
     298, 301
- R.M.S. strain, 400, 412
- Radiative relaxation, 488, 504
- Radiative transitions, 329
- Random  
     anisotropy, 189, 191, 227,  
     229–230, 242  
     exchange, 226, 229  
     frustration, 225–227
- Rare-earth, 335, 337, 341,  
     342, 344
- Red-shift, 485–486
- Reflection coefficient,  
     formula, 67  
     magnetic field dependence,  
         70, 71  
     relative change, 58
- Resonator, 60

- Restricted Kohn-Sham (RKS), 170, 173, 176–178  
 Rhodamine, 279, 281–282, 286, 291, 293, 296, 299–301, 304  
 Rietveld method, 398  
 Scaling, 189, 191  
 Seed-mediated growth, 117, 118  
 Sensitizer, 322, 326, 339  
 Shape control, 118  
 Single domain, 126, 129  
 Single-occupied molecular orbital (SOMO), 178  
 Singlet, 474, 502–505  
 Singlet-triplet splitting, 176, 180  
 Single-walled carbon nanotube (SWCNT), 166–181  
 Size control, 117  
 Sol-gel, 270  
 Specific absorption rate, 129, 130  
 Specific loss power, 129, 130  
 Sperimagnet, 228  
 Speromagnet, 228  
 Spin Hall effect, 28–29  
 Spin valve, 186–187, 235–236, 239–240  
 Spin-glass, 191, 226–229  
 Spin-mixing, 11  
 Spin-orbit, 224, 230, 237  
 Spin-orbit coupling, 479, 488, 494  
 Spin-polarized Kohn-Sham (BS-KS), 170, 173, 176–178  
 Spin-polarized supercurrents, 5, 29, 38  
 Spin-polarized transport, 186, 203, 208, 233–234, 237–238, 240, 242  
 Spin-states, 169, 170  
 Spintronics, 233–234, 236–237  
 Spin-valve, 15, 30–32  
 Sputter deposition, 25  
 SQUID, 27–28  
 Stoke shift, 329  
 Stokes shift, 282, 293  
 Strain energy, 169, 174–176  
 Structure development, 119, 120  
 Sulfides, 267  
 Superexchange,  
     correlation exchange, 201–202, 212  
     kinetic exchange, 201–202, 218  
     pathways, 197, 217, 221–223  
     potential exchange, 201, 218–219, 221, 224, 242  
     spin polarization exchange, 188, 201–202, 211, 214, 218, 220, 233–234, 240  
 Superparamagnetism, 126, 129  
 Surface coating, 122  
 Susceptibility, 67  
 Tamm-Dancoff approximation, 178–180  
 Theranostic nanomedicine, 154  
 Theranostics, 142, 143, 145, 146, 154  
 Thermoelectric effects, 32–38  
 Time-Dependent DFT (TD-DFT), 170–171, 178–180  
 Tissue engineering, 145  
 Transition metal ions, 282–283, 287, 289–290  
 Transmission coefficient,  
     formula, 68  
     magnetic field dependence, 70, 71  
     relative change, 58  
 Triphenylamine, 279, 281–282, 288, 295  
 Triplet, 494, 502–504  
 Tris(8-hydroxyquinoline) aluminum, 482  
 Twisted intramolecular charge transfer (TICT), 281, 306  
 Two-photon spectroscopy, 359

- Unrestricted Kohn-Sham, 170, 176,  
177, 180  
Usadel equation, 19–21
- Vertical absorption energy, 178–179
- Waveguide, 58
- Wavenumber, 65, 66
- Work function, 494, 496,  
498, 501  
Wurtzite, 392–393, 402, 414
- Zero-field-splitting, 225, 231  
Zinc-blende, 392–393, 402–403,  
413–414  
Zinc-doped ferrites, 144, 145



## **Also of Interest**

### **Check out these published volumes in the Advanced Materials Series**

#### **Advanced Magnetic and Optical Materials**

Edited by Ashutosh Tiwari, Parameswar K. Iyer, Vijay Kumar and Hendrik Swart

Published 2016. ISBN 978-1-119-24191-1

#### **Advanced Surfaces for Stem Cell Research**

Edited by Ashutosh Tiwari, Bora Garipcan and Lokman Uzun

Published 2016. ISBN 978-1-119-24250-5

#### **Advanced Electrode Materials**

Edited by Ashutosh Tiwari, Filiz Kuralay and Lokman Uzun

Published 2016. ISBN 978-1-119-24252-9

#### **Advanced Molecularly Imprinting Materials**

Edited by Ashutosh Tiwari and Lokman Uzun

Published 2016. ISBN 978-1-119-33629-7

#### **Intelligent Nanomaterials (2<sup>nd</sup> edition)**

Edited by Tiwari, Yogendra Kumar Mishra, Hisatoshi Kobayashi and

Anthony P. F. Turner

Published 2016. ISBN 978-1-119-24253-6

#### **Advanced Composite Materials**

Edited by Ashutosh Tiwari, Mohammad Rabia Alenezi and Seong Chan Jun

Published 2016. ISBN 978-1-119-24253-6

#### **Advanced Surface Engineering Materials**

Edited by Ashutosh Tiwari, Rui Wang, and Bingqing Wei

Published 2016. ISBN 978-1-119-24244-4

**Advanced Ceramic Materials**

Edited by Ashutosh Tiwari, Rosario A. Gerhardt and Magdalena Szutkowska  
Published 2016. ISBN 978-1-119-24244-4

**Advanced Engineering Materials and Modeling**

Edited by Ashutosh Tiwari, N. Arul Murugan and Rajeev Ahuja  
Published 2016. ISBN 978-1-119-24246-8

**Advanced 2D Materials**

Ashutosh Tiwari and Mikael Syväjärvi  
Published 2016. ISBN 978-1-119-24249-9

**Advanced Materials Interfaces**

Edited by Ashutosh Tiwari, Hirak K. Patra and Xumei Wang  
Published 2016. ISBN 978-1-119-24245-1

**Advanced Bioelectronics Materials**

Edited by Ashutosh Tiwari, Hirak K. Patra and Anthony P.F. Turner  
Published 2015. ISBN 978-1-118-99830-4

**Graphene****An Introduction to the Fundamentals and Industrial Applications**

By Madhuri Sharon and Maheswar Sharon  
Published 2015. ISBN 978-1-118-84256-0

**Advanced Theranostic Materials**

Edited by Ashutosh Tiwari, Hirak K. Patra and Jeong-Woo Choi  
Published 2015. ISBN: 978-1-118-99829-8

**Advanced Functional Materials**

Edited by Ashutosh Tiwari and Lokman Uzun  
Published 2015. ISBN 978-1-118-99827-4

**Advanced Catalytic Materials**

Edited by Ashutosh Tiwari and Salam Titinchi  
Published 2015. ISBN 978-1-118-99828-1

**Graphene Materials****Fundamentals and Emerging Applications**

Edited by Ashutosh Tiwari and Mikael Syväjärvi  
Published 2015. ISBN 978-1-118-99837-3

**DNA Engineered Noble Metal Nanoparticles  
Fundamentals and State-of-the-art-of Nanobiotechnology**  
By Ignác Capek  
Published 2015. ISBN 978-1-118-07214-1

**Advanced Electrical and Electronics Materials  
Process and Applications**  
By K.M. Gupta and Nishu Gupta  
Published 2015. ISBN: 978-1-118-99835-9

**Advanced Materials for Agriculture, Food and Environmental Safety**  
Edited by Ashutosh Tiwari and Mikael Syväjärvi  
Published 2014. ISBN: 978-1-118-77343-7

**Advanced Biomaterials and Biodevices**  
Edited by Ashutosh Tiwari and Anis N. Nordin  
Published 2014. ISBN 978-1-118-77363-5

**Biosensors Nanotechnology**  
Edited by Ashutosh Tiwari and Anthony P. F. Turner  
Published 2014. ISBN 978-1-118-77351-2

**Advanced Sensor and Detection Materials**  
Edited by Ashutosh Tiwari and Mustafa M. Demir  
Published 2014. ISBN 978-1-118-77348-2

**Advanced Healthcare Materials**  
Edited by Ashutosh Tiwari  
Published 2014. ISBN 978-1-118-77359-8

**Advanced Energy Materials**  
Edited by Ashutosh Tiwari and Sergiy Valyukh  
Published 2014. ISBN 978-1-118-68629-4

**Advanced Carbon Materials and Technology**  
Edited by Ashutosh Tiwari and S.K. Shukla  
Published 2014. ISBN 978-1-118-68623-2

**Responsive Materials and Methods**

**State-of-the-Art Stimuli-Responsive Materials and Their Applications**

Edited by Ashutosh Tiwari and Hisatoshi Kobayashi

Published 2013. ISBN 978-1-118-68622-5

**Other Scrivener books edited by Ashutosh Tiwari**

**Nanomaterials in Drug Delivery, Imaging, and Tissue Engineering**

Edited by Ashutosh Tiwari and Atul Tiwari

Published 2013. ISBN 978-1-118-29032-3

**Biomedical Materials and Diagnostic Devices Devices**

Edited by Ashutosh Tiwari, Murugan Ramalingam, Hisatoshi Kobayashi and Anthony P.F. Turner

Published 2012. ISBN 978-1-118-03014-1

**Intelligent Nanomaterials (first edition)**

**Processes, Properties, and Applications**

Edited by Ashutosh Tiwari Ajay K. Mishra, Hisatoshi Kobayashi and Anthony P.F. Turner

Published 2012. ISBN 978-0-470-93879-9

**Integrated Biomaterials for Biomedical Technology**

Edited by Murugan Ramalingam, Ashutosh Tiwari, Seeram Ramakrishna and Hisatoshi Kobayashi

Published 2012. ISBN 978-1-118-42385-1

## **WILEY END USER LICENSE AGREEMENT**

Go to [www.wiley.com/go/eula](http://www.wiley.com/go/eula) to access Wiley's ebook EULA.